MAGNETOMETRIC TECHNIQUES FOR THE MEASUREMENT OF INITIAL SUSCEPTIBILITY AND FOR NON-CONTACT SENSING OF DISPLACEMENT

by

M.P. Cooke, BSc.

A thesis submitted to the University of Newcastle upon Tyne for the degree of Doctor of Philosophy.

April, 1984.

DECLARATION

Unless otherwise stated, the work described in this Ph.D. thesis is original and was carried out in the Department of Geophysics and Planetary Physics at the University of Newcastle upon Tyne between October 1979 and November 1982. None of the material that is presented has been submitted for any other academic award or qualification.

Michael Peter Cooke.

27. 4. 84.

ACKNOWLEDGEMENTS

I am grateful to the people who have helped me to produce this thesis; I am especially grateful to my wife Diane, Professor K. Runcorn, my supervisor Dr. A. de Sa, Dr. A. Stephenson, Mr. E. Simpson, Mr. H. Bolland, Mrs. D. Taylor, my sponsors the Natural Environment Research Council and my employers Plessey Research (Caswell) Ltd.

ABSTRACT

Magnetometric techniques for the measurement of initial susceptibility and for non-contact sensing of displacement.

M.P. Cooke, April 1984.

Part 1 of the thesis describes a new instrument that simultaneously measures the real magnetic susceptibility X' and the imaginary magnetic susceptibility X". The instrument measures the temperature dependences of X' and X" in rock samples between 16°C and 800°C; natural developments are working down to -200°C and measuring the anisotropy of susceptibility. The instrument's heart is a tuned circuit driven at its natural frequency by a 5MHz crystal oscillator. The tuned circuit's inductance is a sample coil that encloses a furnace. The random noise level in the signal for X' is 7.4×10^{-13} m^3 r.m.s., the noise level in the signal for X" is 2×10^{-12} m^3 r.m.s. Sample volumes are 0.1 cm^3 or less.

Equations describing the instrument are derived and verified, particular attention is paid to the sample coil. Circuit diagrams are included. Some results are presented and equations that broadly describe the observed temperature dependences of X' and X" are developed. Some methods for substantially improving the instrument's performance are outlined.

Part 2 of the thesis describes a new method for non-contact sensing of displacement. A magnet is mounted on the object whose displacement is to be measured. The magnet's field is sensed and fed to a 6502 microprocessor programmed to display the distance between the magnet and the sensor; intervening barriers with a permeability very close to unity do not affect the readings. The accuracy is better than 2.0% of full scale deflection (FSD) over the useful range of 250 mm and better than 0.1% FSD over a range of 110 mm. The magnet's volume is 400 mm^3 and the moment is 3.1×10^{-7} Wbm. Circuit diagrams are presented and a complete

software listing is included, the design will work with any magnet and magnetometer. There are directions for greatly improving the instrument's performance.

A GLOSSARY OF SYMBOLS

References

Papers from journals are identified in the list of references by superscripted numbers in brackets, for instance[36] refers to a paper on Q multiplication by Harris. When a book is referred to there are two superscripted numbers: the first number identifies the book and the second identifies the page in the book, for example [49,250] points to page 250 in Advanced Electronic Circuits by Tietze and Schenk.

Symbols used in part 1 of the thesis

Greek symbols have been avoided as far as possible for convenience in typing. Unfortunately this means that symbols from the English alphabet are often used more than once. Where a symbol has two definitions, the correct meaning will always be obvious through the context in which the symbol is used.

Symbol	Units	Meaning
a	FV^{x}	A constant in the voltage/capacitance relationship for the varicap diode
A		The gain of an amplifier
A	m^2	A cross sectional area
b	m	The length of a sample coil
B	Hz	A bandwidth
B	T	A magnetic flux density
B(s)	V or A	The feedback signal in a feedback system
c	Jm^{-3}	The anisotropy energy of a single domain magnetic grain
C	F	A capacitance
C(s)	V or A	The output of a feedback system
d	m	The diameter of a sample
D	m	The diameter of a sample coil

Symbol	Units	Meaning
D		The gain of a peak rectifier
e_o	Fm^{-1}	The permittivity of free space: 8.854×10^{-12}
e_r		The relative permittivity
E	Vm^{-1}	An electric field strength
E(s)	V or A	The error in a feedback system
f	Hz	A frequency
F		A filling factor
g	CKg^{-1}	The gyromagnetic ratio: 1.759×10^{11}
G	Ω^{-1}	A conductance
G	Ω^{-1}	The transconductance of an amplifier
G(s)		A transfer function
h_{FE}		The forward current gain of a bipolar transistor
H	Am^{-1}	A magnetic field strength
H_A	Am^{-1}	The anisotropy field in a ferromagnetic specimen
H(s)		A transfer function
i	A	An alternativing current
I	A	A direct current
j		The square root of -1
k	JK^{-1}	Boltzmann's constant: 1.381×10^{-23}
K	$Vrad^{-1}$	The gain of a phase detector
K_p	Vm^{-3}	The sensitivity of the new instrument to the real susceptibility
K_Q	Vm^{-3}	The sensitivity of the new instrument to the imaginary susceptibility
K_u	Jm^{-3}	The uniaxial anisotropy constant for single domain grains
K_1	Jm^{-3}	An anisotropy constant
l	m	The length of a sample
L	H	An inductance

Symbol	Units	Meaning
m	Kg	A mass
M		Figure of merit for a sample coil
M	Am^{-1}	Magnetization or moment per unit volume
M_M	Am^2Kg^{-1}	The specific or mass magnetic moment
M_s	Am^{-1}	The saturation magnetization per unit volume
M_T	Am^2	The total, or dipole, moment
n		The number of turns on a single layer wire coil
n	$V/\sqrt{Hz}$	A spot noise voltage generator
N		A noise factor
N		The demagnetizing factor of a magnetic grain
p		A damping factor for a group of coupled electron spin vectors.
P	$Js^{-1}m^{-3}$	Rate of change of energy per unit volume
q	C	The charge on one electron: 1.602×10^{-19}
r	m	A radius
R	m	A radius
R	Ω	A resistance
R(s)	V or A	A stimulus for a feedback system
s		The Laplace transform variable
s		The length/diameter ratio for a sample coil
S	m	The skin depth
t	s	Time
T	K	An absolute temperature
T_B	K	A blocking temperature
u	V^{-1}	The gain of a varicap diode
U	Hm^{-1}	The Rayliegh hysterysis constant
v	V	An a.c. voltage
V	V	A d.c. voltage

Symbol	Units	Meaning
V	m^3	A volume
V_c	m^3	The volume of a coil
V_s	m^3	The volume of a sample
w	rad s^{-1}	An angular frequency
W	J	Energy
X		A volume susceptibility
X_a		The apparent volume susceptibility
X_i		The intrinsic volume susceptibility
X'		The real volume susceptibility
X"		The imaginary volume susceptibility
X_M	m^3Kg^{-1}	The specific, or mass, susceptibility
X_T	m^3	The total susceptibility
z	Ω	An impedance
Z	V^{-1}	The gain of a Q-multiplier
μ	Hm^{-1}	The total permeability
μ_o	Hm^{-1}	The permeability of free space: $4\pi \times 10^{-7}$
μ_r		The relative permeability
ρ	Ωm	A resistivity
σ	$\Omega^{-1}m^{-1}$	A conductivity
τ	s	A magnetic relaxation time for a group of coupled electron spin vectors
τ	s	An electrical time constant
$\emptyset$	rad	A phase difference
$\emptyset$	V	A p-n junction potential

Symbols used in part 2 of the thesis

Symbol	Units	Meaning
a	m	A separation
A	m^2	A cross sectional area

Symbol	Units	Meaning
b		A binary bit
B	T	A magnetic flux density
B_r	T	A remanent induction
e	V	The quantization error
f	Hz	A frequency
f_s	Hz	The sampling frequency
f(x)	m	A displacement estimated as a result of interpolation
G(jw)		A fourier transform
G(z)		A z transform
h	bits	A look up table entry spacing
H	Hm^{-1}	A magnetic field strength
H_c	Hm^{-1}	A coercive force
H(z)		A digital transfer function
i(t)		The Dirac delta function
I(t)		A train of Dirac delta functions
k	VT^{-1}	The sensitivity of a fluxgate magnetometer
l	m	A length
L		The normalisation factor in the bilinear transform
M	Am^{-1}	A magnetization or moment per unit volume
M_T	Am^2	The dipole moment or total moment
N		The number of bits at the output of an analogue to digital converter, or the number of bits at the input of a digital to analogue converter
p(e)		The probability density function of the quantization error
r	m	A separation
s		The Laplace transform variable
t	s	Continuous time

Symbol	Units	Meaning
T	s	A discrete time interval
V	V	A voltage
w	rad s^{-1}	An angular frequency
W	s	The width of a flat topped sampling pulse
x	bits	The output of an analogue to digital converter
x_i	bits	A collocation point in a look up table
z		The z transform variable
u_o	Hm^{-1}	The permeability of free space: 4×10^{-7}
θ	rad	A phase shift or an angle
$\phi(t)$		A clock signal

CORRIGENDA

Page 22, equations (1.43) and (1.44), replace

(1 - jwt) by (1 - jwτ)

Page 27, after equation (1.66), replace $X_i' \gg 1$ by $X_i' \ll 1$

Page 29, equation (2.3), replace $\mu_o\mu_r n^2 Ab$ by $\mu_o\mu_r n^2 A/b$

Page 33, equation (2.19), replace W by ΔW

Page 36, table 5, replace Direction by Direct

Page 43, equation (2.40), replace $w_o L/R_p$ by $R_p/w_o L$

Page 46, equation (2.48), note that $GR_f \gg 1$

Page 47, equation (2.52), note that in practice ΔQ is always

< 1% and is nearly always < 0.1%, thus Q may be regarded

as constant when calculating $d\phi$

Page 58, after equation (3.22), replace $\Delta V_p \ll 0.1V_c$ by $\Delta V_p \leq 0.1V_c$

Page 75, last paragraph, replace 5Hz by 5MHz

Page 125, paragraph 2, replace El-Hanary's by El-Hanany's

CONTENTS

PART 1

A NEW RADIO FREQUENCY INSTRUMENT FOR THE MEASUREMENT OF INITIAL MAGNETIC SUSCEPTIBILITY.

CHAPTER 1

SOME OF THE PHYSICS OF SUCEPTIBILITY AT RADIO FREQUENCIES

1.1 INTRODUCTION

The first part of this thesis is about a new instrument that measures the temperature dependence of susceptibility at an operating frequency of 5 MHz. This chapter describes enough of the background physics to allow the experimental results produced later to be correctly interpreted. It will be seen that the measured susceptibility is affected by the sample's temperature, conductivity, shape, size and structure; the instrument's operating frequency is important too.

For convenience and brevity, the term ferromagnetic is meant to encompass ferrimagnetic, antiferromagnetic and parasitic-antiferromagnetic materials as well; but distinctions will be made where necessary. To give some examples: iron is ferromagnetic, magnetite (Fe_3O_4) is ferrimagnetic and haematite (α-Fe_2O_3) is parasitic-antiferromagnetic. It is assumed that the reader is familiar with the origins of ferromagnetism and its relatives, if not, any of references (1),(2), (3), (4) and (10) may be turned to for guidance. Unfortunately, these references create some confusion by using three different systems of magnetic units. The first job is therefore to define the system of magnetic units used in this thesis and to show how conversions to the other systems may be made.

1.2 THE DEFINITIONS AND THE UNITS OF MAGNETIC FLUX, MAGNETIC FIELD, SUSCEPTIBILITY AND PERMEABILITY

The modern system of Sommerfeld S.I. magnetic units is used throughout this thesis. Table 1 may be very useful to those who wish to make conversions from Sommerfeld S.I. to other systems, the table is based on one originally produced by Dr. A. Stephenson.

The magnetic flux density $\underline{B}$ is a vector associated with electric currents. A current carrying wire that is intercepted by lines of

Table 1. Magnetic units, definitions and conversions.
$\mu_o = 4\pi \times 10^{-7}$ Hm^{-1}

MAGNETIC PARAMETER	DEFINITIONS		
	The system adopted	Other common systems	
	MKS (Sommerfeld)	MKS (Kennelly)	E.M.U.
Total flux in a magnetizable medium	$\underline{B} = \mu_o (\underline{H} + \underline{M})$	$\underline{B} = \mu_o \underline{H} + \underline{I}$	$\underline{B} = \mu_o \underline{H} + 4\pi \underline{J}$
Volume susceptibility	$X = \underline{M} / \underline{H}$	$X = \underline{I} / \mu_o \underline{H}$	$X = \underline{J} / \underline{H}$
	UNITS AND FACTORS TO CONVERT FROM SOMMERFELD		
Flux density, $\underline{B}$	$T(NA^{-1}m^{-1})$	Wbm^{-2}	$10^4 G$
Field strength, $\underline{H}$	Am^{-1}	Am^{-2}	$4\pi \times 10^{-3}$ Oe
Magnetization (moment p.u. volume), $\underline{M}$	Am^{-1}	μ_o Wbm^{-2}	$10^{-3} G$
Total (dipole) moment, $\underline{M}_T$	Am^2	μ_o Wbm	$10^3 Gcm^3$
Specific (mass) moment, $\underline{M}_M$	Am^2Kg^{-1}	$\mu_o WbmKg^{-1}$	Gcm^3g^{-1}
Volume susceptibility, X	———	———	$1/4\pi$ GOe^{-1}
Total susceptibility, X_T	m^3	m^3	$10^6/4\pi Gcm^3Oe^{-1}$
Specific (mass) susceptibility, X	m^3Kg^{-1}	m^3Kg^{-1}	$10^3/4\pi Gcm^3g^{-1}Oe^{-1}$

magnetic flux will experience a deflecting force. If the flux is everywhere normal to the wire, then one unit of $\underline{B}$ is that flux density which exerts a force of one newton on one metre of wire carrying one amp of current. The units of $\underline{B}$ that follow from this are $NA^{-1}m^{-1}$ which are commonly known as tesla, T.

The flux density exists in a medium through which it will produce a magnetic field strength $\underline{H}$. If the medium contains no magnetizable particles - for instance a vacuum, or a very weakly magnetic gas - the relation between the field $\underline{H}$ and the flux density $\underline{B}$ is

$$\underline{B} = \mu_o \underline{H} \ , \qquad (1.1)$$

where μ_o is known as the permeability of free space. The magnetic field at the centre of a plane, single turn coil in a vacuum is

$$H = \frac{i}{2r} = \frac{B}{\mu_o} \ , \qquad (1.2)$$

in which r is the radius of the coil and i is the current in it. One unit of $\underline{H}$ is the field at the centre of a plane coil one metre in diameter carrying a current of 1 amp. The units of H are clearly Am^{-1} and those of μ_o are NA^{-2} or Hm^{-1}. The value of μ_o is $4\pi \times 10^{-7}$ Hm^{-1}.

Where $\underline{B}$ exists in a magnetizable medium equation 1.1 has to be modified, for the medium's own elemental magnetic dipoles will become partially aligned and add to the applied flux. The additional component is the magnetization $\underline{M}$ per unit volume. The total flux density is

$$\underline{B}_T = \underline{B}_A + \mu_o \underline{M} = \mu_o(\underline{H} + \underline{M}) \ , \qquad (1.3)$$

where $\underline{B}_A$ is the applied flux density. The units of $\underline{M}$ are Am^{-1}, the same as $\underline{H}$. Equation 1.3 assumes that the magnetized material is both isotropic and infinite in extent.

The magnetization in a medium is related to the inducing field by the medium's susceptibility X such that

$$X = \frac{\underline{M}}{\underline{H}} \quad . \qquad (1.4)$$

X is dimensionless and is known as the volume susceptibility; in words, it is the ratio of the induced magnetization to the inducing flux density that would exist were the magnetized material replaced by a vacuum.

The magnetic permeability μ and the relative magnetic permeability μ_r are closely related to X. By definition the total flux in a magnetized medium can also be written

$$\underline{B} = \mu \underline{H} = \mu_r \mu_o \underline{H} \, . \qquad (1.5)$$

Recalling equation 1.3 it is apparent that

$$\mu_r \underline{H} = \underline{H} + \underline{M}$$

and $\underline{H}$ can be removed using 1.4 to give

$$\mu_r = 1 + X \, . \qquad (1.6)$$

Both μ and μ_r are dimensionless.

Although X is dimensionless it is sometimes not a convenient quantity to use: the total susceptibility X_T and the specific, or mass, susceptibility X_M are more often met with. The first relationship is

$$X_T = XV \, , \qquad (1.7)$$

where V is the volume of material so that X_T has the units m^3. The second relationship is

$$X_M = X \frac{V}{m} \, , \qquad 1.8$$

where m is the mass of material so the units of X_M are $m^3 Kg^{-1}$.

1.3 RESTRICTIONS ON THE SAMPLE'S STRUCTURE

The operating frequency of 5MHz will be seen to have advantages, but it does limit the type of sample that can be measured. The purpose of this section is to show what the limits on the sample's structure are.

The susceptibility of a material is most commonly found by noting its response to an alternating magnetic flux. It is important that the changes in the flux due to the sample's susceptibility are clearly separable from all other sources of change. Unfortunately, at the 5 MHz operating frequency the sample's conductivity makes an unwelcome appearance through the skin effect and eddy current losses.

The skin depth[1,236] of an electrically conducting body is

$$S = \left[\frac{2\rho}{w\mu}\right]^{0.5} = \left[\frac{2\rho}{w\mu_o\ (1 + X)}\right]^{0.5}, \qquad (1.9)$$

where ρ is the resistivity of the body and w is the angular frequency of the incident electromagnetic radiation. In this application it has to be ensured that S is much greater than the dimensions of the specimen being analysed, for this ensures that the flux penetration is uniform throughout. As an illustration, let's calculate the skin depth of a natural sample of pyrrhotite at 5 MHz. The susceptibility of pyrrhotite can be as high as 0.1 whilst its conductivity can be as low as $10^{-5}\Omega$ m. In the worst case S is 7×10^{-4}m and so the sample's dimensions should be $< 2 \times 10^{-4}$m.

The eddy currents induced in the sample continually dissipate heat and constitute a power loss P. Eddy current losses are discussed more fully later in this chapter, for now it is enough to note that the losses grow dramatically as the particle size or the measurement frequency is increased.

The problems of flux penetration and power loss can be conveniently side stepped by finely dividing a sample and then separating the resulting grains. The power loss is automatically reduced because r is much smaller and the requirement that S>> r is much more likely to be satisfied. This new instrument is specifically designed to measure the susceptibility of samples in which the ferromagnetic content consists

of grains well dispersed in a non-conducting, non-magnetic matrix. Rocks are nearly always in just this form - the pyrrhotite ore mentioned earlier could easily be ground and dispersed in a neutral medium such as lithium flouride or aluminium oxide.

This half of the thesis has a geophysical flavour because rock samples have been readily available to test the instrument with, and because rock magnetism is an important and well documented area of application. It must be stressed that the new technique is not limited to rocks. The instrument will work equally well on any natural or synthetic sample having the required structure.

1.4 THE INITIAL SUSCEPTIBILITY OF AN ARRAY OF FERROMAGNETIC GRAINS AT AUDIO FREQUENCIES

As the title suggests, this section deals with the suceptibility that is measured by applying a flux alternating at less than $\sim 6 \times 10^4$ rads s^{-1}. The foundations are laid here for the next section on susceptibility at radio frequencies where the issues are much more complicated. Rock samples are used as a model for discussion. Rocks usually contain between 1% and 5% by weight of ferrimagnetic or antiferromagnetic mineral grains well dispersed in a paramagnetic or diamagnetic matrix. In a typical case, the particles range from 0.1 μm to 10 μm in size; an extreme range is about 100Å to 1 mm. It is considered that these particles do not interact magnetically. Most rocks and minerals are semiconductors so their resistivity decreases with increasing temperature. The most important minerals are oxides and sulphides of iron and titanium and they may well be mixed. Collinson[2] has written a concise review of the compounds that are important to rock magnetism.

The initial susceptibility of a ferromagnetic substance can depend on the magnitude of the applied flux; if the applied flux is less than 1mT the initial magnetic susceptibility is found. Within

this bound the induced magnetization is reversible and the measured susceptibility is independent of the applied flux. For comparison, the scalar value of the earth's magnetic field at Greenwich is currently about 50 μ T.

When a finite body is magnetized by an external field H_e it can be conveniently considered that free magnetic poles are formed at the body's ends. These poles produce a demagnetizing field H_d in opposition to the magnetization, see figure 1. For a regularly shaped body.

$$H_d = NM \ , \tag{1.10}$$

where the demagnetizing factor N depends mainly on the shape of the body. The body's internal field H_i is

$$H_i = H_e - NM \ , \tag{1.11}$$

and so the intrinsic susceptibility X_i is

$$X_i = \frac{M}{H_i} = \frac{M}{(H_e - NM)} \ . \tag{1.12}$$

The experimentally observed susceptibility is

$$X_a = \frac{M}{H_e} = \frac{X_i}{1 + NX_i} \ , \tag{1.13}$$

where equation 1.12 has been used to replace M. Equation 1.13 is important. X_a is called the apparent susceptibility. When X_i is large $X_a \longrightarrow 1/N$, thus X_a is a poor measure of X_i for a strong ferrimagnetic such as magnetite. X_i is observed for a material with a weak susceptibility such as haematite; haematite is parasitic-antiferromagnetic[3,11].

It is now clear that the demagnetizing factor N makes the susceptibility of an array dependent on the shape of the constituent grains. Craik[4,22] tabulates N for ellipsoids of revolution. As an example, an ellipsoid of dimension ratio 1.5:1 has a polar axis demagnetizing factor N_a of 0.233 and an equatorial axis demagnetizing factor N_b of 0.383. A sphere has $N_a = N_b = 0.333$. Along the

Figure 1. The poles created on the surface of a magnetized body.

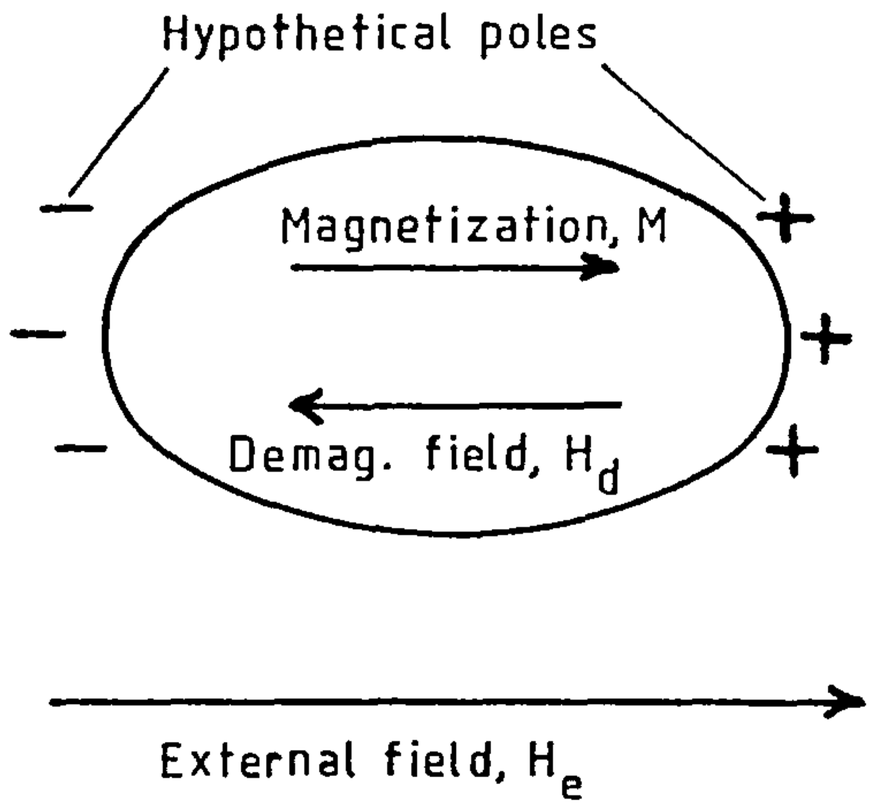

Figure 2. The variation of observed susceptibility with grain size over the range 0.8 μm to 112 μm. Data from Day, Fuller and Schmidt[5].

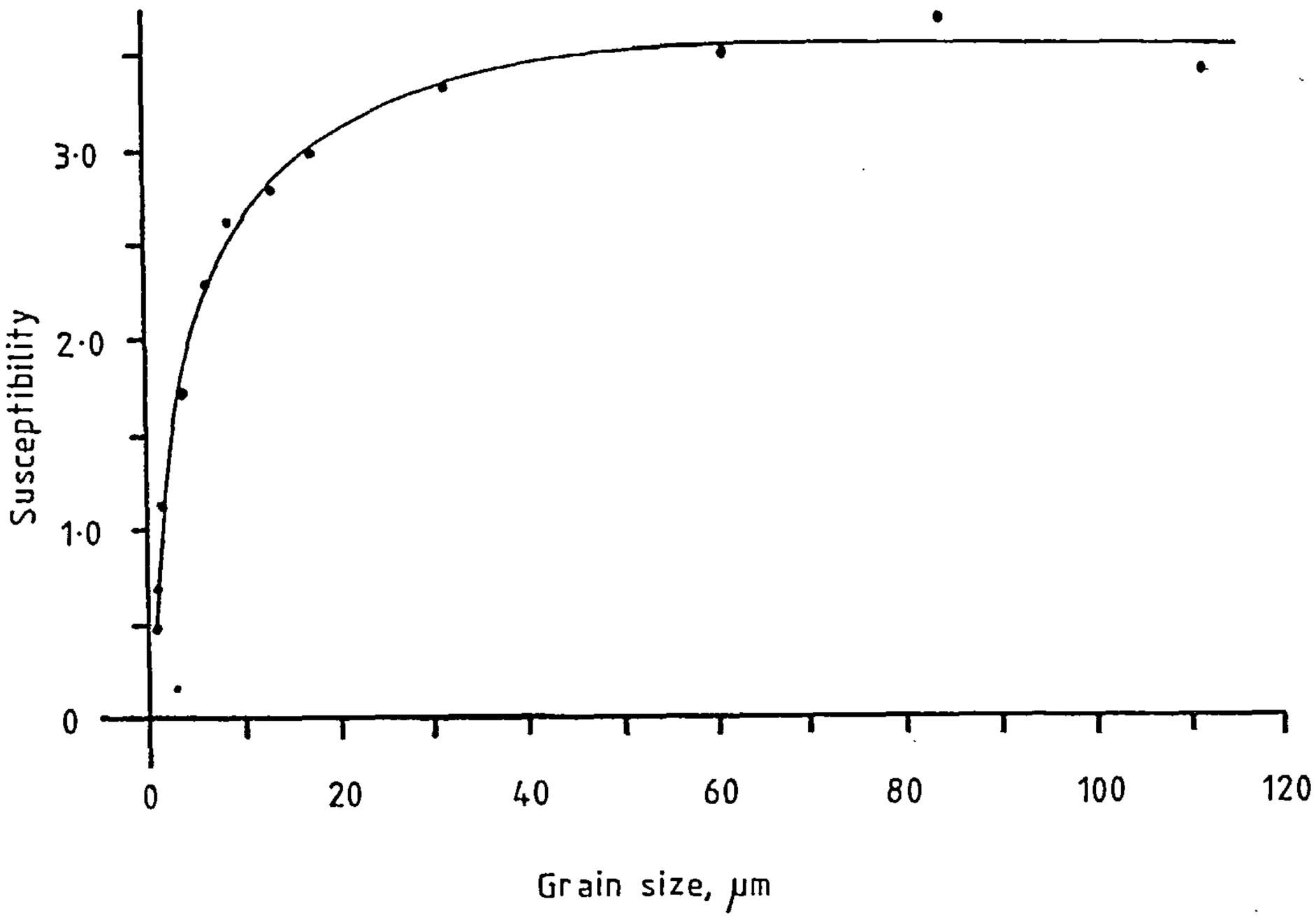

length of a rod, $N \longrightarrow 0$. An ideal rock contains many randomly oriented, non-interacting grains. Therefore, the demagnetizing factor of the rock sample has to be deduced as an appropriate average of an individual particle's demagnetizing factors. Stacey[5,71] has analysed this problem for ellipsoids of revolution having a dimension ratio of 1.5:1 which is a realistic shape in practice. He calculated that the average demagnetizing factor is $\overline{N} = 0.31$.

Having discussed the effect of the grain's shape on susceptibility, it may well be wondered what effect the grain's volume has on susceptibility. Large grains are multidomain; that is, they subdivide themselves into many adjoining magnetic domains to minimise the magnetostatic energy of the notional surface poles[4,164]. The susceptibility X_i is high because magnetization occurs through domain wall motion which is an easy process energetically. X_i varies only slightly with grain size in this region. Small grains that are below a certain critical size[4,164] are single domain where magnetization occurs through domain rotation. Their susceptibility is lower than that of multidomain grains. Very small grains are superparamagnetic[4,146] and can have larger values of apparent susceptibility than multidomain grains[6]. A superparamagnetic grain is one whose direction of magnetization can be spontaneously reversed by ambient thermal agitation. The meanings of large, small and very small depend on the mineral in question, the shape of the grain and the temperature at which susceptibility is measured. Collinson[2] gives more detailed information and references on the subject. Figure 2 illustrates the variation of susceptibility with grain size for a titanomagnetite of composition $0.4Fe_2TiO_4.0.6Fe_3O_4$. The data are taken from Day, Fuller and Schmidt[7] who state that the behaviour changes from single domain to multidomain at about 1 μm.

The initial susceptibility of a particulate array need not be isotropic. For an ellipsoidal particle the demagnetizing factor varies according to which axis the flux is applied along. If the grains are aligned and the intrinsic susceptibility is high, such that $X_a \longrightarrow 1/N$, the susceptibility is obviously anisotropic. Once more, Collinson[2] may be turned to for a proper account.

In summary, the initial magnetic susceptibility of a non-interacting array of particles is an ambiguous quantity. The hidden variables of grain size, grain shape and grain alignment all combine to lower the worth of absolute values of initial susceptibility. However, changes in the value of a sample's initial susceptibility represent a powerful diagnostic tool. Magnetic anisotropy can be turned to advantage because it yields information about the sample's structure - such as the direction of a sedimentary bedding plane. Furthermore, the temperature dependence of a rock's susceptibility can indicate which mineral or minerals are present. The new instrument was developed specifically to monitor the temperature dependence of initial susceptibility between room temperature and $> 700^{o}C$.

1.5 THE INITIAL SUSCEPTIBILITY OF AN ARRAY OF FERROMAGNETIC GRAINS AT RADIO FREQUENCIES

1.5.1 Introduction

The ideas introduced in the last section are valid when the frequency of the inducing field is low, say less than 10KHz. At higher frequencies the susceptibility splits into two components: the real susceptibility X' and the imaginary susceptibility X". X' represents the induced motion of domain walls and the rotation of domain magnetization. X' is in phase with the applied field. X" represents losses in the sample through hysterysis, eddy currents and what are for now termed lattice losses. X" is in quadrature to the applied field. This section concentrates on the mechanisms that contribute to X" and shows which mechanism is most important to an array of ferromagnetic grains when the inducing field is very weak.

One of the problems in writing this section was that there has previously been little geophysical interest in measuring susceptibility at high frequencies, so the theory has been taken piecemeal from a number of different sources and then collated. One of the most useful sources was a text by Smit and Wijn[8] on the properties of ferrites. A ferrite is a member of a group of iron oxides with the general formula $MO.Fe_2O_3$, where M is a divalent metal ion such as Mn^{2+}, Fe^{2+}, Co^{2+}, Ni^{2+}, Cu^{2+}, Zn^{2+}, Mg^{2+} or Cd^{2+}. Many magnetic materials of geophysical interest are ferrites, magnetite ($FeO.Fe_2O_3$) is one example.

A further problem has been a lack of suitable data with which to make illustrative calculations and comparisons. The only ferromagnetic array on which sufficient data were available was compressed carbonyl iron powder[3,498]. It consists of spherical particles of $Fe(CO)_5$ pressed together with an insulating binder. A typical particle diameter range is 3 μm to 20 μm but the calculations suppose that all the particles are 3 μm in diameter. The inital susceptibility of the powder is 19, this shows that the magnetic grains cannot be considered to be non-interacting; if they were the susceptibility would be $1/N = 3$ as N for a sphere is 0.333. However, this factor simply makes the tests stiffer and the ultimate conclusions of this subsection more believable. Some data on carbonyl iron and the experimental values for the applied flux are included in table 2 below.

Table 2 A collection of data on carbonyl iron powder together with experimental values for the applied field. The data on carbonyl iron were found in Chikazumi[3].

Parameter	Value
Particle radius, r	1.5×10^{-6} m
Initial permeability, μ_r	20
Saturation magnetization, $\mu_o M_s$	1.56 T
Coercive field, H_c	1.2×10^3 Am^{-1}
Hysterysis constant, U	0.013 $\mu_o mA^{-1}$
Anisotropy constant for an elongated single domain particle, K_u	4.6×10^5 Jm^{-3}
Intrinsic conductivity, σ	$10^7 \Omega^{-1}$ m^{-1}
Frequency of applied flux, f	5×10^6 Hz
Amplitude of applied flux, B_m	9×10^{-7} T

1.5.2 The Skin Depth

It was mentioned in section 1.3 that the skin depth ought to be greater than the ferromagnetic grain size so that there is an even flux penetration, this is also a necessary condition in the following subsections on X". Because of the importance of the skin depth, it is worth calculating its values in a few examples. The range of examples is restricted by the lack of suitable data, but some results for the conductivity and permeability of a few natural ores were found in Parasnis[9,11]. The skin depths are calculated using equation 1.9, but before they are tabulated mention must be made of an underlying assumption. Equation 1.9 is only true if the ratio of the conductive current to the displacement current in the medium is much greater than one[1,236], that is if

$$\frac{\sigma}{we_o e_r} \gg 1 , \qquad (1.14)$$

where e_o is the permittivity of free space and e_r is the relative permittivity of the medium. Unfortunately, both e_r and σ/ω are frequency dependent, for they decrease as the frequency at which they are

determined increases[8,240]. No values of e_r have been seen for materials of geophysical interest. The largest value of e_r that has been come across is 1.5×10^5 for Mullard Ferroxcube type A at 1KHz. This value has been combined with the examples' conductivities to make a conservative test of condition 1.14. The results for the tests and the skin depths are given in table 3.

Table 3 A conservative test of the ratio of the conductive to displacement current, σ/we_oe_r, and of the skin depth for various solids of geophysical interest. e_r is taken as 1.5×10^5 and $w = 3.14 \times 10^7$ rads^{-1}.

Solid	Conductivity σ, $\Omega^{-1}m^{-1}$	Initial permeability, μ_r	σ/we_oe_r	Skin depth S, m
Pyrrhotite ore	10^3 - 10^5	1.001 - 1.1	1×10^{13}	7×10^{-4} -7×10^{-3}
Pyrite ore	10^{-1} - 10^4	1.0001 - 1.005	1×10^9	2×10^{-3} -7×10^{-1}
Haematite ore	10^{-2} - 10^1	1.00042- 1.01	1×10^8	7×10^{-2} -2.25
Magnetite ore	10^{-1} - 10^2	1.07 - 15	1×10^9	6×10^{-3} -7×10^{-1}
Compressed carbonyl iron powder	1.1×10^7 intrinsic	20	1×10^{17}	1.5×10^{-5}

Two conclusions may be drawn from table 3. The first is that the tests on the ratio σ/we_oe_r show that equation 1.9 for the skin depth is valid. Secondly, if the reasonable assumption is made that the ferromagnetic grains in rock samples have similar properties to the ores mentioned above, then the grain sizes, having a typical range of 0.1 μm to 10 μm, are nearly always very much less than one skin depth at a 5MHz operating frequency.

Table 4, also using data from Parasnis[9,129], shows some room

temperature conductivities typical of the paramagnetic and diamagnetic matrices in which the ferromagnetic grains may be embedded.

Table 4 The electrical conductivities of some rocks and sediments.

Material	Conductivity σ, $\Omega^{-1}m^{-1}$
Marble (limestone)	$< 10^{-12}$
Quartz	$< 10^{-10}$
Rock salt	$10^{-7} - 10^{-6}$
Granite	$10^{-6} - 2 \times 10^{-4}$
Sandstones	$2.5 \times 10^{-4} - 2.9 \times 10^{-2}$
Morain	$2.5 \times 10^{-4} - 1.3 \times 10^{-1}$
Limestones	$2.5 \times 10^{-3} - 8.3 \times 10^{-3}$
Clays	8.3×10^{-3} -1

The conductivities of the matrices are so low that fears about the skin depth in them can be forgotten.

1.5.3 The hysterysis loss

It is well known that the induced magnetization $\underline{M}(t)$ in a ferromagnetic material exhibits hysterysis when responding to an alternating flux $\underline{B}(t)$. The area of the hysterysis loop represents the work done per cycle by the inducing flux in overcoming impediments to domain wall motion - such as lattice dislocations and interstitial impurities. When the applied field is small, as is the case when measuring initial susceptibility, the hysterysis loop is leaf shaped and the energy loss may be calculated. It will be shown that hysterysis leads to the appearance of X" in quadrature to the applied field.

The form of the initial portion of the low field magnetization curve is given by[3,296]

$$M = XH + \frac{1}{2} UH^2 , \qquad (1.15)$$

where X is the initial susceptibility and U is the Rayliegh constant. The first term in 1.15 is the reversible, lossless magnetization

whilst the second term is the irreversible, lossy magnetization. Using 1.15, the leaf like Rayliegh hysterysis loop in figure 3 is described by

$$M + M_m = X(H + H_m) + \frac{1}{2} U(H + H_m)^2 \ , \qquad (1.16)$$

for the ascending branch and

$$M - M_m = X(H - H_m) - \frac{1}{2} U(H - H_m)^2 \qquad (1.17)$$

for the descending branch. Putting $M = M_m$ when $H = H_m$ in 1.16 yields

$$M_m = XH_m + UH_m^2 . \qquad (1.18)$$

The loop can now be reformulated to resemble 1.15 by substituting 1.18 into 1.16 and 1.17. For the ascending branch

$$M_a = (X + UH_m)\, H + \frac{1}{2} U(H^2 - H_m^2) \ , \qquad (1.19)$$

and for the descending branch

$$M_d = (X + UH_m)\, H - \frac{1}{2} U\,(H^2 - H_m^2) \ . \qquad (1.20)$$

The area of the loop is the hysterysis loss per cycle, this is given by

$$W_h = \int_{-H_m}^{+H_m} M_a . dH + \int_{+H_m}^{-H_m} M_d . dH, \qquad (1.21)$$

which gives

$$W_h = \frac{4}{3} U H_m^3 \ . \qquad (1.22)$$

Recalling that

$$H_m = B_m / \mu_o \mu_r \ ,$$

the rate of loss of power per m^3 is given by

$$P_h = \frac{4}{3} Uf(B_m / \mu_o \mu_r)^3 \ , \qquad (1.23)$$

Figure 3. The Rayliegh hysteresis loop for low magnetizations.

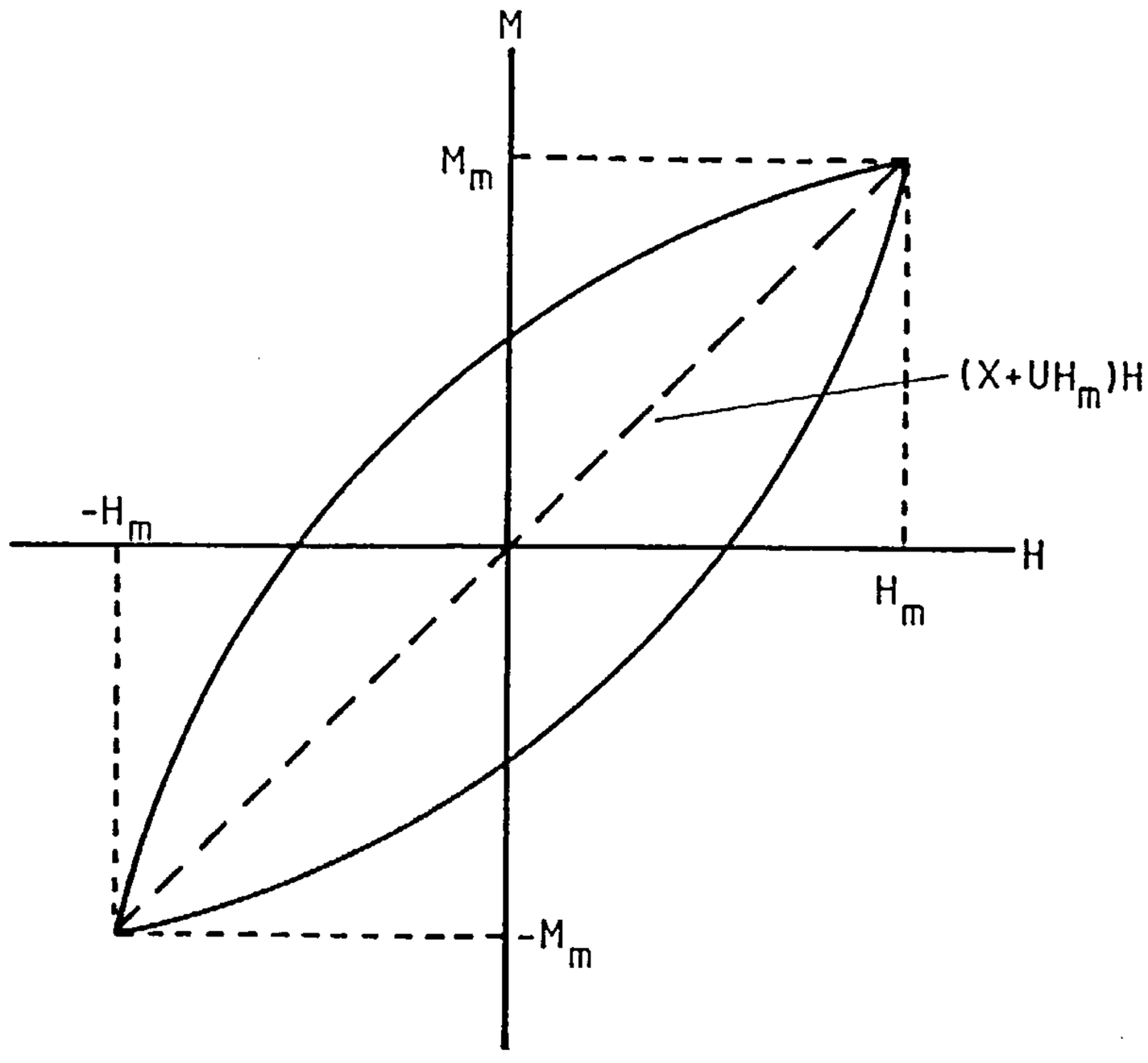

Figure 4. The phase shift and distortion of M(t) due to the Rayliegh loop.

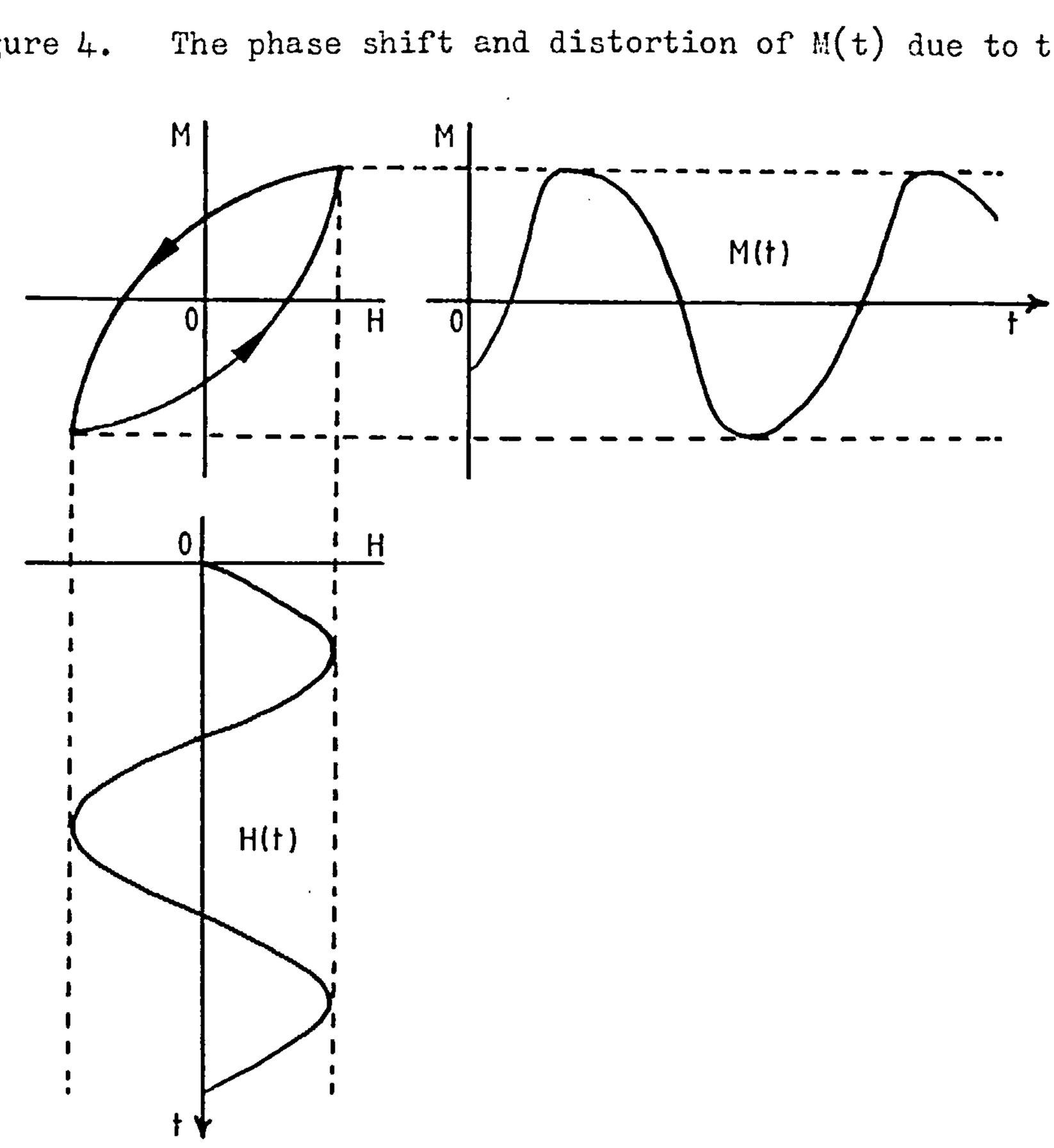

where f is the frequency of the applied flux. Table 2 contains data on carbonyl iron powder and on the flux applied by the new instrument. Fitting these values into 1.23 gives

$$P_h = 5.0 \times 10^{-6} Js^{-1}m^{-3} .$$

This result will later be compared with results for eddy current and lattice losses.

Now let's examine the magnetization M(t) due to an applied field H(t) where

$$H(t) = H_m \cos wt . \qquad (1.24)$$

Equations 1.19 and 1.20 are now

$$M(t) = (X + UH_m)H_m \cos wt \pm \frac{U}{2} H_m^2 \sin^2 wt. \qquad (1.25)$$

Figure 4 gives a pictorial impression of this distortion. The $\pm \sin^2 wt$ term in 1.25 can be expressed as a Fourier series, when this is done equation 1.25 becomes

$$M(t) = (X + U H_m) H_m \cos wt + \frac{U}{2} H_m^2 \left[\frac{8}{3\pi} \sin wt - \frac{8}{15\pi} \sin 3wt - \ldots \right] . \qquad (1.26)$$

Equation 1.26 clearly shows that hysteresis introduces a sin wt component that is in quadrature to the applied flux. This component is part of the imaginary susceptibility X".

1.5.4 The eddy current loss

When the magnetic flux in a conducting medium changes with time, an electromotive force is generated at right angles to the direction in which the flux is changing - so there is a resulting flow of eddy currents within the material. A simple example of this is drawn in figure 5. The eddy currents will continually dissipate energy through ohmic heating; the magnetization M(t) will therefore lag behind the inducing flux B(t). Once again, the energy loss splits the susceptibility into real and imaginary parts. The mathematical steps to arrive

Figure 5. The eddy currents in a homogeneously magnetized cylinder oppose the current that induces them.

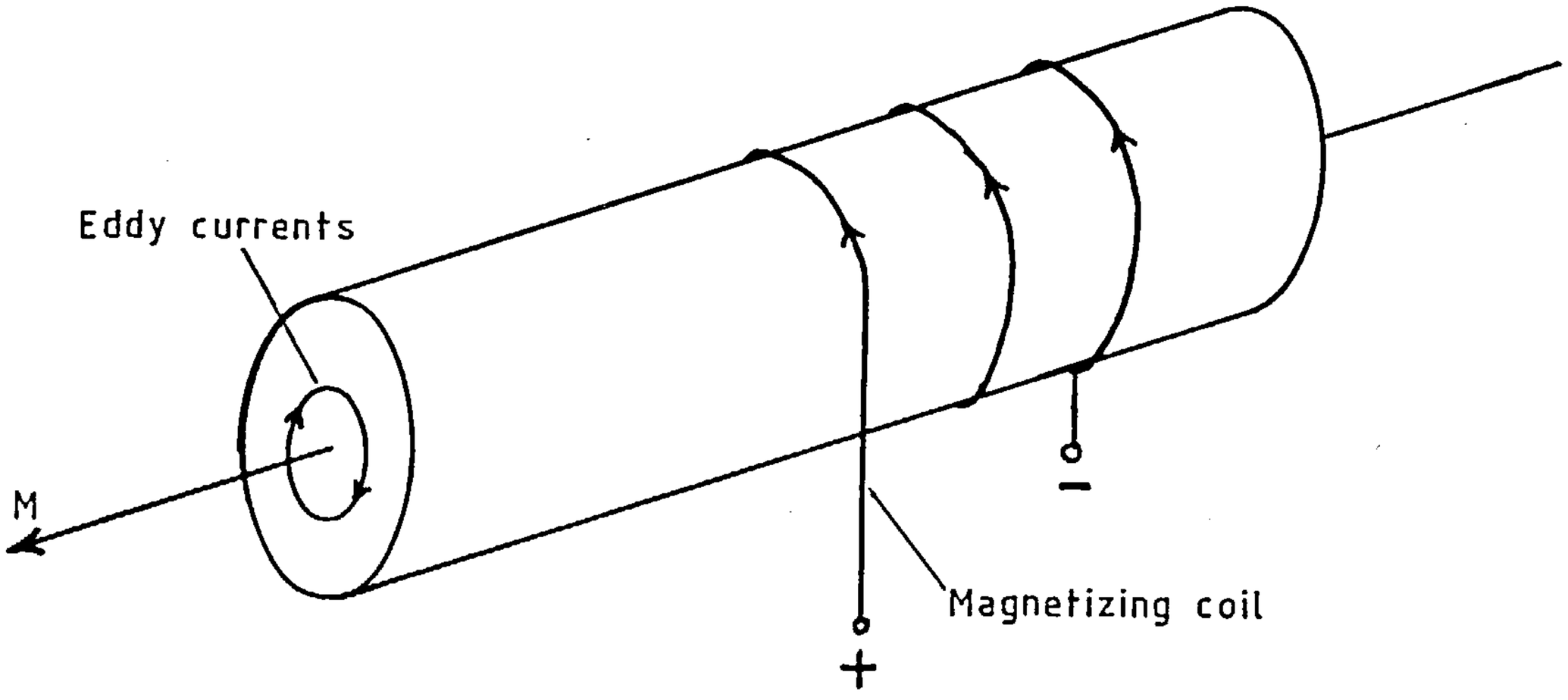

Figure 6. A cylindrical model for calculating eddy current losses when magnetization changes through the motion of a single domain wall.

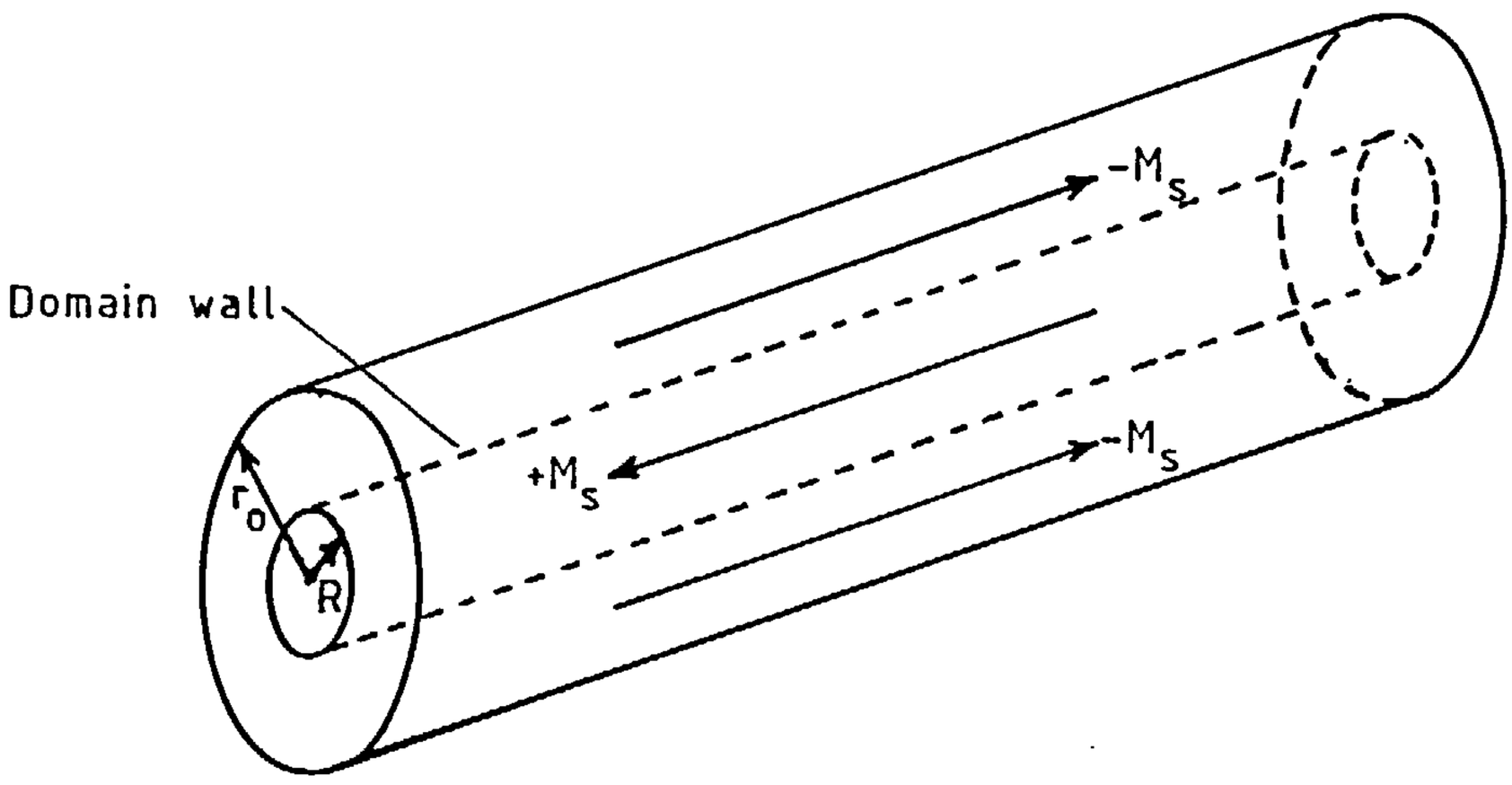

at the power loss in the case of a cylinder are well known[10,174][3,321] and are not repeated as only the result is needed. The model to which the result applies is shown in figure 6. A cylindrical wall of radius R separates two antiparallel domains in a rod of radius r_o. The magnetization of the cylinder as a whole is changing through the expansion of the wall. The instantaneous rate of loss of energy per unit volume is

$$P_e = \frac{\mu_o^2 r_o^2}{2\rho} \left[\frac{dM}{dt}\right]^2 \ln\left[\frac{r_o}{R}\right], \qquad (1.27)$$

where (dM/dt) is the rate of change of magnetization at the cylinder wall and ρ is the resistivity of the cylinder. Equation 1.27 shows that the power loss depends on the size of the wall. If the magnetization is fully reversed, the averaged power loss is

$$\overline{P_e} = \frac{r_o^2 \mu_o^2}{2\rho} \left[\frac{dM}{dt}\right]^2 . \qquad (1.28)$$

Of course, real domain distributions are far more complicated than that considered, so equation 1.28 only gives a rough indication of the losses to be expected.

Equation 1.28 is now going to be used to make a crude estimate of $\overline{P_e}$ in the test case of compressed carbonyl iron powder. The magnetization is forced to change by a driving flux $B_m \cos wt$.

Since $M = XH$ and $B = \mu_o \mu_r H$,

$$M = \frac{XB_m}{\mu_o \mu_r} \cos wt \qquad (1.29)$$

and

$$\left[\frac{dM}{dt}\right]^2 = \frac{B_m^2}{\mu_o^2} \left[\frac{\mu_r - 1}{\mu_r}\right]^2 w^2 \sin^2 wt \qquad (1.30)$$

in which X has been replaced by $(\mu_r - 1)$. Fitting 1.30 into 1.28 gives

$$\overline{P_e} = \frac{r_o^2 w^2 B_m^2}{4\rho} \left[\frac{\mu_r - 1}{\mu_r}\right]^2 \qquad (1.31)$$

since $\sin^2$ wt averages to 0.5. Taking data from table 2,

$$\overline{P_e} = 4.1 \times 10^{-3} Jm^{-3} s^{-1}.$$

The eddy current losses are 800 times larger than the hysterysis losses in this example.

In both this and the hysterysis analyses it has been assumed that M = XH. However, when finding the eddy current losses in the presence of hysterysis the relation ought to have been written as M = (X' - jX")H. The same is true when finding hysterysis losses in the presence of eddy currents: the result is that the two losses are slightly mixed. There is nothing of value to be gained by pursuing this more complex argument.

1.5.5 The lattice loss

Magnetization occurs through domain wall motion and domain rotation. Both mechanisms require the rotation of coupled electron spins, this is on the scale of a domain wall width for domain wall motion and throughout the whole domain for domain rotation. There are two types of losses connected with this rotating electron spin vector, one is due to a relaxation mechanism and the other to a rotation mechanism. Both losses transfer energy from the spin vector to the lattice. The lattice is therefore heated and the driving field loses energy. As before, this can be accounted for by introducing an imaginary susceptibility X". This subsection shows how the lattice losses arise where the magnetization is alternating by domain rotation. An estimate is made of how big these losses are for the example of carbonyl iron grains.

To start with, it is best to introduce the magnetic relaxation time τ. Picture the magnetization vector due to the aligned spins of a cluster of atoms. When the applied flux is changed, the vector

will move to find a new equilibrium position. This position corresponds to the optimum balance between the potential energy due to the applied flux and the direction dependent magnetostatic energy arising from the crystalline field and the demagnetizing field. If the vector is ever to settle into this stable position, rather than just precess about it, there must be a finite damping factor p. This necessity points to a relaxation time τ in that the damping prevents the magnetization instantaneously following the applied flux. The magnetic relaxation time τ is defined as the time that elapses after the application of a flux B before the magnetization differs by less than 1/e from its equilibrium value.

An equation of motion can be written and solved for a spin vector that is free to rotate into parallelism with an applied flux; Anderson[10,18] gives a good account. Such an analysis interrelates the damping factor p, the relaxation time τ and the applied flux B. The results are:

$$\tau = \frac{1 + p^2}{w_o p} \qquad (1.32)$$

where

$$w_o = gB = g\mu_o H; \qquad (1.33)$$

w_o is the natural precession frequency in the absence of damping and g is the charge to mass ratio of an electron ($1.759 \times 10^{11} CKg^{-1}$). In the presence of damping, the spin vector precesses about the applied flux at a frequency

$$w = \frac{1}{p\tau} = \frac{w_o}{1 + p^2} . \qquad (1.34)$$

When $p = 0, \tau \longrightarrow \infty$ and equilibrium is never reached after the applied flux is changed, see figure 7a. When $p >> 1, \tau \longrightarrow p/w_o$ corresponding to motion in a viscous medium with a long settling time - figure 7b. Between these two extremes p = 1 gives critical damping with a minimum settling time $\tau_{min} = 2/w_o$. In general $0 < p \ll 1$ and

Figure 7. The motion of a precessing spin vector in response to an applied field H.

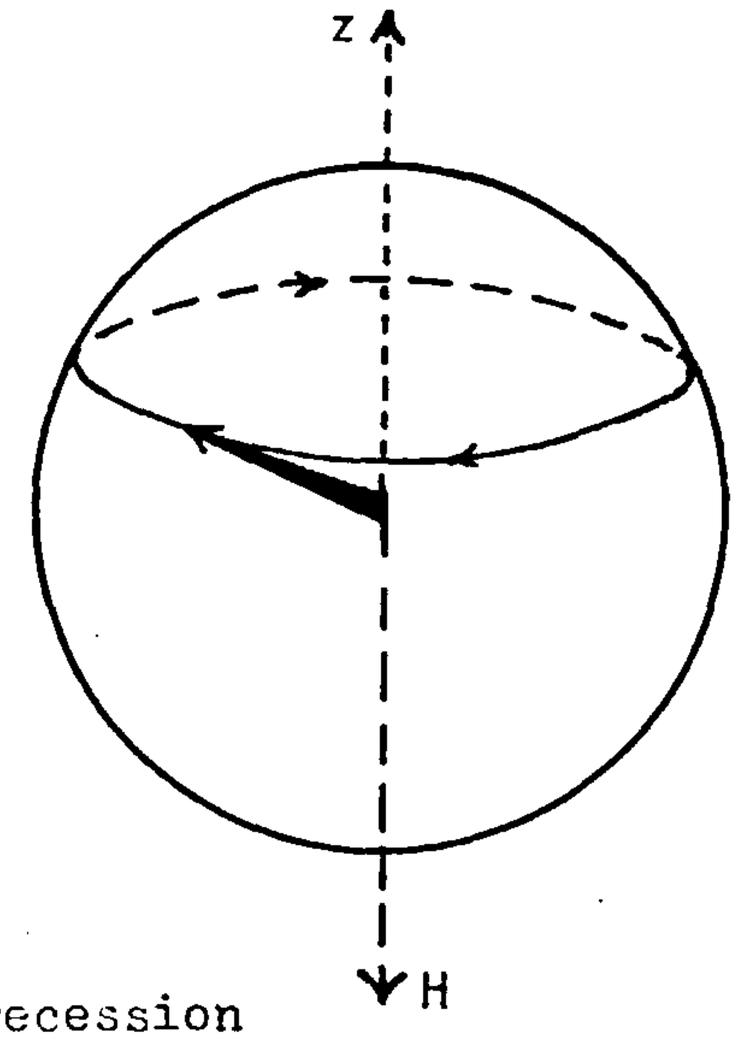

a. p = 0, continuous precession

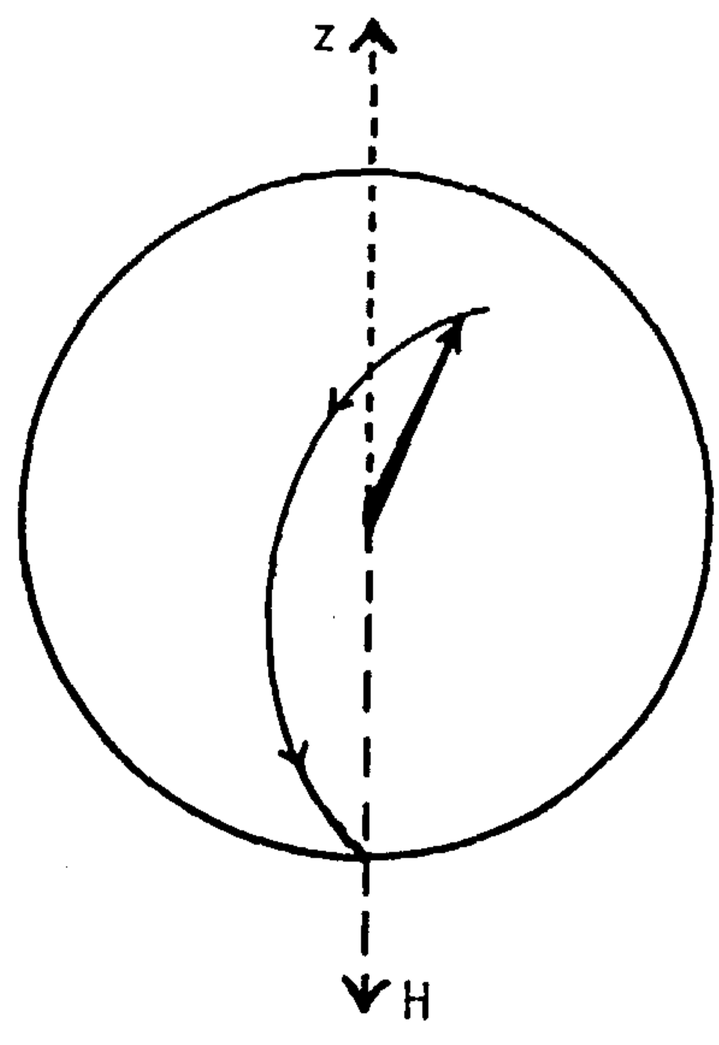

b. p>>1, overdamped

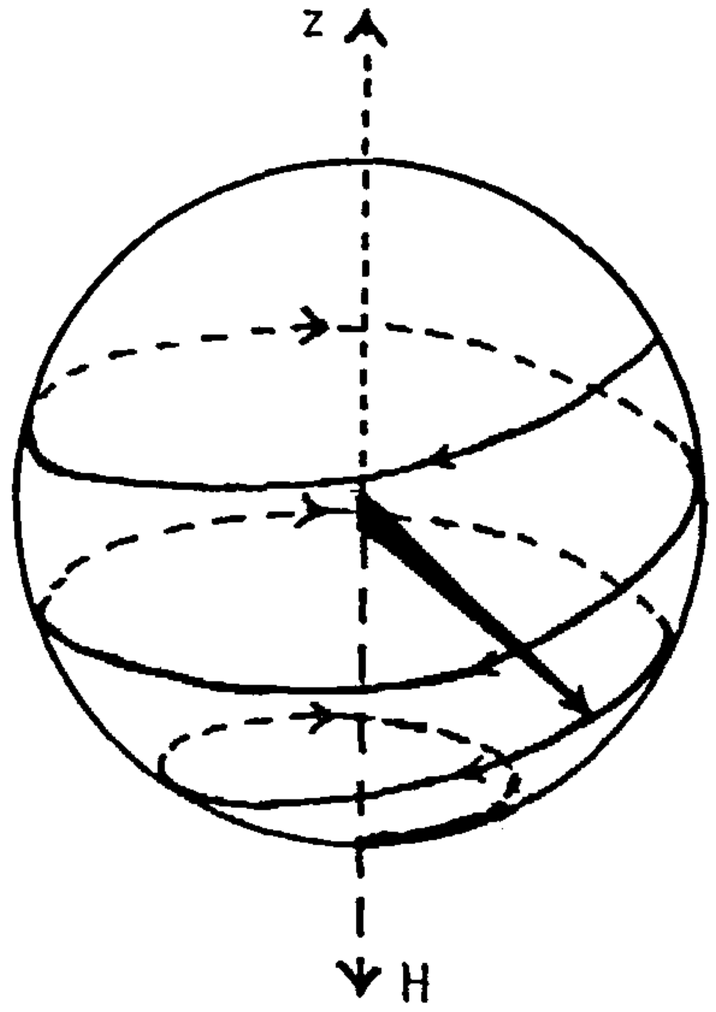

c. p<<1, underdamped

$\tau > \tau_{min}$, figure 7c. These relations are now used to formulate the resonance and relaxation phenomena.

Ferromagnetic and ferrimagnetic resonances are studied in detail by Smit and Wijn[8,268]. They are complex topics with dependances on macroscopic and microscopic crystal structure, the type of magnetization and demagnetizing factors. Fortunately, it is adequate for the present purposes to briefly discuss ferromagnetic resonance alone. The most important point to be made is that w_o in equation 1.33 is not, in this instance, related to the applied flux: instead, it is related to an internal anisotropy field H_A.

If a ferromagnetic specimen is rotated in an applied field, the magnetization tends to remain parallel to an easy direction that is specific to the type of crystal lattice. A crystal anisotropy field $\underline{H}_A$ lying along the easy direction can be postulated to account for this effect, for there is then a torque $\mu_o \underline{H}_A \times \underline{M}$ tending to keep the internal magnetization vector aligned with the easy direction. Let K_1 be a characteristic anisotropy constant for a crystal with cubic crystalline anisotropy[3,138][4,139], and recall that M_s is the saturation magnetization:

$$H_A = \frac{2K_1}{\mu_o M_s} \qquad (1.35)$$

if K_1 is positive and

$$H_A = -\frac{4K_1}{3\mu_o M_s} \qquad (1.36)$$

if K_1 is negative. Equations 1.35 and 1.36 are not valid for magnetization by domain wall motion.

In the presence of H_A, the initial magnetization in a very small driving flux is due to domain rotation about the easy direction. If the driving frequency is equal to the natural precession frequency there is a ferromagnetic resonance. The natural precession is driven

constant amplitude against the effects of damping and the energy to do this is sapped from the driving field. The real susceptibility X' drops rapidly as the driving frequency is increased above the precession frequency. To be more precise, for regions in the material where the applied alternating flux has a component perpendicular to H_A the resonance frequency is predicted to be

$$w_o = \mu_o g H_A \qquad (1.37)$$

using 1.33. In the presence of finite damping, the resonance peak is broadened and the resonant frequency is shifted[10,188] to

$$w_r = \frac{w_o}{(1 + p^2)^{0.5}} \quad . \qquad (1.38)$$

Such behaviour would be expected of any resonant system. Experimentally, w_r is the frequency at which X" peaks and X' falls to half its low frequency value. As $p << 1$ it can be seen that $w_r \approx w_o$, putting 1.36 into 1.37 gives

$$w_r = -\frac{4gK_1}{3M_s} \quad , \qquad (1.39)$$

where K_1 is negative. K_1 can be related to the low frequency rotational susceptibility[3,263] by

$$X = -\frac{\mu_o M_s^2}{2K_1} \qquad (1.40)$$

when K_1 is negative. K_1 can now be eliminated from 1.39 to give

$$w_r = \frac{2}{3}\frac{\mu_o g M_s}{(\mu_r - 1)} \quad , \qquad (1.41)$$

where μ_r is the low frequency relative permeability. Exactly the same result would be derived were $K_1 > 0$.

The resonance frequency w_r can be predicted quite successfully using 1.41. Figure 8[4,183] shows how w_r is reduced as μ_r increases. Inserting data from table 2 into 1.41 gives $f_r = 153$MHz for the spherical carbonyl iron grains: this is a reasonable result judging by figure 8.

The starting point in analysing relaxation losses is the equation

Figure 8. Permeability spectra for Ni-Zn ferrites, Philips Ferroxcube IV grades A-E, showing resonance in anisotropy fields

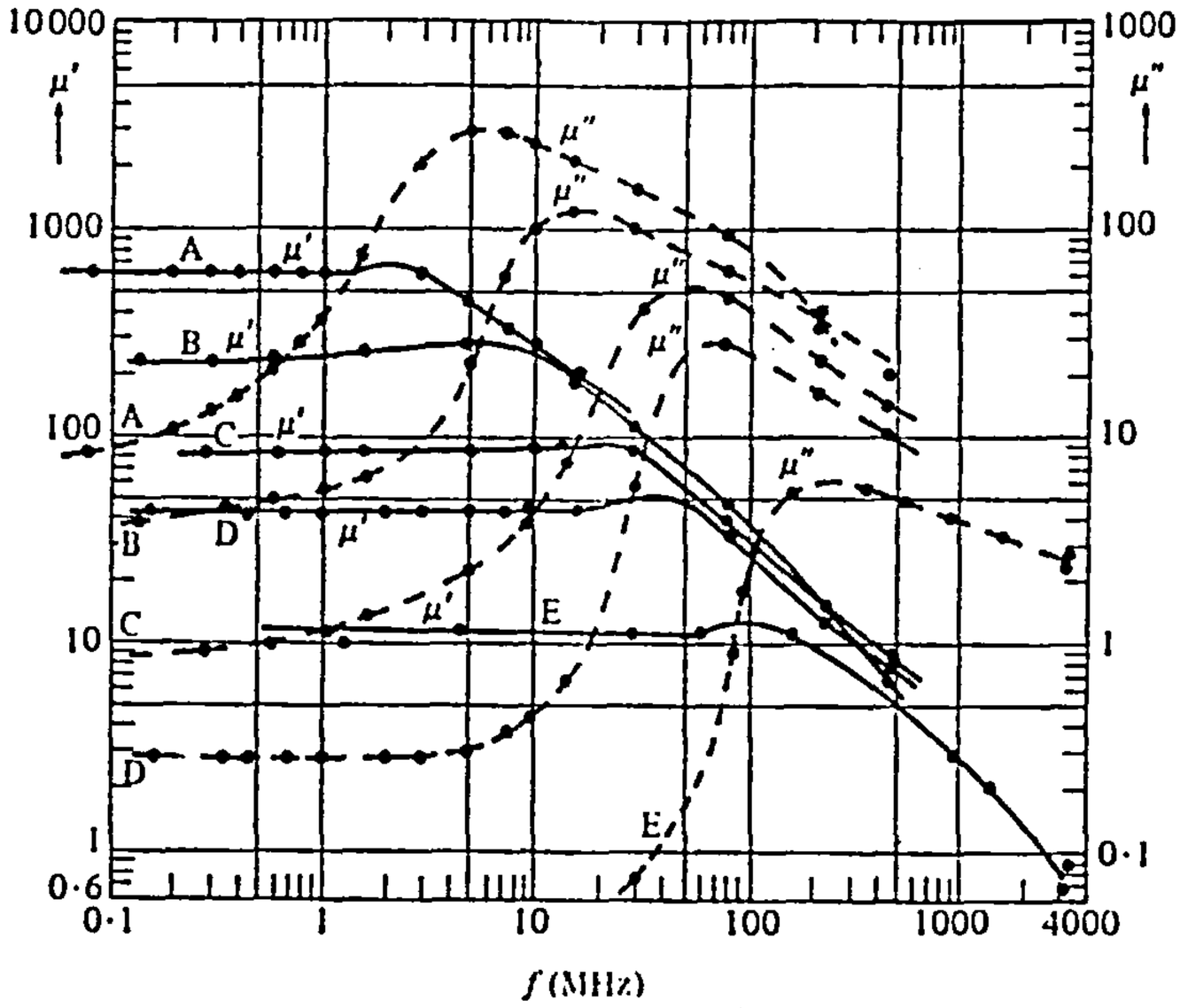

Figure 9. The variation in μ' and μ'' that would be predicted for a relaxation with a single time constant

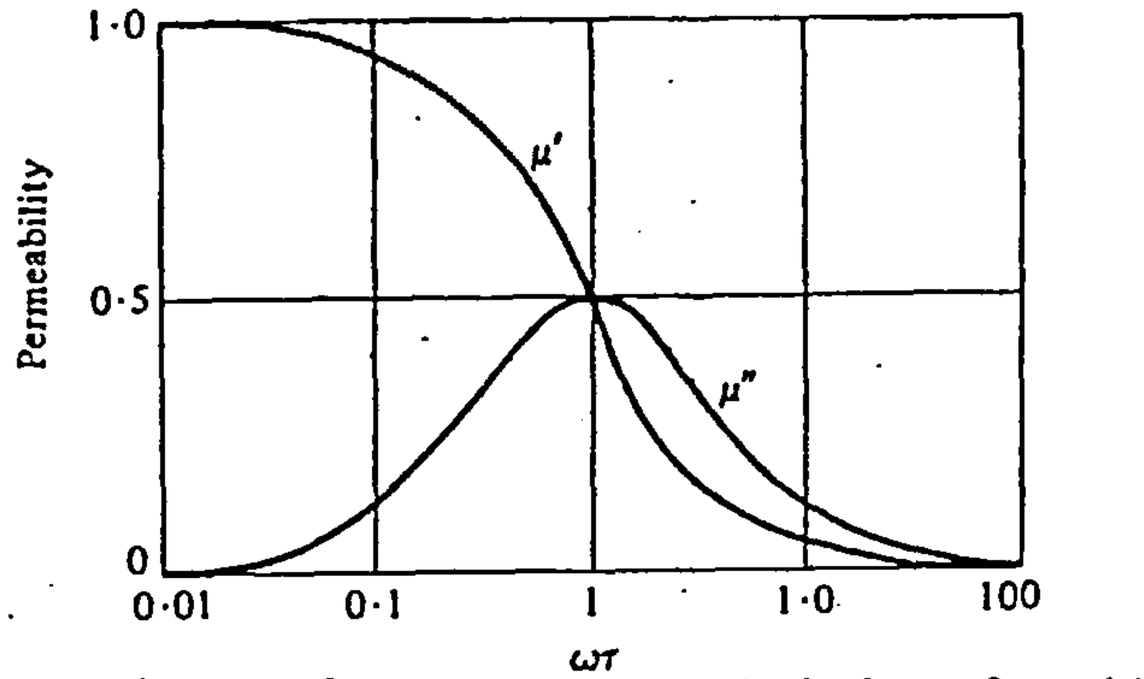

Figure 10. The spectrum of a copper containing ferrite with a spinel structure showing a low frequency rotation relaxation and a high frequency precession.

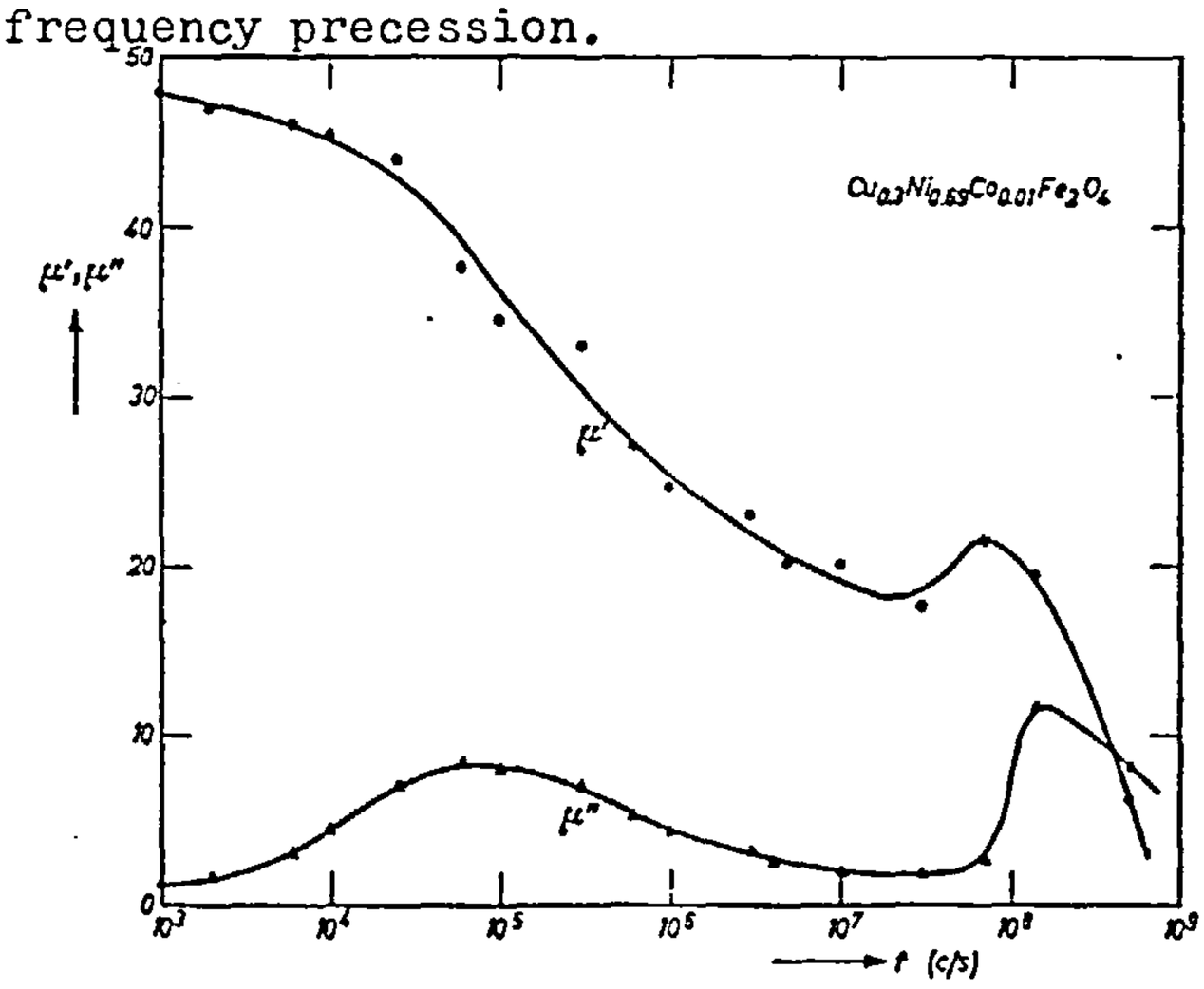

of motion[10,194] for the component of magnetization parallel to the applied flux when $p << 1$:

$$\tau \frac{dM}{dt} + M = XH \quad . \tag{1.42}$$

For a field of the form $H = H_m \cos wt$ there must be a solution of the form $M = M_m \exp(j(wt - \phi))$. Equation 1.42 may therefore be written as

$$jw\tau M_m \exp(j(wt - \phi)) + M_m \exp(j(wt - \phi)) = XH_m \exp(jwt) ,$$

from which

$$M_m = \frac{XH_m(1 - jwt)}{(1 + w^2\tau^2)} \quad . \tag{1.43}$$

X is the low frequency susceptibility, it is not the same as X(w) which is the susceptibility as a function of frequency. Using 1.43, $X(w) = M_m / H_m$ or

$$X(w) = \frac{X(1 - jwt)}{(1 + w^2\tau^2)} \quad . \tag{1.44}$$

X(w) is normally split into real and imaginary components

$$X(w) = X' - jX'' , \tag{1.45}$$

such that

$$X' = \frac{X}{(1 + w^2\tau^2)} \tag{1.46}$$

and

$$X'' = \frac{Xw\tau}{(1 + w^2\tau^2)} \quad . \tag{1.47}$$

The relation between the complex permeability and the complex susceptibility is easy to find. At low frequencies

$$\mu_r = 1 + X ,$$

and at high frequencies

$$\mu_r' - j\mu_r'' = 1 + (X' - jX'') ;$$

therefore

$$\mu' = X' + 1 \tag{1.48}$$

and

$$\mu'' = X''. \qquad (1.49)$$

Figure 9 shows the variations in μ' and μ'' that would be predicted from 1.46 to 1.49 if τ was single valued. There is no reason to suppose that τ does not occupy a range of values in practice.

If τ can be estimated for a given case of rotation magnetization, the region of relaxation losses can be predicted. Recalling 1.32,

$$\tau = \frac{(1 + p^2)}{w_o p} \qquad (1.50)$$

where p is always $<<1$ and is typically about 0.01[8,102]; w_r, which is very close to w_o, has already been calculated using 1.41. Combining this result with p = 0.01 in 1.50 gives $\tau = 1 \times 10^{-7}$. This result predicts that the rotation relaxation losses for carbonyl iron will peak at $f = 1 / 2\pi\tau \approx 1.6$ MHz.

These simple calculations on the regions of relaxation and resonance losses show that resonance in the internal anisotropy field can be dropped from consideration, for it occurs at a frequency that is very much greater than the operating frequency of 5MHz. Relaxation losses, on the other hand, are likely to be important. It should be noted that real geophysical materials do not have permeabilities as high as carbonyl iron and so the regions of resonance and relaxation occur at higher frequencies. Maghemite ($\gamma - Fe_2O_3$) is a natural oxide which resonates in its anisotropy field at about 1.2GHz, this puts $1/2\pi\tau$ at 12 MHz so that relaxation losses would still be important to an instrument operating at 5MHz. Figure 10[8,289] shows a high frequency resonance and a lower frequency relaxation in the permeability spectrum of a copper ferrite.

It is not difficult to connect X" and μ" to the power lost to the lattice. The change in energy dW associated with a field H and a

change in flux dB is[1,49]

$$dW = \int_V (\underline{H} \cdot d\underline{B}) \; dV \quad . \tag{1.51}$$

In an isotropic medium,

$$dW = HdB \tag{1.52}$$

per unit volume. The losses are attributable to X" and so,

$$dW = H \; (\mu_o \mu'' dH)$$

$$= \mu_o \; X''H.dH \; . \tag{1.53}$$

as $H = H_m \cos wt$, the power lost per second per unit volume is

$$P_l = \frac{\mu_o X''}{T} \int_{-T/2}^{+T/2} H_m \cos wt \quad (wH_m \cos wt)dt, \tag{1.54}$$

that is

$$P_l = \frac{1}{2} \; \mu_o w X'' H_m^{\,2} \; , \tag{1.55}$$

which is the required result. Using equation 1.47 the final arrangements are:

$$P_l = \frac{1}{2} \frac{\mu_o X}{\tau} \; \frac{H_m^{\,2}}{(1 + 1/w^2\tau^2)} \; , \tag{1.56}$$

and

$$P_l = \frac{1}{2} \frac{\mu_o(\mu_r - 1)}{\tau} \left[\frac{B_m}{\mu_o \mu_r}\right]^2 \left[\frac{1}{1 + 1/w^2\tau^2}\right] \tag{1.57}$$

The value calculated for τ and the relevant data in table 2 can be used in 1.57 to yield $P_l = 1.4 \times 10^{-1} \; Jm^{-3}s^{-1}$ for carbonyl iron grains at 5MHz. For comparison, the hysterysis loss was calculated to be $P_h = 5.0 \times 10^{-6} Jm^{-3}s^{-1}$ and the eddy current loss was $4.1 \times 10^{-3} Jm^{-3}s^{-1}$. The conclusion is that the lattice loss dominates. The most serious competitor is the eddy current loss, but its importance has been exaggerated because natural ferromagnetic grains in a rock matrix are unlikely to have intrinsic conductivities as high as $10^7 \Omega^{-1} m^{-1}$.

Some materials have initial permeabilities that are too high to be due to domain rotation alone. Domain wall motion is dominant in

these cases. Domain walls can exhibit resonance and relaxation[3,349][4,228] and these both occur at about 0.01 of the frequency of rotation resonance in the anisotropy field[3,353]. This is just the same region that rotation relaxation is expected to occur in. Where lattice losses through wall motion are present they are likely to be greater than losses due to rotation, so 1.56 and 1.57 can be presumed to represent the minimum lattice loss. The dynamics of domain walls have not been considered in detail because domain rotation is much simpler and yet yields useful results. It is worth noting that the hysterysis losses are solely due to domain wall motion and that the eddy current losses were calculated under the assumption that the domain walls moved. Finally, when wall relaxation does occur it obeys 1.56 and 1.57 although τ is now the ratio of the wall's damping factor to its stiffness[11].

1.5.6 The temperature dependence of the magnetic relaxation time constant.

The magnetic relaxation time constant τ is temperature dependent in both multidomain and single domain particles. For example, τ in ferrites exhibits a temperature dependence of the form[4,179][8,292][12]

$$\tau = \tau_\infty \exp (E_m/kT) \qquad (1.58)$$

in which τ_∞ is the relaxation time at an infinite temperature and E_m is an activation energy. Galt[12] found that values of $\tau_\infty = (10^{12}\text{Hz})^{-1}$ and $E_m = 0.22$ eV fitted experimental data on $(NiO)_{0.75}(FeO)_{0.25}Fe_2O_3$. Smit and Wijn[8,297] tabulate experimental values of E_m ranging from 0.10eV to 0.40eV for various ferrites. They found that τ_∞ can range from $(3 \times 10^8\ \text{Hz})^{-1}$ to $(10^{13}\text{Hz})^{-1}$.

The temperature dependence of τ in single domain particles has been extensively studied[4,147][13]. In the absence of an applied field the magnetization of a single domain grain is stable through anisotropy. For a grain of volume V this stabilising energy takes a maximum value of cV/2: c is both shape and stress dependent but it can be calculated when only shape anisotropy is important. In reality, the direction

of magnetization in a single domain grain fluctuates through thermal agitation. When $cV/2 \approx kT$ there is a significant probability that the magnetization will spontaneously rotate to reversal.

Whereas τ is a relaxation time, in the case of single domain grains $1/\tau$ can be regarded as the probability per second that the magnetization will reverse through thermal agitation. With this probabilistic point of view in mind, τ is given by[4,147]

$$\tau = \frac{1}{f_e} \exp (cV/2kT) , \qquad (1.59)$$

which is identical in form to 1.58 except that E_m is now calculable. The factor f_e can be identified as a frequency of electron precession, it has a constant value of $10^9 - 10^{10} s^{-1}$ just as it does in 1.58. For a uniaxial particle $c/2$ can be replaced by K_u, the uniaxial anisotropy constant. Equation (1.59) can now be rearranged to relate τ to the particle's volume V

$$\ln \tau = \frac{K_u V}{kT} - 22. \qquad (1.60)$$

By definition, grains with a small enough volume to be flipped at random by ambient thermal energy are superparagnetic: a grain may be thought to flip randomly when $\tau^{-1} \leqslant$ the frequency of the applied flux. Superparamagnetic grains carry no remanance and have zero coercivity.

1.5.7 The effect of the demagnetizing factor on the real and imaginary susceptibilities

The demagnetizing factor N affects the experimental determination of the real and imaginary susceptibilities. The experimentally observed susceptibility is

$$X_a = \frac{X_i}{1 + NX_i} , \qquad (1.14)$$

where X_i is now

$$X_i = X_i' - jX_i'' \quad . \tag{1.61}$$

The result of substituting 1.61 into 1.14 is

$$X_a' - jX_a'' = \frac{X_i' - jX_i}{1 + N\,(X_i' - X_i'')} \quad , \tag{1.62}$$

from which

$$X_a' = \frac{(1 + NX_i')X_i' + NX_i''^2}{(1 + NX_i')^2 + N^2X_i''^2} \quad , \tag{1.63}$$

and

$$X_a'' = \frac{X_i''}{(1 + NX_i')^2 + N^2X_i''^2} \quad . \tag{1.64}$$

Equations 1.63 and 1.64 show that X_i' and X_i'' are mixed in X_a' by the demagnetizing factor. When $X_i' >> X_i''$ equations 1.63 and 1.64 simplify to

$$X_a' = \frac{X_i'}{(1 + NX_i')} \tag{1.65}$$

and

$$X_a'' = \frac{X_i''}{(1 + NX_i')^2} \quad . \tag{1.66}$$

When $X_i' >> 1$ the demagnetizing field is ineffective and so

$$X_a' = X_i' \quad , \tag{1.67}$$

and

$$X_a'' = X_i'' \quad .$$

CHAPTER 2

THE INFLUENCE OF A MAGNETIZABLE MATERIAL ON THE PROPERTIES OF A SOLENOIDAL COIL

2.1 INTRODUCTION

Chapter 1 discussed the effect of an applied flux on a magnetizable sample. Chapter 2 takes a reverse point of view by asking how the magnetized sample affects the source of the flux. This topic is important for it will show what can be measured and it helps in deciding how measurements might best be made.

Samples are most conveniently probed by alternating fields. Such fields, and the induced changes in them, are readily distinguished from any natural remanent magnetization (n.r.m.) that may be locked in the sample[(2)]. The most obvious means of applying an alternating flux is to place the sample in a coil that is energised by an alternating current: this is the scheme that was adopted. It will shortly be seen that X' affects the inductance of the sample coil, whilst X" increases the effective resistance of the sample coil.

Two existing a.c. susceptibility instruments are briefly outlined, both of them were developed to measure the variation of initial susceptibility with temperature. These devices are used to put the present work into a context.

The high frequency circuits developed for nuclear magnetic resonance (n.m.r.) detection can be elegantly simple and yet very sensitive. Two particularly important circuits, the Robinson oscillator and the Rollin Q-meter, are mentioned in the light of the present requirements. This leads to a description of the principle of the new instrument.

2.2 HOW THE COIL AND SAMPLE INTERACT

2.2.1 The field in a solenoidal coil

This subsection presents some useful formulae on single layered air

cored coils. The axial field in the centre of a very long single layered solenoid is

$$H = \frac{n}{b} I \ , \qquad (2.1)$$

where n is the total number of turns of the coil, b is the length of the coil and I is the current in the coil. For any single layered air cored coil, if x is the displacement from the centre of the coil and D is the diameter of the coil (see figure 11a) then the field anywhere on the axis of the coil is[14, 182]

$$H = \frac{In}{2b}\left[\frac{b + 2x}{(D^2 + (b + 2x)^2)^{0.5}} + \frac{b - 2x}{(D^2 + (b - 2x)^2)^{0.5}}\right] \qquad (2.2)$$

Figure 11b shows the variation of H along a coil whose length to diameter ratio is 0.86, a coil of exactly this shape is used in the work described in chapters 5 and 6.

The inductance of a single layered solenoid whose length is long compared with its diameter is

$$L = \mu_o \mu_r n^2 A b, \qquad (2.3)$$

where μ_r is the relative permeability of the material filling the coil and A is the coil's cross sectional area. Wheeler's formula for the inductance of a single layered coil whose length is less than its diameter is[15]

$$L = \mu_o \mu_r \left[\frac{10^3}{4\pi}\right]\left[\frac{D^2 n^2}{102b + 45\ D}\right]. \qquad (2.4)$$

Equation 2.4 is correct to within 3% for $0.25 \leq (b/D) < 1.00$.

2.2.2 The effect of the sample on the solenoidal measuring coil

If a long, air cored solenoid is filled with magnetizable material, the original inductance L_o is changed to

Figure 11. The magnetic field along the axis of a helical, single layer, air cored coil.

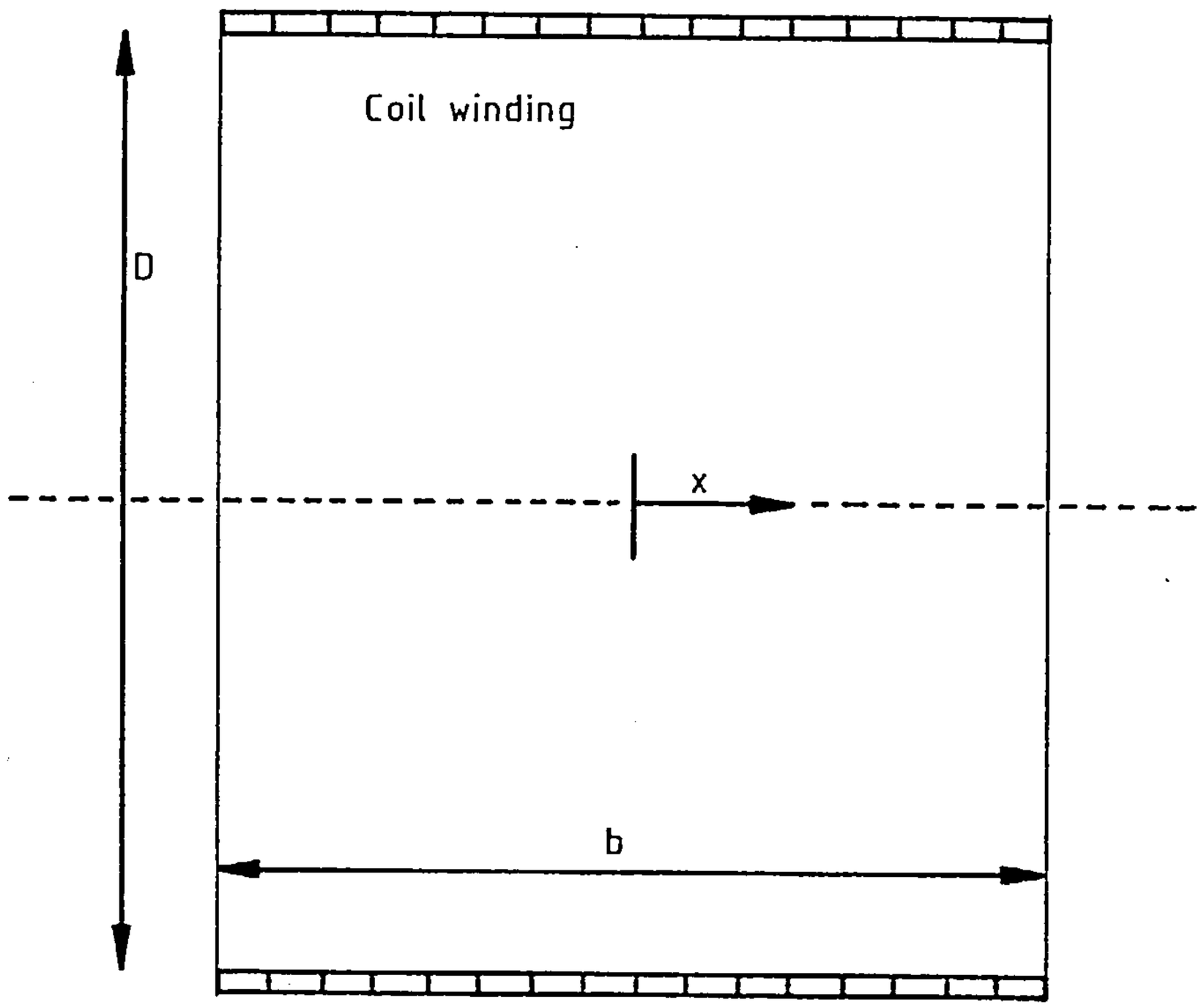

a. The symbols for equation 2.2, s = b/D = 0.83.

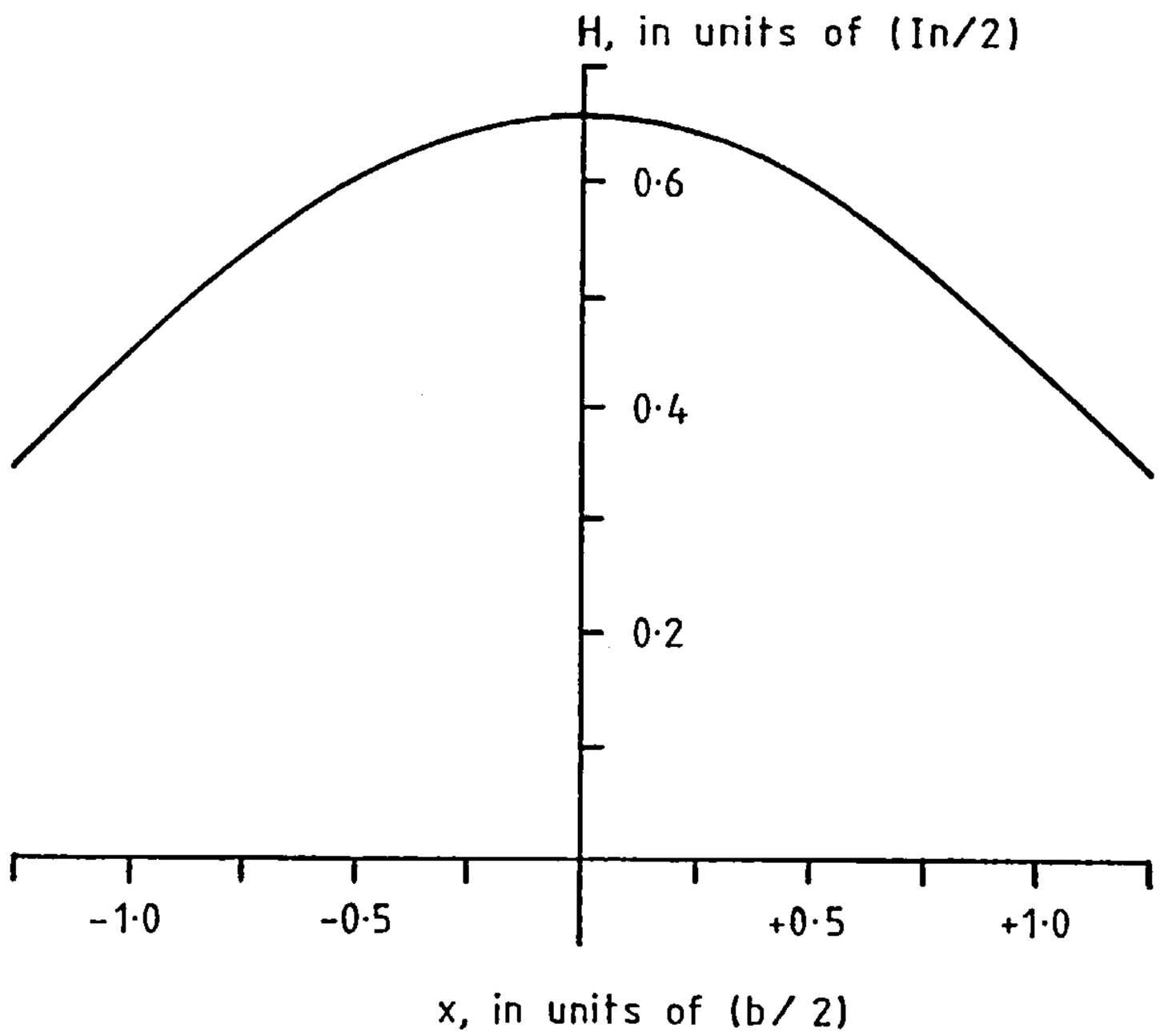

b. The axial field variation for the coil above

$$L_1 = \mu_r L_o \ , \qquad (2.5)$$

in which it has been assumed that the relative permeability of air is one. Equation 2.5 can be rewritten as

$$L_1 = (1 + X)L_o \ ,$$

so that

$$L_1 = (1 + (X' - jX")) \qquad (2.6)$$

at high frequencies. If the solenoid has a d.c. resistance of R_s then the excited, filled coil will have an impedance of

$$R_s + jwL_1 = R_s + wL_oX" + jwL_o\ (1 + X') \ , \qquad (2.7)$$

where w is the angular frequency of the exciting current. The effect of filling the long solenoid with magnetizable material has been to change the inductance by

$$\Delta L = X'\ L_o \ , \qquad (2.8)$$

and to increase the d.c. resistance by

$$\Delta R = X"wL_o \ . \qquad (2.9)$$

ΔL and ΔR are both measurable.

2.2.3 The measuring coil's filling factor

Equations 2.8 and 2.9 are only valid when a long core, tightly wound around by an energised coil, is fully penetrated by flux. The question of flux penetration has already been dealt with in sections 1.3 and 1.5.2. However, because the coil was ultimately designed to have a good quality factor it was short, not long. Furthermore, the inclusion of a furnace within the coil constrained the diameter of the sample to be much less than that of the coil. A filling factor F is required to account for these points.

The filling factor is defined to be the ratio of the magnetic energy in the sample volume to the total magnetic energy produced by coil. If the sample is now required to be much shorter than the measuring

coil, $\leq 0.25b$, and is placed centrally within it then the flux inside the sample is reasonably uniform; equations 2.8 and 2.9 can now be rewritten as

$$\Delta L = FX'L_o \qquad (2.10)$$

and

$$\Delta R = FX'WL_o \ , \qquad (2.11)$$

where F is the filling factor. The condition that the sample's length l be $\leq 0.25b$ has been adopted in practice. (The sample's diameter d is fixed by the sample tube that fits into the furnace.) When the displacement from the centre of the coil = $\pm$ b/8, H has decreased by only 2.4% from its maximum value. Within these bounds the sample's length and homogeneity do not matter because the field is nearly uniform, so results from different samples can be compared if desired. If the sample is allowed to break these bounds, ΔL and ΔR will also depend on the sample's length and the distribution of ferromagnetic material within the sample: this is most undesirable. The restriction on sample length avoids these unwanted dependences at the cost of having to measure weaker signals.

The coil filling factor F is a little considered quantity. Beyond its definition, almost no information has been seen about it in the literature. The one exception is a paper by Becker and Collett[16] who have a result for the filling factor of a short, solenoidal coil. They give

$$F = \frac{V_s}{V_c} \frac{b(b + 0.45D)}{b^2 + D^2} \ , \qquad (2.12)$$

where V_s is the sample volume and V_c is the coil volume. Unfortunately, neither the paper itself nor the references it contains give a clue about the origins or validity of the result. Later on it will be seen that F

is an important design parameter. It is not sensible to design with an equation of uncertain ancestry so the following analysis was carried out to either confirm or find an alternative to Becker and Collett's result.

Imagine a sample of length l diameter d centrally placed in a coil of length b and diameter D having n turns. The restrictions $l \leq b/4$ and $d < D/2$ are presumed, they are certainly obeyed in the new instrument. From the definition of F, the ratio of the magnetic energy in the sample to the magnetic energy produced by the coil must be found. The magnetic energy produced by an inductance due to a current I is,

$$W = \frac{1}{2} LI^2 . \qquad (2.13)$$

The presence of the sample will change the original inductance L_o to a new value,

$$L_1 = L_o(1 + FX) , \qquad (2.14)$$

where $X = X' - jX''$. From 2.4 and 2.14 the total magnetic energy generated by the coil is

$$W = \left[\frac{10^3 \mu_o}{4\pi}\right]\left[\frac{1 + FX}{2}\right]\left[\frac{D^2 n^2}{102\ b + 45\ D}\right] I^2 . \qquad (2.15)$$

The calculation of the energy due to the field within the sample is based on

$$W = \frac{1}{2}\int \underline{H}.\ \underline{B}\ dV \qquad (2.16)$$

recalling 1.62. A sample composed of a distributed ferromagnetic powder or randomly oriented rock chippings is isotropic and so

$$\underline{H}.\ \underline{B} = HB , \qquad (2.17)$$

therefore

$$\Delta W = \frac{1}{2} \mu_o \mu_r H^2 V_s . \qquad (2.18)$$

As far as the sample is concerned, $\mu_r = 1 + X$ and so 2.18 is

$$W = \frac{1}{2}\mu_o\ (1 + X)H^2V_s \quad . \tag{2.19}$$

As $d < D/2$ it is reasonable to neglect the variation of the flux density at right angles to the coil axis. Since $l \leqslant b/4$

$$H = \frac{I_n}{(D^2 + b^2)^{0.5}} \tag{2.20}$$

to within 2.4%, this can be proven by substituting $x = 0$ and $x = \pm$ $b/8$ into equation 2.2. Equations 2.19 and 2.20 can be combined to give the energy in the sample:

$$\Delta W = \frac{\mu_o}{2}(1 + X)\left[\frac{I^2n^2}{D^2 + b^2}\right] V_s \quad . \tag{2.21}$$

Since

$$F = \frac{\Delta W}{W} \ , \tag{2.22}$$

equation 2.21 may be divided by 2.15 to yield

$$F = B\left[\frac{1 + X}{1 + FX}\right] \tag{2.23}$$

where $$B = \frac{V_s}{V_c}\ \frac{b(b + 0.44D)}{(D^2 + b^2)} \quad . \tag{2.24}$$

The final step is to rearrange 2.23:

$$F^2X + F - B(1 + X) = 0 \tag{2.25}$$

such that

$$F = \frac{-1 \pm (1 + 4XB(1 + X))^{0.5}}{2X} \quad . \tag{2.26}$$

Let's put 2.26 through a simple test whose result can be predicted. In the case of a long solenoid (where $b/D >> 1$) filled with magnetizable material $B = 1$. Equation 2.26 then becomes

$$F = \frac{-1 \pm (2X + 1)}{2X} \tag{2.27}$$

$$= 1$$

if the negative root is ignored for being unrealistic. This is exactly the result that would be expected.

Equation 2.26 may be expanded binomially into a more useful form,

$$F = B\,(1 + X) - XB^2\,(1 + X)^2 + \ldots \qquad (2.28)$$

In practice $B \approx 0.01$, therefore if $X \leqslant 2.5$

$$F \approx B\,(1 + X)\ . \qquad (2.29)$$

This is an important result, for it shows that F is a function of X. Therefore, ΔL and ΔR in equations 2.10 and 2.11 are not linearly dependant on X' or X". However, if $X \leqslant 0.1$

$$F \approx B\ , \qquad (2.30)$$

in agreement with Becker and Collett's result.

To conclude this subsection, when the volume susceptibility is less than 0.1 the filling factor is given by equation 2.12. When the volume susceptibility is greater than 0.1, but less than 2.5, the filling factor is given by 2.29. However, equation 2.29 should be treated with caution because the magnetic field over the cross section of the coil becomes increasingly distorted as X increases, and this invalidates the assumption made to obtain 2.20.

2.3 COMMENTS ON TWO EXISTING INSTRUMENTS THAT MEASURE THE TEMPERATURE DEPENDENCE OF SUSCEPTIBILITY

2.3.1 Introduction

The interplay between the rock sample and the measuring coil has now been described. This subsection presents a synopsis of two existing instruments that recognise and record the induced changes in the coil. Both of these instruments had a strong influence on the recent work. They also indicate the existing standard of performance and therefore the success, or otherwise, of the different ideas on which the new instrument is founded.

The first device to be considered makes the measuring coil part of a balanced inductive bridge operating at 1.5KHz. A working version of

this instrument is available in the department and it is popular because it is easy to use. One objective therefore was to combine a similar ease of use with an improved sensitivity. As a well tried and trusted geophysical tool the bridge was adopted as a reference standard during the development of the new instrument. A paper describing this instrument is included in appendix 3.

The second instrument described operates at 10 MHz. In this instance, the measuring coil is made part of a driven series resonant circuit. Inductive and resistive changes in the measuring coil are distinguishable using this technique. The instrument is more difficult to use than the bridge, but the results it obtains are very interesting. In particular, it stimulated an interest in measuring X".

2.3.2 A 1.5KHz Bridge[17]

In use, the bridge is first balanced roughly such that its output voltage is close to zero. When a sample is inserted into the measuring coil the change in output voltage is closely proportional to the susceptibility of the sample; the bridge is linear to within 1% provided that the sample's total susceptibility $X_T \leq 9.4 \times 10^{-7} m^3$. Calibration is done using a standard of known total susceptibility. The temperature dependence of susceptibility can be monitored continuously simply by feeding the bridge's output to an XY chart recorder while the sample is heated in the bridge's furnace.

A block diagram of the bridge is shown in figure 12[17]. A pair of identical solenoids form two of the bridge's arms, the other arms are both resistive and include some provision for balancing adjustments. One of the solenoids houses a furnace for measurements up to 1000K, the other solenoid houses an insulated container for measurements down to 77K. Figure 13[17] shows how the furnace and measuring coil are amalgamated. The furnace consists of a quartz tube of 8 mm internal

Figure 12. A block diagram of Stephenson and de Sa's bridge[17].

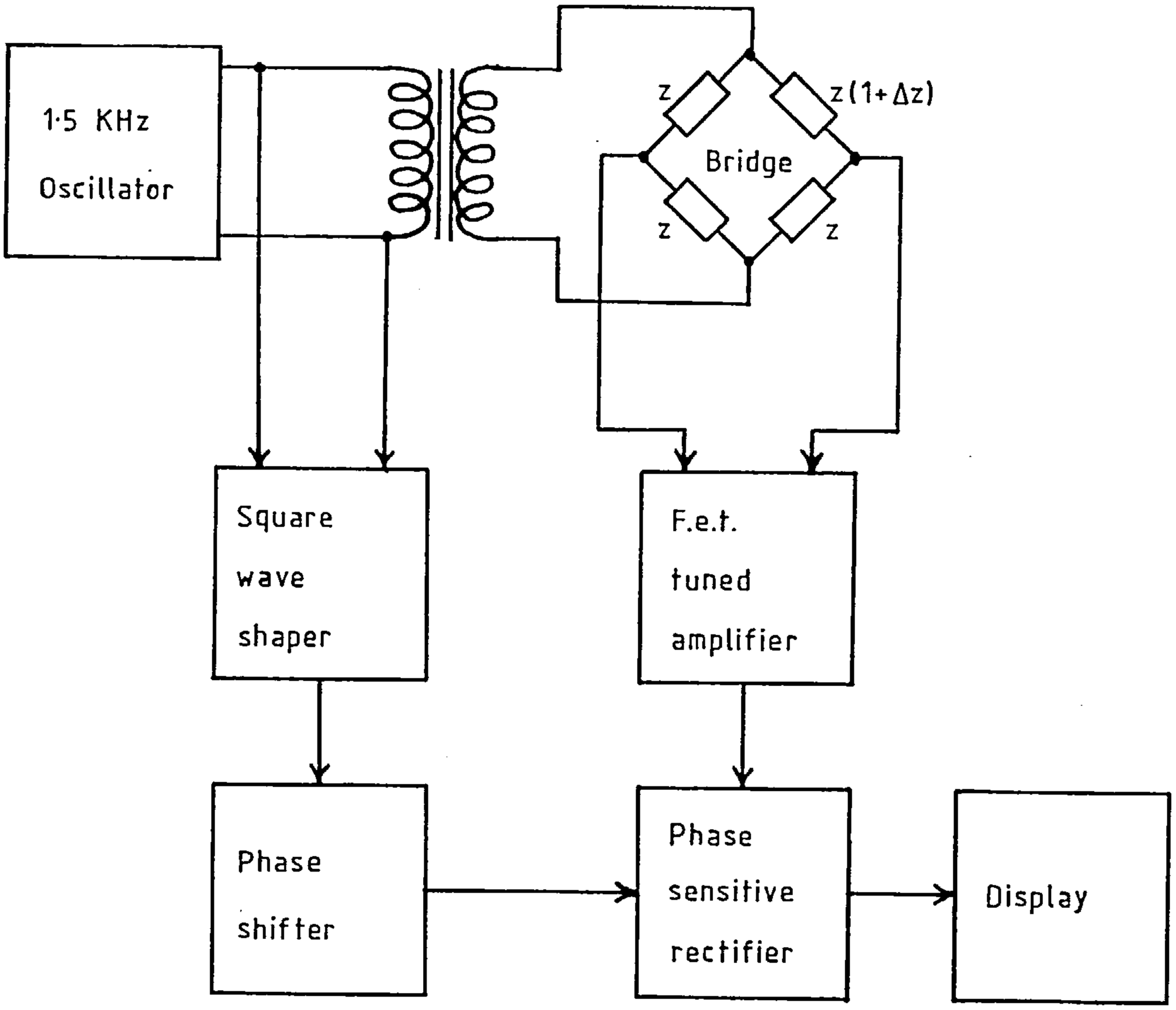

Figure 13. A diagram of Stephenson and de Sa's furnace and measuring coil assembly.

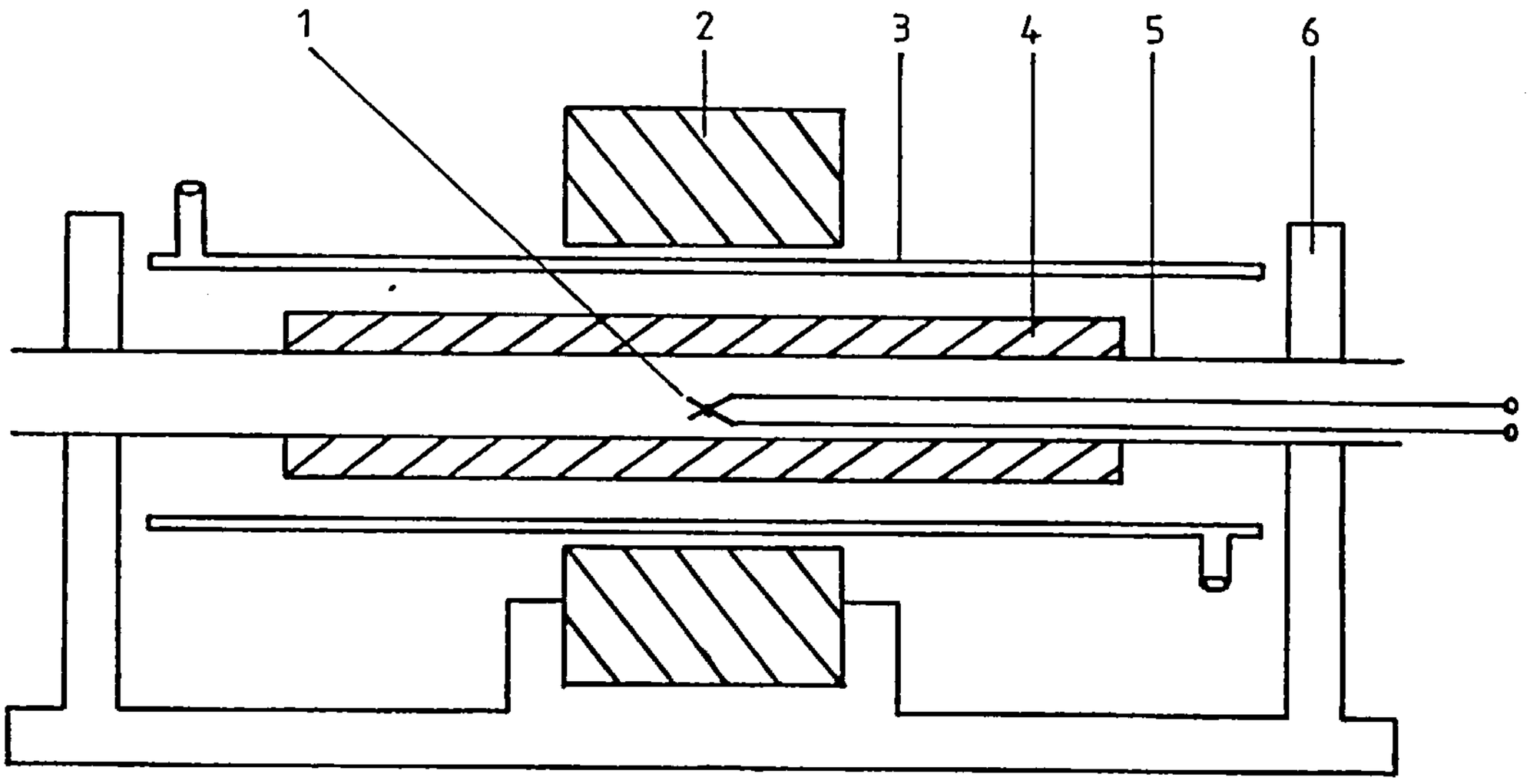

1. Pt-Pt/13%Rh thermocouple
2. Measuring coil
3. Water jacket
4. Furnace winding
5. Quartz tube
6. Supports

diameter wound non-inductively with nichrome wire. Currents of up to 1A can be passed through the furnace without disturbing the bridge. Insulation between the furnace and coil is provided by an air gap and water jacket.

For the purposes of comparison later on, the relevant specifications of the instrument are listed in table 5 below.

Table 5 Some details of the 1.5KHz bridge.

Parameter	Value
Length of sample coil	3.6×10^{-2} m
Internal diameter of sample coil	2.2×10^{-2} m
Construction of sample coil	5,000 turns of 32 s.w.g. enamelled copper wire
Flux at the centre of the sample coil	3.6×10^{-4} T pk.
Sample size	About 10 mm long by 4 mm diameter
Maximum sample strength	$9.7 \times 10^{-7} m^3$
Random noise at the output	$\pm 1.2 \times 10^{-11}$ m^3
Zero drift	$\approx 1.3 \times 10^{-11}$ $m^3 min^{-1}$
Direction reading?	Yes

2.3.3 A 10 MHz Method[18]

The high frequency method of Markert, Trissl and Zimmerman is very different from the technique just described. Markert et al followed a lead given by Petersen[19] in using the high frequency losses of ferromagnetic materials to determine their Curie points. Petersen's apparatus worked at 8MHz.

A block diagram of Markert et al's system is reproduced in figure 14[18]. A crystal oscillator and a voltage controlled regulator are used in conjunction to produce a stable 10MHz signal whose amplitude can be automatically controlled. The regulated signal is fed to a buffer

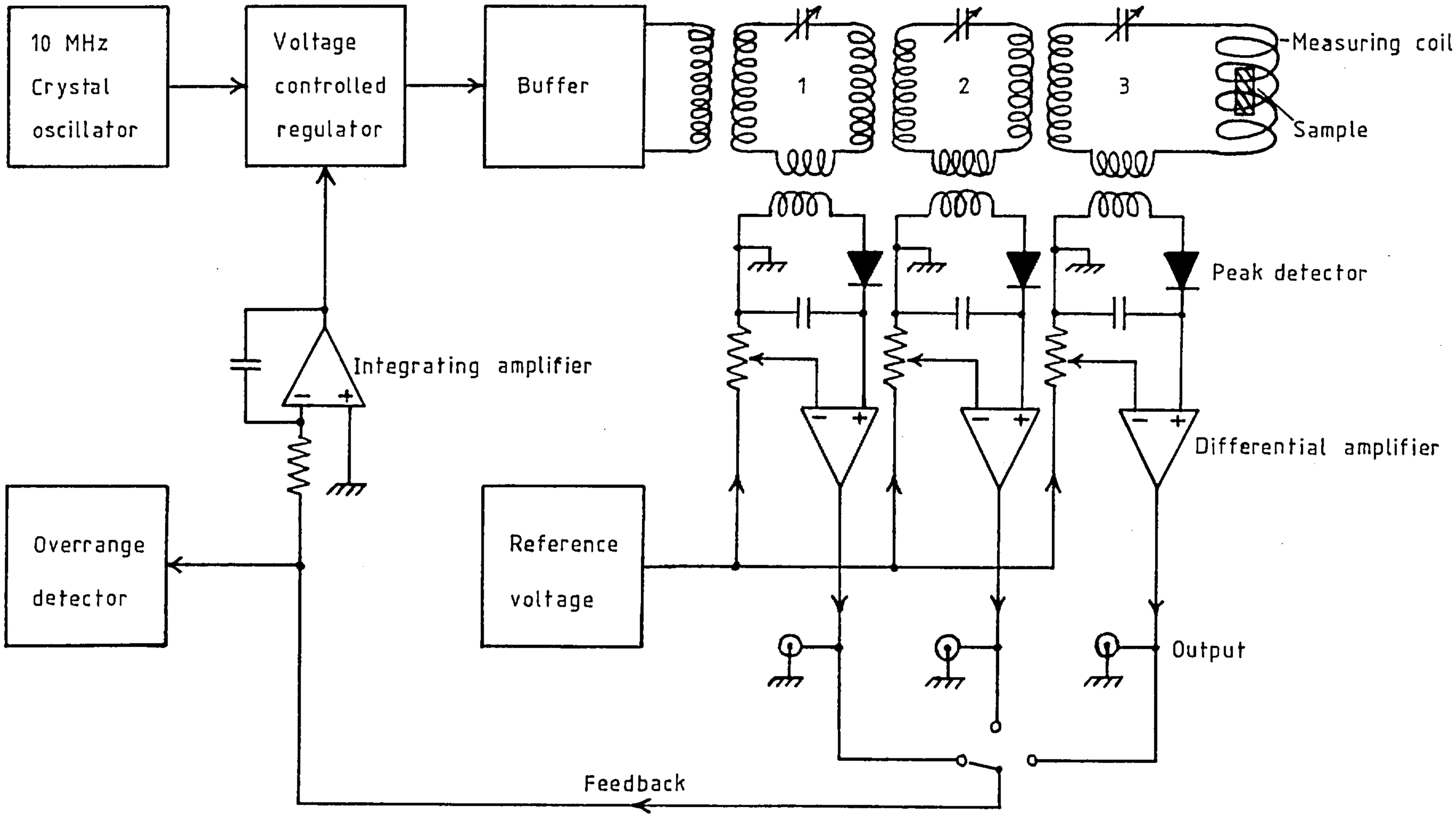

Figure 14. A block diagram of Markert et al's 10MHz system[18].

and thence to three inductively coupled series resonant circuits. As can be seen, the sample is enclosed in a measuring coil in resonant circuit three. The measuring coil consists of $3\frac{1}{2}$ turns of copper tubing, water can be made to flow through the tubing to keep the coil cool. The signal amplitudes in each of the tuned circuits are peak detected and compared with preset reference voltages by differential amplifiers. The output of any one of these amplifiers can be fed back through an integrating amplifier to form an amplitude control loop, the outputs of the other two amplifiers contain information about the susceptibility of the sample. The authors describe three different measuring techniques, but they do not make clear which their favoured method is. One of the methods is outlined below.

Circuit 1 is tuned to resonance and its detected and differentially amplified signal level is fed back to the amplitude regulator. Resonant circuit 1 is now acting simply as a 10 MHz voltage source. Circuit 2 is also set to resonance, but circuit 3 is set off resonance such that the amplitude in it is $1/\sqrt{2}$ of the maximum possible amplitude.

In the absence of a sample the current in circuit 3 is I_{30}. When a sample is inserted into the measuring coil the changes ΔI_2 and ΔI_3, in circuits 2 and 3 respectively, can be measured at the outputs of the differential amplifiers. According to the authors, the increase in resistance of coil 3 due to the insertion of a sample is given by

$$\Delta R_3 = A_1 \left[\frac{\Delta I_2}{I_{30}}\right] - B_1 \left[\frac{\Delta I_3}{I_{30}}\right]. \qquad (2.31)$$

The increase in the measuring coil's inductance is

$$w\Delta L_3 = A_2 \left[\frac{\Delta I_2}{I_{30}}\right] - B_2 \left[\frac{\Delta I_3}{I_{30}}\right]. \qquad (2.32)$$

The constants A_1, A_2, B_1 and B_2 can be determined by calibration using

known samples.

Figure 15 shows the quartz vessel that the sample is placed in. For high temperature measurements the inner quartz tube is evacuated and sealed. The whole vessel is heated in a separate furnace and it is then removed from the furnace and slid into the water cooled sample coil. The changes ΔI_2 and ΔI_3 are simultaneously chart recorded as the sample cools down. A plot of ΔR_3 and ΔL_3 against temperature can then be produced by a series of calculations using equations 2.31 and 2.32.

After theoretically analysing their instrument Markert et al found that in practice it produced results 30% lower than they had predicted. This was because they ignored the coupling factor F by assuming that

$$L = X'L_o$$

and

$$R = X''\omega L_o \ .$$

They also assume that the imaginary susceptibility X" is due to Rayliegh hysterysis losses, a completely different conclusion was drawn in section 1.5.

Markert et al give two examples of results at elevated temperatures and these are reproduced in figures 16a and 16b[18]. The two examples are in marked contrast. Figure 16a is easy to interpret because it has a sharp Curie point[4,37] transition, 16b has a blurred transition which Markert et al attribute to a range of close lying Curie points. In both cases, the losses exhibit a distinct peak and undergo greater changes, as a proportion of their initial value, than the inductive components do. It was stated in section 1.4 that one of the most important applications of susceptibility measurements lies in finding Curie points, the striking changes in figures 16a and 16b show that X" could be of much use in this respect.

To close this subsection, some details of Markert et al's apparatus are given in table 6 below.

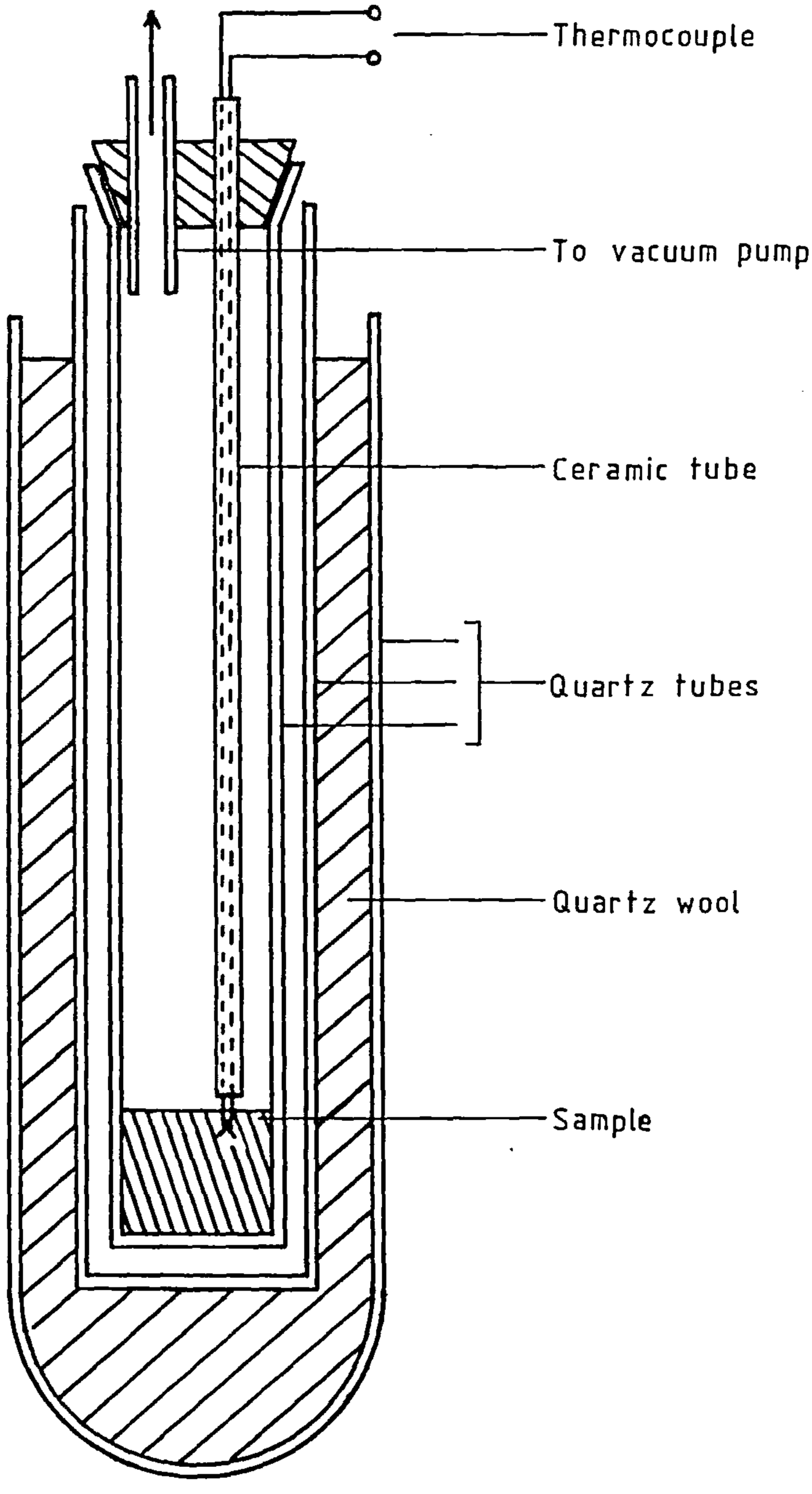

Figure 15. A diagram of Markert et al's quartz sample vessel.

Figure 16. Some results from Markert et al's system[18].

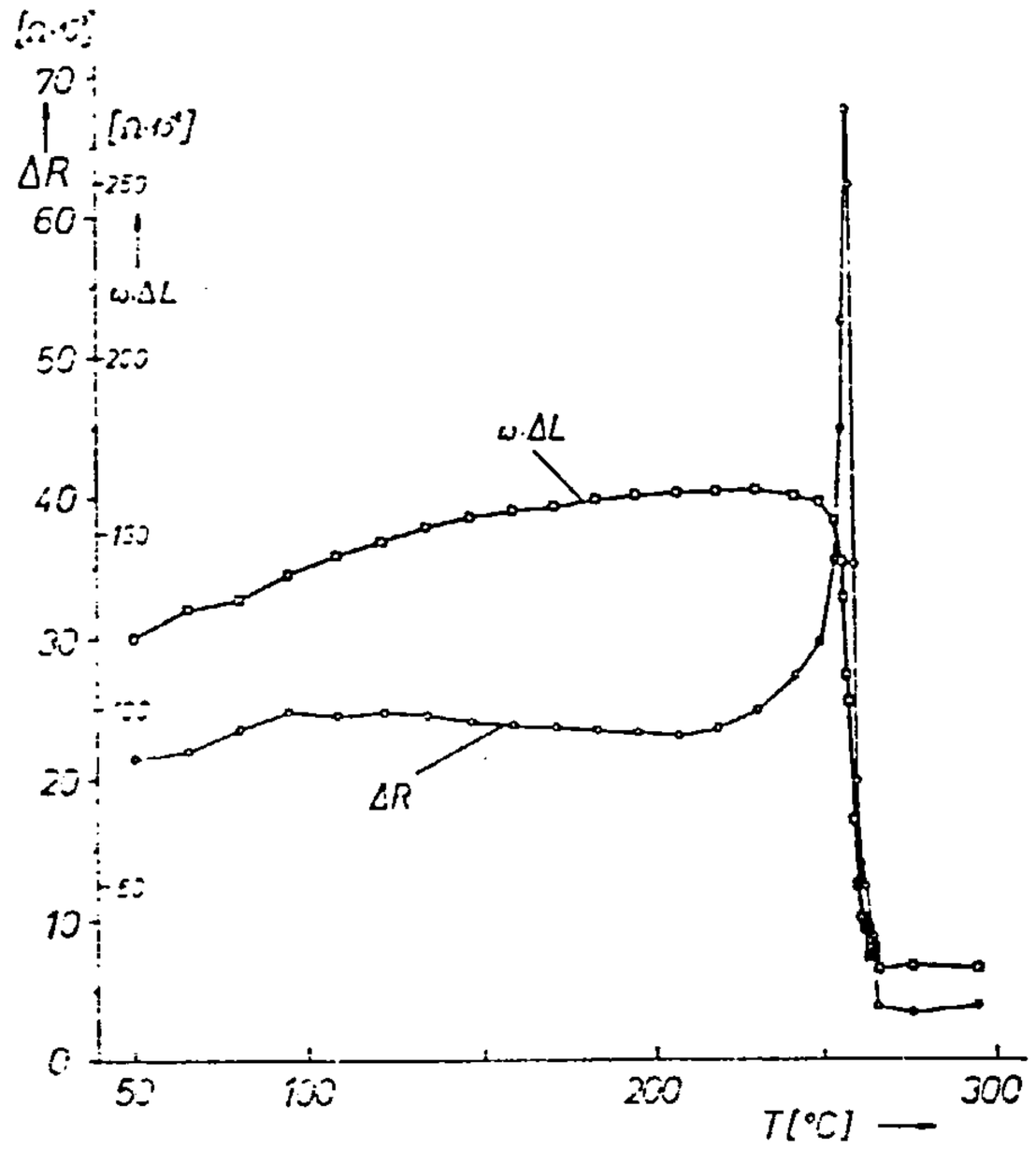

a. Cooling traces showing the Curie point of an yttrium iron garnet (YIG) single crystal. Notice the very sharp peak in X".

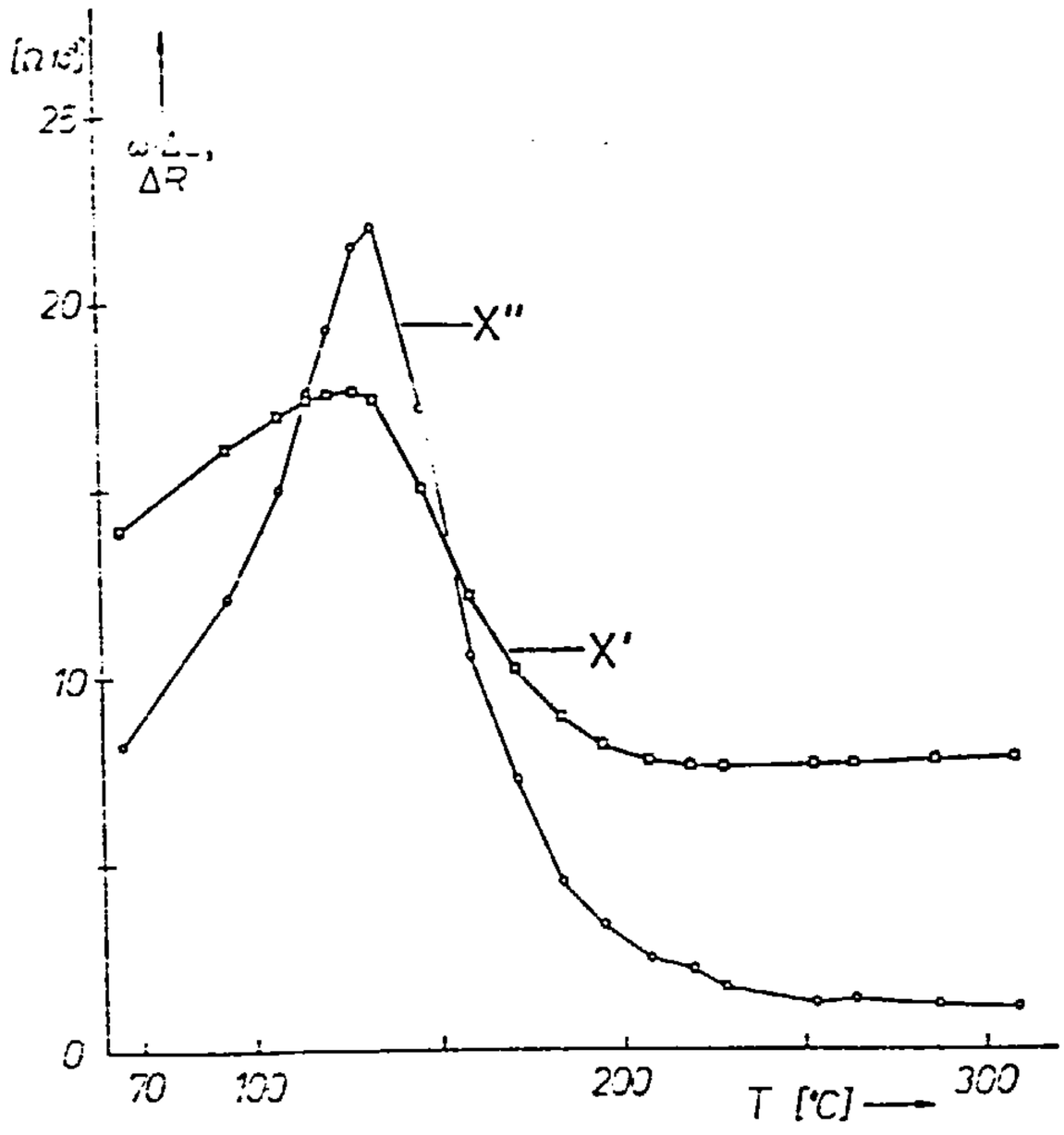

b. The temperature dependence of susceptibility of a standard basalt core of the Rauher Kulm (Bavaria).

Table 6 Some details of the 10MHz method.

Parameter	Value
Length of sample coil	4.5×10^{-2} m
Diameter of sample coil	7.0×10^{-2} m
Construction of sample coil	3.5 turns of copper tube. Internal diameter of tube is 4 mm, external is 6 mm .
Flux at the centre of the sample coil	Not given
Sample size	Up to 30 mm long by 25 mm diameter
Maximum sample strength	Not given
Random noise in X'	$\pm 1.5 \times 10^{-10} m^3$
Random noise in X"	Not given
Zero drifts	Not given
Direct reading?	No

2.3.4 Conclusions

This subsection distils from the preceding comments those features that an experimentalist might desire of a new instrument that measures the temperature dependence of susceptibility.

The 1.5KHz bridge of Stephenson and de Sa is about 13 times more sensitive to X' than the 10 MHz system of Markert et al. A sensitivity at least equal to that of the bridge is desirable as it allows small or weak samples to be successfully dealt with. This sensitivity would be especially useful when examining synthetic materials which might be in short supply.

The amalgamated furnace and sample coil scheme of Stephenson and de Sa is adopted. The advantages are that the rate of heating and cooling can be controlled to suit the sample size, and that the coil is quite effectively insulated from transmitted heat. The price to be paid is a reduced filling factor, and therefore reduced sensitivity, as the

coil has to be large enough to accommodate the furnace and water jacket.

Markert et al are able to evacuate the sample space to minimise the risk of sample oxidation during heating. The standard technique of sealing the samples in an evacuated quartz tube can be used to the same effect in Stephenson and de Sa's arrangement. Changes may occur in a heated sample even in the absence of air. If these changes are irreversible they would be completely missed by an instrument that could not observe the susceptibility during heating.

It is plain from Markert et al's results in figures 16a and 16b that both X' and X" are worth measuring. The temperature dependence of X" in ferromagnetic materials has received very little attention in the past, but X" may be a better indicator of Curie points than X' and it may yield other information too.

Markert et al's apparatus was not automatic as the results it gave had to be manually converted to X' and X". It was hoped that the new instrument would make available outputs directly proportional to X' and X".

2.4 NUCLEAR MAGNETIC SUSCEPTIBILITY SPECTROMETERS

2.4.1 Introduction

A nucleus that contains an odd number of protons has a net spin dipole moment and therefore an associated magnetic moment and susceptibility. This nuclear susceptibility has both real and imaginary parts, and since the mid 1940's a lot of time and effort has been expended in developing ever more sensitive circuits to measure it. Perhaps the most famous of these are the Q-meter circuit of Rollin[20], the marginal oscillator[21], the Pound-Knight-Watkins (PKW) marginal oscillator[22] and the Robinson oscillator[23] with its Faulkner-Holman variant[24]. This section decides which, if any, of this work can be turned to advantage in this project. As the subject is well developed, the decision

can be made quickly, and it will lead to a description of the new instrument's principle in the next section.

Using the aforementioned circuits to measure the temperature dependence of susceptibility is an idea that has been thought of before. Whereas the n.m.r. workers used the changes in the losses of a tuned circuit to measure the imaginary part of the nuclear susceptibility, the geophysical workers used the changes in a tuned circuit's natural frequency to measure the real part of the electronic susceptibility. de Sa[25] utilised a 5 MHz marginal oscillator to find the Curie points of ferrimagnetic materials at elevated temperatures. He pointed out that his method was not sensitive as it was not suitable for initial susceptibilities under 0.5. Riedi[26] used a Q meter to measure Curie points at cryogenic temperatures. Riedi's apparatus worked at frequencies between 1 MHz and 10 MHz and he claimed that his method was significantly more sensitive than de Sa's. These instruments are not suited to the present purposes because they are not sensitive enough, they are not linear and they do not attempt to separate X' and X".

2.4.2 Some useful results on parallel tuned circuits

All of the circuits mentioned for measuring nuclear susceptibility place the sample in a coil which forms part of an LC resonant (tuned) circuit. This subsection presents some useful results that describe the behaviour of a parallel tuned circuit.

Figure 17 depicts a parallel tuned circuit driven by an alternating voltage source through a very large resistance R. The tuned circuit is an inductance L in parallel with a capacitance C, it includes the unwanted d.c. resistance of the coil R_s and the shunt resistance of the capacitor R_c. For high quality silver mica or polystyrene capacitors $R_c > 10^{11}\Omega$ so it can be safely neglected.

The quality factor Q of the tuned circuit is ratio of the reactive

Figure 17. A parallel tuned circuit, including parasitic resistances, driven by a voltage source through an isolating resistance.

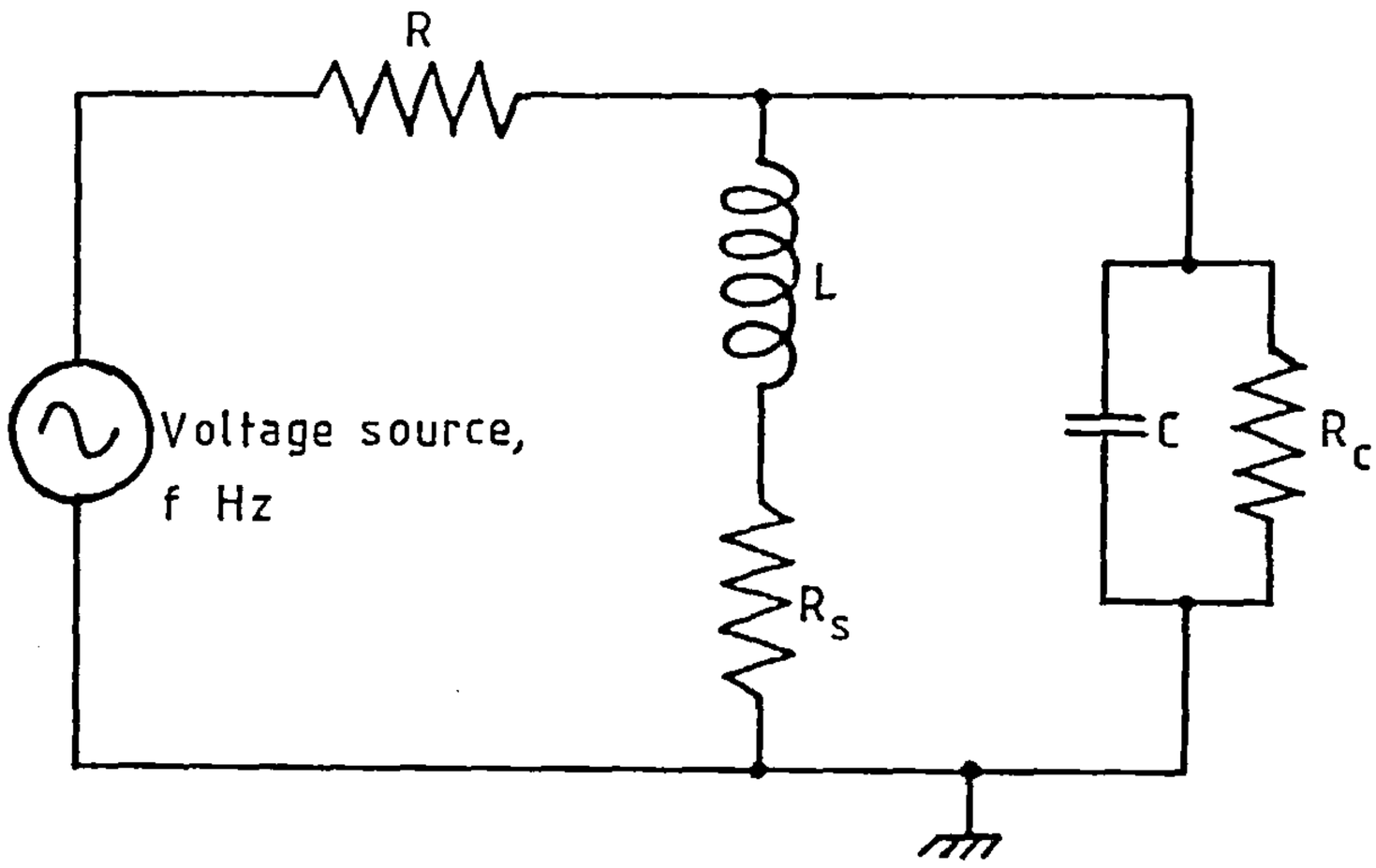

Figure 18. The impedance and phase characteristics of a parallel tuned circuit driven by an alternating current with a frequency close to the natural frequency.

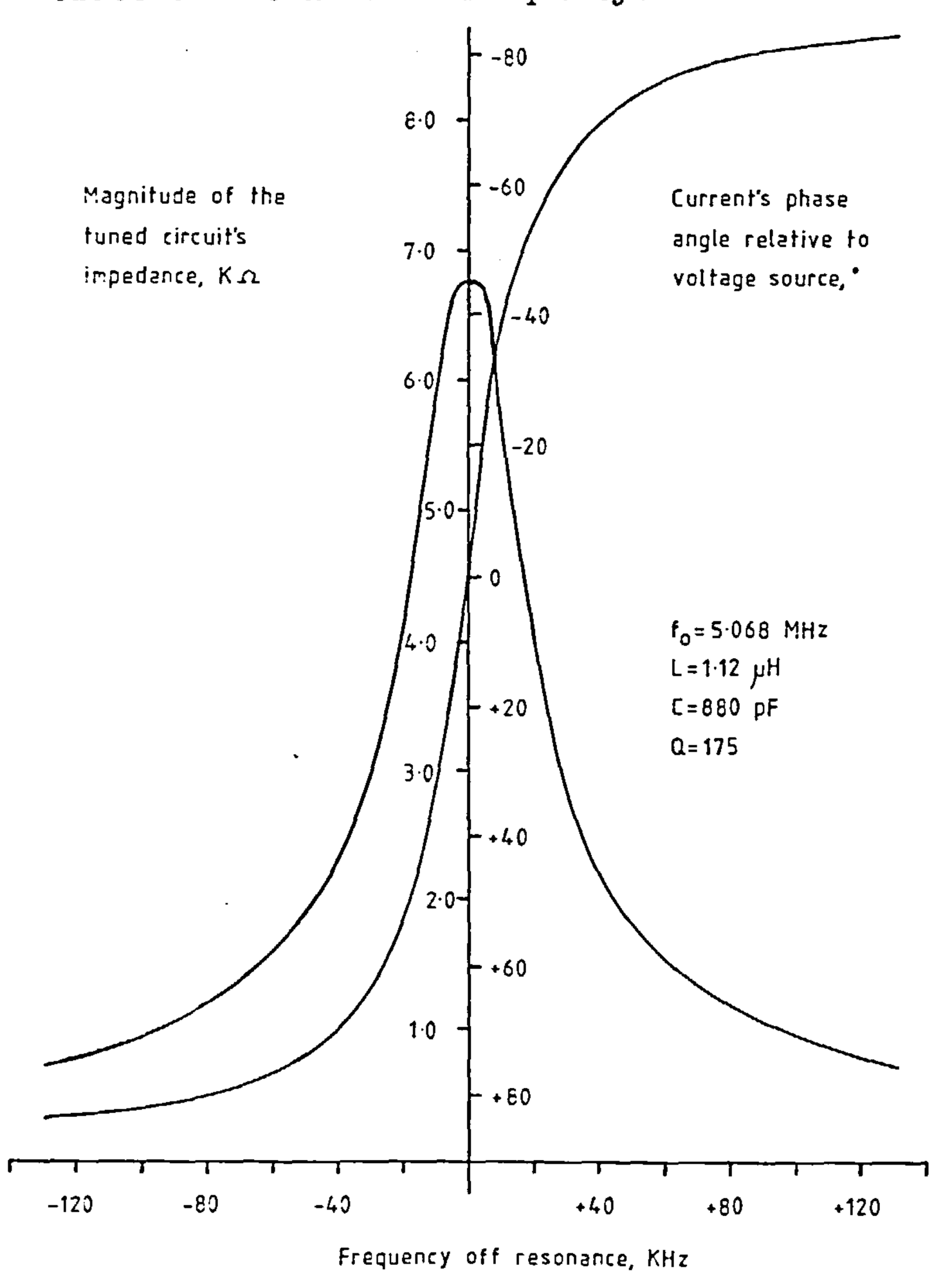

to the dissipative impedance of the coil at the tuned circuit's natural frequency w_o:

$$Q = \frac{w_o L}{R_s} \tag{2.33}$$

provided that R is large enough to be ignored - how large will be seen shortly. Q values of 100 to 300 may be attained over the frequency range 1MHz to 30MHz[15],[27,21].

The natural frequency of the tuned circuit is

$$w_o = \frac{1}{LC}\left[(1 - 1/Q^2) \right]^{0.5}, \tag{2.34}$$

this can be simplified to

$$w_o = (1/LC)^{0.5} \tag{2.35}$$

with an accuracy of better than 1% provided that $Q > 7$. The quality factor of the tuned circuit determines its bandwidth for

$$Q = w_o / \Delta w_o, \tag{2.36}$$

where $w_o \pm \Delta w_o/2$ are the half power frequencies.

The tuned circuit behaves as a real resistance

$$Z = Q w_o L \tag{2.37}$$

when the driving frequency w is equal to the natural frequency w_o; at this frequency the signal across the tuned circuit and the driving signal are in phase. It can now be seen that 2.33 is true if $R >> Q w_o L$. At any frequency other than w_o the phase of the driven relative to the driving current is

$$\phi = + \tan^{-1} (Q(1 - w^2 LC)), \tag{2.38}$$

and the impedance of the tuned circuit is reduced to

$$|Z| = Q w_o L \cos \phi \ . \tag{2.39}$$

These relations are plotted in figure 18 for the case L = 1.12uH, C = 880pF and Q = 175. These values belong to the tuned circuit and furnace arrangement of the final version of the new instrument.

Finally, many papers on n.m.r. do away with the coil's series resistance R_s and replace it with a parallel conductance G or a parallel resistance R_p. It is useful to know that

$$Q = \frac{w_o L}{R_s} = \frac{1}{G w_o L} = \frac{w_o L}{R_p} \quad . \qquad (2.40)$$

2.4.3 The Q meter and the Robinson oscillator

It can quickly be shown that of the four n.m.r. circuits mentioned in 2.4.1, the Q meter and the Robinson oscillator are the most promising candidates for development. A natural starting point is to ask how sensitive these circuits are. The issue is not clear cut, for these instruments are primarily used to detect the peaks in X" due to n.m.r., X' is of incidental interest to them and it is usually ignored in analyses of sensitivity. For the present application X' is of major importance, but the noise sources that limit the accuracy to which it can be measured are also those that pollute the signal for X". On this platform, the results obtained by Wind[28] can be applied. Wind found that the Q meter, the PKW oscillator and the Robinson oscillator are equally sensitive, and that all three are more sensitive than the marginal oscillator. The marginal oscillator is therefore dropped from further consideration. Wind preferred the Q meter and the Robinson oscillator because they are more predictable than the PKW oscillator. The Robinson oscillator has been established as the most popular n.m.r. circuit for some time[24] and it regularly appears in new designs[29,(30)]. Because of its popularity the Robinson oscillator is carried forward for further consideration. The Q meter is carried forward too.

As the Q meter is simplest to understand, it is examined first. Referring to figure 19[31] the points P and Q are not connected, and the current generator is independent of the input voltage. Assume that there is no sample in the coil initially. The tuned circuit is made to resonate with the applied a.c. current by adjusting the capacitor C. The tuned circuit then acts as a pure resistance so that the experimenter observes a signal level

$$V = (w_o LQ)i \ , \tag{2.41}$$

where $w_o = (LC)^{-0.5}$. When a sample is inserted into the coil the quality factor changes to Q_S. If X" is significant and X' is negligible, as would be the case for a paramagnetic sample in the region of nuclear magnetic resonance, the new quality factor is

$$Q_S = \frac{w_o L}{R_s + F w_o X'' L} \tag{2.42}$$

recalling equation 2.11. The decrease in the observed signal level is

$$\Delta V = w_o Li \ (Q_S - Q) \ , \tag{2.43}$$

or

$$\Delta V = w_o Li \left[\frac{w_o L}{R_s + F w_o X'' L} - \frac{w_o L}{R_s} \right] \tag{2.44}$$

using 2.42. In practice $F w_o X'' << R_s$ and so after some simplification

$$V = - QVFX''. \tag{2.45}$$

The change in signal level is directly proportional to X" if X' is not significant.

If a ferromagnetic sample is inserted into the coil the signal's amplitude is affected by X" and X' and the change in amplitude is not informative. A further complication is that in practice it is not possible to set the tuned circuit into exact resonance with the applied

Figure 19. The model used to describe the behaviour of the Q meter and the Robinson oscillator[31].

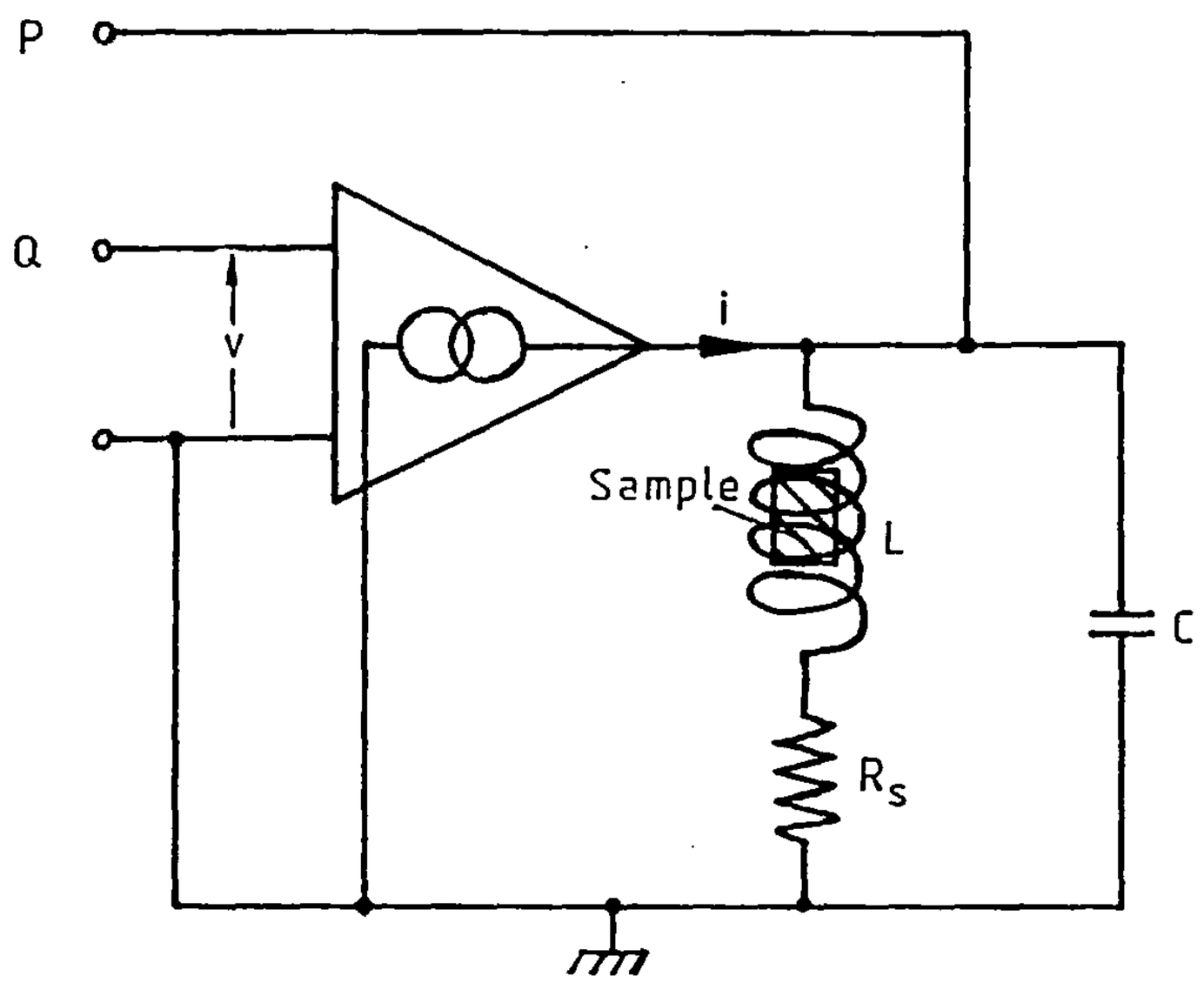

Figure 20. The Robinson oscillator[23].

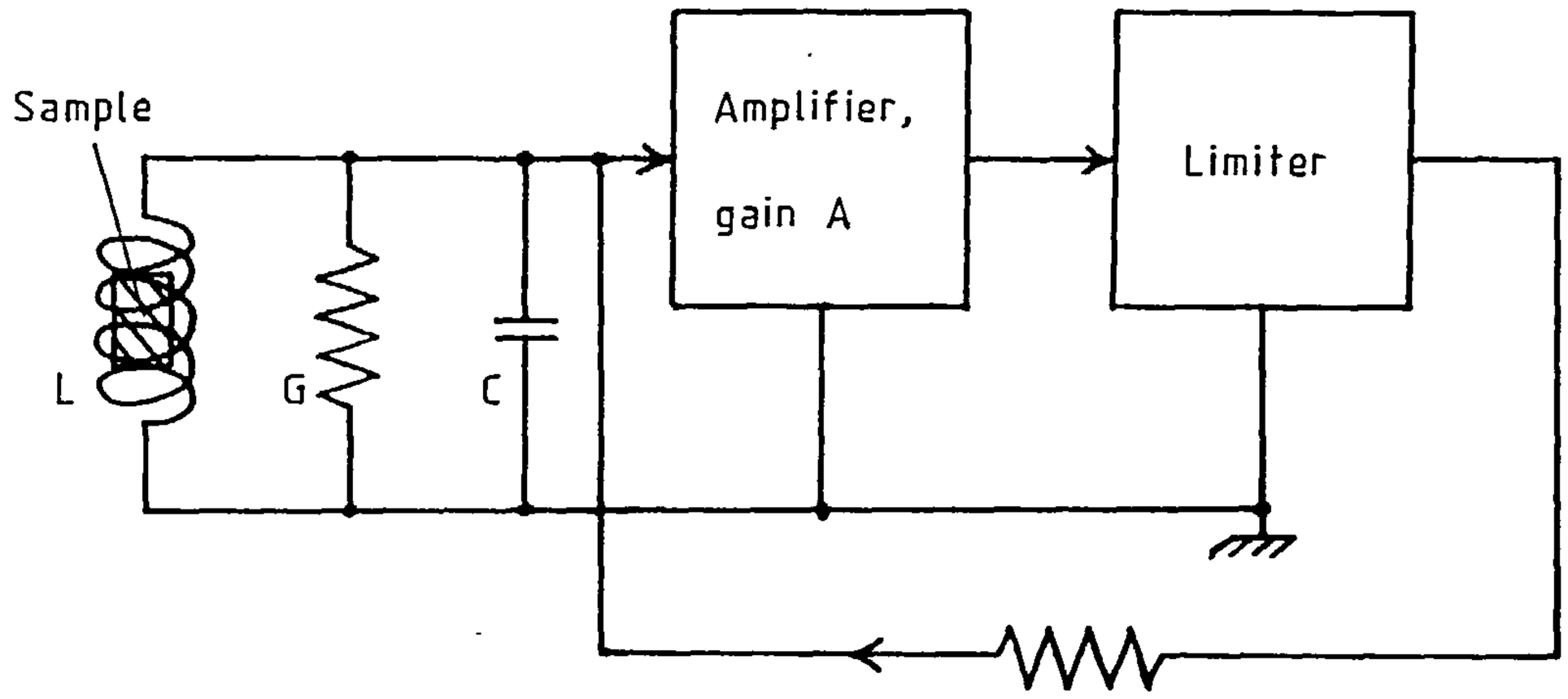

a. A block diagram

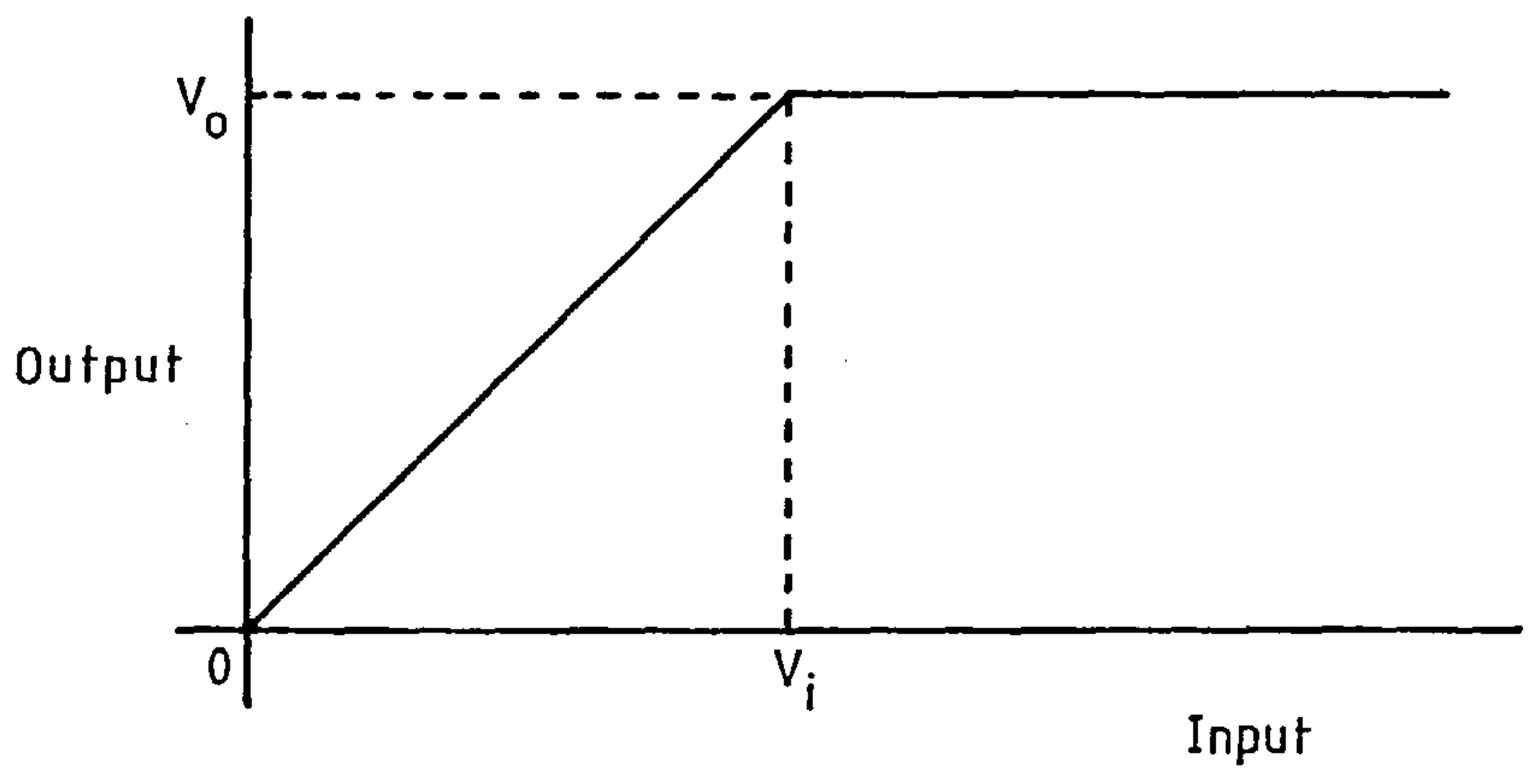

b. The ideal limiter characteristic

alternating current, there is therefore an inital phase difference ϕ between the voltage across the coil and the driving current. When a ferromagnetic sample is inserted into the coil, the change in the phase of V is[31]

$$d\phi = -FQ(w_o/w)(X''\tan\phi - X')\cos^2\phi , \qquad (2.46)$$

where w is the frequency of the driving current. The change in voltage across the coil is[31]

$$dV = -QVF(w_o/w)(X'' + X'\tan\phi)\cos^2\phi , \qquad (2.47)$$

where ϕ is now the sum of the phase differences due to the initial tuning error and the detuning effect of X'. These equations show that the signal observed using a Q meter is unavoidably a mixture of X' and X'' when the sample is ferromagnetic.

A block diagram of the Robinson oscillator is shown in figure 20a[23]. Notice that the series resistance of the coil R_s has been replaced by a parallel conductance G. The principle behind any electronic LC oscillator is to create a negative conductance - G' in parallel with G. Once started, oscillations will carry on forever if G-G' = 0.

The negative conductance has to be non-linear. If, at switch on, G - G' <0 the circuit will spontaneously oscillate and the signal level will grow. As the level rises, the electronic device generating the negative conductance starts to saturate and the average value of the negative conductance falls. When the average value of the negative conductance has dropped to the value of the real conductance the amplitude stabilises. The non-linearity therefore causes the oscillations to start, at a frequency $\approx w_o$, and then limits their growth. Most marginal oscillators allow one transistor to do both jobs, these are classified as Van der Pol oscillators which are analysed in detail by Strauss[32,721].

The Robinson oscillator separates the start up and limiting functions

into two blocks. The limiter's characteristic is shown in figure 20b, it has a gain of V_o/V_i up to limiting. Provided that the total voltage gain is greater than the voltage division of the feedback resistor and tuned circuit, that is if

$$AV_o/V_i > GR_f \quad , \tag{2.48}$$

oscillations will occur. The amplitude of oscillation will be

$$V = \frac{4}{\pi} \frac{V_o}{GR_f} \quad . \tag{2.49}$$

A simple theory of operation dealing with ideal limiters and amplifiers leads to the conclusion that any change in the amplitude of oscillation is due to X", whilst any change in the frequency of oscillation is due to X'. Real amplifiers and limiters have frequency dependent gains and phase shifts; Hughes and Smith[31] have generalised the theory of oscillators to account for this. Referring to figure 19, points P and Q are now connected. An input to the current generator of v = Vexp(jwt) leads to an output of i = I exp (j(wt + ϕ)). ϕ is frequency dependent and allows for delays in the amplifier and limiter. I is also frequency dependent. Their results for the changes in frequency and amplitude due to a ferromagnetic sample are:

$$dw = \frac{w}{2} F \ (X'' \tan \phi - X') \quad , \tag{2.50}$$

and

$$dV = -QVF(X'' + X' \ c/2Q) \quad , \tag{2.51}$$

where c is a constant that is roughly equal to one.

Once again, the observable signals are a mixture of X' and X". It is worth showing how important ϕ is in 2.50. If both the amplifier and limiter have bandwidths of 100 MHz they will each delay a 5 MHz signal by 0.05 radians, the total delay is therefore 0.1 radians or 3.2 ns.

Equation 2.50 should then be written

$$dw = \frac{w}{2} F\ (0.1X'' - X')\ .$$

In fact, the situation is worse than this because the calculation ignored the excess phase shift due to the non-linear behaviour of the limiter.

2.5 THE PRINCIPLE OF THE NEW INSTRUMENT

It has been seen that neither the Q meter nor the Robinson oscillator yield signals directly proportional to X' and X". In an unmodified form, the Robinson oscillator is the most useful of the two when dealing with ferromagnetic samples. However, it is the Q meter that is adopted and changed.

There are three reasons for adopting the Q meter. The first is that the unwanted electronic phase shifts are frequency dependent. The Q meter at least keeps the phase shifts constant by operating at a fixed frequency. Next, the Q meter has not been fully exploited in the past; the information contained in the phase difference between the voltage across the coil and the driving current has been ignored. Finally, the Q meter can be changed to overcome most of its disadvantages.

The phase difference between the driving and driven signals is only zero when the tuned circuit's natural frequency is exactly equal to the driving frequency. It is proposed to measure this phase difference and to use it as the error signal in a negative feedback system which keeps the tuned circuit in exact resonance despite changes in X'.

Recalling 2.46

$$d\phi = -FQ(w_o/w)(X'' \tan \phi - X') \cos^2 \phi,$$

the feedback will ensure that $w_o = w$, $\tan \phi = 0$ and $\cos^2 \phi = 1$, therefore

$$d\phi = FQX' \quad . \qquad (2.52)$$

The phase difference is proportional to X' with no admixture of X". The value of $d\phi$ will be represented by the magnitude of the feedback voltage

necessary to reduce dØ to zero. If the feedback system is linear, then the feedback voltage will be linearly proportional to X'.

Because the tuned circuit is maintained at resonance any change in amplitude is due to the change in Q alone. Recalling 2.43

$$\Delta V = w_o Li\ (Q_S - Q) \quad ,$$

so

$$\Delta V = w_o Li \left[\frac{w_o(L + \Delta L)}{R + \Delta R} - \frac{w_o L}{R} \right] . \qquad (2.53)$$

Equations 2.10 and 2.11 are now put into 2.53 to give

$$\Delta V = w_o Li \left[\frac{w_o L(1 + FX')}{R + w_o LFX"} - \frac{w_o L}{R} \right] \qquad (2.54)$$

$$= Qw_o Li \left[\frac{1 + FX'}{1 + FQX"} - 1 \right] , \qquad (2.55)$$

so

$$\Delta V = FV \left[\frac{X' - QX"}{1 + FQX"} \right] . \qquad (2.56)$$

Under most circumstances FQX"<<1 so that

$$\Delta V = FV\ (X' - QX") \ . \qquad (2.57)$$

Comparing equations 2.57 and 2.51 reveals that the new instrument will be two times worse than the Robinson oscillator in allowing X' to affect the signal for X". This is a price worth paying, for equations 2.52 and 2.50 show that the new instrument can truly measure X' whereas the Robinson oscillator cannot.

Equation 2.52 is only valid if the circuitry used to measure the phase difference introduces no extra phase shifts. By making the circuitry symmetric, any delay affecting the signal from the coil will also affect the reference signal from the driving oscillator. The two therefore cancel and so 2.52 is valid. Similarly, any phase noise in the driving oscillator will be common to the reference and the tuned

circuit signals and will cancel out at the phase detector.

Finally, it should be remembered that X' and X" refer to the real and imaginary volume susceptibility. For convenience in typing, no distinction has been made between the intrinsic and the apparent susceptibility. When the two are appreciably different X' and X" should be replaced by X_a' and X_a'' in the formulae above.

2.6 THE CHOICE OF OPERATING FREQUENCY

It has been stated a number of times that the operating frequency is to be 5MHz. A number of facts need to be considered to justify this choice.

X' can be most accurately measured at low frequencies, say <10KHz, where the complicating effects of rotation relaxation and wall resonance/relaxation can be ignored. However, X" is largest and most easily measured at high frequencies, say > 50 MHz. As both X' and X" are to be found some compromise has to be made in the operating frequency.

The new instrument is least sensitive to X' in equation 2.57 if the Q is large. It will be seen in the next chapter that the signal to noise ratio is greatest if the natural Q, as defined in 2.33, is large. The highest quality factors for single layered, air cored coils are usually obtained at frequencies between 1 and 20MHz[15]. The operating frequency must therefore lie between these values.

Much of the attraction of Stephenson and de Sa's bridge[17] lay in the amalgamation of the furnace and sample coil. The metallic furnace winding is bound to degrade the Q of the coil. To minimise this effect, the operating frequency should be closer to 1MHz than 20MHz.

Finally, the experience of previous experimenters in this field can be called upon. de Sa[25] worked at 5MHz, Reidi[26] worked between 1MHz and 10MHz, Petersen[19] worked at 8MHz and Markert et al[18] worked

at 10MHz - all of these people met with some success.

The evidence available indicates that 5MHz is a reasonable choice of operating frequency.

CHAPTER 3

THE FIRST VERSION OF AN INSTRUMENT TO MEASURE THE TEMPERATURE DEPENDENCE OF INITIAL SUSCEPTIBILITY

3.1 INTRODUCTION

Chapters 1 and 2 have largely concentrated on the physics underlying the measurement of susceptibility. This chapter and the two that follow are concerned with the design, performance and development of the new instrument. The purpose of this chapter is to show that the principle described in section 2.5 works and to point to a more sophisticated embodiment of the same priciple.

Negative feedback plays an important part in the instrument and section 3.2 mentions some of its properties. Armed with this information, the description and analysis in sections 3.3 and 3.4 will be quite clear. Subsection 3.5 presents some results and compares them with the analysis and with a trusted experimental standard. Section 3.6 looks at noise in the instrument.

A research paper on the first version of the instrument has been published in the Journal of Physics E: Scientific Instruments[33]. A paper on the intermediate version of the instrument, which is not described in this thesis, was presented at the 1981 United Kingdom Geophysical Assembly Conference held at the University of Cambridge.

3.2 A SHORT NOTE ON NEGATIVE FEEDBACK

Jones[34] has written a useful article on feedback in instrument design and Shinners[35] can be turned to for a full account of control systems theory.

The feedback loop illustrated in figure 21 is the most primitive possible, yet it has some important properties. The blocks labelled G(s) and H(s) might each be a large subsystem with internal feedback loops, or just a piece of wire. Whatever the blocks contain, the closed

Figure 21. A single loop feedback system

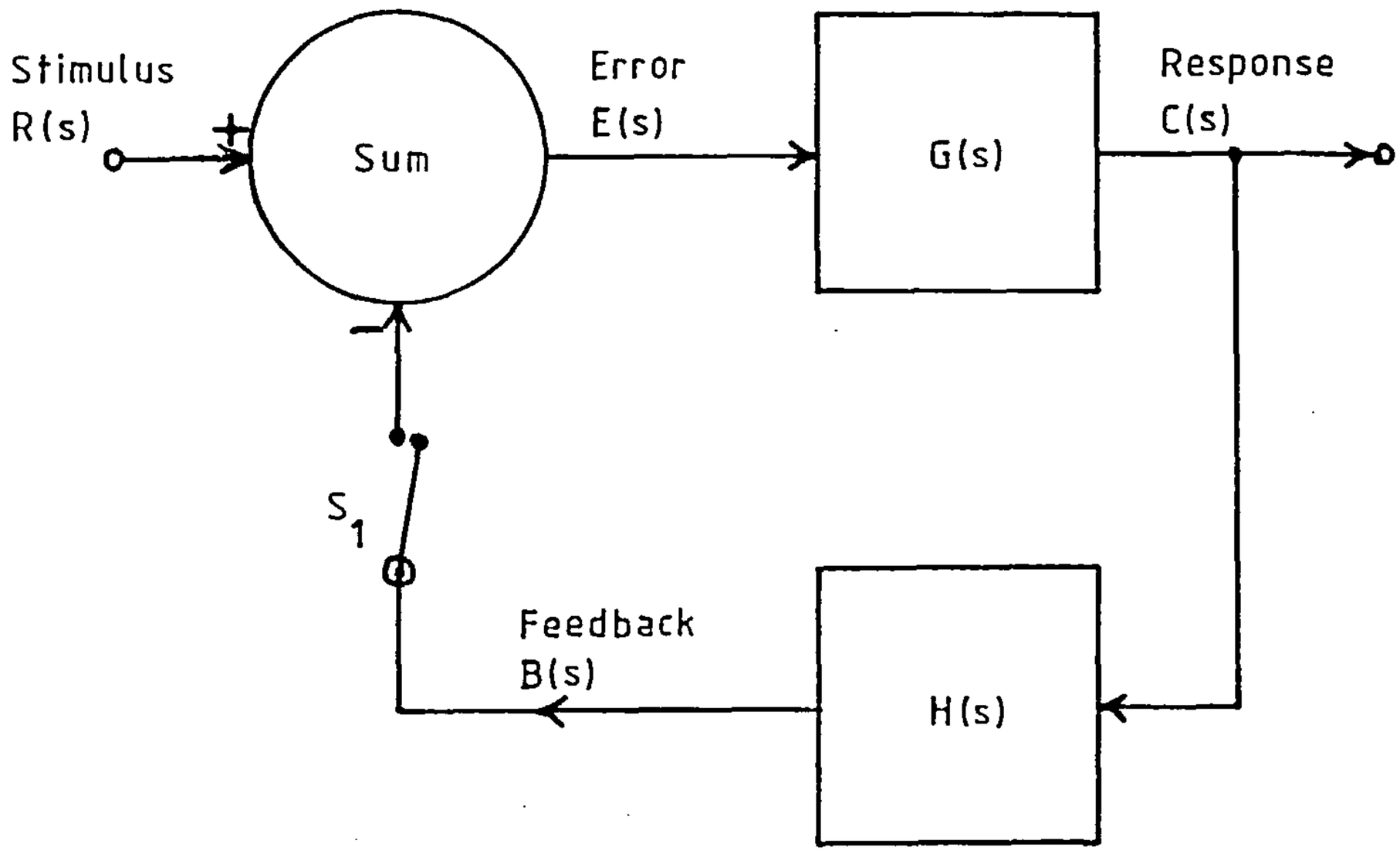

Figure 22. A block diagram of the first version of the instrument. The numbers are explained in the text.

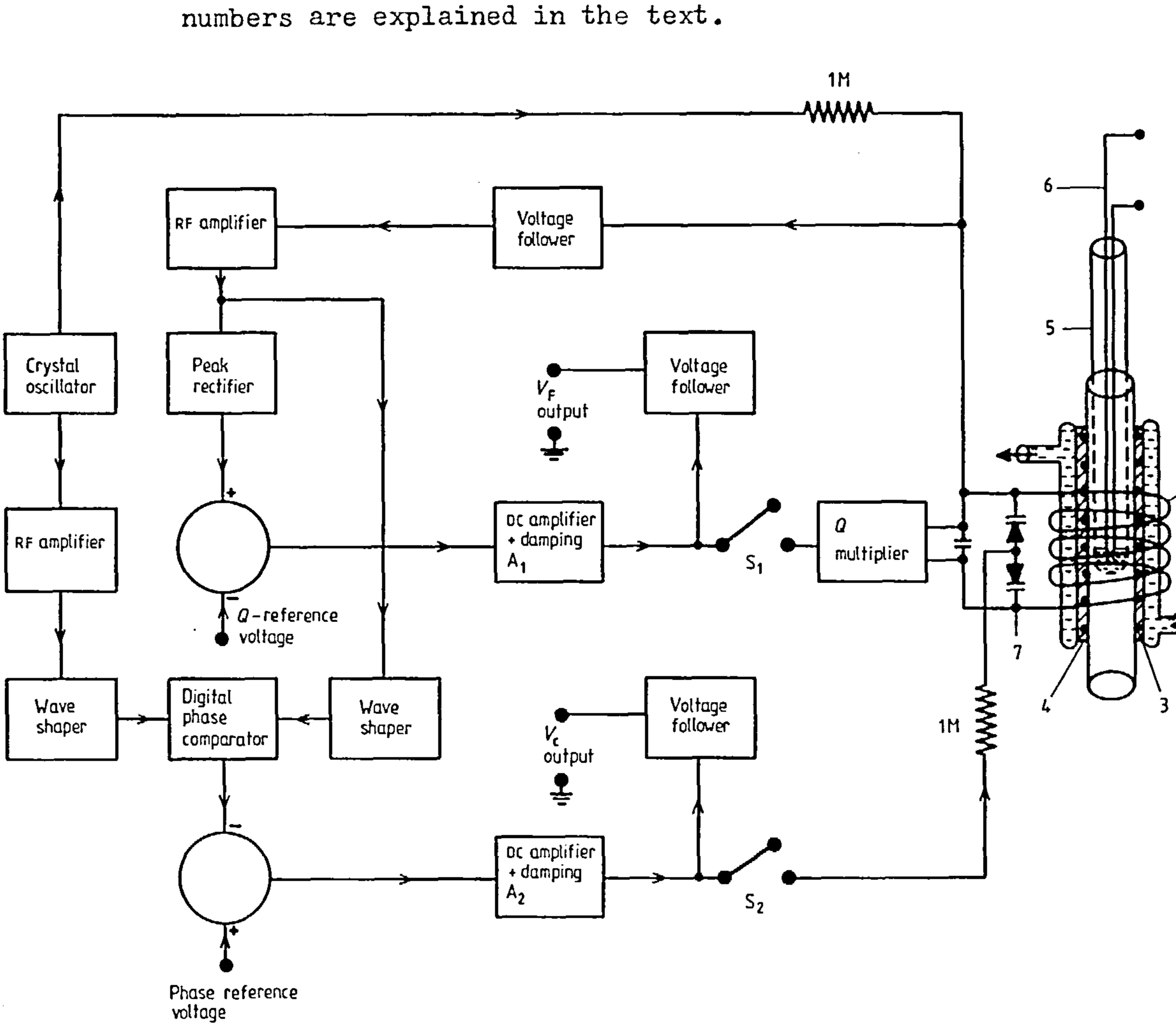

loop transfer function of the feedback system is

$$\frac{C(s)}{R(s)} = \frac{G(s)}{1 + G(s)H(s)} \qquad (3.1)$$

where s is the Laplace transform variable

$$s = \sigma + jw \ . \qquad (3.2)$$

Shinners[35,22] describes the properties of Laplace transforms and the advantages of using them. Referring to figure 21, when the switch S_1 is opened the open loop transfer function is

$$\frac{B(s)}{R(s)} = G(s)H(s) \ . \qquad (3.3)$$

When S_1 is closed a negative feedback loop is formed. The negative feedback loop tries to make the feedback signal B(s) equal to the input signal R(s) so that the error signal E(s) is zero. If the error is to be kept small the open loop gain has to be made large; when this is so the closed loop transfer function is

$$\frac{C(s)}{R(s)} \approx \frac{1}{H(s)} \ . \qquad (3.4)$$

This important result shows that the character of the direct transfer function G(s) is not reflected in the output C(s) when the open loop gain is large. Therefore, if G(s) is a non-linear transducer that measures R(s), a linear feedback device H(s) will force the output C(s) to be linearly proportional to R(s) whatever the characteristic of G(s). The problem with negative feedback is that if the signal delay around the loop is too large the system can be unstable and useless. The stability of the system can be predicted by studying the roots of the characteristic equation:

$$1 + G(s)\,H(s) = 0 \ . \qquad (3.5)$$

A convenient practical approach is to break the loop at S_1 and plot the amplitude and phase of G(jw)H(jw) using a signal generator, a voltmeter and a phase meter. This is known as the Bode Diagram technique

and it is fully described by Shinners[35,213].

3.3 A DESCRIPTION OF THE CIRCUIT

Two feedback loops are used in the first version of the instrument. One of them keeps the natural frequency of the tuned circuit constant by means of a voltage variable capacitance, the purpose of this was explained in section 2.5. The other loop maintains an artificially high Q using a voltage controlled negative resistance. The effects of this are to minimise the error due to X' in equation 2.57 and to keep the signals' amplitudes within the system constant.

The structure of the instrument is shown in figure 22. A 5.0 MHz crystal oscillator drives the resonant circuit (1) through a 1 MΩ isolating resistance. The oscillator, a Salford Electrical Instruments type QC1223S, has a stable output amplitude and a frequency stability of within $\pm$ 2 p.p.m. over a temperature range of $0^{o}C$-$55^{o}C$. The single layer sample coil is wound from silver wire and it has an inductance of 1.3μH. Inside the coil is a water jacket (2) and a furnace (3). The furnace is made of non-magnetic nichrome V wire which is bifilar wound onto a cylindrical quartz former. This wire is 0.122 mm in diameter, the narrowest available gauge is used so that the eddy current losses in the furnace are minimised. The water jacket and Refrasil lagging (4) thermally and electrically isolate the sample coil from the furnace. The sample can be heated in its quartz holder (5) to over $700^{o}C$. The sample's temperature is monitored by a non-magnetic Pt-13%Pt/Rh thermocouple (6) against an ice/water reference. The Q multiplier[36] generates enough negative resistance to produce an overall Q of 1.1×10^{3}; more will be said about the Q multiplier later.

An f.e.t. voltage follower passes the signal from the tuned circuit to a Plessey SL541B high slew rate operational amplifier. The signal then divides to travel along two separate feedback paths.

The Q maintaining loop measures the amplitude of the signal coming from the amplifier with a peak rectifier. The DC output of the peak rectifier represents the Q of the tuned circuit. A fixed reference voltage that represents the Q in the absence of a sample is subtracted from the rectifier's output. The difference is amplified and fed to the voltage controlled negative resistance that is generated by the Q multiplier. The feedback is arranged such that a decrease in the output of the peak rectifier, through sample losses, causes an increase in negative resistance. The increase in negative resistance causes an increase in Q which pushes the output of the peak rectifier back to its old level.

The phase control loop requires two signal inputs. The first of these is the amplified signal from the tuned circuit, this is passed through a limiter and thence to the input of a phase detector. The second signal is an amplified and limited reference from the crystal oscillator. The phase detector turns the relative phases of the two signals into a proportionate DC output. The detector's output is subtracted from a DC reference signal that represents the initial in phase condition. The difference is amplified and passed to a voltage variable capacitance formed from two varicap diodes. The feedback is arranged such that an increase in inductance, caused by X', is compensated by a decrease in capacitance, so keeping the natural frequency fixed.

The two feedback paths are closed using switches S_1 and S_2 (figure 22). The loops' response times are adjusted such that the phase loop acts more quickly than the Q loop for this minimises the interaction between them.

A potential weakness of this system is its poor resistance to mechanical vibration. Vibration can create small changes in the parasitic capacities of the leads and the sample coil, it can also alter the inductance of the sample coil by causing small changes in its dimensions.

To fight this problem the shielded oscillator, tuned circuit and f.e.t. voltage follower are mounted close together on a rigid platform. The platform is contained within a heavy metal case that sits on foam rubber. The platform is thus decoupled from the environment. The sample coil is made rigid by gluing it to its glass former. When the instrument is in use no problems are experienced with mechanical vibrations.

3.4 CIRCUIT ANALYSIS

3.4.1 The phase loop

The phase loop is shown as a feedback system in figure 23. The system's output is ΔV_p volts in response to the system's input X'. The purpose of this subsection is to analytically connect X' to ΔV_p.

The noise sources n_1, n_2 and n_3 are set to zero and S_1 is opened. X' is coupled by the filling factor F to the inductance L. The fractional increase in inductance is $\Delta L/L = FX'$ and this decreases the natural resonant frequency of the tuned circuit by

$$\frac{\Delta w_o}{w_o} = -\frac{1}{2}\frac{\Delta L}{L} \qquad (3.6)$$

$$= -\frac{1}{2} FX' \quad . \qquad (3.7)$$

The tuned circuit's gain converts the change in natural frequency into a phase shift, the phase shift can then be measured against the crystal oscillator. The gain of the tuned circuit $\Delta \phi / \Delta w_o$ can be calculated in the following way:

$$\frac{\Delta \phi}{\Delta w} \approx \frac{d\phi}{dw}$$

$$= \left[\frac{dw}{d\phi}\right]^{-1} \quad . \qquad (3.8)$$

Using equation 2.38

$$w = \left[\frac{1}{LC}\left[1 - \frac{\tan \phi}{Q}\right]\right]^{0.5} \quad , \qquad (3.9)$$

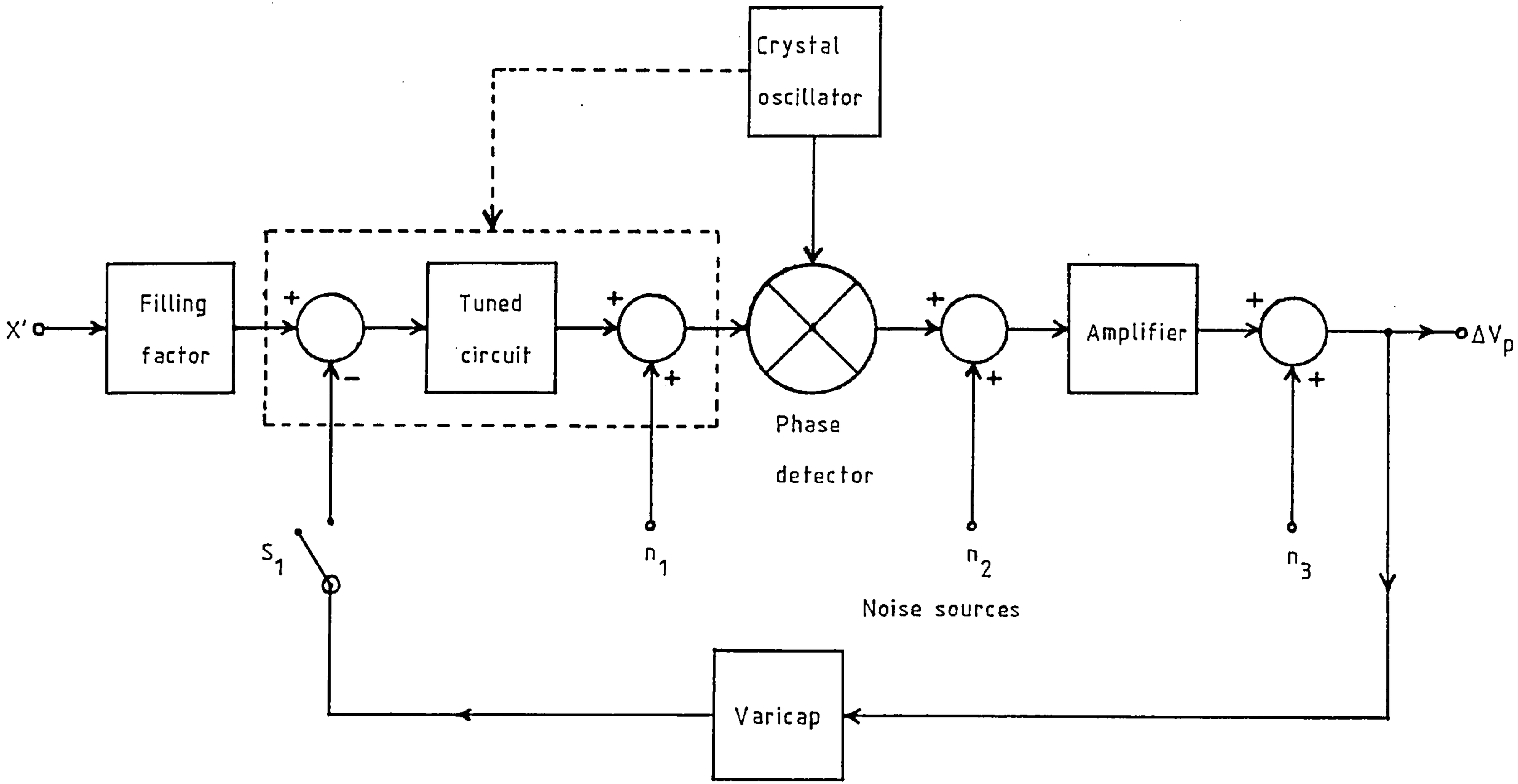

Figure 23. The phase control subsystem.

so

$$\frac{dw}{d\phi} = \frac{w}{2Q} \sec^2\phi. \qquad (3.10)$$

Provided that the change in natural frequency is small

$$\frac{dw}{d\phi} = \frac{w_o}{2Q} \ , \qquad (3.11)$$

and the gain of the tuned circuit is

$$\frac{\Delta\phi}{\Delta w} = \frac{2Q}{w_o} \ . \qquad (3.12)$$

From 3.7 and 3.12 the open loop phase shift due to X' is

$$\Delta\phi = -FQX' \ . \qquad (3.13)$$

The phase shift is measured by a phase detector having a sensitivity of K, $Vrad^{-1}$. The low frequency (< 1Hz) output of the phase detector is amplified by A and passed to the varicaps which have a conversion coefficient of u, V^{-1}. When S_1 is open

$$\Delta V_p = - QFKAX' \qquad (3.14)$$

and the open loop gain is -QKAu.

By analogy with 3.1 the control system's closed loop gain can immediately be written down as

$$\frac{\Delta V_p}{FX'} = \frac{-QKA}{1 - QKAu} \ . \qquad (3.15)$$

The open loop gain is arranged to be much greater than one so that

$$\frac{\Delta V_p}{X'} \approx \frac{F}{u} \ . \qquad (3.16)$$

A result for u is needed to complete this analysis. The depletion capacitance of a varicap is a non-linear function of the applied reverse bias voltage. The equivalent circuit of a varicap is shown in figure 24. The junction capacitance C_j is associated with parasitic resistances R_s and R_p. R_s is usually $< 1\,\Omega$ whilst R_p is normally $> 10^8\,\Omega$.

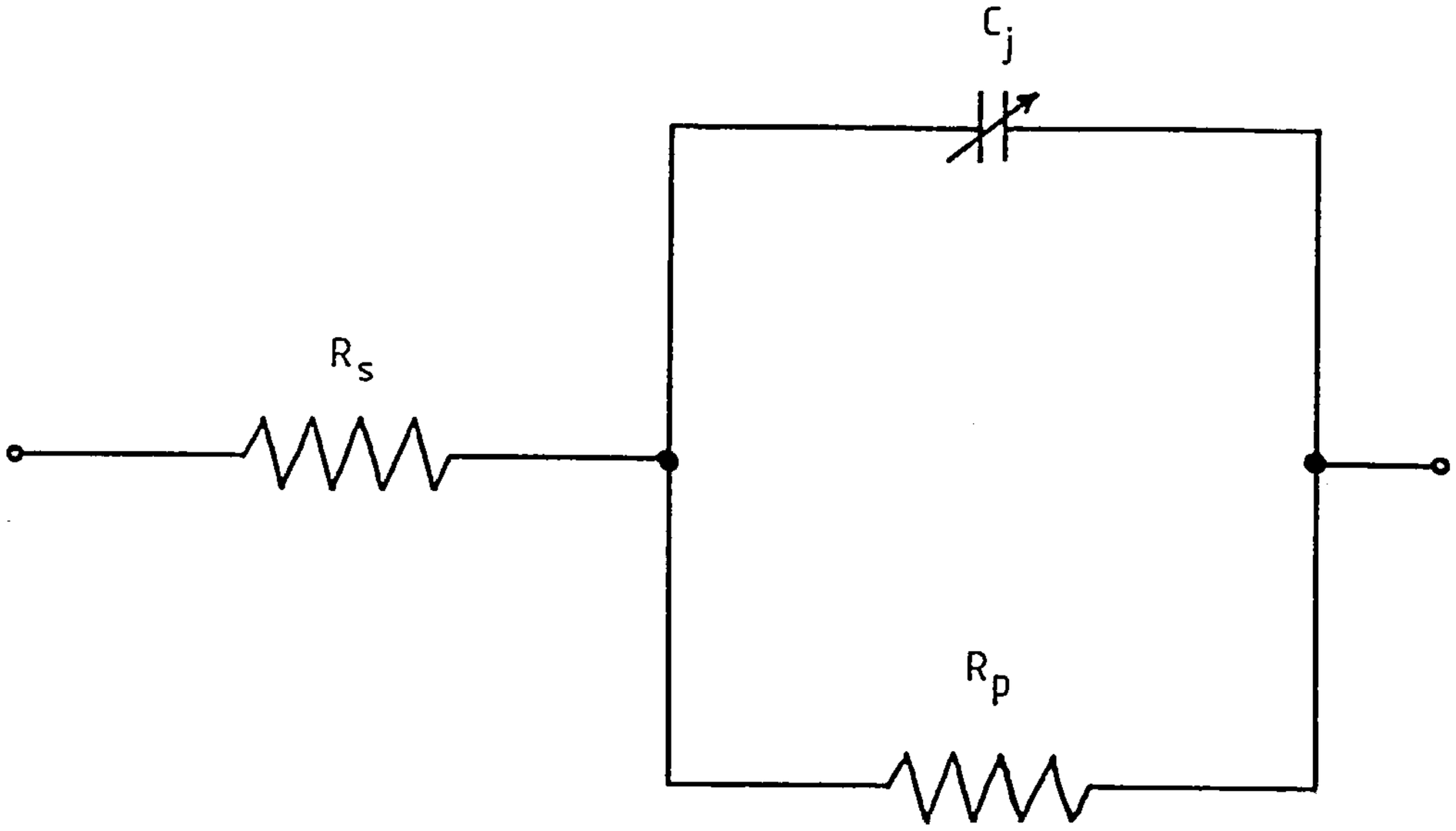

Figure 24. The equivalent circuit of a reverse biased varicap diode.

Both resistances decrease in importance as the reverse bias voltage V_r increases, they are ignored from now on. The behaviour of C_j is given by(37)

$$C_j(V_r) = \frac{C_{jo}}{(1 - V_r/\phi)^m}, \qquad (3.17)$$

where C_{jo} is the capacitance at zero bias, ϕ is a built in barrier potential and m depends on the nature of the p-n junction. For an abrupt junction m = 0.5 and for a linearly graded junction m = 0.333. Note that V_r is negative for reverse bias and positive for forward bias. A good estimate of ϕ is 0.7V. The form of 3.17 is now simplied to

$$C_j(V_c) = \frac{a}{V_c^m}, \qquad (3.18)$$

where "a" is a constant of proportionality and $V_c = (0.7 - V_r)$.

The feedback matches the fractional increase in inductance $\Delta L/L$ with a fractional decrease in capacitance $-\Delta C/C$ so keeping the product LC constant provided the changes are small. Clearly

$$\frac{\Delta C}{C} = u\,\Delta V_c, \qquad (3.19)$$

therefore

$$u(V_c) = \frac{1}{C}\frac{dC_j}{dV_c}. \qquad (3.20)$$

Putting 3.18 into 3.20 produces

$$u(V_c) = -\frac{m}{C}\frac{a}{V_c^{(1+m)}}. \qquad (3.21)$$

In the absence of a sample $V_c = (0.7-V_p)$, in the presence of a sample $V_c = (0.7 - (V_p + \Delta V_p))$. Provided that $\Delta V_p \ll V_p$, u is nearly constant.

Equation 3.16 can now be filled out,

$$X' = - \left[\frac{m}{c} \frac{a}{V_c^{(1+m)}} \right] \left[\frac{1}{F} \right] \Delta V_p \quad . \qquad (3.22)$$

It should be recalled that $V_c = (0.7 - V_p)$ where V_p is a fixed offset voltage. ΔV_p is proportional to X' to within 4.3% providing $\Delta V_p << 0.1 V_c$. The offset voltage V_p can be removed using a differential amplifier so that ΔV_p may be directly chart recorded.

3.4.2 The Q loop

With no sample the offset at the Q loop's output is V_Q, with a sample present the output is $V_Q + \Delta V_Q$. This subsection shows how ΔV_Q is related to X".

Figure 25 is a block diagram of the Q loop. S_1 is open and the noise sources n_1 to n_4 are set to zero. X" causes an increase in the coil's resistance of $\Delta R_s = FX"w_oL$, the fractional change in resistance is

$$\frac{\Delta R_s}{R_s} = FQX" \quad , \qquad (3.23)$$

where Q is the initial quality factor. Equation 2.57 shows that the resulting change in voltage is

$$\Delta V \approx FVQX" \quad , \qquad (3.24)$$

where V is the voltage across the coil in the absence of a sample. X' does affect 3.24, but its contribution is Q times less than that of X". As the Q has been multiplied to 1.1×10^3 the effect of X' is ignored. Equation 3.24 assumes that the tuned circuit is driven by a current source. This is true in practice because the isolation resistance between the crystal oscillator and the tuned circuit is much greater than Qw_oL; see figure 22.

The signal across the coil is pre-amplified before peak detection. For large enough input levels (> 2V peak to peak) the peak detector's

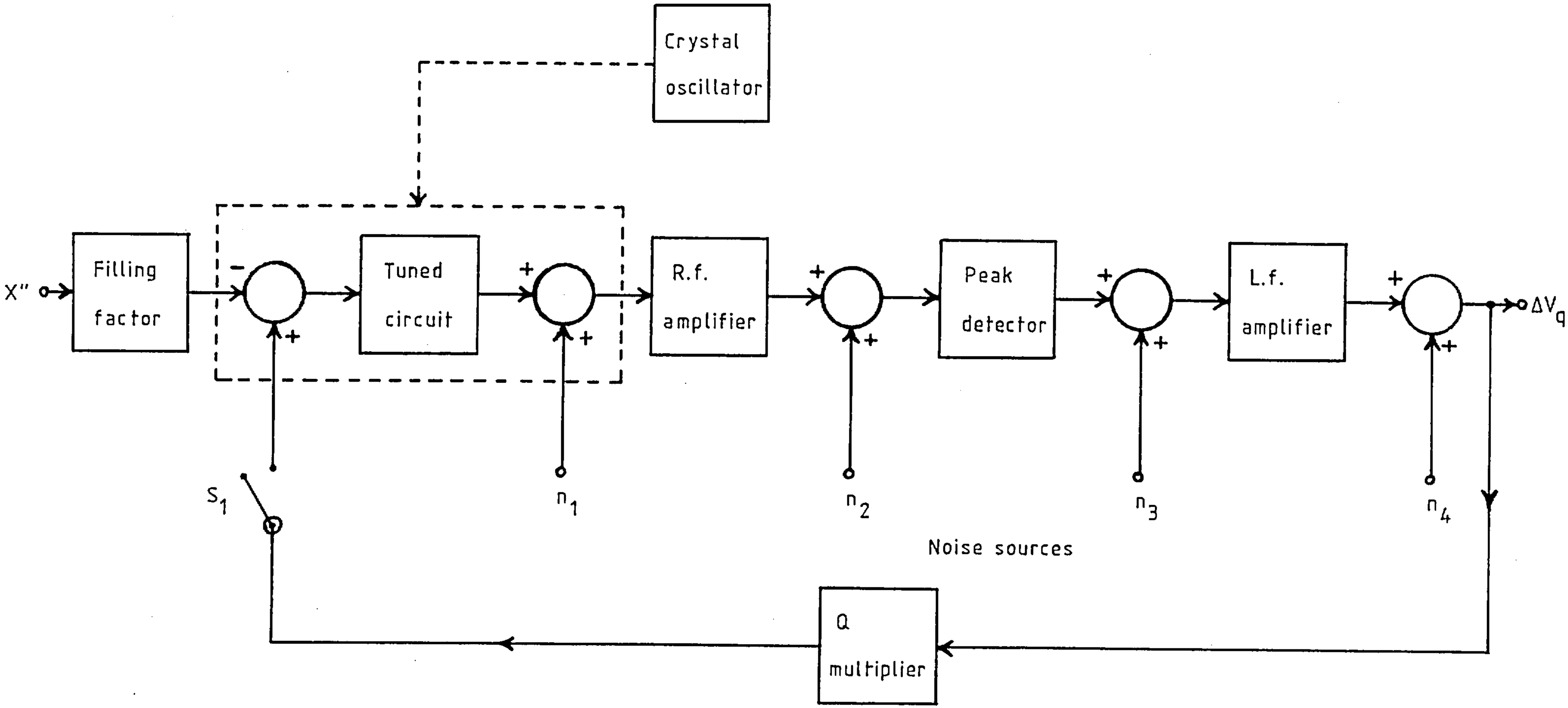

Figure 25. The Q control subsystem.

output responds linearly to changes in input amplitude. From figure 25, when S_1 is open

$$\Delta V_Q = FVQX"A_1DA_2 , \tag{3.25}$$

where D is the gain of the peak detector. The gain of the Q multiplier is

$$Z = \frac{1}{Q} \frac{dQ}{dV_Q} \tag{3.26}$$

and the open loop gain is VA_1DA_2Z.

When S_1 is shut the closed loop gain can be written down from 3.4 to yield

$$X" = \frac{1}{FQ^2} \frac{dQ}{dV_Q} \Delta V_Q . \tag{3.27}$$

It was found experimentally that dQ/dV_Q was constant over a wide operating range, ΔV_Q was therefore proportional to X".

The action of the voltage controlled Q multiplier merits further attention. It will first be shown how a negative resistance is generated, then how the resistance affects the Q and finally how the resistance may be varied. Figure 26a is a model of the Q multiplier block and tuned circuit after the varicaps and isolation resistance have been omitted. The active element has infinite input impedance and zero output impedance, it has a large current gain and unity voltage gain. In reality, the active element is a darlington pair connected as an emitter follower. The resistance connected to the output emitter terminal is split into two to form a voltage divider. The divider ratio can be controlled because one of the resistors, R_v, is voltage variable. Positive feedback is taken from the divider to the tuned circuit through R_f. The tuned circuit capacitance is formed from two capacitors in series.

Figure 26. The voltage controlled Q multiplier

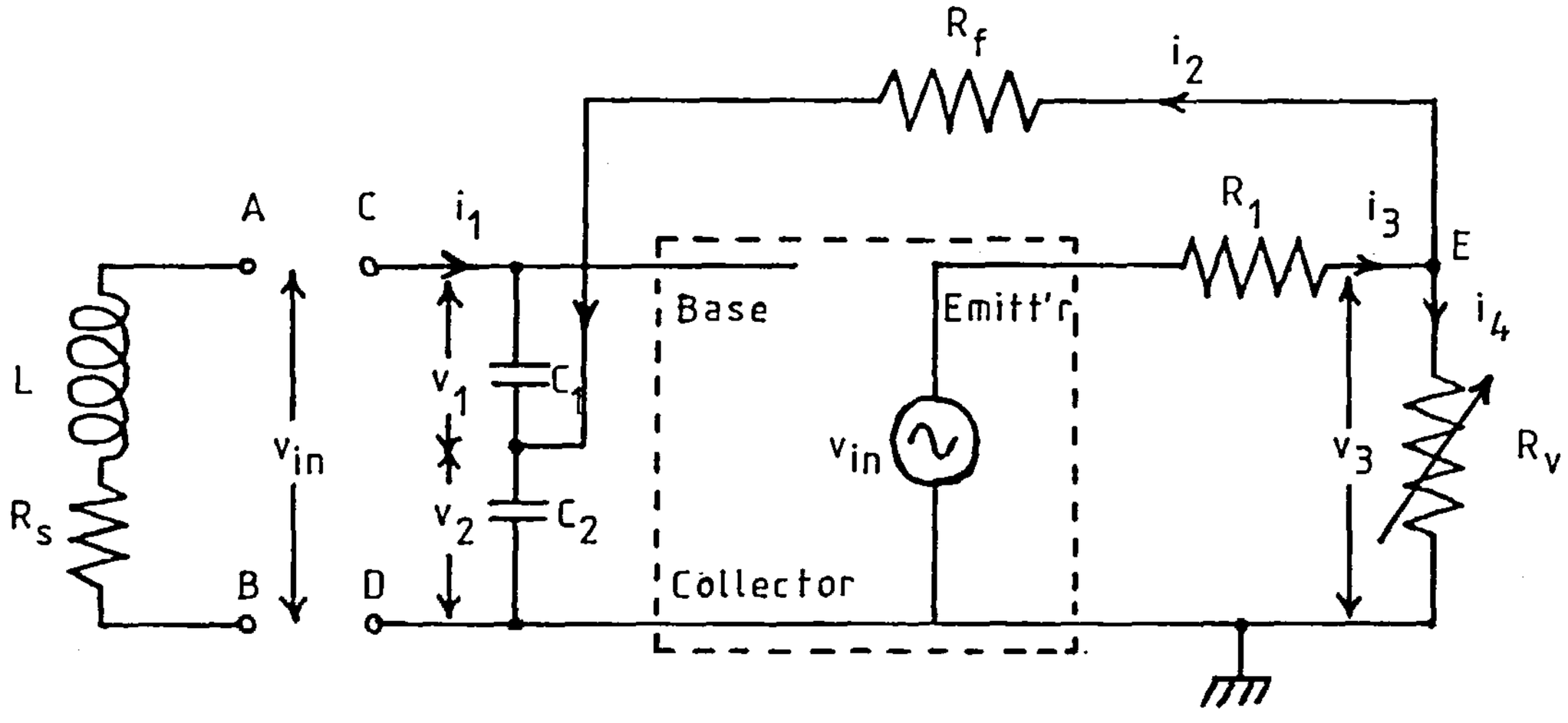

a. A model

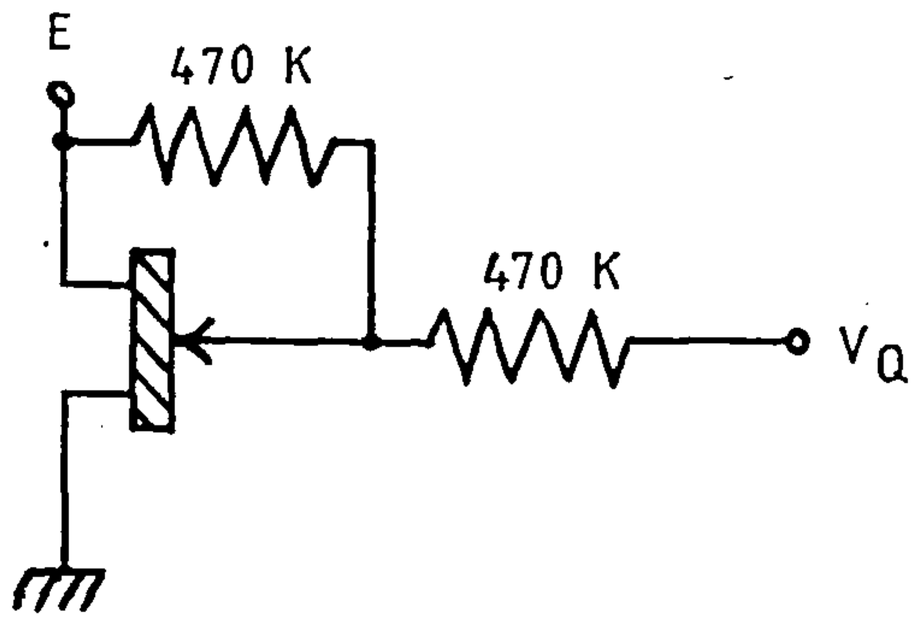

b. The voltage variable resistance R_v.

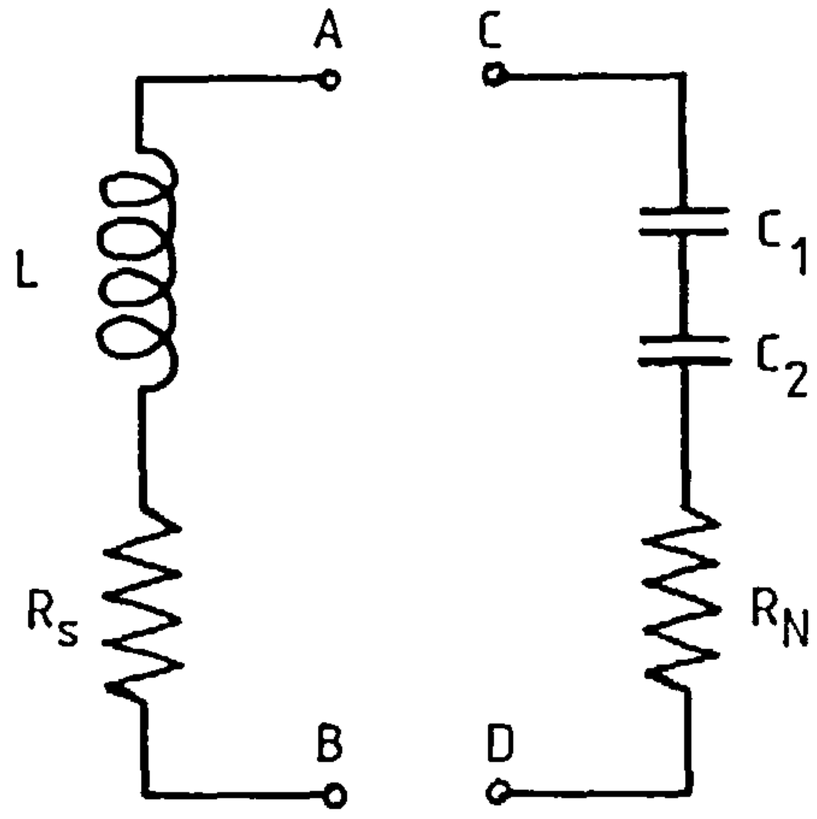

c. An equivalent circuit for the Q multiplier.

A diagram of the voltage variable resistance is shown in figure 26b. As the gate voltage applied to the n-channel f.e.t. is decreased the channel resistance rises. The two 470KΩ resistances apply feedback from the drain to gate so that the dependence of the channel resistance on the drain source voltage is minimised[38,5] .

An alternating voltage of angular frequency w with an amplitude v_{in} is applied to the terminals C and D. An alternating current i_1 is generated and the impedance presented to the terminals A and B is

$$Z_{in} = \frac{v_{in}}{i_1} = \frac{v_1 + v_2}{i_1} \quad . \tag{3.28}$$

As

$$v_1 = \frac{i_1}{jwC_1} \tag{3.29}$$

and

$$v_2 = \frac{i_1 + i_2}{jwC_2} , \tag{3.30}$$

it can be seen that

$$Z_{in} = \frac{1}{jwC_1} + \frac{1}{jwC_2} + \frac{i_2}{i_1}\frac{1}{jwC_2} . \tag{3.31}$$

Using 3.29 in 3.31 yields

$$Z_{in} = \frac{1}{jwC_1} + \frac{1}{jwC_2} - \frac{i_2}{v_1}\frac{1}{w^2C_1C_2} . \tag{3.32}$$

The last term in 3.32 is the negative resistance R_N that is needed for Q multiplication. Equation 3.32 also shows that the equivalent circuit of the Q multiplier is C_1, C_2 and R_N in series; this is drawn in figure 26c. The effective Q of the tuned circuit is

$$Q_{eff} = \frac{w_o L}{R_s + R_N} , \tag{3.33}$$

where R_s is the series DC resistance of the inductance and R_N is negative. The Q multiplication factor is

$$\frac{Q_{eff}}{Q} = \frac{R_s}{R_s + R_N} \quad . \tag{3.34}$$

When $R_N \rightarrow R_s$ the degree of multiplication becomes very large. Now let's see how R_N can be controlled by R_v. As

$$i_2 = \frac{v_3 - v_2}{R_f} \tag{3.35}$$

and

$$v_2 = v_{in} - v_1 \ , \tag{3.36}$$

equation 3.32 can be rewritten as

$$Z_{in} = \frac{1}{jwC_1} + \frac{1}{jwC_2} - \frac{1}{w^2 C_1 C_2 R_f}\left[1 - \frac{(v_{in} - v_3)}{v_1}\right] \quad . \tag{3.37}$$

Because $v_{in} > v_3$ and v_3 is a function of R_v, it is clear that decreasing R_v reduces the amount of negative resistance in the circuit. For small amounts of positive feedback

$$i_2 + i_1 \approx i_1 \tag{3.38}$$

and

$$i_3 \approx i_4 \tag{3.39}$$

so that

$$v_3 \approx v_{in}\left[\frac{R_v}{R_1 + R_v}\right] \tag{3.40}$$

and

$$v_1 \approx v_{in}\left[\frac{C_2}{C_2 + C_1}\right] \quad . \tag{3.41}$$

Using 3.38 and 3.39 the negative resistance is given by

$$R_N = -\frac{1}{w^2 C_1 C_2 R_f}\left[1 - \frac{C_2 + C_1}{C_2}\left[1 - \frac{R_v}{R_1 + R_v}\right]\right] \ ,$$

this result gives the dependence of R_N on R_v. Values of $C_1 = C_2 =$ 1.5nF, $R_f = 1K\Omega$ and $w = 3.14 \times 10^{-7}$ rad s^{-1} are used in the Q multiplier. If $R_1 >> R_v$ (f.e.t. saturated) then $R_N = +0.5\Omega$ and the Q is decreased as would be expected. If $R_1 = R_v$ then $R_N = 0.0\Omega$ and the Q is not affected as $i_2 = 0$. If $R_1 << R_v$ (f.e.t. pinched off) then $R_N = -0.5\Omega$; however, conditions 3.36 and 3.37 are violated in this case so the circuit could never produce as much negative resistance as -0.5Ω. Losses in the coil and connecting wires amount to about 0.4Ω.

3.5 RESULTS

This section provides the proof that the instrument works as predicted by sections 2.5, 3.4.1 and 3.4.2. The response to both X' and X" is shown to be linear to within the accuracy of the measurements. Equation 3.22 is developed so that a calibration factor for X' can be calculated, the result comes within 2% of the measured value. A calibration factor for X" is calculated. Measurements of the noise and drift in the signals for X' and X" are presented. Two plots produced by the new instrument for the temperature dependance of X' are shown to be identical to plots produced by a low frequency susceptibility bridge; this is reassuring because it indicates that the operating frequency of the new instrument is not too high. A summary of the new instrument's performance is presented in table 7, this table should be compared with tables 5 and 6.

3.5.1 Linearity

The linearity of the instrument was checked in the following manner. Varying masses of powdered magnetite were made up to 50 mg samples by dispersing the magnetite in pure LiF. LiF is diamagnetic and gives no signal on its own. No more than 20 mg of magnetite was used in any sample to ensure that the magnetite was well dispersed. The magnetite grains had radii in the range $4.3 < x < 7.7$ μm. Each sample was contained

in a test tube, it was kept in place at the bottom of the tube by a glass wool plug. The samples' volumes varied somewhat as LiF is less dense than magnetite. This was not important because the samples were each less than a quarter of the length of the sample coil (see subsection 2.2.3), and because the instrument responds to the volume susceptibility which is independant of the samples' volumes.

Figure 27 shows the mass of magnetite plotted against ΔV_p and ΔV_Q at room temperature. The linearity of the instrument is seen to be within the error of the measurements.

As a further check on the instrument's operation, a 2.2 mm diameter sphere of amorphous graphite was inserted into the sample coil. Graphite is diamagnetic, so the phase loop ought not to have been affected, but it is a semiconductor so the Q loop should have been affected quite strongly. The measured signals were $\Delta V_Q = -355mV$ and $\Delta V_p = -2mV$, this should be compared with the results in figure 27. The experiment demonstrated that X" was not affecting the output for X'.

3.5.2 Calibration

Referring to figure 22, the DC outputs of amplifiers A_1 and A_2 were adjusted to set the Q multiplier and the varicaps to their predetermined operating points. The feedback loops were then closed using switches S_1 and S_2. With both loops simultaneously locked a pair of calibration factors, K_p and K_Q were found to complete the relations

$$X_T' = K_p \Delta V_p \qquad (3.43)$$

and

$$X_T'' = K_Q \Delta V_Q. \qquad (3.44)$$

The subscript T indicates that the total susceptibility is being referred to; see equation 1.7.

K_p was found experimentally using a standard sample, it was then calculated theoretically from equation 3.22. If the theory was correct

Figure 27. The changes in V_p and V_Q for varying masses of magnetite powder.

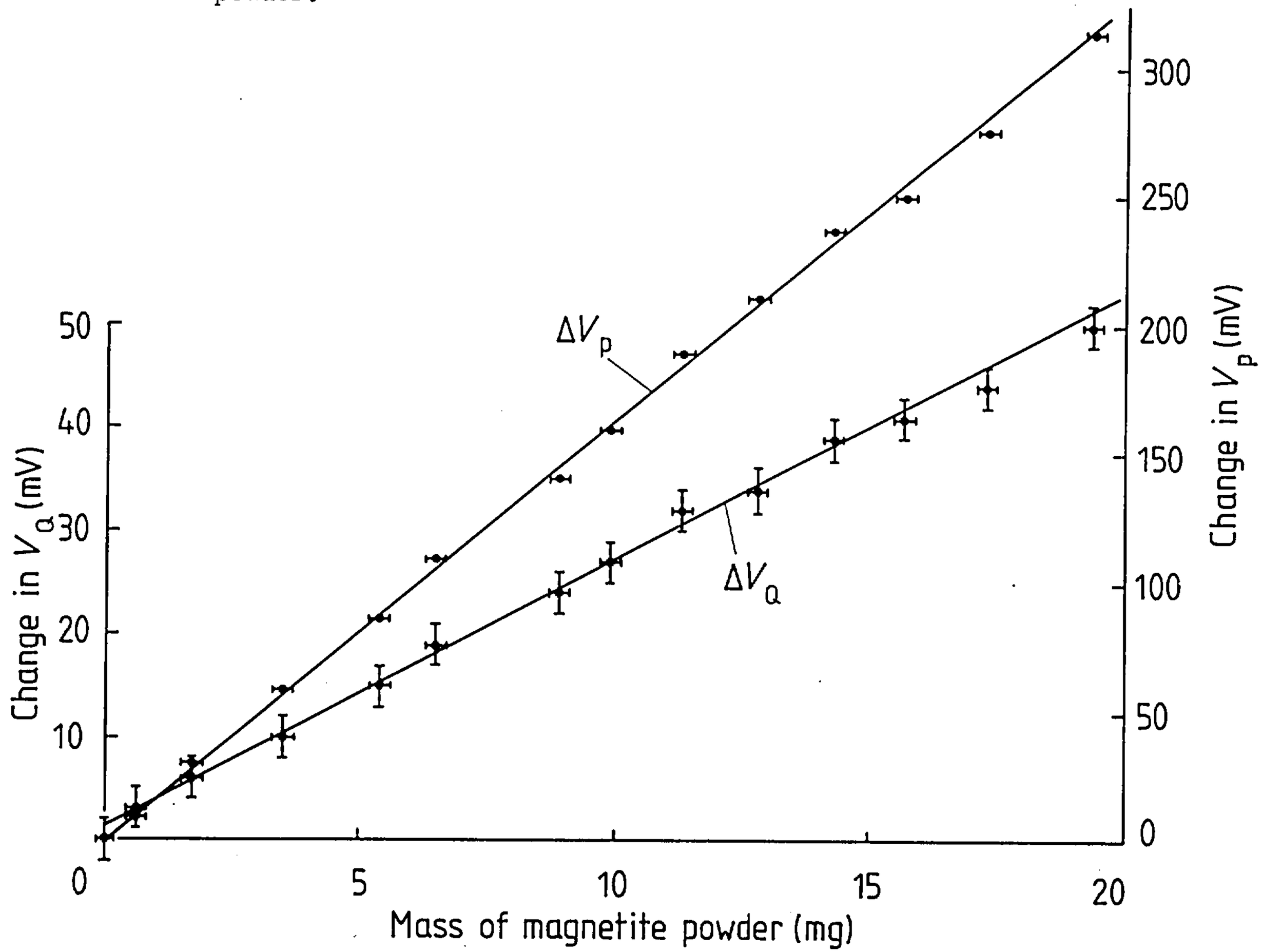

the two results would agree. The standard sample consisted of 238 mg of paramagnetic $FeSO_4.7H_2O$, it had a total susceptibility of $(1.24 \pm 0.02) \times 10^{-10} m^3$. Inserting it into the sample coil gave a signal of

$$\Delta V_p = - (4.9 \pm 0.3) \times 10^{-3} \text{ V}$$

from which

$$K_p = - (2.53 \pm 0.15) \times 10^{-8} m^3 V^{-1} .$$

There was a sizeable uncertainty in K_p because of the weak susceptibility of $FeSO_4.7H_2O$. This substance was chosen because its susceptibility is independent of frequency to well above 5MHz and it is a commonly used standard.

Using equation 3.22, K_p can be expressed as

$$K_p = - \left[\frac{m}{C} \frac{a}{V_c^{(1+m)}} \frac{1}{F} \right] V_s , \qquad (3.45)$$

where V_s is the sample's volume. V_s has been introduced because K_p in equation 3.22 refers to the volume susceptibility, whereas K_p in equation 3.43 refers to the total susceptibility. The varicap's parameters a and m in equation 3.45 were found by fitting equation 3.18 to the manufacturer's data. The varicaps were Mullard BB110G's and it was determined that $m = 0.46$ and $a = 26.5 \text{ pF} V^{0.46}$. The operating offset voltage V_p was -4.99V so that $V_c = + 5.69$V recalling that $V_c = (0.7 - V_p)$. The total capacitance in the circuit was (0.800 ± 0.001)nF. Putting these figures together gives

$$K_1 = 1.204 \times 10^{-3} \frac{V_s}{F} .$$

Using equation 2.30

$$\frac{V_s}{F} = V_c \left[\frac{b^2 + D^2}{b + 0.45D} \right] \frac{1}{b} ,$$

where V_c is the coil's volume, b is the length of the coil and D is the diameter of the coil. The coil's dimensions are b = 43.4 mm and D = 24.5

mm, therefore

$$\frac{V_s}{F} = 2.15 \times 10^{-5}.$$

Finally, the theoretical value for K_p is

$$K_p = 2.58 \times 10^{-8} m^3 V^{-1}.$$

This result is within 2% of the value found experimentally and it is well inside experimental error, the theory is therefore correct. This result also shows that the wire wound furnace and the water in the jacket only slightly worsen the coupling factor. Equation 3.22 shows that K_p will be different if V_p, the fixed offset voltage, is altered. Equation 3.21 shows that the linearity will be better than 4.3% provided that

$$\Delta V_p \leq 0.1 V_c.$$

K_Q is now calculated from equation 3.27:

$$K_Q = \frac{1}{Q^2} \left[\frac{dQ}{dV_Q} \right] \frac{V_s}{F} . \qquad (3.46)$$

dQ/dV_Q was measured and was $-(152 \pm 6) V^{-1}$, Q was found to be $(1.10 \pm 0.03) \times 10^3$ and V_s/F has been calculated to be 2.15×10^{-5}. Using these values

$$K_Q = (2.70 \pm 0.15) \times 10^{-9} m^3 V^{-1} .$$

dQ/dV_Q was linear over a range of 1.4V.

Subsection 1.5.5 has shown that susceptibility is frequency dependent and that the effect is more pronounced when the intrinsic susceptibility is large. Magnetite has a strong susceptibility, see table 3 in subsection 1.5.2, it should provide a good indication of how much X' may be decreased at 5 MHz compared to low frequencies. A 1.5KHz susceptibility bridge[17] and the new instrument were both calibrated against the frequency independent iron sulphate standard. The total susceptibility of 9.6 mg of powdered magnetite well dispersed in LiF was then found on both devices.

The low frequency measurement put the total susceptibility at $(4.1 \pm 0.8) \times 10^{-9} m^3$. The high frequency result was $(4.1 \pm 0.3) \times 10^{-9} m^3$. The weak susceptibility of the standard was a major source of error, but it can be said that the two measurements are in close agreement. It is therefore likely that measurements of X' made on the r.f. device will be directly comparable with measurements made on low frequency devices.

3.5.3 Noise and drift

The noise and drift on both channels were found by monitoring the outputs against time on a chart recorder. With a fast chart speed short term random noise was recorded. With a slow chart speed long term drift was recorded. An analysis of the noise sources and their relative importance is presented in section 3.6.

The noise in the phase loop, averaged over 12 intervals of 10 seconds each, was 0.32mV r.m.s. Using K_p the noise in V_p was equivalent to $8 \times 10^{-12} m^3$ r.m.s. Over an interval of 11 minutes the drift in V_p was monotonic at a rate equivalent to $3 \times 10^{-11} m^3 min^{-1}$.

The noise in the Q loop, averaged over 6 intervals of 10 seconds each, was 1.1mV r.m.s. Using K_Q the noise in V_Q was equivalent to $3 \times 10^{-12} m^3$ r.m.s. Over an interval of 11 minutes the drift in V_Q was monotonic at a rate of $5 \times 10^{-12} m^3 min^{-1}$.

The random noise levels increased by a factor of 2.5 when the furnace was running and water was flowing through the jacket.

3.5.4 Plots of X' against temperature

Chart recordings of the temperature dependence of the real part of the susceptibility were made for a number of samples, two of these recordings are presented below. The temperature dependences of the same pair of samples were also recorded on a 1.5 KHz bridge, these recordings are presented too. The chart recordings from the two instruments are compared to check that they agree. No recordings of the temperature dependence of X" were made at this stage.

Figure 28, obtained on the new instrument, is a plot of X' against temperature whilst heating a 13.0 mg lump of natural magnetite; the trace was very similar on cooling. There is a distinct Curie point at $(580 \pm 3)^{\circ}C$. A proper discussion of the shape of figure 28 is given in chapter 6. For now, it is sufficient to compare it with figure 29 which was produced by heating a 12.9 mg lump of magnetite in the low frequency bridge. The two recordings are almost identical. Figure 29 also puts the Curie point at $(580 \pm 3)^{\circ}C$; the value that would be expected for pure magnetite is $578^{\circ}C$[40].

Some samples have more than one Curie point because they contain a number of magnetizable compounds. An artificial sample was created to prove that the new instrument would faithfully pick out multiple Curie points. Figure 30 depicts X' against temperature for 9.5 mg of magnetite powder mixed with 206 mg of powdered Brazlian haematite, the plot was taken on the new instrument. Figure 30a shows the heating trace; the magnetite powder oxidised but haematite's Curie point is clearly visible. Figure 30b shows the cooling trace; only the haematite's Curie transition is visible. The transition is smeared because it is difficult to maintain a uniform heat throughout a bulky sample while the furnace is running close to its limits. This explains why figure 30 puts haematite's Curie point at $710^{\circ}C$ and not $675^{\circ}C$ as expected.

Figure 31 shows the results of heating and cooling a similar mixture in the low frequency bridge. The exact composition of the mixture was 10.2 mg of magnetite powder mixed with 202 mg of haematite powder. The only difference between the figures is a small hump in the oxidation of the magnetite in figure 31 that is not present in figure 30. It is likely that differences in the rates of heating caused differences in the rates of oxidation, this would account for the dissimilarity.

Table 7 summarises the results presented in this subsection; it should be compared with tables 5 and 6.

Figure 28. A plot of X' against temperature for a 13 mg sample of natural magnetite. This result was obtained at 5 MHz.

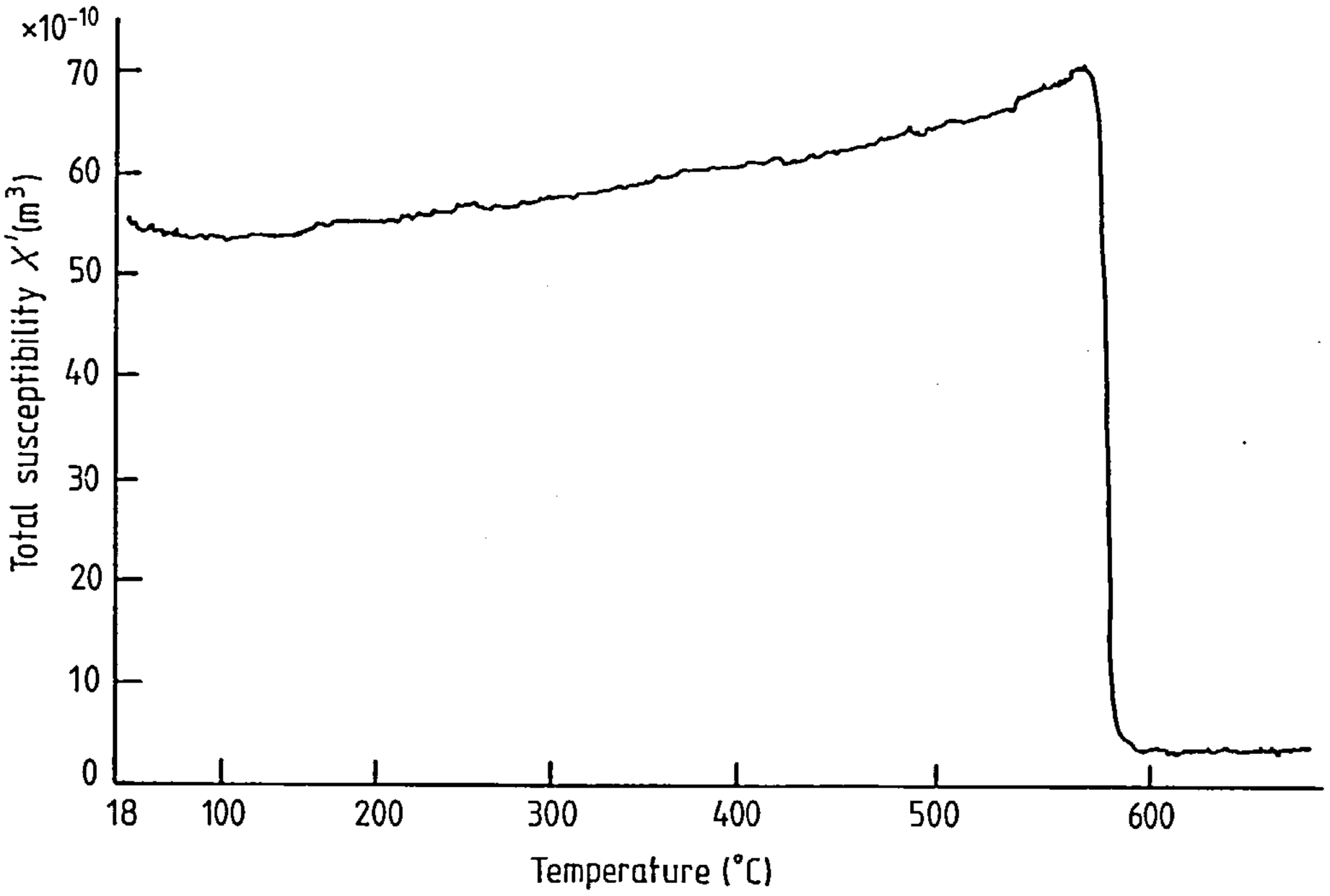

Figure 29. A plot of X against temperature for a 12.9 mg sample of natural magnetite. This result was obtained at 1.5 KHz.

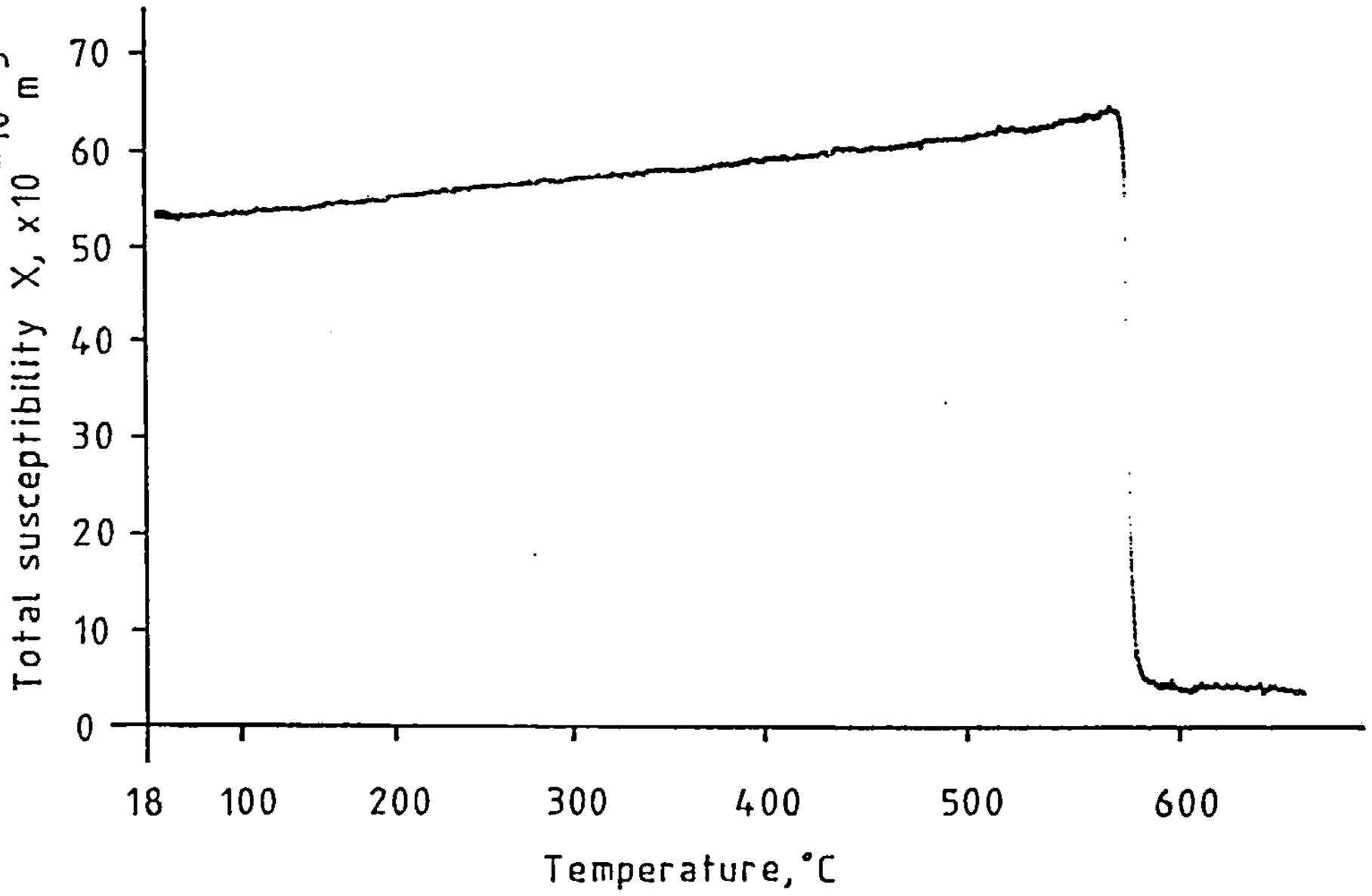

Figure 30. A plot of X' against temperature for 9.5 mg of powdered magnetite mixed with 206 mg of powdered haematite. These results were obtained at 5 MHz.

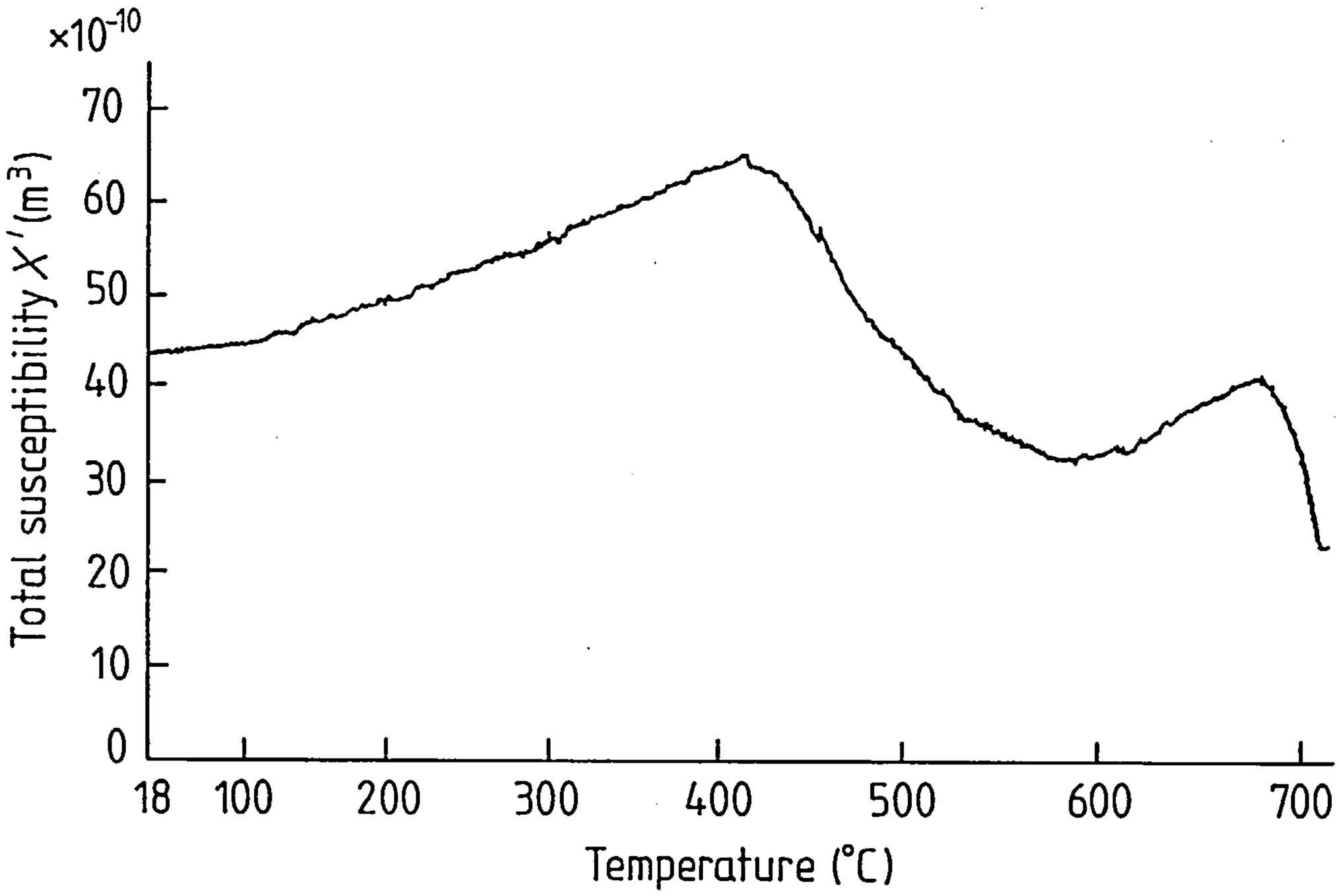

a. Heating

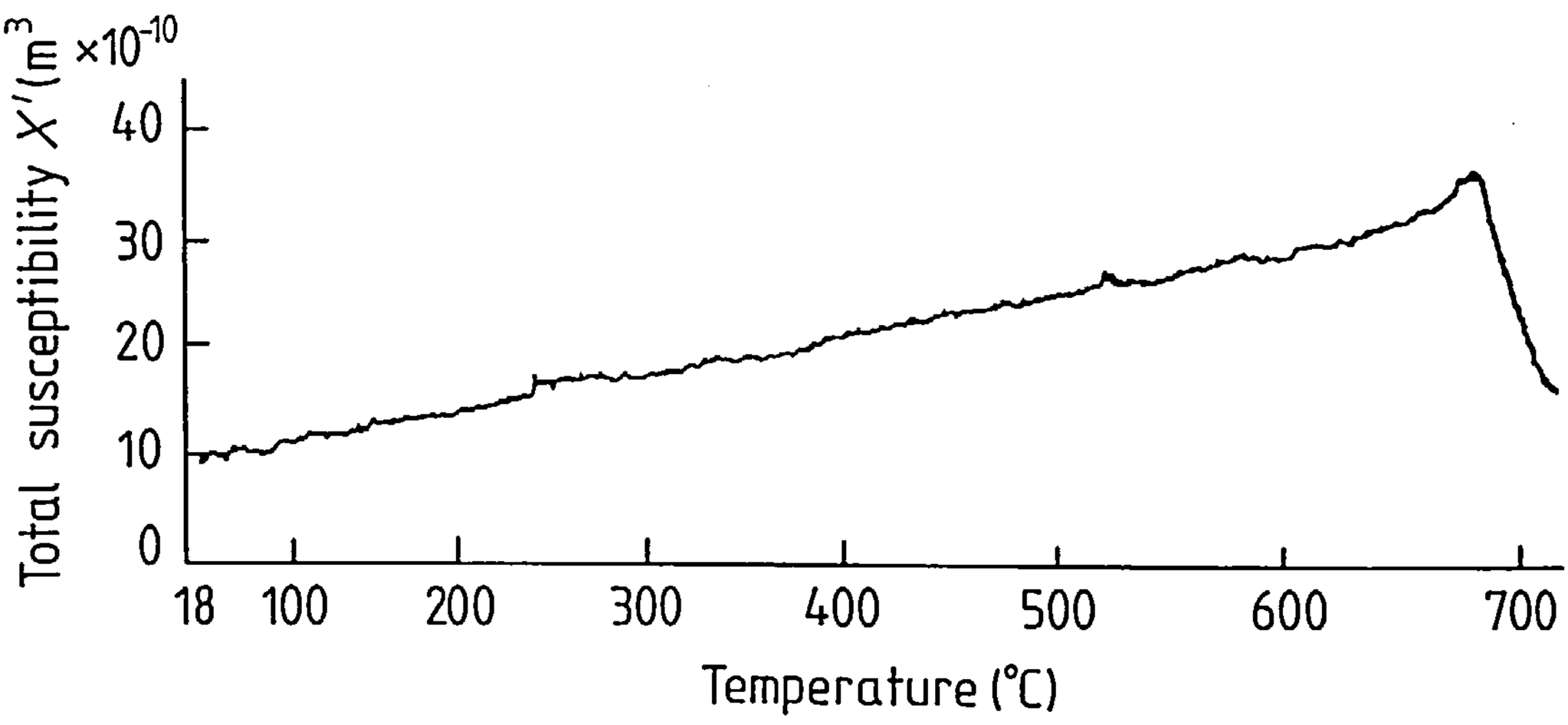

b. Cooling

Figure 31. A plot of X against temperature for a mixture of 10.2 mg of powdered magnetite and 202 mg of powdered haematite. These results were obtained at 1.5 KHz.

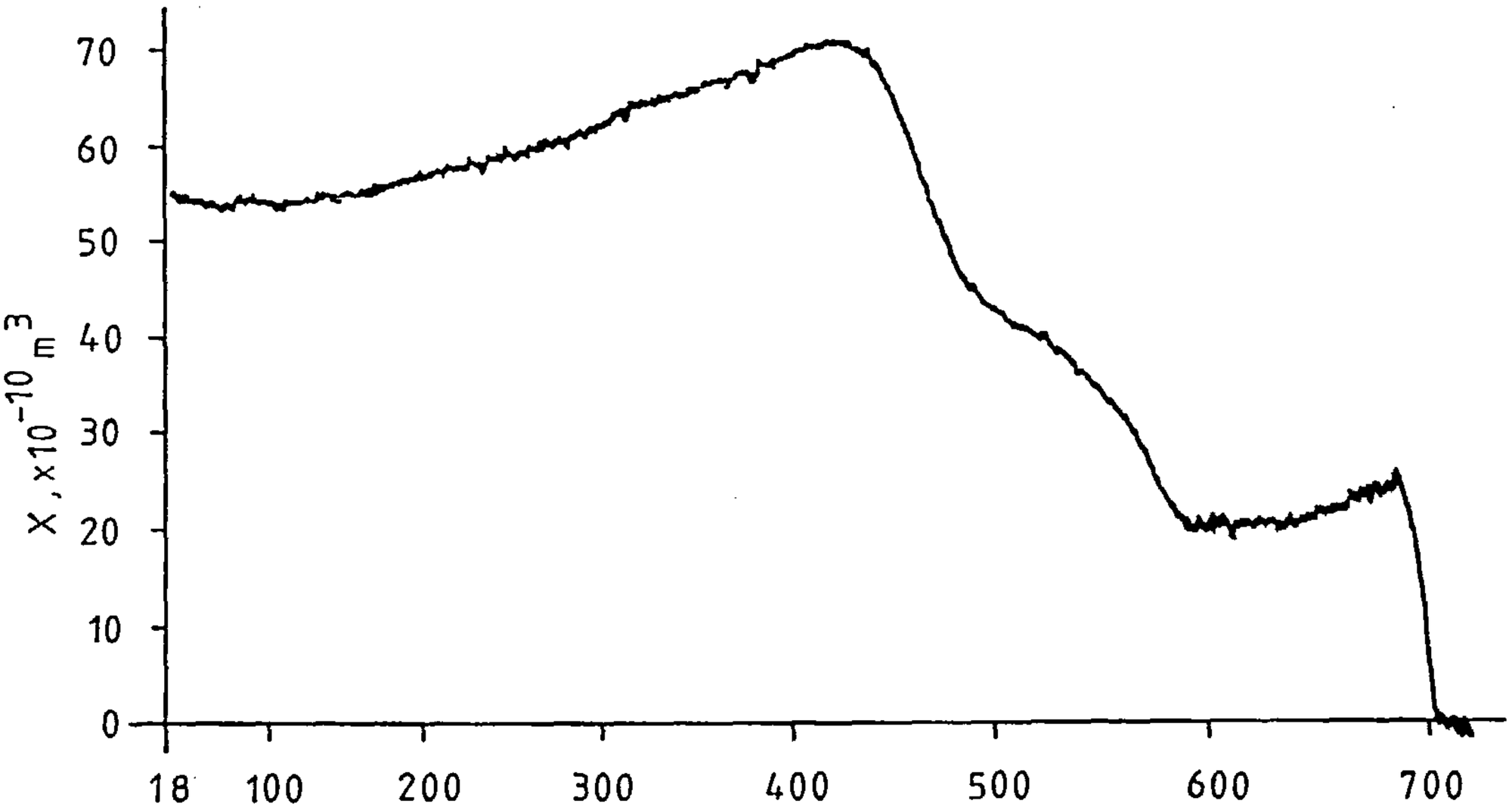

a. Heating

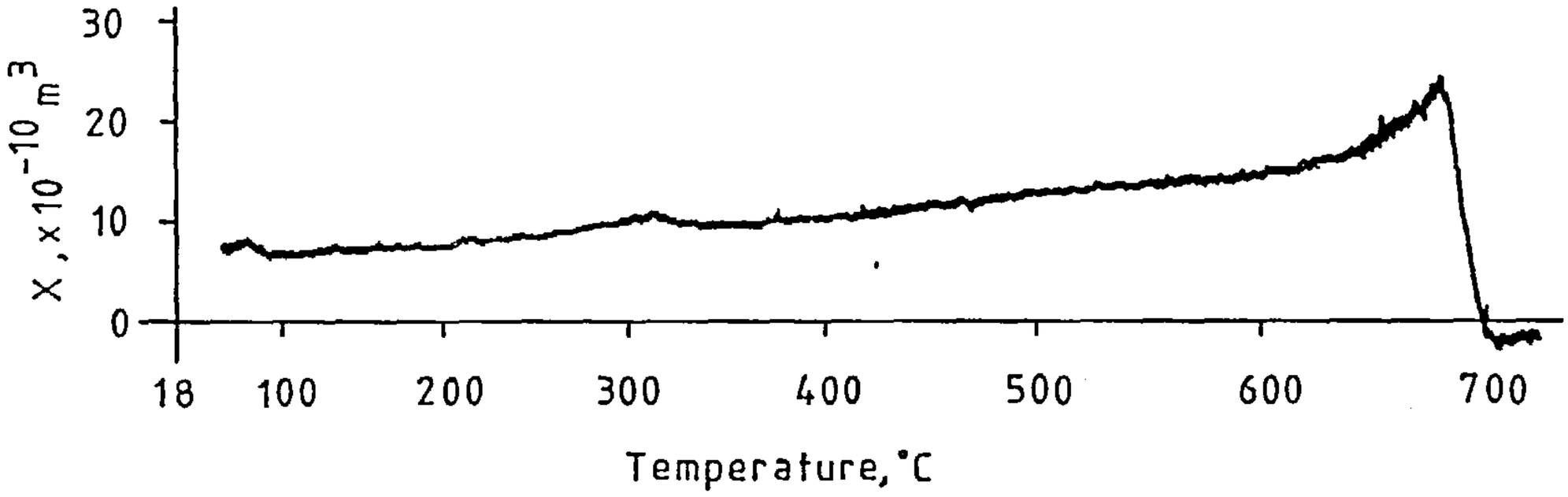

b. Cooling

Table 7. A summary of the performance of the first version of the new instrument.

Parameter	Value
Length of sample coil, m	4.34×10^{-2}
Diameter of sample coil, m	2.45×10^{-2}
Construction of sample coil	10 turns 16 s.w.g. silver wire
Flux at centre of sample coil, T r.m.s.	1.6×10^{-6}
Maximum sample size, m^3	2×10^{-7}
Operating temperature, $^{\circ}C$	16 - 700
Operating frequency, MHz	5.0000
Calibration factor for X_T', m^3V^{-1}	-2.5×10^{-8}
Max. input for X_T', m^3	1.2×10^{-8}
Noise in X_T', m^3 r.m.s.	8×10^{-12}
Drift in X_T, m^3 min^{-1}	3×10^{-11}
Calibration factor for X_T'', m^3V^{-1}	2.7×10^{-9}
Max. input for X_T'', m^3	3.8×10^{-9}
Noise in X_T'', m^3 r.m.s.	3×10^{-12}
Drift in X_T'', m^3 min^{-1}	5×10^{-12}
Direct reading?	Yes

3.6 NOISE ANALYSIS

This noise analysis is directed at improving the instrument by identifying the most critical portions of the device. To do this the instrument is broken down, as illustrated in figures 23 and 25, and a number of independent white noise sources are added in. The most important scurces are then pointed out and analysed in more detail. This leads to some important conclusions about improving the performance in future.

X" is dealt with first. The noise sources n_1 to n_4 in figure 25 each generate white amplitude noise. The source n_1 accounts for the noise generated by the tuned circuit and Q multiplier. The noise fed in from the crystal oscillator also contributes to n_1, but it is ignored as it should be very small compared to the other two constituents. The noise generated by the r.f. amplifier is allowed for by n_2. The peak detector rectifies and smooths the 5MHz signal, it passes undisturbed the random fluctuations in a noise bandwidth[41,518] B from d.c. up to $1/4\tau$ where τ is the peak detector's RC time constant. The disturbances generated within the detector are represented by n_3. As the required information is now at a low frequency n_3 ought to contain a 1/f noise source, but this unnecessarily complicates matters. Finally, n_4 allows for the noise generated by the low frequency amplifier.

The instrument's signal to noise ratio with respect to X" is now going to be found. Q_m is defined to be the quality factor after Q multiplication and Q is the natural quality factor of the coil. Referring to figure 25:

$$d = \frac{\Delta V_Q - n_4}{A_2} \tag{3.47}$$

and

$$c = \frac{d - n_3}{D} , \tag{3.48}$$

that is

$$c = \frac{\Delta V_Q - n_4}{DA_2} - \frac{n_3}{D} \quad . \tag{3.49}$$

Proceeding in a similar manner,

$$a = Z\,\Delta V_Q - Q_m FX''$$

$$= \frac{\Delta V_Q - n_4}{VA_1DA_2} - \frac{n_3}{VA_1D} - \frac{n_2}{VA_1} - \frac{n_1}{V} \quad . \tag{3.50}$$

As the open loop gain ZVA_1DA_2 is much greater than one the output signal is

$$\Delta V_Q \approx \left[\frac{X''FQ_m}{Z}\right] - \left[\frac{n_4}{ZVA_1DA_2} + \frac{n_3}{ZVA_1D} + \frac{n_2}{ZVA_1} + \frac{n_1}{ZV}\right] \quad . \tag{3.51}$$

The first term on the right hand side is signal whilst the second term is noise. As A_1, A_1D and A_1DA_2 are each $>>1$ the dominant noise contribution is n_1 and the signal to noise ratio is

$$SNR = \frac{X''FQ_mV}{n_1} \quad . \tag{3.52}$$

The noise source n_1 now has to be investigated. In figure 32, G is the tuned circuit's loss conductance, -H is the parallel negative conductance and i_1 is the noise current generator for the tuned circuit and Q multiplier. The Johnson noise current generated by the tuned circuit is[23]

$$i_1^2 = \int_{f_1}^{f_2} 4\,kTG.df \tag{3.53}$$

for a small band of frequencies about the resonant frequency. When the Q multiplier is taken into account

$$i_1^2 = \int_{f_1}^{f_2} 4kTGN.df \ , \tag{3.54}$$

where N is the Q multiplier's noise factor[41, 137]. The bandwidth of the

Figure 32. A model to help calculate the noise voltage n_1.

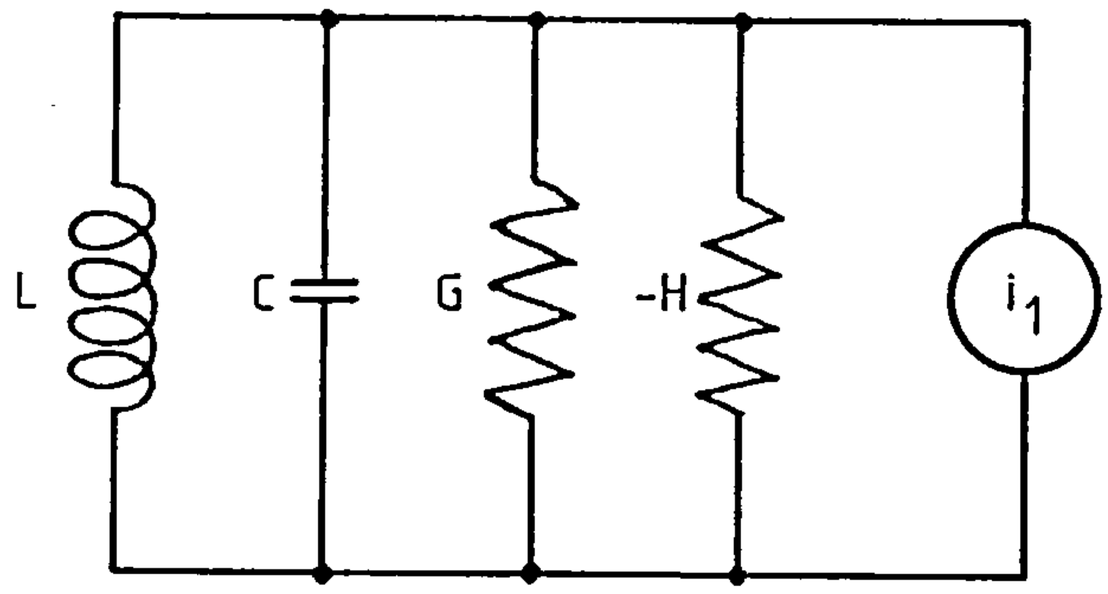

Figure 33. A diagram to show how amplitude noise can create phase noise.

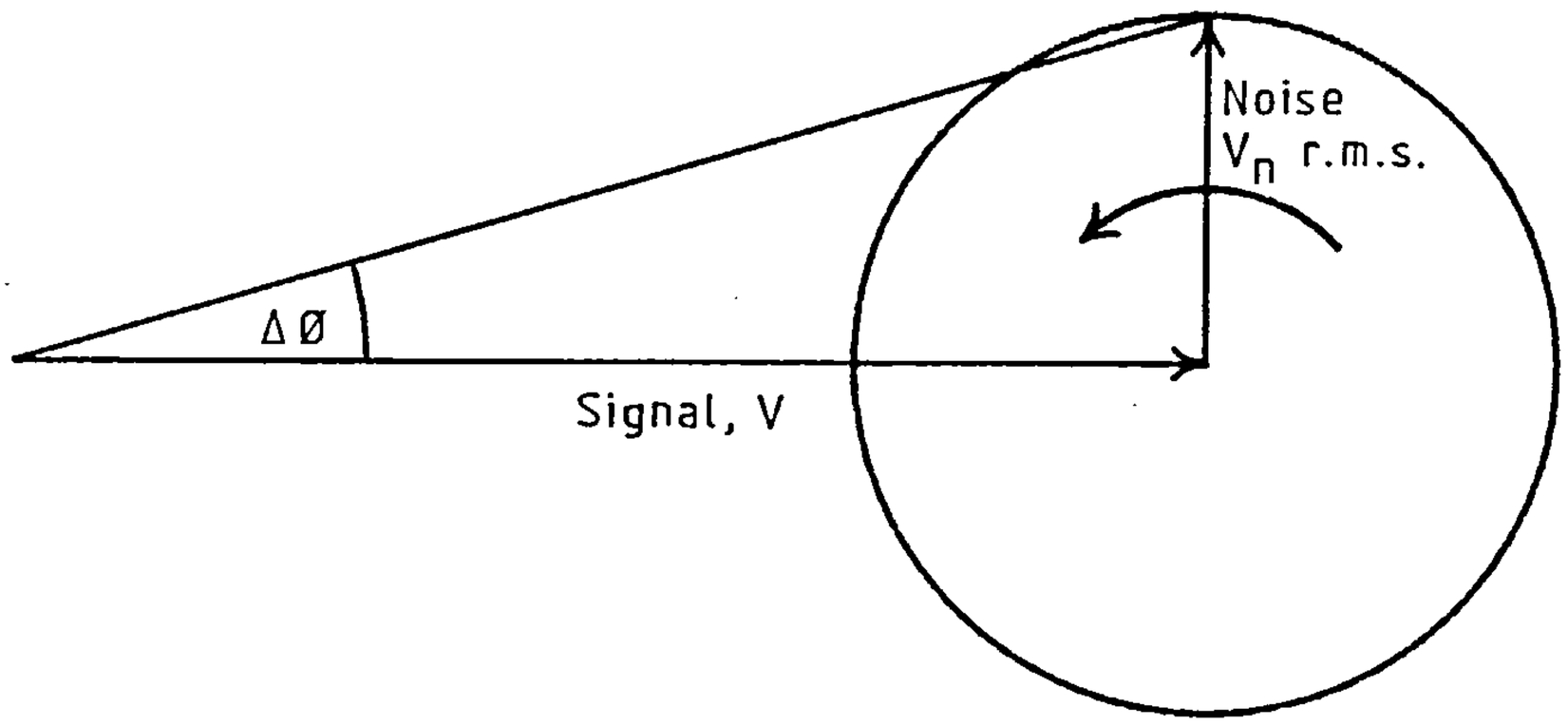

system is determined by that of the detector because the detector's bandwidth is much less than that of the tuned circuit. The result for i_1^2 is thus

$$i_1^2 = 4kTGNB \ . \tag{3.55}$$

The r.m.s. noise voltage developed across the tuned circuit is

$$n_1 = \frac{i_1}{G - H} \ , \tag{3.56}$$

so

$$n_1 = \frac{(4kTGNB)^{0.5}}{G - H} \ . \tag{3.57}$$

When the top and bottom of 3.57 are multiplied by w_oL the result is

$$n_1 = Q_m \left[\frac{4kTBNw_oL}{Q} \right]^{0.5} \ . \tag{3.58}$$

Equations 3.52 and 3.58 can now be combined to give

$$SNR = X''FV \left[\frac{Q}{4kTBNw_oL} \right]^{0.5} \ . \tag{3.59}$$

Equation 3.59 shows that a good coupling factor and a small bandwidth make for a good signal to noise ratio - but this would be expected. What might not be expected is that Q multiplication does not improve the signal to noise ratio. The natural quality factor is important and should be as large as possible. The signal to noise ratio can also be improved by increasing the drive level from the crystal oscillator.

The noise analysis for X' follows a similar course. Using figure 23, the signals at point "a" can be related by

$$u\Delta V_p - FX' = \frac{(\Delta V_p - n_3)}{Q_m KA} - \frac{n_2}{Q_m K} - \frac{n_1}{Q_m} \ . \tag{3.60}$$

The open loop gain $Q_m KAu \gg 1$ so

$$\Delta V_p = \left[\frac{FX'}{u} \right] - \frac{1}{u} \left[\frac{n_3}{Q_m KA} - \frac{n_2}{Q_m K} - \frac{n_1}{Q_m} \right] \ . \tag{3.61}$$

The most important noise source is n_1, therefore

$$SNR = \frac{FX'Q_m}{n_1} . \qquad (3.62)$$

To find n_1 it must first be shown how amplitude noise produces phase noise. The noise centred on a frequency f in an interval df may be represented as a single component of frequency f_n and amplitude $(\overline{V_n^2})^{0.5}$ taken over the interval df. The signal and noise components add together in the manner shown by figure 33. The noise component has an angular velocity $|w_o - w_n|$ relative to the signal. Provided that $V >> (\overline{V_n^2})^{0.5}$ the maximum change of phase is

$$\Delta\phi_{max} = \frac{(\overline{V_n^2})^{0.5}}{V} . \qquad (3.63)$$

As the noise in the interval df is considered to be sinusoidal the r.m.s. phase noise is

$$n_1 = (\overline{\Delta\phi^2})^{0.5} = \frac{(\overline{V_n^2})^{0.5}}{2V} . \qquad (3.64)$$

The amplitude noise has been shown to be

$$\left[\overline{V_n^2}\right]^{0.5} = Q_m\left[\frac{4kTBNw_oL}{Q}\right]^{0.5} \qquad (3.65)$$

where B is now the bandwidth of the phase detector. Phase noise from the crystal oscillator is common to both the signal and reference channels, it therefore cancels out at the phase detector. From equations 3.62 and 3.65 the phase channel's signal to noise ratio is

$$SNR = FX'V\left[\frac{Q}{4kTBNw_oL}\right]^{0.5} . \qquad (3.66)$$

Most of the comments made about equation 3.59 apply to 3.66 also. In particular, equation 3.66 shows once again that it is the natural rather than the multiplied Q that is important to the signal to noise ratio.

CHAPTER 4

THE SYSTEM DESIGN FOR THE FINAL VERSION OF THE INSTRUMENT: A LOCKED PHASE LOOP.

4.1 INTRODUCTION

A lot of thought was put into the design of the improved instrument. It seems best to split the description of the resulting device into two separate chapters. Chapter 4 concentrates on the instrument's large scale make up and chapter 5 deals with the circuit design. This chapter is itself split into two sections. Section 4.2 decides upon the system's structure. Section 4.3 considers issues relevant to the key subsystems.

4.2 THE NEW SYSTEM

4.2.1 Reduction to a single feedback loop

The Q multiplier is dropped because it does not pay its way: section 3.6 has shown that Q multiplication does not improve the signal to noise ratio. The possibility of using feedback to regulate the tuned circuit's Q is lost with the Q multiplier, the instrument is therefore reduced to a single feedback loop. There are mixed blessings in this, the remaining phase loop is now much more easy to stabilise, but it has to be made resistant to the small changes in amplitude created by X".

An improved method of measuring the amplitude of the signal across the tuned circuit is adopted. As the phase loop has to be resistant to amplitude modulation anyway, the signal from the 5 MHz crystal driver is deliberately amplitude modulated at an audio frequency. The 5 MHz carrier is later demodulated using a diode rectifier. The amplitude of the recovered audio signal is measured using a phase sensitive rectifier. Changes in the audio amplitude are directly proportional to changes in the amplitude of the 5MHz carrier. The advantage of this method over simple peak rectification is that it virtually eliminates the needs for d.c. coupling between stages and for d.c. amplification.

4.2.2 Choice of phase loop order

The phase loop operates by locking the phase of the signal from the tuned circuit to the phase of the signal from the crystal oscillator; for this reason it is called a locked phase loop from now on. The well known phase locked loop[42] always contains a voltage controlled oscillator and this distinguishes it from a locked phase loop. The two are nevertheless similar in that they are feedback loops that seek to minimise a phase error and they both employ a phase detector, a low pass filter and a d.c. coupled amplifier. With this justification, results quoted by Gardner[43,127] on optimisation of loop performance are used to help determine the structure of the locked phase loop.

Inserting a sample into the sample coil produces a phase step at the loop's input. The optimum loop transfer function for this type of input is of the form[43,138]

$$\frac{C(s)}{R(s)} = \frac{B}{s + B} \quad , \qquad (4.1)$$

where B is the loop's bandwidth and C(s) and R(s) are defined in figure 21. This is a first order loop tranfer function, it is optimum in the sense that it minimises the mean square loop error

$$(MSE)^2 = \overline{\phi_n^{\,2}} + Y^2 E_T^{\,2} \quad , \qquad (4.2)$$

where $\overline{\phi_n^{\,2}}$ is the phase jitter due to white noise and $Y^2 E_T^{\,2}$ represents the allowable total transient error. The loop's bandwidth B is a variable that depends on the input's signal to noise ratio. B should decrease with worsening input signal to noise ratio and increase with improving input signal to noise ratio. Gardner[43, 139 and 125] shows that a loop that includes a limiter preceded by a bandpass filter automatically varies its bandwidth in a near optimum fashion. In this instrument, the bandpass filter is the parallel tuned circuit that includes the sample

coil and this is followed by a limiter prior to phase detection.

Because the gain of a first order loop is finite the loop error is finite also. Referring to figure 21 the error is

$$E(s) = \frac{R(s)}{1 + G(s)H(s)} , \qquad (4.3)$$

so in this case

$$E \approx \frac{-FX'}{QKAu} \qquad (4.4)$$

using figure 23. In practice, the open loop gain is made large enough to ensure that the loop error is much too small to matter.

4.2.3 The phase sensitive rectifier

The amplitude changes due to X" are likely to be less than 0.1%. The first version observed these changes by rectifying the coil's signal with a diode and the smoothing and amplifying the result. There are two major disadvantages to this method.

The first disadvantage is that the rectifying diodes are temperature sensitive. At a constant current the voltage drop across a silicon diode decreases by $\approx$ 2.1 $mV^{o}C^{-1}$. The 5MHz signal applied to the diode peak rectifier had been amplified to 3V p-p in first version of the instrument. A 0.1% change in this level, allowing for a diode voltage drop of 0.7V, gives a 0.8mV change at the output of the peak rectifier: this is less than that given by a $0.5^{o}C$ change in ambient temperature. The temperature sensitivity of the diodes is therefore unacceptable.

The other disadvantage is that of translating a 5 Hz signal into a d.c. level. At low frequencies, less than 100 Hz say, the spectral density of the noise associated with the rectifying diode and d.c. amplifiers has a roughly 1/frequency (1/f) characteristic[41,150][46,75]. This means that the amplitude spectrum of the random fluctuations goes on increasing in magnitude as the frequency considered decreases. This behaviour is known to be obeyed to frequencies of less than 1 cycle per

month, or 2×10^{-7}Hz. Attempts to improve the signal to noise ratio using a low pass filter are ineffectual against 1/f noise. This is well illustrated by a simple numerical example.

Over a 1 hour measurement period, the time it takes to heat and cool a sample in the furnace, the lowest noise frequency that is likely to disturb measurements has a period of about 4 hours. That sets the lower frequency limit, labelled f_1, to 7×10^{-5}Hz. The upper frequency limit is f_2, where f_2 is roughly the cut off frequency of the low pass filter on the output for X". The combined amplifier and diode noise at the frequency f_1 is represented by a spot noise voltage generator $\overline{n^2}(f_1)$. The random noise generated in the bandwidth f_1 to f_2 is given by

$$\overline{n^2}(f_1).f_1 \int_{f_1}^{f_2} \frac{1}{f}\,df = \overline{n^2}(f_1).f_1 \ln\left[\frac{f_2}{f_1}\right] . \qquad (4.5)$$

The illustration is now completed by finding how much the random noise is reduced if the low pass filter's cut off frequency is shifted from 1Hz to 0.1Hz. For a 1Hz cut off the total noise output is $9.6\overline{n^2}(f_1).f_1$. For a 0.1Hz cut off the total noise output is $7.3\ \overline{n^2}(f_1).f_1$. Reducing the upper cut off frequency by a factor of 10 only reduces the total noise output by a factor of 1.3.

The technique adopted overcomes both of these problems. Phase sensitive rectification, as it is called, has an extensive amount of literature devoted to it. The reviews by Blair and Sydenham[44] and by Meade[45] have good bibliographies.

The application of phase sensitive rectification to this circumstance is shown in figure 34. The output of the 5MHz crystal oscillator is amplitude modulated by an audio signal. The depth of modulation is small so that the audio signal forms an envelope riding on the peaks of the 5MHz carrier. After X" has had its effect, the signal from the tuned circuit

Figure 34. A scheme for measuring the signal amplitude in the tuned circuit using a phase sensitive rectifier.

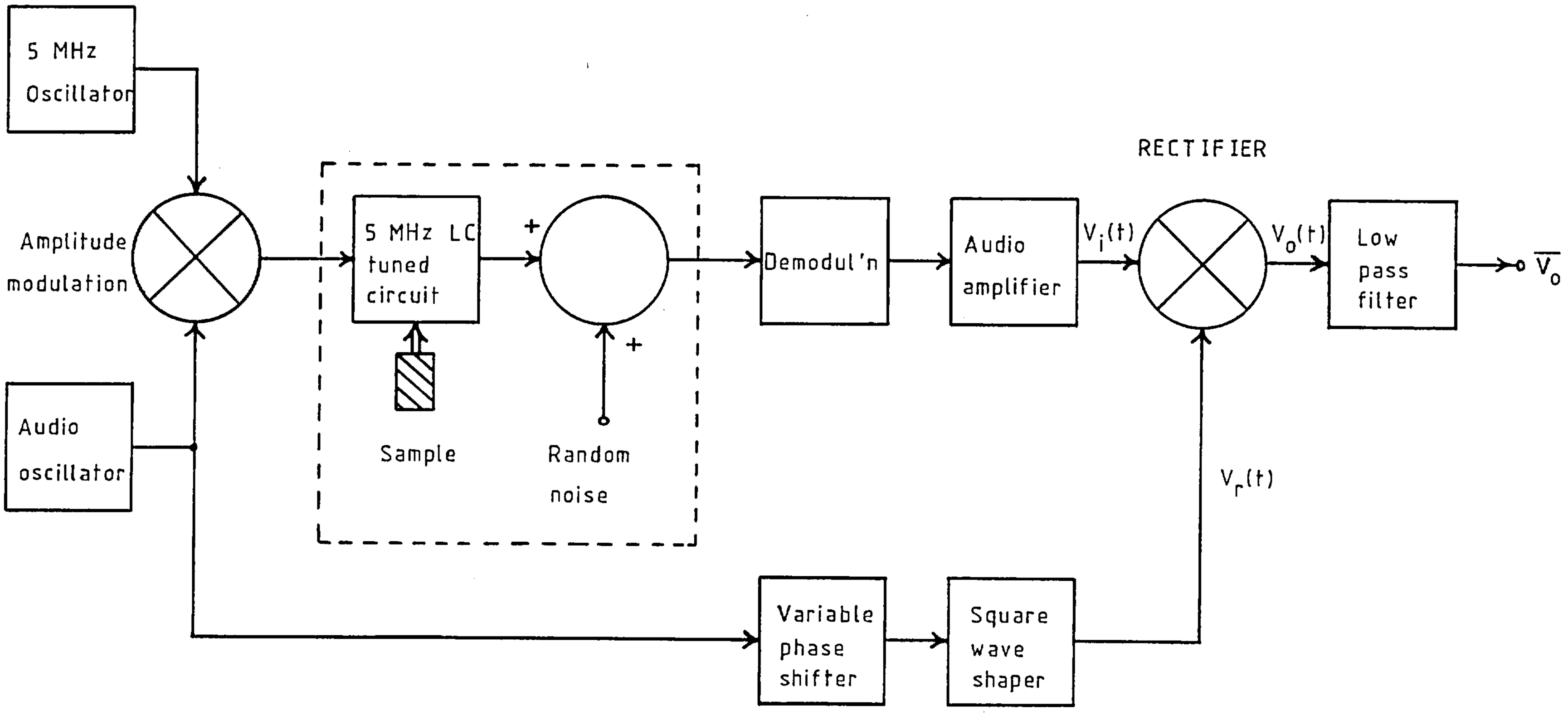

is demodulated to recover the audio signal. Provided that the diode is driven well into conduction, the thermal drift of the diode's internal voltage drop has no effect on the amplitude of the detected audio signal. This is because differential changes are now being sought, the drift prone d.c. component from the demodulator is ignored. The reduction in the tuned circuit's Q due to X" is now reflected in the reduction of the audio signal level. It is sensible to amplify the audio signal as much as circuit constraints allow. The modulating frequency needs to lie well within the white noise region of the amplifier and, if possible, the amplitude detector.

The signal from the audio oscillator also travels along another path as figure 34 shows. The variable phase shifter adds just enough delay in the parallel path to compensate for delays in the amplitude modulator and subsequent stages. The square wave shaper turns the phase shifted output into a switching signal for an analogue multiplier.

The phase sensitive rectifier multiplies the switching signal and recovered audio signal together to produce a d.c. level proportional to the amplitude of the latter. The multiplier's output is

$$V_o(t) = V_i(t).V_r(t) \quad , \tag{4.6}$$

where $V_i(t)$ is the recovered audio signal and $V_r(t)$ is the switching signal:

$$V_r(t) = \begin{cases} +1 \text{ for } 0 < t \leq T/2 \\ \\ -1 \text{ for } T/2 < t \leq T \end{cases} . \tag{4.7}$$

This is depicted in figure 35a. The fundamental frequency of the switching signal is $f_r = 1/T$. The harmonics of the switching signal are mf_r, where $m = 1,2,3$ .....

To complete the process of phase sensitive rectification, V_o is averaged by a low pass filter to produce $\overline{V_o}$. Tietze and Schenk[49,460]

Figure 35. The operation of the phase sensitive rectifier.

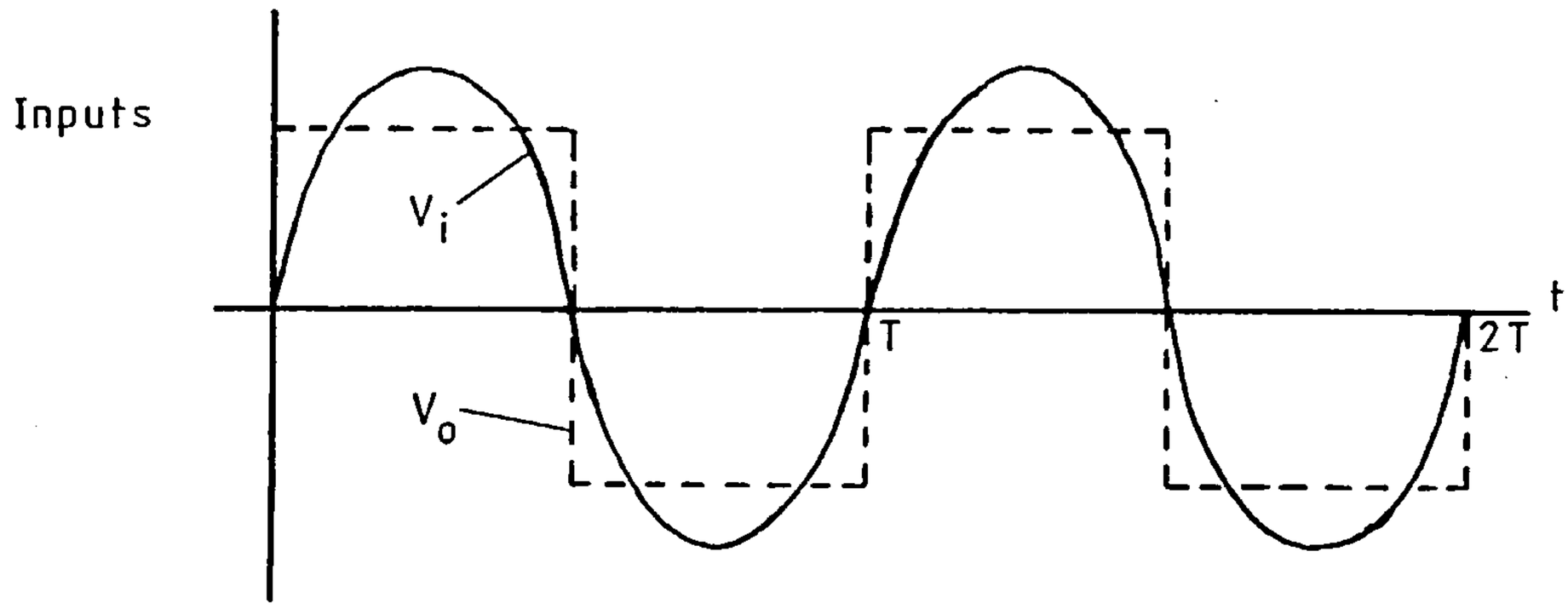

a. The inputs to the phase sensitive rectifier.

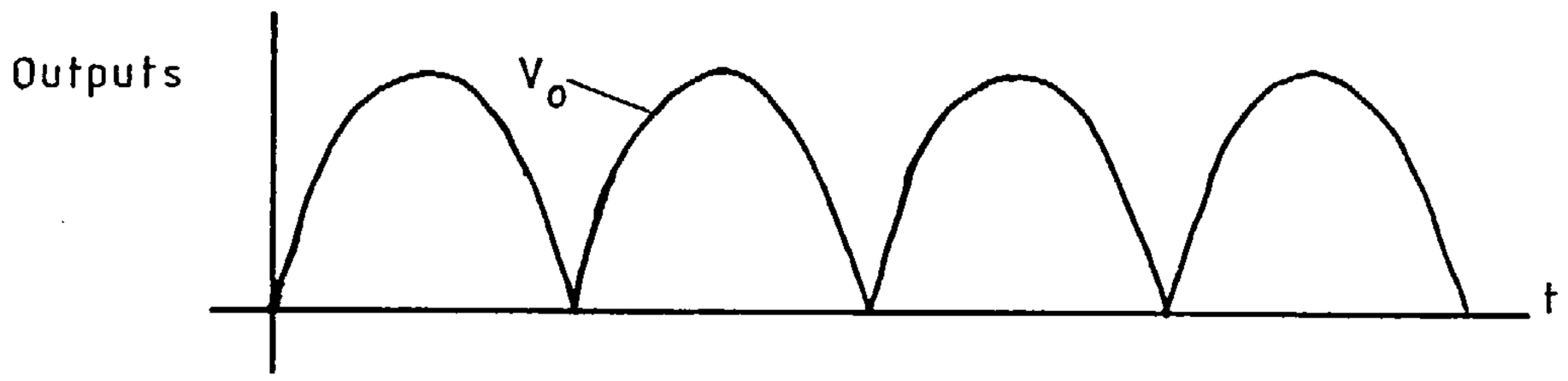

b. The output of the phase sensitive rectifier.

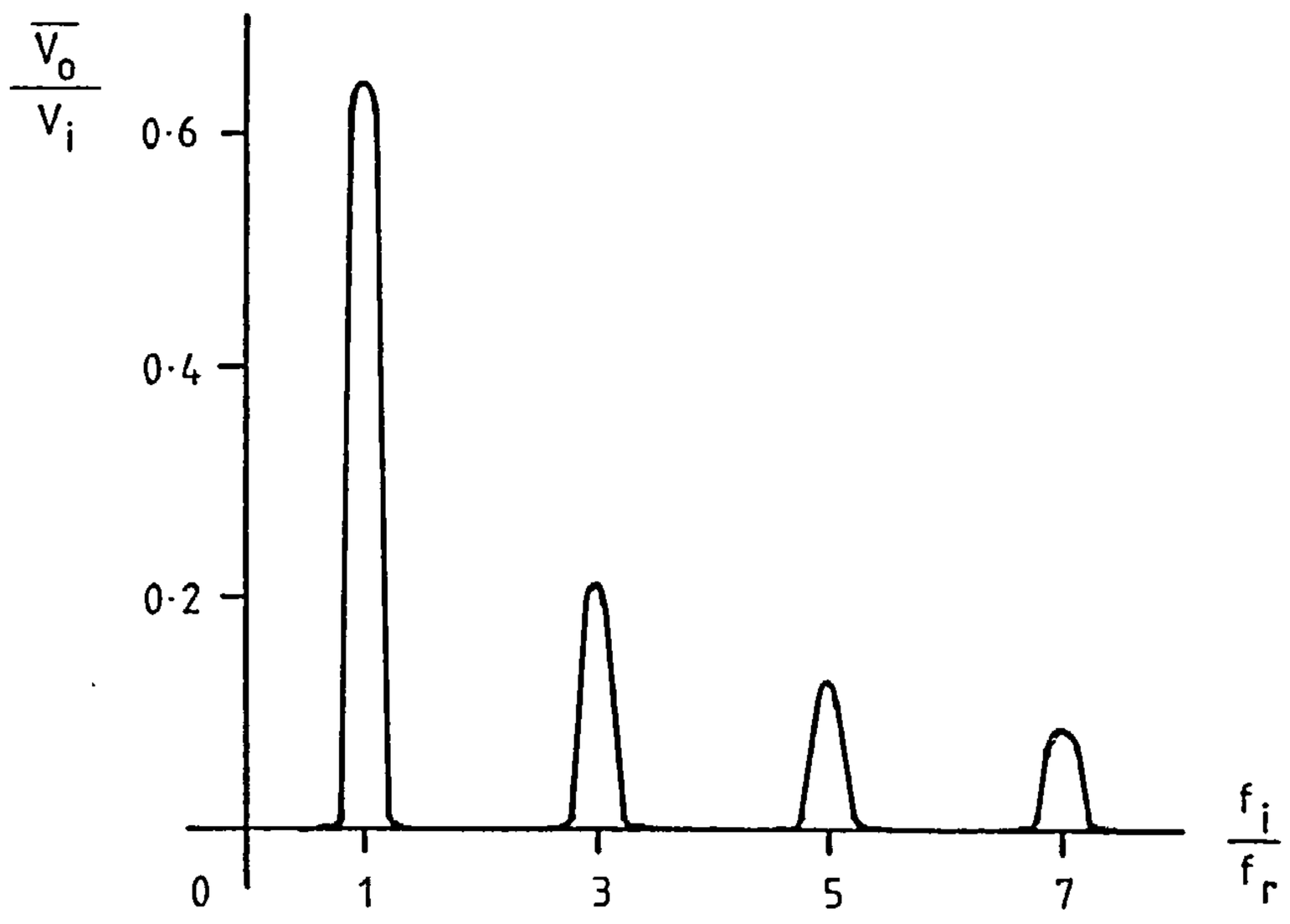

c. The filtering characteristic.

show that the response of the phase sensitive rectifier to an input $V_i(t) = A\cos(2\pi m f_r t + \phi)$ is

$$V_o = \begin{cases} (2/\pi m)\ A\ \cos\phi_m & \text{for } m = 2n + 1 \\ 0 & \text{for } m \neq 2n + 1 \end{cases} \qquad (4.8)$$

where n = 0, 1, 2 ... Because the low pass output filter has a finite time constant, the phase sensitive rectifier responds to frequency bands centred on the discrete frequencies indicated in equation 4.8. For a low pass filter cut off frequency f_c, corresponding to its -3dB bandwidth, the -3dB width of the bands is $2f_c$. Figure 35b shows the filtering characteristic. The Q of the filter in the fundamental band is $f_r/2f_c$, this can be made very large indeed.

The phase sensitive rectifier is an intelligent filter that looks only where it knows the signal lies. The rectification takes place at frequencies where the noise has a white spectrum, so the output signal to noise ratio can be effectively controlled using a low pass filter. The only limit to the noise reduction is the length of time the experimenter can wait for a result, low pass filter cut off frequencies less than 0.01Hz are quite common.

4.2.4 The final structure

The structure that was finally settled on is depicted in figure 36, the figure is self explanatory.

4.3 KEY COMPONENTS

4.3.1 The sample coil

The sample coil's performance is of paramount importance because it is at the start of the processing chain. Equations 3.59 and 3.66 for the signal to noise ratio show that the quantity $Q^{0.5}F$ has to be maximised, Q is the coil's natural quality factor and F is the filling factor. Equation 2.30 has shown that

$$F = \frac{V_s}{V_c} \frac{b(b + 0.44D)}{b^2 + D^2}$$

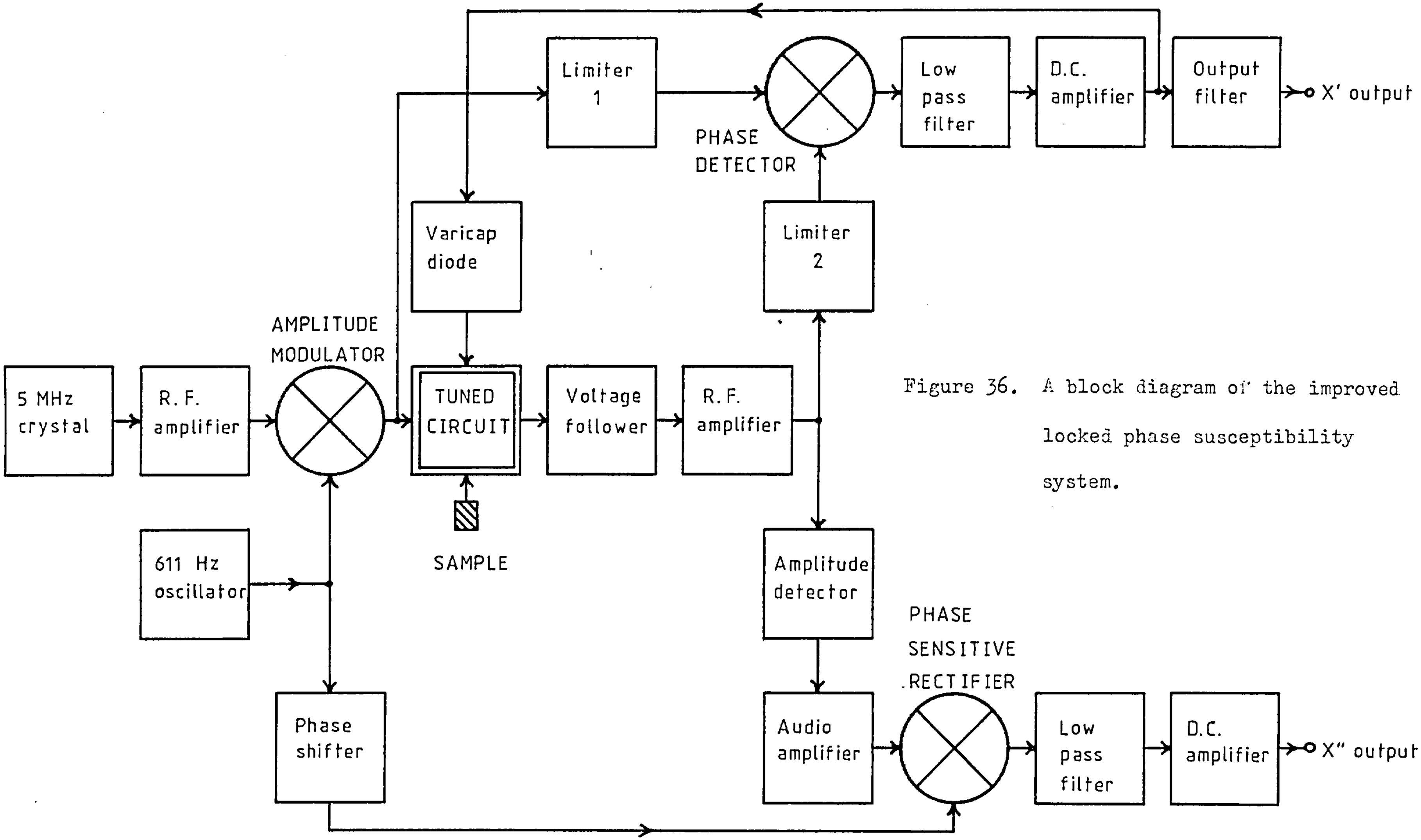

Figure 36. A block diagram of the improved locked phase susceptibility system.

when X' is small. V_s is the volume of the sample, V_c is the volume of the coil, b is the length of the coil and D is the diameter of the coil. Pollack[15] has derived a relationship for the Q of a correctly wound coil:

$$Q \propto \frac{Db}{(102b + 45D)} \quad . \tag{4.9}$$

In practice, the coil's diameter D is determined not by choice but by the furnace with its associated insulation, air gap and water jacket. The only dimension that can be varied to maximise $Q^{0.5}F$ is the coil's length b. For convenience, it is best to work with the product QF^2.

$$QF^2 \propto \left[\frac{V_s}{V_c} \frac{b(b + 0.44D)}{b^2 + D^2}\right]^2 \frac{Db}{(102b + 45D)} \quad . \tag{4.10}$$

Given that

$$V_c = \pi b D^2/4 \tag{4.11}$$

and that

$$102b + 45D = \frac{1000(b + 0.44D)}{\pi^2} \tag{4.12}$$

equation 4.10 can be simplified to

$$QF^2 \propto \frac{16V_s^2}{1000D^3} \frac{b(b + 0.44D)}{(b^2 + D^2)^2} \quad . \tag{4.13}$$

Although D is fixed, the ratio s = b/D is a variable. Dividing the top and bottom of equation 4.13 by D^2 gives

$$QF^2 \propto \frac{16V_s^2}{1000D^5} \frac{s(s + 0.44)}{(s^2 + 1)^2} \quad . \tag{4.14}$$

It is convenient to define a figure of merit M as

$$M = k\left[\frac{1000D^5}{16V_s^2} QF^2\right]^{0.5} \quad , \tag{4.15}$$

k is an unknown constant of proportionality which allows M to be written as

$$M = 10\left[\frac{s(s + 0.44)}{(s^2 + 1)^2}\right]^{0.5} . \qquad (4.16)$$

M is plotted as a function of s in figure 37. The maximum occurs between 0.83 and 0.84, but the maximum is rather broad and small deviations from s = 0.83 - 0.84 make little difference. The coil for this instrument has s = 0.86.

Two other points concerning the quality factor are relevant here. The furnace is wound using just a few turns of the narrowest available gauge of furnace wire. This minimises the reduction of Q by the furnace. Also, the coil is completely enclosed in a metal shield. This shield has the dual effect of decreasing the coil's inductance and increasing its resistance[47]. However, if the ends of the coil are separated by at least a coil diameter from the ends of the shield and the coil diameter is less than half the shield diameter, then the reduction in Q is less than 5-8%. In fact, the coil's ends are no closer than 3 coil diameters from the ends of the shield and the sides of the coil are no less than two coil diameters from the sides of the shield.

4.3.2 The crystal oscillator

The job of the crystal oscillator is to provide a sinusoidal signal at a very stable frequency with a very stable amplitude. The frequency stability of a crystal oscillator is composed of 3 parts [48,14]:

a. Long term frequency drift through aging of the quartz crystal; this is minimised by using a low crystal drive level.

b. Medium term frequency stability; this is affected by environmental changes such as ambient temperature or supply voltage.

c. Short term phase noise; this is reduced by using a high crystal drive level, a high Q crystal and low noise circuitry.

Gardner[43,100] discusses oscillator phase noise generally and gives some references on the subject. The amplitude stability of the oscillator

Figure 37. A plot to determine the sample coil's optimum length to diameter ratio.

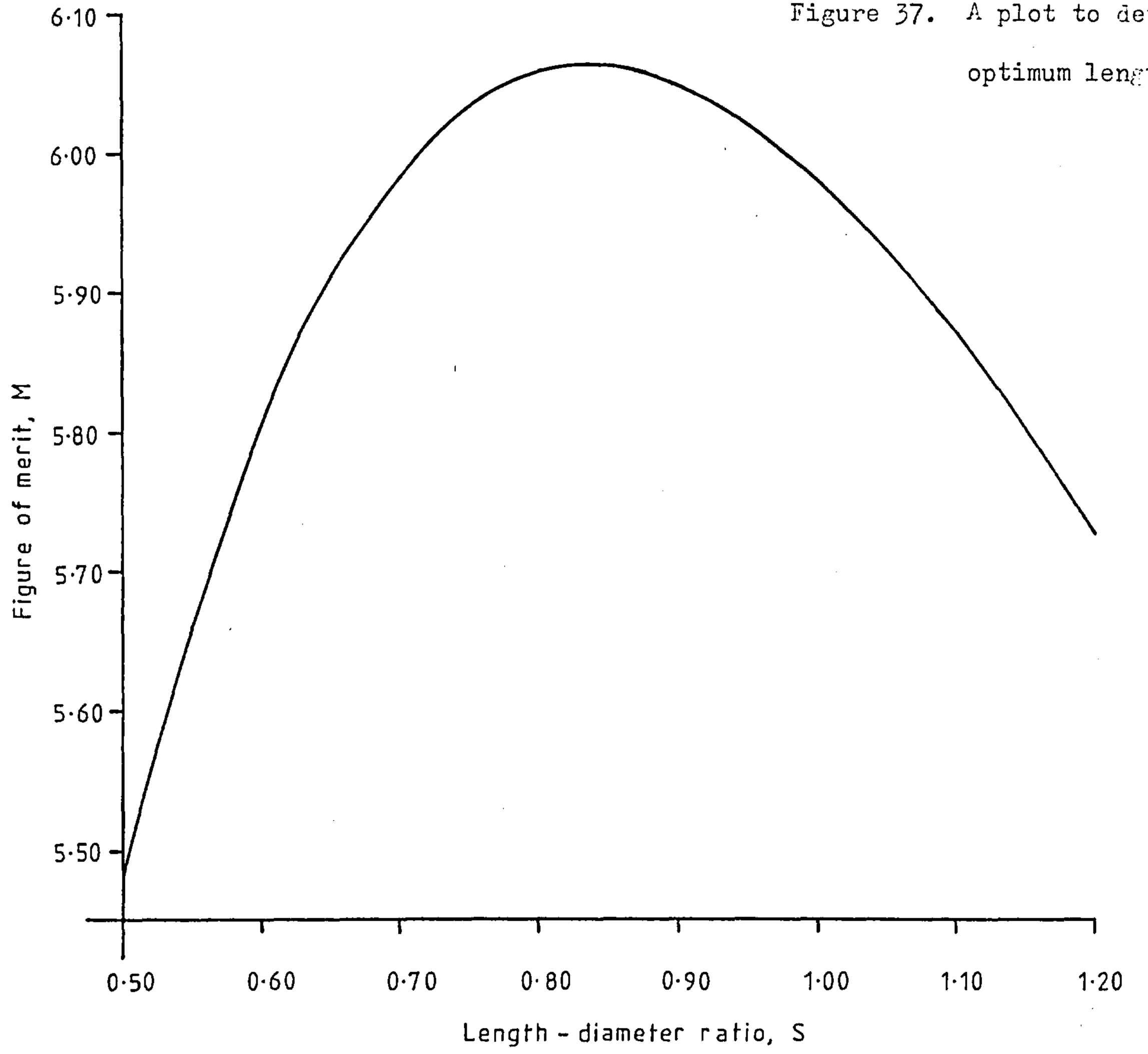

may be broken down in a similar manner.

No attempt has been made to design a suitable crystal oscillator. Instead, a Plessey SL 1680C crystal oscillator maintaining circuit is used and the performance of the resulting oscillator is outlined below. The crystal chosen to partner the integrated circuit is a 5.0688 MHz series resonant unit with a Q of 1.8×10^5 and an equivalent series resistance of 21Ω.

The aging of the crystal is negligible because of the very low drive level delivered by the SL1680. The power dissipated in the crystal is about 0.2 μW compared to more common levels of about 10μW to 500 μW. The rate of aging is less than 15Hz $year^{-1}$.

The circuit ensures that the only contribution to the medium term frequency drift is the crystal's temperature coefficient. The temperature coefficient is about -0.4 $ppm\,^{o}C^{-1}$ over the range $0^{o}C$ - $40^{o}C$, this is insignificant compared to the temperature coefficient of the tuned circuit.

The short term phase noise is large for a crystal oscillator because of the low crystal drive level. This should not be important because the phase noise is common to the coil and reference signals and cancels itself out at the phase detector. Data on the SL1680 puts the base band noise level at -85dB with respect to the carrier (5MHz) in a 1Hz bandwidth. This can be interpreted[48,18] as a phase jitter of 0.005^{o} r.m.s. in a 1 Hz bandwidth.

The amplitude of the sinusoidal output from the SL1680 is feedback stabilised to 0.15 V r.m.s. No further details are given in the specifications.

4.3.3 The radio frequency phase detector

The job of the locked phase loop is to keep the natural resonant frequency of the tuned circuit exactly equal to the frequency of the crystal oscillator. The phase detector produces the error signal that the loop acts on. If the locked phase loop is to do its job properly, the phase detector must fulfil a number of requirements:

a. When the signals from the tuned circuit and the oscillator are in phase the averaged output from the phase detector should be zero volts.

b. The phase detector must be able to sense very small deviations of phase from the in phase condition. To put this in perspective, a 0.6 mg sample of magnetite gave a 10mV signal on the first locked phase loop. This was equivalent to a phase shift of 0.8^{o} or a time delay of 0.45 ns. It was anticipated that the new phase detector would have to respond to phase shifts smaller than 0.03^{o}, that is to time delays of less than 17 ps.

c. The phase detector has to have good noise rejection properties.

d. The phase detector has to be insensitive to the amplitude of the input signals.

Egan[42,98] and Gardner[43,106] discuss a wide range of phase detectors. Of these, the multiplying detector is the one that best satisfies requirements b and c. The exclusive - OR (XOR) logic gate can be used as a multiplying detector if it acts on amplitude limited signals; amplitude limiting brings with it resistance to amplitude modulation. The XOR multiplying detector can therefore satisfy requirements b, c and d. It will shortly be seen that the simple XOR detector can be modified to meet requirement a.

Figure 38a shows a generalised multiplying phase detector, it looks very similar to the phase sensitive rectifier of subsection 4.2.3. When two sinusoidal waves, $\cos(w_i t + \phi)$ and $\cos w_r t$, of nearly identical frequency are applied to the detector the output of the multiplier is

$$V_o = \frac{K}{2}\left[\cos\phi\,\cos(w_r - w_i)t + \cos((w_r + w_i)t + \phi)\right] \qquad (4.17)$$

where K is the multiplier's gain.

In the first instance, let $w_r = w_i$. The filter removes the ripple

Figure 38. The multiplying phase detector.

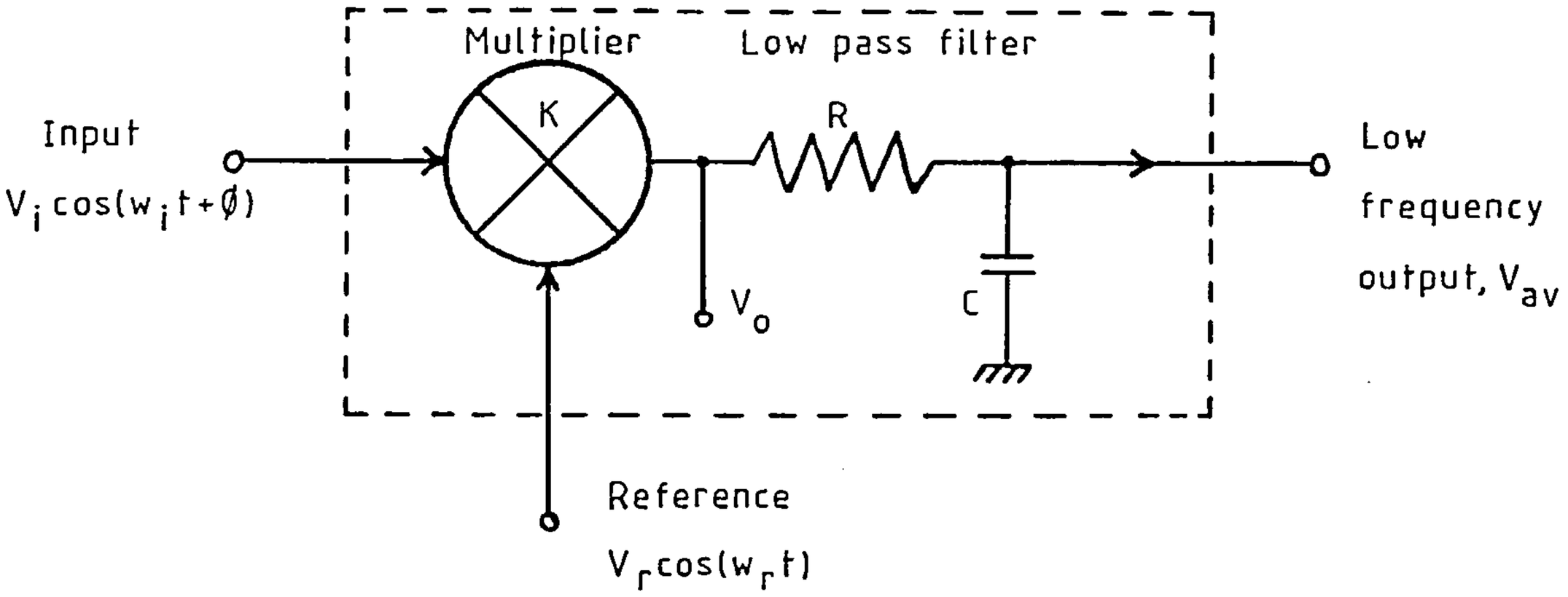

a. A block diagram.

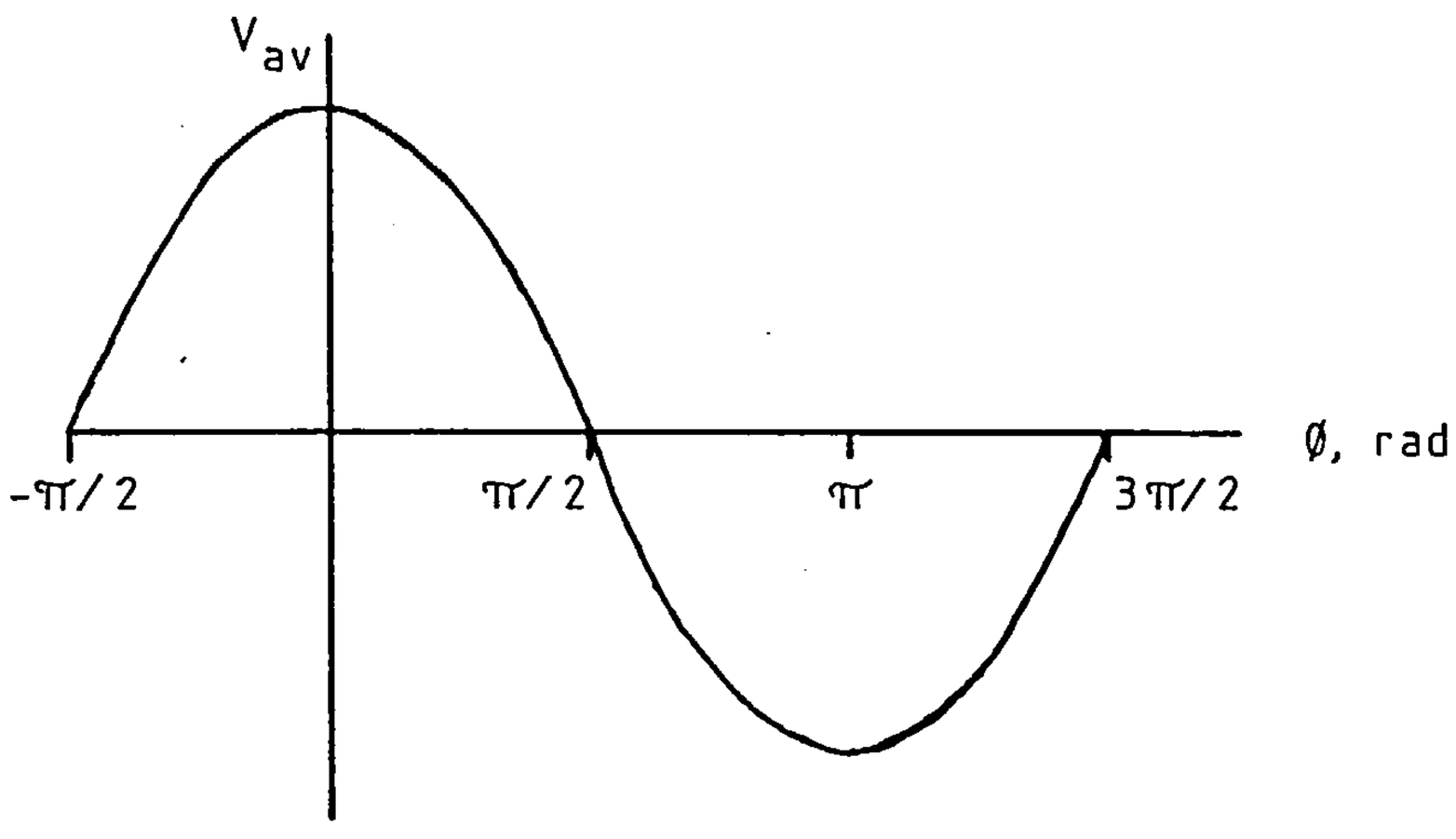

b. The phase detector's output for sinusoidal inputs of equal frequency.

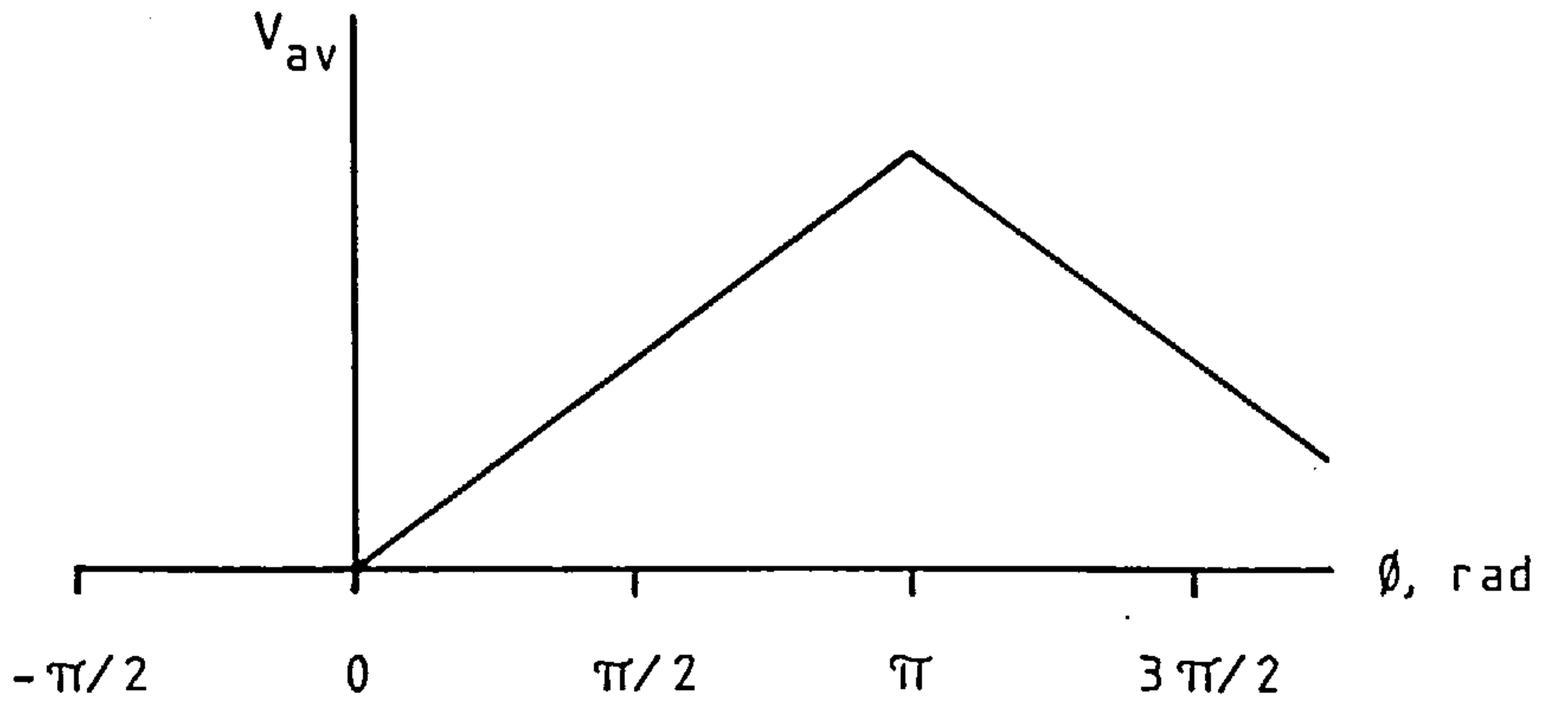

c. An XOR gate's output for square wave inputs of equal frequency.

at $2w_r$ to give

$$V_{av} = \frac{K}{2} \cos \phi \quad . \tag{4.18}$$

Remember that ϕ is the phase difference between the signal from the tuned circuit and the signal from the crystal oscillator. The output is plotted as a function of phase difference in figure 38b. A feedback loop incorporating this detector cannot lock at $\phi = 0$ because the sign of the error signal V_{av} is interdeterminate. The most likely points of operation are $\phi = \pm\pi/2$ where the error signal changes sign. Unfortunately, the locked phase loop will only work properly if $\phi = 0$.

Having seen what happens when $w_r = w_i$, now let $w_i = w_r + \Delta w$ where $\Delta w << w_r$. The averaged output is

$$V_{av} = \frac{K}{2} \cos \phi \cos \Delta wt \quad . \tag{4.19}$$

The equation shows that noise signals lying close to 5MHz are frequency shifted to become low frequency disturbances to the control system. Some of these disturbances are eliminated by the low pass filter. Treating the phase detector as a band pass filter, it has a Q of $w_r/2w_c$ where w_c is the cut off frequency of the averaging filter. For the final version of the instrument $w_r = 3.14 \times 10^7$ rad s^{-1} and $2w_c = 12.6$ rad s^{-1}, therefore $Q = 2.5 \times 10^6$.

When using an XOR gate as a phase detector, the two input signals should both be square waves. By analogy with equation 4.18, it is easy to see that the XOR detector's characteristic is a triangle wave as in figure 38c.

The disadvantages of the XOR gate are the permanent presence of a d.c. offset and the fact that a locked phase loop incorporating it cannot lock at $\phi = 0$. A circuit has been devised that overcomes the d.c. and phase offset problems of the XOR multiplier, it also offers an extended

locking range and low drift. The circuit is shown in figure 39a. The amplitude limited reference and tuned circuit signals are both passed to divide-by-two flip flops. The tuned circuit's signal has deliberately been shifted by 180^{o} by means of an inverting amplifier. The two divided signals are multiplied together, then they are averaged and summed. Figure 39b shows the wave forms at each point in the circuit when $\phi = 0$. The new phase detector's characteristic is shown in figure 39c. The maximum output is about 5 volts because open collector TTL gates are used. The gain is

$$K = \frac{5}{\pi}\,\phi \,, \qquad (4.20)$$

which is identical to that of a simple TTL XOR gate. The advantages of the new detector are:

a. a loop incorporating it automatically locks at $\phi = 0$ rather than $\phi = \pi/2$,

b. there is no d.c. offset,

c. the linear characteristic is extended from π to 2π rad.,

d. the inputs to the multipliers automatically have the optimum 50% duty cycle, and

e. the d.c. drifts of the multipliers cancel when the loop is in lock. The multipliers are on the same chip, at the same temperature and they share the same power rail. Their drifts should be nearly identical and they therefore cancel at the summing amplifier.

4.3.4 Sources of drift

It was expected that measurements of X' and X" against temperature would take about 1 hour of continuous chart recording. On this time-scale instrumental drift is worthy of consideration.

The drift in V_Q is ultimately fixed by the stability of the amplitude control loop in the crystal oscillator, there is no way of correcting this. The drift in V_p reflects slow changes in the natural frequency of

Figure 39. An improved phase detector.

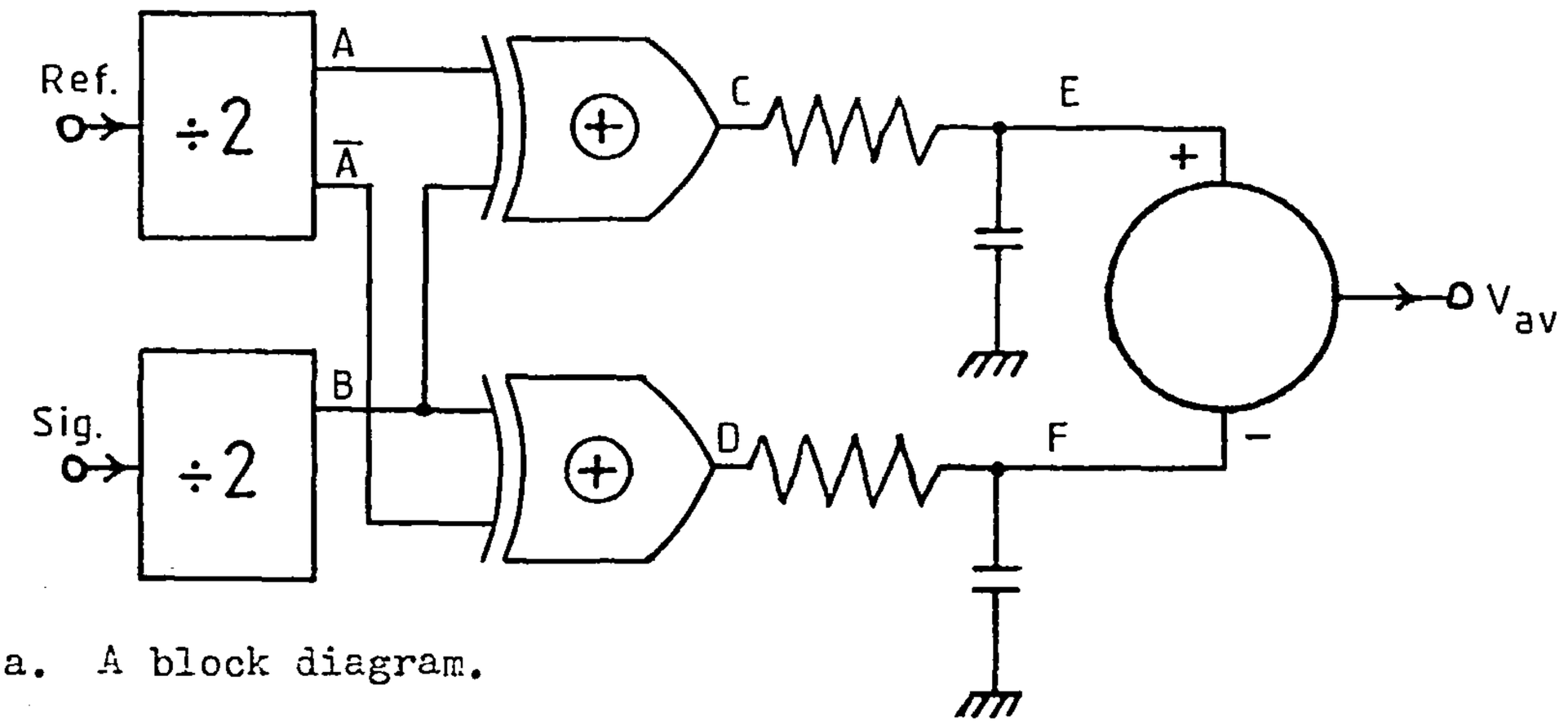

a. A block diagram.

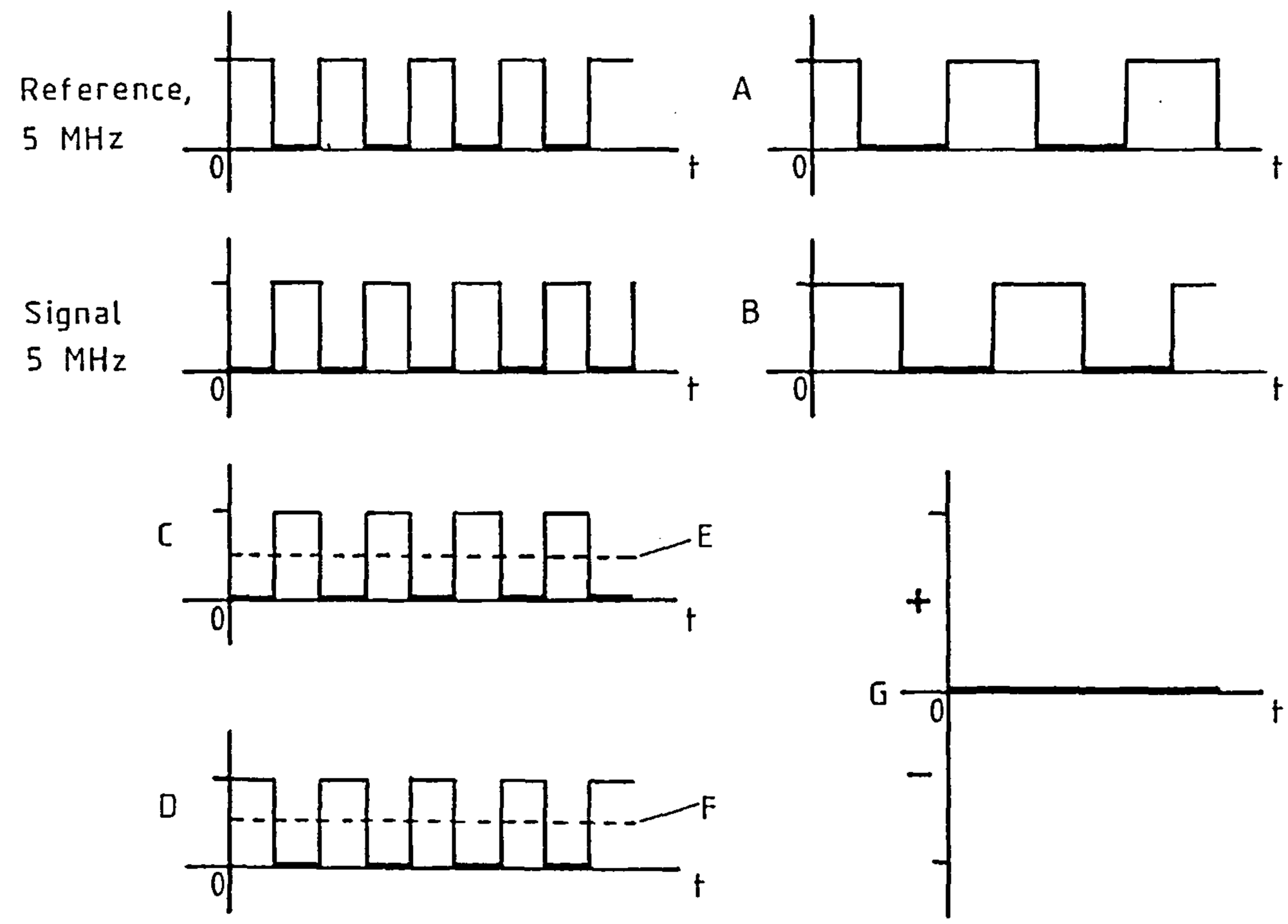

b. Ideal waveforms.

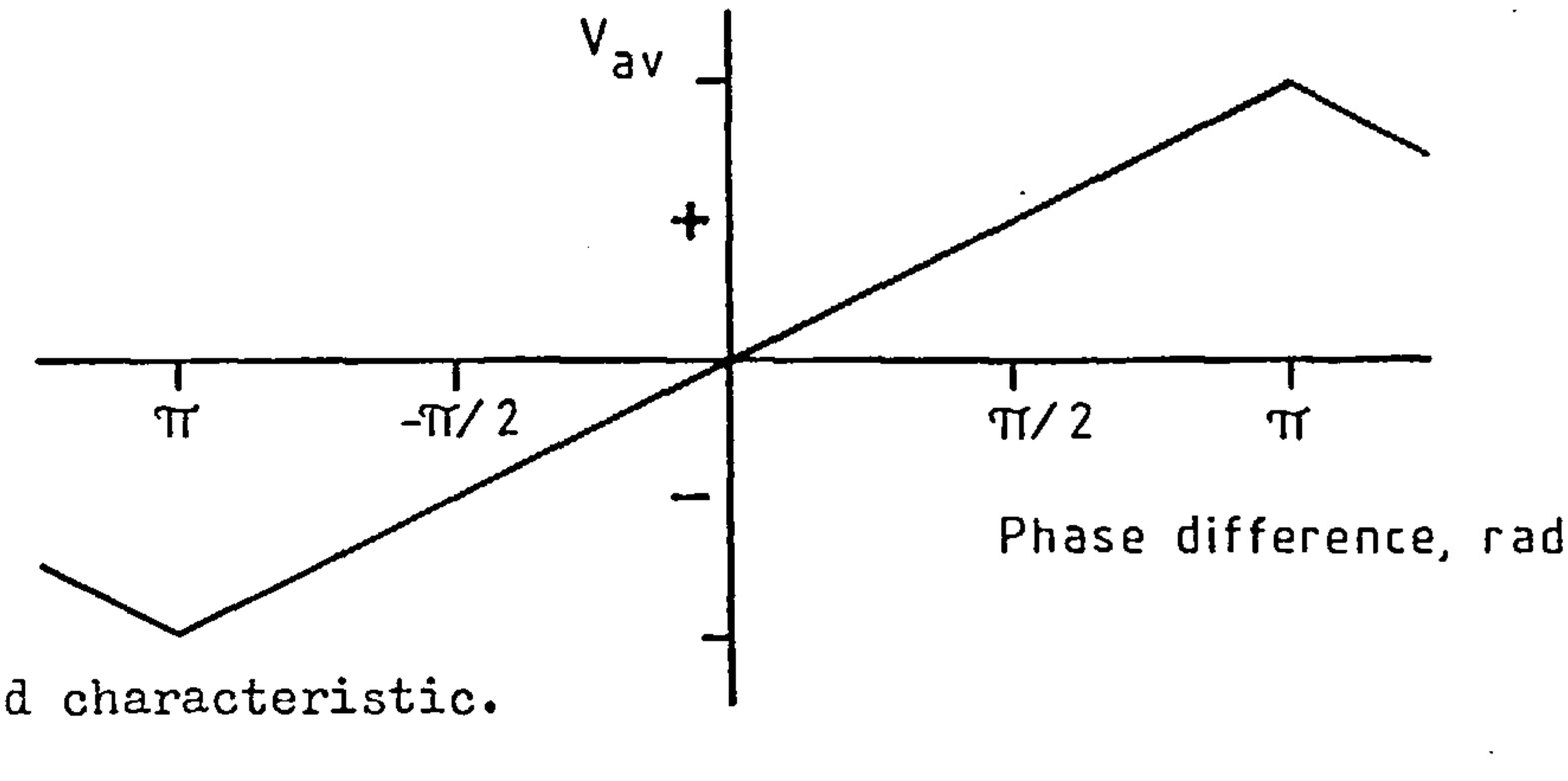

c. The idealised characteristic.

the tuned circuit relative to the much more stable frequency of the crystal oscillator. It is possible to minimise this drift by presuming that it has its roots in the temperature stability of the components in the tuned circuit. The tuned circuit can be broken down into four components: a 1.12 μH inductor, the main capacitance of 865pF, a trimmer capacitance of 12pF and the voltage variable capacitance. The temperature coefficients of each of these are dealt with below.

The trimmer capacitance has a polypropylene dielectric with a temperature coefficient of -200 p.p.m.$^{o}C^{-1}$. The coefficient of the trimmer is therefore -2.4×10^{-3} $pF^{o}C^{-1}$. The effect of this on the natural frequency of the tuned circuit is found from

$$-\frac{1}{2}\frac{\Delta C}{C} = \frac{\Delta f}{f}, \qquad (4.21)$$

where C is the total capacitance in the circuit and f = 5.068MHz. The temperature coefficient of the trimmer is thus equivalent to + $7Hz^{o}C^{-1}$.

The voltage variable capacitance is a Mullard BB105G. Using the manufacturer's data, the combined drifts in the reverse leakage current and the junction capacitance are equivalent to $1 \times 10^{-3} pF^{o}C$, or $-3.5Hz^{o}C^{-1}$ in the configuration used. The crystal's coefficient is $-2Hz^{o}C^{-1}$; the net coefficient of the crystal, the trimmer and the varicap is + $1.5Hz^{o}C^{-1}$.

The temperature dependence of the inductance is found by calculating the effects of thermal expansion in its diameter and length. Wheeler's formula for the inductance of a coil is

$$L = \mu_o \mu_r \left[\frac{10^3}{4\pi} \frac{D^2 n^2}{102b + 45D} \right] \qquad (2.4)$$

where D is the coil's diameter, b is the length of the coil and n is the number of turns. The temperature coefficient of the inductance is

$$\frac{dL}{dT} = \left[\frac{\partial L}{\partial b}\right]\left[\frac{dB}{dT}\right] + \left[\frac{\partial L}{\partial D}\right]\left[\frac{dD}{dT}\right] . \qquad (4.22)$$

This gives

$$\frac{\Delta L}{\Delta T} = L\left[\frac{-102}{(102b + 45D)}\ \frac{\Delta b}{\Delta T} + \frac{(204b/D + 45)}{(102b + 45D)}\ \frac{\Delta D}{\Delta T}\right] , \qquad (4.23)$$

if the changes Δb and ΔD are small. The dimensions of the coil in the improved instrument are $D = 2.372 \times 10^{-2}$m and $b = 2.04 \times 10^{-2}$m, therefore

$$\frac{1}{L}\ \frac{\Delta L}{\Delta T} = 70.0\ \frac{\Delta D}{\Delta T} - 32.4\ \frac{\Delta b}{\Delta T} . \qquad (4.24)$$

The coil is glued rigidly to a cylindrical pyrex water jacket. The coil is easy to stretch or compress along its length, therefore $\Delta b/\Delta T$ can be found from the thermal expansivity of pyrex:

$$\frac{1}{b}\ \frac{\Delta b}{\Delta T} = 3 \times 10^{-6\,o}C^{-1} .$$

The radial expansion coefficient is given by the thermal expansion coefficient of copper:

$$\frac{1}{D}\ \frac{\Delta D}{\Delta T} = 16.7 \times 10^{-6\,o}C^{-1} .$$

Fitting these figures into equation 4.24 gives

$$\frac{1}{L}\ \frac{\Delta L}{\Delta T} = +\ 2.6 \times 10^{-5\,o}C^{-1}$$

which is equivalent to a coil coefficient of $-66 Hz\,^{o}C^{-1}$.

The coil is by far the most temperature sensitive component, but it may be corrected for by appropriately choosing the dielectrics in the main 865pF capacitance. Ceramic capacitors are available with temperature coefficients of 0 p.p.m.$^{o}C^{-1}$ and -150 p.p.m.$^{o}C^{-1}$, whilst silver mica capacitors have a coefficient of + 35 p.p.m.$^{o}C^{-1}$. A combination of (470 + 100)pF silver mica with (100 + 150)pF ceramic at -150 p.p.m.$^{o}C^{-1}$ and 45 pF ceramic at 0 p.p.m.$^{o}C^{-1}$ has a net coefficient of + 51 $Hz\,^{o}C^{-1}$.

This almost cancels the coefficient of the coil.

The arrangement of these components is shown in figure 40. The main capacitance and coil are housed together in a thermally insulated environment. This ensures that their temperatures are always identical so that the compensation works properly. The insulated environment is almost theremostatic for the water that continuously flows in the jacket has beer found to have a temperature stability of $\pm$ 0.25^{o}C per hour. Had the water's temperature stability been a problem, a thermostatted water supply could have been used.

It was anticipated that some sizeable offsets would arise when the furnace was running, these were reduced in two ways. First, it was ensured that heat from the furnace did not reach any of the temperature sensitive parts. Second, the mechanical coupling between the coil and the furnace was minimised to prevent thermal expansion in the furnace distorting the coil.

Figure 40. How the tuned circuit was thermally and electromagnetically isolated from the ambient environment.

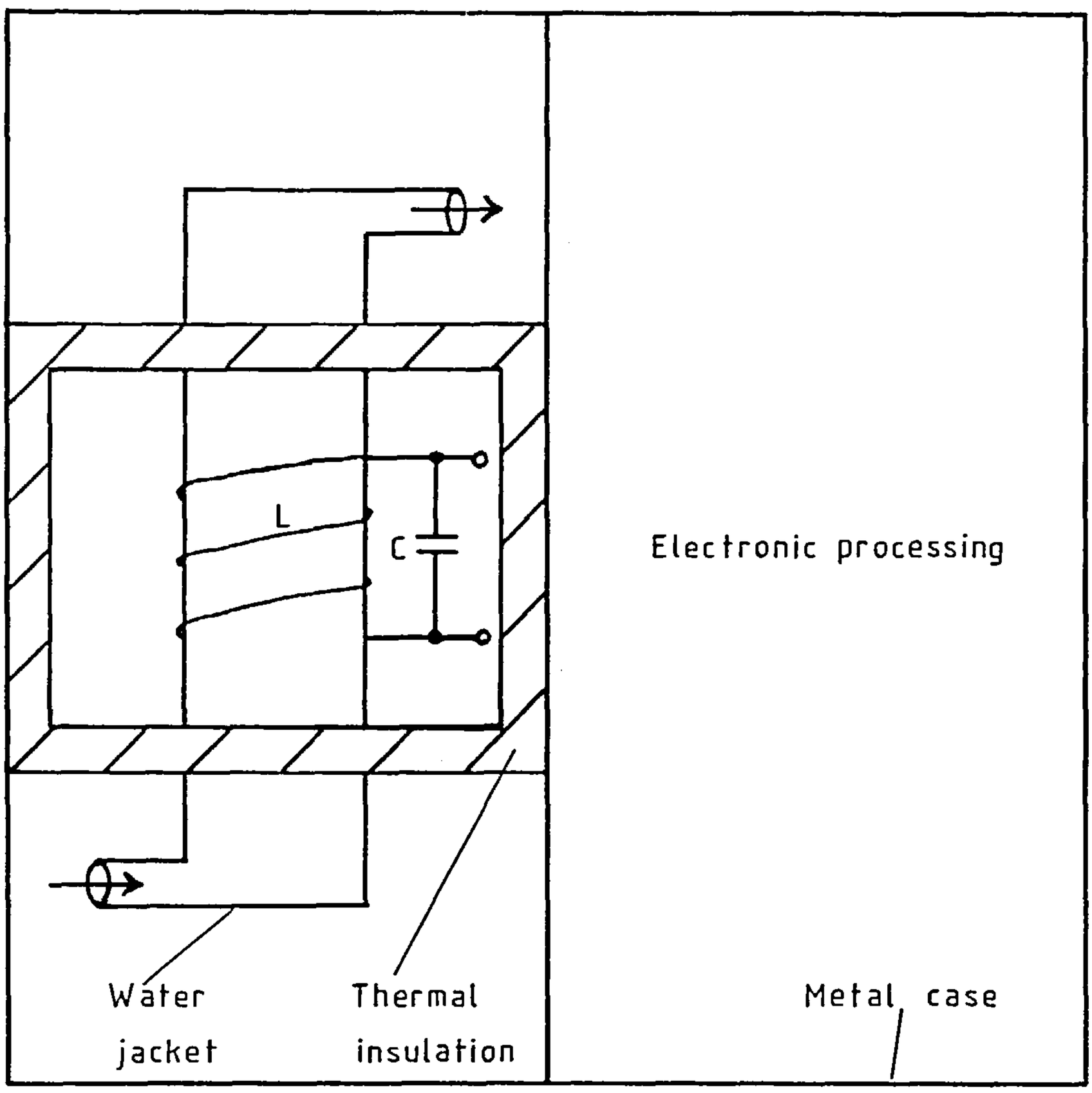

CHAPTER 5

THE CIRCUITRY FOR THE IMPROVED LOCKED PHASE LOOP

5.1 INTRODUCTION

This chapter describes the circuitry that was developed for the improved locked phase loop. Sections 5.2 to 5.4 are devoted to the three circuit boards that carry all of the electronic components. Next, section 5.5 describes the furnace's construction and characteristics. Finally, section 5.6 lists the initial adjustments and presents some photographs of the completed instrument.

Correct grounding and shielding within the instrument are very important both for stability and for low noise. The guidelines set out by Morrison[50] are followed carefully.

The correct choice of passive components matters also. Carbon resistors are more noisy than metal film resistors[46,149], so 1% metal film resistors are used throughout. Electrolytic capacitors are avoided as far as possible, tantalum capacitors are normally used for decoupling power supplies. Ceramic disc capacitors are more noisy than silver mica or polystyrene types, but their low parasitic inductance makes them useful for r.f. decoupling.

The circuitry is built entirely on stripboard for rapid construction and ease of alteration during development. Unfortunately, stripboard is not intended for use above 50KHz. Should other versions of this instrument be built the use of a properly laid out double sided printed circuit board with an earth plane is highly recommended.

5.2 THE TUNED CIRCUIT DRIVER BOARD

5.2.1 Generating a 5MHz drive signal

The circuit that generates the 5MHz drive signal is drawn in figure 41. The SL1680 crystal oscillator maintaining circuit draws power from a simple 6.2V supply, the device has an internal voltage regulator.

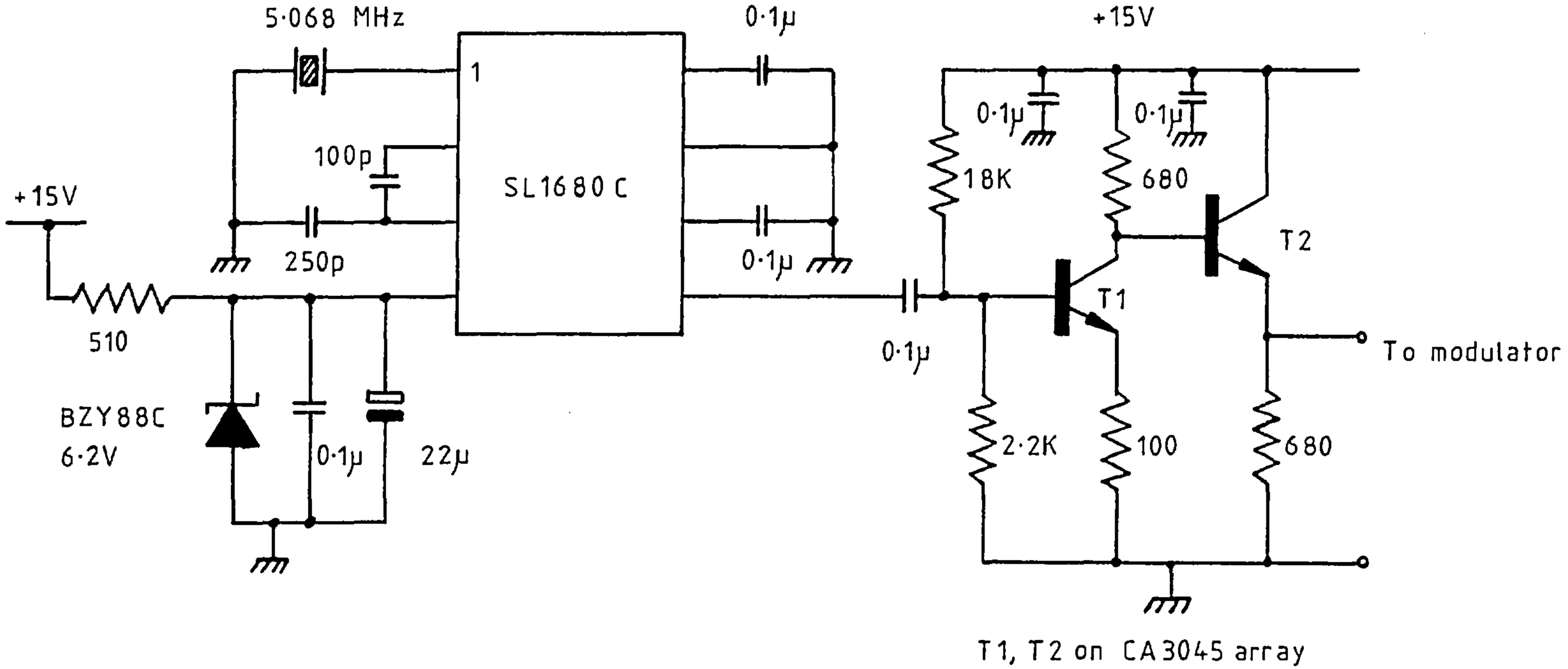

Figure 41. The circuit that generated the 5MHz drive signal.

The SL1680 feeds a sinusoidal 5.068 MHz signal to the outside world from a common collector voltage follower which has a standing current of 1.2mA. The output resistance R_o of the voltage follower should be dominated by the intrinsic resistance r_e of the output transistor's base emitter junction (39,39).

$$R_o \approx r_e = \frac{kT}{qI_c} = \frac{26}{I_c} , \qquad (5.1)$$

where I_c is in mA and the ambient temperature assumed is 25°C. R_o is therefore 22 Ω.

The 5MHz signal is amplified prior to amplitude modulation by a common emitter - common collector amplifier. Two low noise transistors on a CA 3045 package are used, their low base collector capacitance of 0.6 pF reduces the Miller effect(39,83) in the common emitter amplifier. The noise figure of the amplifying stage is minimised by correctly choosing the collector current for a source impedance of 22 Ω. The necessary relationship is(39,138).

$$I_c \text{ (optimum)} \approx 28 \frac{(h_{fe})^{0.5}}{R_s} , \qquad (5.2)$$

where I_c is in mA, h_{fe} is the forward current gain of the transistor and R_s is the source impedance. Knowing that R_s is 22 Ω and that h_{fe} is between 40 and 100 for these devices, I_c (optimum) is between 8.0mA and 12.7mA. The current through T1 is stabilised at 10mA in practice. T2 serves as a high input impedance buffer to preserve T1's gain.

5.2.2 The audio oscillator and modulator

Figure 42 shows the circuit that amplitude modulates the 5MHz waveform and produces the reference necessary for phase sensitive rectification. The oscillator is a 555 astable multivibrator with its output subdivided by 128 from 78.2KHz to 611 Hz. This arrangement reduces the phase noise of the 555 by a factor of 128(43,99). It is also a con-

Figure 42. The circuit for amplitude modulating the 5MHz drive signal.

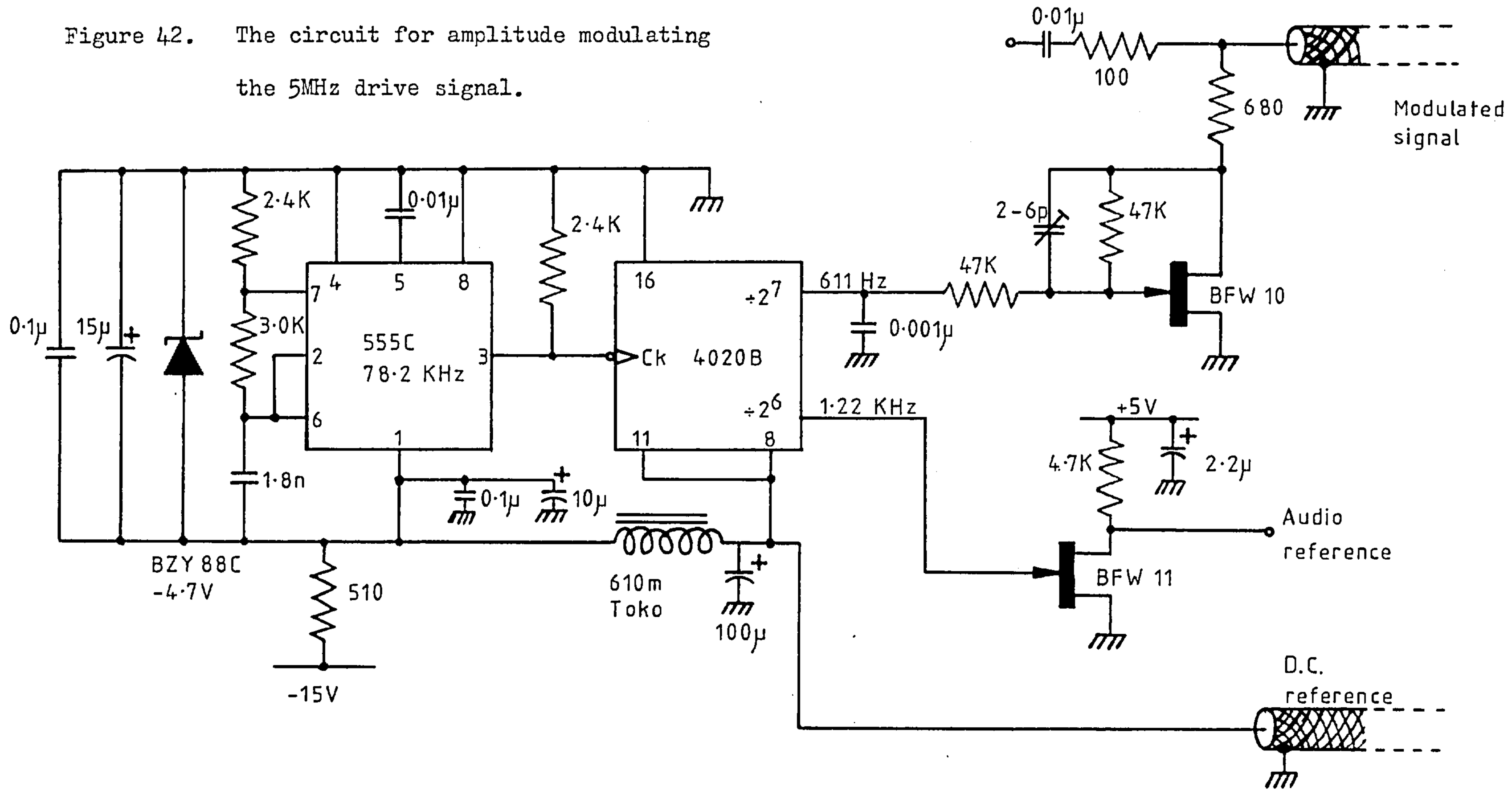

venient way of producing a reference at twice the modulation frequency: subsection 5.4.2 shows that this makes phase shifting easy.

The oscillator and divider run off -4.7V power rails so that the divider's output is of the correct polarity for an n-channel f.e.t. As the divider is CMOS the output is a saturated 4.7V peak to peak square wave. By using the -4.7V rail as a DC reference in the phase sensitive rectifier, any drift in the modulating signal's amplitude is self cancelling and produces no error in X".

The amplitude modulator is an n-channel BFW10 used as a voltage variable resistance. To minimise the 2nd and 3rd harmonic distortion produced by the modulator, feedback is taken from the drain to the gate and a device with a high pinch off voltage is selected[38]. A small 2 to 6 pF trimmer is included to compensate for a parasitic gate-source capacitance of about 5pF. Another n-channel f.e.t. makes the 1.22KHz reference signal acceptable to the TTL circuits used in the phase shifter.

The two output waveforms are shown in figure 43. The drive signal to the tuned circuit, in figure 43a, is 3.25V peak to peak with a 9% modulation depth. The envelope is slightly assymmetric about the 0V line due to a small amount of 3rd harmonic distortion produced by the SL1680 crystal oscillator circuit. Figure 43b shows the clean 0.3V to 5.0V square wave at 1.22KHz that is produced for the phase sensitive rectifier.

5.3 THE SUSCEPTIBILITY SENSING BOARD

5.3.1 The tuned circuit and the r.f. amplifier

The arrangement of the tuned circuit, voltage follower and r.f. amplifier is illustrated in figure 44. The tuned circuit is isolated in its own metal enclosure. The circuitry that buffers, amplifies and further processes the signal from the tuned circuit is screened in another metal enclosure mounted flush with the first. The two enclosures make a very low resistance electrical contact and they are made the reference

Figure 43. The waveforms produced by the r.f. driver board.

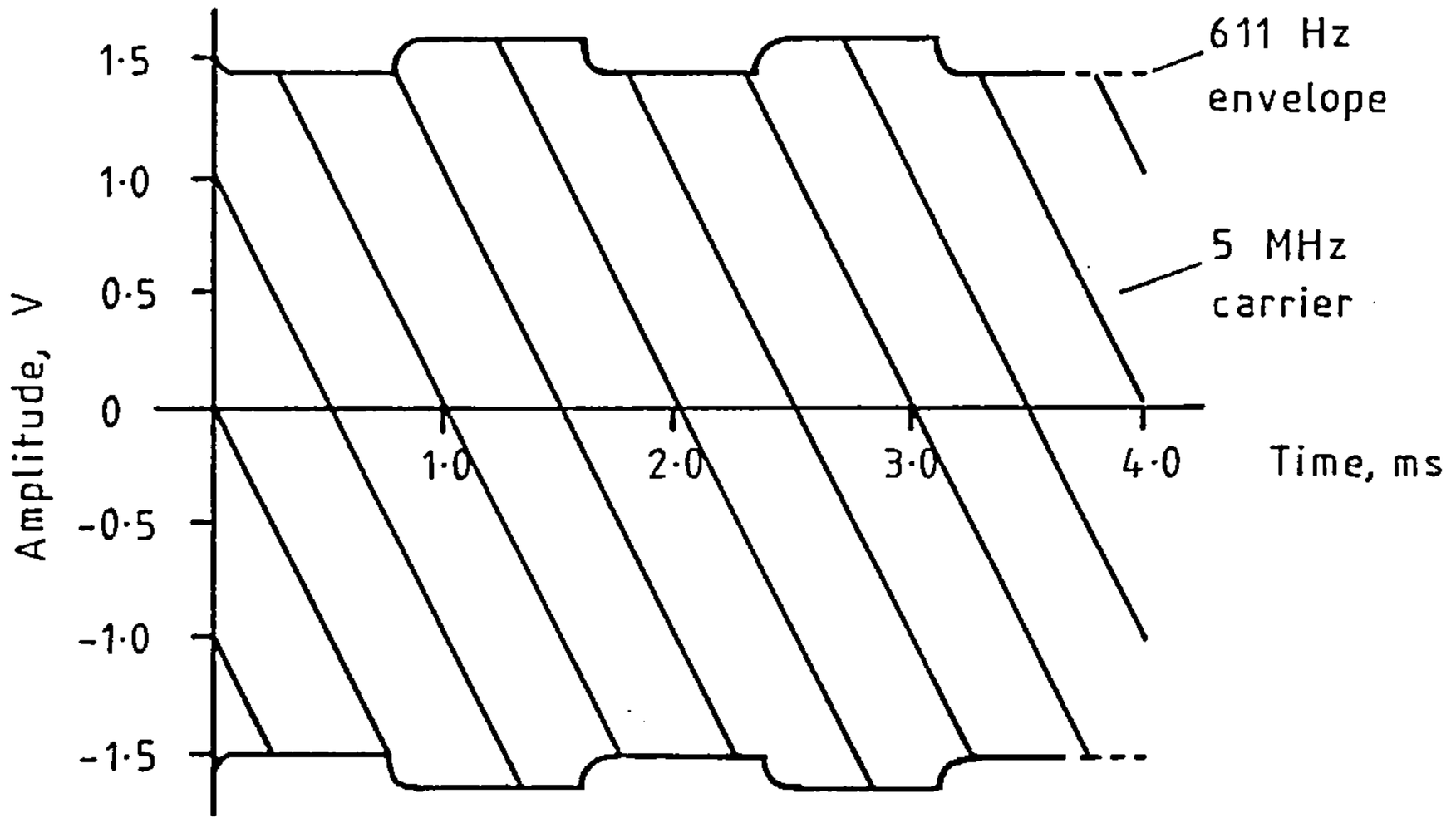

a. The envelope of the 5 MHz signal to the tuned circuit.

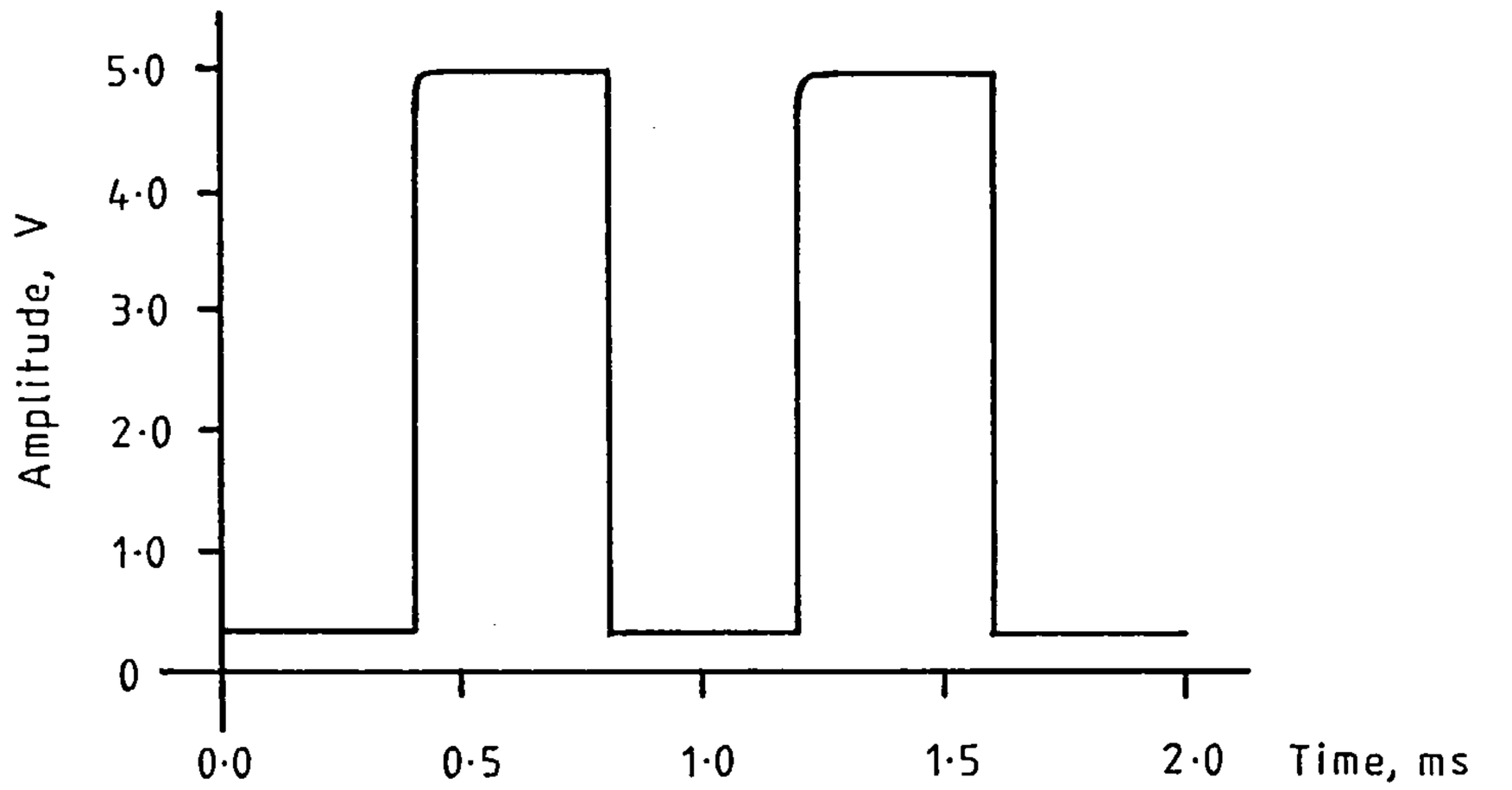

b. The 1.22 KHz reference signal to the phase sensitive rectifier's phase shifter.

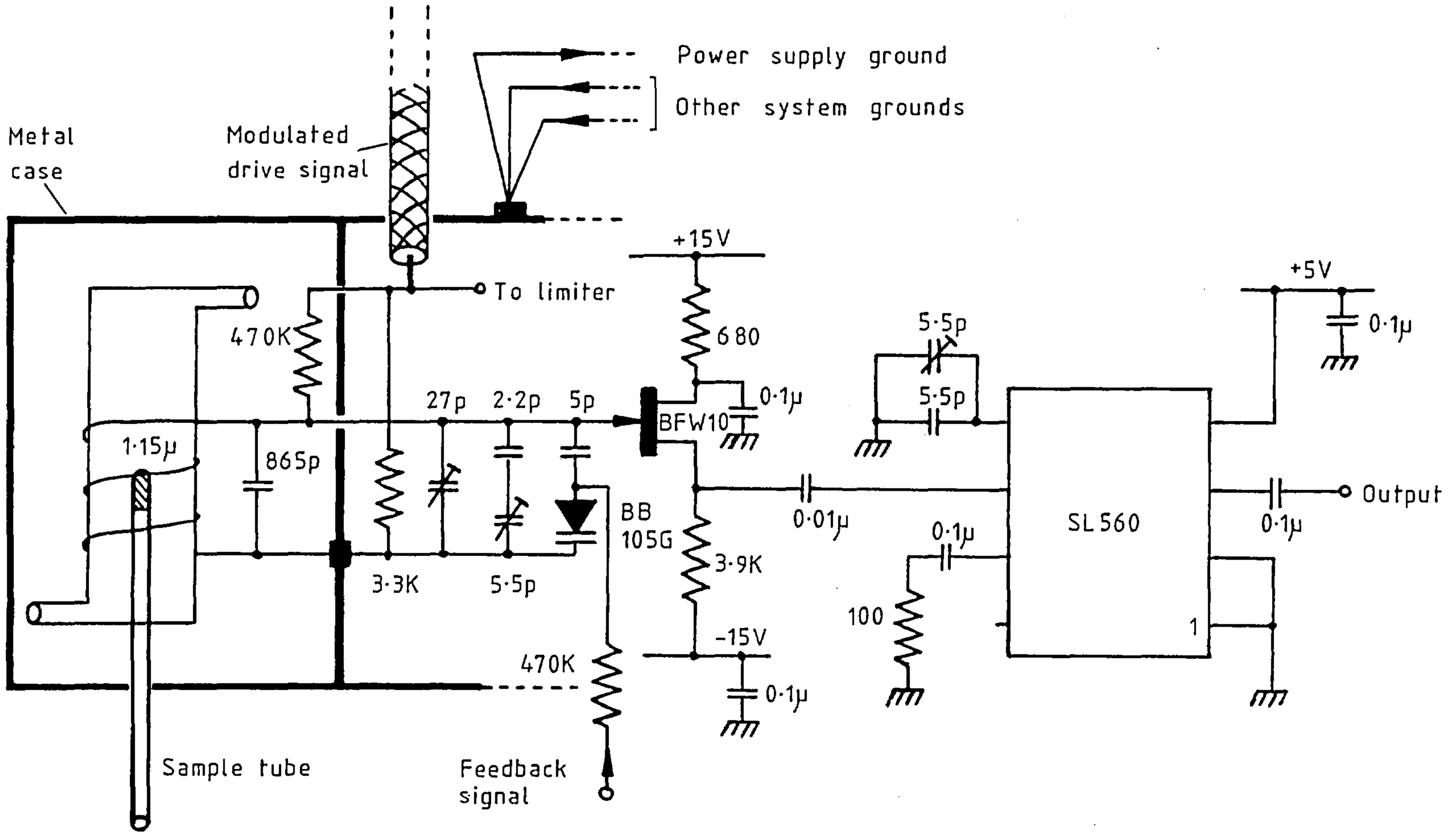

Figure 44. The tuned circuit, the voltage follower and the r.f. amplifier.

ground for whole instrument, low resistance connections are made from here to the power supply ground. The circuitry within the composite enclosure is grounded at one point only, that being the point at which the tuned circuit is grounded[50,40]. The modulated 5MHz drive signal enters the enclosure in a screened coaxial cable. It is fed directly to a limiting amplifier and also through a 470KΩ isolating resistor to the tuned circuit.

The bulk of the tuned circuit's capacitance is located as close as possible to the sample coil. This improves the Q by reducing the resistance in the path of the electrical current alternating between the inductance and capacitance. It also improves the filling factor by minimising the stray inductance associated with the connecting leads to the capacitance. Very little electrical energy flows into the adjoining metal chamber.

The coil is wound with 1.8 mm diameter enamelled copper wire on a 22.0 mm diameter glass water jacket former. It was shown in subsection 4.3.1 that the optimum length to diameter ratio of the coil is 0.84. The highest possible quality factor is attained by ensuring that[15]

$$n = \frac{b}{1.414d} \quad , \tag{5.3}$$

where n is the number of turns on the coil, b is the length of the coil and d is the wire's diameter. In fact, the coil has 8 turns, a length of 20.5 mm and a length to diameter ratio of 0.86. Using Wheeler's formula, equation 2.4, the inductance is calculated to be 1.15 μH. The true value of the inductance is 1.12 μH. Wheeler's formula has been used to optimise the coil's length to diameter ratio and to calculate the filling factor F. The agreement between the predicted and measured inductance is reassuring.

The other capacitors in the tuned circuit are a 2-22pF trimmer, a 1-5.5pF trimmer in a bandspread arrangement with a 2.2pF capacitor and a linearised varicap feedback capacitance. These capacitors are separated from the tuned circuit for convenience in mounting and for access. The

varicap and its series capacitor are carefully chosen to give a large feedback signal swing combined with a linearised capacitance - voltage characteristic. In the first design the largest sample of magnetite (19.4 mg) had caused a shift of 1.0KHz in the tuned circuit's natural frequency. The new coil has a filling factor that is 1.8 times larger than the original coil, so a shift of 2KHz in the natural resonant frequency has to be allowed for. Knowing that

$$\frac{\Delta f}{f} = -\frac{1}{2}\frac{\Delta C}{C}, \qquad (4.21)$$

the variable capacitance has to have a maximum shift of 0.7pF available. This is arranged using a BB105G varicap and a 5pF silver mica capacitor in series. The silver mica capacitor serves three purposes: it makes sure that the varicap can never present a DC load to the tuned circuit, it limits the maximum change of capacitance to produce a large feedback signal swing and it makes the capacitance - voltage characteristic more nearly linear. The resulting characteristic is shown on figure 45. The slope of the best line of fit between $V_r = -4V$ and $V_r = -13V$ is $7.67 \times 10^{-2} pFV^{-1}$. The gain of the feedback capacitance is

$$u = -\frac{1}{C}\frac{dC}{dV_r}, \qquad (3.20)$$

which is 8.72×10^{-5} since C = 880pF. In operation, the feedback capacitance is biased to a quiescent level of -5V by the circuit shown in figure 46. This circuit is included on the r.f. amplifier board, it has a second function of differentially receiving the amplified feedback error signal. Note that the IN827 voltage reference diode has a temperature stability of $0.001\%^{o}C^{-1}$.

The voltage across the tuned circuit is buffered by a low noise, n-channel BFW10 f.e.t. This stage is self biased. The signal from the voltage follower is passed to a Plessey SL560 r.f. amplifier which is

Figure 45. The variation of the feedback capacitance with the feedback voltage.

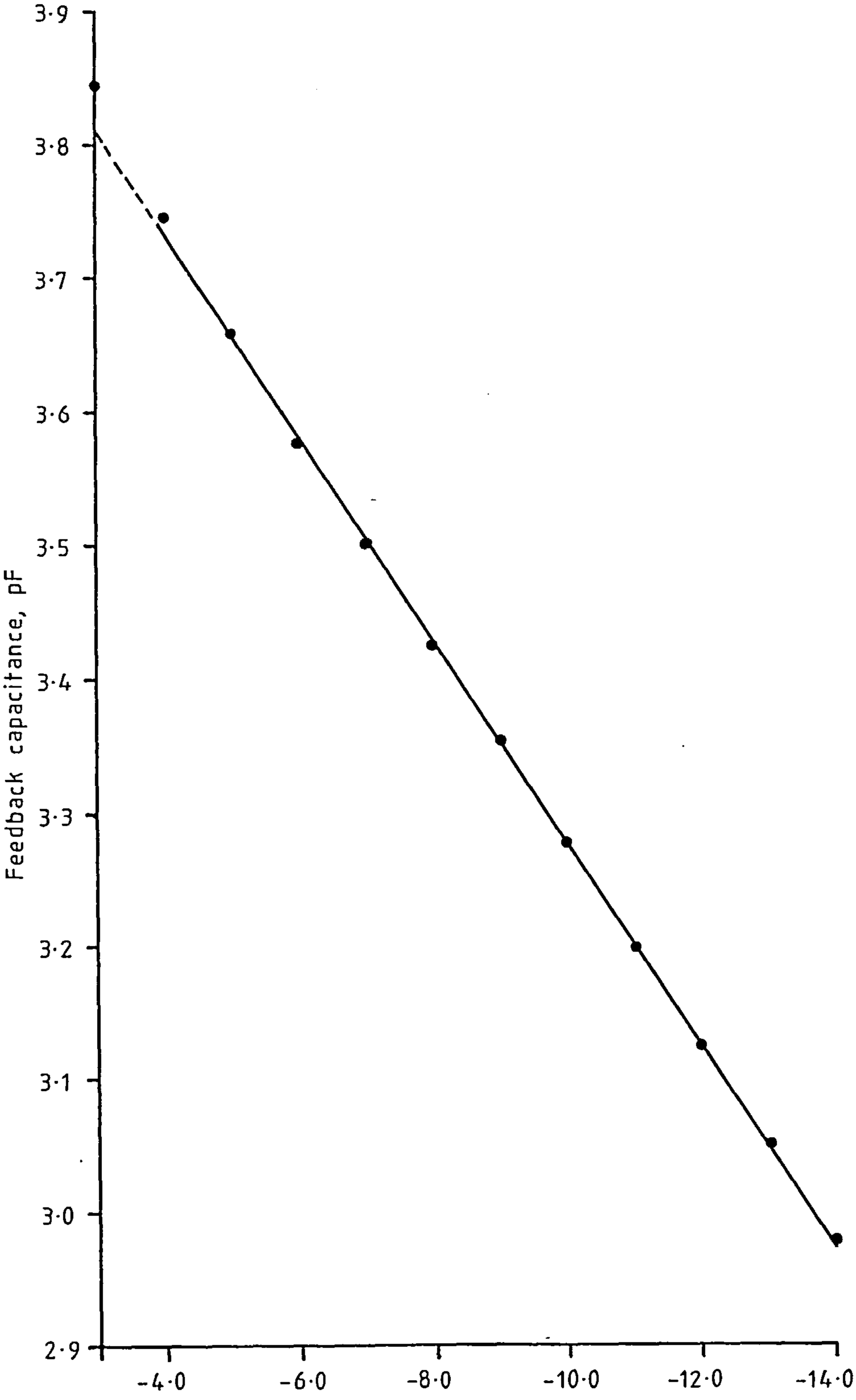

Figure 46. The varicap driver with the bias network.

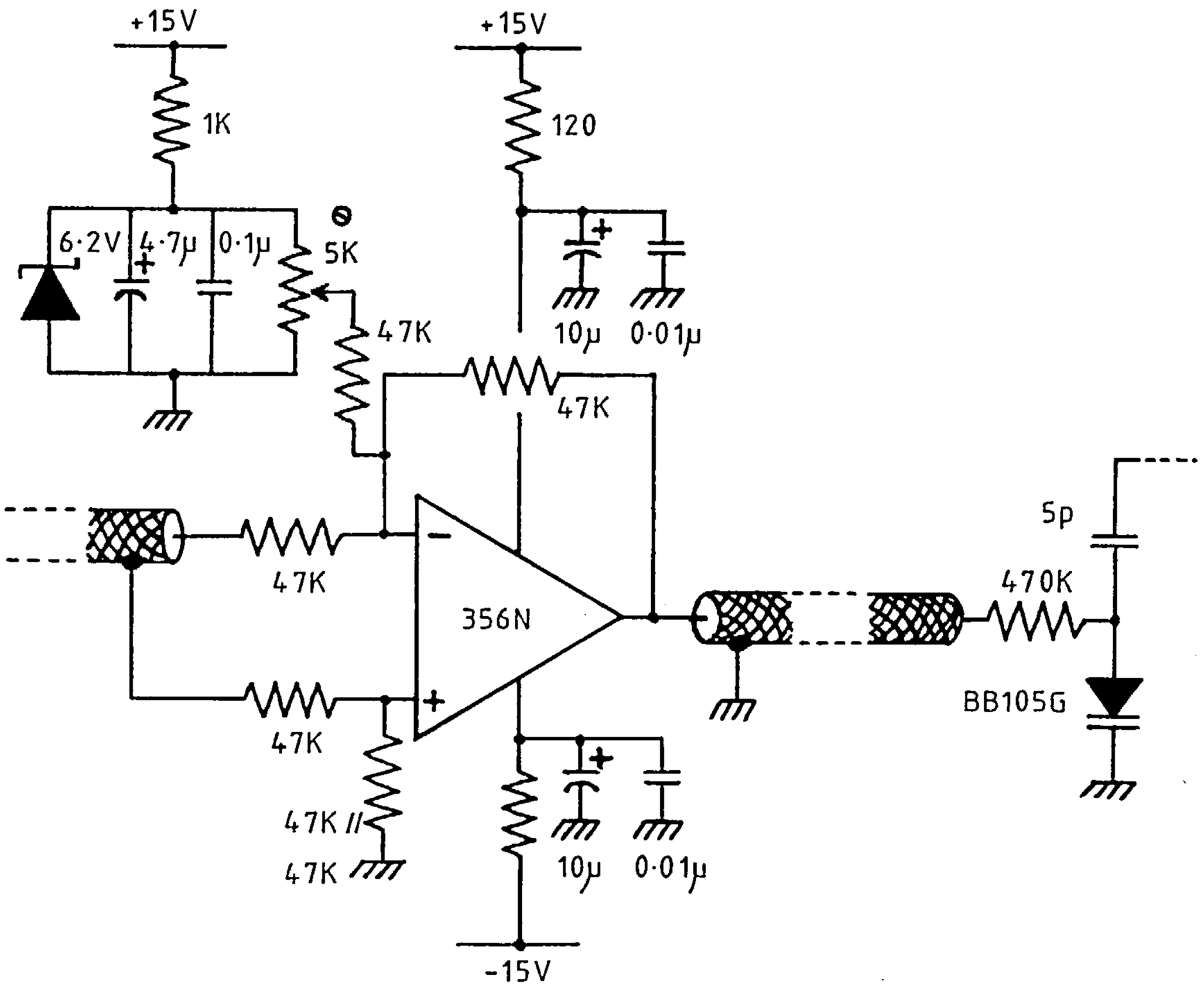

arranged to have an inverting gain of 8.5 and an output impedance of about 2 Ω. The low output impedance is essential for the combined input impedance of the succeeding amplitude detector and limiter is both small and changing. A variable capacitance connected to the SL560 is used to roll off the gain above 40MHz. This improves the amplier's stability on stripboard and allows small adjustments to the intrinsic phase delay.

The noise factor N_b of the BLW10 is[39,343]

$$N_b \approx 1 + \frac{\overline{e_n^2}}{4kTR_s} \qquad (5.4)$$

where $\overline{e_n^2}$ is the spot noise voltage of the BLW10 at 5MHz and R_s is the source impedance. As the bandwidth of the phase loop is much less than the bandwidth of the tuned circuit, equation 5.4 can be rewritten as

$$N_b \approx 1 + \frac{\overline{e^2}_n}{4\,kTw_oLQ} \qquad (5.5)$$

Knowing that Q = 175, L = 1.12uH and $e_n^2 = 5.6 \times 10^{-17} V^2 Hz^{-1}$, it can be calculated that $N_b = 1.5$.

According to Plessey's data, the noise factor of the SL560 common emitter/common collector amplifier is 1.5 when the following conditions all hold:

a the source resistance R_s is 200 Ω,

b the common emitter amplifier has a collector current of 1.1mA, and

c the emitter is a.c. grounded.

The BLW10 is selected to obtain a transconductance g of $4.7 \times 10^{-3} \Omega^{-1}$ at its operating point, it therefore has an output impedance of 1/g = 213 Ω in keeping with the SL560's requirement. The amplifier's collector current is correctly set to 1.1mA. However, there is an external resistance R_e of 83 Ω in series with the emitter. The noise factor N_a

for the amplifier is now

$$N_a = 1.5 + \frac{R_e}{R_s} = 1.9 \ . \qquad (5.6)$$

The noise factor of the combined buffer and amplifier is 2.4.

5.3.2 The amplitude detector

The amplitude detector, figure 47a, is a more elaborate version of the familiar peak rectifier. The germanium OA91 rectifying diodes are biased into slight conduction to improve their detection efficiency. The diodes are used as a differential pair. The waveforms shown in figure 47b are transmitted along a pair of shielded leads to a differential amplifier. The receiving amplifier is thus able to reject any 50Hz breakthrough from the furnace current because it appears as a common mode signal. The input impedance of the circuit is about 450Ω.

5.3.3 The limiters

Originally two CA3045 transistor arrays were used to make a pair of limiters, their design was based on the assymmetric differential amplifier (49,141). They had a high input impedance and a good resistance to amplitude modulation at their inputs. They also had the symmetric limiting characteristic that is required to minimise intermodulation between 1/f noise and the 5MHz signal (43,105). Unfortunately, their wide bandwidth left them only marginally stable on stripboard, they were therefore unreliable and they were dropped. These limiters would be stable on a printed circuit board with a ground plane and their design is presented in section 6.4 on improvements.

The limiters that are used are shown in figure 48a. Their d.c. operating conditions are identical, some small alterations that are needed for limiter 1 (see figure 36) are shown in dotted lines. Each limiter is built using a CA3045 transistor array. The bias conditions of the common emitter limiting amplifier are made thermally stable by taking advantage of

Figure 47. The amplitude detector.

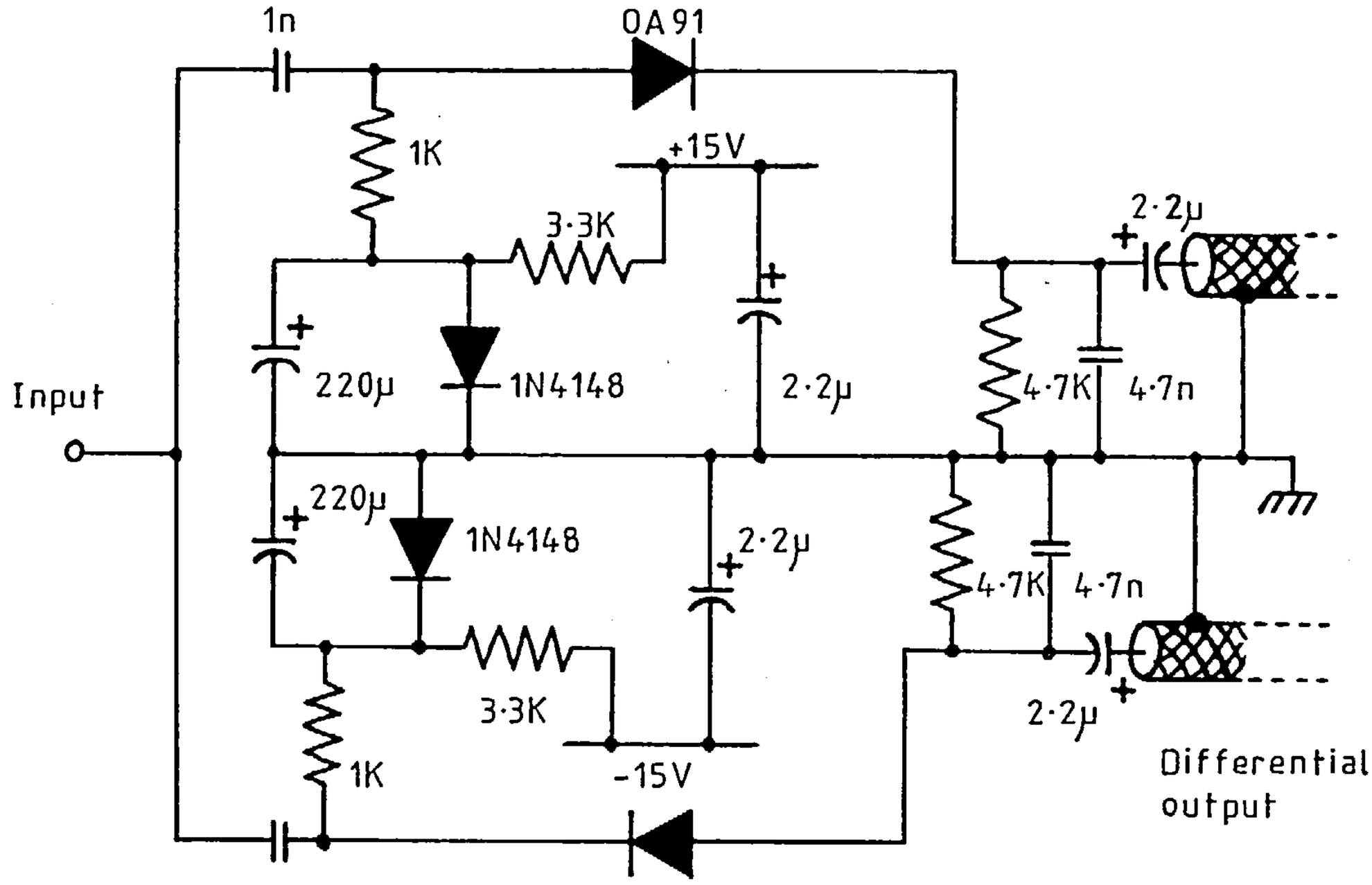

a. The circuit.

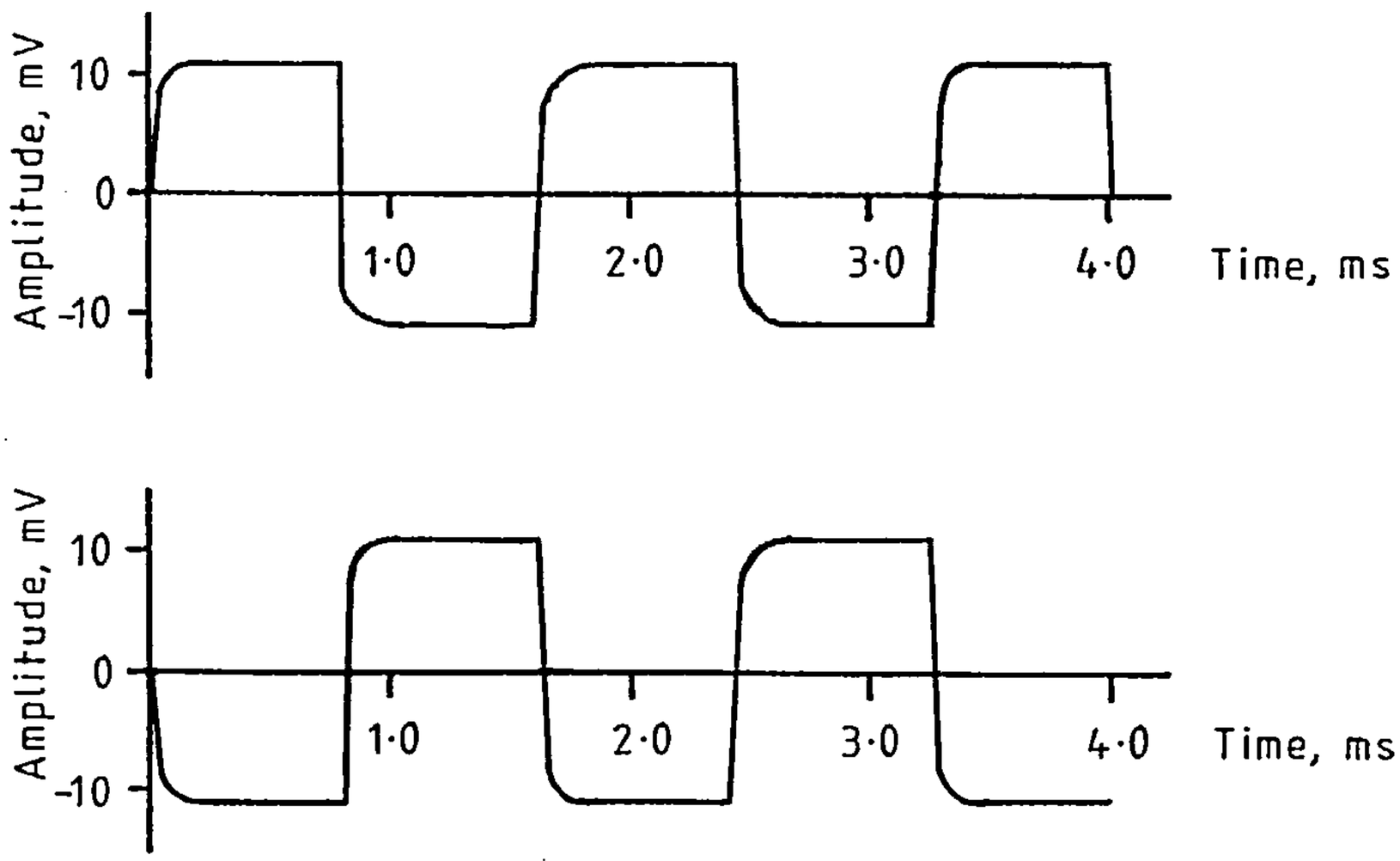

b. The output waveforms.

Figure 48. The limiters.

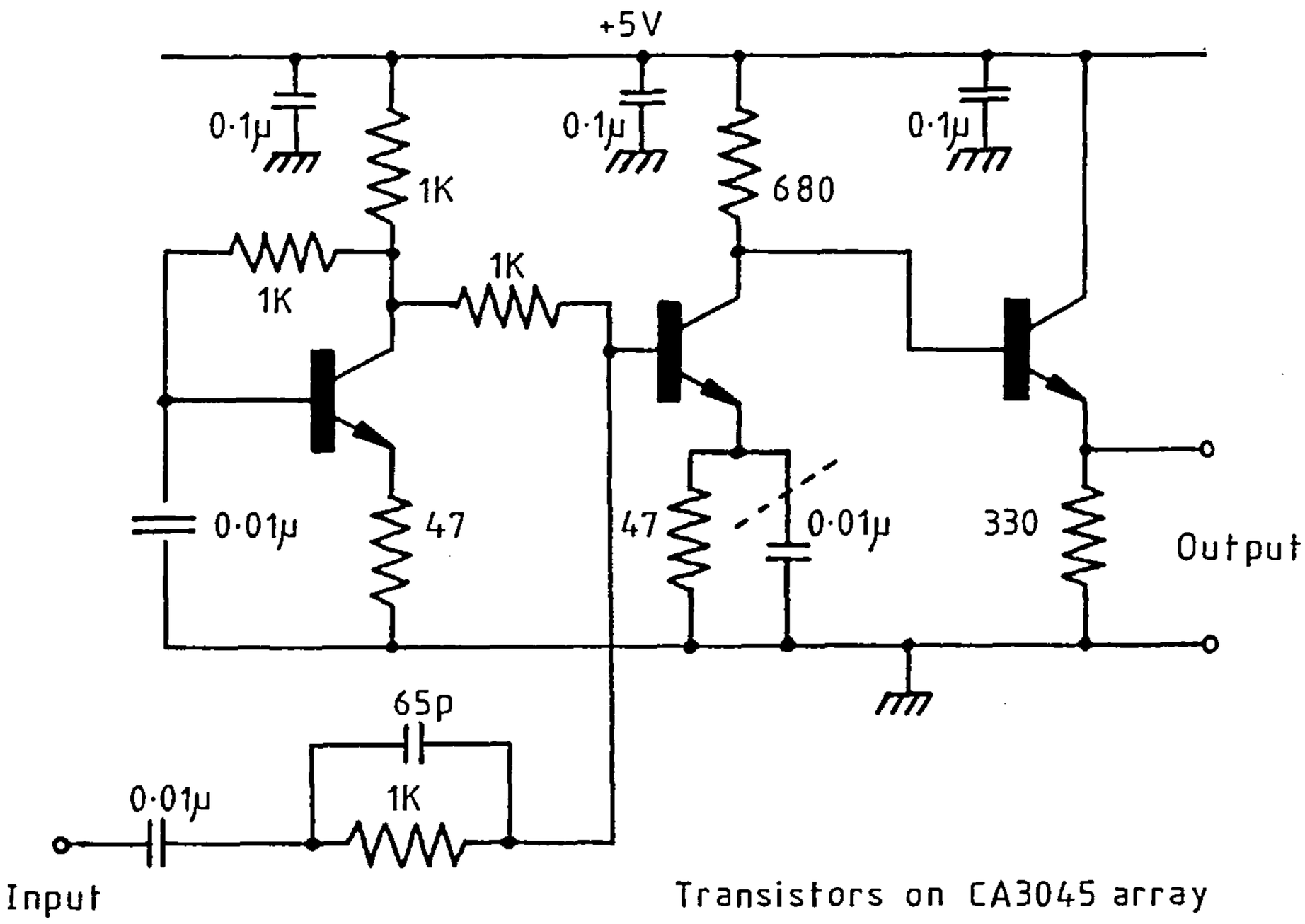

a. The circuits.

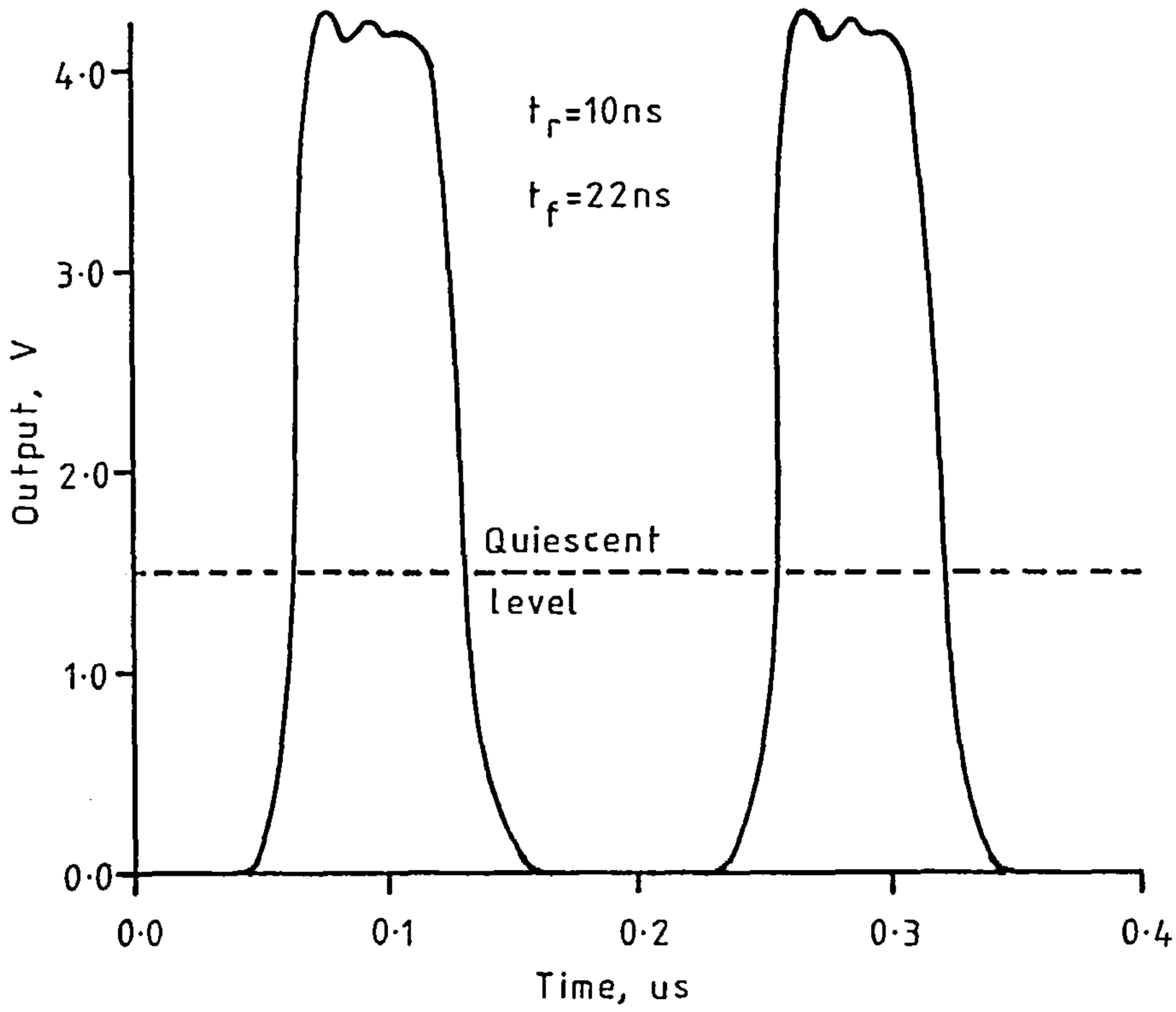

b. The output waveforms.

the close transistor matching. One transistor is connected as a diode such that thermal variations in the base-emitter voltage of the amplifier are automatically tracked by the diode, the DC bias current of the amplifier is therefore stable.

Each limiter is directly connected to a TTL flip flop. TTL recognises an input less than 0.8V as a logical 0 and an input more than 2.0V as a logical 1. The quiescent output of the limiter is set midway between these levels so that the flip flop is switched on the zero crossings of the input to the limiter.

The input to limiter 1 is 1.15V r.m.s. and so it is necessary to reduce its gain by omitting the 0.01uF capacitor. It turns out to be necessary to compensate limiter 1 to reduce the phase shift in it. Calculations founded on the theory of base compensated video amplifiers [51,286] indicate that a 68pF capacitor should be placed in parallel with the 1 KΩ input resistor. In practice, a 65pF capacitor works best.

The output waveform, figure 48b, is identical from both limiting amplifiers. Saturation in the common emitter amplifier prevents the output having a 50% duty cycle. Saturation also causes the limiters' input impedance to change with time, the purpose of the 1KΩ input resistor is to shield other circuits from the effects of this.

5.3.4 The 5 MHz phase detector

The phase detector that is drawn in figure 49 has already been described in subsection 4.3.3, remember that it relies on the input signals being 180^{o} out of phase for correct operation. The output is differential so that any common mode noise is rejected by the amplifier at the receiving end of the shielded leads. The gain of the detector can be positive or negative depending on the initial states of the JK flip flops, this means that the phase loop can provide positive or negative feedback. Fortunately there are only two possible states, each with a probability

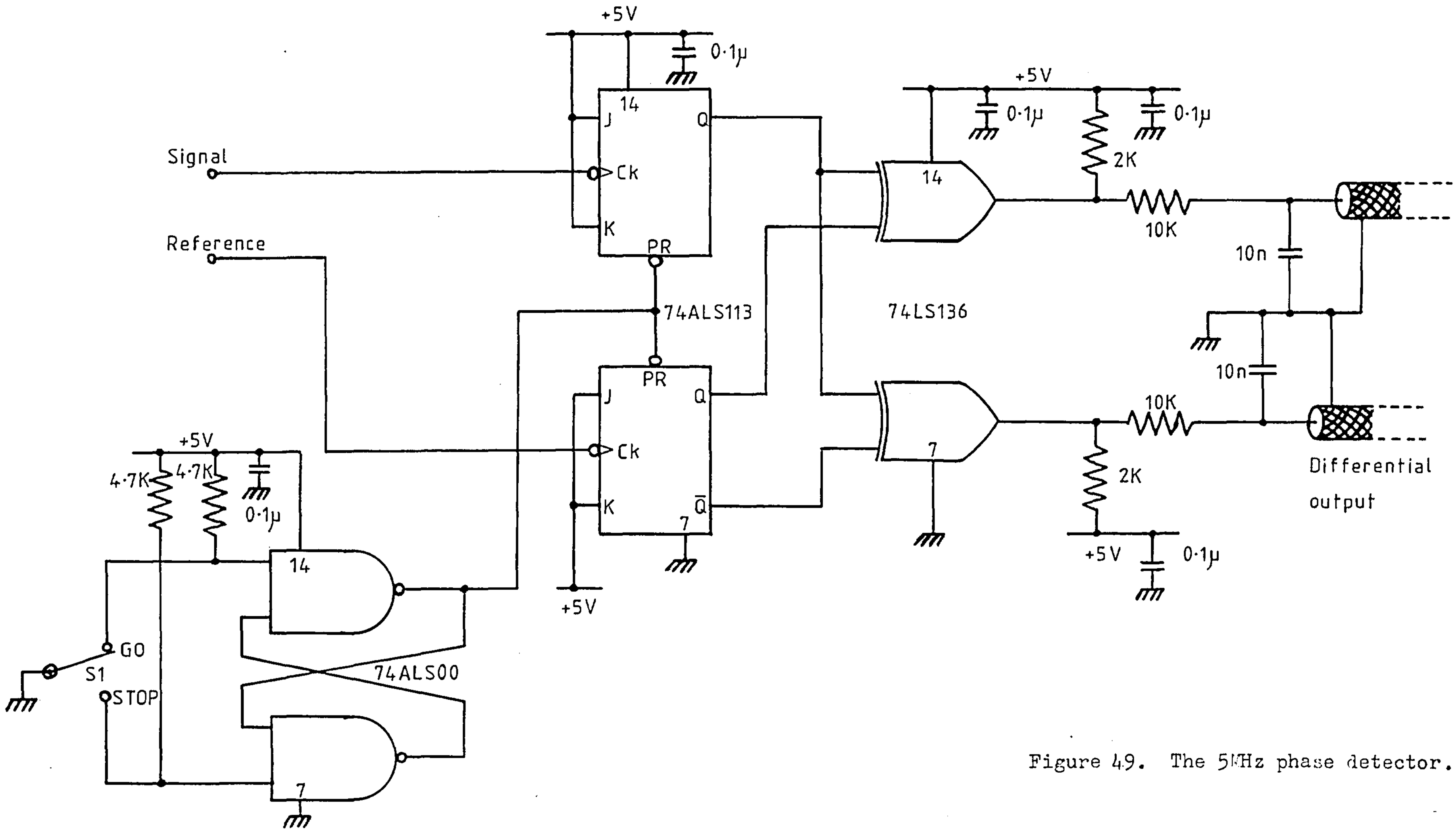

Figure 49. The 5MHz phase detector.

of 0.5 at switch on. A debounced mechanical switch is used to repeatedly turn the flip flops off and on until the loop locks correctly, no more than two or three attempts are ever needed. An automatic correction circuit is described in section 6.4. Finally, advanced low power schottky (ALS) TTL is used in the flip flops because of its low gate delay. At the time the experimental work was done ALS exclusive - or gates were not available.

5.4 THE LOW FREQUENCY BOARD

5.4.1 The amplifier for the phase sensitive rectifier

The differential square wave signals from the amplitude detector, each 22mV peak to peak, are summed and amplified to a level of 7.5V peak to peak prior to phase sensitive rectification. The circuit used is that in figure 50a, it needs little explanation. The 1/f noise corner frequency for the low noise 356N bifet amplifiers is 100Hz; the 611Hz signal being amplified is thus well clear of their 1/f noise regions.

The operational amplifiers' ability to reject noise in their $\pm$ 15V supplies decreases with increasing noise frequency. Simple low pass filters, shown in figure 50b, are included in the amplifiers' taps to the power rails to progressively absorb power supply noise above 160Hz. This arrangement is used on every operational amplifier in the instrument.

5.4.2 The phase shifter for the phase sensitive rectifier[41]

The 1.22KHz output from the CMOS 4020B divider, figure 42, is sent to the TTL 74LS123 monostable circuit in figure 51. The output of the monostable is normally at a low level, but a positive going transition at the input makes the output switch to a high level. The output remains in this metastable state for a period τ, where $\tau = 0.45\ R_{EXT}C_{EXT}$, before returning to its stable low state. The duration of the metastable state can be varied in this configuration using the 100KΩ multiturn potentiometer. The waveforms at the input and output of the monostable are drawn in figure 52. The required 611Hz reference square wave is generated by passing the monostable's output through a 74LS73 JK flip flop configured

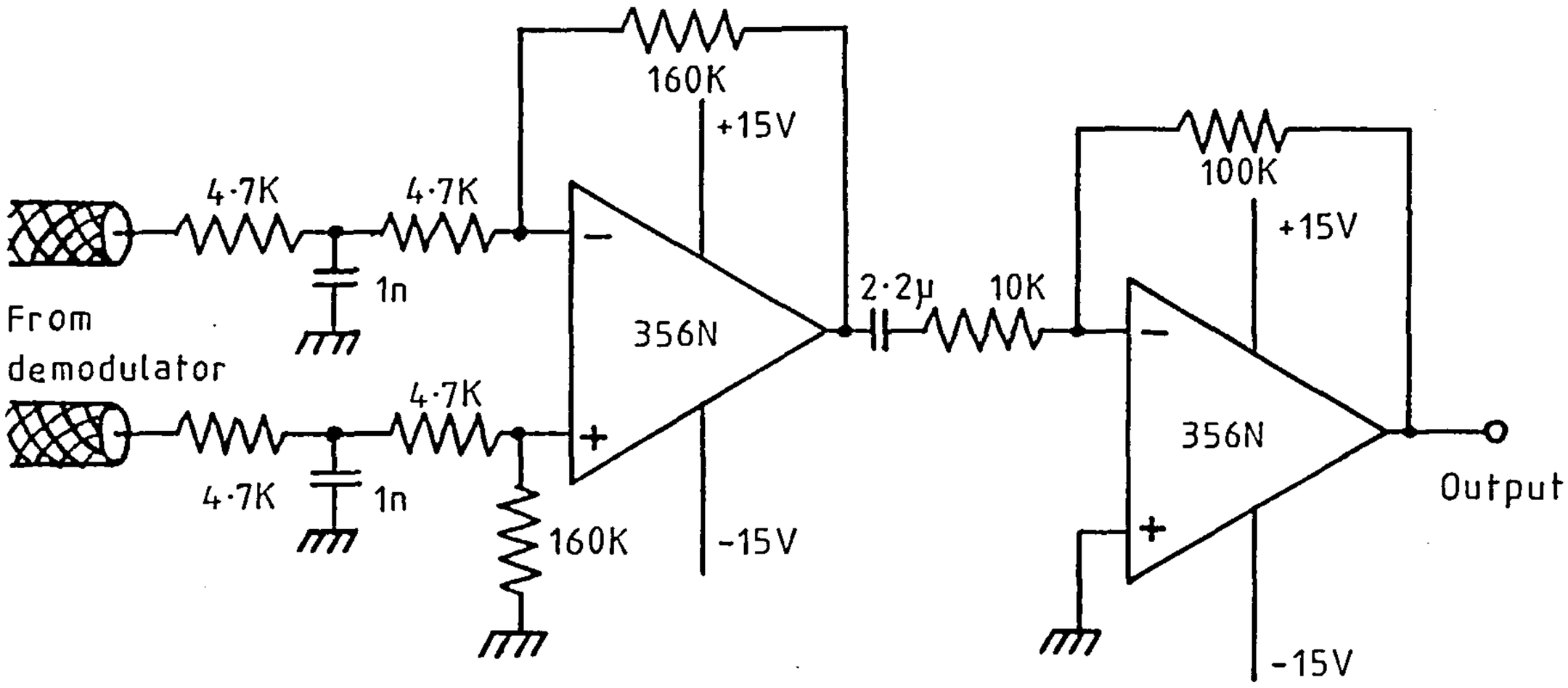

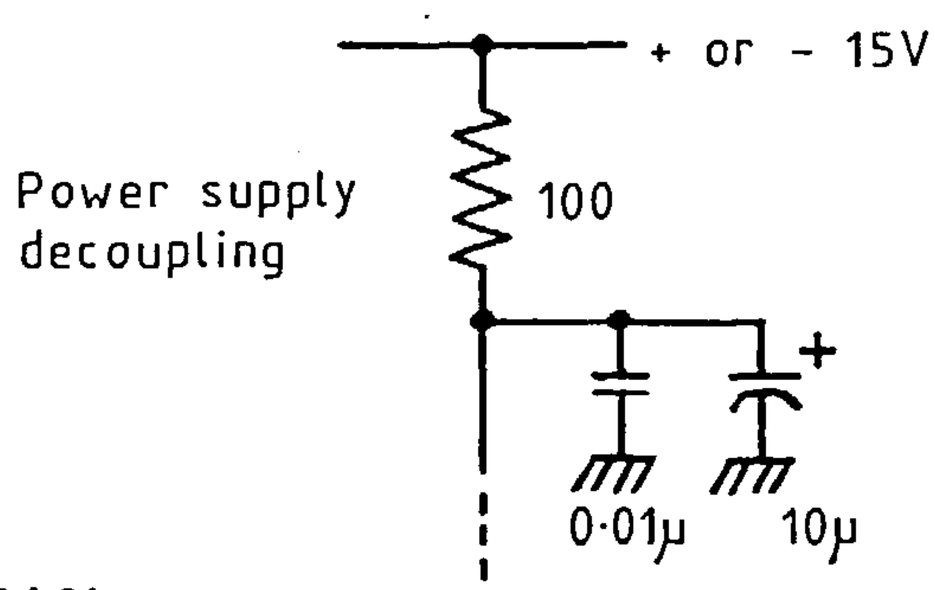

Figure 50. The audio amplifier.

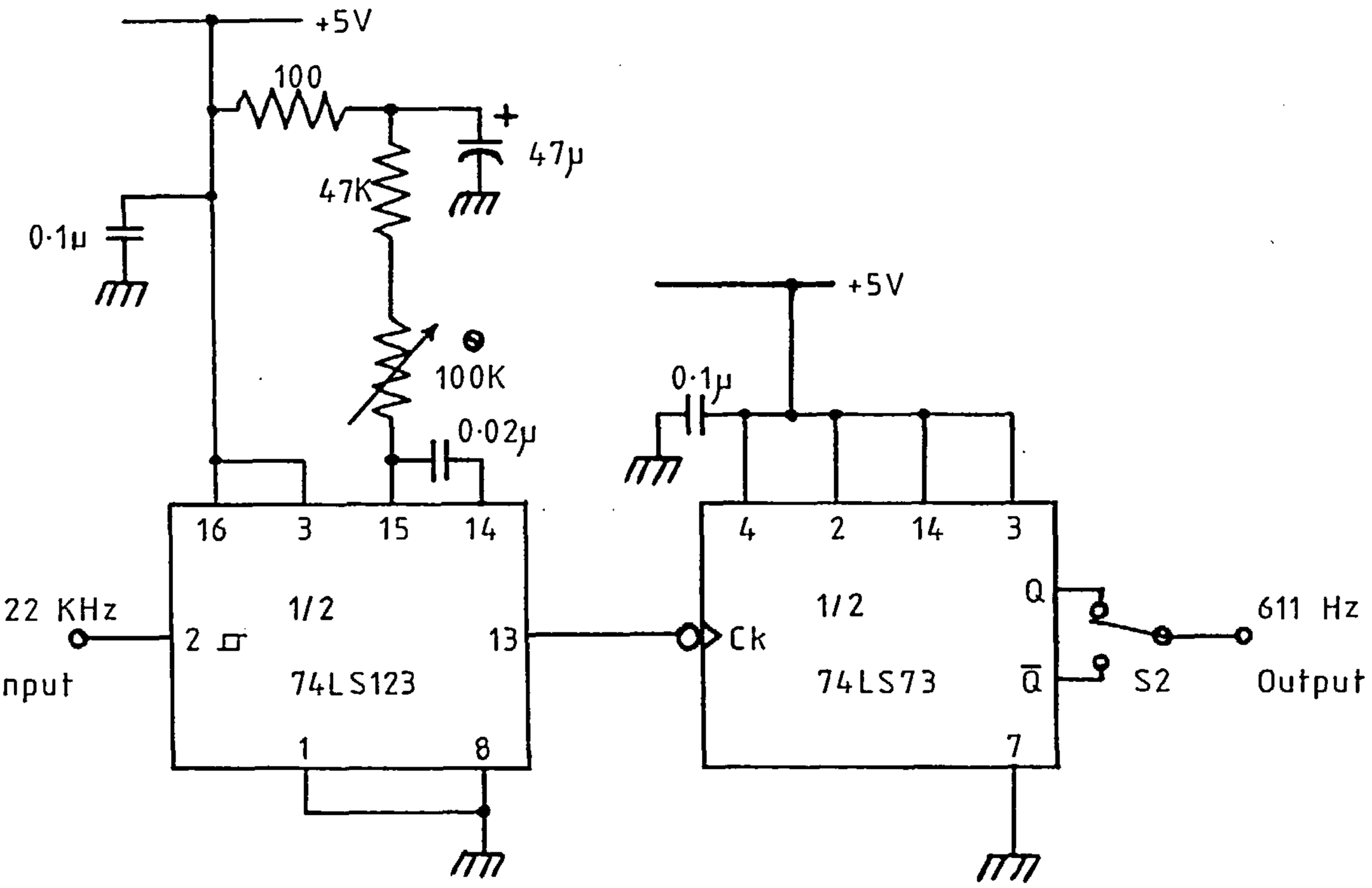

Figure 51. The reference signal's phase shifting circuit.

Figure 52. The waveforms in the phase shifting circuit.

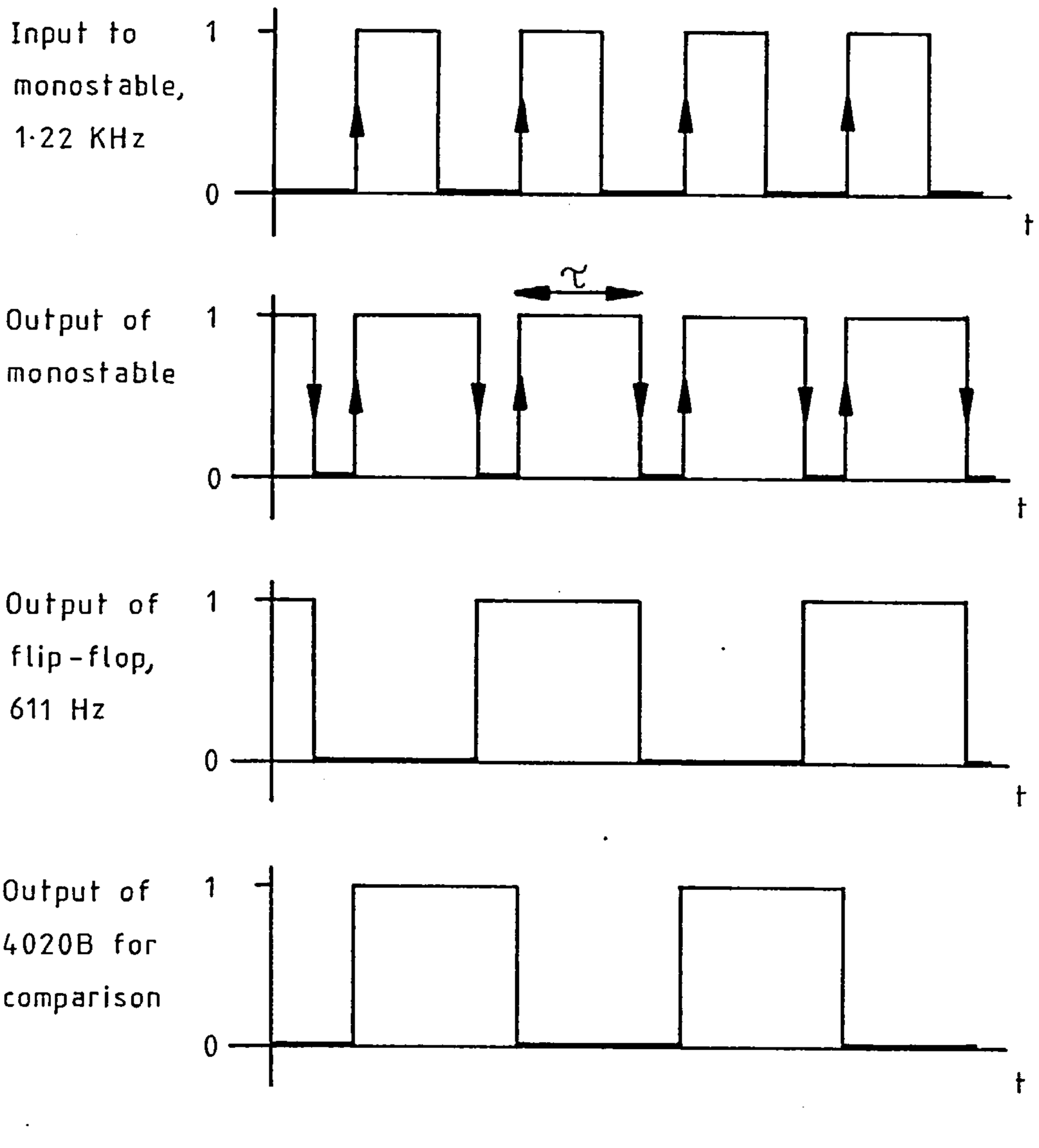

as a divide by two circuit. Referring once more to figure 52, it can be seen that the output of the flip flop is a phase shifted version of the modulating signal.

The phase shifter provides $\pm$ 99° of continuously variable phase shift at 611Hz, the switch S_2 provides a fixed shift of 0 or 180°.

5.4.3 The phase sensitive rectifier and averaging filter

The phase sensitive rectifier drawn in figure 53 is a simplified version of that described by Caplan and Stern[52]. In the present circuit four CMOS analogue transmission gates, all contained on a TTL compatible DG303 integrated circuit, are used to create a pair of shunt - series choppers. These are switched in antiphase by the reference signal V_R to alternately open or ground the inverting and non-inverting terminals on the OP-07D operational amplifier. One problem with CMOS switches is that the reference signal leaks into the wanted signal through inter-electrode capacitances. However, the switches are well matched so the leakage will be a symmetric effect that will be removed by the low pass filter. When the switching signal and the analogue signal are in phase the output of the OP-07D is like that in figure 35a.

A d.c. offset voltage is added in to make the averaged output zero in the absence of a sample. This offset is derived from the audio oscillator's power rail as shown in figure 42. The advantage of this scheme is that any drift in the amplitude of the modulating signal is automatically cancelled in the phase sensitive rectifier.

The output averaging is performed by a unity gain Bessel filter with 1 Hz low pass cut off frequency. The Bessel characteristic is chosen for its rapid settling and low phase distortion. An excellent discussion on the design and analysis of active filters is given by Tietze and Schenk[49,76].

The Analogue Devices OP-07D and 517KH are high quality amplifiers chosen for their low offset voltage, low drift and low noise. The 517KH

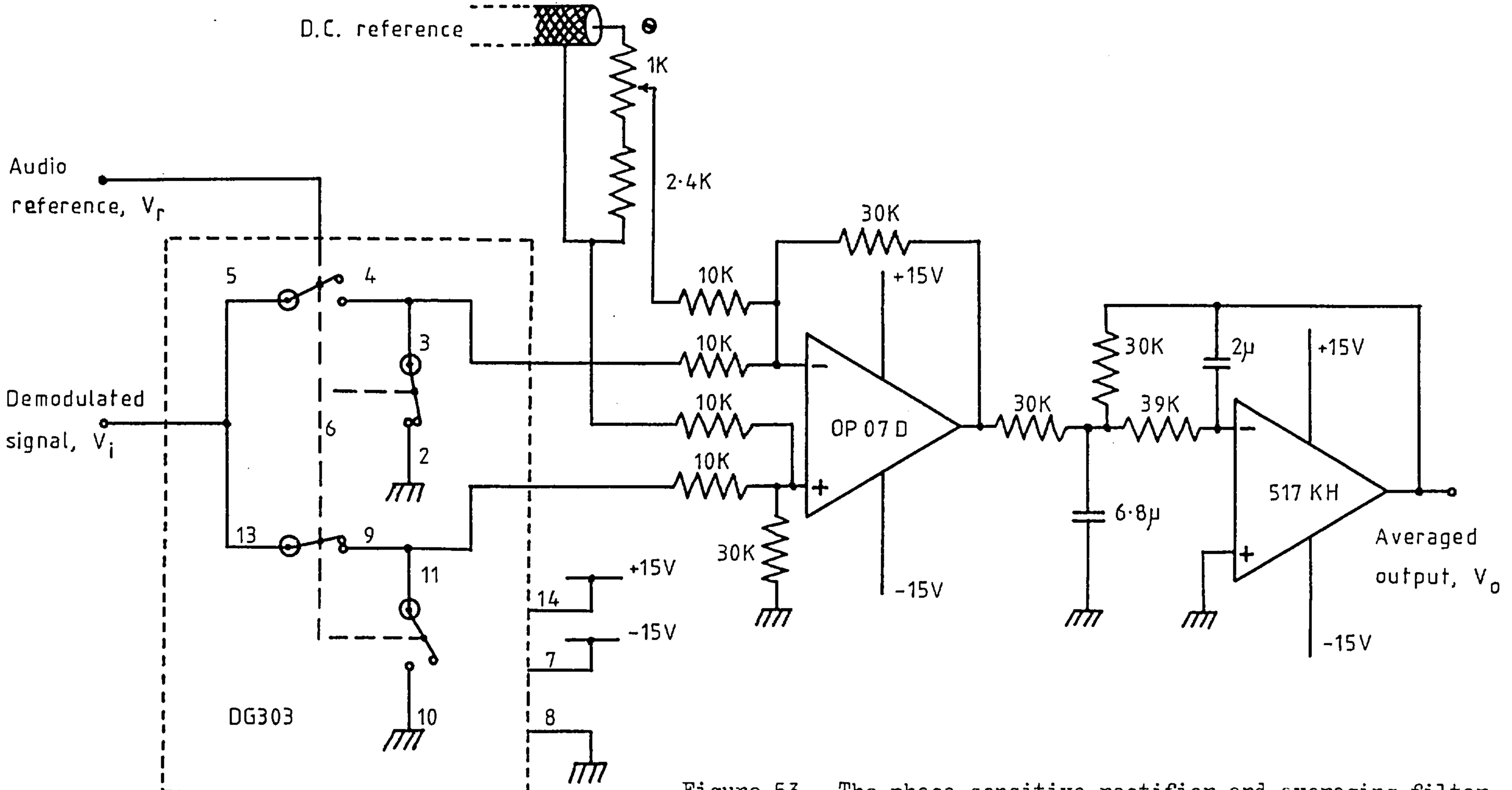

Figure 53. The phase sensitive rectifier and averaging filter.

has an input bias current of 1nA which makes it suitable for use with fairly high source resistances.

5.4.4 Bode plots for the locked phase loop

The bode diagram technique is commonly used to help design linear feedback control systems. Readers not familiar with Bode diagrams will find the text by Shinners[35,213] helpful. Experimentally, the technique involves plotting the open loop gain and phase shift as a function of frequency. The information so gained is used to ensure that the opened phase loop has a frequency response that will guarantee closed loop stability.

Figure 54 shows how the measurements were made. A sinusoidal signal was fed to the varicap through the varicap driver, see figure 46. The signal caused the natural resonant frequency of the tuned circuit to be sinusoidally varied and created corresponding phase changes that were measured by the phase detector. The outputs of the two open collector exclusive - or gates were filtered, summed and amplified to produce the system's open loop response to an input disturbance. The gain of the leading differential amplifier was $100/(47 + 10 + 2) = 1.7$, the following amplifier had a gain of 30. The open loop gain, $20 \log_{10}(V_2/V_1)$ and phase shift are plotted as a function of frequency in figure 55.

The results show that the loop had a stable first order characteristic up to the point at which the loop gain dropped to unity. After this the roll off in gain corresponded to a second, third and ultimately fourth order characteristic. The open loop gain had dropped by 3dB at 1.68KHz, the unity gain crossover frequency was 4.13KHz. The gain and phase response below 4.13KHz is determined by the low pass filter at the output of the exclusive-or gates.

As the first order characteristic had to be retained, see subsection 4.2.2, it was decided to increase the open loop gain to 100, or 40 dB, in order to keep the loop error below 1%, see equation 4.4. The two

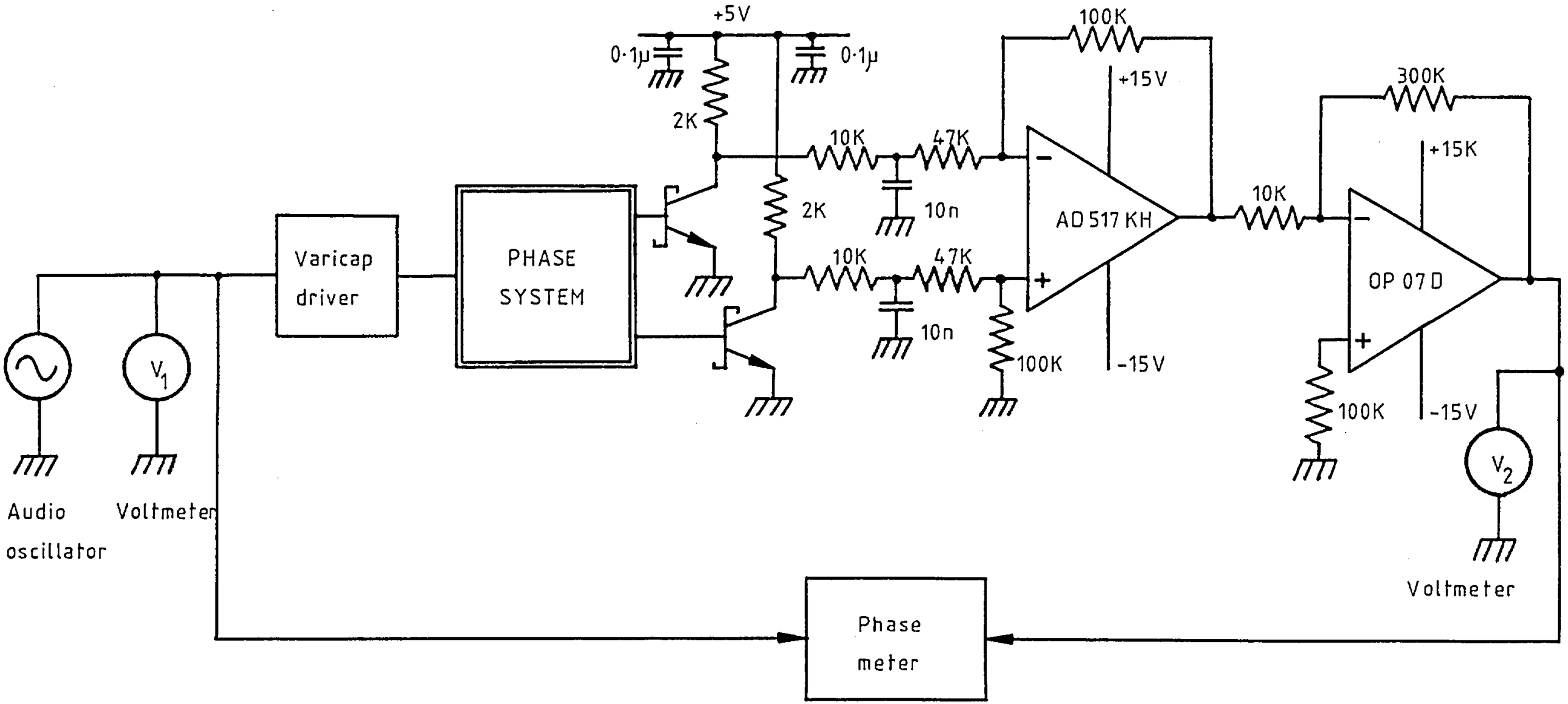

Figure 54. The experimental set up used to obtain Bode plots for the locked phase loop.

Figure 55. The Bode plots for the locked phase loop prior to alteration.

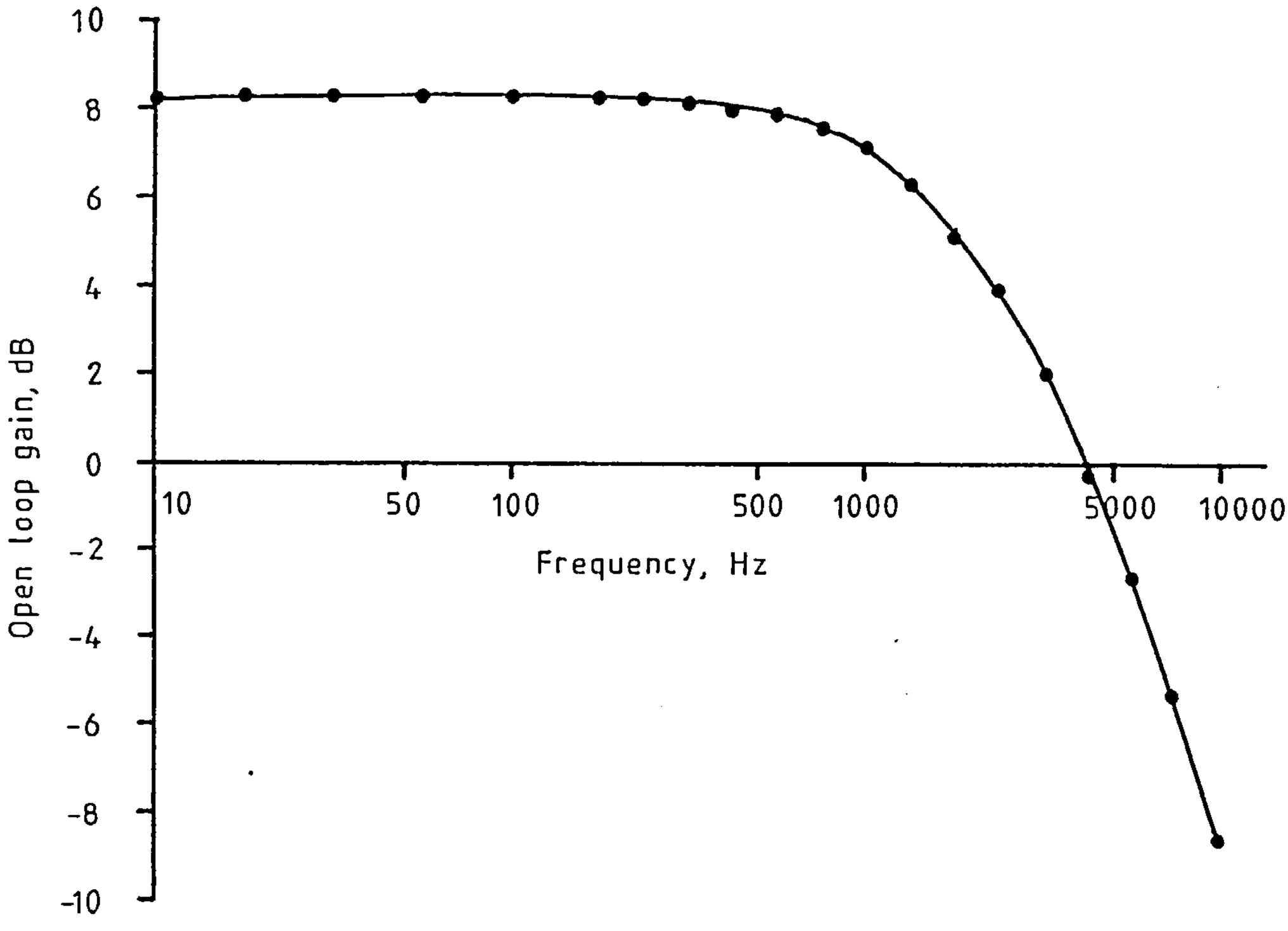

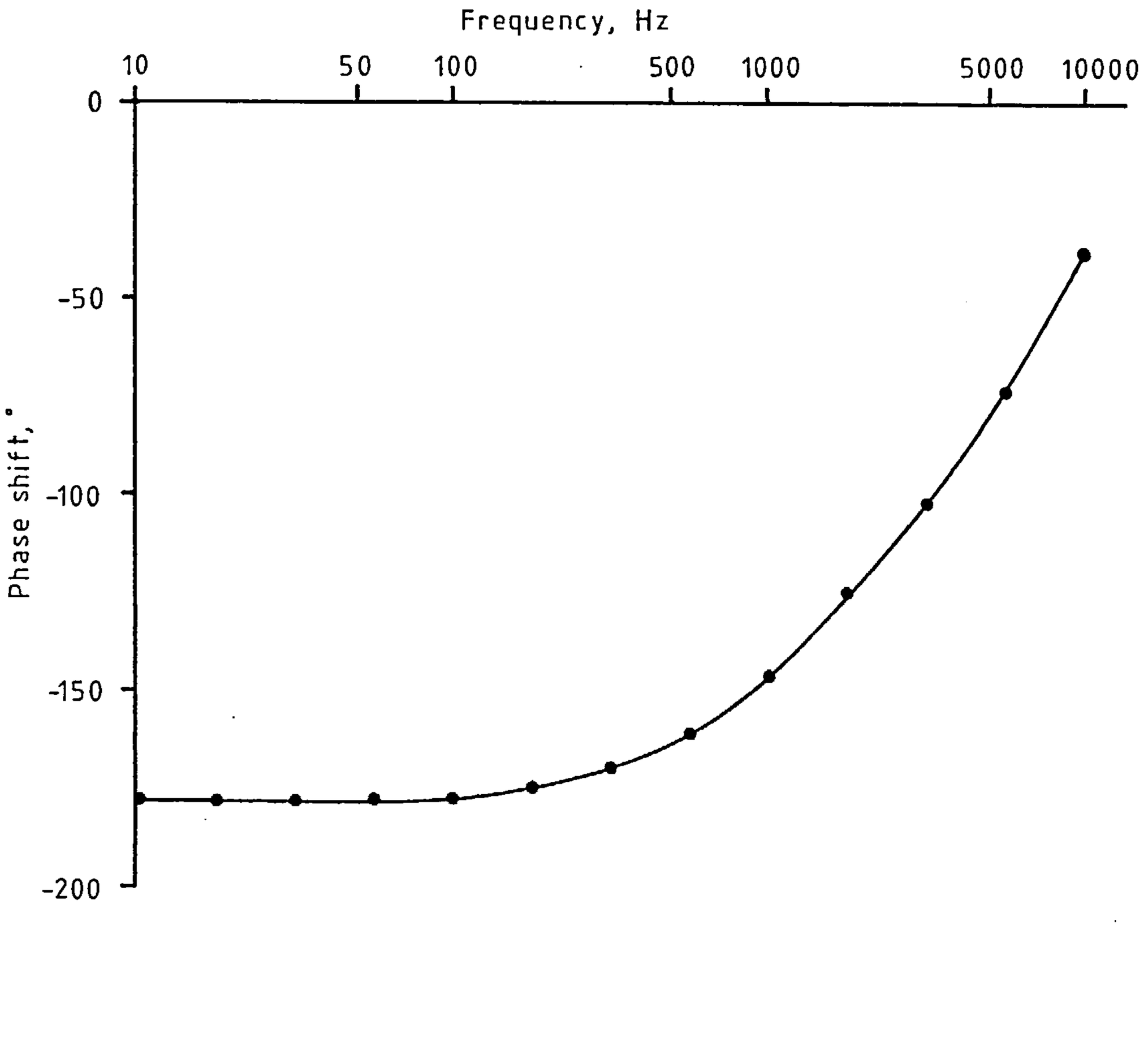

amplifiers in figure 54 therefore have to have a combined gain of 1,954 or 65.8dB. The frequency response of the loop then had to be altered to keep the loop stable when closed. The simplest way of doing this was to insert another first order roll off at some frequency much less than 1.68 KHz. The exact roll off frequency was decided by adhering to some advice given by Tietze and Schenk[49,466]: setting the loop's phase margin to 65^{o} at the unity gain crossover frequency minimises the loop's settling time after a transient input disturbance. This was arranged by inserting a new RC time constant for which $1/2\pi RC = 7.23Hz$. The new unity gain crossover frequency was about 723 Hz at which the phase shift due to the new time constant was virtually 90^{o}. To this had to be added the loop's original phase shift of 25^{o} at 723Hz. The total phase shift was therefore 115^{o} giving a phase margin of $(180-115) = 65^{o}$ as required.

The final arrangement of the phase loop's error amplifier is shown in figure 56. It is necessary to alter the low pass filter at the input to the differential amplifier. The modification shifts the filter's -3dB frequency from 1.68 KHz to 1.73KHz, this leaves the calculations on phase margin intact. The dominant time constant is formed using a 22 nF capacitor in parallel with the 1MΩ feedback resistance on the second amplifier. An output was taken from this amplifier to the varicap driver to complete the feedback loop. The output is also passed through a 1.0Hz Bessel low pass filter[49,104] to improve the signal to noise ratio to the monitoring chart recorder or voltmeter.

5.5 THE FURNACE

5.5.1 The furnace's power supply

The circuit for the furnace's power supply is shown in figure 57. A variac controls the furnace current through a 5:1 step down transformer. An LC filter preceding the transformer absorbs mains transient voltages and variac wiper noise. The a.c. current supplied to the furnace is symmetric

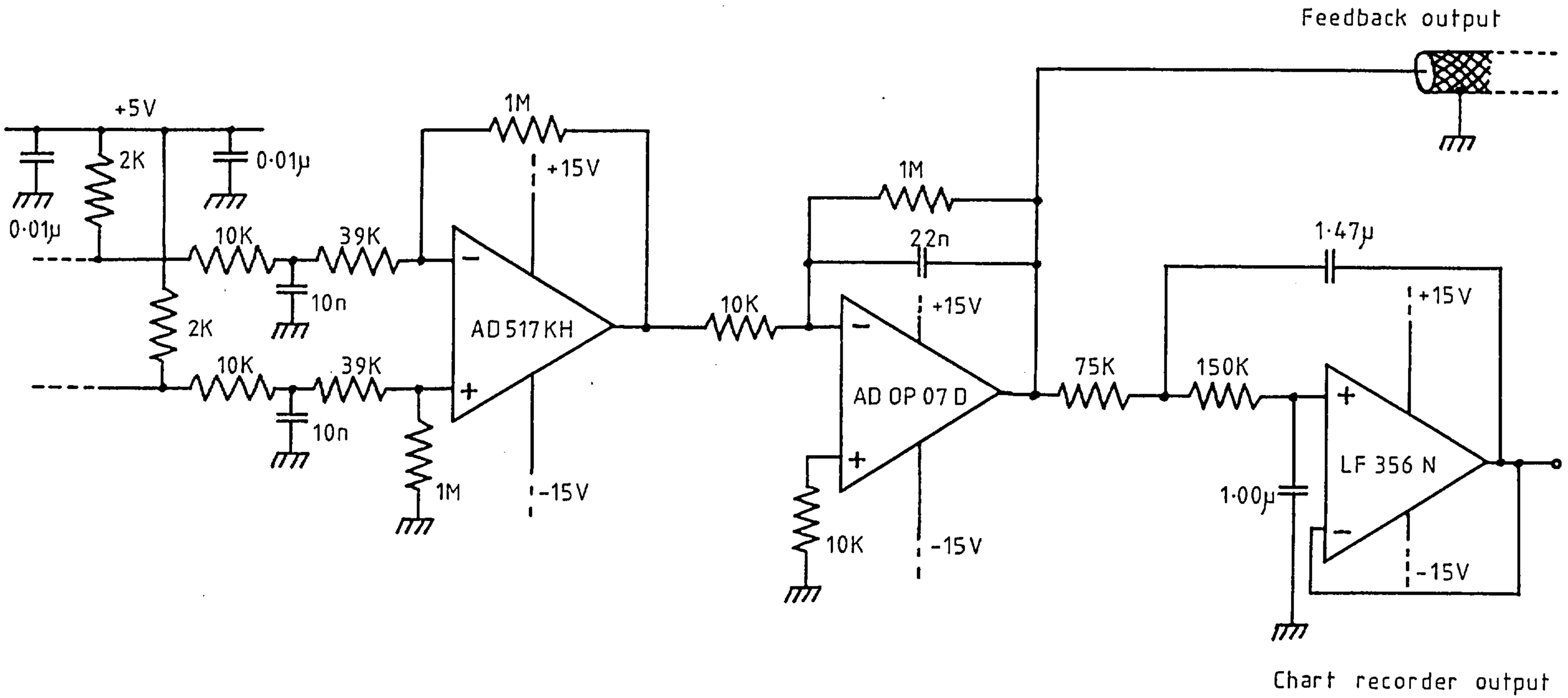

Figure 56. The locked phase loop's error amplifier and 1.0 Hz low pass output filter.

Figure 57. The furnace's power supply.

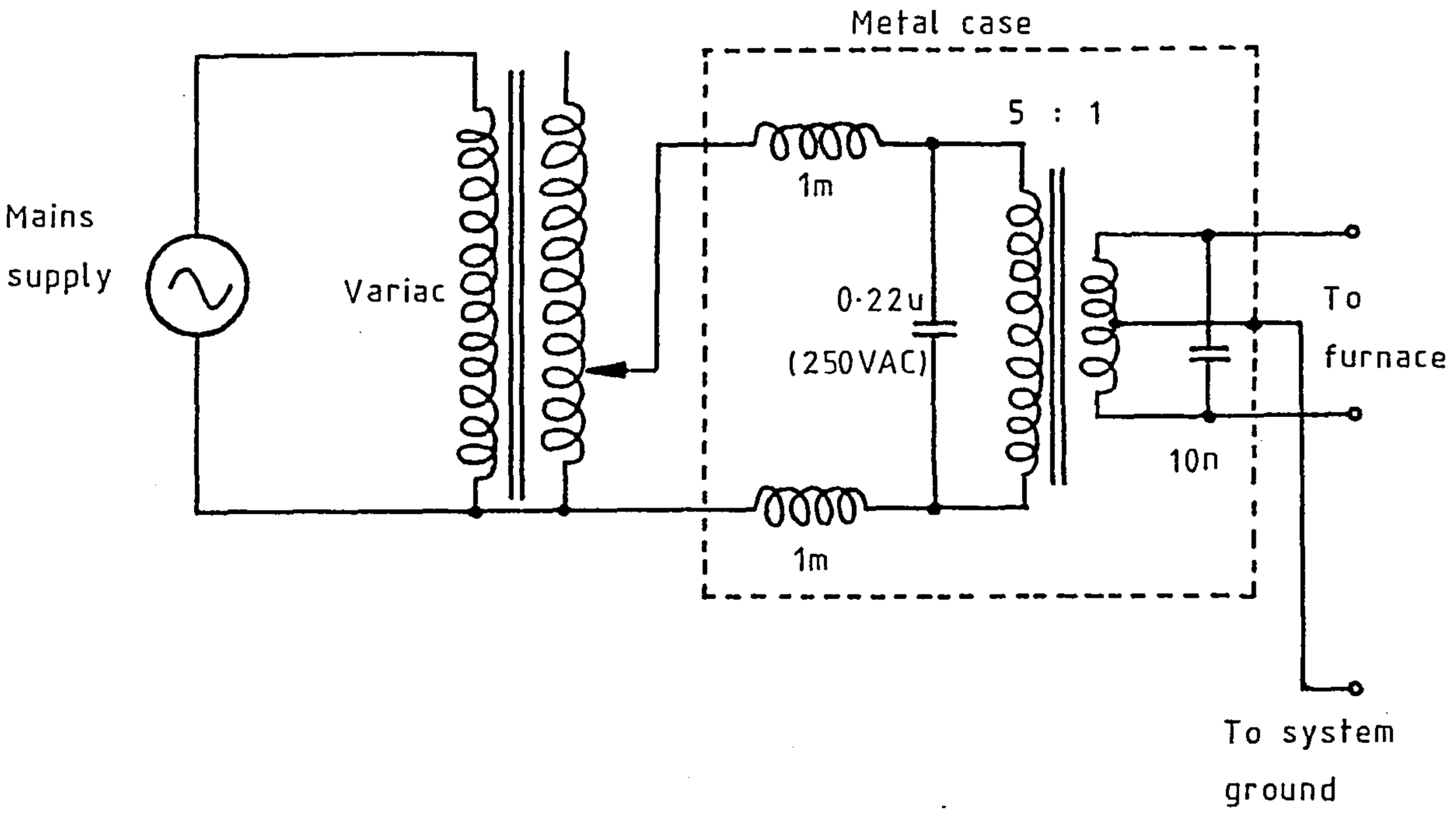

Figure 58. The construction of the furnace.

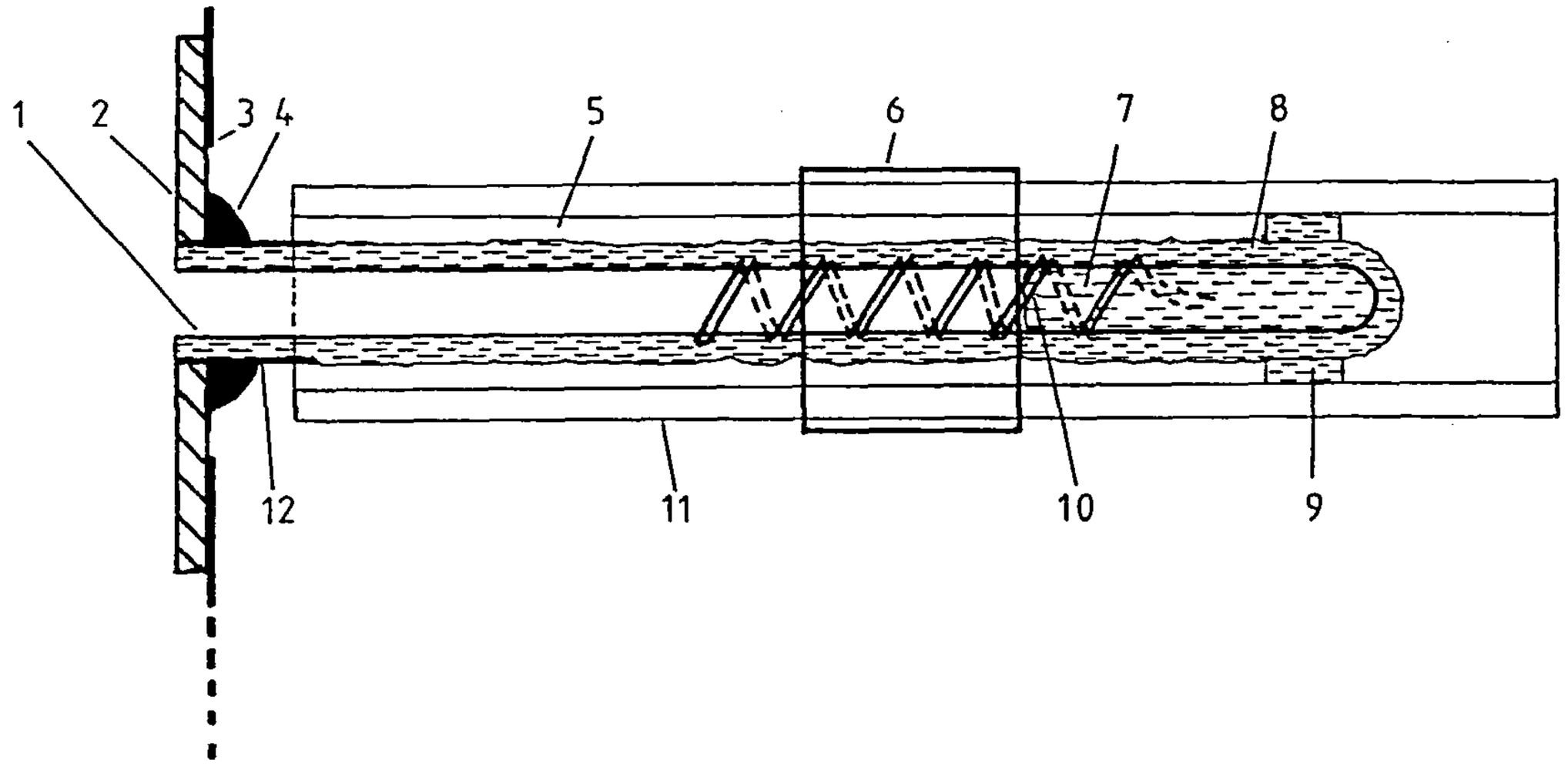

1. Quartz furnace tube
2. Metal fixing flange
3. Metal shield
4. Araldite
5. Air Gap
6. Sample coil
7. Refrasil wool thermal insulation
8. Refrasil tape insulation
9. Furnace support to water jacket.
10. Bifilar wound furnace coil
11. Water jacket
12. Pyrex supporting collar.

about the system's ground. This means that any undesirable leakage of 50Hz current through stray capacitances is self cancelling.

5.5.2 The construction of the furnace

Figure 58 illustrates the construction of the furnace. The quartz furnace tube is supported at its open end by a pyrex collar in an aluminium fixing flange. At its closed end it is supported by the water jacket using heat resistant refrasil cord wedging. The sample coil is located directly over a 4 cm long heating element. The heating element consists of 12 bifilar wound turns of 0.0048" diameter nichrome V wire; bifilar winding ensures that no stray 50Hz magnetic field is created. A good deal of care is taken over insulation to reduce heat losses and thereby minimise the number of turns required by the furnace. The furnace tube is wrapped in 3 layers of insulating Refrasil tape. The closed end of the quartz tube is filled up to the edge of the sample coil with quartz wool. There is a still air gap between the furnace and the water jacket.

The mounting of the furnace and water jacket inside the metal shield is depicted in figure 59a. Heat escaping from the ends of the water jacket passes harmlessly through ventilation holes in the shield. The coil and capacitors are located inside a thermally insulated compartment as mentioned in subsection 4.3.4. A pair of perspex pillars hold the water jacket firmly in their yokes.

5.5.3 Details of the furnace's performance.

A profile of air temperature against penetration into the furnace, at a power consumption of 56W, is shown in figure 59b. The profile's plateau was very nearly at the position that samples rested at during heating. For a maximum sample size of 0.5 cm the temperature difference between the sample's ends is about 12°C at an average temperature of 716°C. At lower temperatures the difference shrinks.

The furnace has been tested at power consumptions of up to 80W, this consumption produces a temperature of 880°C at the plateau. The

Figure 59. More details of the sample coil and furnace.

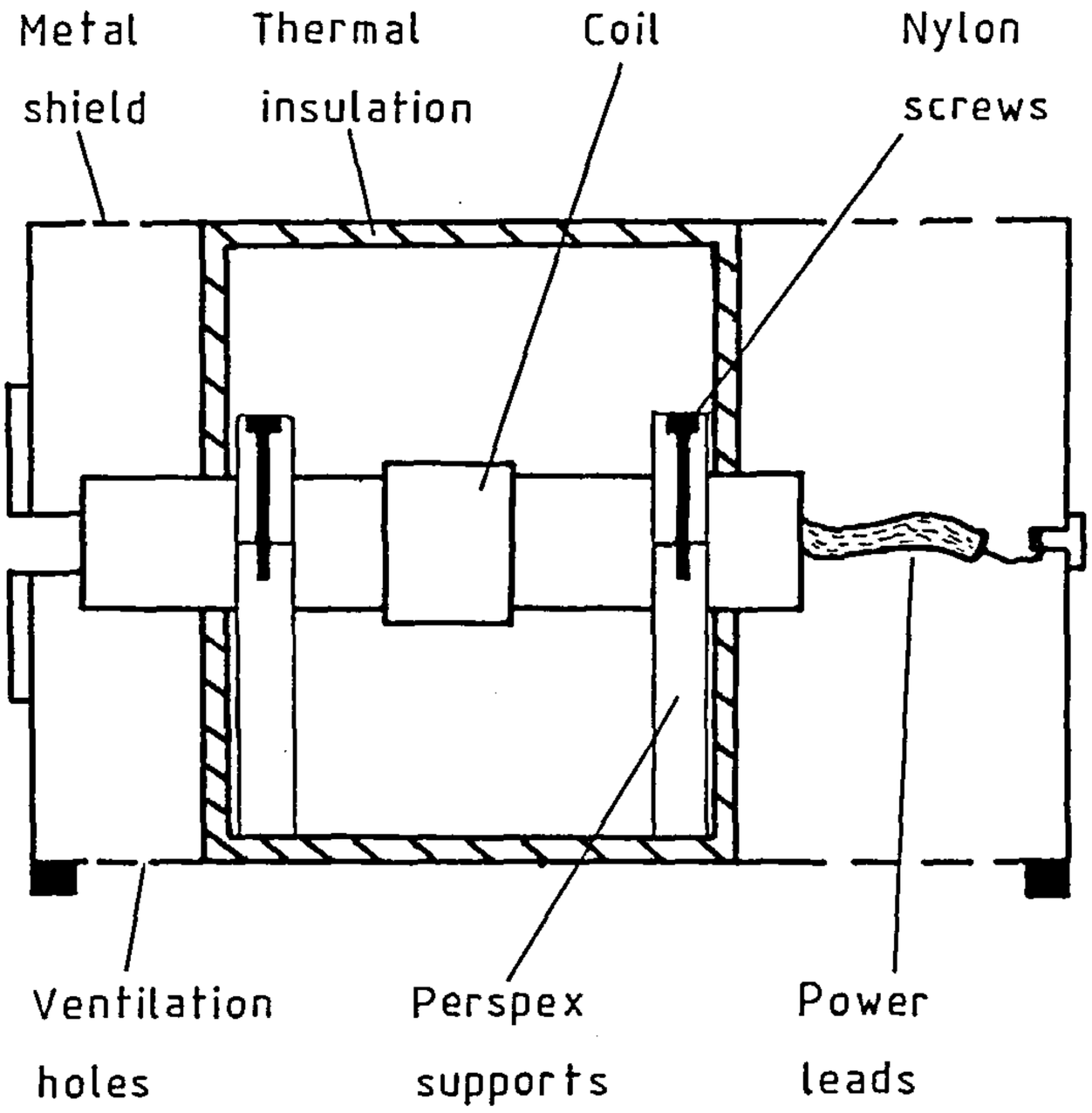

a. A side view of the sample coil's housing.

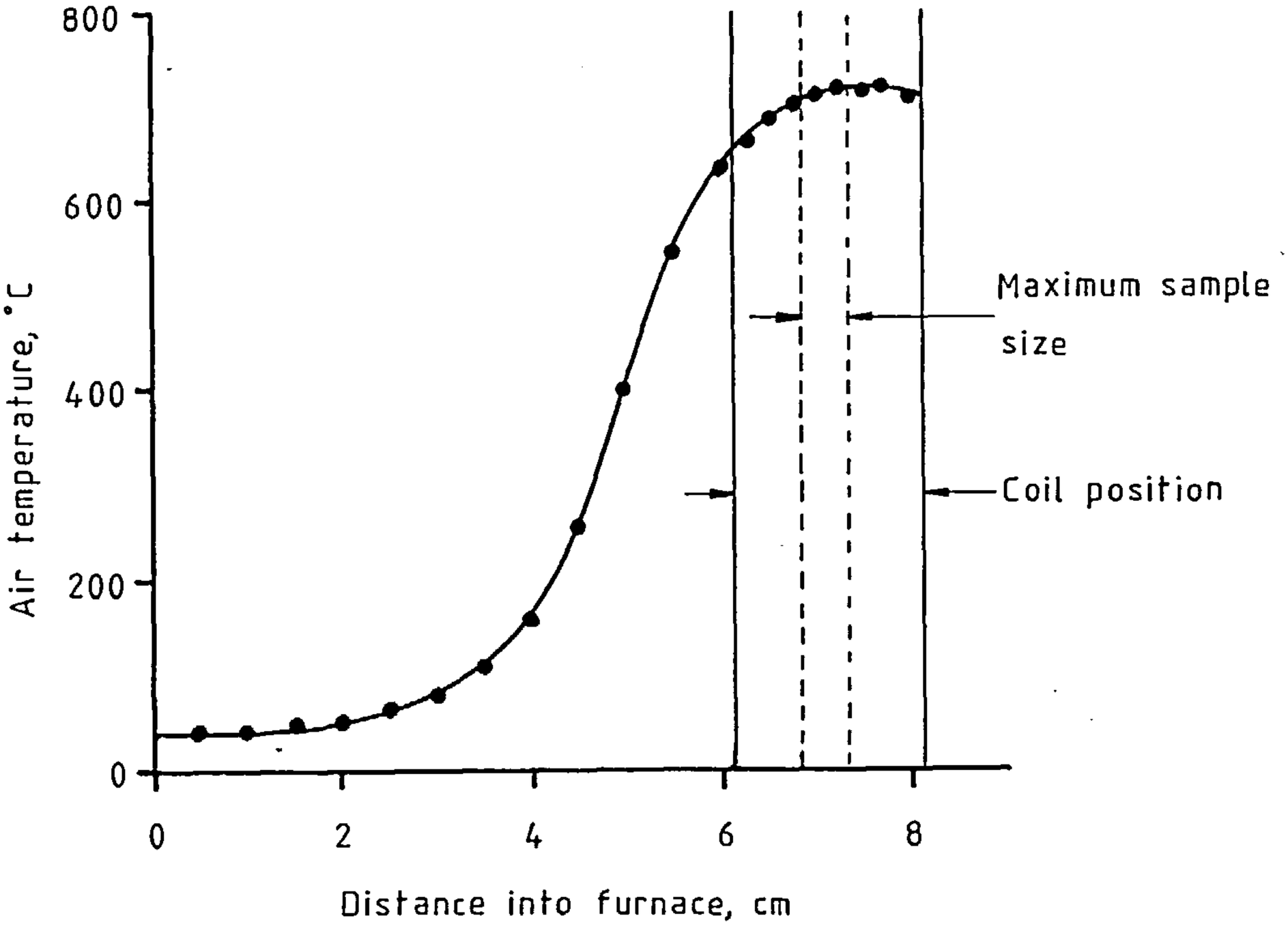

b. The variation of the air temperature within the furnace. The furnace current is 1.10A r.m.s. and the power input is 56W.

resistance of the furnace varies between 45.4 Ω at room temperature and 47.0Ω at 880°C. The furnace has a time constant of 67s.

Both the water flowing through the jacket and the nichrome heating element alter the behaviour of the tuned circuit. In the absence of the furnace, filling the jacket with water causes a 13% drop in Q, a 9% drop in the coupling factor F and a shift of 0.15% in the tuned circuit's natural frequency. When the jacket is drained of water, inserting the furnace causes a 2% drop in Q, a 2% drop in F and a 0.02% shift in natural frequency. When the water and furnace are present the Q of the tuned circuit is 175.

The temperature of the furnace is monitored using a Pt-13%Pt/Rh thermocouple in the arrangement shown in figure 60. To keep losses in the thermocouple down to a minimum, the thinnest available wire is used and the fused junction is made as small as possible. The wires are 0.245 mm in diameter and the fused junction blob is 0.6 mm in diameter. Thermocouple wire 0.1 mm thick can be obtained and this ought to be used in the future.

5.6 THE INITIAL ADJUSTMENTS

1. The power rails required for the electronic circuitry are + 15V at 100mA, -15V at 60 mA and + 5V at 75 mA.

2. The power rail and coolant water supply are switched on and the instrument is left to stabilise for 1/2 hour.

3. The locked phase loop is opened by disconnecting the lead from the error amplifier to the varicap driver. The bias at the output of the varicap driver is set to -5V using the multiturn potentiometer, see figure 46.

4. By monitoring the output of the SL560 amplifier with a digital r.f. voltmeter, see figure 44, the tuned circuit is set to exact resonance with the crystal oscillator using the trimmer capacitors on the tuned

Figure 60. A diagram of the sample holder.

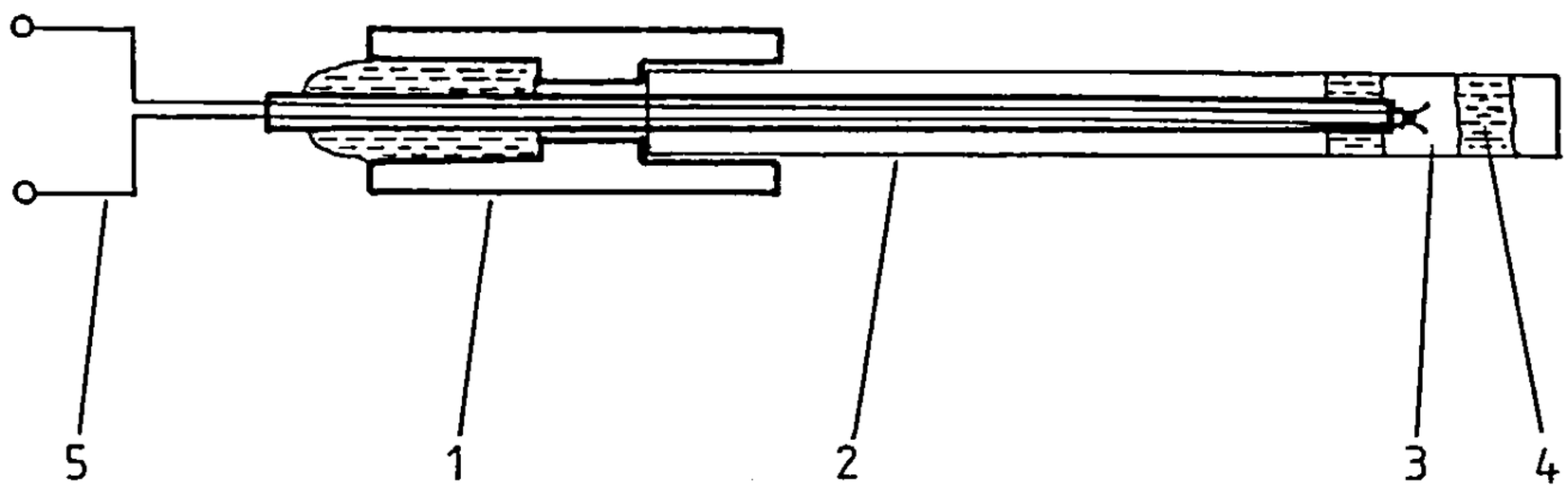

1. The holder.
2. Quartz sample tube.
3. The sample
4. Refrasil lagging.
5. Pt - 13% Pt/Rh thermocouple.

circuit.

5. The phase loop's offset error is measured at the output of the differential amplifier in figure 56, the error is then reduced to zero using the trimmer capacitor on the SL560.

6. The phase loop is then closed by reconnecting the lead from the error amplifier to the varicap driver.

7. Adjustments 3 - 6 do not need to be repeated in the future.

8. The switch S_1 on figure 49 is flicked once or twice until the loop locks.

9. The initial adjustments to the phase sensitive rectifier are quite simple. The reference signal is moved into phase with the detected signal, see figure 51. The output of the phase sensitive rectifier is then reduced to zero using the variable d.c. offset, see figure 53.

Some photographs of the completed instrument are shown in figures 61a to 61c.

Figure 61. Some photographs of the completed instrument.

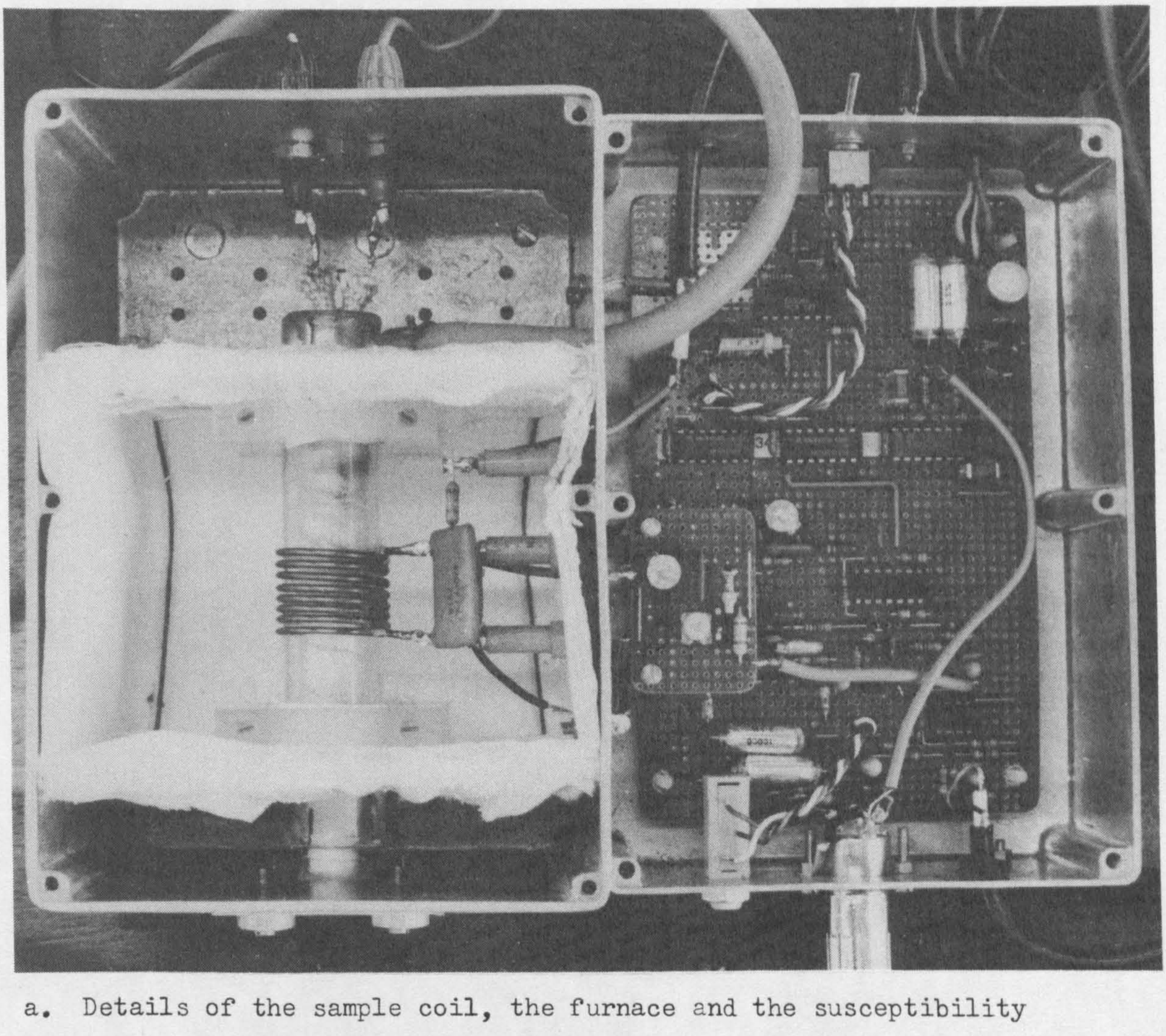

a. Details of the sample coil, the furnace and the susceptibility sensing board.

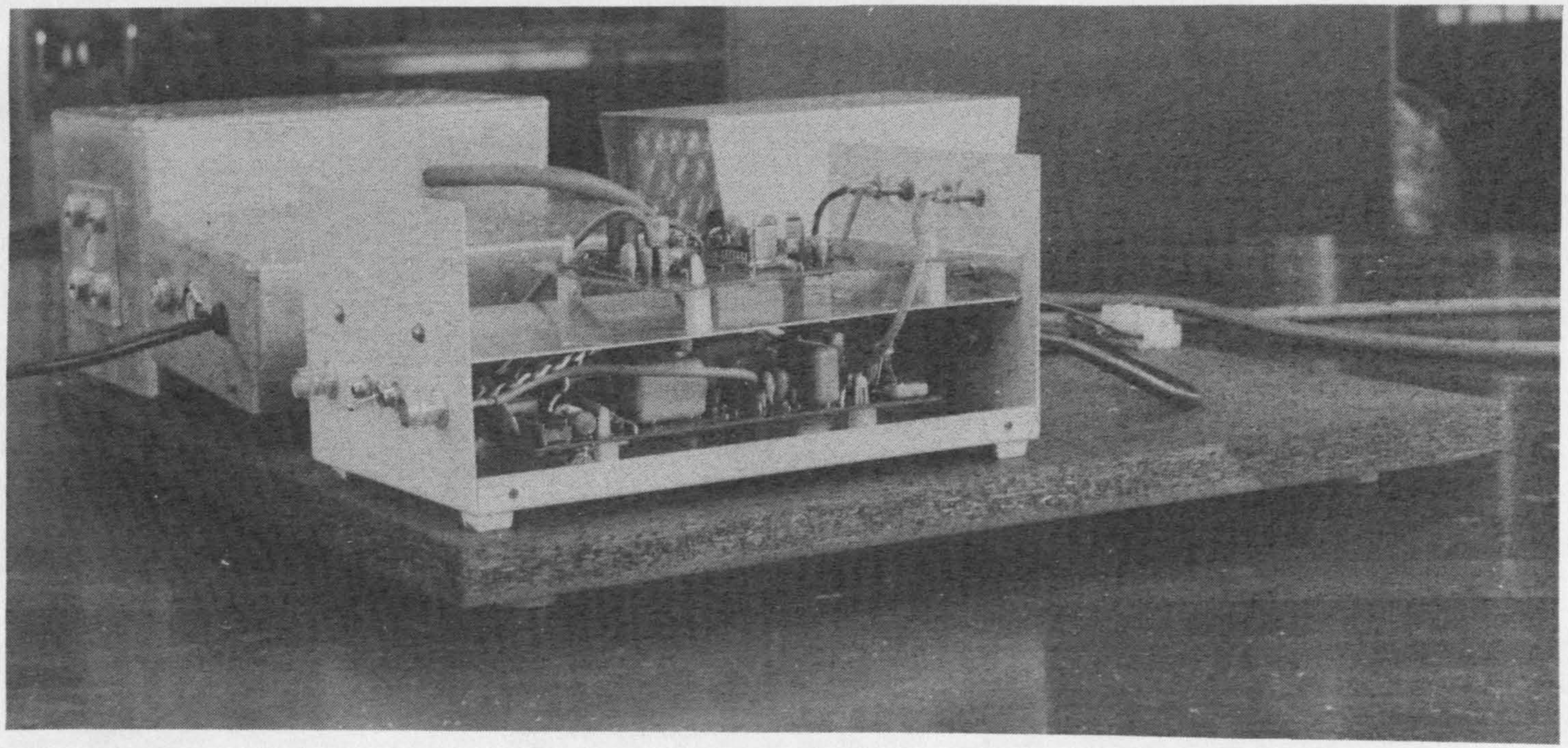

b. The mounting of the tuned circuit driver board (uppermost) and the low frequency board.

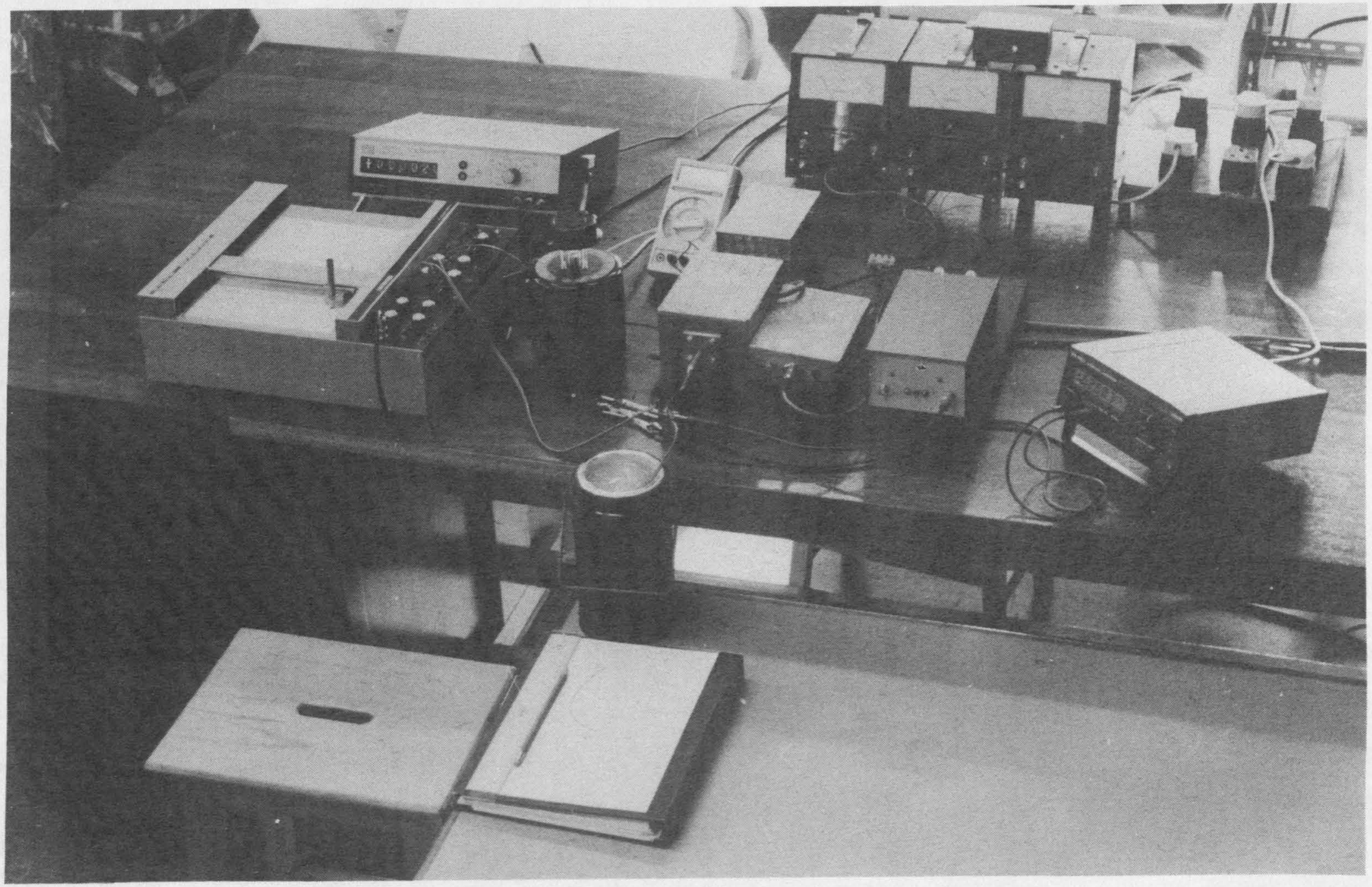

c. The complete system in operation.

CHAPTER 6

RESULTS, APPLICATIONS, IMPROVEMENTS AND THE TEMPERATURE DEPENDENCE OF SUSCEPTIBILITY

6.1 INTRODUCTION

This chapter concludes the description of the new radio frequency instrument for measuring the temperature dependence of initial magnetic susceptibility. Section 6.2 presents the results that have been obtained using the improved locked phase loop, these show a vast improvement over the results obtained using the first working version. The temperature dependences of both X' and X" have been successfully measured and a number of examples are shown. The section is rounded off by an analysis of the temperature dependences of X' and X" in terms of magnetic relaxation times.

Section 6.3 discusses the applications of the instrument. It points out the information that may be gained from the high temperature dependence of susceptibility. It also describes the uses to which room temperature measurements of susceptibility may be put. A number of promising applications have not been tried out. However, modifications to the coil and capacitors are all that is required to measure the low temperature dependence of susceptibility and the anisotropy of susceptibility. The ways towards realising these untried applications are pointed out.

Since completing the experimental work a number of circuit refinements have been thought of, these are outlined in section 6.4. Finally, section 6.5 is the conclusion to chapter 6 and to this part of the thesis.

6.2 RESULTS

The tests and results are set out below in the same order that they were for the first version in section 3.5, this facilitates direct comparison between the two instruments. All of the measurements have been made with the coolant water flowing and with the furnace in place.

6.2.1 Linearity

The linearity was checked using two sets of test tube samples. The first set consisted of varying masses of magnetite dispersed in LiF, these had been made up for the first version. The magnetite grains had radii between 4.3μ and 7.7μ. The second set was a new series of haematite samples each dispersed in LiF. The radii of the haematite grains were less than 40μ. Whereas magnetite was one of the strongest ferromagnetic materials likely to be met in rock magnetism, haematite was one of the weakest. The two sets made a good pair to test the large and small scale behaviour of the instrument. A pure LiF control sample gave a signal of -13mV.

The results for the real part of the susceptibility, X', are shown in figures 62 and 63. Here, the change in the feedback voltage V_p is plotted against the mass of ferromagnetic material. The plots prove that the instrument is linear in its response to X'.

The variations in V_Q for the imaginary part of the susceptibility, X", are not shown. 19.4mg of magnetite gave a signal of $\Delta V_Q = -10.4$mV and 24.4 mg of haematite gave a signal of -1.0mV. When compared to ΔV_p, the changes ΔV_Q at room temperature are thought too small to be useful.

6.2.2 Calibration

Calibration factors K_3 and K_4 are needed to complete the relations

$$X_T' = K_3 \Delta V_p \qquad (6.1)$$

and

$$X_T'' = K_4 \Delta V_Q \ , \qquad (6.2)$$

where the subscript T indicates that the total susceptibility is being referred to.

The phase loop was calibrated using the paramagnetic salt $MnCl_2.4H_2O$. This substance had an 87% larger susceptibility than the $FeSO_4.7H_2O$ that was used to calibrate version 1. 112.8 mg of

Figure 62. The changes in V_p for varying masses of magnetite powder.

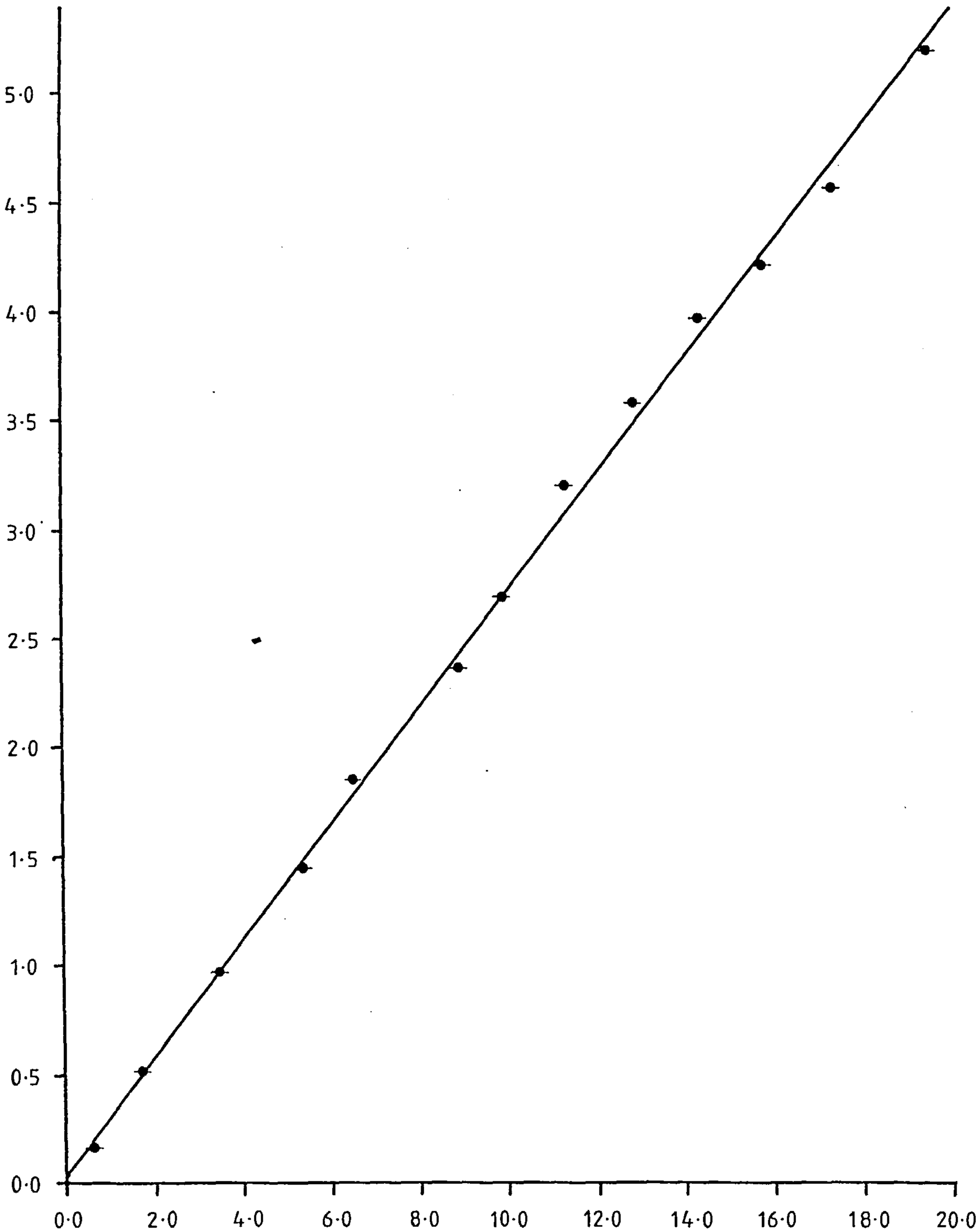

Figure 63. The changes in V_p for varying masses of haematite powder.

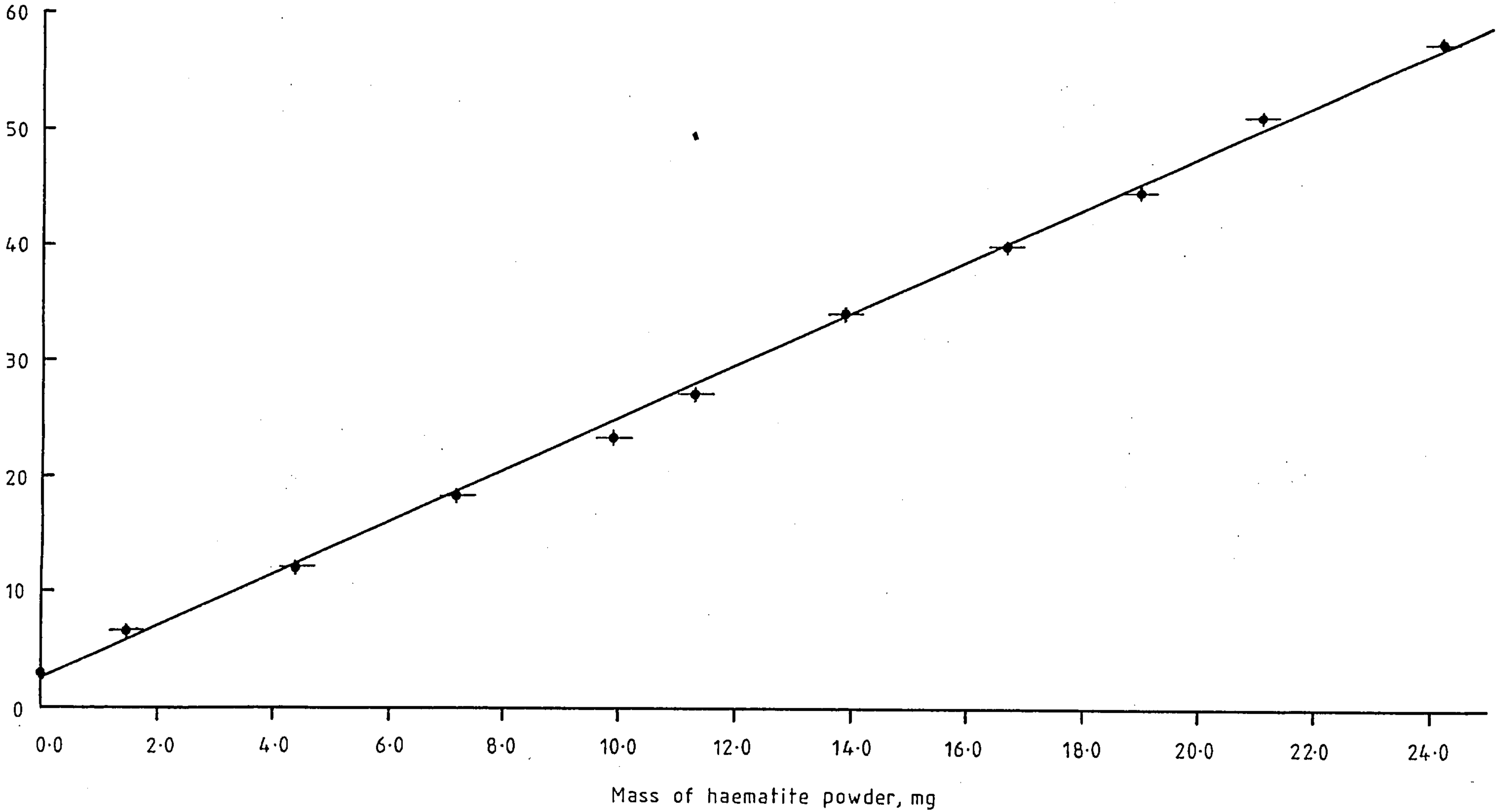

$MnCl_2.4H_2O$ had a total susceptibility of $1.07 \times 10^{-10} m^3$, it gave a signal of $\Delta V_p = -(72.1 \pm 0.7)mV$. The measured calibration factor for the phase loop was therefore

$$K_3 = -(1.480 \pm 0.014) \times 10^{-9} m^3 V^{-1}.$$

It is instructive to compare the measured value of K_3 with the value predicted from circuit parameters. Subsection 3.5.2 showed that the two values agreed well for version 1. Using equations 3.21 and 3.45,

$$K_3 = u \frac{V_s}{F} . \qquad (6.3)$$

The gain of the linearised feedback varicap was calculated in subsection 5.3.1:

$$u = -8.72 \times 10^{-5} V^{-1}.$$

The sample volume V_s divided by the coupling factor F is

$$\frac{V_s}{F} = V_c \left[\frac{b^2 + D^2}{b + 0.45D} \right] \frac{1}{b} , \qquad (2.30)$$

where V_c is the volume of the coil, b is the length of the coil and D is the diameter of the coil. The length of the coil is

$$b = (2.05 \pm 0.05) \text{ cm}$$

and

$$D = (2.38 \pm 0.02) \text{ cm} .$$

This gives

$$\frac{V_s}{F} = (1.41 \pm 0.04) \times 10^{-5} m^3 .$$

However, there is an $(11 \pm 1)\%$ decrease in F through the combined effects of the water and sample coil, and an effective 1% decrease in F through the finite closed loop gain. The corrected value for V_s/F is thus

$$\frac{V_s}{F} = (1.62 \pm 0.06) \times 10^{-5}, \ m^3 .$$

Finally, the theoretical value for K_3 is

$$K_3 = u\frac{V_s}{F} = -(1.41 \pm 0.05) \times 10^{-9},\ m^3V^{-1}.$$

The measured value of K_3 is

$$K_3 = -(1.480 \pm 0.014) \times 10^{-9}, m^3V^{-1}.$$

The two results agree well.

The value of V_s/F can be used to find K_4 for the imaginary signal. A similar procedure was adopted for version 1. From equation 3.24

$$\Delta V_Q \approx FV_oQX",$$

where ΔV_Q is the change in output from the phase sensitive rectifier on inserting a sample and V_o is the output of the phase sensitive rectifier prior to nulling in the absence of a sample. This is rearranged to give

$$X_T" = \frac{V_s}{F}\frac{1}{V_oQ}\Delta V_Q,\ m^3 \qquad (6.4)$$

so that

$$K_4 = \frac{V_s}{F}\frac{1}{V_oQ}. \qquad (6.5)$$

The best value for V_s/F is $(1.70 \pm 0.02) \times 10^{-5}$, m^3 which is calculated from the measured values of K_3 and u. V_o is 11.617V and Q is 175 ± 1. This gives

$$K_4 = -(8.4 \pm 0.1) \times 10^{-9}m^3V^{-1}.$$

It is simple to calculate the maximum values of X_T' and $X_T"$ that the instrument can cope with. Referring to figure 45, X_T' is dealt with first. The quiescent voltage for the varicap is -5V, but applied levels down to -13V are within the linear region. This puts the locked phase loop's linear operating range at 8V or $1.18 \times 10^{-8}m^3$.

If the filtered output of the phase sensitive rectifier is not nulled it stands at 11.6V. Sample losses due to $X_T"$ cause this level to drop. The limit of the allowable drop is the operational amplifier's linear

working range: this is about -12V. The maximum operating range is therefore 23.6 V or 2.0 x 10^{-7} m^3.

6.2.3 Noise and drift

The noise and drift on both channels were measured by monitoring their outputs against time on a chart recorder. With a fast chart speed, short term random noise was recorded. With a slower chart speed, longer term drift was recorded.

Two 30 second recordings were made to find the r.m.s. noise in X', portions of these recordings are shown in figure 64. A room temperature measurement took 10 seconds typically; the two traces were used to estimate the random noise over this time span. The traces were divided into 10 second segments and the value of the output was noted at 1/2 second intervals within the segment. The standard deviation of these values was taken as the r.m.s. noise within the segment. The standard deviations for the six segments were averaged to produce the estimate that the random noise amplitude was 0.5mV r.m.s. This corresponds to a noise level of 7.4 x 10^{-13} m^3 r.m.s. in X_T'. A distinct change in output level can be seen near the beginning of trace a in figure 64, more will be made of this shortly.

It is interesting to note that 0.5mV r.m.s. corresponds to a phase noise level of $(3.4 \times 10^{-4})^o$ r.m.s. at the operating frequency of 5.068MHz. This level is fourteen times less than the $(5 \times 10^{-3})^o$ r.m.s. fluctuations in the phase of the signal from the crystal oscillator, see subsection 4.3.2. The assumption that the crystal oscillator's phase noise cancels out at the 5 MHz phase detector is therefore proven.

Two 5.5 minute recordings were made of the phase loop's output. The drift in each was estimated by noting the output's value at six second intervals and then finding the slope of the least mean square error line of fit. Results of -0.26 mV $minute^{-1}$ and + 0.42mV $minute^{-1}$ were thus obtained.

Figure 64. Two recordings of the short term noise in the signal for X_T'.

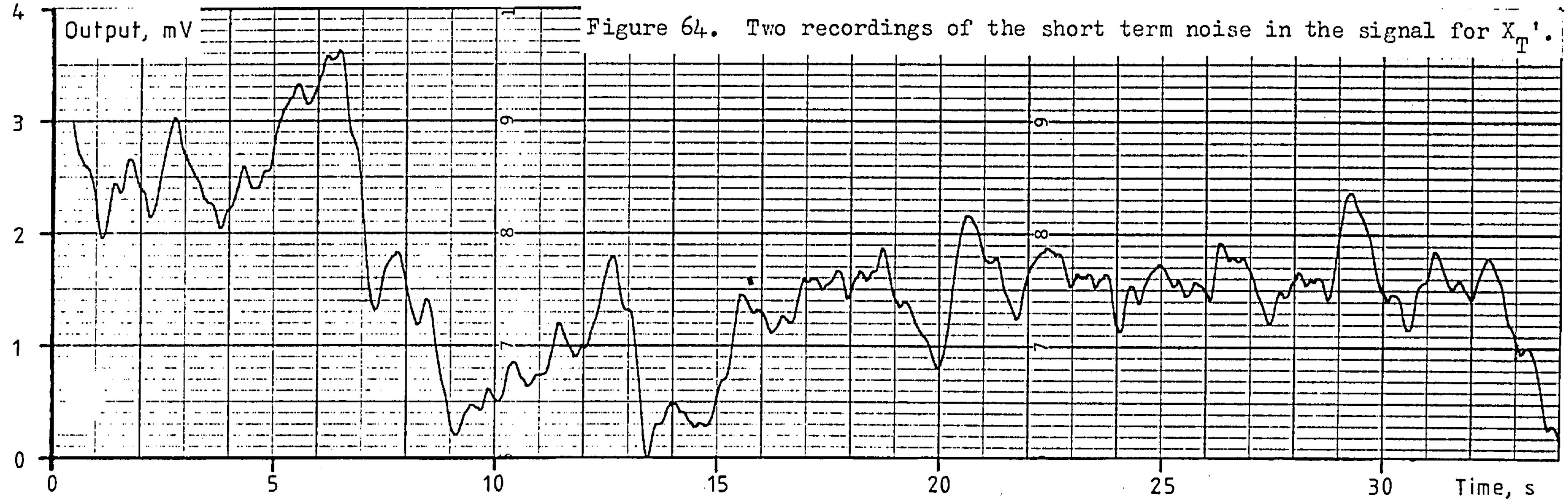

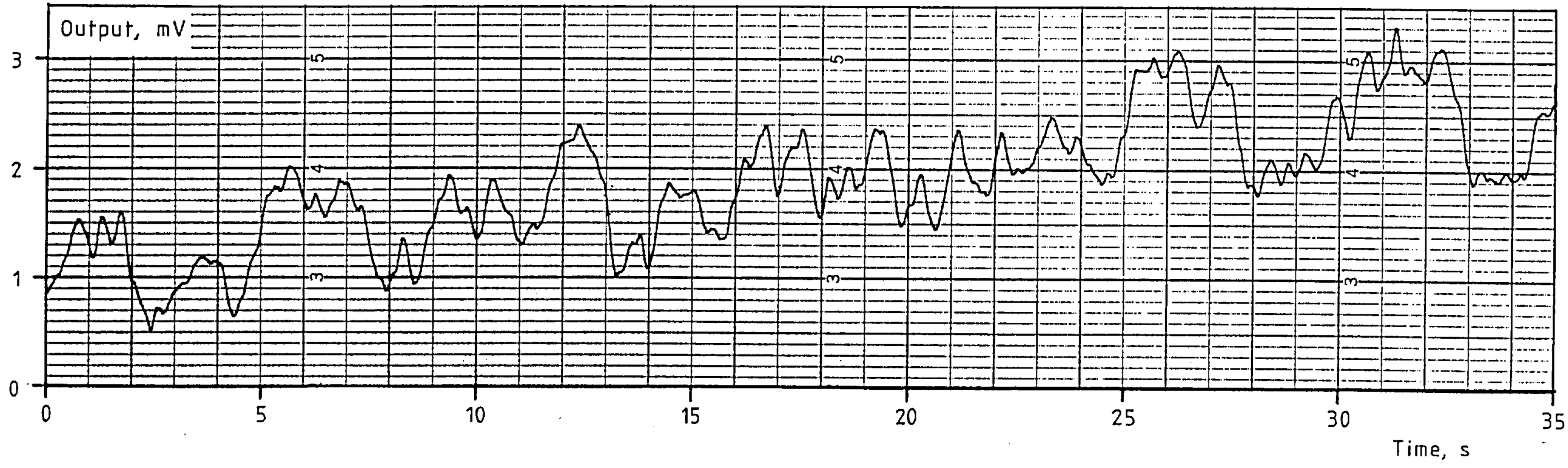

Of these, + 0.42 mV minute^{-1} was used to give an estimate of 6.2 x 10^{-13}m^3 minute^{-1} for the drift in the signal for X_T'.

The recording whose drift was - 0.26mV minute^{-1} is shown in figure 65. It shows distinct shifts in output of the type already seen in figure 64a. These shifts, appearing and disappearing at random intervals in time, are known as popcorn or burst noise. The most likely source of the popcorn noise was the TTL circuitry in the 5MHz phase detector.

The random noise and drift in the channel for X_T" was measured in the same way as that for X_T'. The averaged random noise was 0.22mV r.m.s., equivalent to 2 x 10^{-12}m^3. A portion of a short term noise recording is shown in figure 66. The amplitude noise is equivalent to random variations in Q of 3.3 x 10^{-3} r.m.s. in a natural Q of 175. The random noise can be reduced by increasing the phase sensitive rectifier's time constant, see figure 53. The drift in X_T" was 0.54mV min^{-1} or 5 x 10^{-12}m^{3}minute^{-1}. The main source of noise and drift in X_T" must have been the SL1680C crystal oscillator maintaining circuit.

The short term random noise levels were completely unaffected by the furnace current. For steady furnace currents the drifts were also unchanged, but changing the current induced a marked drift. Figures 67a and b show typical examples of the drift in the signals for X_T' and X_T" as the furnace is heated to 700^{o}C and is slowly brought back to room temperature. A complete cycle takes about 80 minutes. Two drift mechanisms are evident in the figures: the first is the drift with time that has already been discussed, the second is a drift with temperature that is discussed below.

It is likely that two mechanisms are contributing to the drift with temperature. The first is that the water jacket on which the coil is wound will be distorted in a complex manner as the furnace temperature is raised. The reason for this is that whilst the water jacket's outer tube is kept cool by the flowing water, the inner tube is heated up by the

Figure 65. One of the plots used to determine the drift in the signal for X_T'.

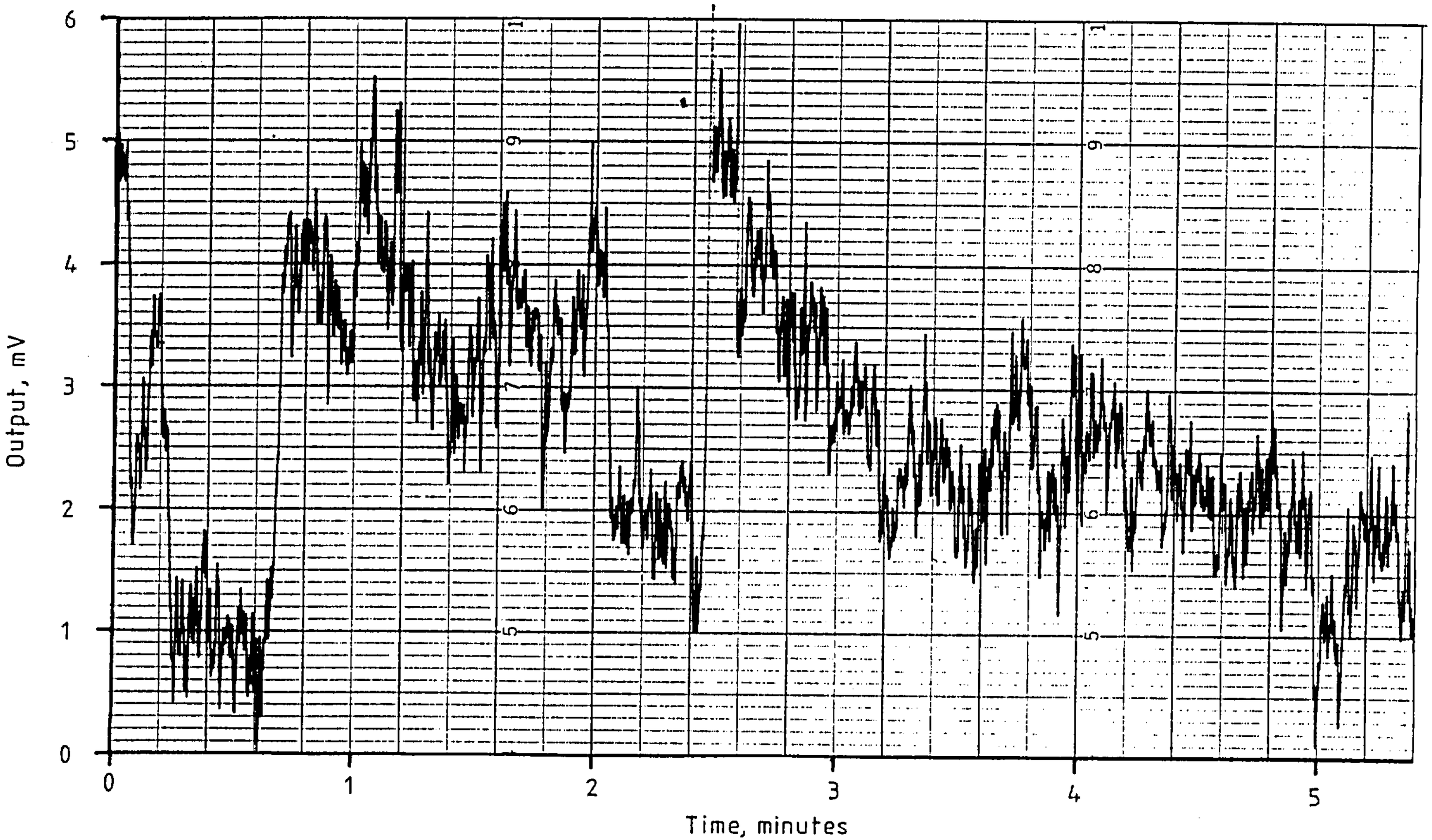

Figure 66. A recording of the short term noise in the signal for X_T".

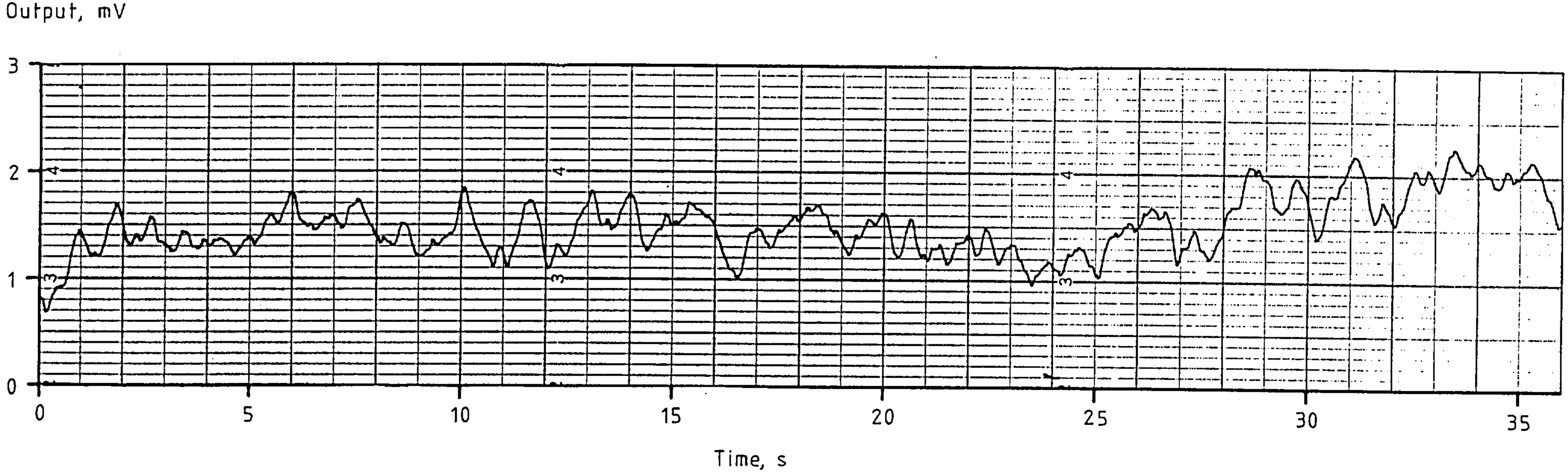

Figure 67. The temperature induced drifts.

a. The drift in the signal for X_T' over a heating and cooling cycle lasting 80 mins.

b. The drift in the signal for X_T'' over a heating and cooling cycle lasting 80 minutes. The heating and cooling curves have been separated for clarity.

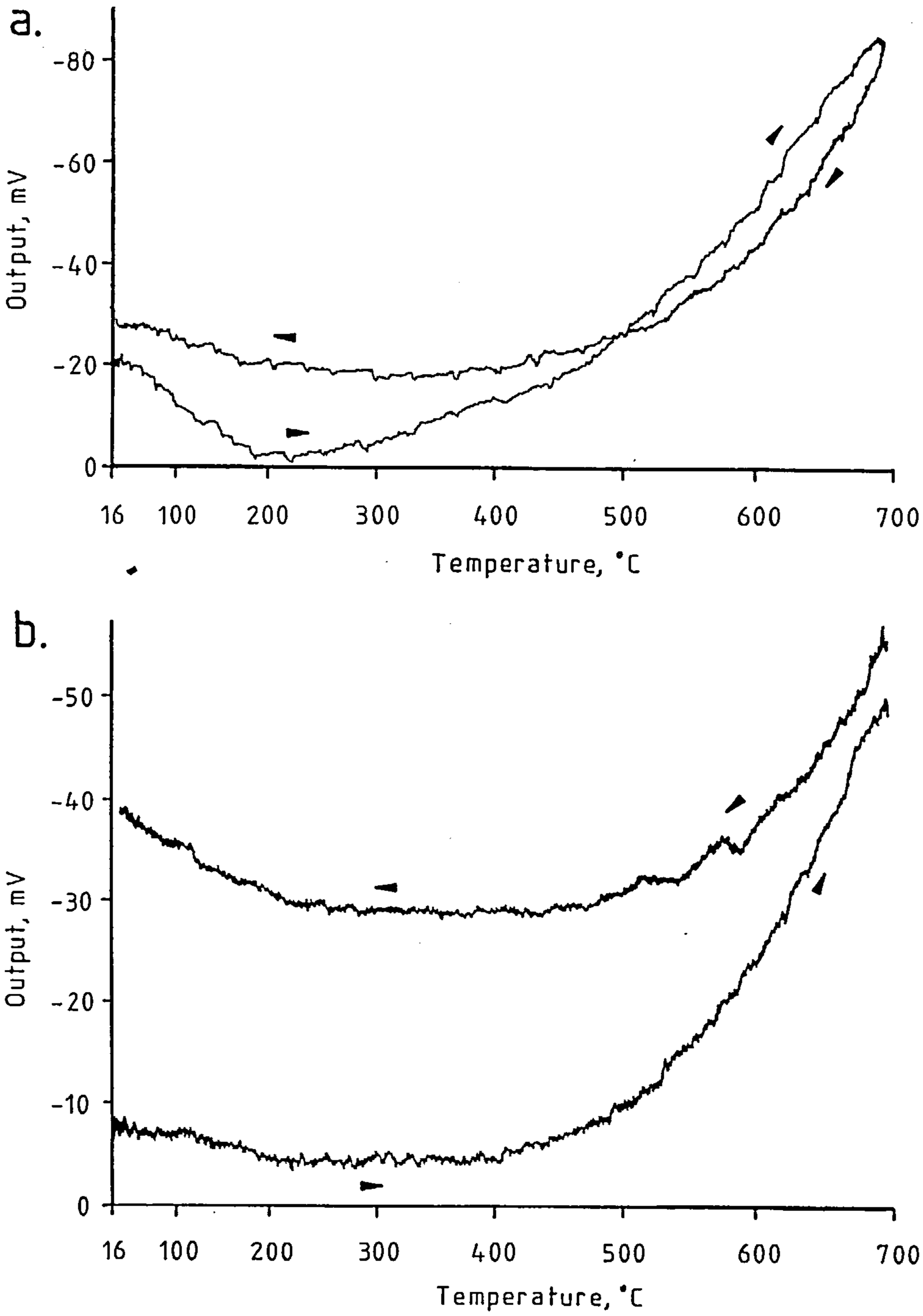

furnace - see figure 58. The second mechanism is that the sample coil does get slightly warmer as the furnace gets hotter, this will increase the coil's resistance and decrease its Q. The effects of both mechanisms could be reduced by winding the coil on a former that does not touch the water jacket. The price to be paid is a decrease in the filling factor F, but this should be no worse than 30%.

Looking in more detail at figure 67a, a series of blips are evident on the trace. These correspond to points at which the Variac in figure 57 was used to alter the furnace current. These blips will disappear if an electronic controller is used to continuously and smoothly vary the furnace current.

6.2.4 Comparing the improved locked phase loop with the first version.

This subsection shows how much effect the improvements described in chapters 4 and 5 have had on the locked phase loop's performance. Table 8 lists the values found for noise, drift and so on.

Parameter	Value	
	First Version	Final Version
Length of sample coil, m	4.34×10^{-2}	2.05×10^{-2}
Diameter of sample coil, m	2.45×10^{-2}	2.38×10^{-2}
Construction of sample coil	10 turns 16 s.w.g. Ag wire	8 turns 15 s.w.g. Cu wire
Flux at centre of sample coil, T r.m.s.	1.6×10^{-6}	0.5×10^{-6}
Maximum sample volume, m^3	2.6×10^{-7}	8×10^{-8}
Operating temperature range, ^oC	16 - 700	16 - 800
Operating frequency, MHz	5.000	5.068
Calibration factor for X_T', m^3V^{-1}	-2.5×10^{-8}	-1.5×10^{-9}
Maximum input for X_T', m^3	1.2×10^{-8}	1.2×10^{-8}
Noise in X_T', m^3 r.m.s.	8.2×10^{-12}	7.4×10^{-13}
Drift in X_T', m^3 min^{-1}	3×10^{-11}	6.2×10^{-13}
Calibration factor for X_T'', m^3V^{-1}	2.7×10^{-9}	8.4×10^{-9}
Maximum input for X_T'', m^3	3.8×10^{-9}	2.0×10^{-7}
Noise in X_T'', m^3 r.m.s.	3×10^{-12}	2×10^{-12}
Drift in X_T'', m^3 min^{-1}	5×10^{-12}	5×10^{-12}
Direct Reading?	Yes	Yes

Dealing with X_T' first of all, it is clear that there has been a very substantial improvement in all quarters. The only factor that has not been improved is the maximum value of X_T' that can be handled, the original value is adequate for the samples that are likely to be met.

The results for X_T'' are disappointing. There is only a slight improvement in performance and that is a 33% decrease in the random noise level. The improvement in maximum input level is no advantage at all, the range of version 1 had been satisfactory. The nub of the problem here is the wideband amplitude noise generated by the SL1680 crystal oscillator maintaining circuit. Section 6.4 has some useful suggestions to make.

Table 9 compares the improved locked phase loop to the instruments of Stephenson and de Sa[17] and Markert et al[18] with regard to the noise and drift in X_T'. Markert et al do not give enough information to permit a comparison of performances with respect to X_T''.

Table 9 A brief comparison of the improved locked phase loop to the instruments of Stephenson and de Sa[17] and Markert et al[18].

Parameter	Instrument		
	Version 2	Stephenson & de Sa	Markert et al
Noise in X_T', m^3 r.m.s.	7.4×10^{-13}	1.3×10^{-11}	3×10^{-10}
Drift in X_T', m^3 min^{-1}	6.2×10^{-13}	1.3×10^{-11}	Not given
Frequency of operation, Hz	5.068×10^{6}	1.5×10^{3}	1×10^{7}
Field in sample coil, Am^{-1} r.m.s.	0.4	200	Not given

The noise level of the improved locked phase loop is seventeen times lower than the low frequency bridge of Stephenson and de Sa, and it is 400 times lower than the r.f. tuned circuit technique of Markert et al.

6.2.5 Plots of X_aT' and X_aT'' against temperature

This subsection shows plots of X_{aT}' and X_{aT}'' against temperature for

a series of four samples. The subscript "a" is used to denote the apparent susceptibility that was discussed in sections 1.4 and 1.6. For convenience in typing, the extra subscript "T" for total susceptibility is omitted from now on. The first two samples to be discussed are lodestone (magnetite ore) and haematite.

Figures 68a and b show the variations in the real and imaginary susceptibility of a 14.0 mg sample of lodestone. The sample's real susceptibility X_a' prior to heating was $5.03 \times 10^{-9} m^3$. Figure 68a shows that X_a' had risen by a factor of 1.05 by the time the sample reached the Curie transition. X_i' rose more than this, but the rise was masked by the magnetic grains' demagnetizing factors - see equations 1.63 and 1.65. The appearance of a peak in susceptibility immediately before the Curie transition is known as the Hopkinson effect, this effect is discussed in the next subsection. The Curie temperature was taken to be the point of intersection of lines produced from the Curie transition and from the trace just above the transition. The Curie temperature was determined to be $(567 \pm 2)^{o}C$ on both the heating and the cooling paths. The close agreement shows that the rate of change of the furnace's temperature was slow enough for the thermocouple to accurately register the sample's temperature. The complete cycle, from $12^{o}C$ to $603^{o}C$ and back again, took about 1 hour. The susceptibility had decreased slightly at the end of the run because heating in air oxidised the sample's outer skin to haematite.

Figure 68b shows the thermal variation of X_a'' for the lodestone sample. For clarity the cooling curve alone has been reproduced, the heating curve was identical. Below the sharp peak in X_a'' at the Curie temperature, the losses continually decrease with decreasing temperature. The drop in the magnitude of X_a'' at the Curie transition was 5.8 times its absolute value at room temperature. The transition put the Curie temperature at $(568 \pm 2)^{o}C$, this is in agreement with the result from figure 68a.

Figure 68. The temperature dependence of susceptibility for a 14.0 mg sample of lodestone.

a. The real part of the apparent total susceptibility

b. The imaginary part of the apparent total susceptibility

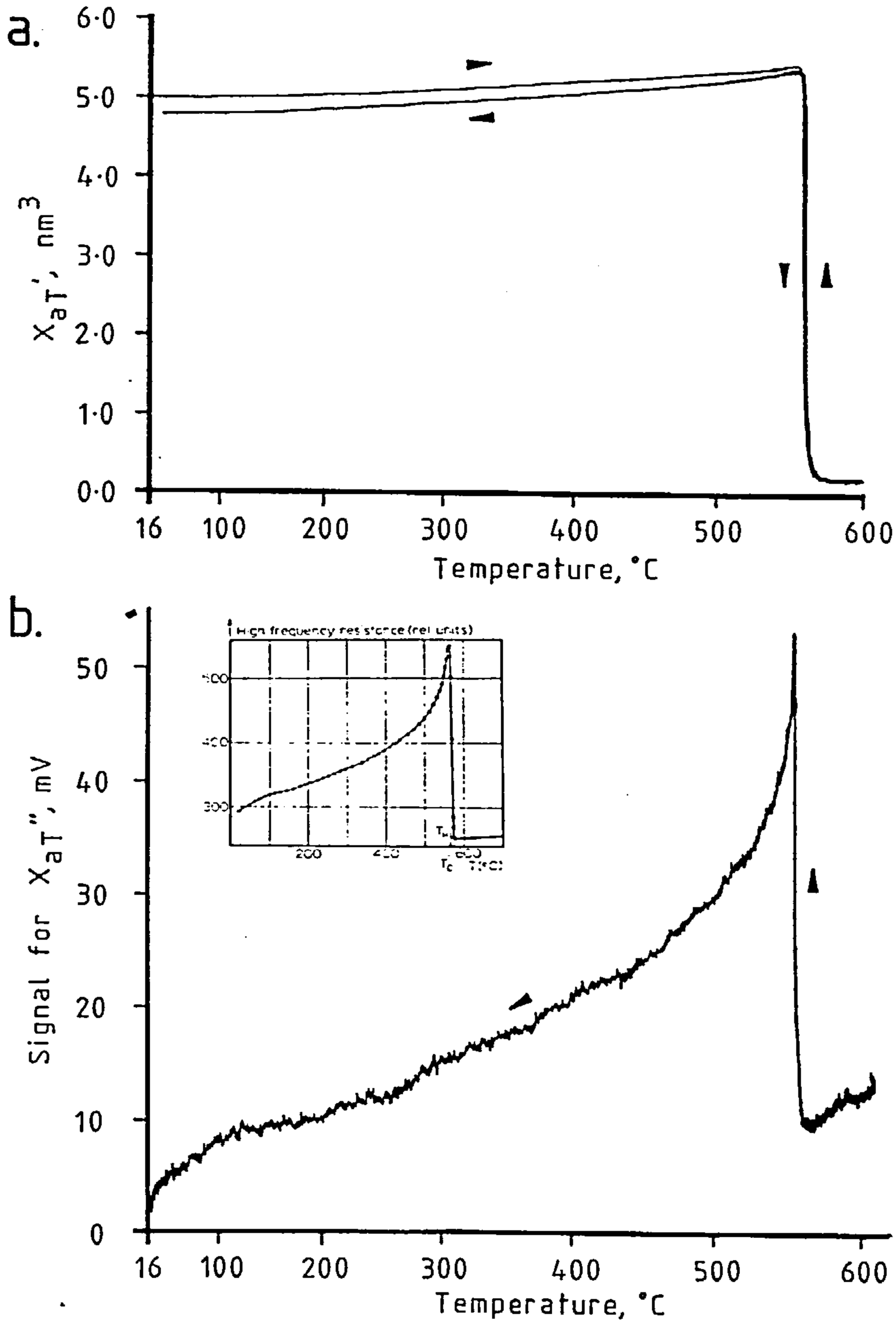

The contrast between figures 68a and 68b provides clear evidence that figure 68b is genuinely tracing X_a". There is no way that the trace in figure 68b can be ascribed to a detuning effect due to X_a', for X_a" describes a sharp spike whereas X_a' undergoes a rectangular step transition. Furthermore, the small growth in X_a' caused an increase in the coil's Q whereas the dramatic rise in X_a" represented a decreasing Q. Petersen's[19] results on the temperature dependance of X_a" for lodestone are shown inset in figure 68b. The results are identical even though Petersen used a completely different technique.

The temperature dependences of the real and imaginary susceptibilities of a 101.4 mg sample of haematite are shown in figures 69a and b. The radii of the haematite grains were known to be less than 40 μm. Starting with figure 69a, the real susceptibility prior to heating was $3.48 \times 10^{-10} m^3$. In contrast to figure 68a the Hopkinson peak was very pronounced for the susceptibility had increased by a factor of 3.1 just below the Curie point. The Curie point was $(673 \pm 2)^{o}C$. Once again, the transitions on heating and cooling overlapped. The complete run from $16^{o}C$ to $698^{o}C$ and back again took 80 minutes. A sizeable offset was visible after the Curie point. A small portion of this, about $3 \times 10^{-11} m^3$, was due to the formation of paramagnetic Fe_2O_3, the rest was the result of the temperature induced drift. The return cooling path below the transition was different from the heating path. This cannot be completely accounted for by the drift's hysterysis, but it can be explained as follows. When the haematite passed through the Curie point its magnetic domains were destroyed. When the haematite was subsequently cooled it is likely that the domains did not reform exactly as they were and so their combined susceptibility had a different temperature dependence. The relationship between temperature, susceptibility and magnetic structure is discussed in more detail shortly.

Figure 69b shows a sharp peak in losses as the haematite cooled

Figure 69. The temperature dependence of susceptibility for a 101.4 mg sample of haematite.

a. The real part of the apparent total susceptibility.

b. The imaginary part of the apparent total susceptibility.

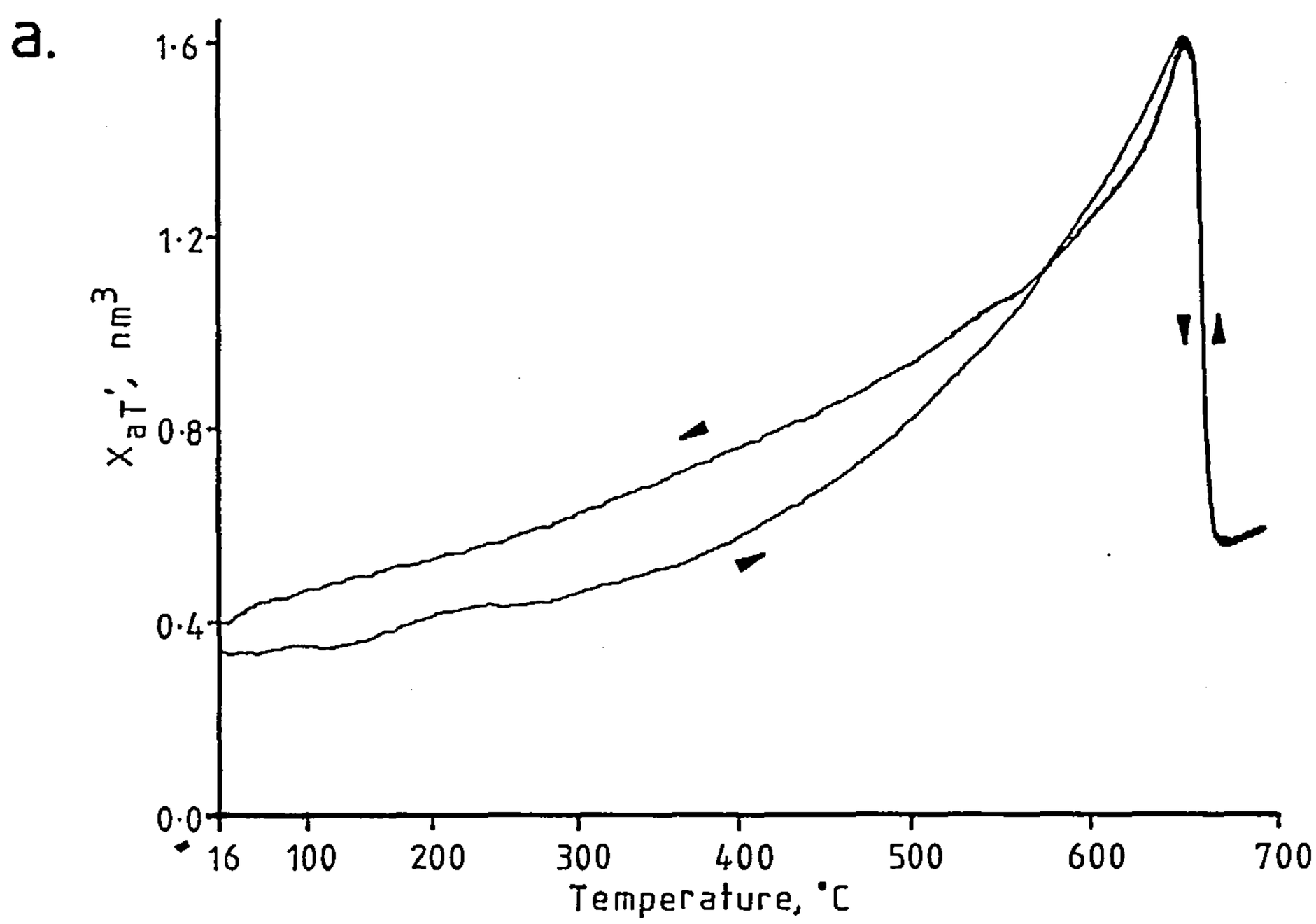

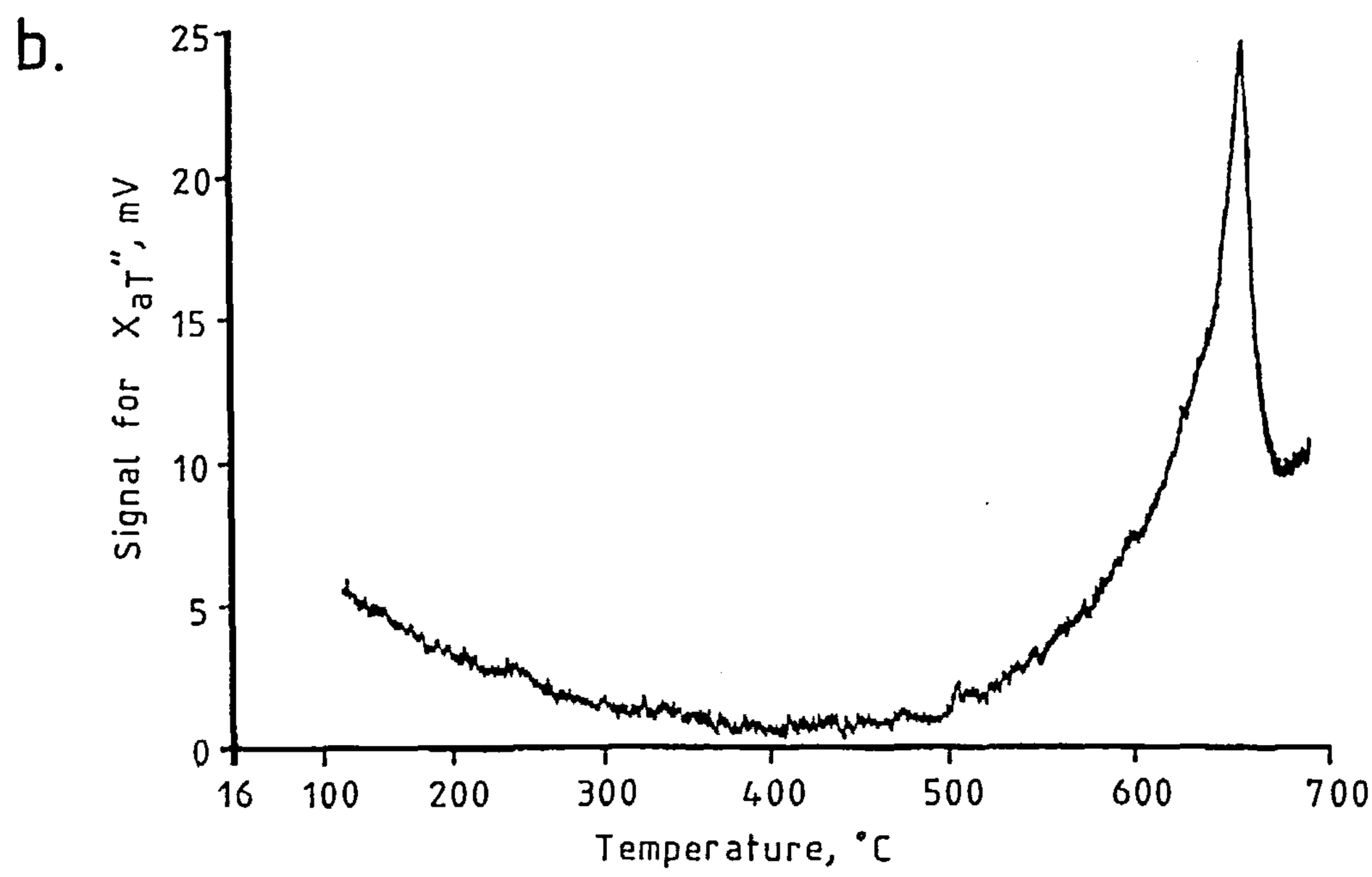

through its Curie point. For the sake of clarity, only the cooling trace has been reproduced because the heating trace was identical. The magnitude of the transition, $2.5 \times 10^{-10} m^3$, was seven times larger than the room temperature value of X_a". Figure 69b put the Curie point at $(673 \pm 2)^{\circ}C$ in agreement with figure 69a. One significant difference between the traces of X_a" for lodestone and haematite was that the losses in haematite only increased significantly when quite close to the Curie point, whereas those for lodestone had increased gradually all the way up from room temperature.

The results for another two samples are presented now, each sample consisted of chippings from a 1" rock drill core. Probably between 1% and 5% by weight of the chippings were useful ferromagnetic grains, the rest was the non-magnetic matrix in which the grains were suspended. These samples are more complicated than the lodestone (magnetite) and haematite just seen. Some comments are made on the traces for X_a' but not on the traces for X_a" because these are not so clear. The shapes of all the curves are discussed in more detail in the following subsection.

Figures 70a and b are the heating and cooling curves for British tertiary dyke NW5.21E. Its susceptibility X_a' prior to heating was $4.29 \times 10^{-10} m^3$. This had increased by a factor of 2.0 just below the Curie point at $(506 \pm 2)^{\circ}C$. From the very different shape of the cooling curve, it is evident that some physical change took place above the Curie point.

Figures 71a and b are the heating and cooling curves for sample 33-3-100, site 524, leg 73 of the Deep Sea Drilling Project. The mineral's concentration was about 6% by weight and the ferromagnetic grain sizes fell in the range $(50\text{-}300)\mu m$. The sample's DC room temperature susceptibility was $1.65 \times 10^{-5} m^3 Kg^{-1}$, this measurement had been made with a translation balance[53].

Figure 70. The temperature dependence of susceptibility for a 91.1 mg sample of NW 5.21E.

a. The real part of the apparent total susceptibility.

b. The imaginary part of the apparent total susceptibility.

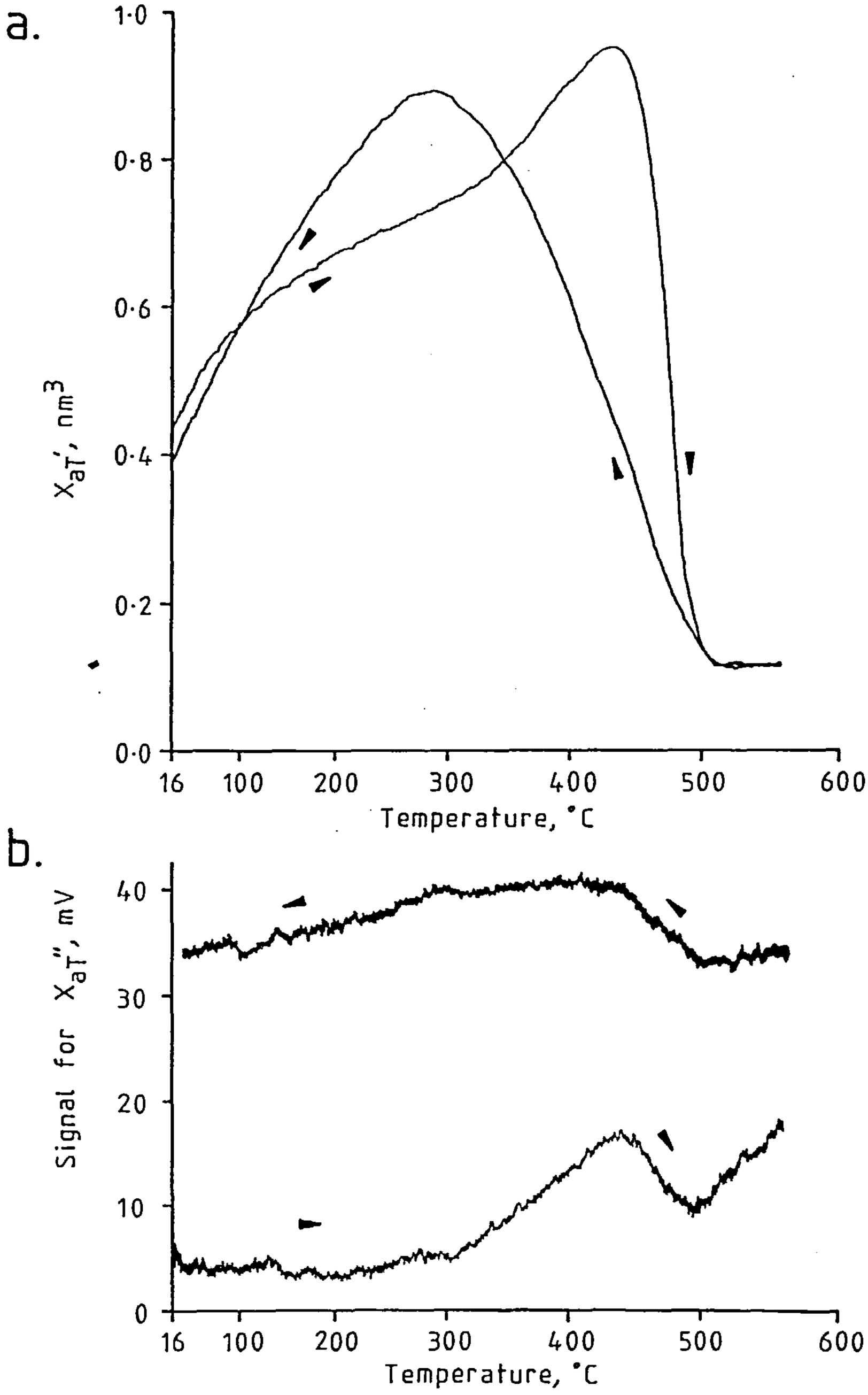

Figure 71. The temperature dependence of susceptibility for a 104 mg sample of 33-3-100.

a. The real part of the apparent total susceptibility.

b. The imaginary part of the apparent total susceptibility.

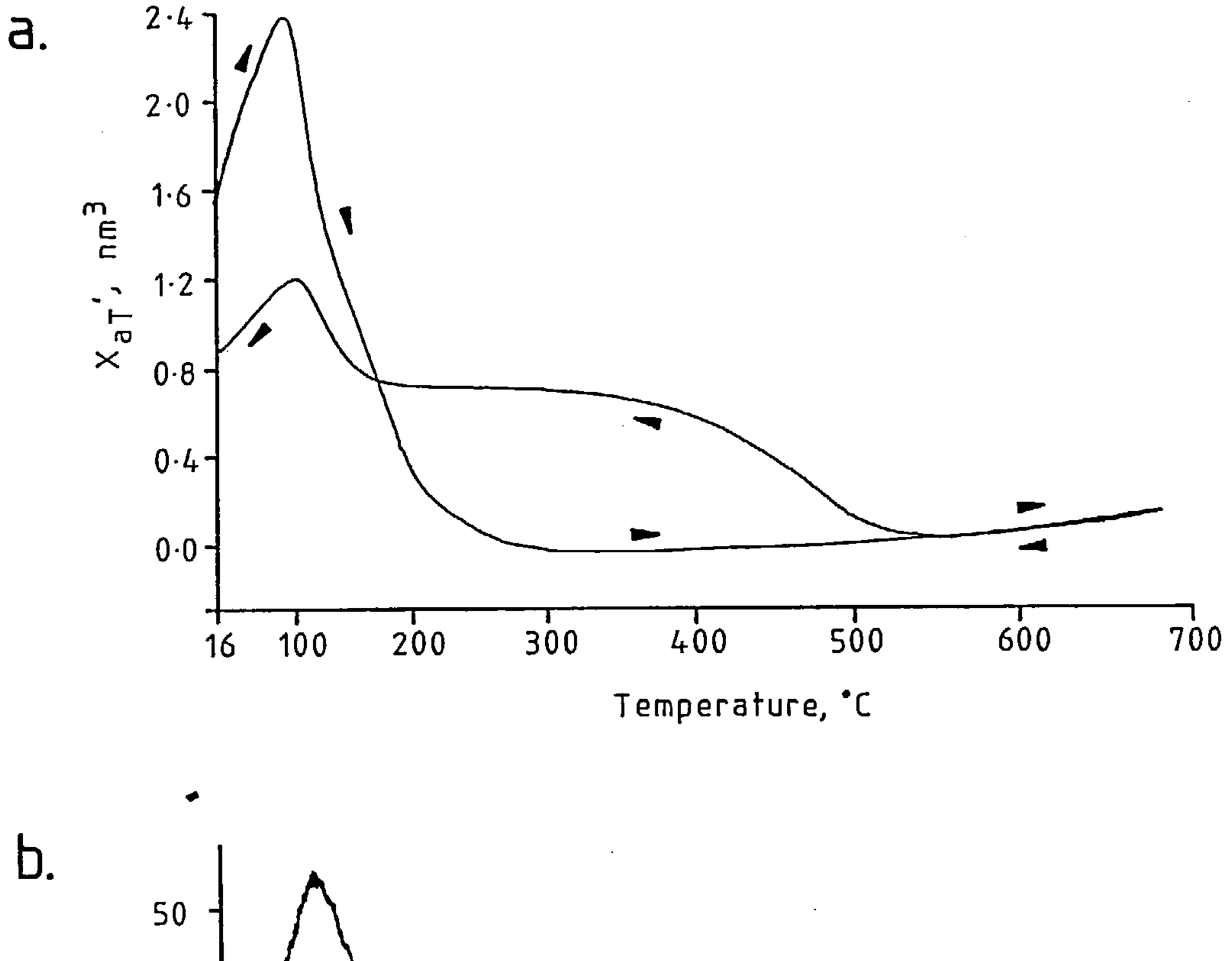

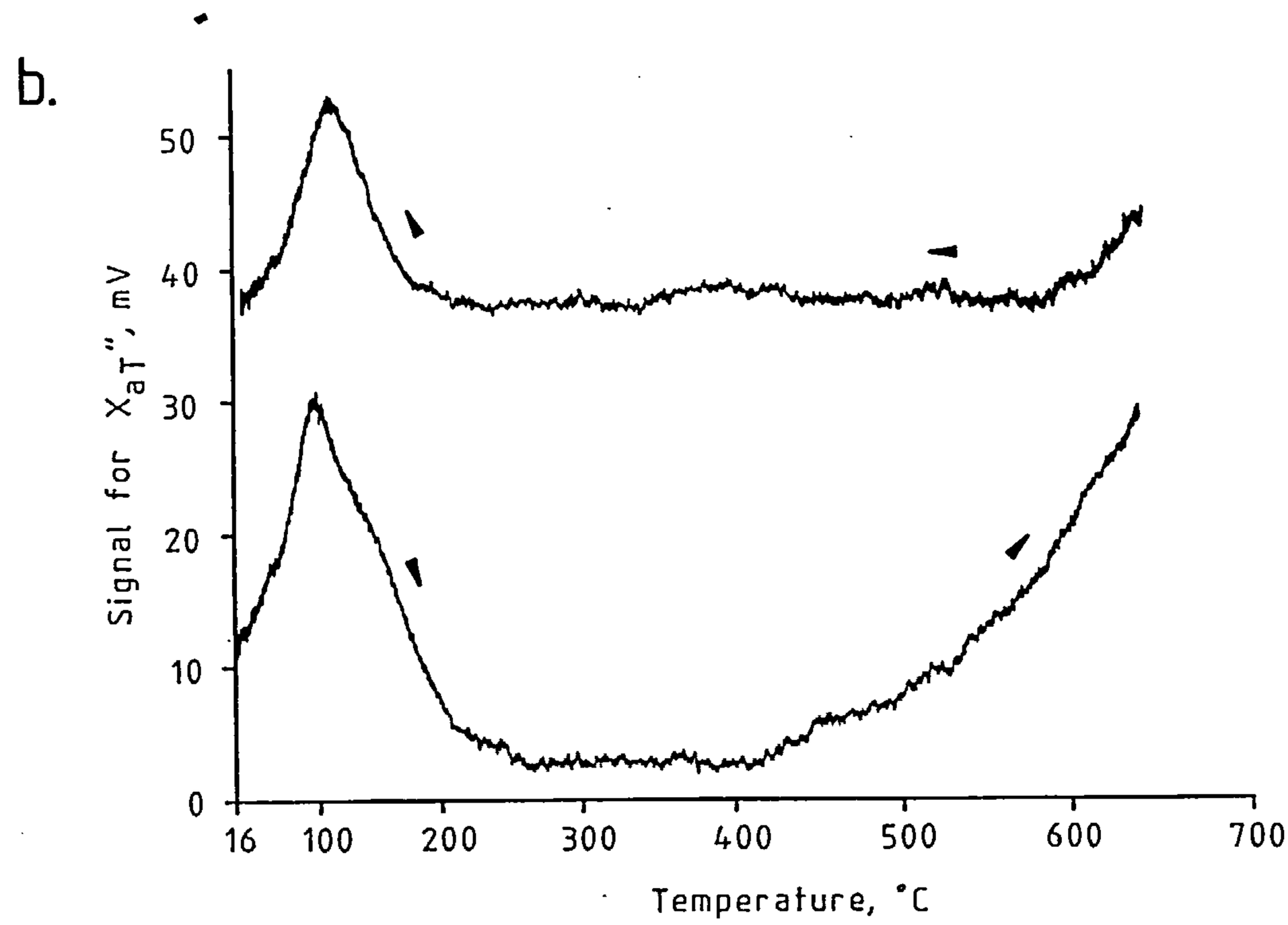

Measurements on a quantity of this sample using the new instrument gut the room temperature susceptibility at $1.56 \times 10^{-9} m^3$ or $1.5 \times 10^{-5} m^3 Kg^{-1}$. Bearing in mind that the rock sample was unlikely to be homogeneous, the result from the new instrument at 5.068 MHz was in good agreement with that from the DC translation balance. On heating, the peak real susceptibility was 1.5 times the room temperature susceptibility. The Curie transition was quite complex as it had two distinct slopes and a long tail off. The Curie point was taken to be the end of the tail at which the susceptibility finally disappeared, this was $(304 \pm 10)^{\circ}C$. On cooling from $688^{\circ}C$ two new Curie points appeared showing that chemical changes had taken place.

6.2.6 An investigation into the shapes of the traces for $X_a'(T)$ and $X_a''(T)$

It has been seen that the temperature dependence of susceptibility amounts to more than a simple transition at the Curie point. The traces have characteristic shapes that must contain information about the magnetic structure of the sample. The purpose of this subsection is to mention some work that has already been done on explaining the temperature dependence of susceptibility, and then to propose an extension to this work by piecing together some of the ideas mentioned in chapter 1. One of the proposal's advantages is that it unifies the treatment of X' and X".

An important component in any discussion on the temperature dependence of susceptibility is the notion of superparamagnetism. Superparamagnetism has already been mentioned in chapter 1 but a brief reminder of what it means is worthwhile. In essence, below a temperature known as the blocking temperature single domain grains have a susceptibility due to stable rotation magnetization. Above the blocking temperature the single domain grains become superparamagnetic and have a much stronger susceptibility because of the magnetization's ability to completely flip in sympathy with the applied field. Following the lines of an argument set out by Stephenson[6], the blocking temperature T_B of a grain of volume V which

is amongst a randomly oriented array of uniaxial single domain grains is

$$T_B = \frac{K_u V}{k}\left[\frac{1}{22 + \ln \tau_m}\right] . \qquad (6.6)$$

K_u is the grains' uniaxial anisotropy constant, k is Boltzmann's constant and τ_m is a time constant associated with the method of measuring susceptibility. Equation 6.6 follows from equation 1.70. Using equation 1.50, if the magnetizing field is oriented at an angle ϕ to a uniaxial grain's easy direction the rotational initial susceptibility is

$$X_r = \frac{\mu_o M_s^2}{2K_u} \sin^2 \phi \quad , \qquad (6.7)$$

in which M_s is the saturation magnetization of a grain. For the assembly of non-interacting randomly oriented grains the composite susceptibility is

$$X_r = \frac{\mu_o M_s^2}{3K_u} \quad , \qquad (6.8)$$

since $<\sin^2\phi> = 2/3$. Above the blocking temperature the susceptibility of the random assembly of superparamagnetic grains is[6]

$$X_s = \frac{\mu_o V M_s^2}{3kT} \quad . \qquad (6.9)$$

There are three points to make about these results. Firstly, the ratio of the susceptibility of a grain when it is just above the blocking temperature to when it is just below the blocking temperature is

$$\frac{X_s}{X_r} = \frac{K_u V}{kT_B} \qquad (6.10)$$

$$= 22 + \ln \tau_m \qquad (6.11)$$

from equation 6.6. At an operating frequency of 5 MHz τ_m =

$(2\pi \times 5 \times 10^{6})^{-1} = 3.18 \times 10^{-8}$, thus

$$\frac{X_s}{X_r} = 4.74.$$

In words, the susceptibility of a random array of superparamagnetic uniaxial grains drops by a factor of 4.7 as it cools through the blocking temperature when the measurement frequency is 5MHz. The second point is that the susceptibility drops off as 1/T above the blocking temperature. The third point is that a real sample contains a range of grain sizes so that at any given temperature some grains will be above their blocking temperatures and others will be below. For an operating frequency of 5MHz the blocking volume V_B at a temperature T is

$$V_B = \frac{kT}{K_u} \quad (4.7) \; . \qquad (6.12)$$

Relations 6.6 to 6.12 show that the temperature dependence of susceptibility for a random array of single domain uniaxial grains may vary in quite a complex manner. They also show that the variation depends on the distribution of grain sizes, the uniaxial anisotropy constant and the frequency of measurement. These concusions provide some insight into the behaviour of real samples. Equation 6.13 may be stretched to explain the rise in the intrinsic susceptibility of multidomain grains just below the Curie temperature T_c: as $T \longrightarrow T_c$, $K_u \longrightarrow 0$ so V_B becomes very big and even large multidomain grains will become superparamagnetic. However, these superparamagnetic susceptibilites are not always large as M_s^2 in equation 6.9 may be close to zero.

The work that has been seen on understanding the temperature dependence of susceptibility has been wholly concerned with the real part of the susceptibility at frequencies of 5 KHz or less where $X'' \approx 0$. Radhakrishnamurty and Likhite[54] propose three different categories for X(T) traces, these are illustrated in figure 72. They considered the

Figure 72. Idealised categories for X'(T) traces, after Radhakrishnamurty and Likhite[54].

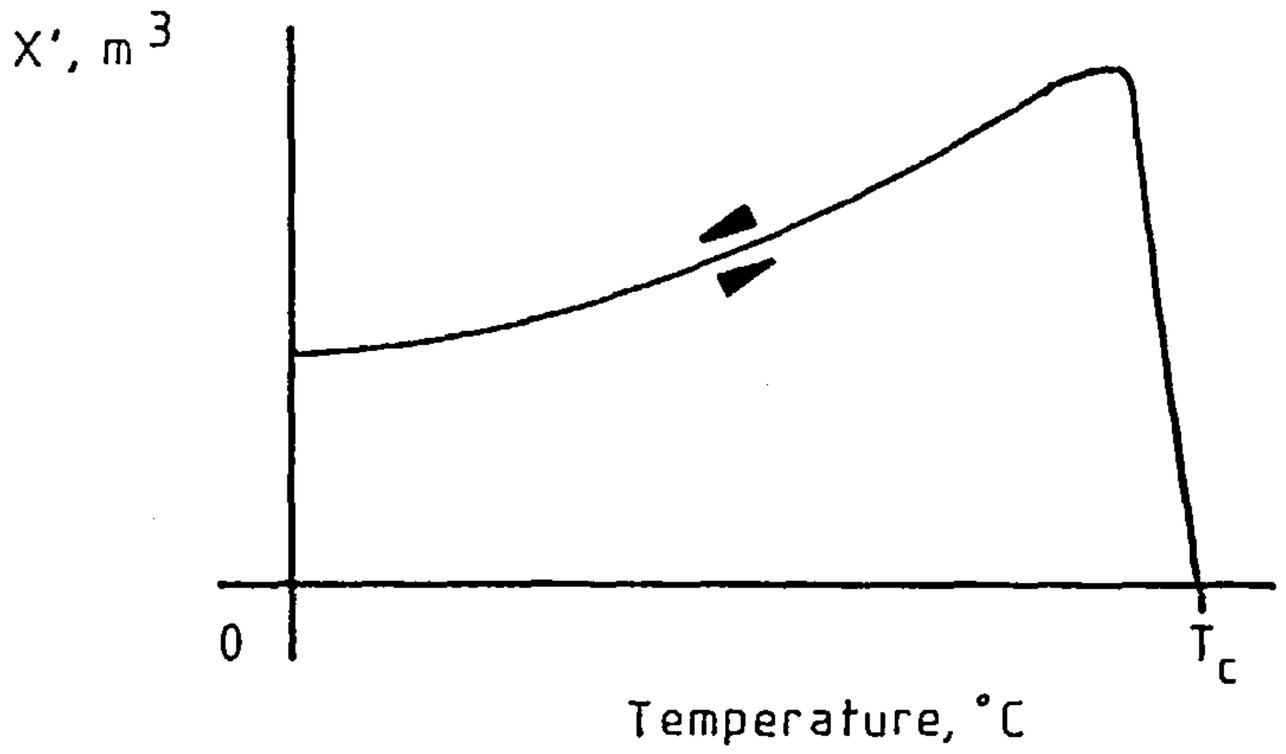

a. The Hopkinson multidomain type, or H type.

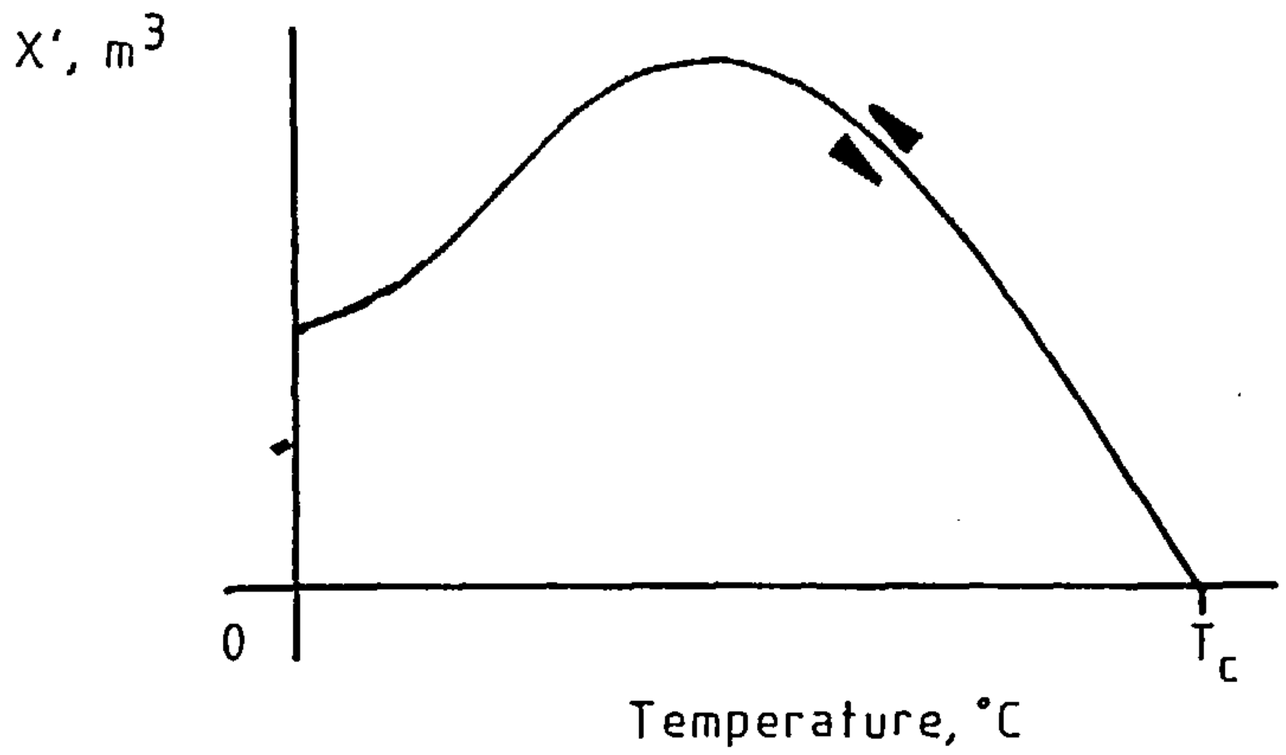

b. The single domain type, or SD type.

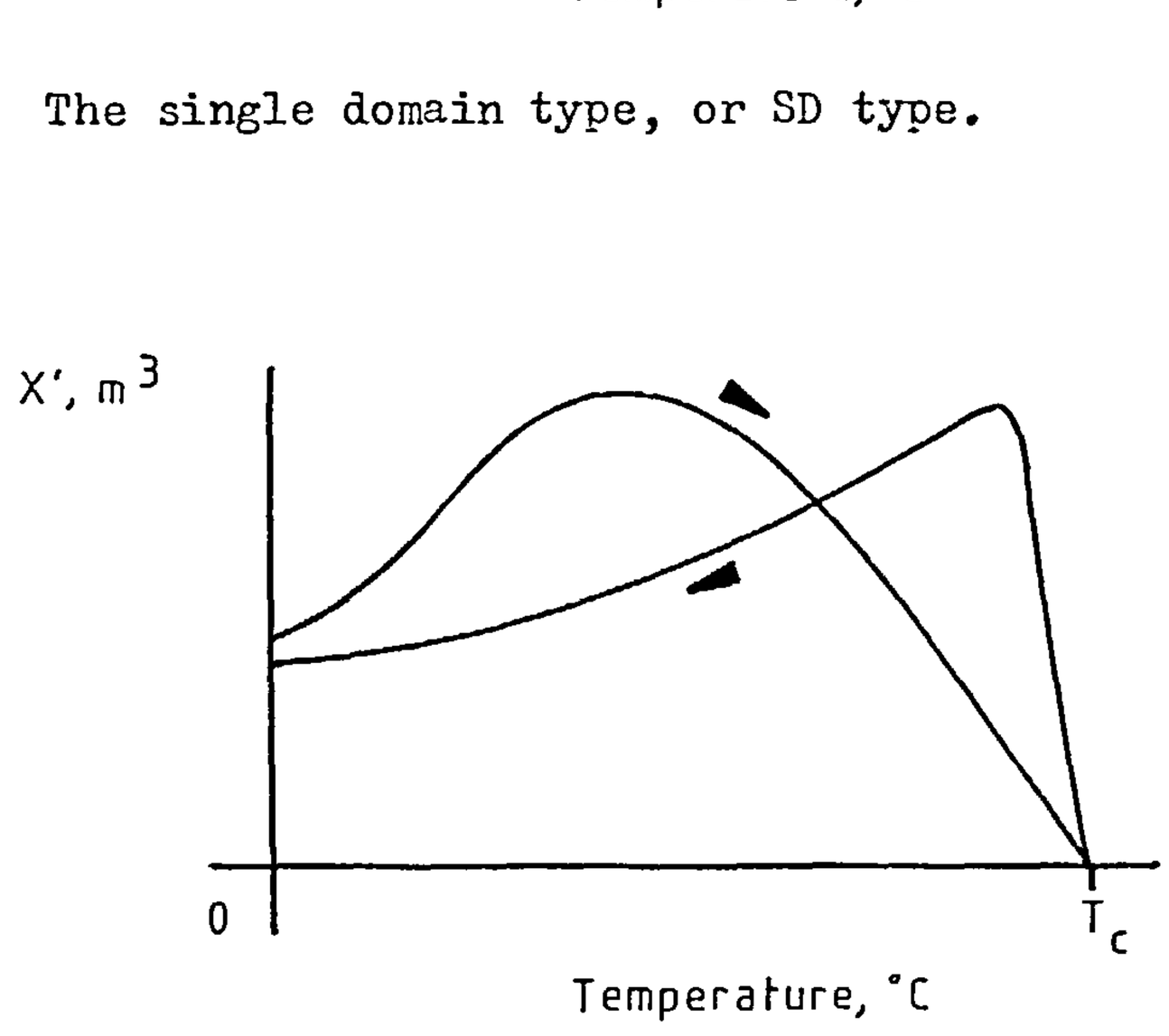

c. The quasi-single domain type, or QSD type.

Hopkinson or H type curve, figure 72a, to be characteristic of multi-domain materials. Examples of H curves for X'(T) have been presented in figures 68a and 69a. The second category was that of single domain materials. If a material contains purely single domain grains that are too large to be superparamagnetic at room temperature, it will exhibit a rising susceptibility as it is heated. This is because more and more grains will be passing through their blocking temperatures. Ultimately, the material's susceptibility will start to decrease because of the 1/T dependence of X_s - see equation 6.9. Figure 72b depicts an ideal single domain (SD) curve. Figure 71a would probably have been of this type had it not been chemically altered by heating. Finally, the quasi single domain (QSD) category, figure 72c, was proposed to account for samples undergoing physical alteration on heating. A physical alteration might be a change in mechanical stress or a change in grain shape. Figure 70a is a beautiful example of a QSD curve.

Dunlop[55] taps a similar vein of thought in a paper on the thermal enhancement of magnetic susceptibility. He also notes that samples with braod ranges of blocking temperatures exhibit broad peaks in susceptibility, whilst samples with a narrow range of blocking temperatures exhibit sharper peaks. A recent review by Dunlop[56] contains a number of references if more information on superparamagnetism and blocking temperatures is required.

Stephenson[6][13] has calculated the temperature dependence of susceptibility for random arrays of uniaxial grains with various grain size distributions. However, he limits his analysis to temperatures well below the Curie point where the uniaxial anisotropy constant can be considered to be independent of temperature; furthermore, he does not deal with the imaginary component of susceptibility. What follows is an attempt to add to Stephenson's work by modelling the behaviour of the real and imaginary susceptibility of uniaxial single domain grains right up to the

Curie point. No attempt is made to account for chemical or phase changes in the sample and only the low field initial susceptibility is considered. The uniaxial grains are assumed to be fine enough for hysterysis and eddy current losses to be ignored; see equation 1.57 and the succeeding comments.

The starting point for the model comes from equations 1.46 and 1.47:

$$X'(T) = \frac{X_o}{(1 + w^2\tau^2)} \tag{1.46}$$

and

$$X''(T) = \frac{X_o w \tau}{(1 + w^2\tau^2)} \quad . \tag{1.47}$$

X_o is the intrinsic d.c. susceptibility of the random array of uniaxial single domain grains, w is the operating angular frequency and τ is the grains' magnetic relaxation time constant which is defined in subsection 1.5.5. Both X_o and τ are temperature dependent. The next step is to represent X_o properly. Above the blocking temperature $w\tau << 1$ and the grain is superparamagnetic. Substituting $w\tau << 1$ into equation 1.46 shows that $X'(T) \approx X_o$ above the blocking temperature; this indicates that equation 6.9 for the superparamagnetic susceptibility is the correct form to choose for X_o. The intermediate results are therefore

$$X'(T) = \frac{\mu_o M_s(T)^2 V}{3kT} \left[\frac{1}{1 + w^2\tau^2} \right] \tag{6.13}$$

and

$$X''(T) = \frac{\mu_o M_s(T)^2 V}{3kT} \left[\frac{w\tau}{1 + w^2\tau^2} \right] , \tag{6.14}$$

where V is the volume of a grain.

The temperature dependance of τ for a single domain uniaxial particle was discussed in subsection 1.5.5:

$$\tau = \frac{1}{fe} \exp\left[\frac{K_u V}{kT}\right], \qquad (6.15)$$

in which f_e is a frequency of electron precession. Craik[4,147] puts f_e at about 10^9, this is in reasonable accord with Stephenson[6] who takes $\ln f_e$ to be 22; Stephenson's value is used throughout the following calculations. It is assumed that f_e is independent of temperature.

K_u is not independent of temperature, but in some cases its variation can be linked to the temperature dependence of M_s. Chapter 1 made a number of calculations on the magnetic behaviour of an array of carbonyl iron grains, this array is considered again. The grains in the array are small enough to be single domain and they are taken to be ellipsoidal in shape. The uniaxial anisotropy constant for an elongated single domain grain is given by[3,361]

$$K_u = \frac{1}{4}\mu_o M_s^2 , \qquad (6.16)$$

therefore

$$K_u(T) = \frac{1}{4}\mu_o M_s(0)^2 \left[\frac{M_s(T)}{M_s(0)}\right]^2 . \qquad (6.17)$$

Note that for polycrystalline iron the temperature dependence of K_u is given by[3,151][10,132]

$$\frac{K_u(T)}{K_u(0)} = \left[\frac{M_s(T)}{M_s(0)}\right]^{10} .$$

Experimental data on the temperature dependence of M_s for iron were taken from a paper by Tyler[57]. Table 2 contains a note of the saturation magnetization for carbonyl iron at room temperature: $\mu_o M_s = 1.56T$.

Equations 6.13 and 6.14 for X'(T) and X"(T) are not yet complete

because they do not allow for a rotational susceptibility.

$$X_r = \frac{\mu_o M_s^2}{3K_u} \tag{6.8}$$

below the blocking temperature. To correct this a new term will be added to equation 6.13:

$$X_r' = \frac{\mu_o M_s(T)^2}{3K_u(T)} \left[\frac{w^2\tau^2}{1 + w^2\tau^2} \right]^2 . \tag{6.18}$$

The extra factor in X_r' is simply a means of making X_r disappear above the blocking temperature. Below the blocking temperature $w\tau >> 1$ and

$$X_r' \longrightarrow X_r \ ;$$

above the blocking temperature $w\tau << 1$ and

$$X_r' \longrightarrow 0$$

which is as it should be. No addition needs to be made to equation 6.14 for X" is negligibly small when $w\tau >> 1$. The final equations are:

$$X'(T) = \frac{\mu_o M_s^2}{3K_u} \left[\frac{w^2\tau^2}{1 + w^2\tau^2} \right]^2 + \frac{\mu_o V M_s^2}{3kT} \left[\frac{1}{1 + w^2\tau^2} \right] \tag{6.19}$$

and

$$X''(T) = \frac{\mu_o V M_s^2}{3kT} \left[\frac{w\tau}{1 + w^2\tau^2} \right] , \tag{6.20}$$

where

$$K_u(T) = 5.2 \times 10^5 \left[\frac{M_s(T)}{M_s(0)} \right]^2 \tag{6.17}$$

and

$$\tau = 2.8 \times 10^{-10} \exp \left[\frac{K_u V}{kT} \right] . \tag{2.15}$$

The graphs in figures 73, 74 and 75 show the results of calculations for grains with volumes equal to spheres of radii 1 nm, 3 nm and 10 nm. The graphs show a number of features that are observed in practice even though real samples contain a distribution of grain sizes.

In figures 73 and 74 the blocking temperature is not close to Curie temperature. It can be seen that X' tails off only gradually as the Curie temperature is approached. This is also seen on figures 70a and 71a. Figures 73 and 74 show that X" exhibits a strong peak at the blocking temperature and is small elsewhere. This is also observed in figure 71b. Figure 70b exhibits broader peaks; this may be because it contains a larger range of grain sizes or because its blocking temperature is further from the Curie temperature, it may be a combination of both reasons. In figure 75 the blocking temperature is close to the Curie temperature, the behaviour of X' and X" is very similar to that shown in figures 69a and 69b.

The model shows that X" tends to underestimate the Curie point of single domain materials. Petersen[19] appears to believe that the decrease in losses on the high temperature side of their peak can be used to measure the Curie point. This is true, but the model suggests that X' is better sustained than X" up to the Curie point; X' is likely to be the more accurate indicator. Markert et al[18] seem to believe that the peak in X" corresponds to the Curie point. This is wrong, the peak in X" corresponds to the blocking temperature, or the average blocking temperature for a real sample. Where samples are multidomain the peak and the succeeding decrease in X" are very close to the Curie point. Even then, it is no easier to measure the Curie point using X" than it is using X'. In summary, there are only disadvantages in using X" rather than X' to measure Curie temperatures. This conclusion is contrary to the beliefs of Petersen[19] and Markert et al[18].

Figure 73. The calculated susceptibility as a function of temperature for a uniaxial carbonyl iron grain with a volume equal to that of a sphere of radius 1 nm.

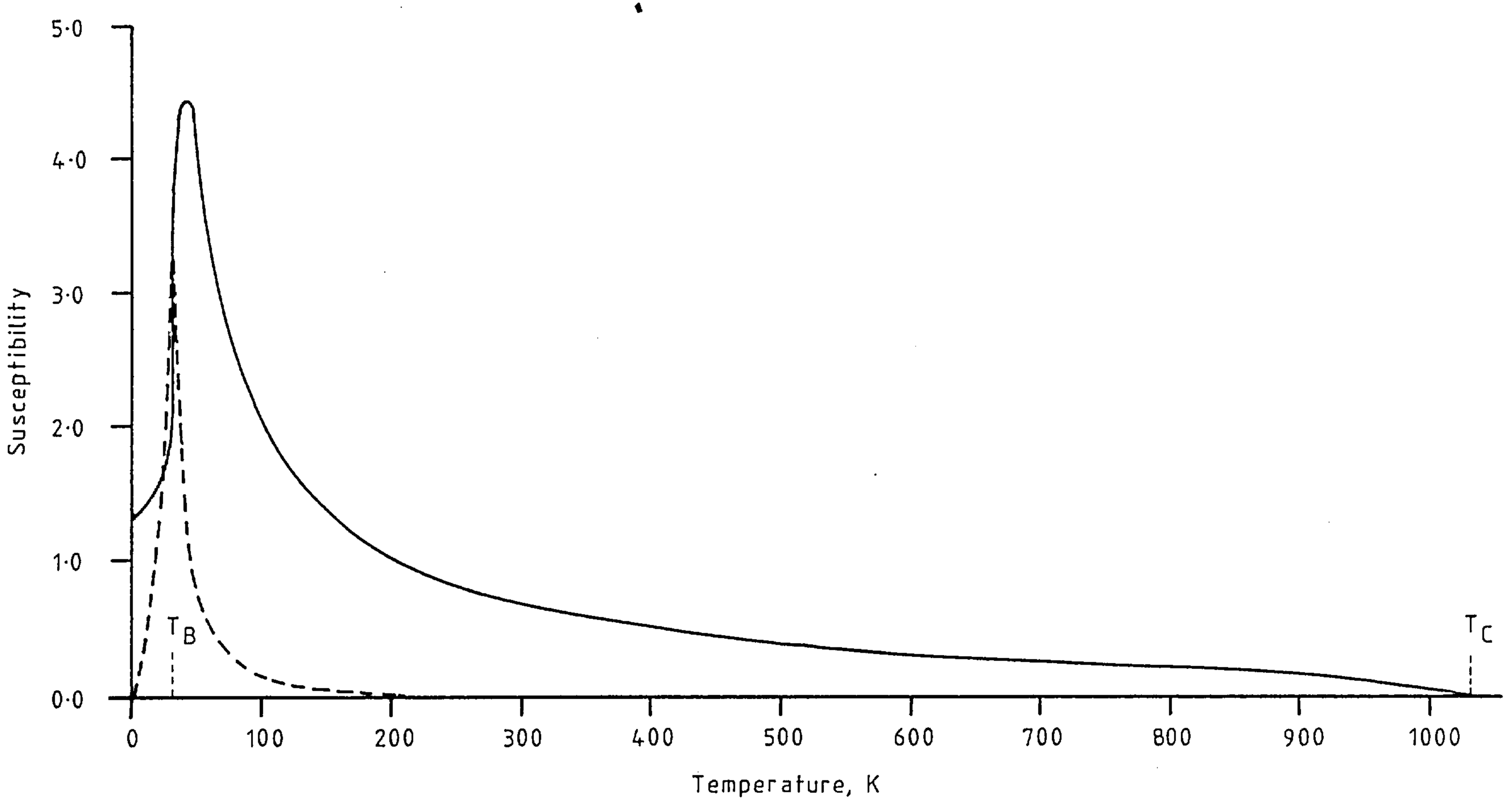

Figure 74. The calculated susceptibility as a function of temperature for a uniaxial carbonyl iron grain with a volume equal to that of a sphere of radius 3 nm.

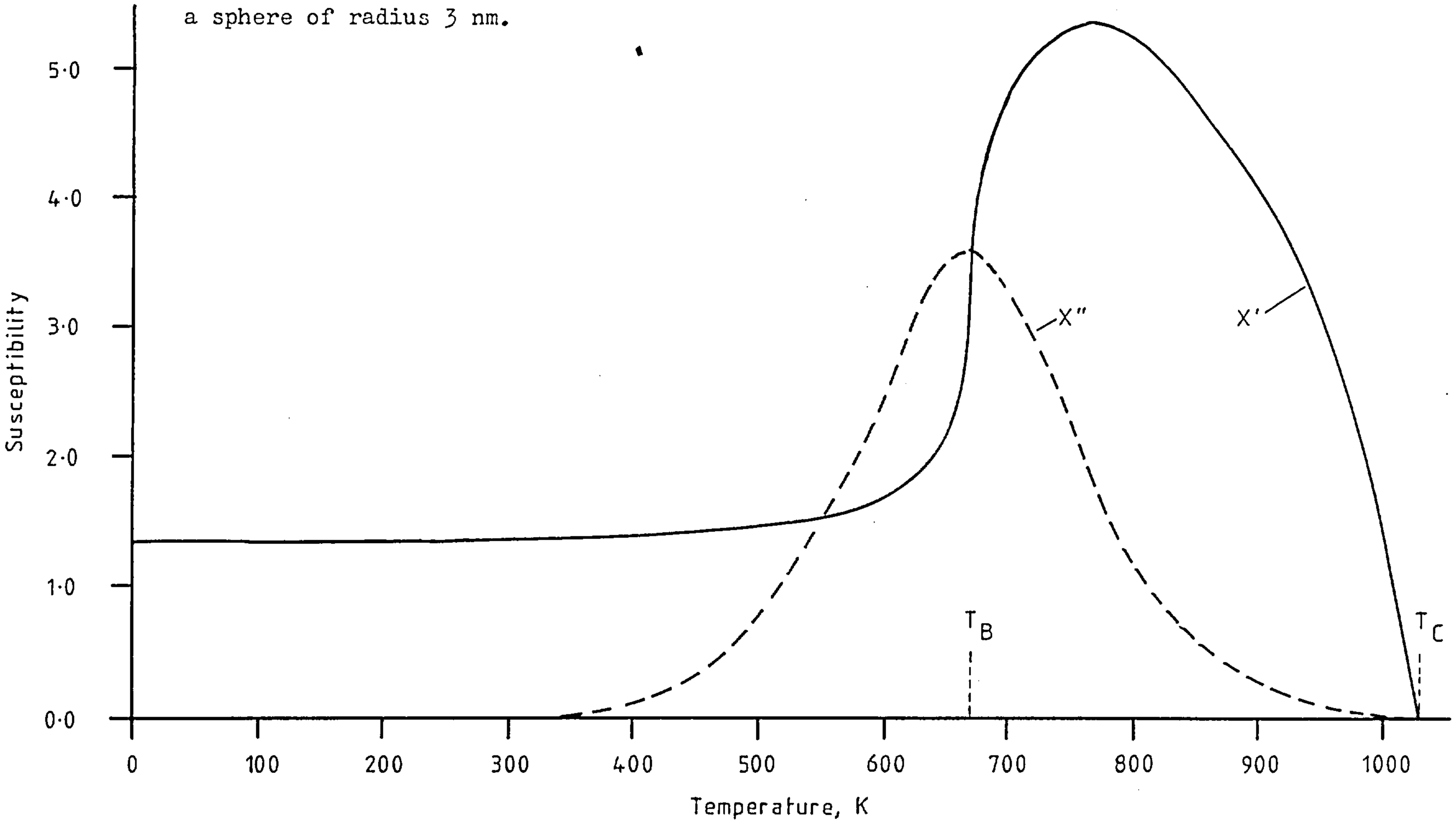

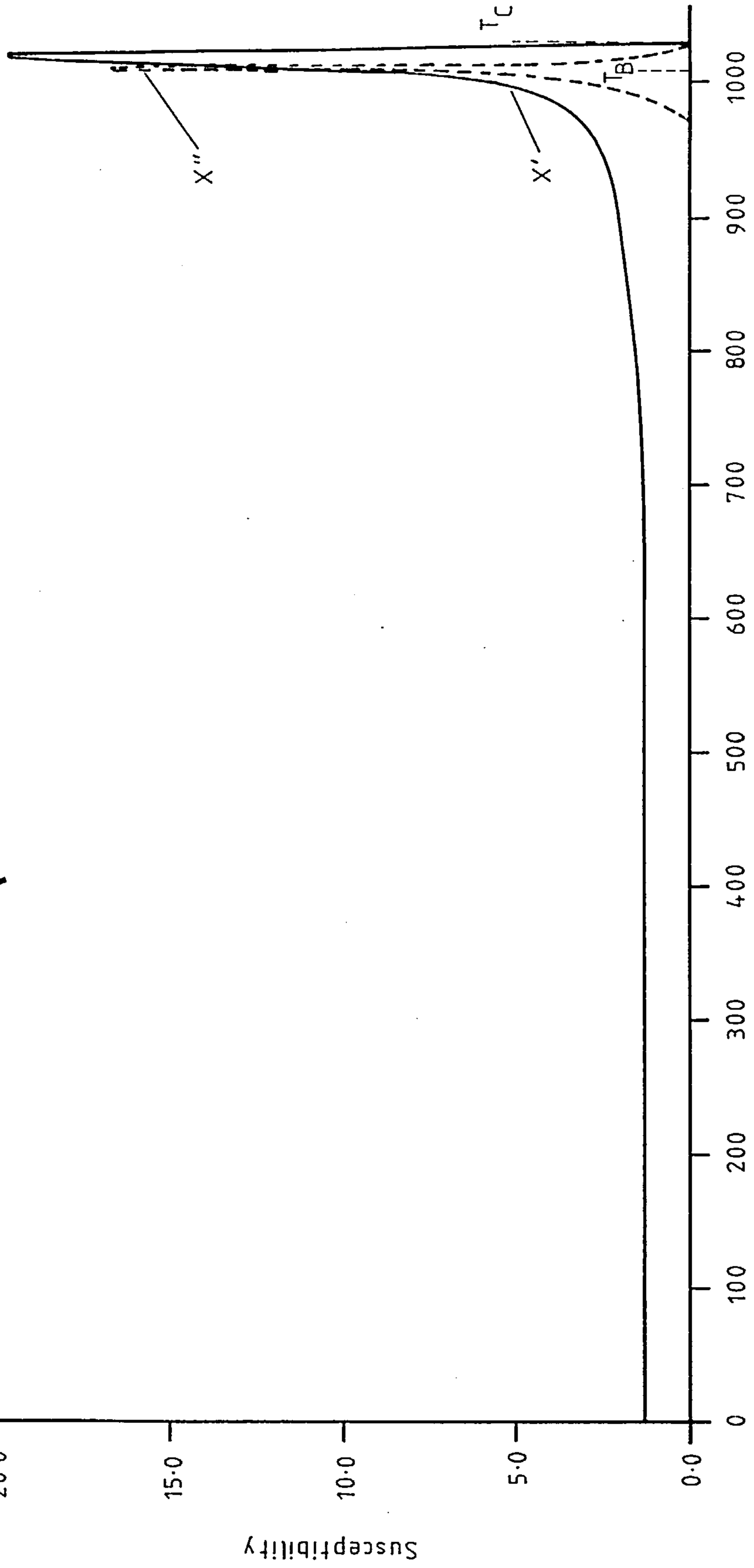

Figure 75. The calculated susceptibility as a function of temperature for a uniaxial carbonyl iron grain with a volume equal to that of a sphere of radius 10 nm.

The model that has been developed is realistic because it allows X' and X" to vary continuously as a grain passes through its blocking temperature; Stephenson's model predicts a discontinuous jump at the blocking temperature. One way in which the new model differs from the measurements is that it predicts that X" should peak before X', neither figure 70 nor figure 71 support this. It would be interesting to apply the model to a sample with a distribution of grain sizes. Stephenson's paper[13] on the distribution of single domain iron grains in lunar dust contains a good example to experiment with. Stephenson found that lunar dust from the Apollo 11 mission had a susceptibility that was constant to within $\pm$ 10% from -196°C to 400°C. He deduced that the iron grains had volumes V ranging from $<1.1 \times 10^{-25} m^3$ to $>1.3 \times 10^{-23} m^3$ with a distribution $n(V) \propto V^{-2}$. Starting with these deductions, a computer could be programmed to find out whether the model predicted a fairly constant X' between -196°C and 400°C.

6.3 APPLICATIONS

The purpose of this subsection is to mention the applications of the new instrument and to show how versatile it is. The instrument has a number of good features: it is very sensitive to X', it separates X' and X" and yields voltages linearly proportional to each, it applies an alternating field so it is unaffected by any natural remanent magnetization in the sample, it measures the true initial susceptibility because it applies an extremely low field, it is easily screened from electromagnetic interference because its operating frequency is 5MHz, it requires no special mounting to shield it from mechanical vibration, it has no moving parts, it is compact and its performance can still be substantially improved. The subsection is broken into two halves. The first half concentrates on the applications of the instrument in its present form. The second half describes applications requiring small changes to the

arrangement of the sample coil and capacitor, these applications have not been tried.

6.3.1 Applications that require no modifications

6.3.1.1 The volume fraction V_f

The susceptibility of many rocks is due almost entirely to the ferrimagnetic minerals they contain. Knowing a sample's susceptibility and the mineral type it is possible, with a restriction, to estimate the amount of the mineral that is contained in the sample. As the susceptibility is determined not only by the mineral type, but also by the grain size, grain shape and internal stresses the method is restricted to use within a particular group of rocks where these extra factors are likely to be similar. The apparent susceptibility of the rock sample is:

$$X_a' = V_f \left[\frac{X_i'}{1 + NXi'} \right] \qquad (6.2)$$

where X_a' is the volume susceptibility and the volume fraction V_f is

$$V_f = \frac{\text{volume of ferrimagnetic mineral}}{\text{volume of the rock sample}} \qquad (6.22)$$

Equation 6.21 is only true when $V_f << 1$ which it is in most cases. Even if X_i' is not known, the variations of V_f amongst a group of rocks can be found.

6.3.1.2 The Koenigsberger ratio Q_n

A convenient definition of the Koenigsberger ratio is[2]

$$Q_n = \frac{\mu_o M_{n.r.m.}}{X' B_e} \quad , \qquad (6.23)$$

where $M_{n.r.m.}$ is the natural remanent magnetization acquired in the earth's field B_e and X' is the volume susceptibility. It is most applicable to igneous rocks where it gives the ratio of a rock's permanent magnetization to the magnetization induced in it by the earth's field. The instrument's

contribution lies in accurately measuring X'. Collinson[2] discusses the use of Q_n as an indicator of the stability of n.r.m. Q_n is of most utility in the interpretation of geometric field intensity variations where it measures the relative contributions of induced and remanent magnetization in the underlying rocks. Parasnis[9,13] mentions Q_n in this context and tabulates a number of examples.

6.3.1.3 Finding the average resistivity or the average size of weakly magnetic, electrically conducting grains

When a sample is only weakly magnetic and yet is a reasonably good conductor, induced eddy currents are the dominant source of power loss. This fact is exploited in El-Hanary's technique[58] for finding the average grain size of metallic powders if the metal's resistivity is known. Conversely, if the grain size of the powder is known the resistivity of the metal can be found. By heating the samples the temperature dependence of resistivity can be found too.

The technique involves mixing the metallic, or perhaps semi-conducting, powder with an inert powder such as LiF to prevent the electrically conducting grains clogging together. The mixture is inserted into the sample coil and the reduction in quality factor is measured. One obvious restriction is that the skin depth in the conducting grain has to be larger than the radius of the grain. If the restriction is observed the change $\Delta(1/Q)$, where

$$\Delta(1/Q) = \frac{1}{Q_{sample}} - \frac{1}{Q_{original}} , \qquad (6.24)$$

is given by [58]

$$\Delta(1/Q) \approx 0.2 \left[\frac{V}{V_c}\right] \left[1 + 0.45\frac{b}{D} + \left[\frac{b}{D}\right]^2\right]^{-1} x \left[\frac{a}{S}\right]^2 \left[1 - \frac{4}{105}\left[\frac{a}{S}\right]^4\right] . \qquad (6.25)$$

V is the total volume of the conducting grains, V_c is the volume of the sample coil, b is the length of the coil, D is the diameter of the coil, a is the average radius of the conducting grains and S is the skin depth given by equation 1.9. The factor (V/V_c) is meant to represent the coil's filling factor F, it would be better to replace this with equation 2.24.

To experiment with this technique an amorphous diamagnetic graphite sphere was made. The idea was to insert it into the sample coil and compare the change in Q predicted by theory with that found in practice. The radius of the sphere was 0.55 mm and its resistivity was taken as $1.4 \times 10^{-5} \Omega$ m[59]. The change $\Delta(1/Q)$ predicted by 6.26 was 4×10^{-5}, the measured change was also 4×10^{-5}. The good agreement has to be treated with caution because of the uncertainty in the true resistivity of amorphous graphite.

6.3.1.4 Identifying magnetic minerals in rocks through their Curie points

Magnetic minerals can be identified through their characteristic Curie points. While the method is not as exact as chemical or X-ray analysis it is nonetheless very useful. Mineral identification through Curie points works best if the samples are sealed in evacuated quartz capsules to prevent oxidation. The method is simple to use. Nagata[40] gives experimental results which show that the Curie temperatures of minerals in the titanomagnetite solid solution series, $xFe_2TiO_4.(1 - x) Fe_3O_4$, vary almost linearly with x from $T_c = 578^oC$ $(x = 0)$ to $T_c = -170^oC$ $(x = 1)$. For the haematite - ilmenite series, $yFeTiO_3.(1 - y) \propto Fe_2O_3$, the Curie temperatures vary almost linearly with y from $T_c = 675^oC$ $(y = 0)$ to $T_c = -205^oC$ $(y = 1)$.

The Curie point of the natural lodestone in figure 68a was $(568 \pm 2)^oC$; this indicates, as expected, that it was almost pure magnetite. The Curie point of the haematite in figure 69a was $(673 \pm 2)^oC$ as it should have been.

6.3.1.5 Using the temperature dependence of susceptibility to uncover the domain structure of magnetic minerals

This has already been discussed at length in sections 6.2.5 and 6.2.6. Once again, it is best if the samples under investigation are enclosed in evacuated quartz containers. X" is of use here because it peaks at the dominant blocking temperature.

6.3.2 Applications that require alterations to the tuned circuit

6.3.2.1 Measuring the temperature dependence of susceptibility from 77K to 300K

There is a considerable amount of interest in measuring susceptibility at low temperatures. Many Curie points occur in the range 77-300K and the shapes of the susceptibility curves harbour information on domain structure. One advantage of working at low temperatures is that rock samples do not undergo chemical changes. Both magnetite and haematite undergo structural phase transitions in this temperature range and these can be located through anomalies in the susceptibility. Creer[60] discusses these transitions whilst Stephenson and de Sa[17] and Markert et al[18] have examples of the low temperature dependence of susceptibility.

The alteration necessary is very easy to carry out and stems from the scheme used by Stephenson and de Sa[17]. At present the axis of the sample coil is horizontal so that the sample holder can be slid slowly into the sample tube until the best signal is obtained. The axis of the sample coil now needs to be vertical and the closed end of the sample tube, see figure 58, has to be brought closer to the sample coil. The sample holder will therefore be slotted into a glass well and the bottom of the well will locate the sample in the central region of the coil where the field is most nearly uniform, see figure 11b.

The sample under investigation would be wrapped in a little ball of cotton wool and pushed to the bottom of a test tube container. When in place in the coil, the sample would be cooled by dropping liquid nitrogen

onto it. After the liquid nitrogen had boiled off, the sample would start to warm and the temperature dependence of susceptibility would be measured. The Refrasil furnace lagging would prevent the sample warming too quickly; if the rate of warming was too slow, a small current could be passed through the furnace. The thermally insulating housing around the sample coil, see figure 59, will protect the coil from cold vapours. The water jacket, the air gap and the Refrasil will prevent the coil cooling by conduction.

With this simple change of orientation the instrument would be easier to use, because the sample would always locate itself properly, and the one arrangement would serve for low temperature, room temperature and high temperature measurements.

6.3.2.2 Measuring anisotropic susceptibility

If the magnetic grains in a rock sample are not randomly oriented but are aligned in some way, then the rock sample will have an anisotropic susceptibility. Natural processes that can cause alignment are lava flows in igneous rocks, stream flow in sediments and geological stresses. The interest in anisotropy therefore lies in the information it contains about the alignment mechanisms.

Anisotropy measurements are usually made on cyclindrical rock samples with height to diameter ratios between 0.85 and 1. A typical diameter is 2.54 cm. For this application, the requirement is to build a large sample coil in which the rock cylinder can be oriented as required. The coil must be large enough to spread a uniform field over the sample. A suitable coil would be 10 cm long by 4 cm wide, this would give no more than 1.1% variation in field strength over the sample. Winding the coil in 1.8 mm wire would result in an inductance of 14 μH. The parallel tuning capacitance therefore needs to be reduced to 70 pF. The filling factor would be improved to 0.06 from its present value of 0.01. Taking this in conjunction with the larger sample volumes it is clear that the range of measurement for X' has to be increased drastically. Fortunately, the

reduction in the value of the tuning capacitors automatically improves this range 12.5 times. It is worth noting that this modification simplifies the measurement of volume susceptibilibity because the volume of a rock core is easily found; it is therefore easier to measure the Koenigsberger ratio and the volume fraction.

6.4 IMPROVEMENTS

Various ways of refining the instrument's performance have already been mentioned in this chapter and in chapter five. For convenience these points are collected together below and some new ideas are added for good measure.

6.4.1 Alterations to the furnace and sample coil

It was suggested in subsection 6.2.3 that the sample coil ought to be wound on a separate glass sleeve concentric with, but mechanically isolated from, the water jacket. This will stop the inductance of the sample coil being altered by the thermal distortion of the water jacket, it will also improve the thermal insulation between the furnace and sample coil. Careful construction should limit the drop in the filling factor to about 30%. Of course, the thermal insulation of the sample coil's compartment and the temperature compensation of the coil by the capacitors are still necessary measures. The purpose of a sleeve that is separate from the water jacket is to isolate the tuned circuit from the furnace, the purpose of the insulation and compensation is to protect the tuned circuit from changes in the ambient air temperature. With regard to temperature compensation, it appears that the temperature coefficient of silver mica capacitors is unpredictable. Polystyrene capacitors have a temperature coefficient that is more predictable but is too large unless they are combined with other capacitors which have a lower temperature coefficient; the use of high quality air dielectric capacitors ought to be considered.

It would be sensible to mount the sample coil, former and water-jacket

such that their axis was vertical and not horizontal. The reasons for this have just been explained in subsection 6.3.2.1.

Eddy current losses in the furnace and thermocouple could be significantly reduced by using thinner wire for each, this would improve the quality factor of the tuned circuit. At present the nichrome wire used in the furnace is 0.122 mm in diameter, this might be decreased to 0.0813 mm diameter. The thermocouple wire is 0.245 mm in diameter, this could be shrunk to 0.1 mm.

6.4.2 General electrical improvements

All of the circuitry should be mounted on double sided copper printed circuit boards. One side of the printed circuit board should be used as the earth plane, the other should be used for connections between components. Holes should be drilled in the circuit board such that the components can be mounted on the earth plane side. To prevent the components' leads shorting to the earth plane, a small area of copper should be removed from around the holes on the earth plane side of the board; this is simple to do using a drill with a countersinking tool. The earth plane should be cleared away from any trimmer capacitors belonging to the tuned circuit.

The crystal oscillator with its amplifier and audio modulator should be mounted in a screened compartment adjoining the tuned circuit compartment. The oscillator and modulator should have their own regulated and filtered power supply. The radio frequency phase detector should also be mounted in its own screened compartment and should have its own regulated power supply.

The unregulated power lines to the radio frequency portions of the instrument should be passed between compartments using feedthrough capacitors. The precautions described in chapter 5 concerning decoupling and grounding should be observed.

6.4.3 A lower noise, self correcting phase detector

Examples of what is believed to be popcorn noise from the 5MHz phase detector have been shown in figures 64 and 65. Subsection 6.2.6 mentioned that one of the most likely sources of the popcorn noise is the pair of 74LS136 exclusive - OR gates. Replacing these and the 2.2 KΩ collector resistors with a pin compatible high speed CMOS 74HC86 should substantially reduce the problem. The 74HC86 is a quad exclusive - OR gate. It was never intended for low noise analogue circuitry, but its output will limit at the 0V and 5V supply lines. If the 5V supply line is carefully filtered and is separate from the supply to the rest of the digital circuitry, then the amplitude noise from the modified phase detector should be considerably less than that from the original phase detector.

The phase loop can have positive or negative gain depending on the initial states of the flip flops in the phase detector, see figure 49. If the gain should be positive it has to be manually corrected by using a de-bounced switch to reset the flip flops. An automatic correction circuit has recently been devised, it is illustrated in figure 76. When the loop gain is positive the phase loop feedback signal is driven into saturation at $\pm$ 13V. When the absolute value of the feedback signal is > 12V the output of the comparator goes high to +5V. This turns the l.e.d. "in lock" indicator off and causes the output of a TTL monostable circuit to go from +5V to 0V. This disables the dividers for a period determined by the monostable delay. During this period the loop error voltage will settle to zero and the input to the monostable will return to the low state. When the output of the monostable switches to its normal state of +5V the flip flops are enabled and there is a 50% chance of the loop locking. The mechanism continues to act until the loop successfully locks. Experience with the de-bounced switch has shown that two or three attempts always suffice, the automatic correction circuit should

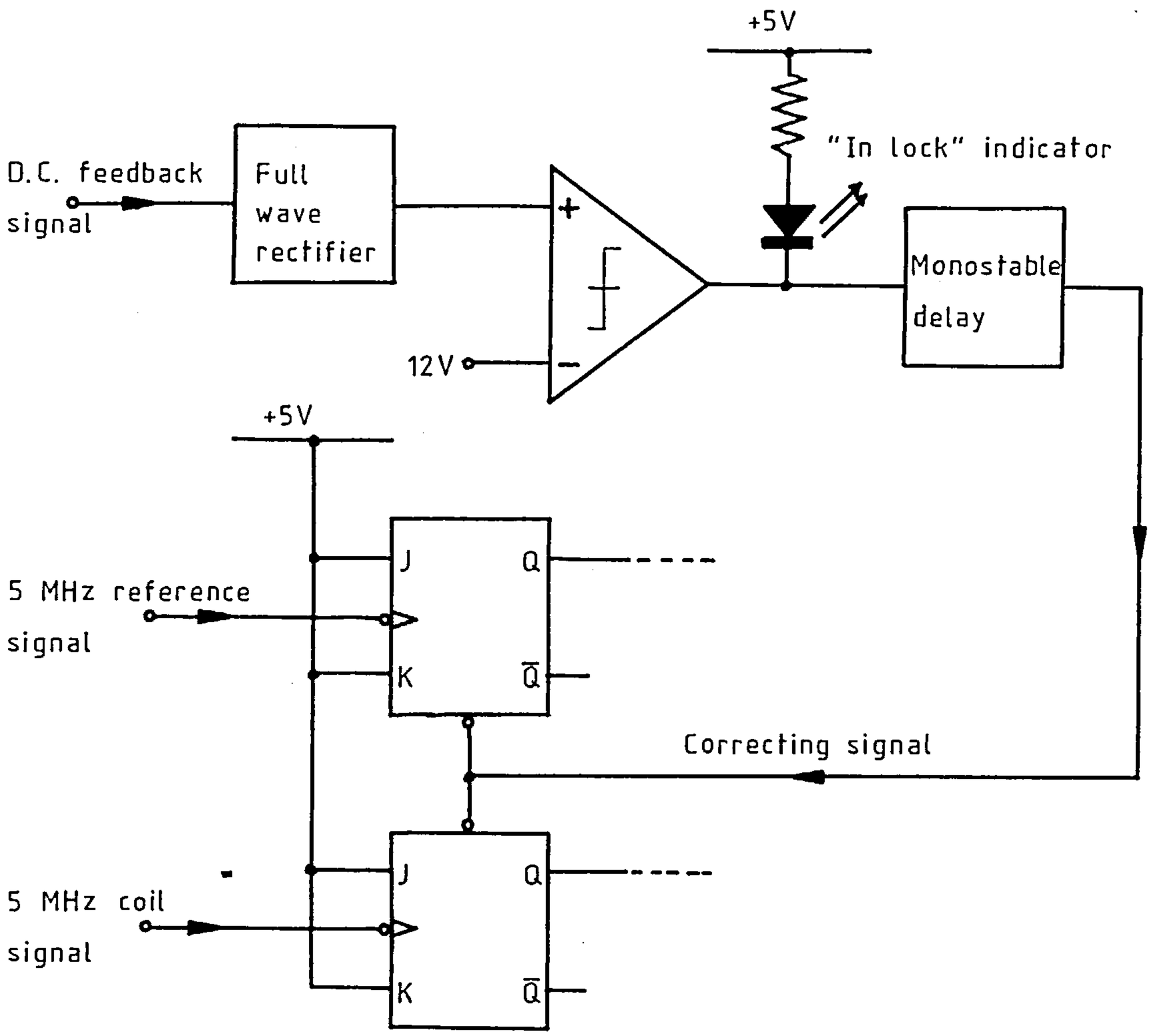

Figure 76. An untried automatic correction circuit for the 5 MHz phase detector.

therefore achieve lock within one second.

6.4.4 Improvements to the analogue radio frequency circuits

A linear active detector for r.f. demodulation is shown in figure 77a. The circuit's advantages are that it is a good linear detector for small changes in a strong signal and it has a high input impedance. If the circuit is designed correctly, transistor T_2 is turned off by a positive voltage that is small compared to the amplitude of the signal V_{in}. When T_2 is turned off the circuit acts as a linear half wave detector and the current through R_2 increases as V_{in}/R_1. The detector's characteristic is shown in figure 77b, the noise performance is discussed by Robinson(46,200).

The r.f. amplifier and demodulator shown in figure 78 was designed by Robinson(29). The optimum source resistance for the lowest noise is about 6KΩ; the 6KΩ impedance presented by the tuned circuit is therefore ideal and the amplifier can be expected to have a noise factor of somewhat less than 1.3. The amplifier's gain is 20. The signal across the tuned circuit should be between 50 and 100 mV p.p.

The circuit of an improved limiting amplifier is shown in figure 7. The output of the amplifier has been designed to drive a TTL logic gate, the maximum swing is $\pm$ 1.1V about a quiescent level of 1.4V. It comes much closer to the ideal symmetric limiter than the predecessor described in subsection 5.3.3. The transistor Q_A can never enter saturation so there is no delay due to charge storage in Q_A's collector. The emitter degeneration resistors improve the amplifier's linearity. The transistors on the Plessey SL 3145C array have f_T's of 2.5GHz, this is a considerable improvement on the RCA 3045 array. The limiter's gain is 5.5, it is likely that an extra amplifier between the tuned circuit amplifiers and the limiter will be needed.

The Plessey SL1680C is a very convenient crystal oscillator maintaining circuit, but the amplitude noise and harmonic distortion in its output

Figure 77. An improved amplitude demodulator.

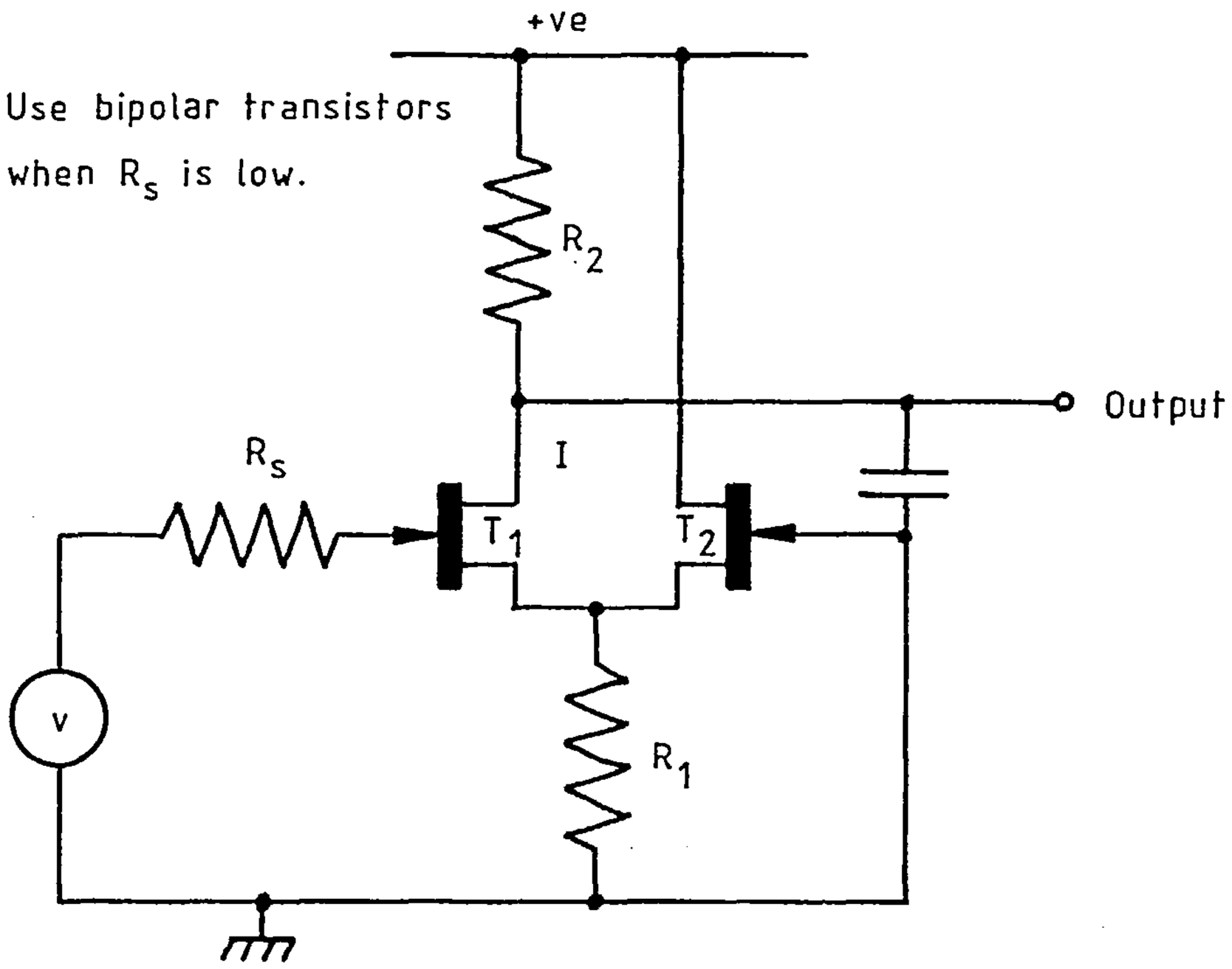

a. The circuit

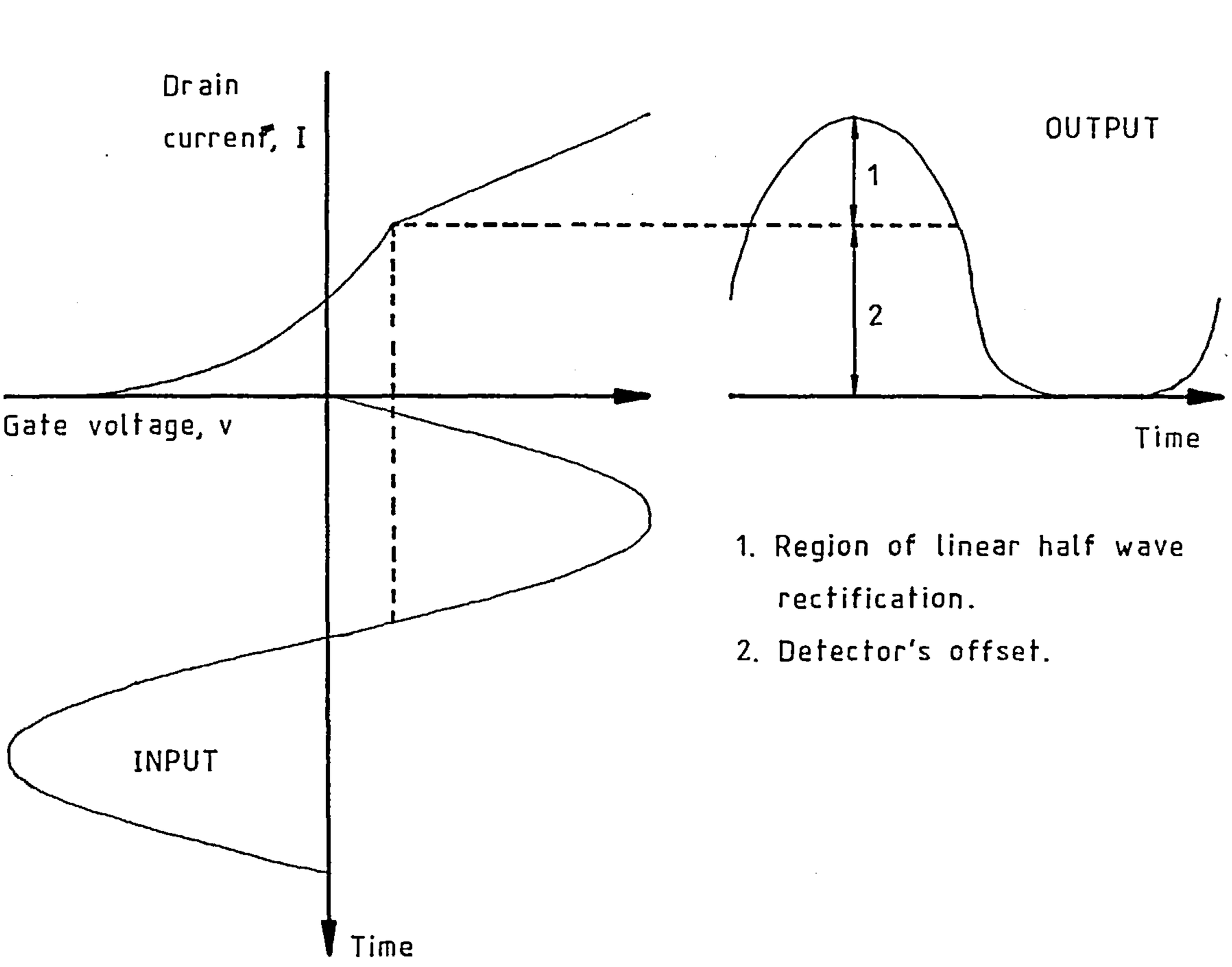

1. Region of linear half wave rectification.
2. Detector's offset.

b. The characteristic

Figure 78. An improved tuned circuit amplifier with an amplitude demodulator. This circuit is described by Robinson[29].

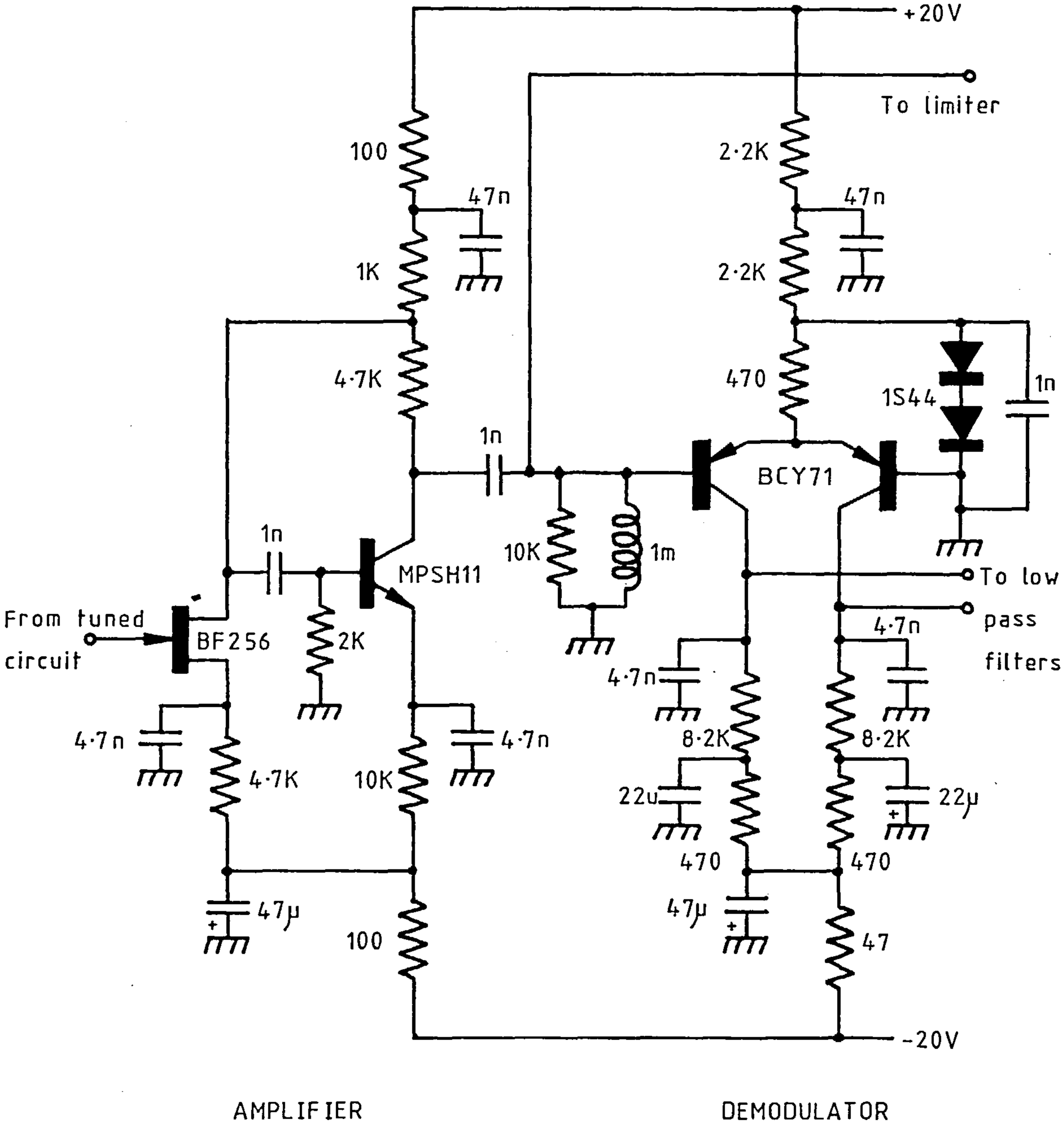

AMPLIFIER DEMODULATOR

Figure 79. An untried design for an improved limiting amplifier.

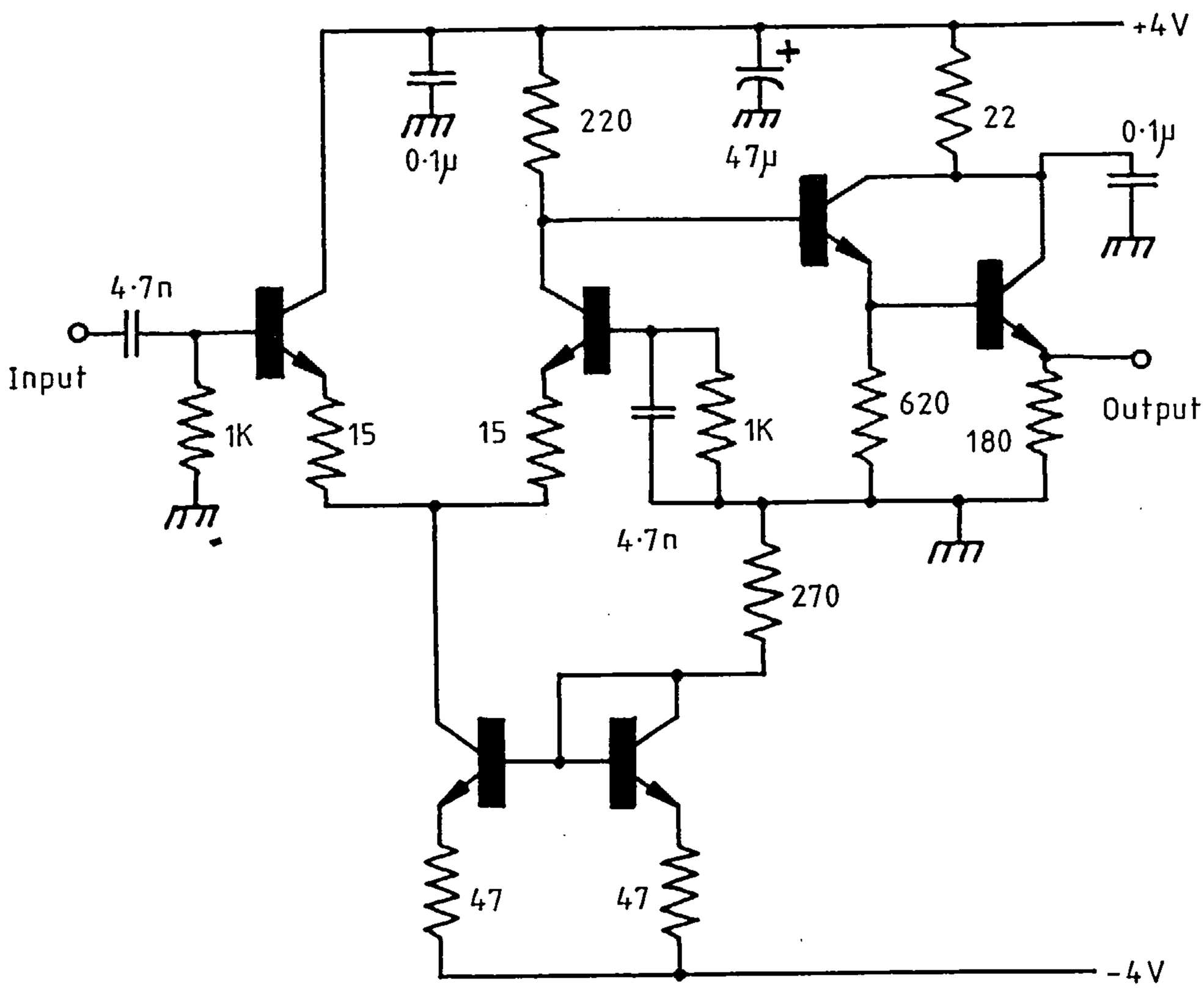

Transistors on two SL3145C arrays.

are too high. The harmonic distortion can be removed by incorporating a tuned amplifier into the circuit shown in figure 41. The effects of the amplitude noise and drift can be removed by closing an amplitude control loop around the r.f. amplifier. If the control loop is carefully designed, the low frequency amplitude noise can be reduced almost to that of an external voltage reference. The control loop also makes a convenient point to introduce amplitude modulation for subsequent phase sensitive rectification.

6.5 CONCLUSION OF CHAPTERS 1 TO 6

Chapters 1-6 have described the evolution of a brand new means of measuring susceptibility. Operating at 5 MHz the instrument separates and measures both the real and the imaginary parts of a sample's initial magnetic susceptibility. The instrument is sensitive and versatile. Most of the experiments so far made with it have been concerned with the temperature dependence of susceptibility between room temperature and 800°C.

Chapter 1 assembled the information needed to understand how the initial susceptibility is affected by sample size and shape and by the frequency of the applied magnetic field. The chapter commenced by defining the system of magnetic units used throughout this thesis, this was necessary because there are three systems in common use. Calculations of the skin depth in various materials were used to show that 5MHz is a reasonable operating frequency if samples are restricted to those consisting of fine ferromagnetic grains in an inert matrix; rock samples fall into this category. It was shown that magnetic grains have internal demagnetising factors which create an apparent susceptibility X_a that is always less than the intrinsic susceptibility X_i. It was also explained that the grains could be multidomain, single domain or superparamagnetic depending on the constituent material, the temperature, the grain size and

the frequency of the applied field. At radio frequencies, magnetic power losses in the sample become significant and cause the susceptibility to split into real and imaginary components. Three sources of power loss were considered: the hysterysis loss, the eddy current loss and the lattice loss. These losses were estimated for an array of carbonyl iron grains and it was seen that the lattice loss was most important, although the grains are very good electrical conductors the eddy current loss was only second in importance. It seems to be generally assumed that either hysterysis or eddy current losses dominate. The magnetic relaxation time that underlies the lattice loss was discussed in some detail. The time constant used to decide whether single domain particles are superparamagnetic or not was identified as an example of a magnetic relaxation time. Finally, a result was produced to account for the effect of the demagnetizing factor on the real and imaginary susceptibility.

Having discussed susceptibility from the sample's point of view, chapter 2 focussed attention on how the susceptibility might be sensed. A simple air cored coil was chosen both to apply the field and to measure the sample's response. It was shown that the real part of the susceptibility increased the inductance of the coil and the imaginary susceptibility increased the resistance of the coil. A very useful expression for the coil's magnetic filling factor was derived, the derivation has not been seen elsewhere and the result does not seem to be widely known. Two existing instruments were introduced as a yardstick to judge the new instrument by. One was a 1.5KHz[17] bridge measuring the real susceptibility alone whilst the other, a series of 10 MHz inductively coupled tuned circuits[18], measured both the real and imaginary susceptibilities. Results from the 10 MHz instrument indicated that the imaginary susceptibility was a potent tool for identifying Curie points. When searching for an improved approach to measuring the real and imaginary susceptibility, work on nuclear

magnetic resonance was examined and found to be promising. The popular Robinson oscillator was rejected in favour of the unpopular Q-meter; the Q-meter had a lot of room for development and an elegant potential for separating the real and imaginary susceptibilities. The principle of a new instrument was then described and the choice of a 5MHz operating frequency was explained.

Chapter 3 described the first working version of the instrument which consisted of two feedback loops acting on a driven tuned circuit. The sample was placed in an air cored coil which formed the inductance of the tuned circuit. One of the feedback loops used a voltage controlled capacitance to keep the natural frequency of the tuned circuit fixed, this loop's feedback voltage was a signal for the real susceptibility. The other feedback loop used a voltage controlled Q-multiplier to keep the signal amplitude across the tuned circuit constant, this feedback voltage was a signal for the imaginary susceptibility. The voltage controlled Q-multiplier was shown to be equivalent to a voltage controlled negative resistance. A theory of operation was developed for both loops. Calibration showed that the theory was correct and that the linearity was within the error of measurement. Plots of the temperature dependence of the real susceptibility were shown for magnetite and haematite. The performance of this version was as good as the 1.5 KHz bridge and 10 times better than the 10 MHz instrument. Finally, a study of noise sources was carried out with the object of improving the new instrument's design. A research paper on some of this work was published in J. Phys. E: Sci. Instrum. [33]; a paper on it was presented at the 1981 United Kingdom Geophysical Assembly.

Chapter 4 described the system design for an improved instrument. The theory of phase locked loops was drawn upon to decide that the loop

controlling the tuned circuit's natural frequency ought to be first order. The amplitude loop was dispensed with. The amplitude of the signal across the tuned circuit was to be measured by phase sensitive rectification following audio frequency amplitude modulation at the crystal oscillator, the theory and advantages of this method were discussed. Using the result for the coil's filling factor and the conclusions of the noise analysis, optimum sample coil dimensions were derived. Drift within the phase loop was discussed and the sample coil was pinpointed as the major source. The temperature coefficient of the sample coil's inductance was calculated and a method of compensation was explained. A novel type of multiplying phase detector was described. The output of the detector is 0 volts for 0^{o} phase difference, whereas for other multiplying detectors the output is 0 volts at 90^{o} phase difference. This characteristic is very desirable and means that the detector should find use in many other applications.

After the system design, chapter 5 presented the electronic circuit design. The complete set of circuit diagrams and explanations will allow the instrument to be reproduced by other interested workers. The linearity of the remaining feedback loop was considerably improved. The construction and performance of the furnace was described in detail. Finally, the initial adjustments to the completed instrument were listed and some photographs of it were displayed.

Results for the final version were presented in chapter 6. The performance with respect to the real susceptibility was considerably improved: random noise was reduced 11 fold and drift was reduced by a factor of 48. The improvement in performance with respect to the imaginary susceptibility was disappointing, there was a 33% reduction in random noise and the drift was unchanged. The blame for the small improvement was allotted to amplitude noise in the crystal oscillator. The results of the calibration tied up with theory once more. Some very interesting plots of the temperature

dependences of the real and imaginary susceptibility were shown for magnetite, haematite and two other samples. The shapes of these plots were discussed and related to the samples' internal magnetic domain structures. Stephenson's[6] account of the temperature dependence of the low frequency susceptibility of an array of uniaxial single domain grains was extended by including the effects of the temperature dependent magnetic relaxation time. These new equations give a continuous transition from rotational to superparamagnetic behaviour, Stephenson[6] predicts a step transition. The equations naturally account for the temperature dependence of the imaginary susceptibility. They indicate that the imaginary susceptibility should peak at the blocking temperature; they also indicate that the imaginary susceptibility is not a good marker for Curie points and this is contrary to the impression given by Markert et al[18] and by Petersen[19]. The temperature dependence of an array of single domain carbonyl iron grains was calculated. The results were similar to what had been observed for samples which were believed to have predominantly single domain grains. A number of applications were discussed, some of these have not been tried but they require nothing more than a simple modification to the sample coil and parallel capacitance. As it stands, the instrument will measure Curie points in the range 20°C to 800°C for mineral identification, it will yield information on blocking temperatures and domain structures, it will determine the volume fraction of the ferromagnetic mineral in a sample, it can help determine the Koenigsberger ratio and it can find the resistivity or the size of the grains in weakly magnetic samples. It was shown that it is possible to measure Curie points from -200°C to 800°C merely by turning the sample coil upright. If the sample coil is enlarged, then it is possible to measure anisotropic susceptibilities. Lastly, a number of ways of significantly reducing noise and drift and some useful modifications to the phase detector were described.

PART 2

A NEW INSTRUMENT FOR NON-CONTACT MAGNETIC SENSING OF DISPLACEMENT.

CHAPTER 7

THE MEASUREMENT PRINCIPLE, SOME BACKGROUND INFORMATION AND THE CHOICE OF MAGNET AND MAGNETOMETER.

7.1 INTRODUCTION

This new instrument for non-contact sensing of displacement exploits the fact that the field from a permanent magnet varies with distance. In principle, if the total moment of the magnet is known, and if the field from the magnet is measured using a magnetometer, then the displacement between the magnet and magnetometer can be calculated. This principle is not new, but it has never been popular because of the non-linearity of the field/displacement characteristic. Analogue function circuits, for instance the National Semiconductor LH0094, are not suited to low frequency (<10Hz) linearisation because they are noisy and drift prone. Digital linearisation has been prohibitively expensive in the past. On top of this, magnetic materials with a very strong magnetization, for an adequate signal to noise ratio combined with reasonable magnet volume, have often lacked the stability necessary for use in adverse environments.

The problem of non-linearity has previously been tackled using special magnet configurations which manage to produce linear field/displacement characteristics over a few millimetres or so. The magnetometer's sensor has to be attached to the object whose displacement is to be measured. This is a clumsy arrangement because the fixed magnets restrict access to the moving object, also because the object is shackled by the wires necessary to the magnetometer's sensor and finally because the range of useful operation is so limited. Wieder[64,99] describes an unusually good magnetostatic quadrupole which generated an almost linear field gradient over a distance of 80 mm. More typically, other arrangements described by the same

author can be used to measure displacement over a ± 2 mm range to an accuracy of 1.5%.

The current availability of strong and stable magnetic materials, sensitive magnetometers and low cost microcomputers injects a new life into this technique. The instrument to be described makes accurate and continuous non-contact measurements of displacement along a single axis. In this arrangement, the magnetometer is fixed and a small permanent magnet is attached to the moving object. As can be seen from figure 80, it is the nature of the link to the moving object that gives each type of displacement transducer a set of unique properties. The only link in this case is a magnetic field. The only force on the moving object is that needed to accelerate a magnet weighing about 3 grammes. DC magnetic fields pass unattenuated through many solid materials, for instance: brass, lead, copper, silver, aluminium, glass, plastic, water, wood, flesh and many others. Furthermore, the accuracy is immune to oil, grease, dirt, smoke and many other environmental pollutants. The frequency response is limited only by the magnetometer or by the skin depth of the material between the magnet and magnetometer. No other technique can lay claim to all these attributes.

At the moment, the accuracy is better than 2% of full scale deflection (FSD) over the entire useful range of 250 mm and better than 0.1% FSD for displacements less than 110 mm. A research paper on the instrument has been published in the Journal of Physics E: Scientific Instruments [65].

The design and development of the hardware and software are described in chapters 8 and 9. The resulting instrument will work with any choice of magnet and magnetometer. Chapter 10 discusses the performance of the instrument together with some improvements. The remainder of this chapter first puts the new technique in context by

Figure 80. The basic sections of a displacement transducer.

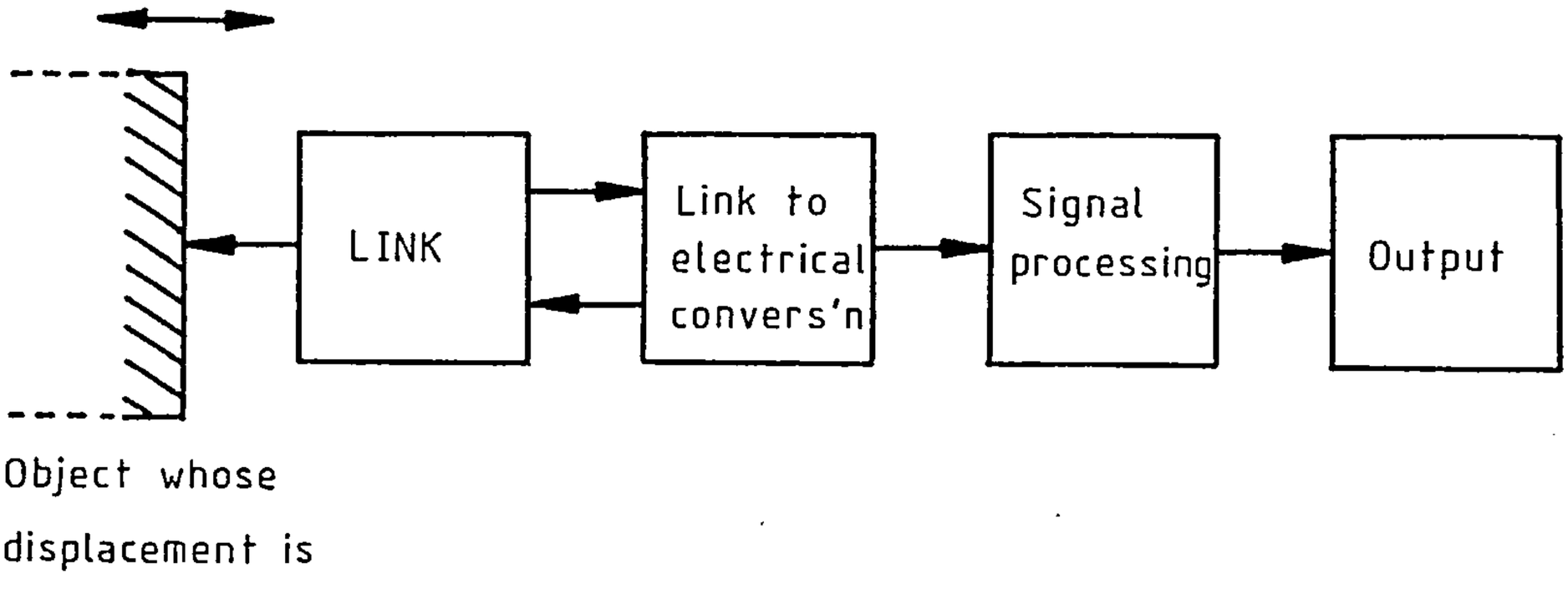

Figure 81. Demagnetization and energy product curves of a permanent magnet. A minor hysterysis loop associated with magnet stabilisation is also illustrated.

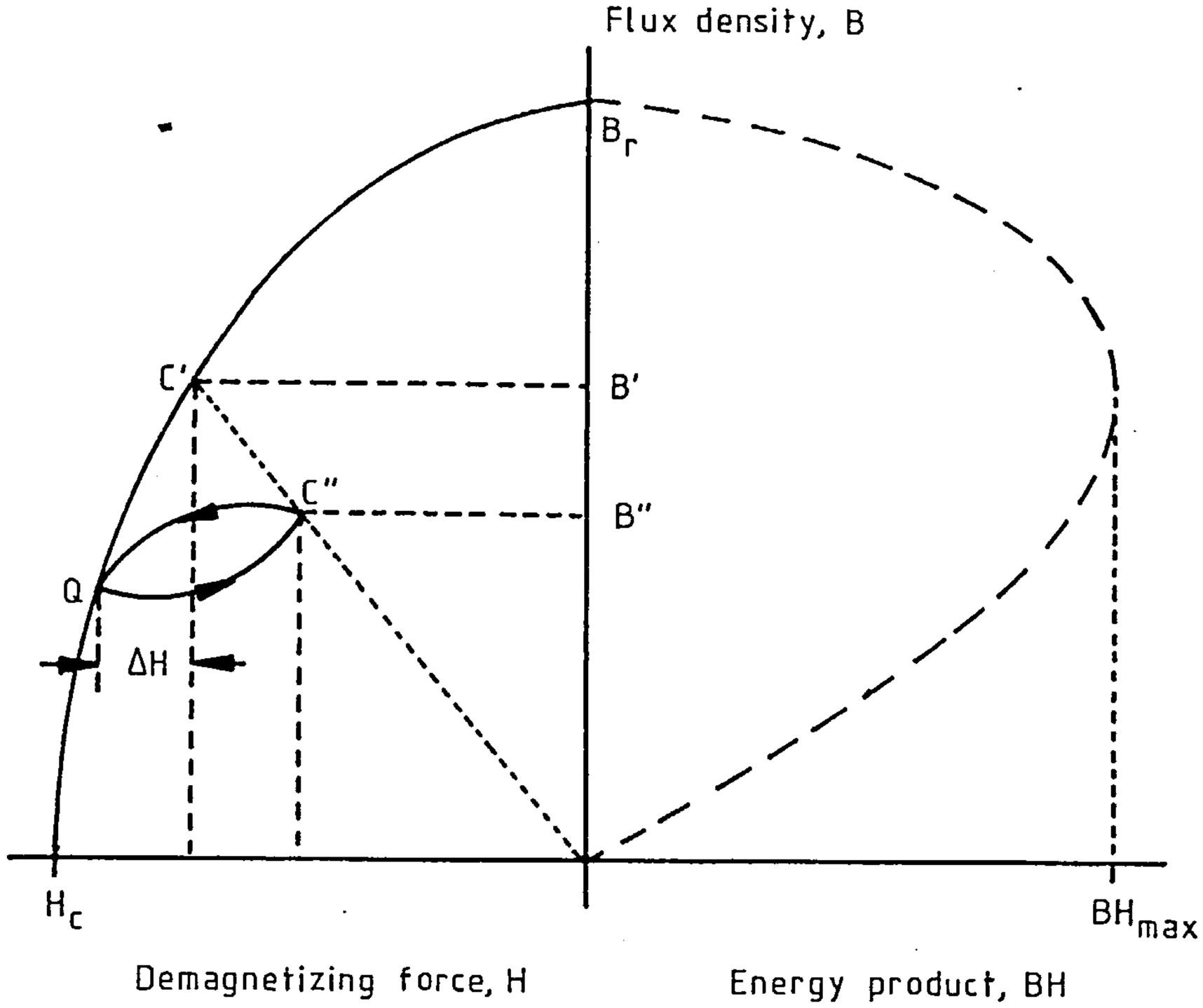

mentioning other methods of non-contact sensing of displacement. It then discusses the factors affecting the choice of magnet and magnetometer.

7.2 OTHER METHODS FOR NON-CONTACT SENSING OF DISPLACEMENT

This section mentions some of the better known methods of non-contact sensing of displacement. These methods fit into the broad categories of inductive, capacitive, ultrasonic and optical. A review by Garratt[66] and a readable book by Sydenham[67] give more details and an extensive list of references. A review by Hugill[68] is also useful.

Non-contact inductive transducers can be subdivided into variable reluctance, variable mutual inductance and variable Q types. They all require a.c. excitation: driving amplitudes between 2 and 15 V r.m.s. at frequencies between 1 and 10 KHz are common. The variable mutual inductance type is known as a linear variable displacement transformer (LVDT). It consists of a solenoid tapped half way along its length within which moves a ferromagnetic core. The centre-tapped solenoid is often excited by a separate primary coil. As the core moves relative to the winding the alternating flux cutting each half of the solenoid varies, this creates an imbalance in the amplitude of the induced voltages from the two halves. The amount of imbalance is linearly related to the core's displacement from the coil's centre. For a non-contact LVDT, the core is attached to the moving object. The core is free to move along the axis of the coil, but the coil itself prevents any motion perpendicular to the axis. Typically, this type of LVDT has a range of 50 mm with a resolution of 2 μm and a frequency response of 500 Hz. The linearity is often better than 0.5% FSD and the temperature coefficient is about 0.005% FSD$^{o}C^{-1}$. A small LVDT with a range of 0.2 mm could have a resolution

of about 5 nm.

Non-contact variable reluctance transducers come in two types. The first type uses a pair of electrically separate coils that are physically joined end to end as a differential pair. Once again, a ferromagnetic plunger is attached to the object whose displacement is to be found. As the plunger moves within the excited coils the flux paths change and so the coils' inductances alter. This is known as a variable leakage path (VLP) sensor and its performance is similar to that of the LVDT. The second type is the non-contact reluctance transducer which allows a displacement to alter a short air gap in an otherwise high permeability circuit. The air gap is between a ferromagnetic plate attached to the moving object and a fixed coil wound on a ferromagnetic pot core. As the air gap between the pot core and the plate alters the inductance of the coil varies non-linearly. This transducer typically has a 5 mm range with a 5% of FSD linearity if a separate linearisation circuit is used. The temperature stability is about 0.2% FSD $^{o}C^{-1}$. An electrical system incorporating it would have a frequency response of about 500 Hz and a resolution of 2μm.

After part 1 of this thesis, the principle of the variable Q inductive transducer should be readily appreciated! The moving object should have a highly conducting surface, or have one attached to it. Magnetic flux lines passing from a fixed sensing coil into the moving surface induce eddy currents which reduce the Q of the coil. The Q of the coil is a non-linear function of the coil to surface displacement. The range can be up to 50 mm with a resolution of 5μm and a frequency response of 10^4 Hz. The linearity is within about 2% of FSD when using a linearisation circuit. The temperature coefficient is about 0.2% FSD$^{o}C^{-1}$.

Capacitive transducers also require an a.c. excitation but the driving voltages required are somewhat larger than those applied to the inductive types. The non-contact capacitive transducer relies on the capacitance between two plates being inversely proportional to their separation. The working range is limited to about 5 mm with a resolution of 12μm. They can be made linear to about 1% of FSD. Their temperature coefficient is typically $-0.1\%^{o}C^{-1}$ and their frequency response is up to 3 KHz.

Inductive and capacitive transducers are perhaps the most popular means of non-contact sensing of displacement. Their resolution depends on their range of operation, a larger range goes with a lower resolution. None of the devices mentioned exert any static force on the moving object, this can be a very important advantage. With the exception of the LVDT and the VLP, the existing non-contact inductive and capacitive transducers are more susceptible to interference and changes in ambient temperature than the contacting types. This is because they cannot be used in differential circuits in which unwanted signals and dependances can be made to cancel. A disadvantage of the LVDT and VLP devices is that they cease to work if the object moves laterally. The other devices continue to work, albeit at a reduced accuracy, and do not restrain the object in any way.

The new transducer stands out from the pack for it has a superior working range and a unique ability to penetrate barriers. The variable reluctance and variable Q transducers share this ability only to a limited extent because they are forced to rely on a.c. fields: a 1 KHz magnetic field has a skin depth of only 7 mm in lead. Their operating frequencies can be lowered, but the penalty is a reduced sensitivity. Provided the object is not moving

too quickly, the new transducer has no such limitation for the magnetic field varies at a very low frequency: a 0.1 Hz magnetic field has a skin depth of 700 mm in lead.

Ultrasonic sensors can measure displacement if the propagation velocity of a longditudinal wave in the intervening medium is known. The displacement is found from the transit time of the transmitted waves, a resolution of 2μm is possible. Mehrdadi et al[69] describe a means of finding the level of irregular surfaces by timing the arrivals of ultrasonic echoes from the surface.

Optical systems, such as laser interferometers, have resolutions that are independant of range together with an inherent linearity. A dual frequency laser interferometer, which requires a reflector to be attached to the object, can have a 1 nm resolution over a range from a few millimetres to hundreds of metres. The disadvantages of interferometers are that they are very expensive, they can be bulky and, because of their precision optics, they are sensitive to changes in temperature, humidity, pressure and also to vibration.

Television cameras can be used to gauge displacement. They have an accuracy of about 0.1% of the image size independent of the intermediate optical scaling used. A pair of cameras can make three dimensional assessments. There is quite a lot of interest in this technique because measurements can be made on objects inside isolation chambers simply by letting windows into the protective walls. The new transducer has applications in this area, especially if its range can be increased: it will shortly be seen that the range can be considerably increased.

7.3 THE PERMANENT MAGNET

From now on, the new transducer is called the field gradient transducer. Two important players in the performance of the field

gradient transducer are the permanent magnet and the magnetometer. This section discusses the behaviour of the magnet and suitable magnetic materials.

Ideally, a permanent magnet would produce a very large field from a small volume and it would be completely unaffected by extraneous demagnetizing fields, changes in temperature and the passage of time. The diagram in figure 81 shows a BH energy product curve with its parent demagnetization curve, it also shows a minor hysterysis loop associated with magnet stabilisation. As a start in explaining the diagram, assume that a permanent magnet is magnetized to saturation and then the magnetizing field is removed. When the demagnetizing field is zero, as would nearly be the case for a toroidal magnet, the resulting flux density B_r is the residual induction. H_c is the demagnetizing field, or coercive force, that reduces the induction to zero. When the magnetizing field is removed and the demagnetizing field is not zero, as in the case of a bar magnet, the magnet acquires a state that is displaced from B_r on the demagnetizing locus; this is the state C' in figure 81. At this point the flux density in the magnet is B' and the total flux generated is B'A, where A is the cross sectional area of the magnet. The magnetomotive force per unit length of the magnet is H', so the total magnetomotive force applied to the air circuit surrounding the magnet is H'l where l is the length of the magnet. The total energy developed in the air circuit is (B'A) H'l). The natural magnet quality factor is BH which measures the magnetic energy available per unit volume of magnet. The magnet should be operated at the point where BH is at its maximum, this gives the optimum compromise between the flux generated and the resistance to demagnetization.

A transient external demagnetizing field, ΔH, will shift the operating point from C' to Q. When the field is removed the operating point will return to C" rather than C'. However, if ΔH is reapplied the operating point will return to Q and then go back to C" when ΔH disappears. This process is used to stabilise the permanent magnet. Deliberately applying a demagnetizing field ΔH reduces the energy product BH, but it means that transient external fields less than ΔH cannot permanently alter the magnet. In the present context, this means that the displacement transducer's calibration can be made lasting and reliable.

Sintered samarium cobalt, $SmCo_5$, has one of the largest BH energy products of any permanent magnet material currently available[70], [71]. It has a remanent induction of 0.99-1.05T and a coercive force of 710-800 KAm^{-1}. The maximum energy product is 190-220 KJm^{-3}. It may be stabilised by heating at 100°C in a reverse field of about 400 KAm^{-1}, this reduces the remanent induction by roughly 1%[71]. The closest competitor is probably Alcomax III. Alcomax III has a superior remanent induction of 1.25T but a far inferior coercive force of 50 KAm^{-1} and a maximum energy product of only 45 KJm^{-3}. Vacomax 200 has a reversible temperature coefficient of $-0.036\%^{o}C^{-1}$ from 20°C to 100°C and $-0.045\%^{o}C^{-1}$ from 20°C to 250°C.

A cylindrical magnet is the most suitably shaped for use with a field gradient transducer. The magnet is set to its operating point by correctly choosing the length to diameter ratio. A length to diameter ratio of about 0.4[70] sets $SmCo_5$ to its maximum BH operating point. A pair of formulae exist for the magnetic field H from a slender cylindrical magnet. In this case, the magnet is not slender but the formulae are useful nonetheless. The terms used in the formulae are defined in figure 82. The magnet's magnetiz-

Figure 82. A diagram to define the terms used in calculating the field from a bar magnet.

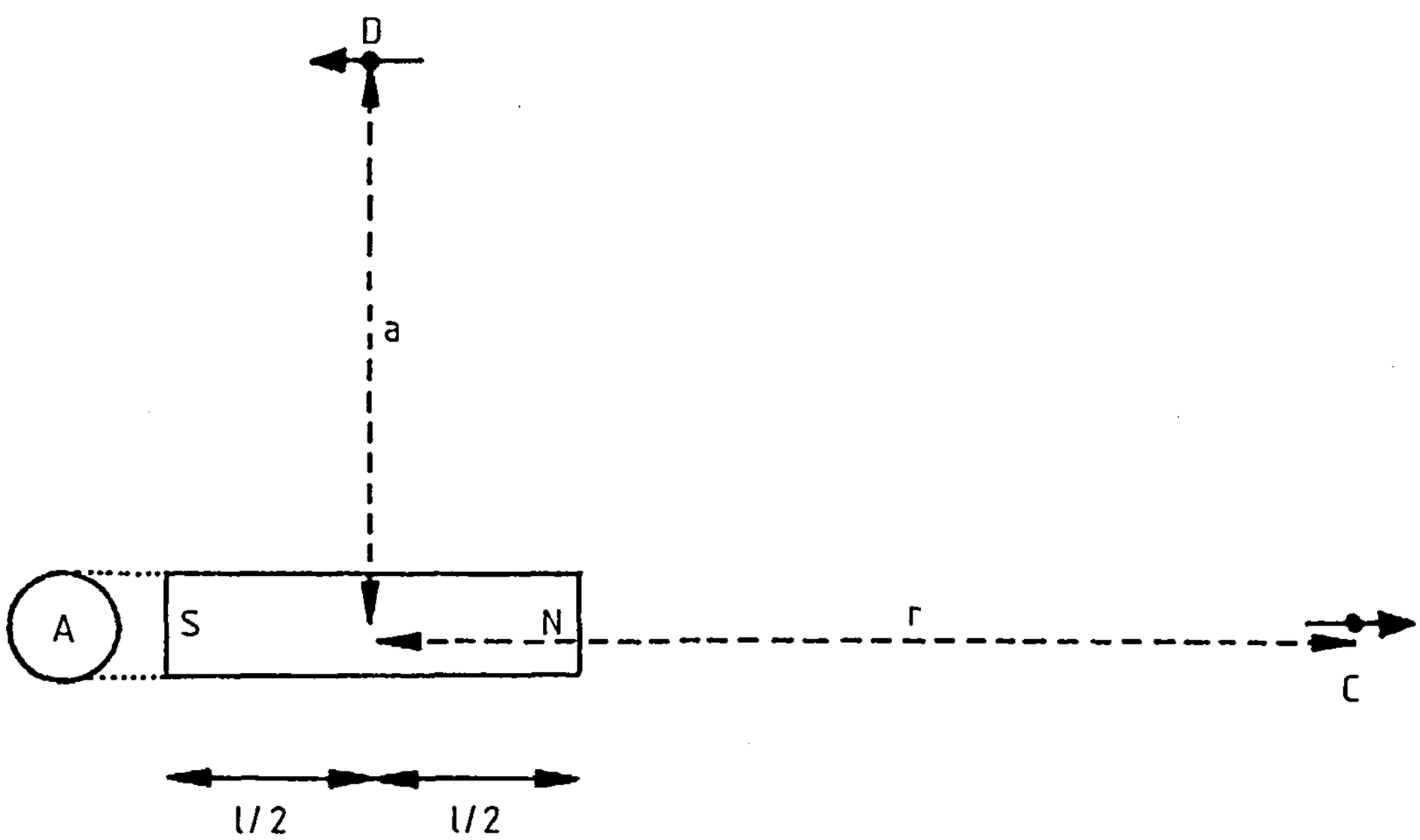

Figure 83. The relative responses of a single sensor magnetometer and a twin sensor gradiometer to an axial magnetic dipole.

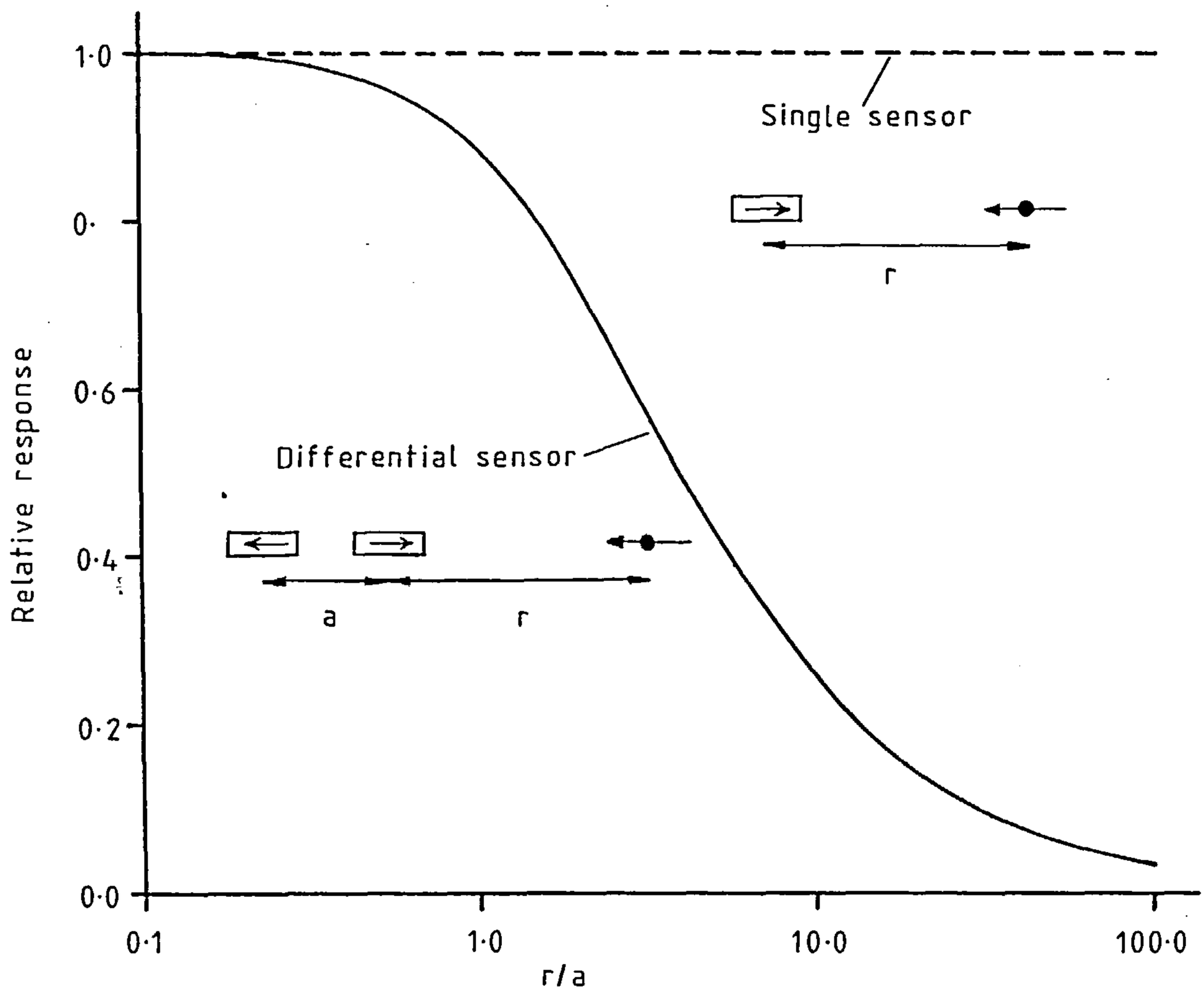

ation per unit volume is M. If the magnet's circular end faces are each uniformly magnetized they are equivalent to point poles of magnitude $\pm$ MA. By superposition the field at C is

$$H_C = MA\left[\frac{1}{(r-l/2)^2} - \frac{1}{(r+l/2)^2}\right] \qquad (7.1)$$

which simplifies to

$$H_C = (MAl).\frac{2r}{(r^2-l^2/4)^2} \quad . \qquad (7.2)$$

Similarly the field at D is

$$H_D = (MAl).\frac{1}{(a^2+l^2/4)^{1.5}} \quad . \qquad (7.3)$$

Equations 7.2 and 7.3 break down close to the magnet because internal demagnetizing fields ensure that the magnetizations of the end faces are not uniform.

This section is concluded by recording the details of the magnet that was used to test the principle of the field gradient transducer. The magnet used was an offcut of a larger $SmCo_5$ magnet, it was used because it was immediately available. Its dimensions were 11 mm x 9.8 mm x 4 mm and its volume was 430 mm^3. It was magnetized parallel to its longest dimension with a dipole moment of $2.46 \times 10^{-1} Am^2$. A magnet made of Vacomax 200 with an identical dipole moment and properly dimensioned for the maximum BH product would have a diameter of 12.5 mm, a length of 5 mm and a volume of 618 mm^3.

7.4 THE CHOICE OF MAGNETOMETER

The job of the magnetometer is to convert the magnetic field impinging on its sensor into a voltage. The five most popular magnetometer mechanisms in current use are proton precession, optically pumped alkali vapour, Hall effect, fluxgate and superconducting quantum interference (SQUID). The types suitable for use in the field gradient transducer are picked out below. There is no attempt to explain how the magnetometers work, references to

review papers are given instead.

A suitable magnetometer would have an ability to follow changing fields (a bandwidth of, say, 5Hz or more), low noise, wide dynamic range and a vector response. The last feature allows differential sensor pairs to discriminate against interfering environmental fields. The magnetometer must also be stable with time and temperature to facilitate monitoring of displacement over long periods. With these requirements, the proton precession[72] and optically pumped alkali vapour[72] magnetometers can be dropped from consideration. Neither has a vector response and the frequency responses of both are very poor.

Hall effect devices[64] do have a vector response and they have an excellent frequency response. Their rather severe temperature dependence can be corrected for. Wilson and Jones[73] describe a Hall effect magnetometer with feedforward temperature compensation. Their magnetometer has a bandwidth of 70KHz and a resolution of 10μT. By sacrificing the bandwidth, this resolution could be improved by employing phase sensitive rectification.

The fluxgate magnetometer[74] is the best suited to the task in hand. The most stable fluxgate magnetometer is the feedback type where the sensor is used as a null sensing device within a field-cancelling coil. The bandwidth is up to about 500Hz which is more than adequate. Noise levels in the 0.01Hz to 10Hz frequency range can be from 10pT r.m.s. to a few nT r.m.s. The temperature stability can be better than 30×10^{-6} of FSD$^{\circ}C^{-1}$. The long term amplitude stability depends on the stability of the instrument's sensitivity and offset. As an example, Primdahl[74] measured $\pm$ 3.5nT peak fluctuations in a fixed high field over a period of

90 days.

Geomagnetic noise is of the order of 10pT r.m.s. in a 1Hz bandwidth centred on 1Hz and of the order of 10nT r.m.s. at 0.01Hz[75]. To this may be added the contributions of electrical machines, electrical switches, electrical furnaces and other interfering noise sources (such as underground electric trains in the case of these experiments). Man made noise may be many orders of magnitude greater than geomagnetic noise. It is clear that environmental noise, rather than magnetometer noise, will limit the performance of the field gradient transducer in most instances. Fortunately, differential fluxgate magnetometers, called gradiometers, are available. A pair of sensors mounted in opposition can be made to detect the field gradient due to a nearby source and reject the uniform field of a distant source. In this application, the gradient from the permanent magnet will be detected and interfering fields will be ignored.

Figure 83 shows the relative responses of single and differential sensor magnetometers to an axial dipole. The distance between the leading sensor and the dipole is r, and the separation between the differential sensors is a. If the sensitivity of the magnetometer is k, VT^{-1} and the dipole moment is M_T, Am^2, then the output for a single sensor is

$$\text{Output (single)} = \mu_o M_T \, 2k \cdot \frac{1}{r^3} \quad . \qquad (7.4)$$

The output of the gradiometer is

$$\text{Output (grad)} = \mu_o M_T \, 2k \cdot \frac{1}{r_3} \left[1 - \frac{1}{(1+a/r)^3} \right] . \qquad (7.5)$$

These responses are plotted as a function of r/a assuming that r

remains fixed. Twin sensor gradiometers can be obtained either by buying a pair of matched feedback sensors[76] and constructing the necessary electronics, or by remounting two of the probes from a triaxial fluxgate unit[77].

The ultimate performance would be obtained using a SQUID gradiometer[75] which can achieve noise levels of about 2×10^{-13} $Tm^{-1}\ Hz^{-\frac{1}{2}}$. At present, these are too bulky and too costly for their use to be justified in many field gradient transducer applications.

The field gradient transducer was developed using a fluxgate magnetometer that had been designed for another application, it was used because it was immediately available. The magnetometer's performance was far from ideal as it was a single sensor device and it had a rather high noise level, these points should be borne in mind. The magnetometer's sensitivity was $1.5 \times 10^{-4}\ VT^{-1}$, it had a noise level of 40nT r.m.s. over a DC-2Hz bandwidth in its working environment. It had a drift of about $\pm$ 70nT per hour and a linear range of $\pm$ 900μT. Its unfiltered bandwidth was 10Hz. It is worth contrasting this performance with that of a PWB unit from Domain Micro-Systems[77]. Their device has 1.8nT r.m.s. noise per channel over a DC-10Hz bandwidth. In the differential mode, the noise will be 2.5nT r.m.s. If the probes were separated by 25 cm a magnet identical to that used in these experiments would give the transducer a useful range of 2.3 m and a bandwidth of 10Hz. The magnetometer used produced a useful range of 0.25 m at a bandwidth of 1Hz.

CHAPTER 8

HARDWARE FOR THE NON-CONTACT DISPLACEMENT TRANSDUCER

8.1 INTRODUCTION

Chapters 8 and 9 describe the hardware and software designed for the non-contact displacement transducer. The objective was to produce and test a working instrument to prove that the principle described in section 7.1 was practical. The resulting hardware and software will work independently of the choice of magnet and magnetometer. The instrument went through a number of stages of development. Ultimately, the boundaries between hardware and software become blurred in the cause of more rapid operation. Section 8.2 explains the hardware's function using a block diagram of the penultimate version of the instrument. This provides a framework to which the details of the finalised circuitry can be attached in section 8.3.

It will be assumed that the reader has some knowledge of the theory of analogue signal sampling and reconstruction, of the signal distortion that occurs in practice and of the z transform. For those who wish to use it, appendix 1 provides a short, self contained account of these topics.

8.2 THE FUNCTION OF THE HARDWARE

A block diagram of the penultimate hardware configuration is shown in figure 84. The samarium cobalt magnet is mounted on a perspex carriage which moves along the line AB. The sensor of the feedback fluxgate magnetometer and the magnetic dipole are fixed in permanent alignment with the axis of motion. This arrangement eliminates the unwanted orientational dependance and ensures that the magnetometer generates the strongest possible signal.

To improve the limited dynamic range of the analogue to digital

Figure 84. A block diagram of the penultimate version of the hardware.

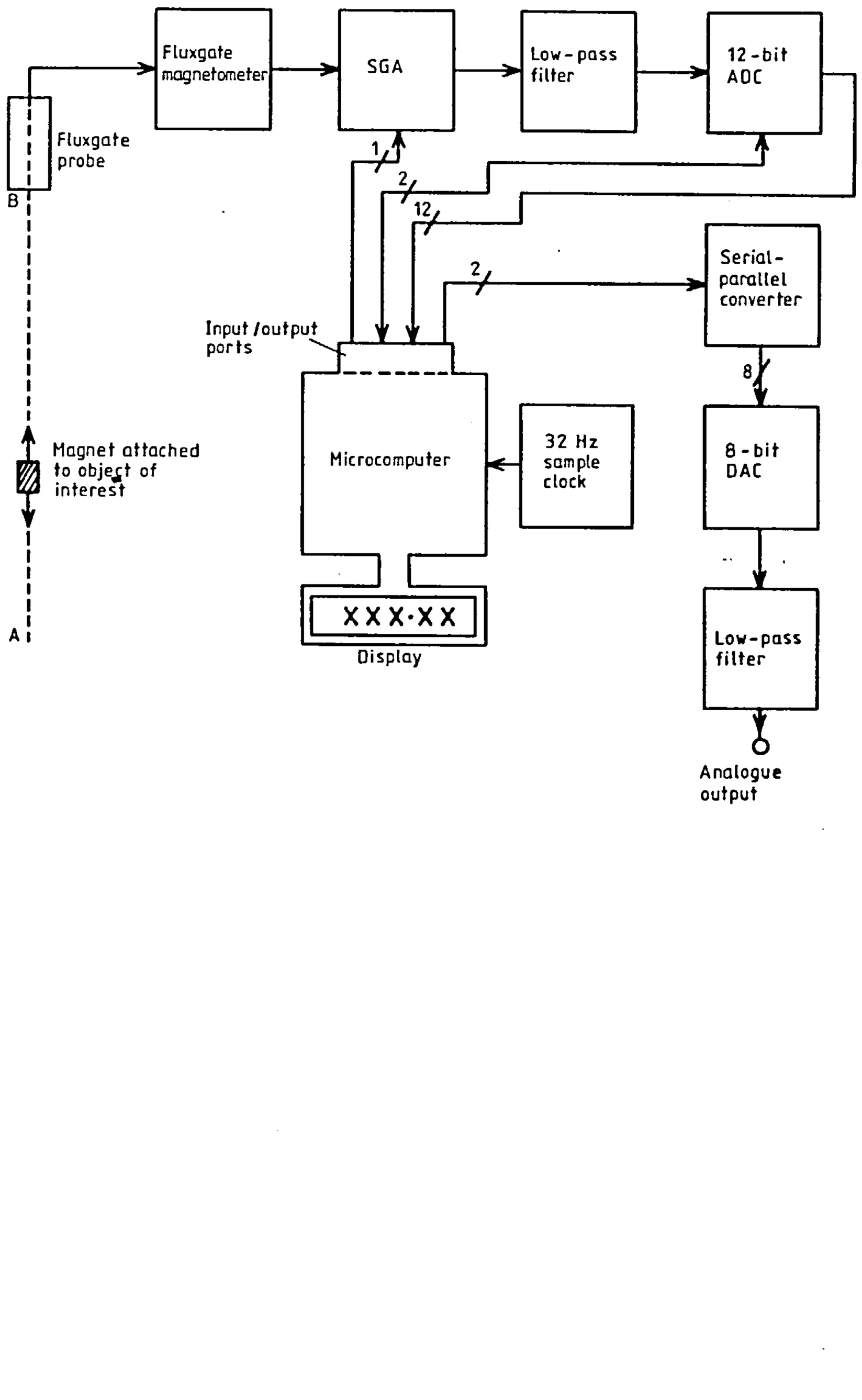

converter (ADC) a switched gain amplifier (SGA) follows the magnetometer. When the magnet is close to the fluxgate probe, and the magnetic field is large, the microcomputer selects a gain of 2.00 so that the amplifier's output does not overload the ADC. When the magnet is distant and the magnetic field is weak a gain of 16.0 is selected. The higher gain makes sure that the ADC's quantization noise (see appendix 1) is well below the magnetometer's noise, in this way none of the information in the weak field is wasted. The gain of the SGA is altered by using CMOS analogue switches to change the gain-setting resistors about an operational amplifier.

The amplified signal from the magnetometer is digitized at the request of the microcomputer. The ADC takes 32 samples each second, this puts the aliasing frequency (see appendix 1) at 16Hz. Signals above 16Hz would be folded below it as aliasing noise. The magnetometer has a 3dB response roll off at 12Hz. A 6th order low pass Chebyshev filter, with a 0.5dB passband ripple and a 3dB attenuation at 7.0 Hz, is used to suppress the unwanted frequency components in the magnetometer's output. The Chebyshev filter's desirable amplitude characteristics outweigh its poor phase performance (see appendix 1).

How the microcomputer handles the data from the ADC forms the content of chapter 9. In brief, the microcomputer uses each new sample as a pointer in an inbuilt displacement calibration table. Stored values in the vicinity of the pointer are combined with the sample by an interpolation routine to produce a new result for the displacement. The result is digitally filtered and then sent to an alphanumeric display and a digital to analogue converter (DAC). The display is updated only twice a second to prevent it flickering too rapidly, the DAC is updated 32 times a second so that the analogue output to the chart recorder traces the magnet's motion

correctly. Strictly speaking, a low pass reconstruction filter is required to smooth the analogue output samples. In this case the filter is obviated by the chart recorder's own time constant.

The microcomputer used in this version is the Rockwell AIM 65 equipped with an 8 kilobyte monitor program. The input/output ports to the slave circuitry are all part of one R6522 versatile interface adaptor (VIA). The 32Hz sample clock, which orchestrates information flow through the instrument, is included on the VIA as a programmable timer. The R6502 microprocessor is programmed using a mnemonic representation of machine code. A high level language such as BASIC could be used, but this would be at the expense of the instrument's bandwidth. When it comes to short program execution times, a general purpose high level language cannot compete with carefully tailored machine code routines.

The publication[65] described the instrument in this penultimate form. One of the main reasons for developing the hardware and software further can be understood by examining the program cycle times. Sampling at 32Hz, the software executed 32 complete cycles every second. One cyle in each half second sent a result to the display and the DAC. The other 30 cycles sent a result to the DAC only. A cycle that sent a result to the display took 29ms giving a maximum possible sampling rate of 34.5Hz. A software cycle that did not send a result to the display took only 4.7 ms. The huge disparity was due principally to the 23ms taken by the display subroutines in the AIM 65's monitor. If the display operation could be reduced to a few μs the displacement transducer's bandwidth could be quadrupled, this would open up a broader range of applications.

Another reason for change was that the microprocessor had to use the VIA as an intermediary when communicating with the SGA, ADC and DAC. This was much slower than direct communication using

the microprocessor's address and data busses. Finally, the AIM 65 was too sophisticated and versatile for the job it had to do. Most of its circuitry and stored software was wasted, this made it unnecessarily bulky and power hungry.

8.3 THE DESIGN OF THE HARDWARE

This section describes the final combination of microcomputer and input/output circuitry. The combination is compact and efficient, it makes full use of the computing power of the microprocessor. A block diagram and microcomputer memory map are shown in figures 85 and 86. Note that the hexadecimal numbers 0...9,A,B,C,D,E,F represent the decimal numbers 0-15. The hexadecimal notation used in figure 86 is a handy way of identifying memory addresses. A 16 bit binary number, corresponding to 16 address lines, can be represented as four hexadecimal (base 16) numbers. As an example $91A8_{16}$ = $1001, 0001, 1010, 1000_2 = 37,288_{10}$.

8.3.1 The microcomputer board

The CUBIT[78] microcomputer board was chosen for the instrument. The CUBIT uses the R6502 microprocessor so software and hardware could be developed and tested on the more sophisticated AIM 65 and then transferred to the CUBIT. The CUBIT is constructed on a 100 mm x 160 mm Eurocard.

Figure 87 is a circuit diagram of the CUBIT taken from the manufacturer's data sheet. The 6502 microprocessor, IC4, is governed by a 1MHz clock. Two antiphase square waves, $\emptyset_1$ and $\emptyset_2$, are generated from the clock's signal by the microprocessor. The 6522 versatile interface adaptor (VIA) incorporates the 16 bit counter / timer which is used to generate the sample clock. The board can house up to 4 kilobytes of random access memory (RAM) as IC6-IC13. Less than 1 kilobyte of RAM is required so IC6 and IC10 alone are inserted. The permanent program is stored in a 2 kilobyte 2716 erasable

Figure 85. A block diagram of the hardware for the final version of the displacement transducer.

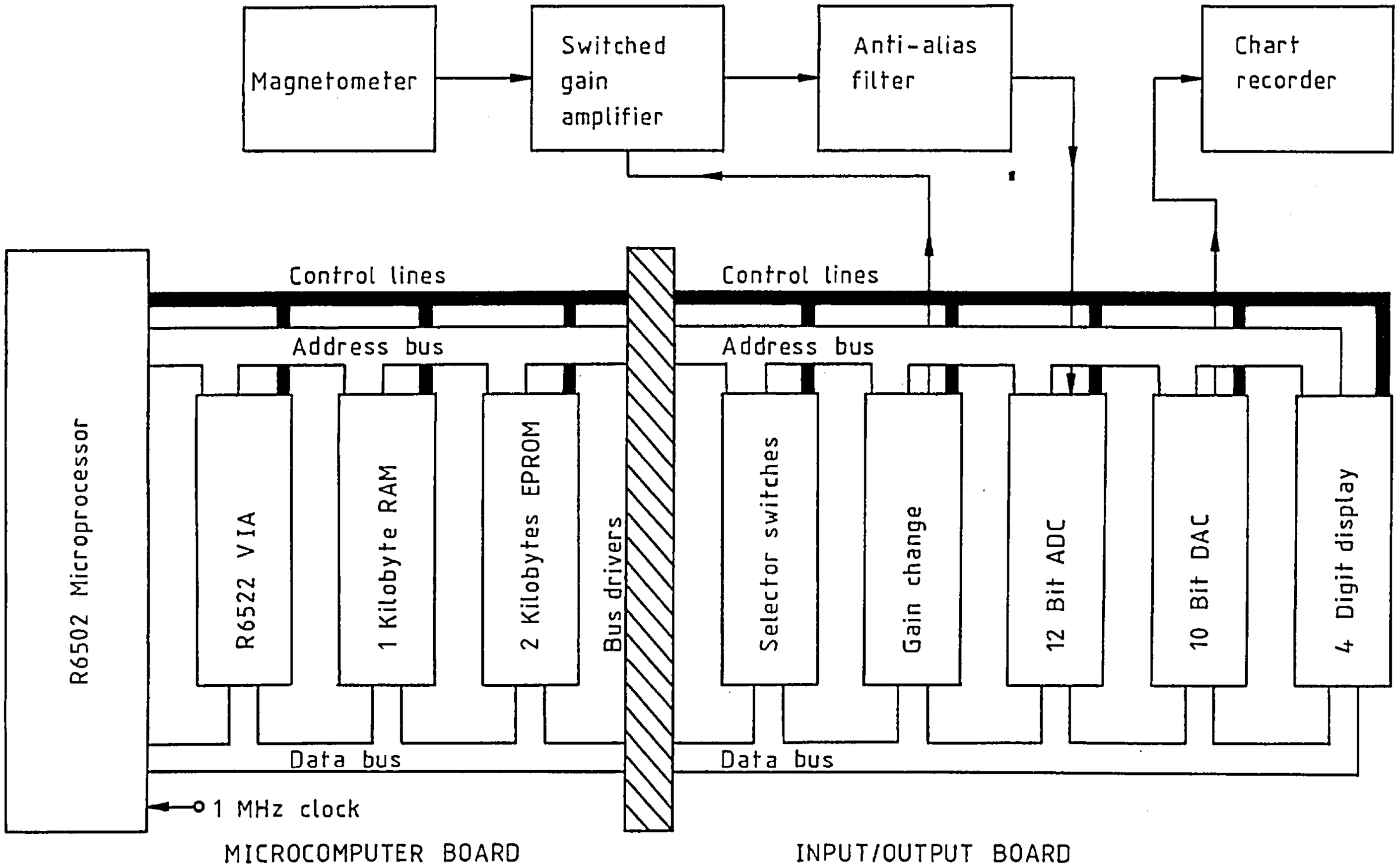

Figure 86. A hardware memory map.

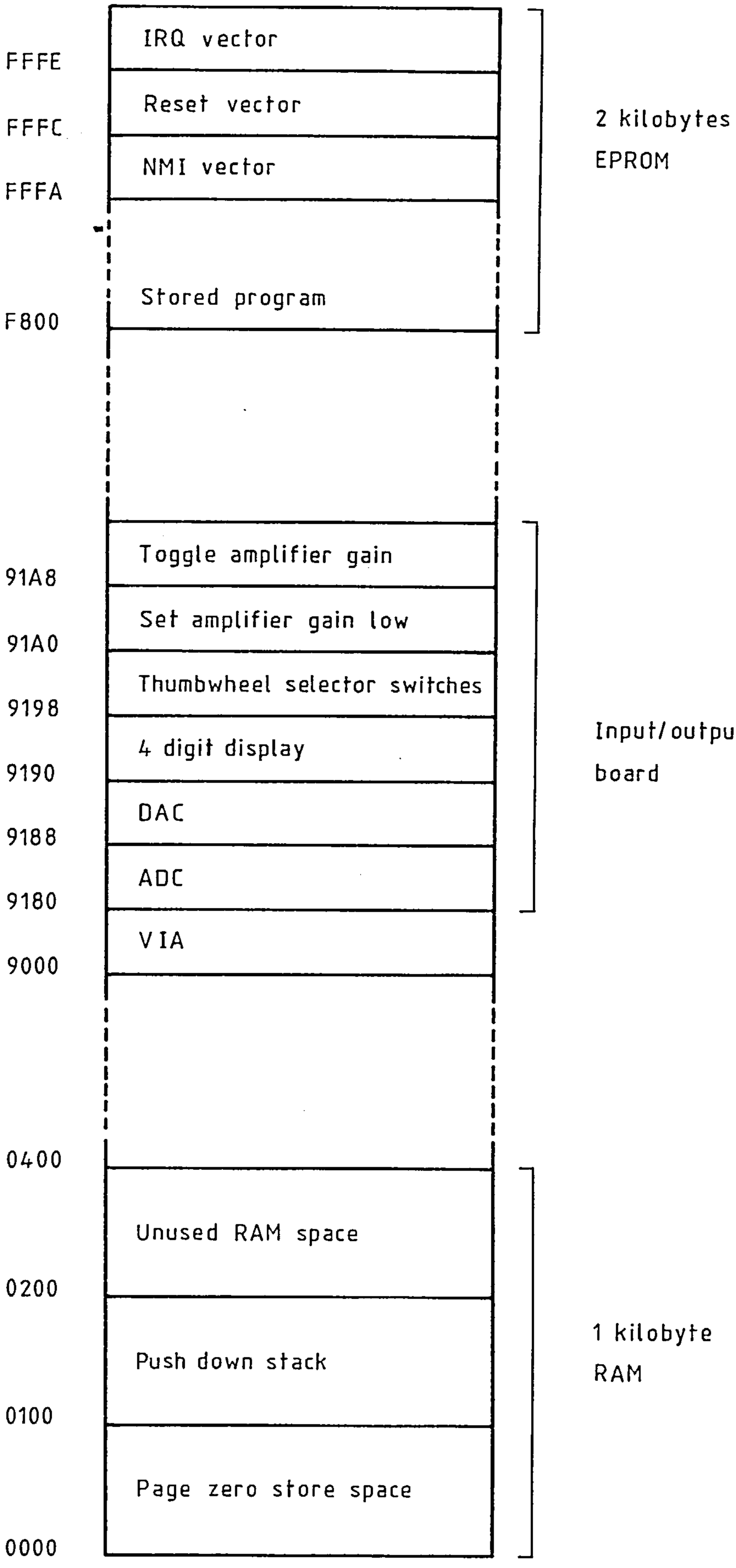

Figure 87. A circuit diagram for the CUBIT microcomputer board[78].

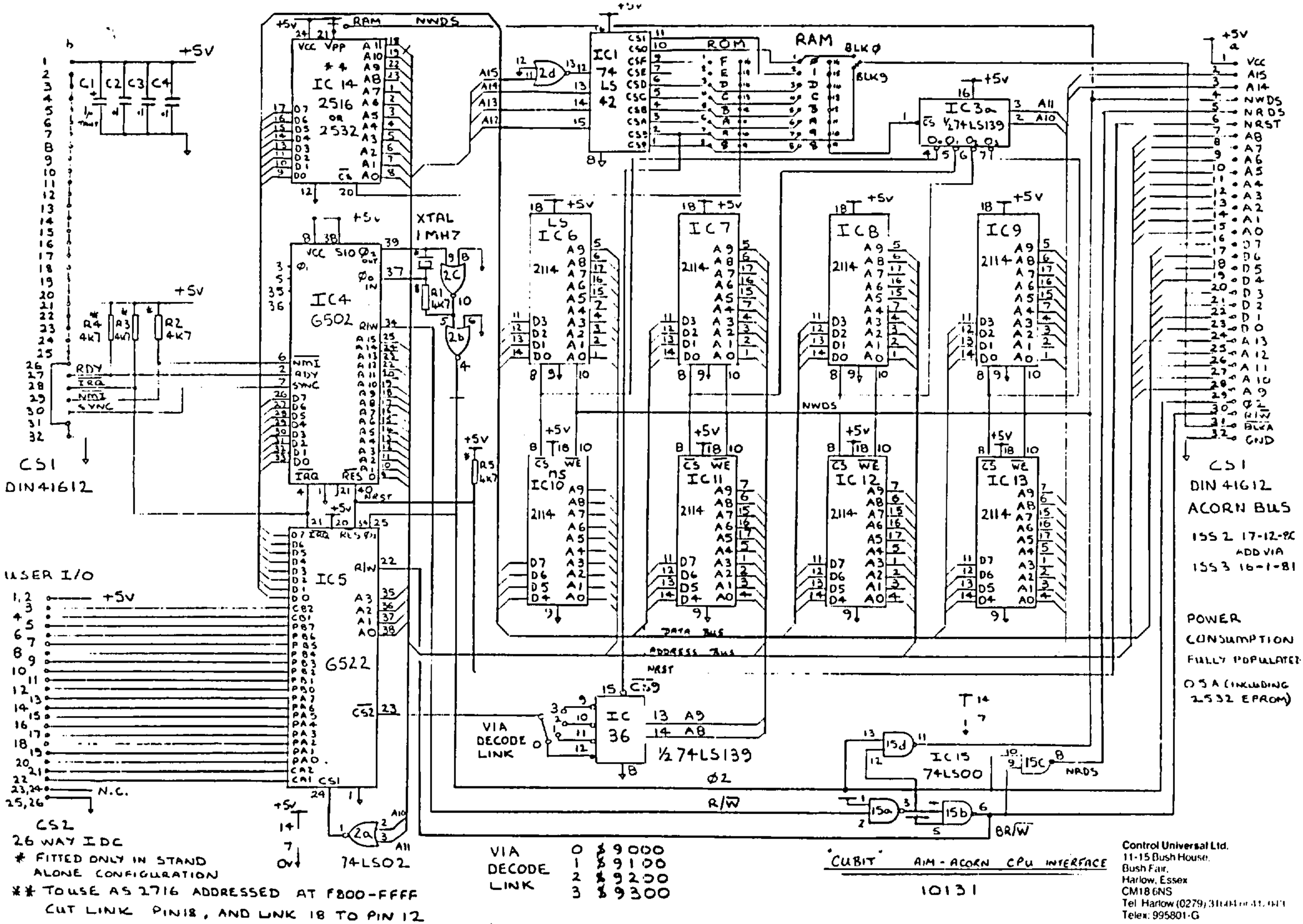

Control Universal Ltd.
11-15 Bush House,
Bush Fair,
Harlow, Essex
CM18 6NS
Tel Harlow (0279) 31481 or 31 6871
Telex: 995801-G

programmable read only memory (EPROM), IC14. The areas of memory in which the RAM, EPROM and VIA are addressed can be altered using a pair of sliding switches.

The microprocessor communicates with other devices through the address and data busses. The direction and synchronisation of data flow is determined by the microprocessor's control lines. When the R/$\overline{W}$ line is high, the microprocessor reads an 8 bit data word in the location selected by the 16 bit address bus. When R/$\overline{W}$ is low, the microprocessor overwrites the selected location. The two anti-phase clock signals $\emptyset_1$ and $\emptyset_2$ split each microsecond into two intervals. In the first interval, the microprocessor adjusts its address and control busses to select a location and to inform the location whether it is to be read or overwritten. During the second interval, data passes from source to destination. If the location addressed cannot work this quickly, then logic belonging to the location can pull the RDY line low and put the 6502 into suspended animation. The location releases the RDY line when it has finished.

The microprocessor can be made to respond to external events through its non-maskable interrupt ($\overline{NMI}$), interrupt request ($\overline{IRQ}$) and reset ($\overline{RST}$) lines. $\overline{RST}$ is used to make the instrument start properly when power is turned on. It can also halt the microprocessor in its tracks and make it go back to the beginning of the stored program. When power is switched on, the operation is as follows. $\overline{RST}$ has to remain low while the power lines establish themselves. When $\overline{RST}$ goes high the microprocessor waits 6 clock cycles (6μs) before it does anything. It then automatically reads the locations $FFFD_{16}$ and $FFFC_{16}$ for it knows that these locations hold the starting address of the stored program. The microprocessor jumps to the start of the program and commences execution.

The CUBIT board makes nearly all of the address, data and control lines accessible in a 64 pin DIN 41612 socket. Three extra lines are connected to unused pins on the socket. These lines are $\emptyset_1$ (pin 3 on IC4), $\overline{R/W}$ (pin 3 on IC15) and $\overline{\text{SELECT PAGE } 91_{16}}$ (pin 11 on IC3). The latter pin went low whenever the addressed location was in the range 9100_{16} to $91FF_{16}$.

Figure 88 shows a worst case timing diagram for read/write cycles using a 1MHz clock. The diagram is valid for loads of up to 130 pF in parallel with 1 TTL input on each data, address and control output line. The lines are all TTL compatible. The input/output board which is described next has to keep within these times if the instrument is to function properly.

8.3.2 Microcomputer to input/output board bus drivers and input/output device select

The worst case timings of figure 88 are only true if the microprocessor's output line drivers are not loaded by more than 130 pF in parallel with 1 TTL input. At the design stage, the capacitative loading of an input/output board is an unknown quantity. For safety, all of the necessary address, data and control lines are buffered using LS TTL transmitter and transceiver chips. With these buffers the system could be considerably expanded should this ever be required. The intrinsic delays in the buffers are small enough to be ignored. When the transmitter and transceiver chips are not selected their outputs enter a high impedance state.

All of the input/output devices are located in page 91_{16} of the microprocessor's address space, this has been shown on figure 86. A 74LS138 three to eight decoder is activated by the $\overline{\text{SELECT PAGE } 91_{16}}$ line from the CUBIT. When activated, the decoder pulls one of the 8 output lines low to alert an input/output device that it is required. As two of the eight outputs are unused, two

Figure 88. Worst case timings for a 1MHz 6502.

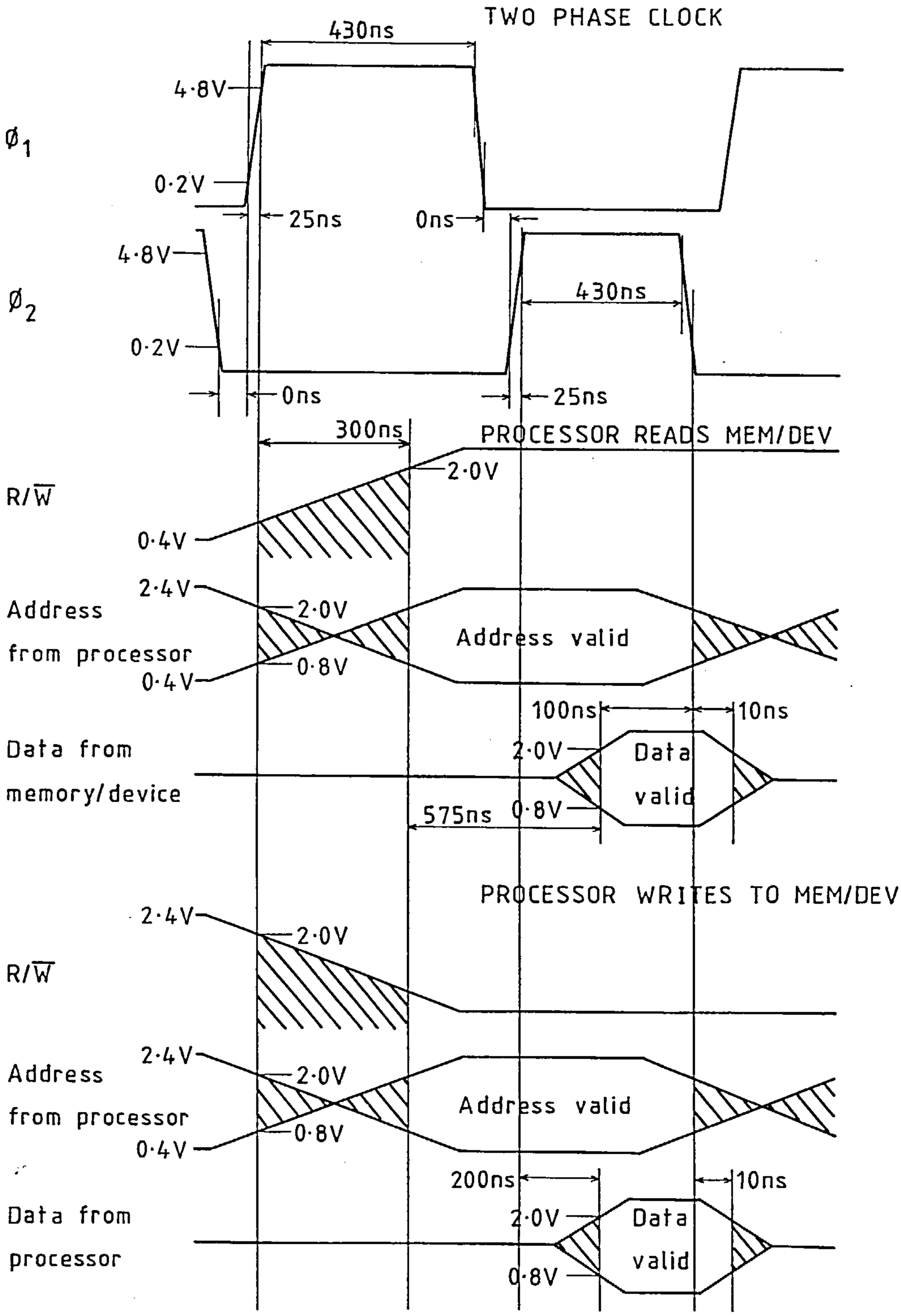

more devices could be added to the input/output board in future. A circuit diagram for this bus interface and decoding section is shown in figure 89.

8.3.3 The input/output board

8.3.3.1 The thumbwheel switches

A pair of hexadecimal thumbwheel switches are included to allow an operator to manually input data or instructions to the microprocessor. Chapter 9 will show how the switches are used to select a sampling rate and to choose between calibration or measuring displacement. The circuit diagram is shown in figure 90a. When asked to do so, the 74LS244 forces the switch settings onto the data bus. At other times the outputs of the 74LS244 are in a high impedance state. Note that the switch settings are the inverse of what the hexadecimal numerals on the thumbwheels show, this has to be accounted for by the software.

Figure 90b shows the input/output board's power rail decoupling and the push-to-RESET switch. A 4.7K pull up resistor for the switch is mounted on the CUBIT board.

8.3.3.2 The switched gain amplifier

The circuit diagram of the switched gain amplifier is shown in figure 91. The gain can be altered manually, when calibrating the instrument, or by software when making measurements of displacement. An l.e.d. is lit when the gain is high, this is an aid when testing the software. A gain of 16 or 2 is selected using a CMOS dual analogue switch to pick one of the two input resistors to OA3. It is important that the ratio of the gains is as close to 8 as possible. In practice the gains are 1.997 ± 0.001 and 15.97 ± 0.01, their ratio is 8.002 ± 0.006. When the inputs to

Figure 89. Microcomputer to input/output board interface buffer.

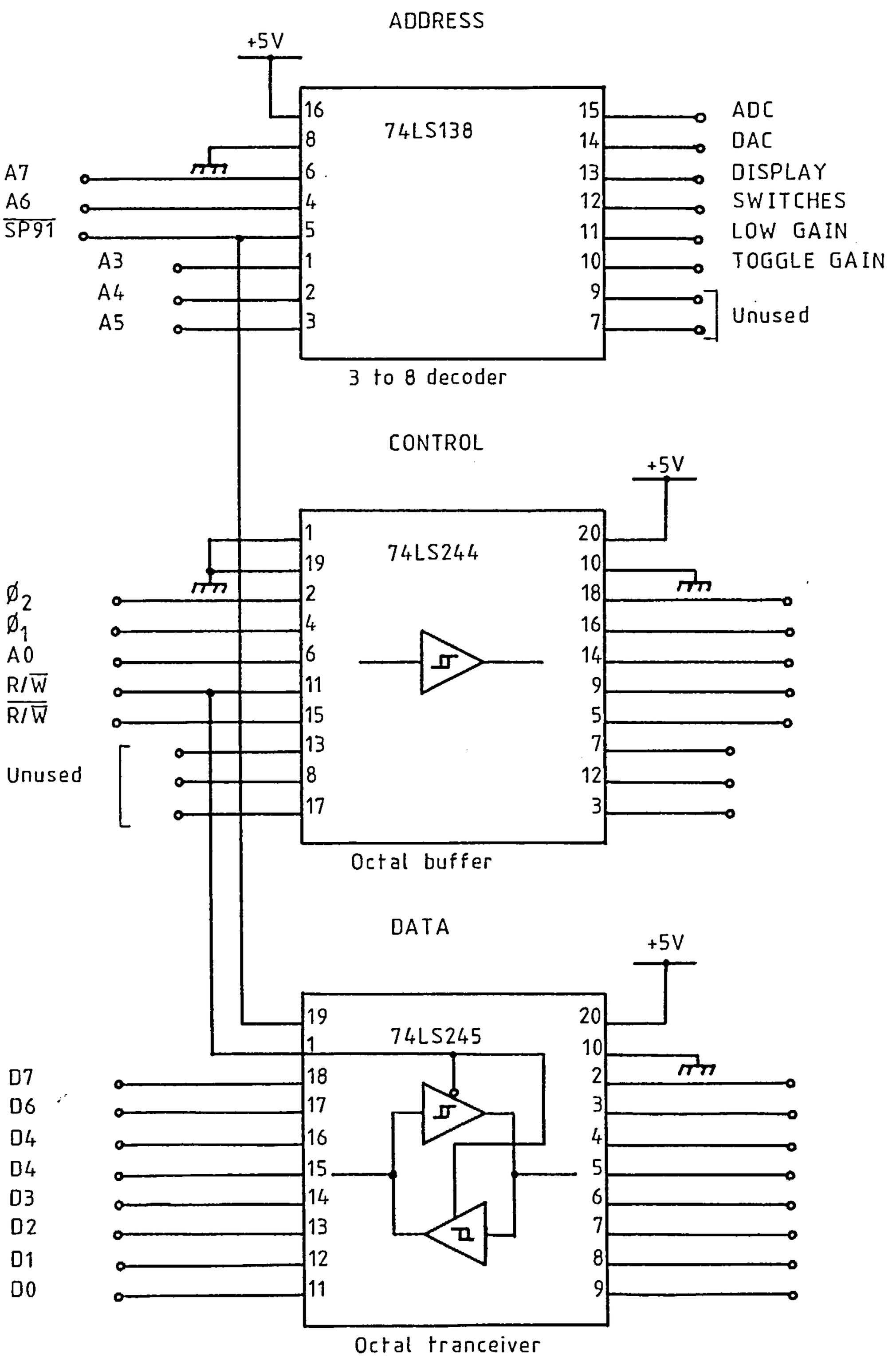

Figure 90.

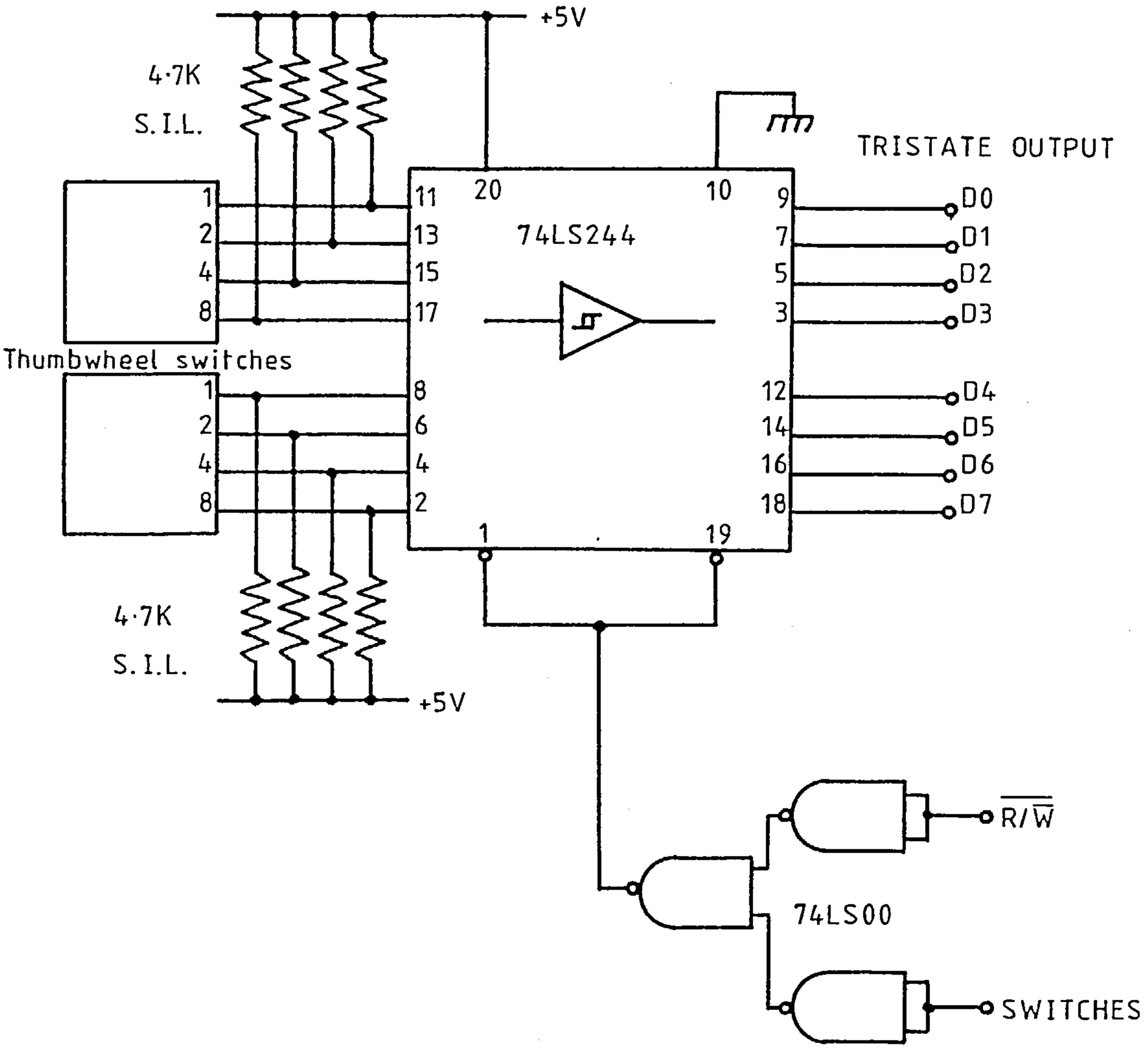

a. The operator's thumbwheel input switches.

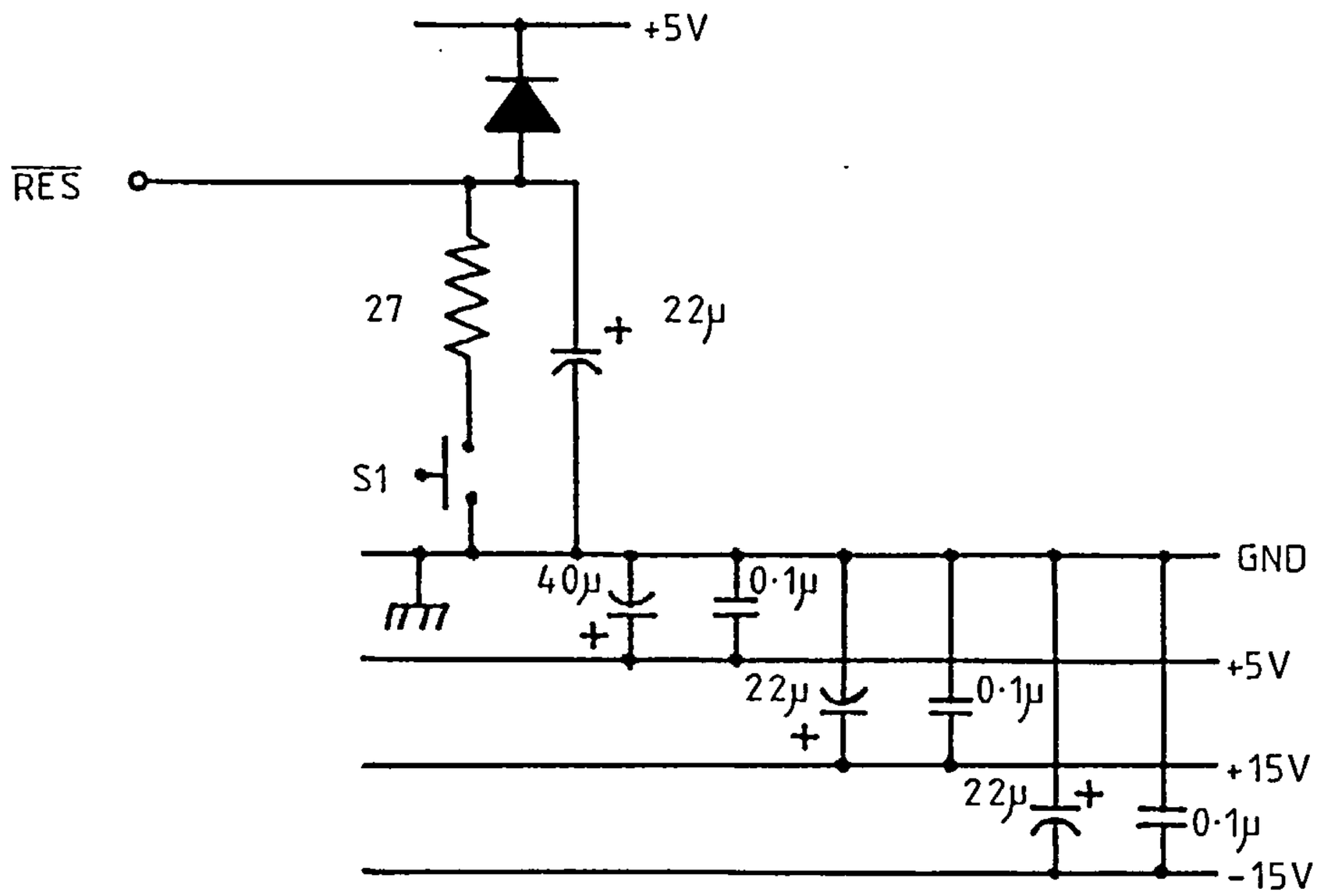

b. The reset switch and power rail decoupling.

Figure 91. The switched gain amplifier.

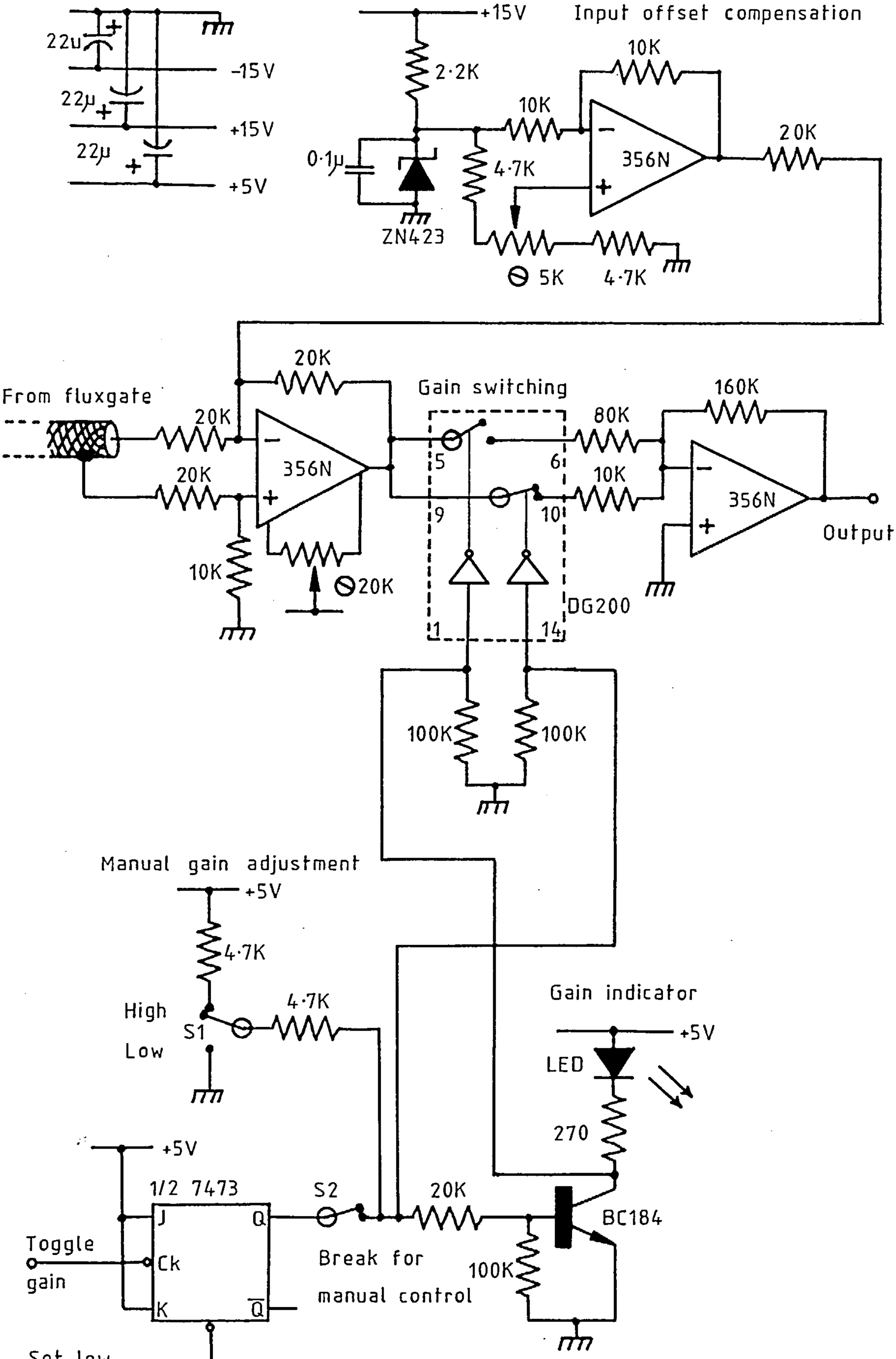

OA2 are grounded, the offset at the output of the succeeding anti-alias filter is 8.9 mV when the gain is 16 and 8.7 mV when the gain is 2. With a gain of 16 the noise and drift at the output of the anti-alias filter is less than 0.15 mV over a period of an hour.

The magnetometer has a sizeable zero offset of -200 mV, this is probably due to d.c. magnetic fields in the laboratory. The fluxgate's signal is added to a d.c. level from OA1 to remove this offset. OA1 can generate adjustable bipolar output levels of $\pm$ 400 mV.

8.3.3.3 The anti-alias filter

The circuit diagram of the anti-alias filter is shown in figure 92a, its frequency response is shown in figure 92b. Tietze and Schenk[49,76] describe the procedure with which the filter was designed.

8.3.3.4 The analogue to digital converter

The Analogue Devices AD574K is a 12 bit successive approximation analogue to digital converter with a typical conversion time of 35μs. It is contained in a 28 pin dual-in-line package and it is microprocessor compatible. A full description of its operation and timing requirements are given in the maker's data book[79]. The configuration of the AD574K is shown in figure 93, one or two notes on it are made below.

The signal from the anti-alias filter is received by a unity gain differential amplifier. The anti-alias filter and switched gain amplifier are contained in a screened enclosure that is separate from the enclosure housing the digital electronics. The signal from the filter is sent along a coaxial cable whose screen is grounded at the filter's enclosure. The common mode rejection ratio of differential amplifier makes it possible to receive the signal with-

Figure 92. A 6th order low pass Chebyshev anti-alias filter. The passband ripple is 0.5 dB, the cut off frequency is 7Hz.

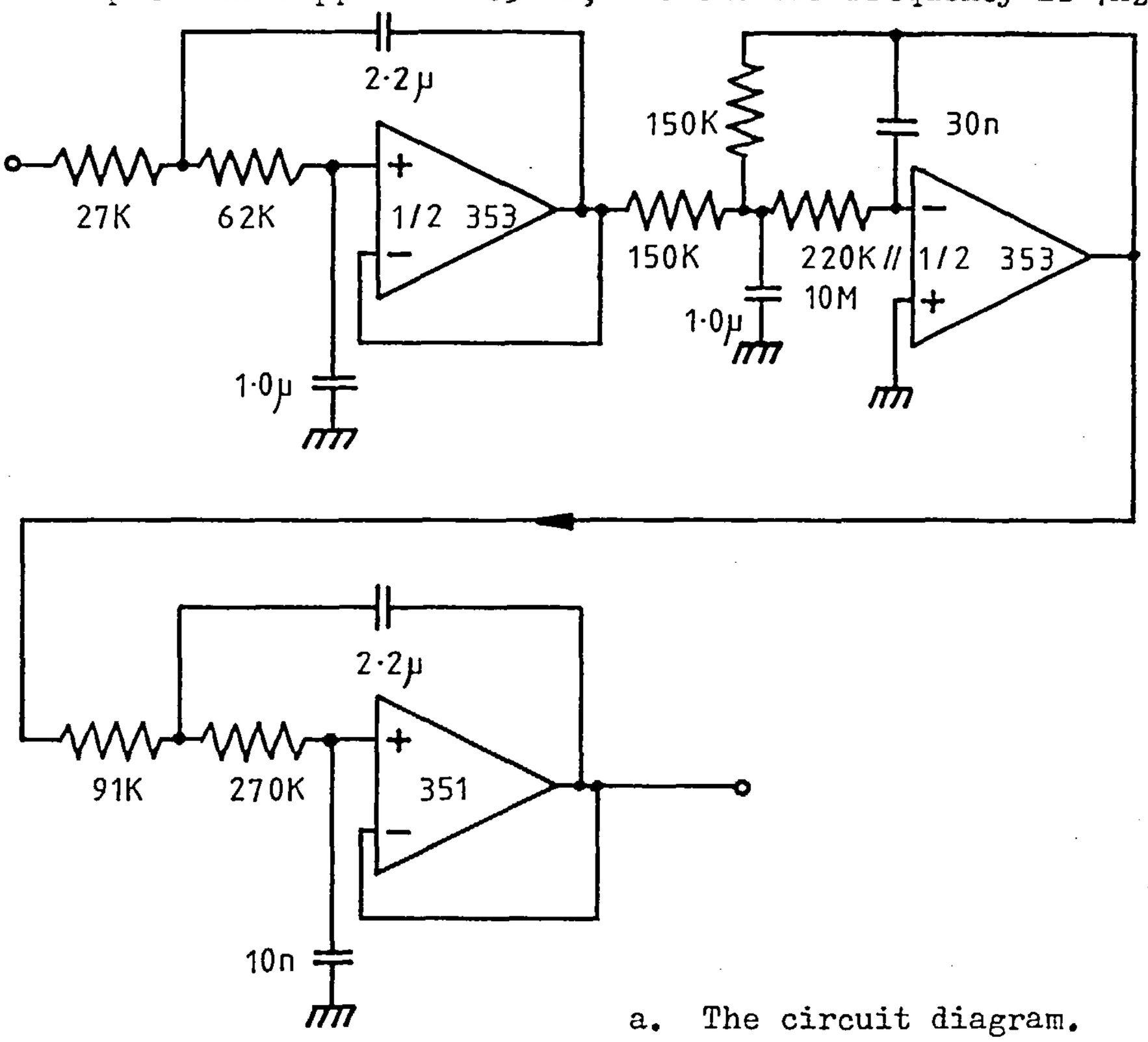

a. The circuit diagram.

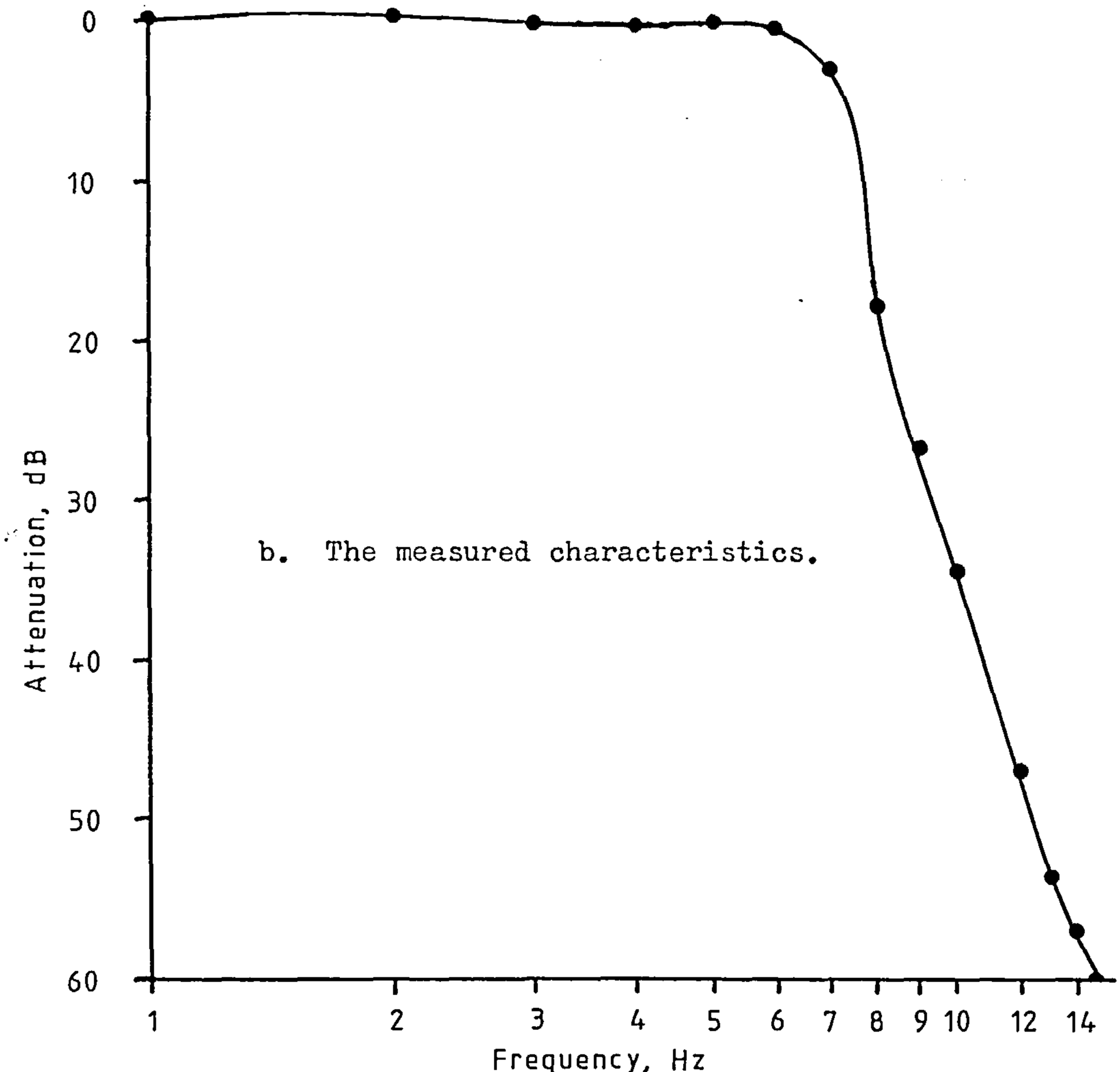

b. The measured characteristics.

Figure 93. The configuration of the analogue to digital converter.

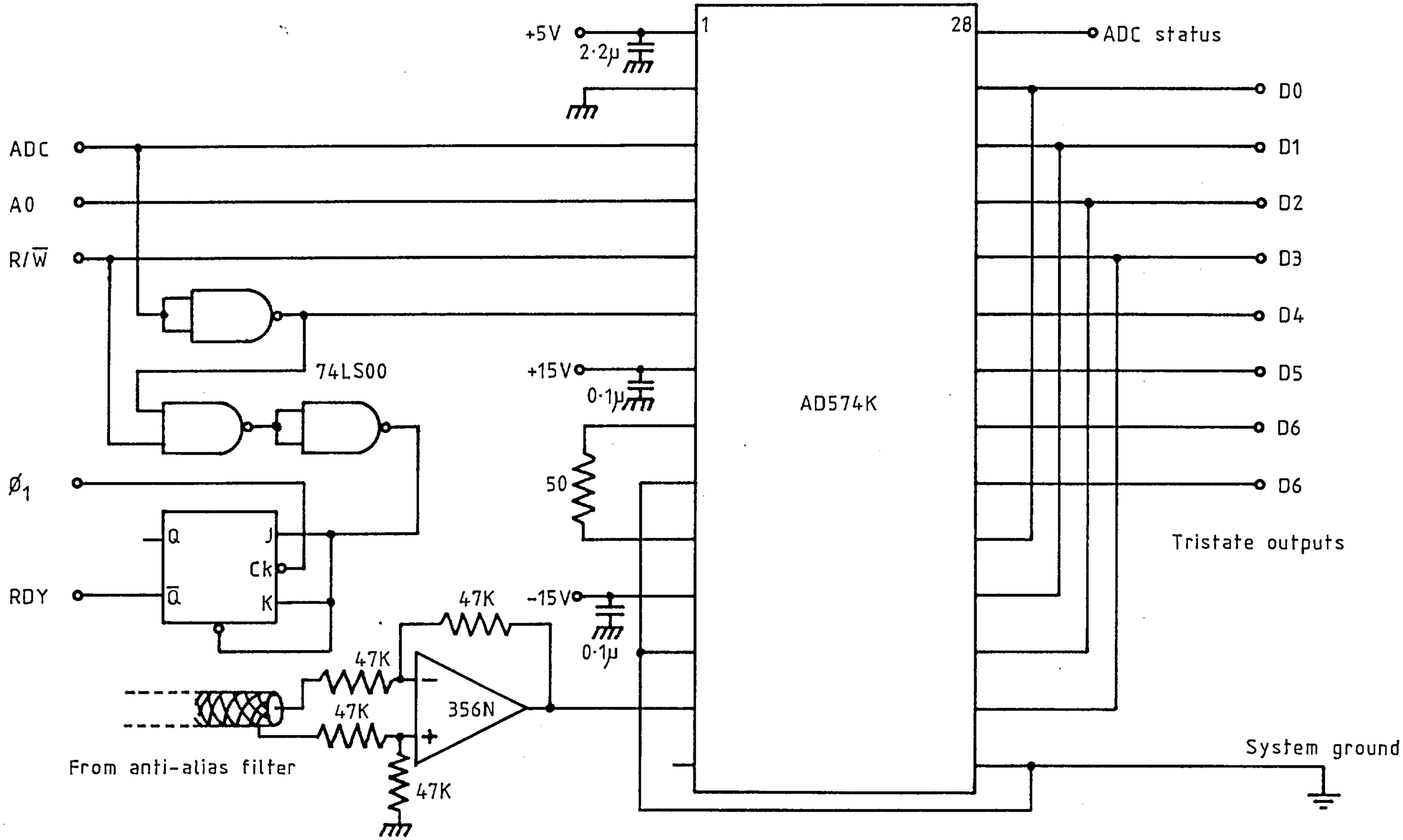

out creating a hum loop. An incidental advantage is that the amplifier's low output impedance prevents errors being created by a changing ADC input impedance during a conversion cycle.

In the configuration shown, the ADC handles unipolar input voltages between 0V and 10V. The magnitude of one least significant bit (LSB) is $10/2^{12}$ = 2.44 mV. The tristate data output lines of the AD574K are connected directly to the data bus. The ADC appears in locations 9180_{16} and 9181_{16} in memory-space. The microprocessor initiates a conversion cycle by trying to store its accumulator at 9180_{16}. After a maximum wait of 35μs the digitized result is ready for processing. The most significant 8 bits of the result are contained in 9180_{16}, the least significant 4 bits are in 9181_{16}. The ADC is not able to make its data available quickly enough to fit in with the microprocessor's read cycle, see figure 88. To get over this problem, some extra circuitry was designed to make the microprocessor stop and wait for 1μs before carrying on as normal. Under normal circumstances the output of NAND gate 3 is low, the RDY line is therefore high and the microprocessor busily executes instructions. When the ADC is addressed and $R/\overline{W}$ is high, the output of NAND gate 3 goes high and the RDY line is forced low which stops the microprocessor. NAND gate 3 also forces the flip-flop's J and K inputs high putting the flip-flop into its toggle (÷ 2) mode. When $\emptyset_1$ goes high again, about 1 μs later, $\overline{Q}$ toggles from low to high and the read cycle is completed successfully.

8.3.3.5 The liquid crystal display

The four digit liquid crystal display is driven by an Intersil ICM 7211 MIPL CMOS display decoder/driver. The operating and timing requirements are described in the manufacturer's data sheet[80].

Figure 94. The liquid crystal display.

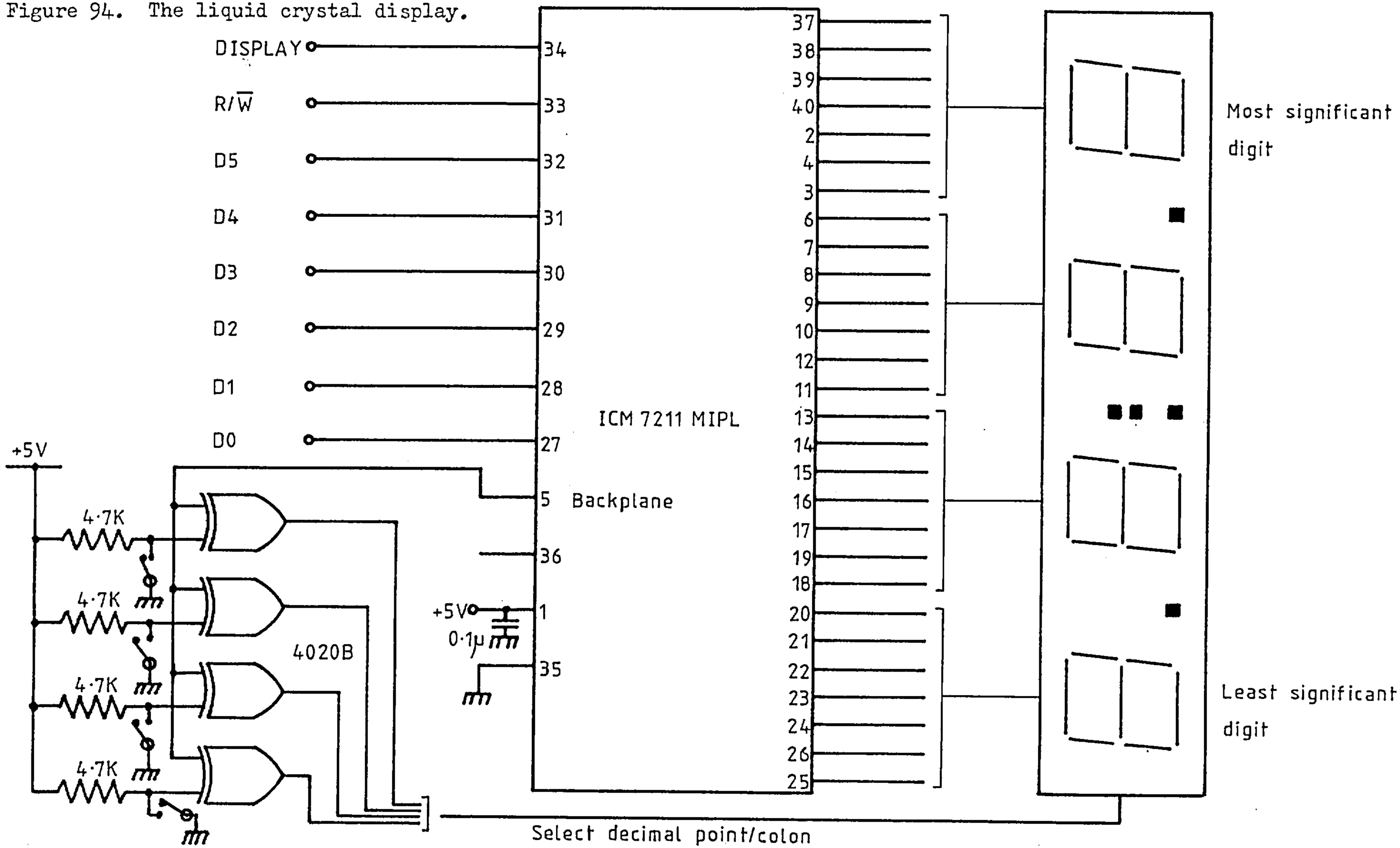

The ICM 7211 MIPL is microprocessor compatible and appears as a location in memory space. The wiring diagram is shown in figure 94. When the device is addressed and R/$\overline{W}$ is low the states of the data lines D_0 to D_5 are stored. Lines D_0 to D_3 specify the hexadecimal number that is to be displayed, lines D_4 and D_5 tell which position the number is to be displayed at. It requires four write cycles to completely alter the display. An alternating back-plane output is fed to four CMOS exclusive - OR gates. These gates determine which of the three decimal points and colon are to be made visible. Closing the appropriate switch turns a symbol on, opening the switch turns the symbol off.

8.3.3.6 The digital to analogue converter

An analogue output for a chart recorder is created using a 10 bit microprocessor compatible National Semiconductor DAC 1000 digital to analogue converter (DAC). The operation and timing requirements are described in the manufacturer's data book[81]. The DAC is arranged to appear at locations 9189_{16} and $918A_{16}$ in memory, see figure 95. The analogue output is updated by first writing the least significant 8 bits into 9189_{16} and then writing the most significant 2 bits into $918A_{16}$. The second write operation causes the 10 bit word to be turned into an analogue level within 3μs. A National Semiconductor LH0071 generates a 10.24V reference voltage. The magnitude of 1 LSB is $10.24/2^{10}$ = 10mV. The inverting voltage to current converter turns a full scale input of $03FF_{16}$ into a full scale output of -10.23V.

8.3.4 Comments

The major reason for designing this specialised hardware was the potential reduction in software cycle time. Running almost identical software, the maximum cycle time using the AIM 65 was 29 ms

Figure 95. The digital to analogue converter.

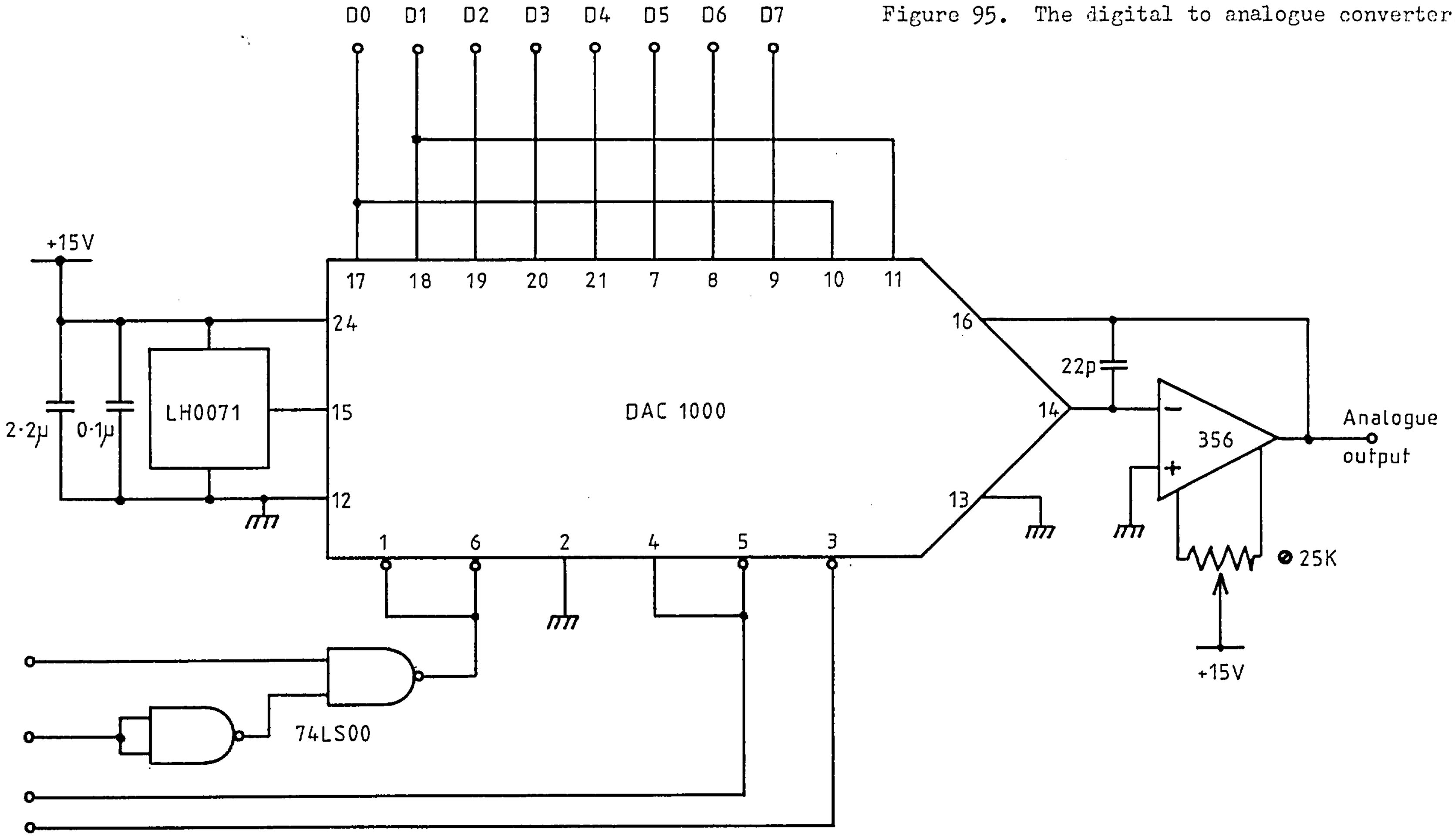

whereas the maximum cycle time on the new hardware was 6.0 ms, a 480% improvement in efficiency. A point not to be dismissed lightly is that a Cubit microcomputer board is about $\frac{1}{4}$ of the price of an AIM 65. The other reason for the design was the urge to build a more compact instrument. The photographic plates in figures 96 and 97 show that this object was achieved too. Figure 96 shows the switched gain amplifier plus filter and the microcomputer. Figure 97 shows the ~~innards~~ contents of the digital and the analogue enclosures. It can be seen that the microcomputer is constructed on two main boards. The lower of the two is the microprocessor board and the upper board, with its rider, is the input/output board.

Figure 96. The innards of the analogue and digital enclosures.

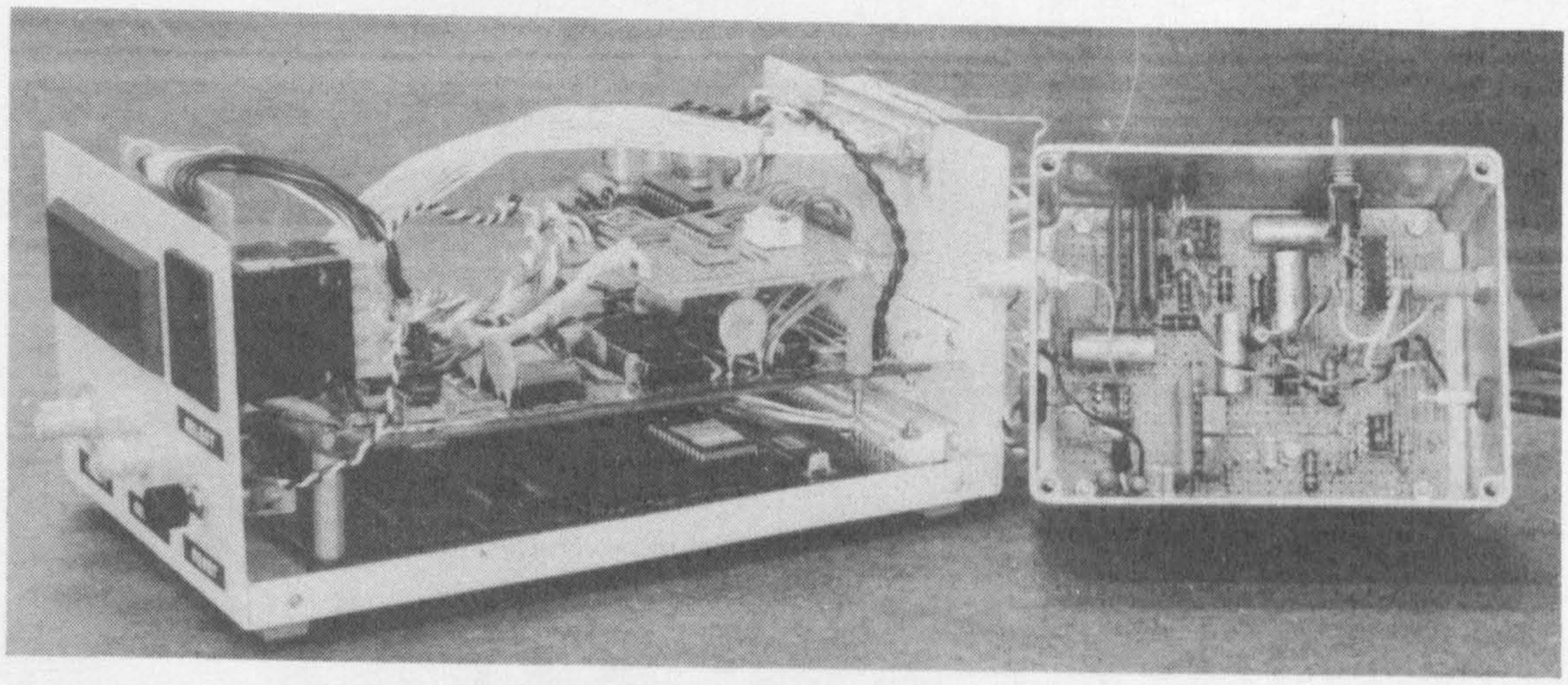

Figure 97. The appearance of the switched gain amplifier and filter

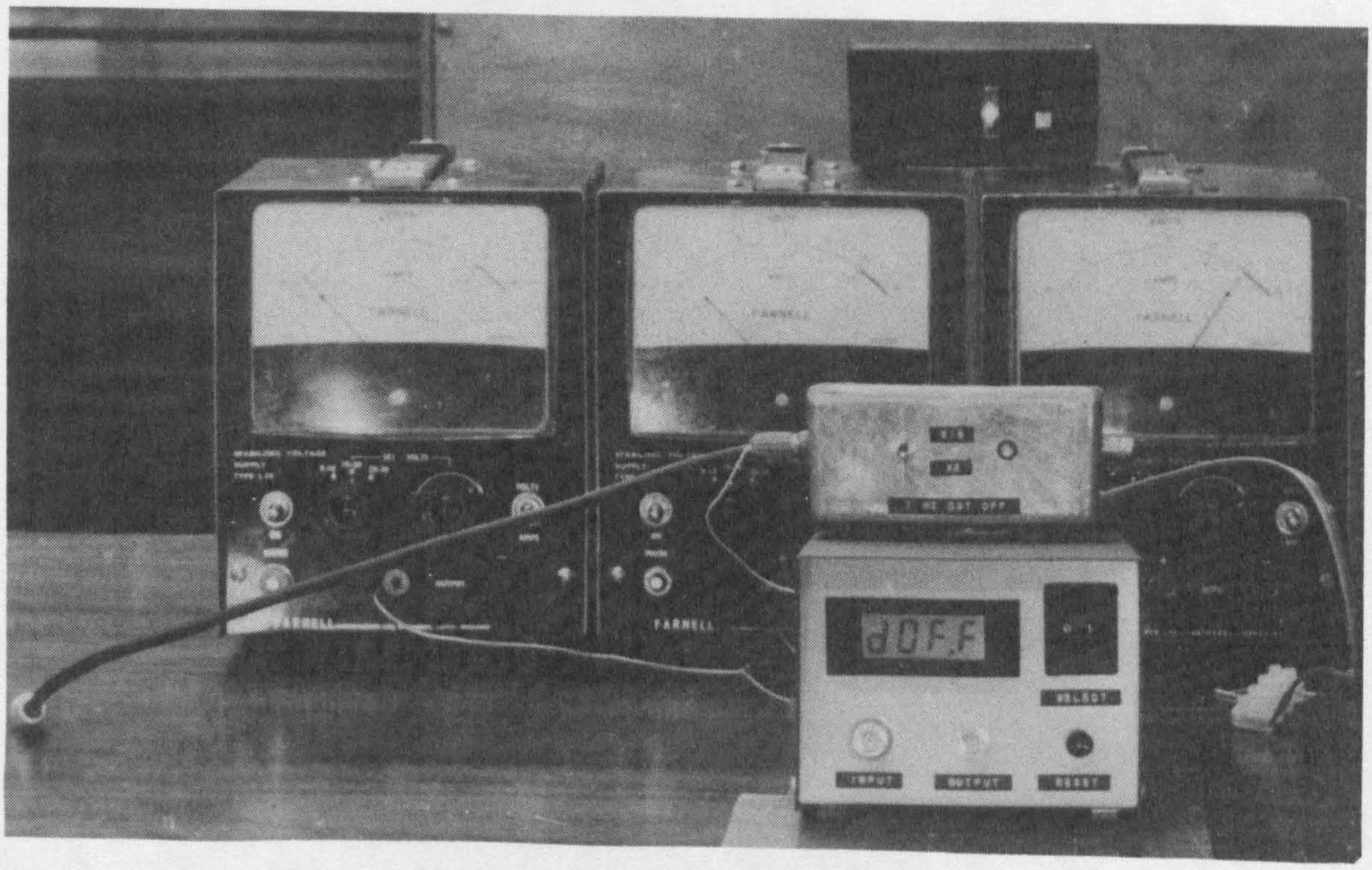

CHAPTER 9

SOFTWARE FOR THE NON-CONTACT DISPLACEMENT TRANSDUCER

9.1 INTRODUCTION

This chapter describes the software for the non-contact displacement transducer. The chapter is split into two parts. The first part is devoted to general aspects of the software design and the second part describes the program itself. The program code is listed and annotated in appendix 2. The code will run only on a 6502 microprocessor, but the description and flowcharts that define the code will much simplify the task of implementing the program on another microprocessor.

9.2 AN OVERVIEW OF THE SOFTWARE DESIGN

9.2.1 The 6502 microprocessor

The 6502 has enjoyed a lot of success and it is currently used in many microcomputers. It is an old device in microprocessing terms, but it has worn well and it is still being built into new designs. Enhanced CMOS versions of it have appeared and these guarantee that it will remain popular for some years to come.

Figure 98 shows the model of the 6502 that is used by the programs. Figure 99 lists the memory addressing modes that are available and figure 100 displays the microprocessor's instruction set. All three figures are taken from Rockwell International data sheets. A few notes on the 6502's features are made below.

The 6502 has an efficient pipelined architecture. Many instruction execution cycles consist of fetching an instruction from memory, decoding the instruction and then fetching the data or address on which the instruction is to operate. Pipelining means that instruction decoding and data, or address, fetching are going on simultaneously. This makes the best use of the slow address and

Figure 98. A 6502 programming model.

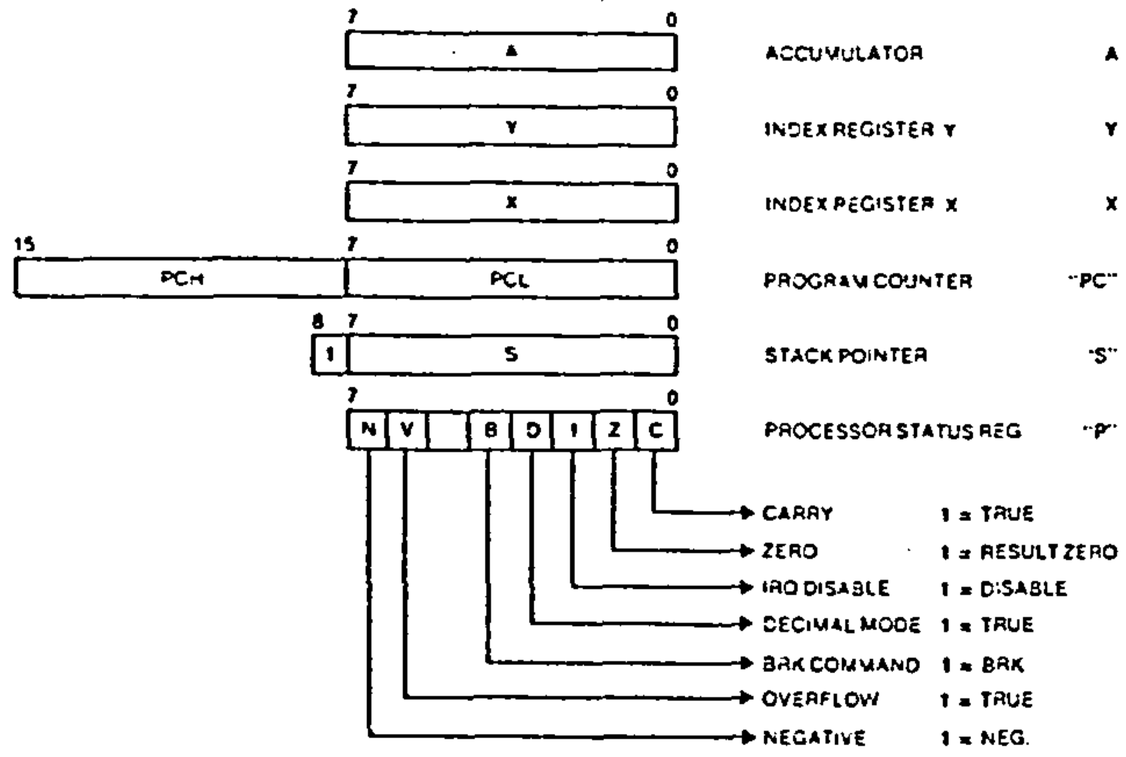

Figure 99. A list of memory addressing modes.

The R6500 features 13 addressing modes. The first byte of each instruction is the operation code specifying both the instruction and the addressing mode. The addressing modes are summarized below.

- ACCUMULATOR ADDRESSING – A one byte instruction, operating on the accumulator.
- IMMEDIATE ADDRESSING – The operand is in the second byte of the instruction.
- ABSOLUTE ADDRESSING – The second and third bytes of the instruction specify the effective address in 65K bytes of addressable memory.
- ZERO PAGE ADDRESSING – Allows shorter code and execution times by assuming a zero page address.
- INDEXED ZERO PAGE ADDRESSING (X or Y, indexing.) – Zero page addressing used with an index register.
- INDEXED ABSOLUTE ADDRESSING (X or Y, indexing) – Absolute addressing used with X or Y index registers.
- IMPLIED ADDRESSING – The register containing the operand is implicitly stated in the operation code.
- RELATIVE ADDRESSING – Used only with branch instructions. The second byte is an "Offset" added to the contents of the program counter.
- INDEXED INDIRECT ADDRESSING – Uses an indirect zero page address indexed by X to fetch the effective address.
- INDIRECT INDEXED ADDRESSING – Uses a zero page address to fetch the effective base address to be indexed by Y.
- ABSOLUTE INDIRECT – Used only with JMP, the second and third bytes point to a two-byte effective address.

Figure 100. The 6502 instruction set.

		Execution Time (clock cycles)												
		Accumulator	Immediate	Zero Page	Zero Page, X	Zero Page, Y	Absolute	Absolute, X	Absolute, Y	Implied	Relative	(Indirect, X)	(Indirect), Y	Absolute Indirect
ADC	Add Memory to Accumulator with Carry	•	2	3	4	•	4	4*	4*	•	•	6	5*	•
AND	"AND" Memory with Accumulator	•	2	3	4	•	4	4*	4*	•	•	6	5*	•
ASL	Shift Left One Bit (Memory or Accumulator)	2	•	5	6	•	6	7	•	•	•	•	•	•
BCC	Branch on Carry Clear	•	•	•	•	•	•	•	•	•	2**	•	•	•
BCS	Branch on Carry Set	•	•	•	•	•	•	•	•	•	2**	•	•	•
BEQ	Branch on Result Zero	•	•	•	•	•	•	•	•	•	2**	•	•	•
BIT	Test Bits in Memory with Accumulator	•	•	3	•	•	4	•	•	•	•	•	•	•
BMI	Branch on Result Minus	•	•	•	•	•	•	•	•	•	2**	•	•	•
BNE	Branch on Result not Zero	•	•	•	•	•	•	•	•	•	2**	•	•	•
BPL	Branch on Result Plus	•	•	•	•	•	•	•	•	•	2**	•	•	•
BRK	Force Break	•	•	•	•	•	•	•	•	•	•	•	•	•
BVC	Branch on Overflow Clear	•	•	•	•	•	•	•	•	•	2**	•	•	•
BVS	Branch on Overflow Set	•	•	•	•	•	•	•	•	•	2**	•	•	•
CLC	Clear Carry Flag	•	•	•	•	•	•	•	•	2	•	•	•	•
CLD	Clear Decimal Mode	•	•	•	•	•	•	•	•	2	•	•	•	•
CLI	Clear Interrupt Disable Bit	•	•	•	•	•	•	•	•	2	•	•	•	•
CLV	Clear Overflow Flag	•	•	•	•	•	•	•	•	2	•	•	•	•
CMP	Compare Memory and Accumulator	•	2	3	4	•	4	4*	4*	•	•	6	5*	•
CPX	Compare Memory and Index X	•	2	3	•	•	4	•	•	•	•	•	•	•
CPY	Compare Memory and Index Y	•	2	3	•	•	4	•	•	•	•	•	•	•
DEC	Decrement Memory by One	•	•	5	6	•	6	7	•	•	•	•	•	•
DEX	Decrement Index X by One	•	•	•	•	•	•	•	•	2	•	•	•	•
DEY	Decrement Index Y by One	•	•	•	•	•	•	•	•	2	•	•	•	•
EOR	"Exclusive OR" Memory with Accumulator	•	2	3	4	•	4	4*	4*	•	•	6	5	•
INC	Increment Memory by One	•	•	5	6	•	6	7	•	•	•	•	•	•
INX	Increment Index X by One	•	•	•	•	•	•	•	•	2	•	•	•	•
INY	Increment Y by One	•	•	•	•	•	•	•	•	2	•	•	•	•
JMP	Jump to New Location	•	•	•	•	•	3	•	•	•	•	•	•	5
JSR	Jump to New Location saving Return Address	•	•	•	•	•	6	•	•	•	•	•	•	•
LDA	Load Accumulator with Memory	•	2	3	4	•	4	4*	4*	•	•	6	5*	•
LDX	Load Index X with Memory	•	2	3	•	4	4	•	4*	•	•	•	•	•
LDY	Load Index Y with Memory	•	2	3	4	•	4	4*	•	•	•	•	•	•
LSR	Shift Right One Bit (Memory or Accumulator)	2	•	5	6	•	6	7	•	•	•	•	•	•
NOP	No Operation	•	•	•	•	•	•	•	•	2	•	•	•	•
ORA	"OR" Memory with Accumulator	•	2	3	4	•	4	4*	4*	•	•	6	5*	•
PHA	Push Accumulator on Stack	•	•	•	•	•	•	•	•	3	•	•	•	•
PHP	Push Processor Status on Stack	•	•	•	•	•	•	•	•	3	•	•	•	•
PLA	Pull Accumulator from Stack	•	•	•	•	•	•	•	•	4	•	•	•	•
PLP	Pull Processor Status from Stack	•	•	•	•	•	•	•	•	4	•	•	•	•
ROL	Rotate One Bit Left (Memory or Accumulator)	2	•	5	6	•	6	7	•	•	•	•	•	•
ROR	Rotate One Bit Right (Memory or Accumulator)	2	•	5	6	•	6	7	•	•	•	•	•	•
RTI	Return from Interrupt	•	•	•	•	•	•	•	•	6	•	•	•	•
RTS	Return from Subroutine	•	•	•	•	•	•	•	•	6	•	•	•	•
SBC	Subtract Memory from Accumulator with Borrow	•	2	3	4	•	4	4*	4*	•	•	6	5*	•
SEC	Set Carry Flag	•	•	•	•	•	•	•	•	2	•	•	•	•
SED	Set Decimal Mode	•	•	•	•	•	•	•	•	2	•	•	•	•
SEI	Set Interrupt Disable Status	•	•	•	•	•	•	•	•	2	•	•	•	•
STA	Store Accumulator in Memory	•	•	3	4	•	4	5	5	•	•	6	6	•
STX	Store Index X in Memory	•	•	3	•	4	4	•	•	•	•	•	•	•
STY	Store Index Y in Memory	•	•	3	4	•	4	•	•	•	•	•	•	•
TAX	Transfer Accumulator to Index X	•	•	•	•	•	•	•	•	2	•	•	•	•
TAY	Transfer Accumulator to Index Y	•	•	•	•	•	•	•	•	2	•	•	•	•
TSX	Transfer Stack Pointer to Index X	•	•	•	•	•	•	•	•	2	•	•	•	•
TXA	Transfer Index X to Accumulator	•	•	•	•	•	•	•	•	2	•	•	•	•
TXS	Transfer Index X to Stack Pointer	•	•	•	•	•	•	•	•	2	•	•	•	•
TYA	Transfer Index Y to Accumulator	•	•	•	•	•	•	•	•	2	•	•	•	•

*Add one cycle if indexing across page boundary
**Add one cycle if branch is taken, and one additional cycle if branching operation crosses page boundary

data busses and reduces program execution times.

The 6502 is a memory mapped device. This means that there are no specific input/output instructions to activate devices which communicate with the outside world. Instead, displays, keyboards and so on appear as addresses in memory - this has already been seen in the hardware design. The advantages of this scheme are that it is simple and that the full power of the microprocessor can be brought to bear on input/output data handling. Klingman(82,282) has more to say on the matter.

Microprocessors spend much of their time simply moving data from place to place, this makes the flexible memory addressing modes on the 6502 very valuable. Some of these modes may be indexed. The index is stored in an internal register and it is then used as a memory pointer with a variable offset from a fixed memory address. By incorporating indexed addressing within an instruction loop that increments the index, large chunks of memory may be moved or processed with a minimum of effort from the programmer. The zero page addressing mode is useful because it assumes that an address is somewhere within the first 256 bytes of memory. This assumption eliminates one of the two memory fetch cycles of direct addressing, thus both execution time and memory consumption are reduced. Klingman(82,267) discusses addressing modes in some detail.

Referring to figure 98, the status register contains test flags that may be set or reset depending on the microprocessor's recent history. These flags allow conditional program branching and they are the source of a computer's power. The 6502 has a powerful set of flags. Of particular interest is the break (BRK) command flag. The flag is set if a BRK instruction in software forces the microprocessor to interrupt what it was doing. This

instruction and its signalling flag aid software debugging. Using a software development system, matters may be arranged such that on detecting a software BRK instruction the microprocessor prints out the contents of its key registers. The designer can then check whether the microprocessor is running the course he hoped it would.

9.2.2 Software development

The Rockwell AIM 65 microcomputer was used as a 6502 software development system. The AIM 65's monitor permitted the use of mnemonic instruction names rather than the less comprehensible machine code symbols. The monitor also provided simple software debugging aids and took care of a keyboard, a display, a printer and a cassette tape recorder. The hardware input/output board described in chapter 8 was designed to be plugged directly into the AIM 65's address, data and control busses. When the software had been developed and checked, the input/output board was unplugged from the AIM 65 and connected to the CUBIT microcomputer board. The completed software was loaded into an EPROM which was inserted into a socket on the CUBIT board. The instrument was then complete.

Writing a fairly large program in a low level language is complex and prone to error. Leventhal[83,238] weighs up the ingredients of good programming discipline. The software was written by first defining the task on a large scale and then breaking it down into a number of modular units. A master flowchart was drawn up to define the order in which these modules were to be performed. Then each module was itself closely defined and broken down into a detailed flowchart that could be turned into mnemonic program code. The modules were tested and debugged separately because this limited the complexity of the problems encountered. Assembling the modules into one program was quite easy because the structure imposed by the

master flowchart ensured that each module worked happily with its neighbours. Three programming rules were observed as far as possible:

1. Each conditional test should have a definite result.
2. Unconditional jumps should be avoided.
3. Each module should have just one entrance and one exit.

If followed to the letter, rules 2 and 3 ensure that there is only one path between any two system states S_1 and S_2, corresponding to points P_1 and P_2 in the programme. Rule 1 ensures that this path will be clearly marked.

9.2.3 The master flowchart

A set of flowchart symbols are defined in figure 101. Before describing the master flowchart, it is worth recalling that a calibration curve of the magnetometer's output against the magnet's displacement is stored as a table in memory. Though the exact co-ordinates of the curve are known only at a few points along its length, the curve between these points will be recovered by interpolation. If the magnet and magnetometer are ever changed, all that has to be altered is the calibration table. The instrument must therefore provide calibration facilities.

The master flowchart is shown in figure 102. When the reset button is pushed, or power is switched on, the microprocessor jumps to the start of the program. The program first makes the microprocessor initialise its status register and store spaces. The settings of the two thumbwheel switches are then examined. One thumbwheel switch indicates the user's choice of sampling rate, the other switch tells whether the displacement or calibration mode has been selected. There is considerable room for expansion here because up to 16 sample rates and 16 programs could be decided between, but

Figure 101. Flowchart symbol definitions.

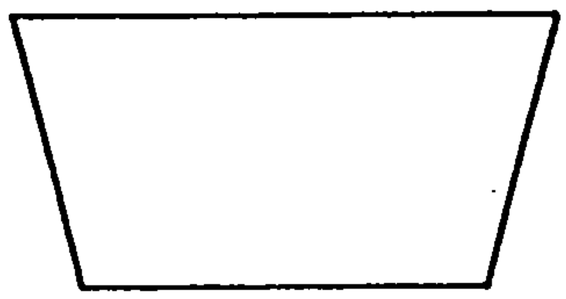

Input or output

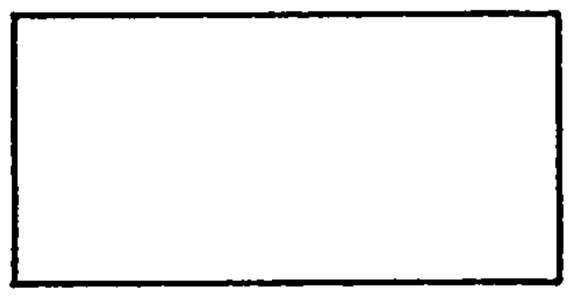

Control, arithmetic, or data movement

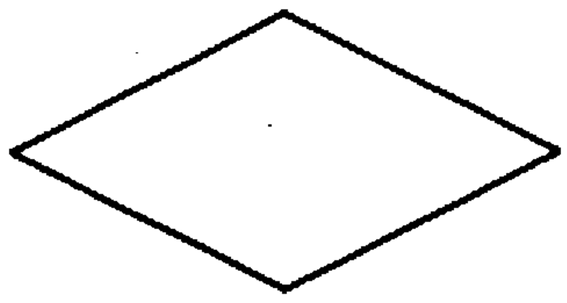

Decision

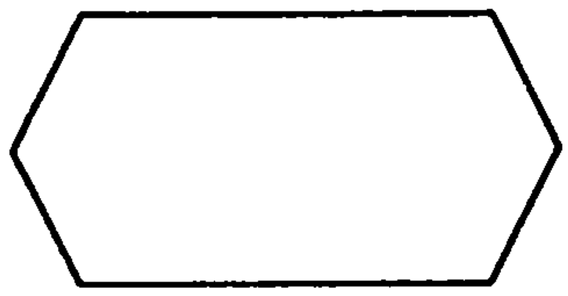

Subroutine

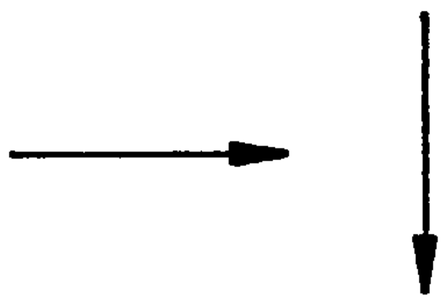

Program flow

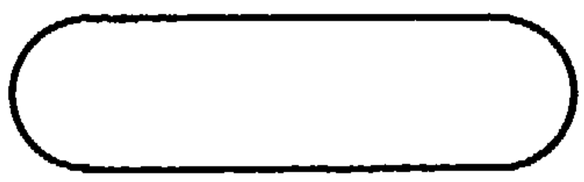

Start, stop, entrance or exit

Figure 102. The master flowchart.

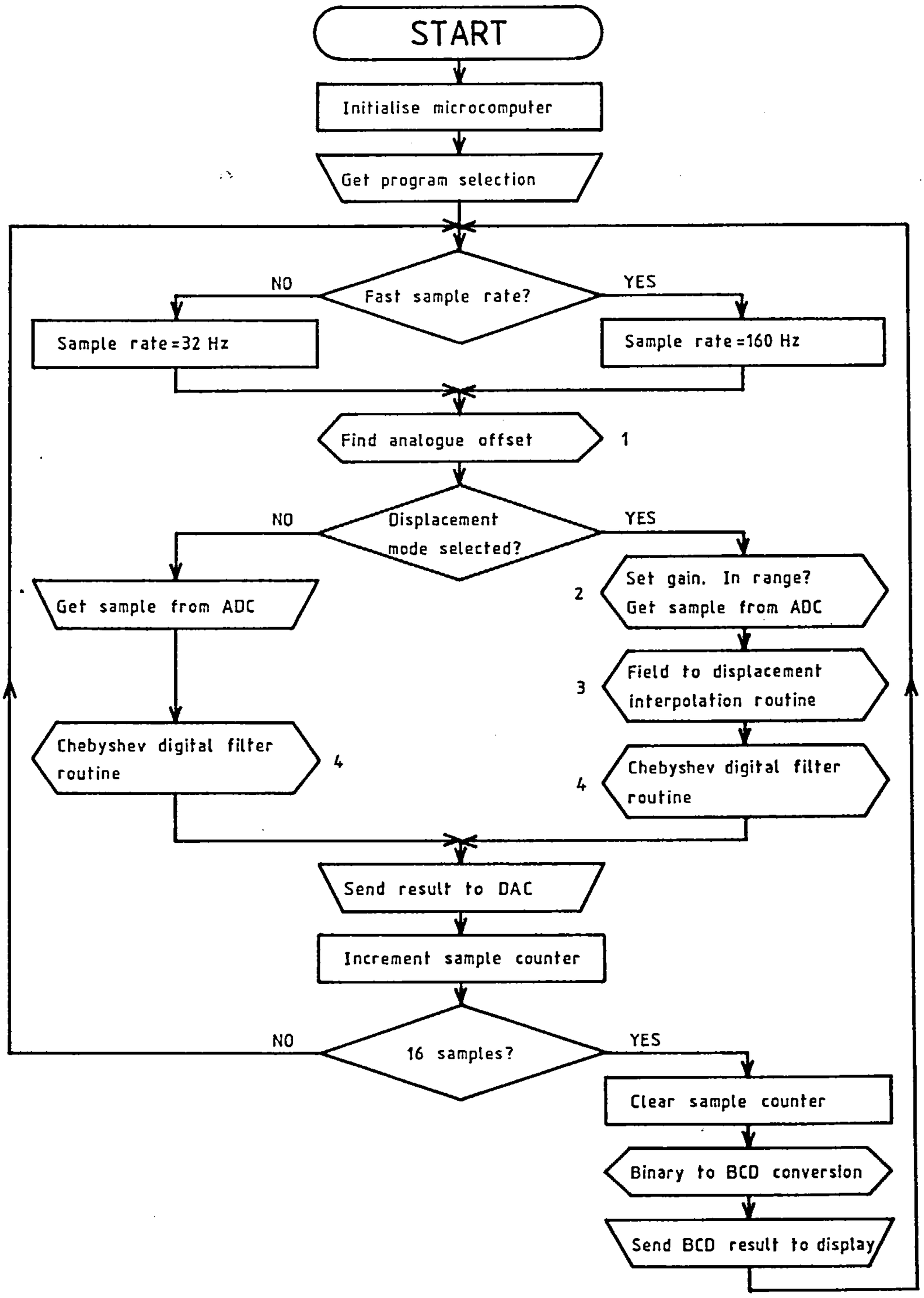

two of each is sufficient to show the principle. The switches could also be used to pass calibration data to the microprocessor.

Subroutine 1 compensates for long term drifts in the analogue circuitry or changes in the ambient magnetic environment. The subroutine assumes that the magnet is sited at its maximum useful displacement. The analogue gain is automatically set to 16 and the digitized output of the magnetometer is averaged over 256 samples. This average is compared with the expected output that was obtained while calibrating the instrument. The difference represents a shift in offset and is accounted for in subsequent calculations. The offset pertaining to a gain of 2 is exactly 1/8 of the previous result.

Assuming that the displacement mode is selected, the function of subroutine 2 is to find the best amplifier gain and to check that valid measurements can be made. The choice of gain is based upon the magnetometer's output, a weak signal requires a high gain and a strong signal requires a low gain. The high-to-low and low-to-high gain thresholds are offset to produce hysterysis, see figure 103. This prevents random noise causing repeated changes of gain when the magnetometer's output is close to the gain transition region. A delay is added to allow the analogue filter to settle after a change in gain. Subroutine 2 also checks that the magnet is in a valid measurement range by seeing if the magnetometer's output is too large or too small. If either of these conditions is detected, the operator is informed accordingly. No measurements will be made until the condition is rectified; when it is rectified measurements recommence automatically.

The program now has a valid sample which subroutine 3 can use to make a new estimate of displacement. The subroutine first selects either the high gain or the low gain calibration table.

Figure 103. A diagram relating the actions of subroutine 2 to displacement.

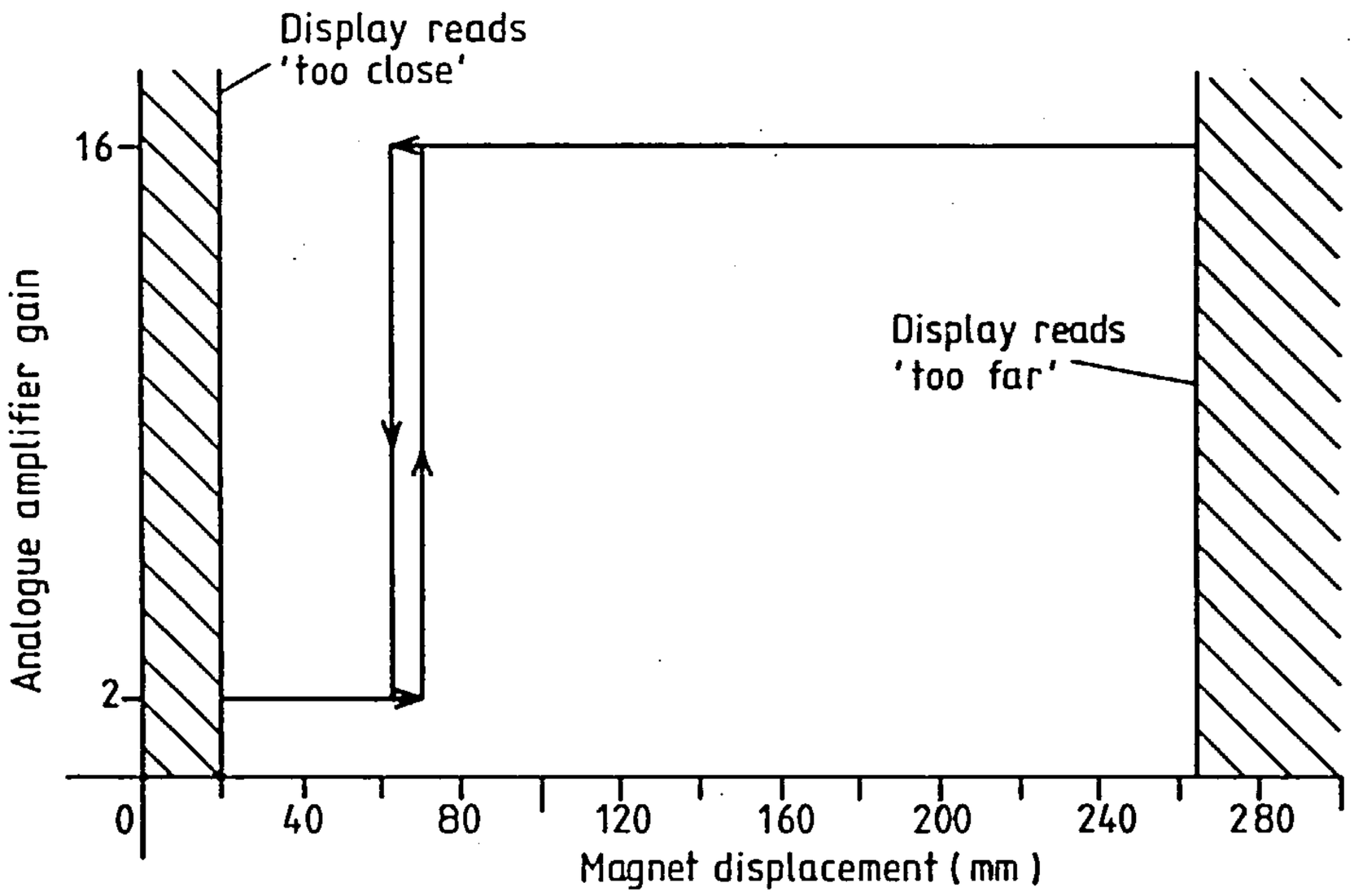

It calculates an offset into the table chosen and picks out the relevant displacement data. Newton's second order forward difference interpolation method is then used to calculate the displacement.

The new estimate of displacement is placed into a 16 bit digital filter. The filter attenuates the high frequency noise components and determines the instrument's bandwidth. The filter has the amplitude characteristic of a second order low pass Chebychev filter with 0.5dB ripple in the passband. Its -3dB cut off frequency is $f_s/32$ Hz where f_s is the sampling frequency; the dependence of a digital filter's cut off frequency on the sampling rate can be useful.

It now remains to display the filtered result before repeating the cycle. The most significant 10 bits of the binary result are sent to the DAC in each cycle. This permits a proper reconstruction of the magnet's motion. The liquid crystal display is updated once every 16 cycles. An algorithm is used to convert the result from binary to binary coded decimal (BCD) before it is passed to the display. The instrument now loops back to make another measurement.

Now let's go back to the middle of the program to see what happens if the user wants to calibrate the instrument. The program's course is similar to that just described. The user manually sets the amplifier's gain and then moves the magnet through a series of known displacements. The instrument, now acting as a voltmeter with a filter, gives the value of the magnetometer's output at each position. This generates a calibration table which can be loaded into an EPROM.

The reader may be wondering why the digital filter was placed after the interpolation subroutine rather than before. To answer this, consider what happens if the filter is placed before the

interpolation subroutine. A change in the amplifier's gain will then present the digital filter with a voltage step. This would be a nuisance because of the filter's poor settling behaviour. More subtly, the magnet velocity that could be successfully followed would be greater at large displacements than at small displacements. For a given magnet velocity, the rate of change of magnetometer output increases dramatically as the displacement decreases. The slew rate of the filter is fixed and is increasingly less able to follow the accelerating change at its input. Both problems have been avoided by placing the filter after the subroutine. There are two more points to make about this. As the filter is used to generate data for the look up table and then to filter data from the look up table, it must have a d.c. gain that is very close to unity to avoid creating systematic errors. Secondly, the random noise from the magnetometer should have a Gaussian probability density function and therefore a zero mean value. After interpolation to a non-linear characteristic, the noise will no longer have a Gaussian probability density function and will not have a zero mean. Passing the interpolated noise through a linear filter will therefore create an offset. Fortunately, for normal noise amplitudes the conversion looks sufficiently linear for the offset to be well below the accuracy of the arithmetic.

Finally, it is interesting to compare the speed of a BASIC program with one written in mnemonic code. The digital filter subroutine was written in both languages. The BASIC version had an execution time of 71.2 ms, the mnemonic version was 29.1 times faster at 2.45 ms. The pains taken to write everything in mnemonic code were well rewarded.

9.3 DETAILS OF THE SOFTWARE DESIGN

The detailed description of the software is broken down into

smaller sections called modules and larger sections called sub-routines. In the main, these correspond to the contents of the blocks on the master flowchart. The last piece to be presented is the controller routine which corresponds to the master flowchart itself. A listing of the code is given in appendix 2.

It will be remembered that memory referencing instructions have shorter execution times if the location they address is in page 0 - the first 256 bytes of memory. To exploit this, all of the microprocessor's temporary arithmetic and control stores are located in page 0. There is no shortage of store space so each location is devoted to just one variable. A page 0 memory map is shown in figure 104, the labels will be given meanings as this section progresses. All addresses are given in hexadecimal.

9.3.1 The analogue to digital conversion module

The subroutine assumes that the counter/timer T1 in the 6522 versatile interface adaptor has been configured by the controller routine to run continuously as a sample clock. At the beginning of each cycle T1 sets a flag in the 6522's interrupt flag register at address 900D. This subroutine waits until the flag is set, it then initiates a conversion and leaves the microprocessor to twiddle its thumbs while the ADC does its job. It next clears the flag ready for the following cycle. The most significant 8 bits of the result are taken from 9180 and loaded into 0001. The least significant 4 bits are taken from 9181 and loaded into 0000. The 12 bit result in 0001 and 0000 has four unwanted trailing zeros. These are removed by shifting the result four spaces to the right. The module is now done. A flowchart is shown in figure 105.

9.3.2 The binary to BCD conversion module

The purpose of this module is to convert a 12 bit binary

Figure 104. A page 0 memory map. All the hexadecimal addresses are preceded by 00.

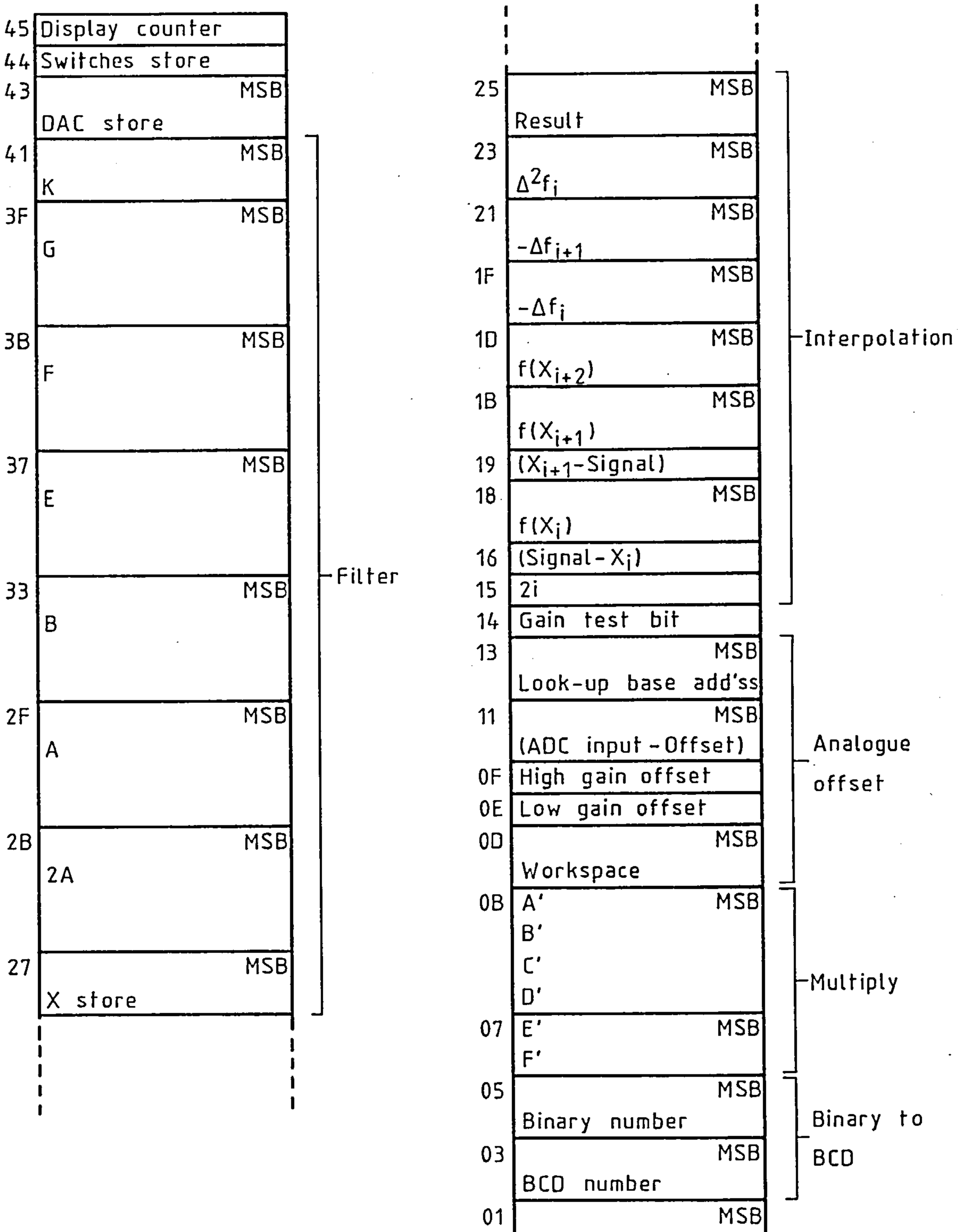

Figure 105. The analogue to digital conversion module.

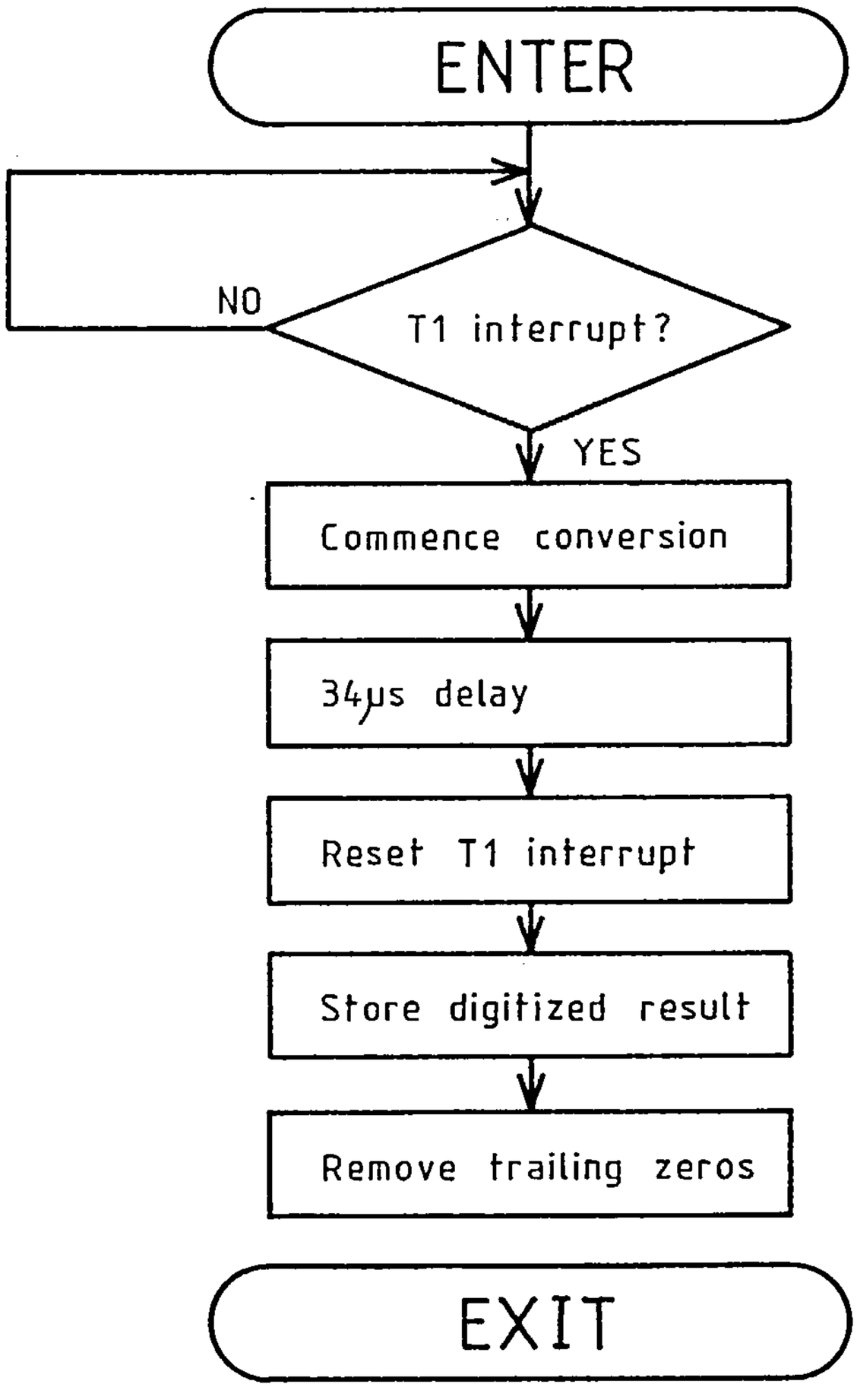

number in 0005 and 0004 into a two byte binary coded decimal (BCD) number in 0003 and 0002. The algorithm used is described in detail by Peatman[84,400]. An 8 bit binary number BNUM has a decimal value of

$$BNUM = b_7 \times 2^7 + b_6 \times 2^6 + b_5 \times 2^5 + ... \qquad (9.1)$$

where b_n refers to a bit. Equation 9.1 can be rewritten as

$$BNUM = ((((((b_7\ 2 + b_6)2 + b_5)2 + b_4)2 + b_3)2 + b_2)2 + b_1)2 + b_o\ . \qquad (9.2)$$

If equation 9.2 is evaluated with the microprocessor set to its decimal mode, a BCD result DNUM is automatically formed. The same principle applies to turning a 12 bit BNUM into a 4 digit DNUM. Apart from this module, the microprocessor always uses binary arithmetic as this is far more efficient on a binary machine. The flowchart is shown in figure 106.

9.3.3 An unsigned binary multiply module

The purpose of this module is to multiply two unsigned 16 bit numbers to produce a 32 bit result. The module will be required by the filter and the interpolation subroutines. The program is based on an algorithm described by Peatman[84,417]. Referring to the model of the algorithm in figure 107a, the multiplier is placed in C', D' and the multiplicand in E', F'. The four bytes A', B', C' and D' are shifted right as a block. The least significant bit of D' is now in the microprocessor's CARRY slot. If CARRY = 1 the multiplicand in E', F' is added to A', B'. If CARRY = 0 there is no addition and A', B', C', D' are rotated once more. After 16 repetitions the 32 bit result resides in A', B', C', D'. The multiplicand remains unaltered in E', F'. The flowchart is shown in figure 107b.

Figure 106. The binary to BCD conversion module.

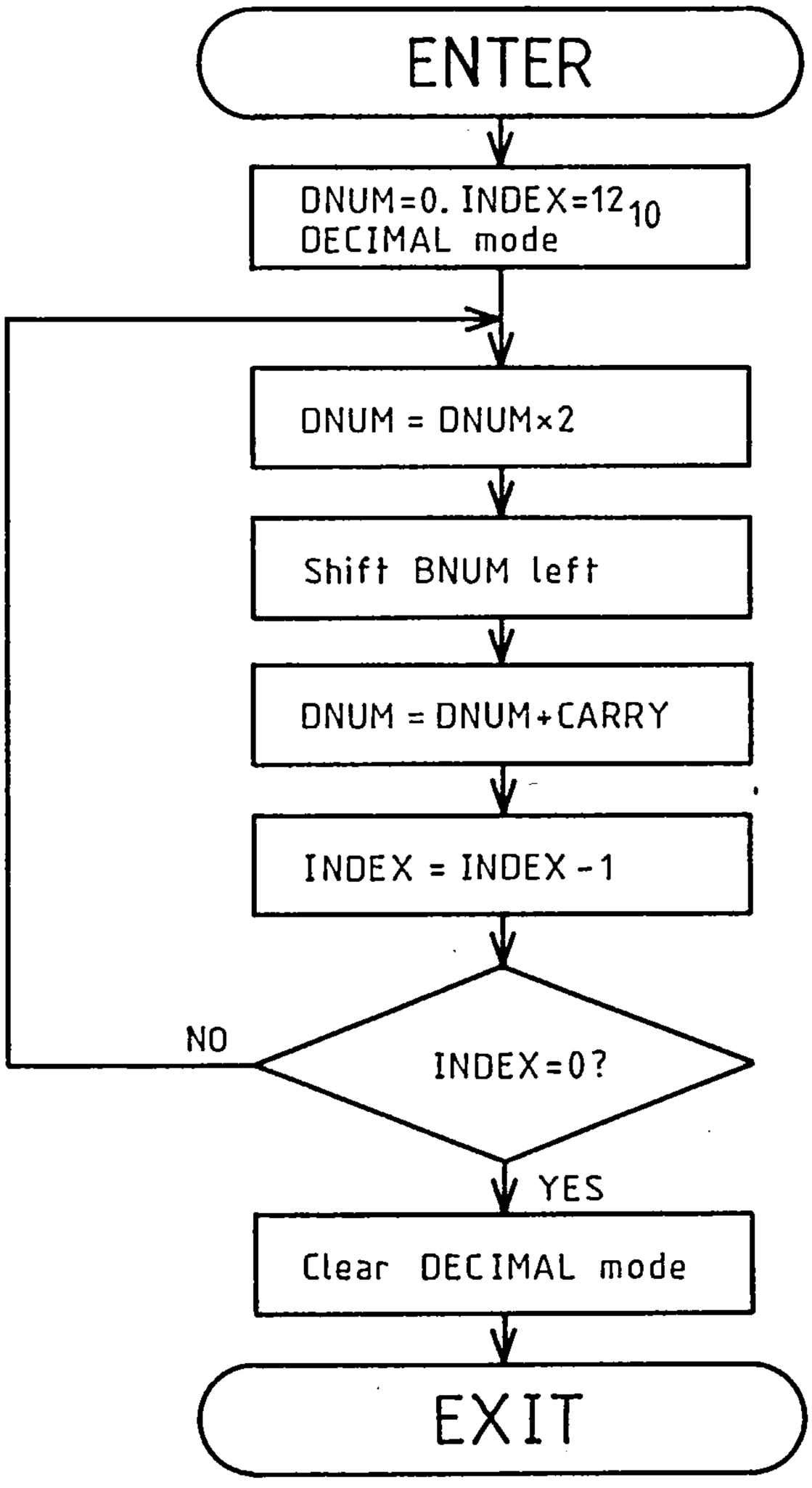

Figure 107. The 16 x 16 unsigned multiply algorithm.

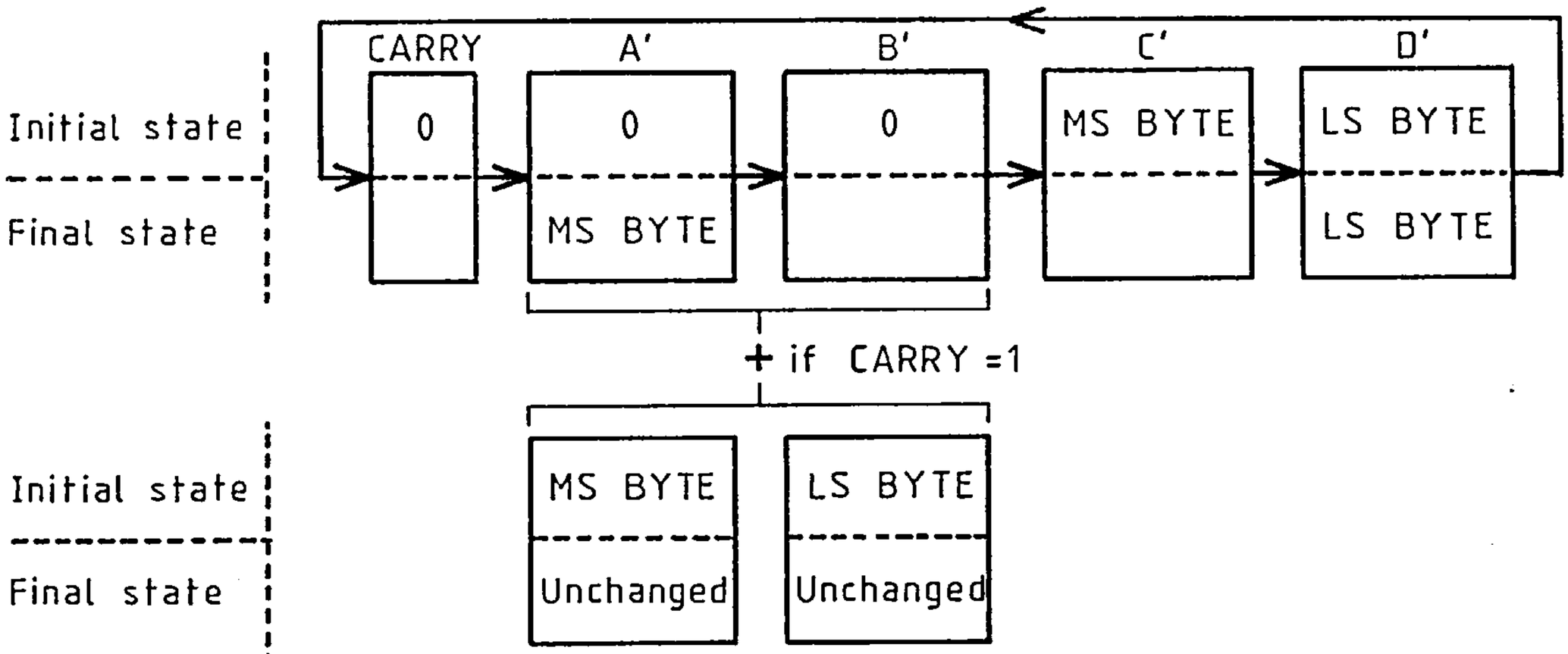

a. A model

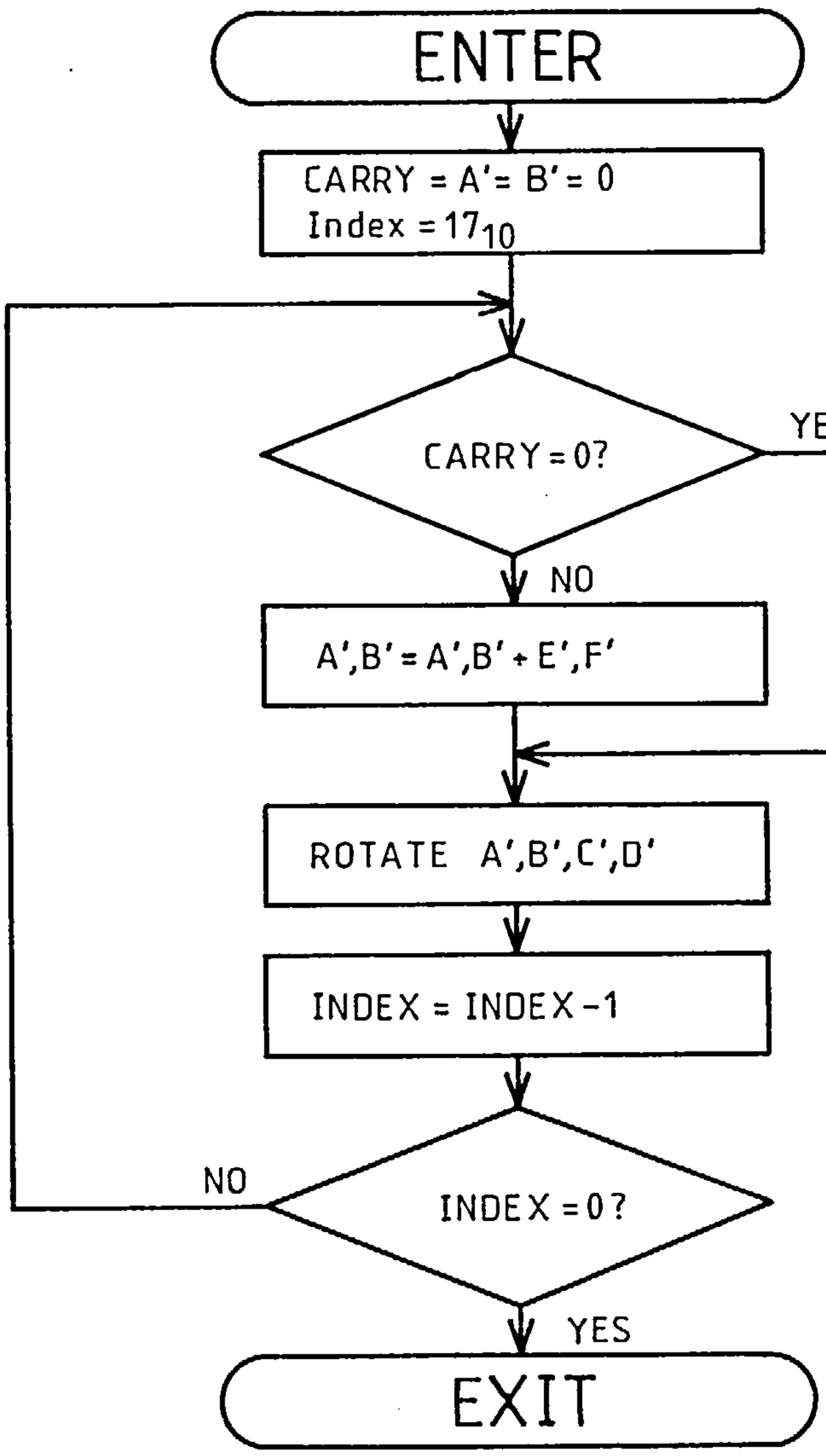

b. A flowchart

9.3.4 The analogue filter's settling delay module

This module is called by the microprocessor when it has just changed the analogue gain. The module gives the analogue filter time to settle down. The microprocessor simply counts out 35 clock cycles and then carries on where it left off. In retrospect, this module would have been better if it had accounted for the sample rate. It ought to count out more cycles on a fast sample rate than on a slow sample rate.

9.3.5 The analogue offset subroutine

This subroutine allows for drifts in the analogue circuitry or changes in the ambient magnetic field. When the instrument is calibrated the fluxgate offset compensation (figure 91) is used to adjust the output of the ADC to 128 bits with the magnet at its maximum useful displacement and with the gain at 16. When the offset subroutine is entered, the microprocessor assumes that the magnet is at its maximum displacement and it sets the gain to 16. In synchronism with the sample clock, it collects and averages 256 readings from the ADC. This operation takes upto 8 seconds, so the microprocessor writes DOFF, for device offset, on the display to let the user know what is going on. The average of the 256 readings is compared with the original result of 128 bits. The difference between the two represents the high gain's offset, the low gain's offset is exactly 1/8 of this result. Fluxgate offset changes of upto $\pm$ 19.5 mV can be accounted for. A flowchart is shown in figure 108.

9.3.6 The gain setting and range checking subroutine

The purpose of this subroutine is to choose the correct gain and to check that the magnet is not too far away or too close. The

Figure 108. The analogue offset subroutine.

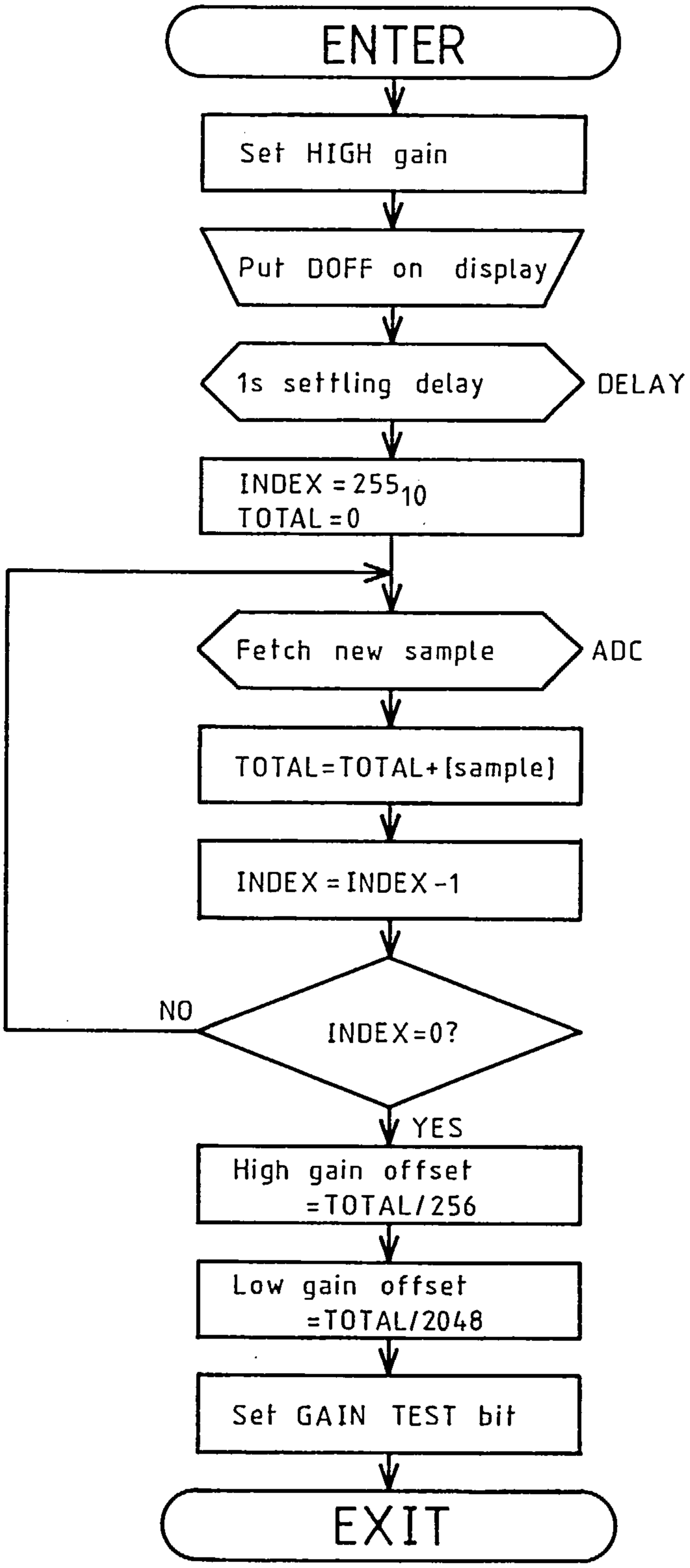

operation of the subroutine has been explained in some detail in subsection 9.2.3 and figure 103. For clarity, the flowchart in figure 109 is less detailed than the preceding flowcharts. All of the decisions in figure 109 are based on the current value of the gain and the output of the ADC. The decisions are summarised in table 10 below.

Table 10 The gain setting and range checking subroutine's decision table.

ADC output, x bits(base 10)	Current gain	Action
$x > 3,839$	Low	Signal "Too Close"
$384 \leq x \leq 3,839$	Low	Gain OK
$x < 384$	Low	Change to high gain
$x > 3,711$	High	Change to low gain
$5 \leq x \leq 3,711$	High	Gain OK
$x < 5$	High	Signal "Too Far"

9.3.7 Calibration data fetching subroutine

This subroutine needs little description. Upon command it simply fetches a sample from the ADC so that the instrument can be calibrated.

9.3.8 Field to distance interpolation subroutine

Before describing the interpolation subroutine, the reasons for using interpolation need to be mentioned. It might be thought that a calculation using the $(\text{displacement})^{-3}$ law of a magnetic dipole would be more direct and save calibration. However, this law does not work well in practice because the magnet is not a point dipole and the fluxgate sensor is far from the invisible point receiver assumed when deducing the law. Anyway, the dipole law would be of no value if a gradiometer were used (see equation 7.5), whereas an interpolation approach is unaffected by the choice

Figure 109. The gain setting and range checking subroutine.

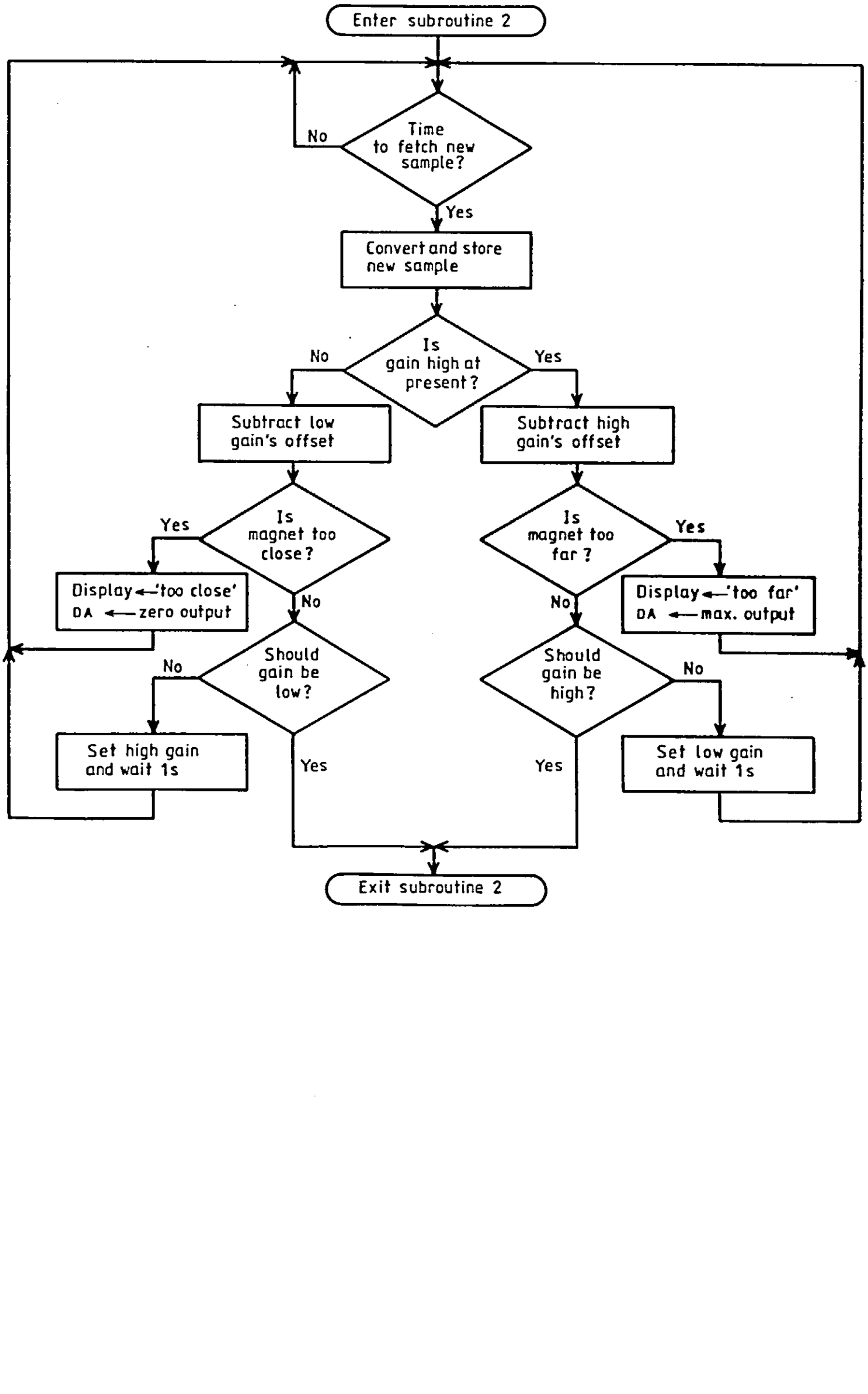

between single and differential sensors. Further, calibration and interpolation permits non-linearities in the magnetometer and allows for fixed magnetizable objects distorting the field from the magnet. Finally, computers are much more efficient at using look up tables than they are at calculating cube roots; the best way of calculating a cube root would be to use interpolation within a pre-calculated look up table. Calibration with interpolation is an accurate, flexible and efficient means of turning a magnetometer's output into a measured displacement.

Calibration generates a table of values relating the magnetometer's output x to the magnet's displacement f(x). There are two overlapping tables because there are two values of gain. Interpolation is used to estimate f(x) when x is not equal to one of the tabulated values. The tabulated values are called pivotal values or collocation points, in this case the pivotal values are evenly spaced in x. Interpolation is based on the assumption that at the x value of interest the original function f(x) can be approximated by some polynomial p(x) whose value at x can be calculated. A polynomial $p_n(x)$ of degree n is uniquely determined by its values at (n+1) points. Therefore a second order interpolation method requires 3 pivotal values. In general, a polynomial p_n is required such that

$$p_n(x_o) = f_o,\ p_n(x_1) = f_1\ ,\quad \ldots\ .\quad p_n(x_n) = f_n\ , \tag{9.3}$$

where

$$f_o = f(x_o),\ \ldots\ldots\ f_n = f(x_n)$$

are the pivotal values of f in the table.

There are many different methods of interpolation [85,774],[86,87]. They can be broken down into forward, backward and central difference

methods depending on how the necessary pivotal values are distributed around the argument x. The choice of method was decided by the form of the calibration table and the nature of the task in hand. Imagine that p_m is to be calculated for some argument $x_n \leq x < x_{n+1}$ in which the x_n are pivotal points. A forward difference method estimates f(x) by fitting $p_m(x)$ to x_n, x_{n+1} ..... x_{n+m}. A backward difference method fits $p_m(x)$ to x_{n-m+1}, x_{n-m+2}, ... x_n, x_{n+1}. A central difference method, such as Everett's formula[85,776], uses pivotal values spread evenly about x and for any order n is naturally more accurate than either of the two previous methods. Which method ought to be used? Look at figure 110. If the interpolation polynomial is of order greater than 1 neither the central nor the backward methods can estimate f(x) when x is between pivotal values 1 and 2. Both methods throw away 64 mm of the high gain table's range of 204 mm. A forward method of order greater than 1 cannot estimate f(x) when x is between points 30 and 31, but it loses only 1 mm for this. A forward difference formula is clearly the one to use.

Newton's forward difference interpolation formula is

$$f(x) \approx p_n(x) = f_o + c\,\Delta f_o + \frac{c(c-1)}{2!}\,\Delta^2 f_o \qquad (9.4)$$

$$+ \frac{c(c-1)(c-2)}{3!}\,\Delta^3 f_o + \ldots\ldots + \frac{c(c-1)\ldots(c-n+1)}{n!}\,\Delta^n f_o \ ,$$

where

$$x_o \leq x < x_1 < x_2 \ ,$$

and

$$h = x_{n+1} - x_n \ ,$$

$$x = x_o + ch \ ,$$

$$c = \frac{x - x_o}{h} \ , \quad 0 < c < h \ ,$$

$$\Delta f_o = f(x_1) - f(x_o) \ ,$$

$$\Delta^2 f_o = (f(x_2) - f(x_1)) - (f(x_1) - f(x_o)) \ .$$

Figure 110. A plot of the pivotal points in the high gain's look up table.

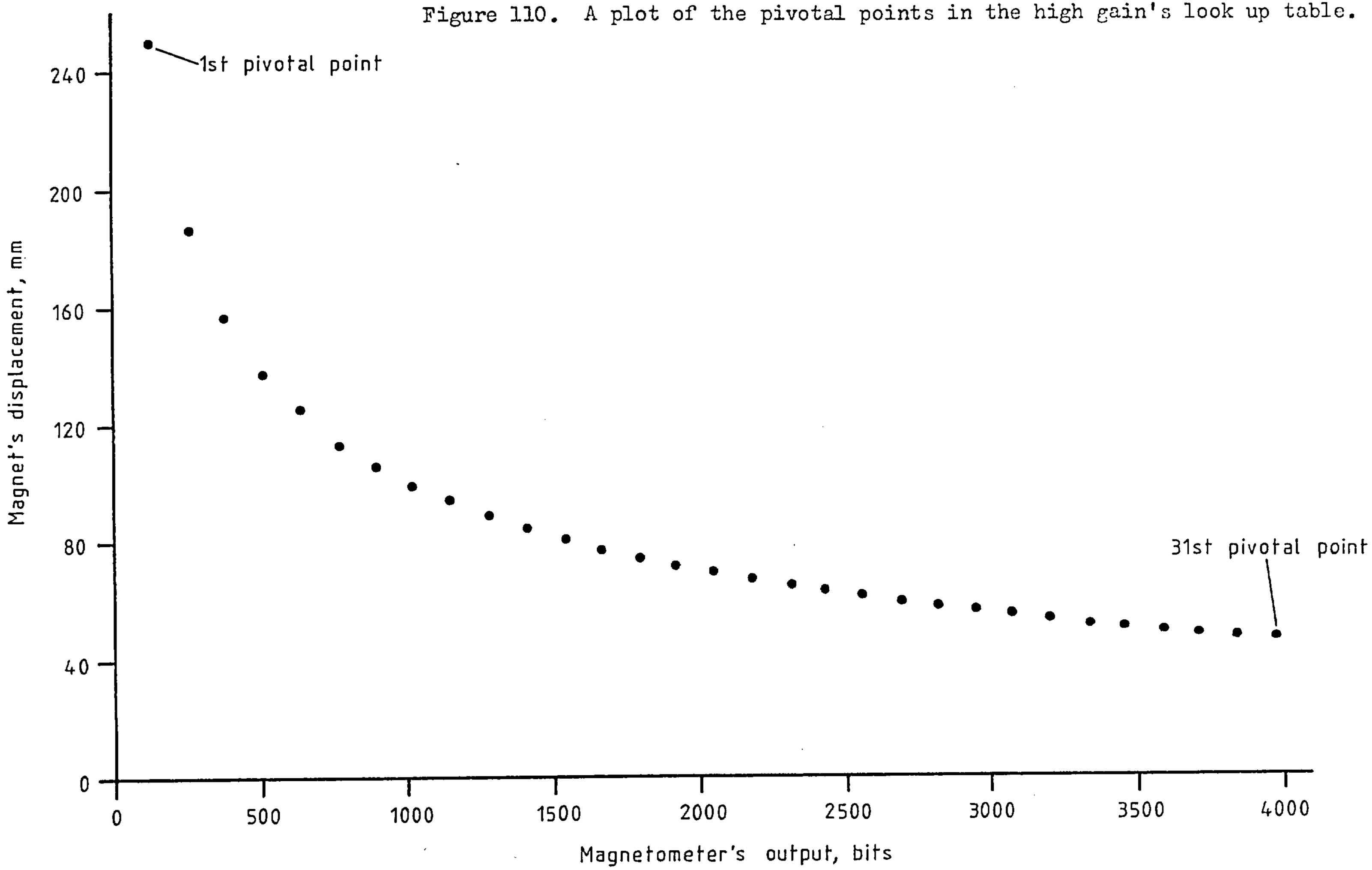

Taking the first two, three or four terms in 9.4 gives interpolation to first, second or third order respectively. The error of interpolation is reduced by increasing the order of interpolation and by decreasing the increment h. Unfortunately, the first suggestion increases computation time and the second increases the calibration effort. If f(x) is known, it is possible to calculate an upper bound to the interpolation error for any order and for any tabular increment[86,87]. To give a feeling for the accuracy of the technique, let's assume that the field/displacement characteristic is that of a true dipole:

$$r \approx \left[\frac{\mu_o M_T 2k}{V}\right]^{0.33}$$

from equation 7.4. M_T is the dipole moment of the magnet, k is the sensitivity of the magnetometer, V is the output of the magnetometer and r is the displacement. For convenience $\mu_o M_T 2k$ is set to 1,000. Table 11 is a portion of the look up table that would be generated if the spacing in V was 1 volt.

Table 11. Example look up table with 1 Volt spacing.

V	r = f(V)
1	10.0000
2	7.9370
3	6.9336
4	6.2996

Table 12 shows the accuracy of Newton's first, second and third order methods of forward interpolation when estimating f(1.5).

Table 12 Comparing the interpolated values with the true value of f(1.5) for a 1 volt spacing

	f(V)	Error, %
True value	8.7358	———
1st order	8.9685	+ 2.66
2nd order	8.8361	+ 1.15
3rd order	8.7929	+ 0.65

Table 13 is a portion of the look up table that would be generated if the spacing in V was halved.

Table 13 Example look up table with $\frac{1}{2}$ volt entry spacing

V	f(V)
1.25	9.2832
1.75	8.2983
2.25	7.6314
2.75	7.1377

Table 14, when compared with table 12, clearly shows the advantage of reducing the spacing between pivotal points.

Table 14 Comparing the interpolated values with the true value of f(1.5) for a $\frac{1}{2}$ volt spacing.

	f(V)	Error, %
True value	8.7358	———
1st order	8.7907	+0.62
2nd order	8.7510	+0.17
3rd order	8.7419	+0.07

It was decided that 2nd order interpolation should be used. This was a suitable compromise between execution time and accuracy. Seim [87]

describes how 2nd order interpolation may be implemented with an 8080 microprocessor. A few relevant points are made below.

The algorithm that is implemented is

$$f(x) \approx f(x_n) + (x-x_n)\frac{\Delta f(xn)}{h} + (x-x_n)(x-x_{n+1})\frac{\Delta^2 f(x_n)}{2h^2} \qquad (9.5)$$

where $x_n \leq x < x_{n+1}$. The table's spacing h is arranged to be 2^n bits as suggested by Seim[87]. This makes the divisions by h and h^2 in equation 9.5 very simple, for division by 2^n corresponds to n right shifts. An offset into the table has to be calculated, this acts as a pointer to the correct pivotal values for the input value of x bits. The spacing h is 128 bits. The maximum ADC output is 4096 bits, so there are 32 pivotal values (32 x 128 = 4096) in each of the high and low gain look up tables. Each pivotal value is two bytes long and so the table offset pointer is given by

$$\text{Offset pointer} = \frac{\text{ADC output value x 2}}{128} . \qquad (9.6)$$

The table's values are pulled out using indexed indirect addressing. The address of the first entry in the high or the low gain look up table is contained in addresses 0013 and 0012. The choice of table is fixed by the gain setting and range checking subroutine which alters the contents of 0013 appropriately. The microprocessor adds the table offset to the address in 0013 and 0012 to form the address of x_n, the first of the three pivotal values needed. The algorithm is arranged such that any numbers multiplied together are both positive. This ensures that the unsigned binary multiply routine can be used.

The final form of the algorithm is

$$f(x) \approx f(x_n) - (x - x_n)\frac{(f(x_n) - f(x_{n+1}))}{128} - (x - x_n)(x_{n+1} - x)\frac{((f(x_n) - f(x_{n+1})) - (f(x_{n+1}) - f(x_{n+2})))}{32,768} \qquad (9.7)$$

where

n = ADC output/128

and

table pointer = 2n.

The flowchart is shown in figure 111.

9.3.9 The digital filter subroutine

The digital filter improves the instrument's signal to noise ratio by reducing the instrument's bandwidth. Digital filters have powerful advantages in that their bandwidths are proportional to the sample rate and the filters' characteristics can be changed simply by altering some numerical constants. The instrument's sample rate is software controlled and the operator can select bandwidths of 1Hz or 5Hz. The 1Hz bandwidth rejects the most ambient noise giving the best estimates of displacement when the magnet is far away. The 5Hz bandwidth allows a more rapidly moving magnet to be followed.

In the earliest versions of the instrument a moving average filter was used. Acting on the results from the interpolation subroutine, a new output was produced by finding the mean of the current and several previous results. The filter was a simple non-recursive estimator for d.c. signals[88,87]. In this case the signal was not d.c. but varied with time, this made the frequency response of the filter important. This topic is dealt with below.

A model of the filter is shown in figure 112a. The blocks labelled z^{-1} represent a time delay of T seconds - see appendix 1. The current output y_m is formed from the present and (n - 1) previous input samples:

$$y_m = \frac{1}{n} \sum_{j=o}^{n-1} x_{m-j} \quad . \qquad (9.8)$$

Figure 111. The field to distance interpolation subroutine.

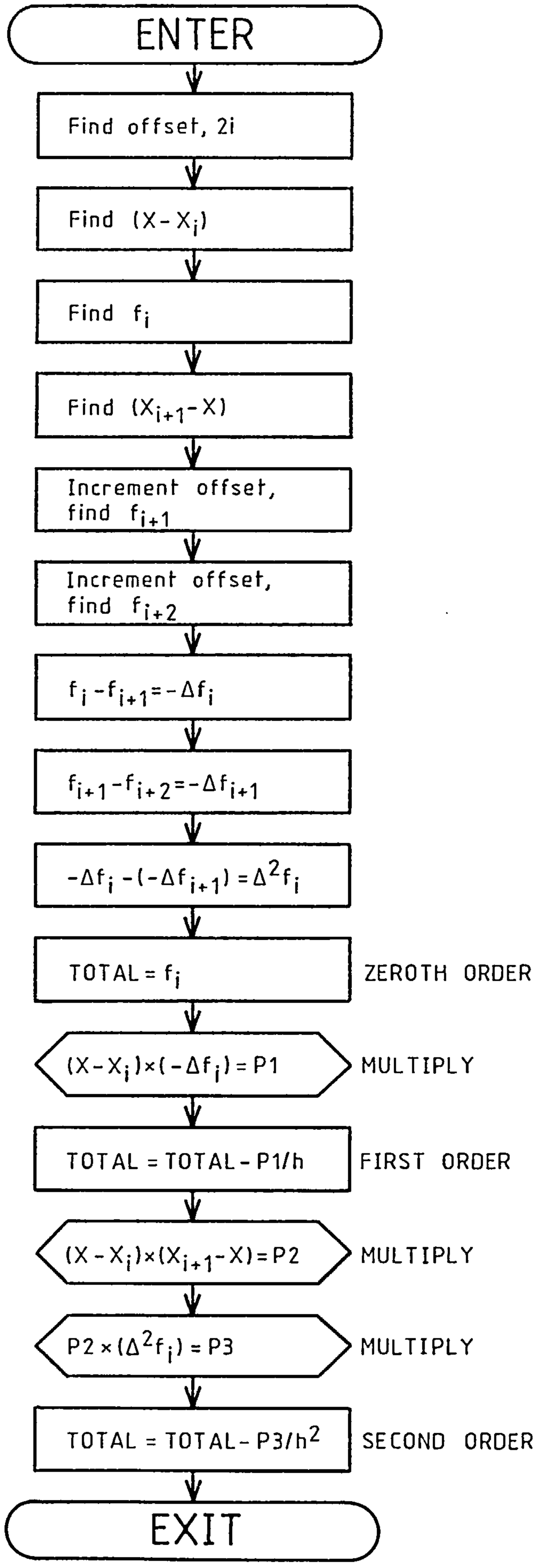

Using the z transform (see appendix 1) the filter's transfer function is

$$H(z) = \frac{Y(z)}{X(z)} = \frac{1}{n} \sum_{j=o}^{n-1} z^{-n}. \qquad (9.9)$$

From the formula for the sum of a geometric progression,

$$H(z) = \frac{1}{n} \cdot \frac{1 - z^{-n}}{1 - z^{-1}} . \qquad (9.10)$$

The frequency response is now found by substituting

$$z = \exp(jwT) \qquad (9.11)$$

which gives

$$H(jw) = \frac{1}{n} \cdot \frac{1 - \exp(-njwT)}{1 - \exp(-jwt)} . \qquad (9.12)$$

After multiplying top and bottom by $\exp(jnwT/2)$ and then by $\exp(jwT/2)$ and simplifying, the result is

$$H(jw) = \exp(-(n-1)jwT/2) \cdot \frac{\sin(nwT/2)}{n\sin(wT/2)}, \qquad (9.13)$$

which is the frequency response of the moving average filter.

The modulus of the frequency response is

$$|H(w)| = \frac{\sin(n\pi w/w_s)}{n\sin(\pi w/w_s)} , \qquad (9.14)$$

where w_s is the sampling frequency in $rads^{-1}$. The argument is

$$\theta = -\tan^{-1}\left[\frac{\sin((n-1)w\pi/w_s)}{\cos((n-1)w\pi/w_s)}\right] . \qquad (9.15)$$

In practice, n was set to 16 and the sampling frequency was 32Hz i.e. $w_s = 2\pi.32$ $rads^{-1}$. The amplitude characteristic of the filter, figure 112b, was very poor; it had no well defined pass-band or stopband and its high frequency attenuation was weak.

An improved filter design was sought. Non-recursive filters can have excellent amplitude and phase characteristics and they are quite easy to design[88,33][63,102]. Unfortunately they are not suited to real time filtering with a microprocessor because of

Figure 112. A non-recursive estimator.

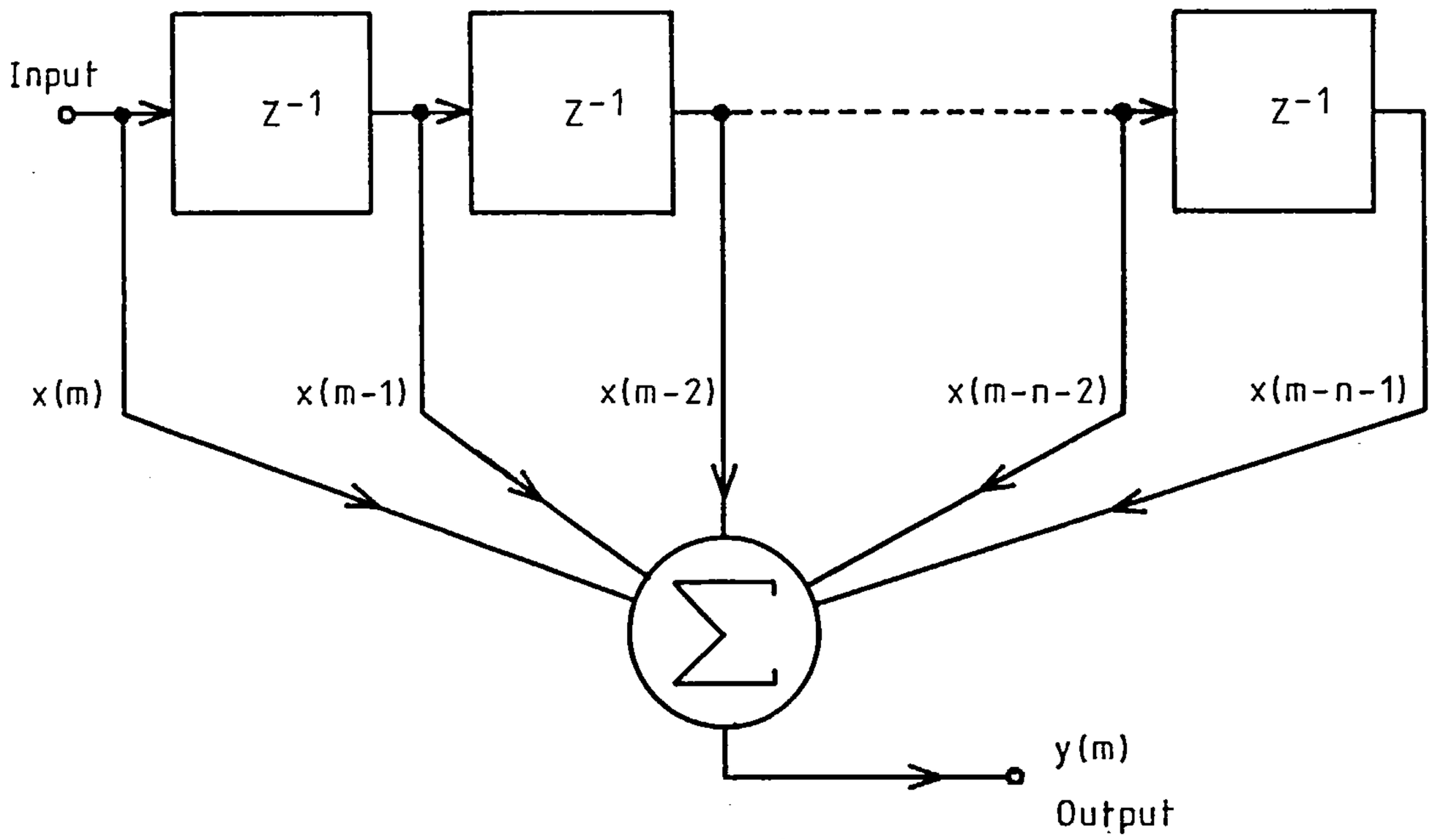

a. A model

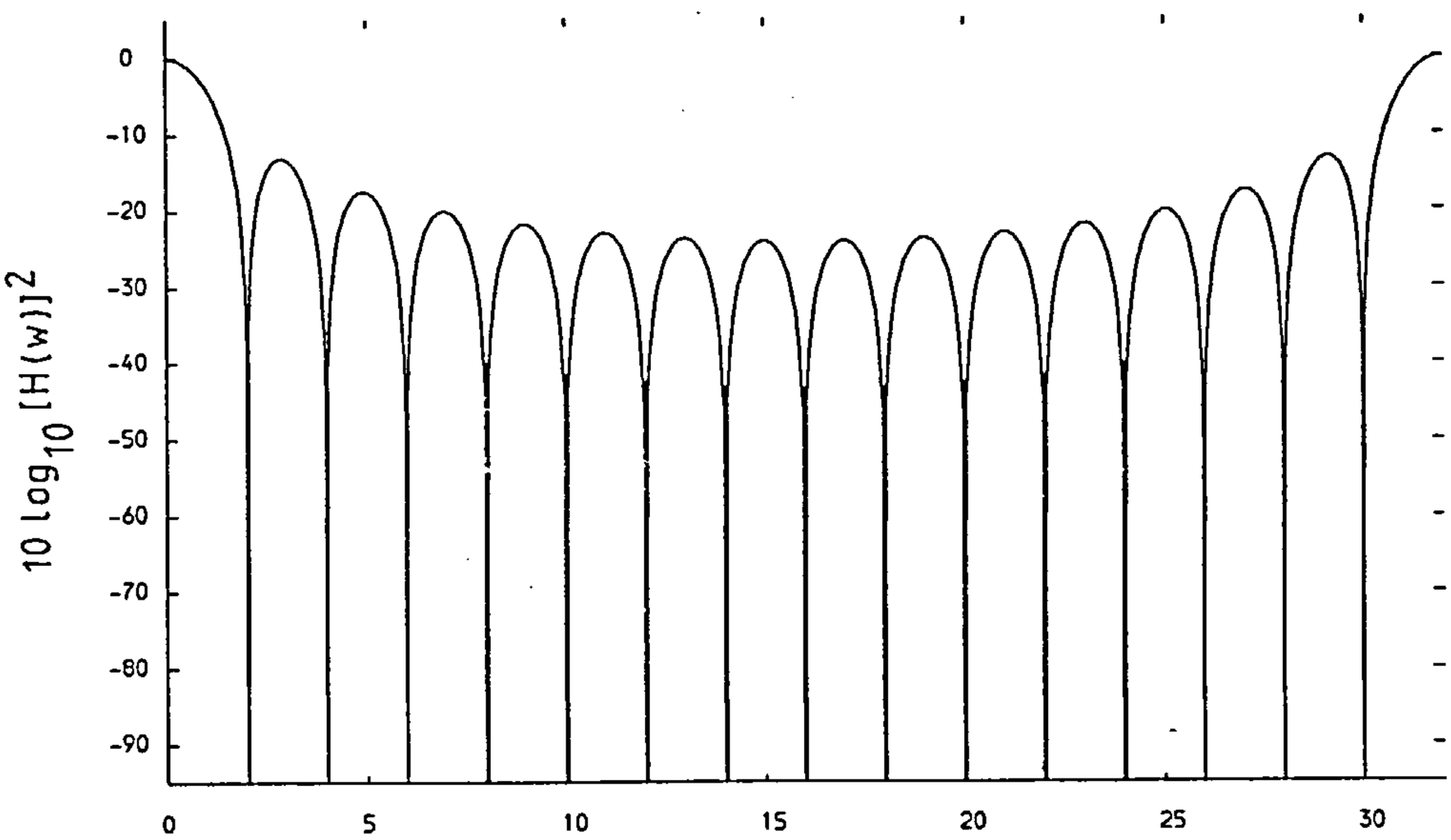

b. The amplitude-frequency response when n = 16 and f_s = 32 Hz.

the large amount of time consuming computation they require. Recursive filters[88,45][63,121] are rather like analogue filters in that they employ feedback and can therefore be unstable. They are well suited to real time filtering but they are more difficult to design than non-recursive filters. Standard analogue filters, such as the Chebyshev and Butterworth types, are optimal in the sense that they achieve their desired aims using the minimum possible number of poles and zeros. For a digital filter the aim, once again, is to minimise the number of poles and zeros to reduce the amount of calculation required to produce each new output value. Simulating the analogue characteristics in the digital domain is therefore a sensible and powerful approach to digital filtering.

There are a number of ways of digitally simulating continuous systems[63,155] but the bilinear transformation is one of the most popular when it comes to filter design. The purpose of the bilinear transform is to map the analogue frequency range $0 < f < \infty$ into the useful digital range $0 < f_s < f_s/2$ (see appendix 1). The spectrum of the transforming function

$$H(z) = \frac{(z - 1)}{(z + 1)} \tag{9.16}$$

is found by setting $z = \exp(jwT)$ with the result

$$H(jw) = \frac{\exp(jwT) - 1}{\exp(jwT) + 1} \quad . \tag{9.17}$$

Multiplying top and bottom by $\exp(-jwT/2)$ gives

$$H(jw) = j \tan(w'T/2) \tag{9.18}$$

or

$$H(jw) = j \tan(w'\pi/w_s) \ , \tag{9.19}$$

where w is the frequency in the analogue domain and w' is the transformed frequency in the digital domain. As $w \rightarrow \infty$, $w' \rightarrow w_s/2$ or $f' \rightarrow f_s/2$; as $w \rightarrow 0$, $w' \rightarrow 0$ also. The transform in 9.16 does

indeed map the analogue frequency range $0 \leqslant f < \infty$ into the digital range $0 \leqslant f' < f_s/2$. What is more, it actually improves the amplitude characteristics of the analogue low pass filters by giving the digital versions flatter passbands and sharper cutoffs[63,194]. On the other hand, phase/frequency characteristics are seriously distorted so Bessel filters ought not to be modelled in this way. Tietze and Schenk[49,380] describe digital filter design using the bilinear transform in some detail.

It was decided that a second order Chebyshev filter should be simulated. The filter was to have $\leqslant$ 0.5dB ripple in the passband and a cut off frequency of 1Hz for a sampling frequency of 32Hz. A general second order analogue transfer function is

$$H(s) = \frac{d_o + d_1 s + d_2 s^2}{c_o + c_1 s + c_2 s^2} \quad , \tag{9.20}$$

in which s is the Laplace transform variable. The transfer function of an analogue second order Chebyshev filter with a 1Hz cut off and 0.5dB ripple is[49,76]

$$H(s) = \frac{1}{1 + 1.3614s + 1.3872s^2} \quad . \tag{9.21}$$

A general second order digital transfer function is

$$H(z) = \frac{D_o + D_1 z + D_2 z^2}{C_o + C_1 z + C_2 z^2} \quad , \tag{9.22}$$

the transfer function of a second order low pass digital filter is

$$H(z) = D_o \frac{1 + 2z + z^2}{C_o + C_1 z + z^2} \quad . \tag{9.23}$$

Tietze and Schenk[49,382] use a modified transform

$$s = L \frac{z - 1}{z + 1} \quad , \tag{9.24}$$

where

$$L = \cot(\pi f_o T) \tag{9.25}$$

and f_o is the desired cut off frequency. The factor L ensures that the cut off frequency of the digital copy coincides with that of

the analogue master. Using equations 9.20, 9.22 and 9.24 the unknown constants in 9.23 can be identified as

$$D_o = \frac{d_o - d_1 L + d_2 L^2}{c_o + c_1 L + c_2 L^2} \tag{9.26}$$

$$C_o = \frac{c_o - c_1 L + c_2 L^2}{c_o + c_1 L + c_2 L^2} \tag{9.27}$$

and

$$C_1 = \frac{2(c_o - c_2 L^2)}{c_o + c_1 L + c_2 L^2} \quad . \tag{9.28}$$

Using 9.21 and 9.25 the constants are

$$D_o = 6.3548 \times 10^{-3},$$

$$C_o = 8.2432 \times 10^{-1}$$

and

$$C_1 = -1.7989 \quad .$$

The cascade second order structure that had to be built into the software is illustrated in figure 113a. The modified version that is used is shown in figure 113b, the modifications are designed to improve the filter's accuracy. The form shown in 113b has an accuracy of $\pm$ 0.5 bit in 4096_{10} bits. The maximum allowable step function input is 0 to 3650_{10} bits; any more than this and the filter overloads itself through overshoot as it cannot cope internally with numbers larger than 4095_{10}. The filter does not recognise numbers less than 10_{10} bits. The multiplication constants are stored to 17 bits accuracy by splitting them into integer and fractional parts. For instance, $-C_1$ is stored as

$$-C_1 = 1.7989 = 1 + 0.7989 \quad .$$

The position of the decimal point is accounted for by correctly ordering the calculations. On this point, the sequence of calculations has to be very carefully arranged to prevent internal overflows. It is also arranged that any numbers to be multiplied are always positive so that the unsigned binary multiply module can be used.

Figure 113. The second order recursive low pass filter.

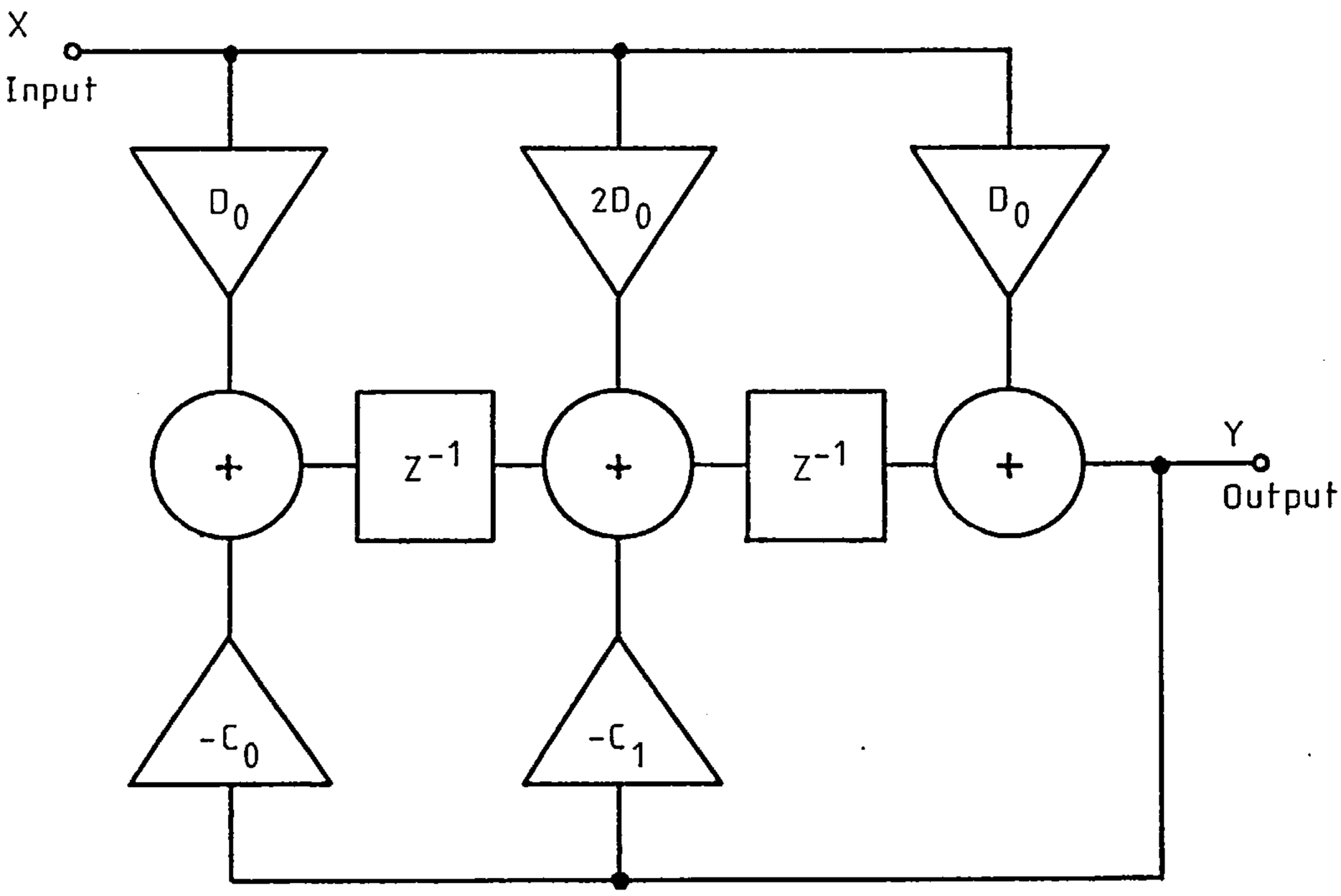

a. The original structure.

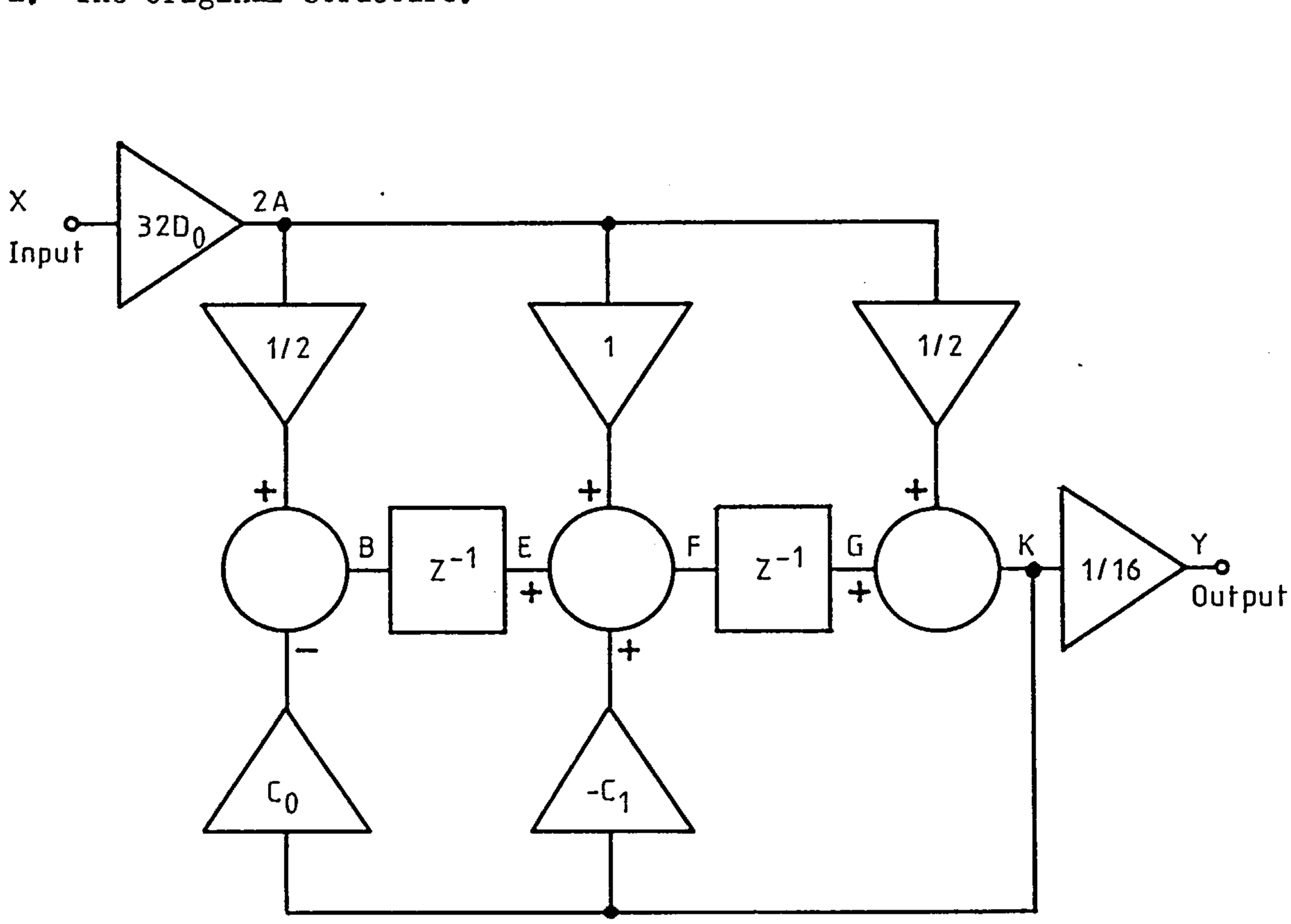

b. The modified structure

Figure 114. The performance of the second order low pass recursive Chebyshev filter when f_s = 32 Hz.

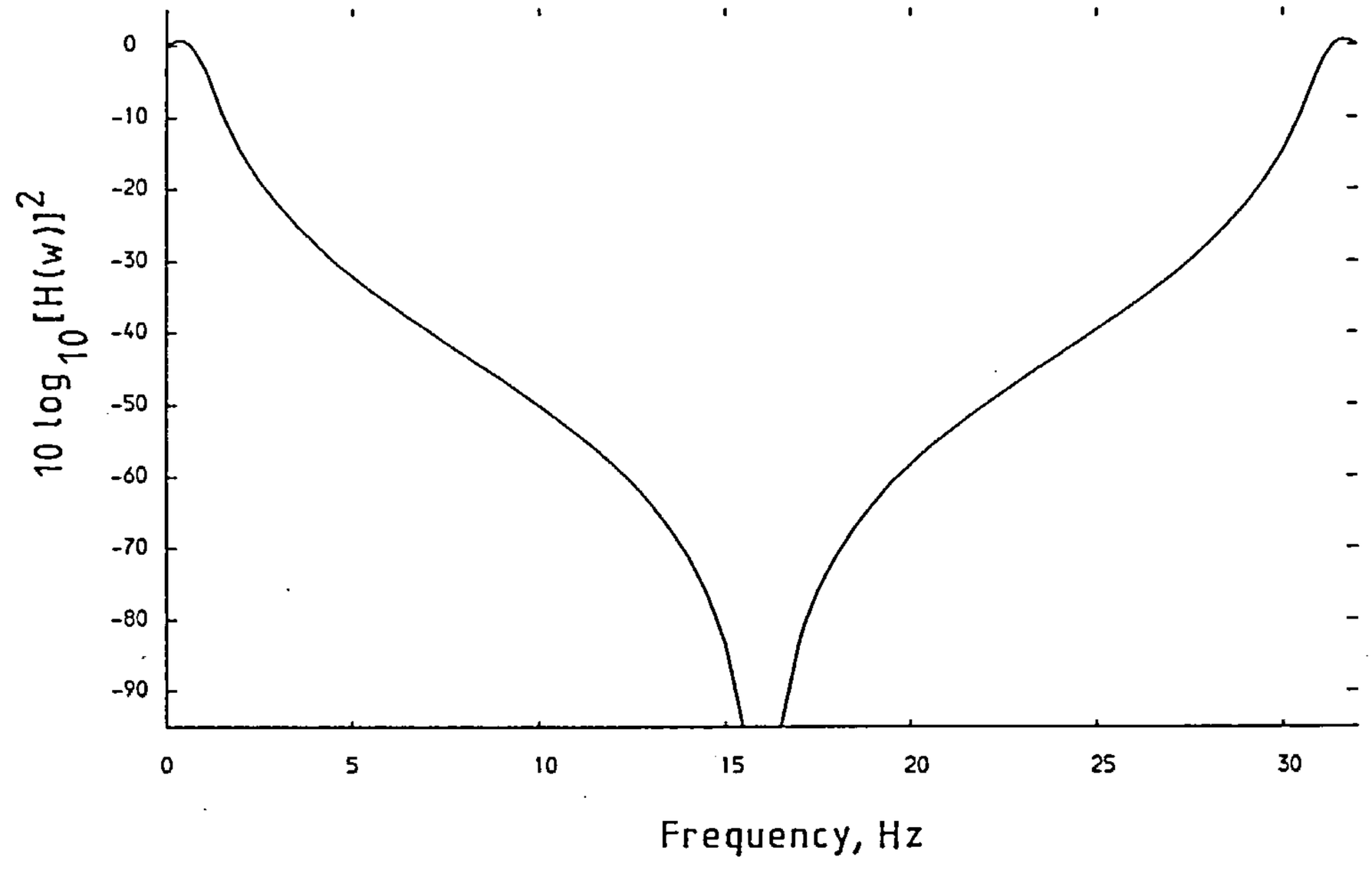

a. The amplitude-frequency response.

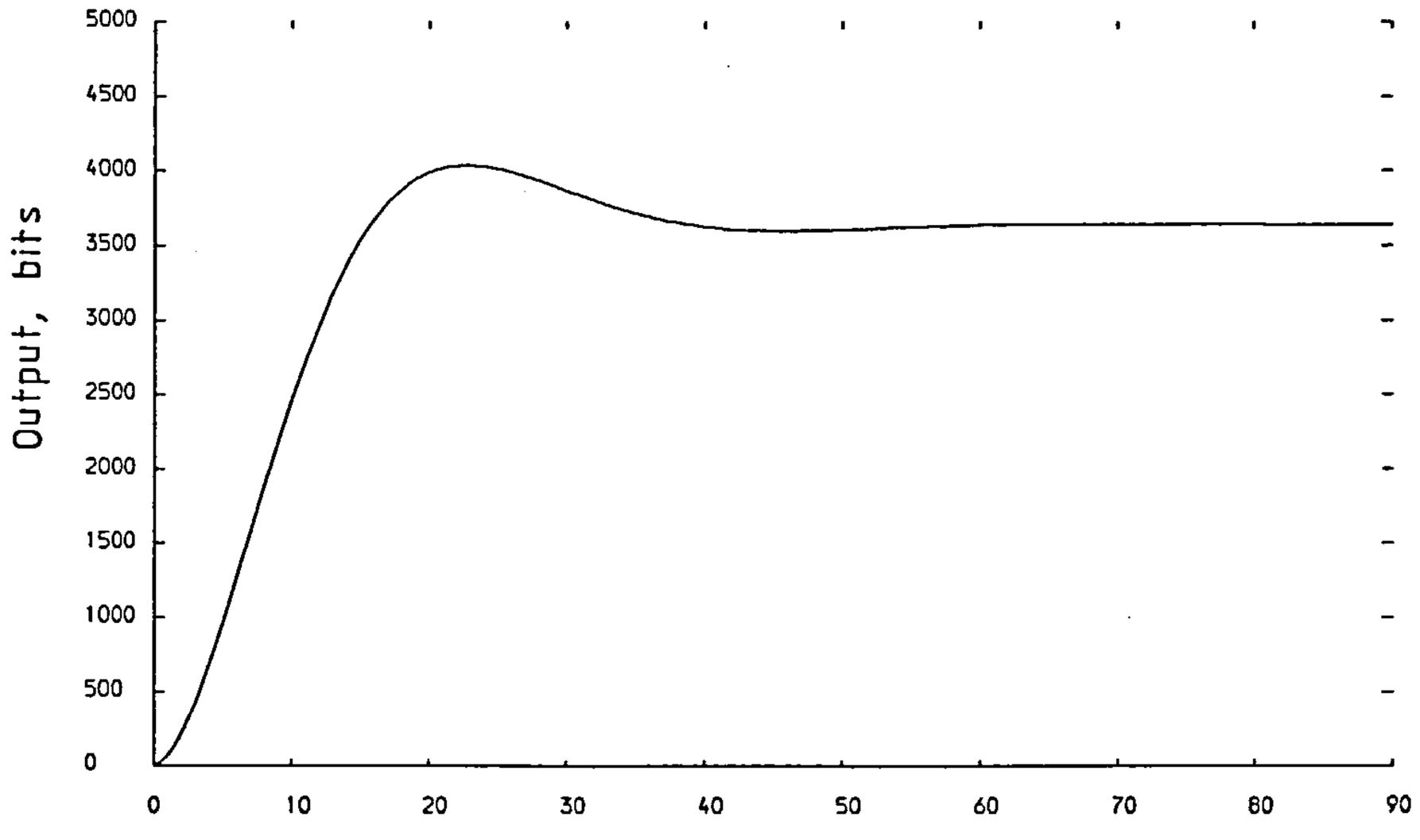

b. The step response.

The internal store spaces are 32 bits long to take the full result of a 16 x 16 bit multiplication. Finally, the number at K in 113b has to be reduced from 32 to 16 bits so care is taken to minimise round off noise.

The calculated frequency response is shown in figure 114a, it is far superior to that shown in figure 112b. The actual step response for an input of 3,644 bits is shown in figure 114b, this was used to check that the filter was performing properly. Table 15 compares the rise time, delay time and overshoot of the analogue filter with that of the digital model given a sampling frequency of 32Hz. The analogue data comes from Tietze and Schenk[49,80].

Table 15 Comparing the analogue and digital filters' step responses at a sampling rate of 32Hz.

Parameter	Analogue filter	Digital filter
Rise time, 10%-90%	0.338s	0.344s
Delay time, 0%-50%	0.251s	0.250s
Overshoot, %	10.7	10.9

The comparison shows that the digital filter performs properly. The flowchart is given in figure 115.

9.3.10 The controller routine

This has already been discussed in subsection 9.2.3. Table 16 shows how the thumbwheel switches on the face of the instrument are used to control it.

Table 16 The thumbwheel switch settings.

Switch 1	Switch 2	Mode	Sample rate, Hz	Bandwidth Hz
0	0	Voltmeter	32	1
0	1	Displacement	32	1
1	0	Voltmeter	160	5
1	1	Displacement	160	5

Figure 115. The digital filter subroutine.

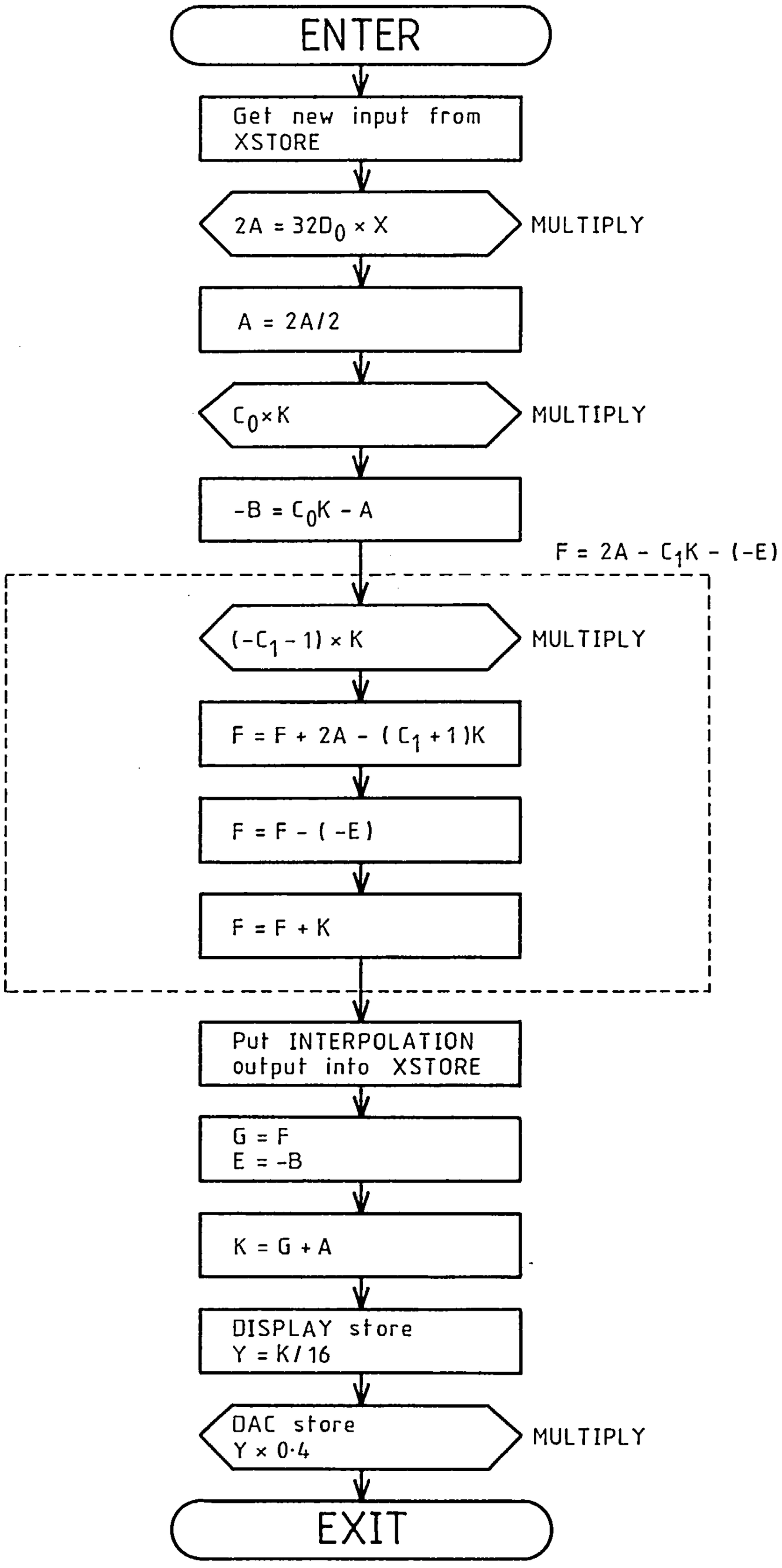

9.3.11 The reset vector

When the power is turned on, or when the reset button is pushed, the microprocessor automatically examines memory locations $FFFC_{16}$ and $FFFD_{16}$ to see where the program starts. The beginning of the code for the controller routine is the start of the program.

CHAPTER 10

CALIBRATION, RESULTS, APPLICATIONS AND IMPROVEMENTS.

This chapter completes the description of the field gradient displacement transducer. It shows first how the transducer was calibrated. Then, a graph of the transducer's measurement error is presented and explained. This is followed by a short discussion on the effects of magnet-sensor alignment errors. Then, the performance of the instrument is quickly summarised prior to short sections on improvements and applications.

10.1 CALIBRATION

The method of calibration has to be accurate so that the performance of the instrument is not obscured by other sources of error. The needs, therefore, are for a precise means of setting a displacement and for an independent and accurate means of measuring displacement.

The displacement was set using a ready built test jig. The jig was constructed entirely of brass and aluminium so it was non-magnetic. It had a sliding bed driven by a screw thread and a laterally fixed bed whose height was adjustable. The permanent magnetic dipole, glued to a perspex carriage, was mounted on the sliding bed such that the dipole was aligned with the direction of travel. The tube shaped fluxgate probe was mounted on the other bed such that the tube's axis was coincident with the dipole's axis. Using this arrangement the probe to magnet separation could be controlled precisely; in addition, the magnetometer's output was maximised and the alignments were stable. A cathetometer was used to measure the positions of the tip of the probe and the leading edge of the magnet to $\pm$ 0.02 mm accuracy. The cathetometer was situated 1.5 m from the magnetometer's probe, this was far enough for the magnetometer not to be influenced in any measurable way. The complete arrangement is drawn in figure 116.

Figure 116. The arrangement of the apparatus used for calibration.

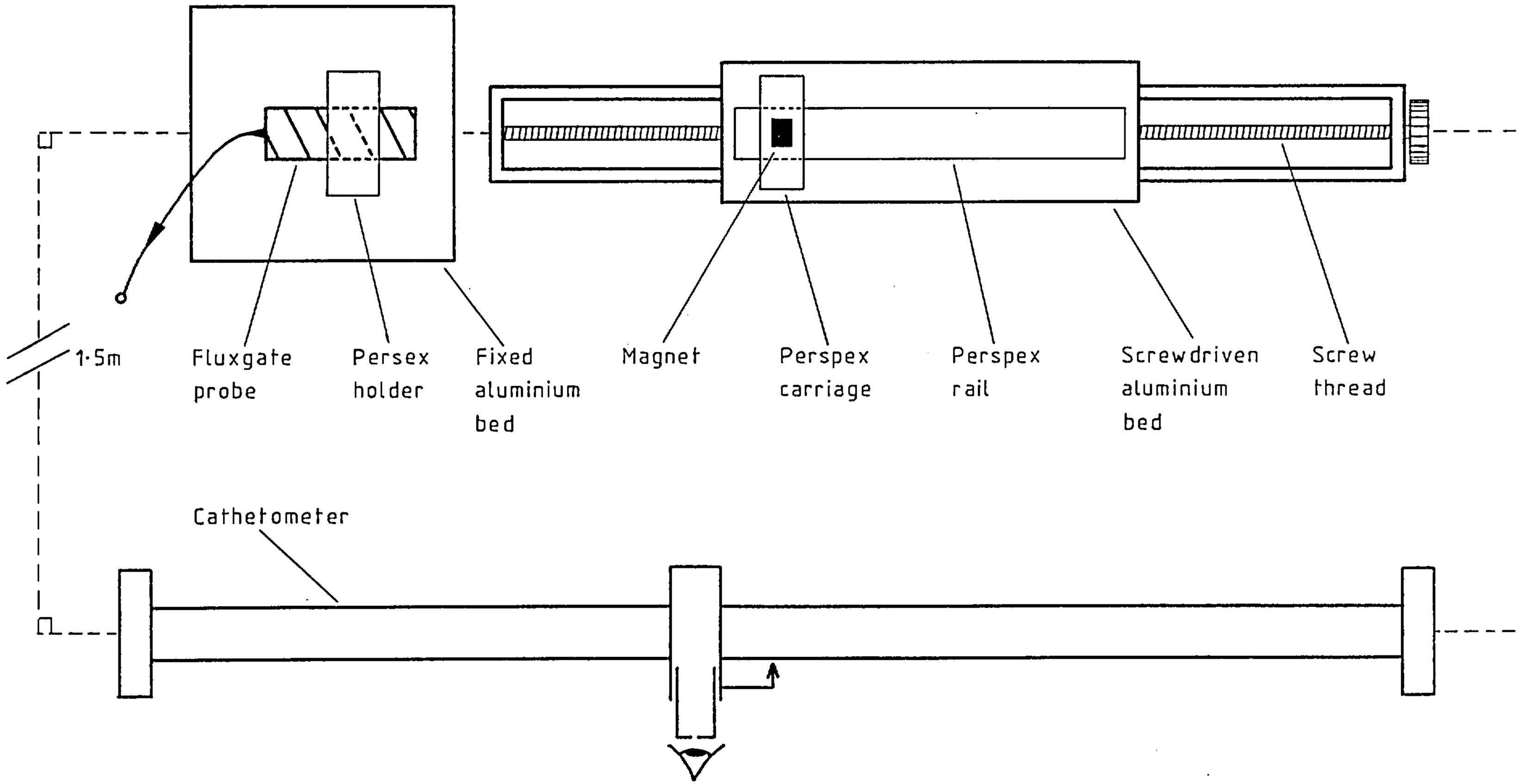

No special precautions were taken to reduce environmental magnetic noise.

The instrument was put into the calibration (voltmeter) mode and the amplifier gain was manually set to x16. The magnet, on its carriage, was moved away from the probe until the magnetometer's output was reduced to 128 bits according to the instrument's display. This probe-magnet separation was noted. The process was repeated in steps of 128 bits, this formed a list of 32 displacements ($128 \times 32 = 2^{12}$) for the high gain look up table. The gain was then switched to x2 and, starting from 128 bits, another 32 displacements were obtained to form the low gain calibration table. Both tables were converted into 16 bit binary code and stored in the microcomputer's memory. The calibration error worsened at large displacements because of the reduction in the magnetometer's signal to noise ratio. The limited resolution of the cathetometer became a significant calibration error at small displacements. The low gain look up table was contained in memory locations $FE7F_{16}$ to $FEBE_{16}$. The high gain look up table was contained in locations $FEBF_{16}$ to $FEFC_{16}$. Each 16 bit entry was split into two bytes, the least significant byte was always placed one location lower than the most significant byte. A log-log plot of the magnetometer's output against probe-magnet displacement is shown in figure 117. The plot curves strongly and demonstrates that calculating displacement using the dipole field law would be inaccurate.

10.2 PERFORMANCE

10.2.1 Accuracy

Having completed the calibration it was possible to find out how accurately the instrument measured displacement. For this test the digital filter subroutine was temporarily arranged to follow the gain set and range check subroutine. The reason was that the displacements were stored to 0.01 mm resolution, so a displacement of 250 mm was

Figure 117. A log-log of the magnetometer's output against displacement.

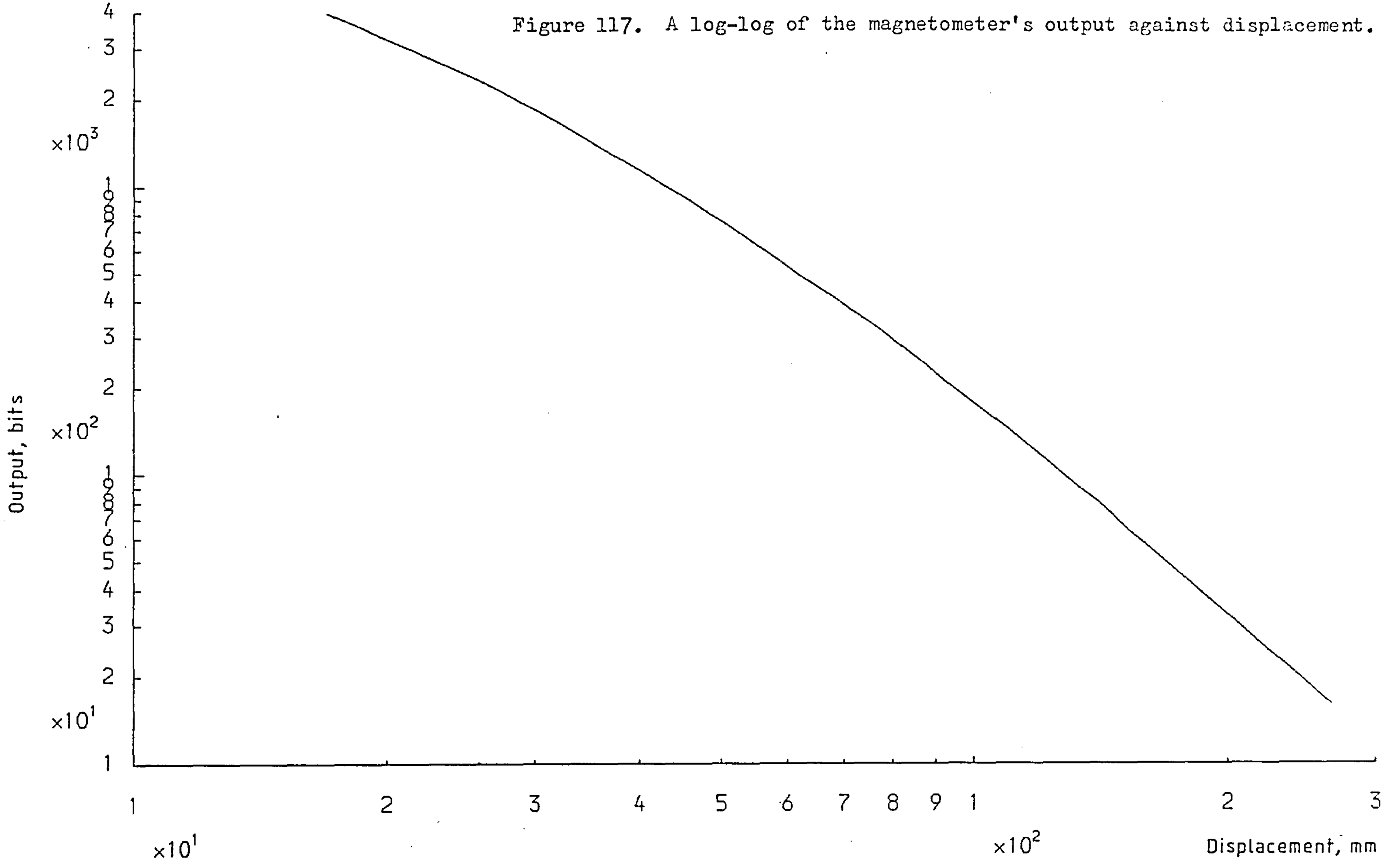

represented as 25,000 bits. The filter could not handle numbers this large, but it had no problems with the ADC output which was obtained from the gain set and range check subroutine. After this test the displacements were re-entered to 0.1 mm accuracy and the filter was put back to its original position following the field to distance interpolation subroutine.

The magnet was set to a series of known displacements using the cathetometer. At each setting the microcomputer's displayed estimate was noted and the instrument's error was found. Figure 118 is a plot of the non-contact measurement error against magnet displacement. The uncertainty in the true displacement was $\pm$ 0.04 mm, this is represented by the broken curves above and below the axis. At large displacements of about 200 mm the interpolation error was dominant. This error could have been reduced using closer spaced entries in the high gain calibration table. The ultimate limit to the reduction of interpolation error was the quantization error of the ADC. At the maximum displacement of 266 mm, a change of one least significant bit corresponded to 0.7 mm, or 0.26% of 266 mm. At the mimimum displacement of 18 mm, a change of one least significant bit corresponded to 4.5μm or 0.025% of 18 mm. The quantization error was always less important than the random noise when the gain was 16. The error bars on figure 118 show the effects of the random noise compared to the interpolation error. Random noise errors, like interpolation errors, shrank in significance as the displacement decreased. At small displacements of about 40 mm or less, the most important errors were those of the method used to test performance. The method exaggerated an underlying increase in calibration error that was itself caused by limited cathetometer resolution.

10.2.2 The effects of probe-magnet misalignment

Correct mechanical alignment is important to any displacement

Figure 118. Non-contact measurement error against magnet displacement.

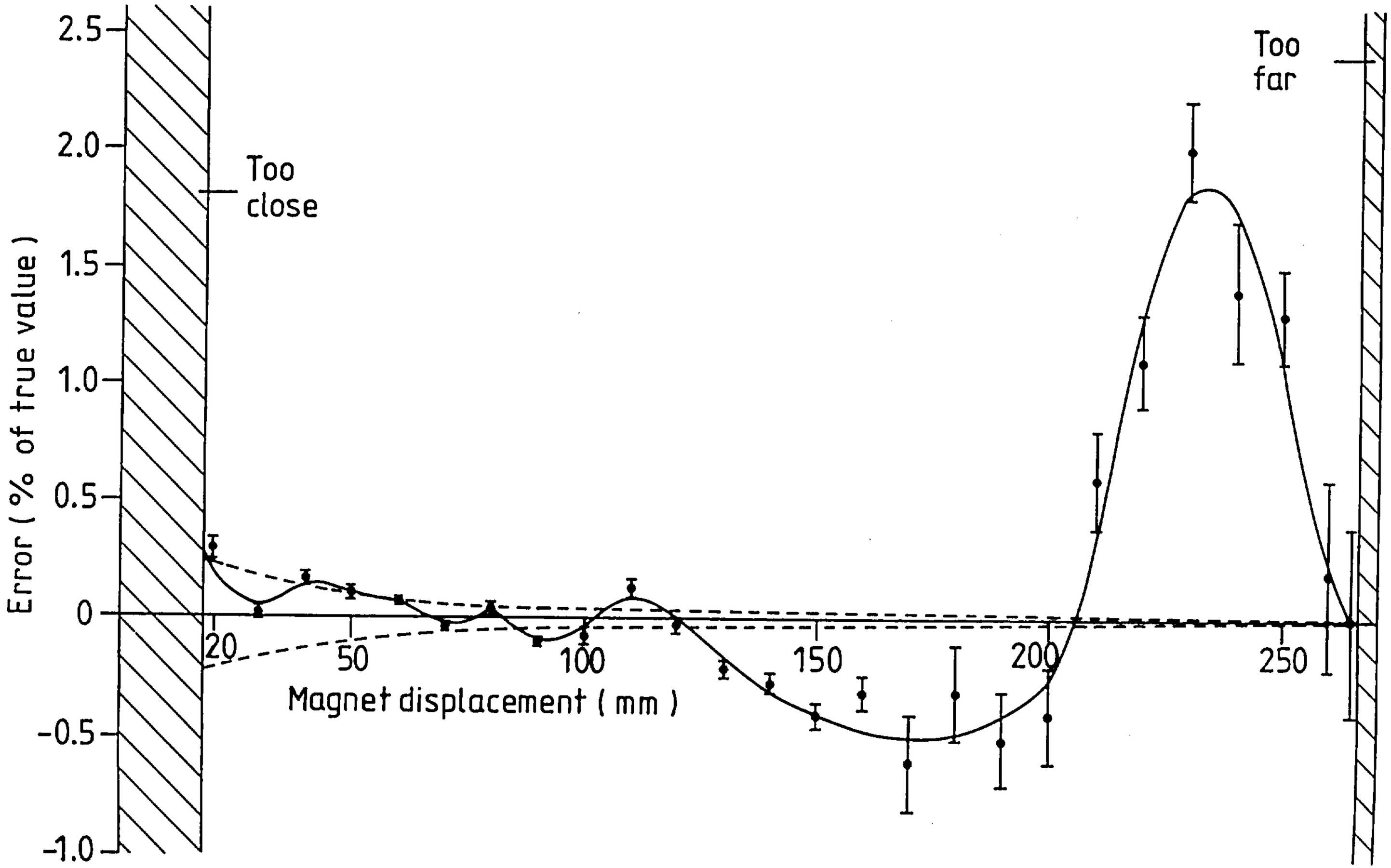

transducer. The purpose of this subsection is to make some short calculations to see how the performance is affected by misalignment. Equation 7.4 is sufficiently accurate to make estimates of error. One point to make is that misalignment is not disastrous providing it is unchanged during and after calibration. Two simple alignment errors are discussed below.

Considered first is the effect of rotating the axis of the magnet relative to the axis of the probe, this is shown in figure 119. If the dipole moment is M_T then the field at any point (r,θ) in a plane containing the dipole at the origin can be specified by the components

$$H_r = \frac{2M_T \cos\theta}{r^3} \qquad (10.1)$$

and

$$H_\theta = \frac{M_T \sin\theta}{r^3} \quad . \qquad (10.2)$$

The fluxgate's sensor is strongly directional. In this example the H_θ component is completely ignored giving

$$V = \frac{\mu_o \, 2kM_T \cos\theta}{r^3} \quad , \qquad (10.3)$$

where k is the magnetometer's sensitivity and V is the voltage at its output. If the error is present during and after calibration the magnetometer's signal to noise ratio is worsened by

$$\frac{V(\theta)}{V(0)} = \cos\theta \quad . \qquad (10.4)$$

A constant rotational alignment error of 8^o worsens the signal to noise ratio by 1%, but it does not prevent the instrument working properly.

If the magnet's rotation is not present during calibration, but occurs afterwards, there will be a measurement error. The micro-computer, unaware of the magnet's rotation away from the calibration

Figure 119. Diagrams used to help calculate the effects of magnet-probe misalignment.

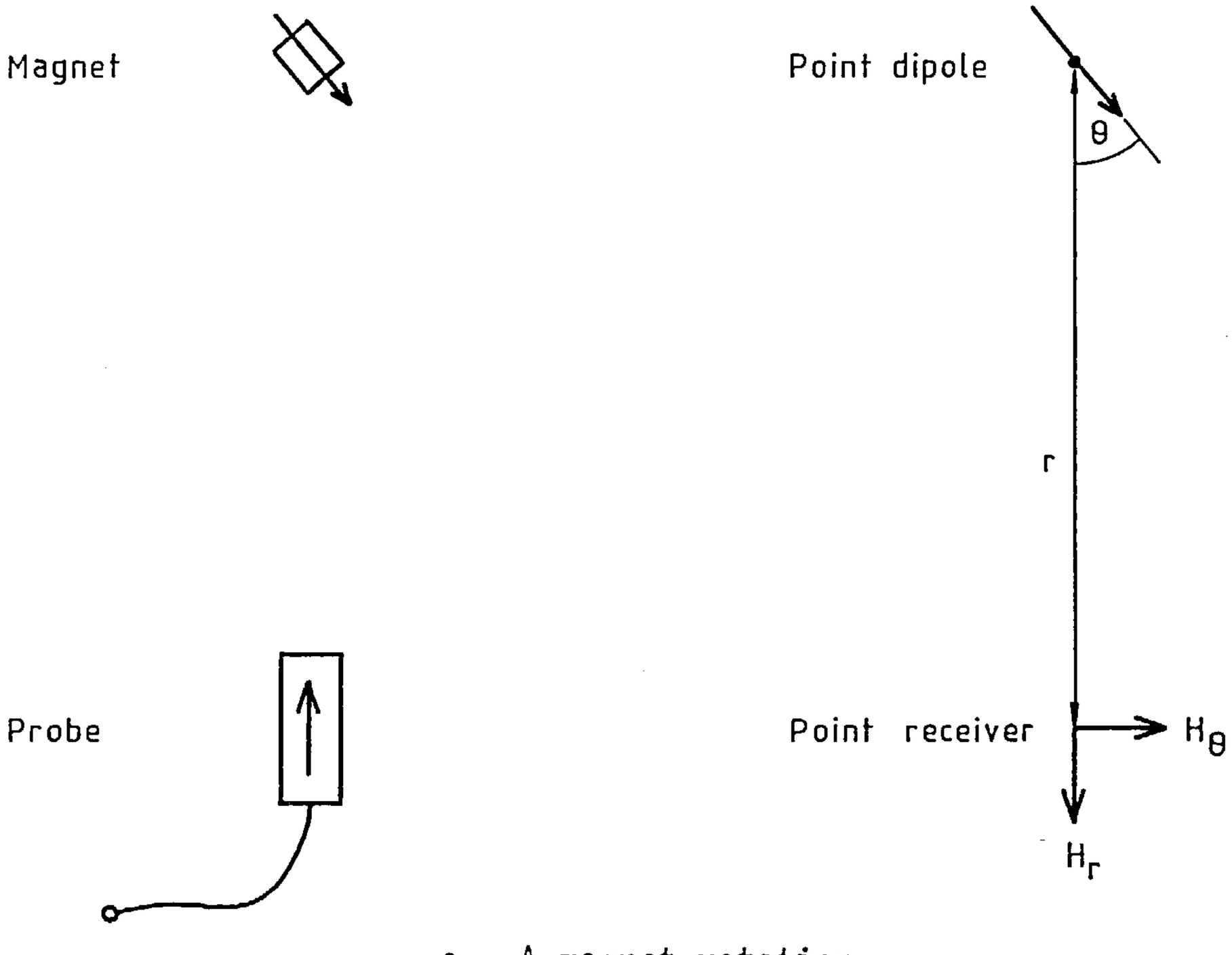

a. A magnet rotation.

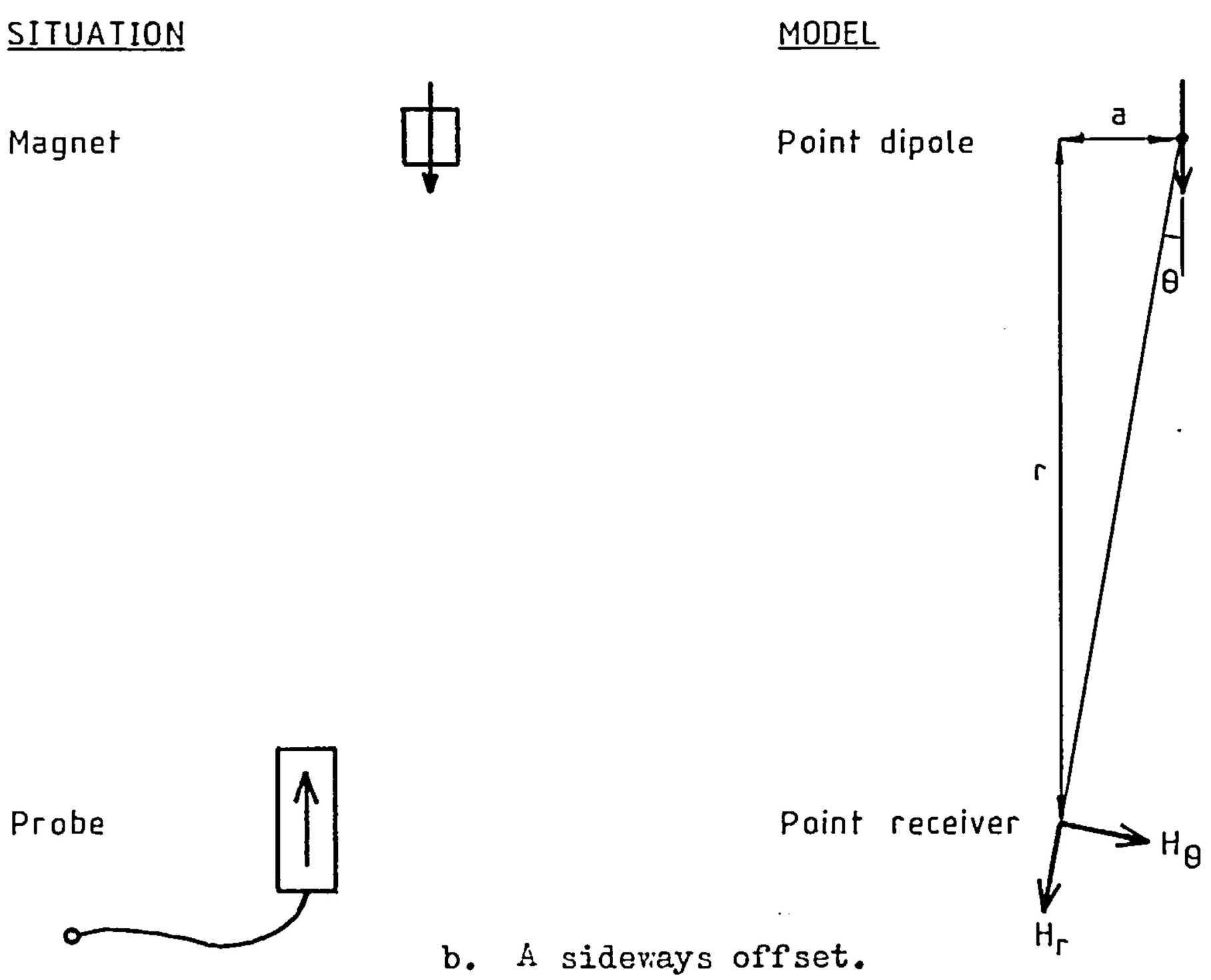

b. A sideways offset.

alignment, treats the decrease in field as an increase of Δr in displacement. Assuming the alignment at calibration was correct:

$$\frac{V(\Delta r)}{V(r)} = 1 - 3\,\frac{\Delta r}{r} \qquad (10.5)$$

if $\Delta r/r \ll 1$. Equations 10.5 and 10.4 may be combined to give the erroneous increase in estimated displacement due to a magnet rotation of θ radians after calibration:

$$\cos\theta = 1 - 3\,\frac{\Delta r}{r},$$

or

$$\frac{\Delta r}{r} \approx \frac{\theta^2}{6} \qquad (10.6)$$

if θ is small. A rotation of 0.14 radian, or 8^o, causes the estimate of displacement to be increased by 0.3%.

The second error to be considered is a sideways shift of the axis of the magnet relative to the axis of the sensor, this is shown in figure 119b. When the field at the sensor is resolved onto the sensitive direction, the signal from the magnet is

$$V(a) = \mu_o k M_T \frac{2\cos^2\theta + \sin^2\theta}{(r^2 + a^2)^{1.5}} \qquad (10.7)$$

using equations 10.1 and 10.2. Next,

$$V(a) = \mu_o k M_T \frac{1}{(r^2 + a^2)^{1.5}} \left[1 + \frac{r^2}{(r^2 + a^2)} \right]$$

$$= \mu_o k M_T \left[\frac{2r^2 + a^2}{(r^2 + a^2)^{2.5}} \right]. \qquad (10.8)$$

Substituting $a = xr$ into 10.8 gives

$$V(x) = \frac{\mu_o kM_T}{r^3} \left[\frac{2 + x^2}{(1 + x^2)^{2.5}} \right] . \qquad (10.9)$$

Assuming that $x << 1$ the binomial theorem can be used to give

$$V(x) \approx \frac{\mu_o kM_T}{r^3} (2 + x^2)(1 - 2.5x^2) ,$$

or

$$V(a) \approx \frac{\mu_o 2kM_T}{r^3} \left[1 - 2\frac{a^2}{r^2} \right] . \qquad (10.10)$$

Finally, the required result is

$$\frac{V(a)}{V(0)} \approx 1 - 2\frac{a^2}{r^2} . \qquad (10.11)$$

For a fixed shift "a" the reduction in the magnetometer's signal to noise ratio is more serious at short distances than at long distances. If the shift is present before and after calibration the instrument will still work properly. If the shift occurs after calibration the microcomputer would interpret the reduction in field as an increase in displacement Δr. Using equations 10.5 and 10.11

$$\frac{\Delta r}{r} \approx \frac{2a^2}{3r^2} . \qquad (10.12)$$

For example, if the instrument was correctly estimating an aligned displacement of 10.00 cm, a sideways shift of 1 cm would cause it to revise its judgment to 10.07 cm.

10.2.3 Other points

The effect of the digital filter is shown in figure 120. Figure 120a shows the unfiltered noise at the output of the field to displacement interpolation subroutine with the magnet set to a displacement of 240 mm. Figure 120b shows the output of the digital filter when the noise in 120a is passed through it.

Figure 120. The effect of the digital filter on noise.

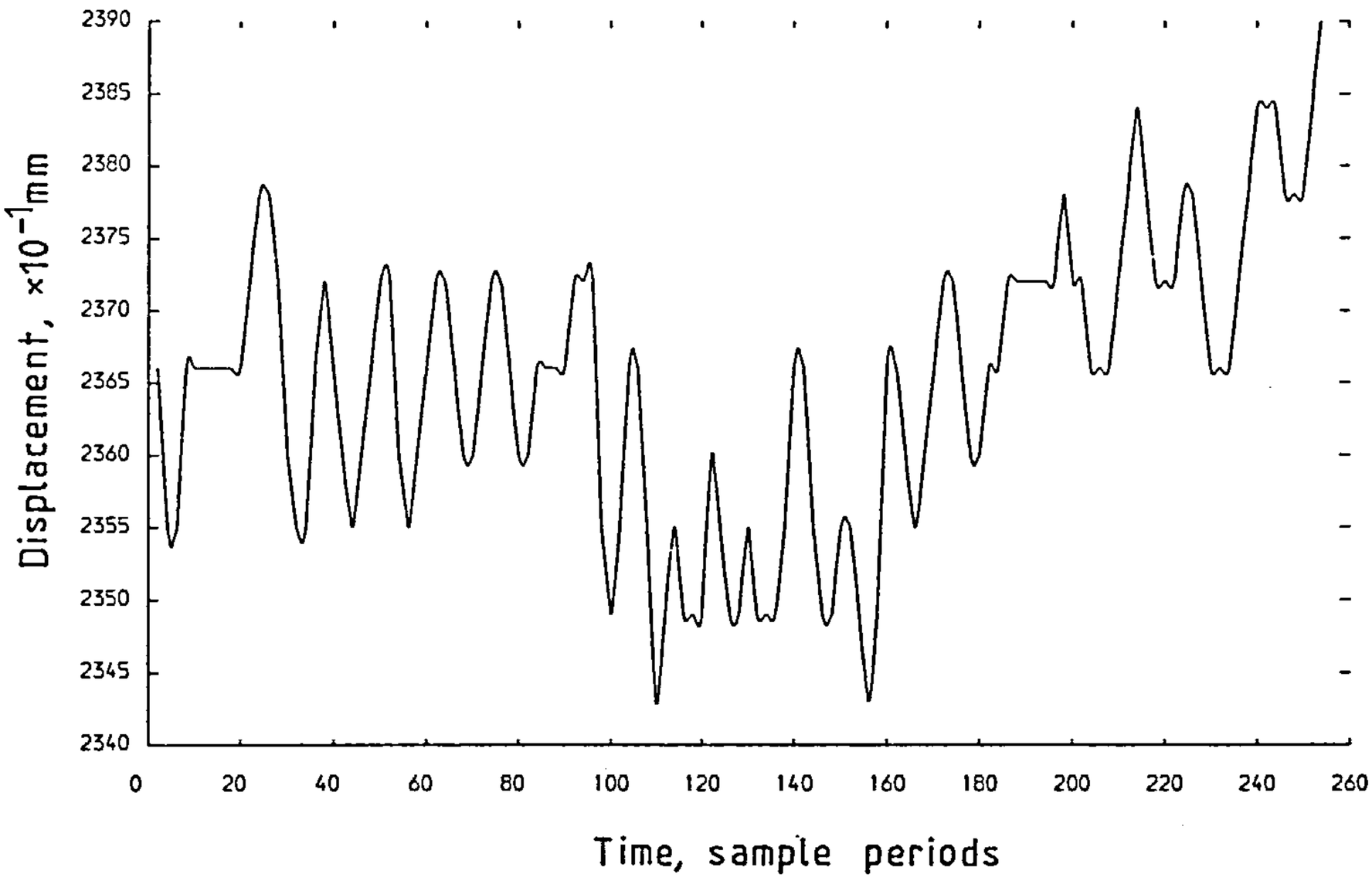

a. Unfiltered signal at the output of the field to displacement interpolation subroutine.

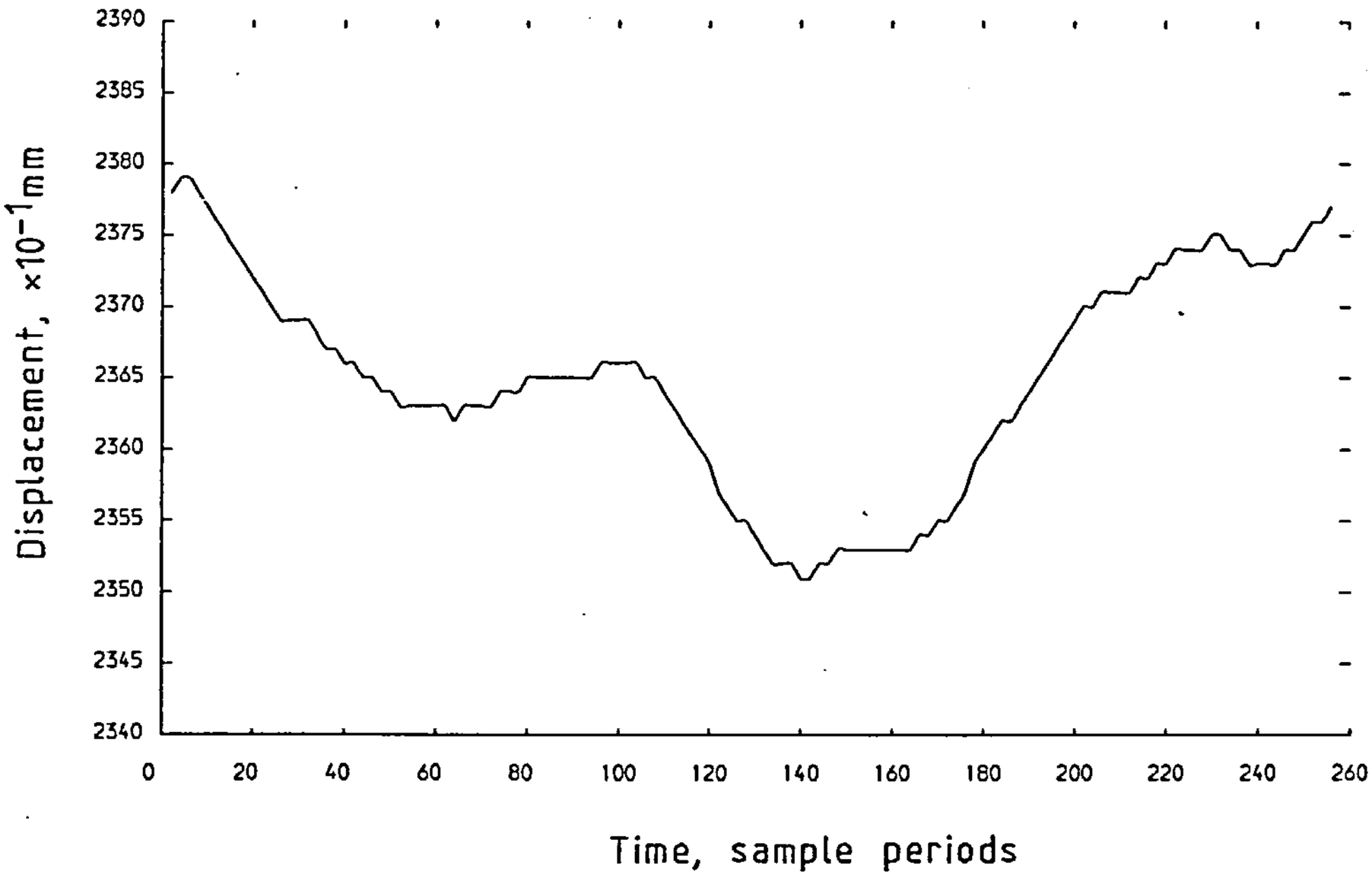

b. The filtered signal.

Figure 121. The signal from the DAC as the magnet was pushed by hand from its minimum to its maximum displacement.

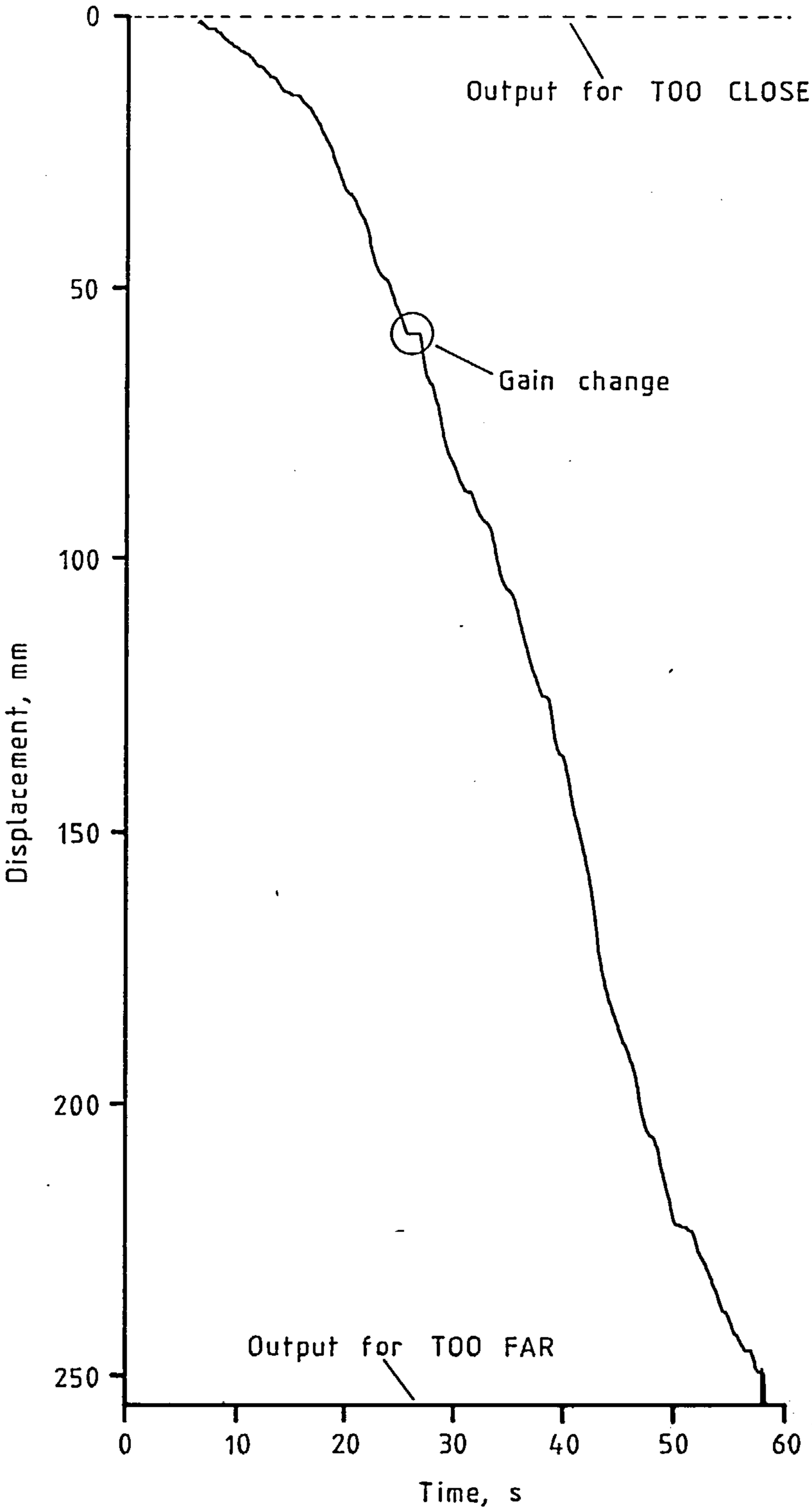

Figure 121 shows the trace from the DAC as the magnet was pushed by hand from its maximum to its minimum displacement. The effect of the delay in the gain change and range checking subroutine can be seen quite clearly. A change of one least significant bit at the output of the DAC represented 0.4 mm change in displacement. It was quickly confirmed that interposing flesh, aluminium or wood between the magnet and probe did not affect the instrument's reading.

10.3 A SUMMARY OF THE PERFORMANCE AT PRESENT

The only link between the sensor and the object whose displacement is to be found is the field from a permanent magnet. This is a great advantage for steady magnetic fields pass unattenuated through many solids and liquids such as: certain stainless steels, brass, lead, copper, silver, aluminium, glass, plastic, wood, water, oil and flesh. The instrument may be made to work over a small range with high resolution or a longer range with lower resolution: the choice is fixed by the magnitudes of the gains in the switched gain amplifier.

At the moment, the instrument is made to work to the maximum limit of its range. The maximum range is determined by the noise level at the output of the magnetometer and by the moment of the permanent magnet. The single probe fluxgate magnetometer that is used has a noise level of 40 nT r.m.s. in its working environment over a DC-2Hz bandwidth. The magnet's dipole moment is 2.46×10^{-1} Am^2. It is normal to quote performance in terms of the full scale deflection (FSD). The minimum measurable displacement is 18 mm and the maximum measurable displacement is 266 mm, this gives a full scale deflection of 248 mm. The instrument has an accuracy of better than 2.0% FSD over the whole working range and better than 0.1% FSD over 18-130 mm. In the range 18-80 mm the measured accuracy is better than 0.02% FSD.

There are two selectable bandwidths of 1.0Hz and 5.0Hz, these correspond to sampling frequencies of 32 Hz and 160 Hz respectively.

The maximum software cycle time is 6.0 ms.

The temperature stability of the permanent magnet determines that of the instrument. The $SmCo_5$ magnet has a temperature coefficient of about $-0.04\%^{o}C^{-1}$ from $20^{o}C$ to $100^{o}C$. Using equation 10.5, this puts the instrument's temperature coefficient at about -0.013% of reading $^{o}C^{-1}$.

Amongst other things, the next section will show how the software cycle time can be reduced to 3.7 ms. It should be recalled that the operating range of the instrument can be improved by a factor of 9 using a fluxgate gradiometer - see section 7.4. The hardware and software are independent of the choice of magnet and magnetometer. Table 17 compares the performance of the field gradient transducer to some of the non-contact transducers mentioned in section 7.2.

10.4 IMPROVEMENTS

A number of improvements are listed below. The first three alter only the analogue circuitry and require little effort. Afterwards, some additions to the digital hardware are recommended and a suggestion is made for further work in digital filter design.

10.4.1 The fluxgate magnetometer

The undesirable effects of alternating and steady magnetic fields in the environment can be minimised using a fluxgate gradiometer which responds only to changes in the local field gradient. This makes it worthwhile employing a more sensitive magnetometer to gain a substantial increase in working range and a reduction in magnet volume. This point was discussed in section 7.4 and it was shown that a commercially available triaxial fluxgate magnetometer, used as a gradiometer, could increase the working range from 0.25 m to 2.3 m at the same time as increasing the bandwidth from d.c.-1 Hz to d.c.-10 Hz.

10.4.2 The switched gain amplifier

The switched gain amplifier proved to be very useful and it is worth

Table 17 Comparing typical performances[66] of the transducers discussed in section 7.2 to the performance of the field gradient transducer.

Parameter	Field gradient transducer		Linear variable differential transformer - inductive	Variable air gap -inductive	Variable Q - inductive	Variable air gap -capacitive
	Present	Potential				
Link from moving object to electrical system	DC - 5Hz magnetic field	DC - 50 Hz magnetic field	Ferromagnetic plunger attached to object	~5KHz magnetic field	50KHz magnetic field	~15KHz electric field
Range, mm	250	2,300*	50	5	50	5
Resolution, μm	4.5, short range <700, long range	<< 1, short range <700, long range	2	2	5	12
Linearity, % FSD	<0.02, short range <2.0, long range	<0.01, short range <1.0, long range	0.5	5	2	1
Frequency response Hz	5Hz	50 Hz, short range 10 Hz, long range	500	500	10,000	3,000
Temperature coefficient, % FSD$^{o}C^{-1}$	-0.001, short range -0.01, long range	-0.001, short range -0.01, long range	0.005	0.2	0.2	-0.1

* With 0.25 Am^2 magnetic dipole.

extending it. Using a quad single-pole-single-throw CMOS analogue switch, such as the DG 303, the amplifier might be given gains of 2, 8, 32 and 128. This drastically extends the dynamic range of the 12 bit ADC so that full advantage can be taken of the improved magnetometer. Used properly, the amplifier would reduce quantization error to insignificance and much reduce interpolation error - see tables 12 and 14. The price for all this is a simple extension to the gain changing and range checking routine and using a high quality amplifier, such as the Analogue Devices AD OP-07 AH, instead of the LF 356.

10.4.3 The anti-alias filter

The anti-alias filter should be put in front of the switched gain amplifier for this would eliminate the settling delays needed when changing the gain. Assuming that a 6th order filter is still to be used, the filter's operational amplifiers must be of high quality to prevent large temperature dependent drifts at the output of the switched gain amplifier. The Analogue Devices AD OP-07 AH and Linear Technology LT 1002 are suitable operational amplifiers; the worst case drift at the output of the switched gain amplifier would be $\pm$ 1.9 x $10^{-4}V^{o}C^{-1}$ so that a change of $\pm$ 6.5^{o}C is equivalent to $\pm$ 1/2 a least significant bit at the ADC.

It will shortly be demonstrated that the sample rate of the digital hardware can be improved. One of the ways this might be exploited is to use an anti-alias filter with a more gentle cut off and much less phase distortion: a sixth order Bessel filter is an obvious choice. A more intriguing possibility is a filter with the minimum possible settling time for a given noise bandwidth. Grimbleby[89] describes such a filter and presents adaptable 3rd and 5th order designs.

10.4.4 Additions to the digital hardware

One very useful addition would be a hardware multiplier because it is much faster than multiplication in software. Tietze and Schenk[49, 287] show that an expandable multiplier may be built quite easily from

TTL 74181 controllable adder circuits; high speed CMOS versions of these circuits should become available. It is estimated that a 1 MHz 6502 in conjunction with an 8 x 8 bit multiplier could perform a 16 x 16 bit multiplication in 120us. In the worst case, a 16 x 16 bit multiplication currently takes 770us in software. Given that there are 6 multiplications per software cycle, it is estimated that the cycle time could be reduced from 6.0 ms to 3.7 ms.

The second addition saves labour. At the moment, recalibration requires the EPROM to be erased by exposure to strong ultraviolet light and then reprogrammed on a special machine. Random access memory that retains it contents when power is turned off has recently become available. An example is the Mostek MK 48Z02 which will store 2 kilobytes for 10 years in the absence of power, yet it behaves just like ordinary static random access memory. If it were used instead of EPROM the operator could enter and permanently store new calibration tables through the instrument's thumbwheel switches, there would be no need for extra equipment and no need to dismantle the instrument.

Finally, it is possible to replace the current 1 MHz 6502 with a 2 or 3 MHz version. This may require faster memory and more use of the RDY control line (section 8.3.1) when communicating with input/output devices. This gives the system a potential sampling rate of about 700 Hz.

10.4.5 The digital filter

A sampling rate of 270 Hz can be attained by adding a hardware multiplier to the present digital system. This allows the instrument a bandwidth of upto 8 Hz with the current digital filter coefficients. It is perfectly reasonable to alter the filter coefficients to extend the bandwidth to 20 Hz or so, this should be adequate for most applications.

One other way of exploiting the extra processing power is to make the digital filter more sophisticated without losing bandwidth. The

instrument's purpose is to estimate a displacement. In the presence of white noise, the optimal linear estimator that produces the least mean square error is the Kalman digital filter. An article by Sorenson[90] provides a useful introduction to Kalman filtering whilst Schwartz and Shaw [61,274] treat the topic in more depth.

10.5 APPLICATIONS

There are many applications for this displacement transducer and a few of them are named below. The only link between the sensor and the object whose displacement is to be found is a magnetic field. The method is therefore ideally suited to situations where a displacement or thickness is to be measured, but some non-magnetizable barrier prevents the use of optical instruments, variable capacitance or reluctance techniques, ultrasonics, X-rays and radioactive sources. Industrially, the instrument might be used to check the thickness or length of pieces of plastic, glass, wood, wads of paper, aluminium struts, brass tubes and so on; it is worth remembering that the instrument is not affected by dirt, grease or water. Medically, it can measure distances through the human body. It makes continuous measurements so it could monitor breathing or the flexing of a muscle. In the laboratory it could measure displacements within a lead lined radiation chamber, or a stainless steel vacuum chamber, from outside the chamber.

Even without barriers, the instrument is a useful displacement transducer. It is entirely automatic and can produce long term records on a chart recording or, with a simple modification,in a permanent digital memory. As the instrument uses a microprocessor, it could easily be adapted to control a system on the basis of displacement measurements. One final suggestion is that it could measure diameters of rotation by attaching the magnet to the outer edge of the rotating body. If the magnitude of the magnetic field were passed to the microprocessor it could easily calculate the difference between maximum and minimum displacements.

APPENDIXES

APPENDIX 1

AN INTRODUCTION TO THE THEORY OF SAMPLING AND RECONSTRUCTING ANALOGUE SIGNALS

A1.1 INTRODUCTION

This appendix is aimed at those who have little or no knowledge of the theory of digital signal processing. It is hoped that the appendix will clarify and underpin the design work in chapters 8 and 9. Fuller explanations and more general treatments are to be found in Schwartz and Shaw[61], Lynn[62] and Stearns[63].

Analogue signals are continuous in amplitude and in time. Amplitude and time can be repeatedly subdivided into finer and finer steps, the practical limit to subdivision is the signal's background noise level. By contrast, a digital signal is discrete in amplitude and in time: amplitude is represented as an integer multiple of an indivisible unit called the bit and time exists only as integer multiples of the host system's clock period T. To tap the signal processing power of a computer an analogue signal must be converted into a flow of digital samples. This appendix shows how the analogue to digital transformation may be brought about and how the analogue signal may be subsequently recovered. It is assumed that the reader is familiar with the Fourier series and the Fourier transform.

A1.2 The ideal sampling and reconstruction process

As a start, let's consider an ideal sampling and reconstruction process where the sampled signal's amplitude remains continuous but time now exists as integer multiples of a sample period T. The aim is to produce a simple model of the sampling process. By comparing the spectra of the original and sampled signals, it will be possible to find out how often the analogue wavefrom has to be sampled to ensure that none of its information content is lost. The look at the ideal model will be concluded by examining the process of reconstructing the original analogue waveform.

The mathematical sampling tool is the Dirac delta function i which is defined such that

$$\int_{-\infty}^{+\infty} i(t).dt = 1 \quad . \tag{1}$$

i(t) is a pulse of infinite height, infinitessimal width and unit area that exists only at t = 0. It may be visualised as a pulse containing one unit of energy. The Fourier transform of the delta function is

$$G(jw) = \int_{-\infty}^{+\infty} i(t)\exp(-jwt).dt \quad . \tag{2}$$

As i(t) exists only at t = 0 this integral is simple,

$$G(jw) = 1 \quad . \tag{3}$$

This result shows that the delta function is a linear superposition of an infinite number of unit amplitude cosine waves over a continuum of frequencies from w = 0 to w = ∞ .

Consider what happens if an analogue signal f(t) is multiplied by a delta function. In the time domain, an instantaneous snapshot is taken of the function f(t) at t = 0 because the product f(t).i(t) exists only at t = 0. However, the product is useless as it stands because it has an infinite height and an infinitessimal width. Integration solves this problem for the energy of the product is finite and is numerically equal to f(t) at t = 0:

$$\int_{-\infty}^{+\infty} f(t)i(t).dt = f(t)\Big|_{t=0} \tag{4}$$

at t = mT where m = 0, 1, 2 ..... .

Looked at in the frequency domain, the delta function is allowing its uniform spectrum to be weighted by the spectrum of f(t).

The analogue waveform must be sampled regularly if its variation over a period of time is to be recorded. Figure A1 shows diagramatically what needs to be done. Mathematically, a train of delta pulses has to be created. This is simply done using i(t - mT) which is defined such that

Figure A1. Sampling an analogue signal.

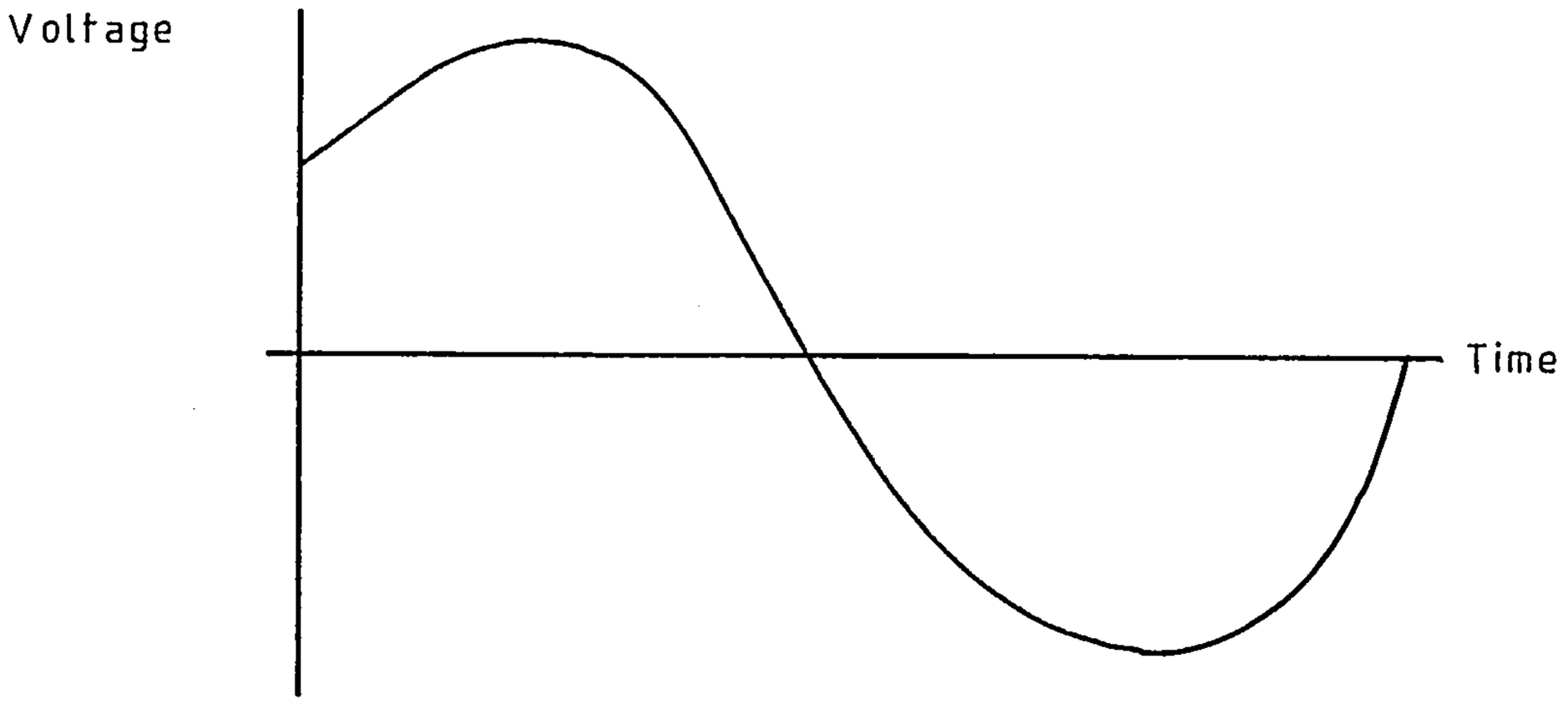

a. The analogue signal...

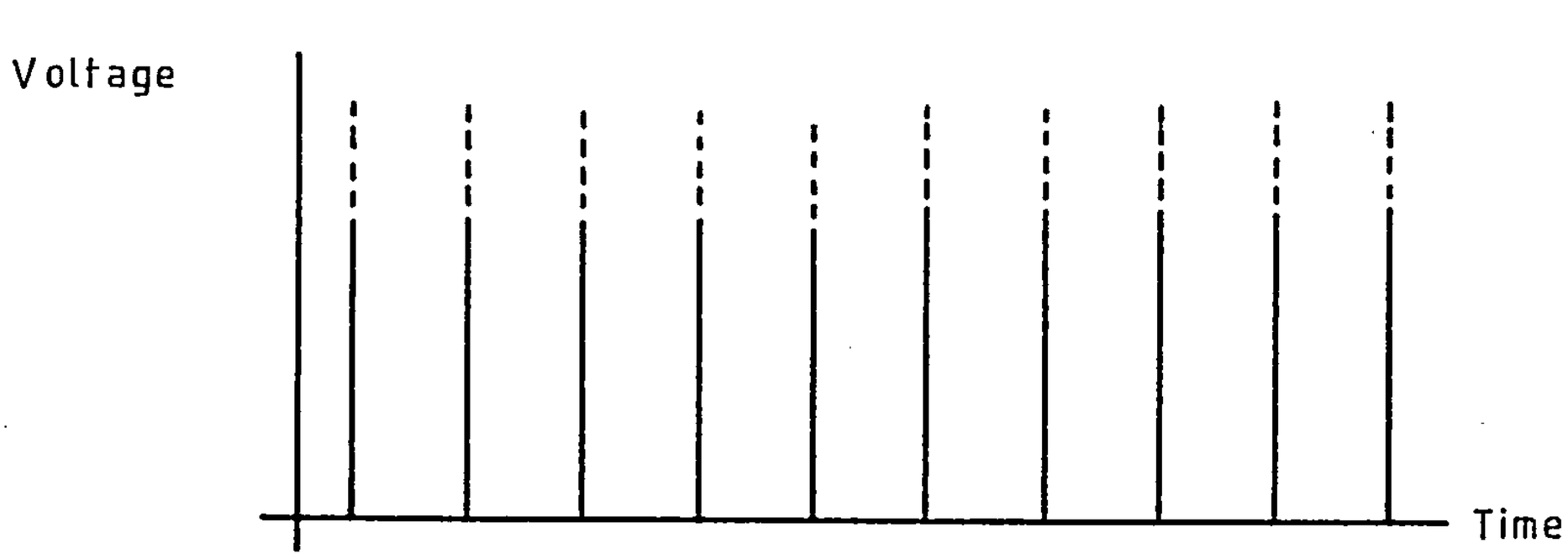

b. ...multiplied by a regular train of delta pulses.....

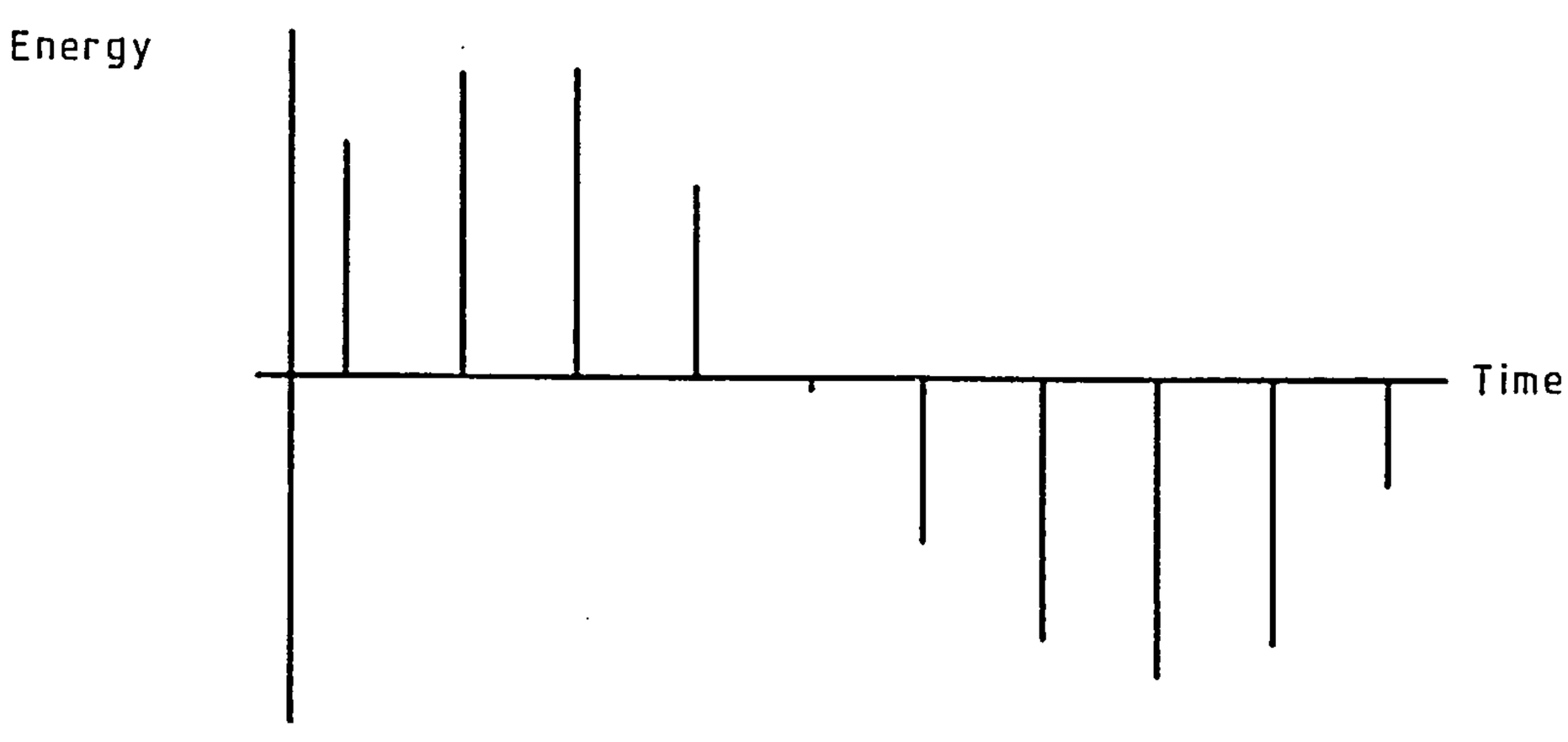

c. .... produces the sampled data.

$$\int_{-\infty}^{+\infty} i(t - mT).dt = 1 \qquad (5)$$

at $t = mT$ where $m = 0, 1, 2 \ldots .$

It is informative to compare the spectrum of a train of delta functions with that of a single delta function. Let I(t) represent the train of delta functions. The pulses are regular with a period T so they can be represented by a Fourier series composed of a fundamental frequency

$$w = \frac{2\pi}{T} \qquad (6a)$$

and its harmonics

$$w_n = \frac{2\pi n}{T} \quad . \qquad (6b)$$

Therefore

$$I(t) = \sum_{n=-\infty}^{+\infty} c_n \exp(j(2\pi n/T)t) \ , \qquad (7)$$

in which the coefficients are

$$c_n = \frac{1}{T}\int_{-T/2}^{+T/2} I(t)\exp(-j(2\pi n/T)t).dt. \qquad (8)$$

As I(t) exists only at $t = 0$ in the interval $-T/2$ to $+T/2$,

$$c_n = \frac{1}{T} \quad . \qquad (9)$$

That is, the delta pulse train consists of an infinite set of cosine harmonics of $w = 2\pi/T$ each of amplitude $1/T$. As shown in figure A2, its appearance in the time domain is identical to its appearance in the frequency domain.

The next step is to find the Fourier transform of the sample set, for this will lead to Shannon's sampling theorem. If the sampled data is labelled $\bar{f}(t)$ then

Figure A2.

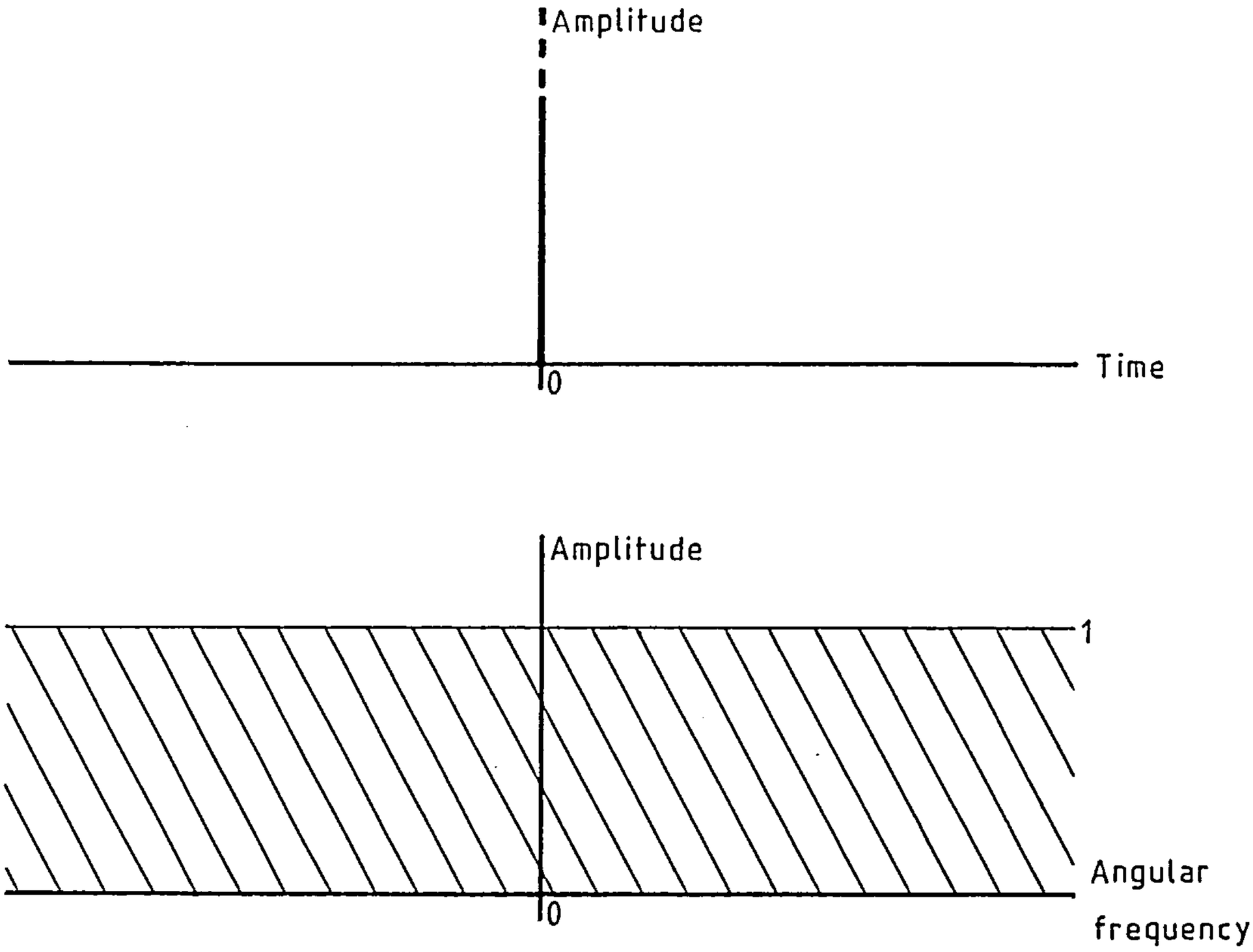

a. A single delta pulse in the frequency and time domains.

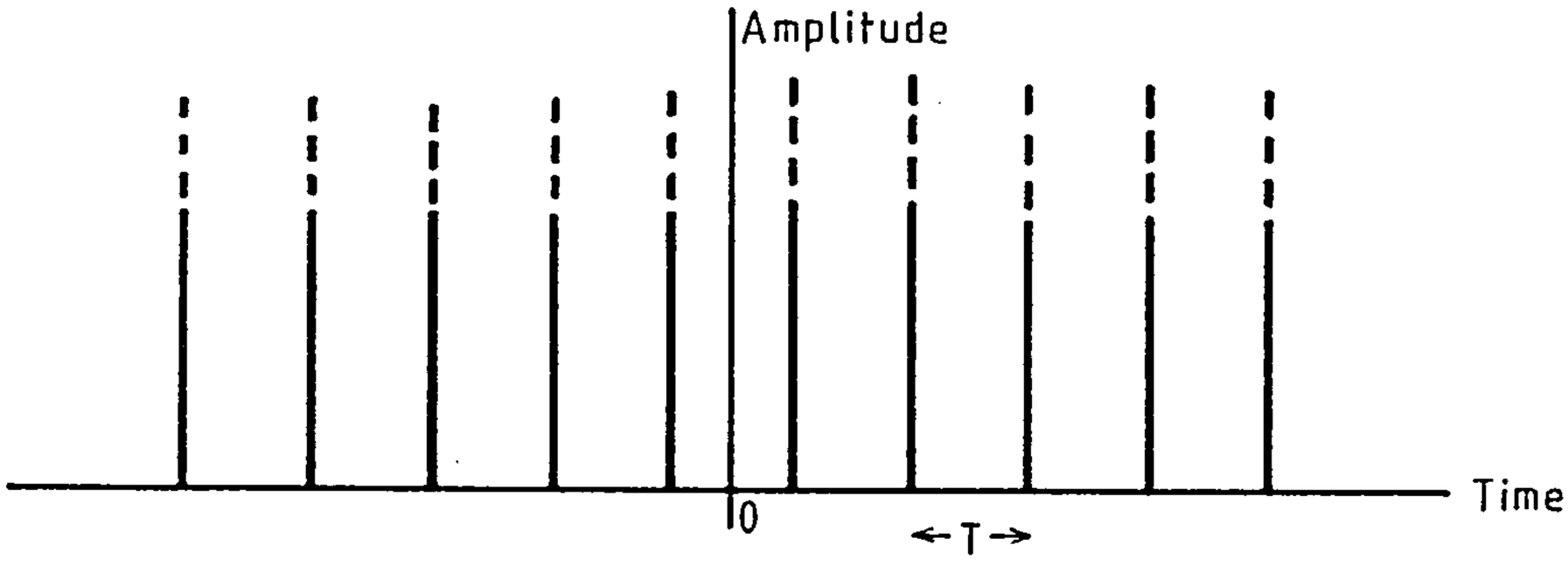

b. A train of delta pulses in the frequency and time domains.

$$\bar{f}(t) = f(t)I(t). \tag{10}$$

Using equations 7 and 9 in equation 10 gives

$$\bar{f}(t) = \frac{1}{T} \sum_{n=-\infty}^{+\infty} f(t)\exp(j(2\pi n/T)t) \; . \tag{11}$$

The Fourier transform of $\bar{f}(t)$ is $\bar{F}(jw)$:

$$\bar{F}(jw) = \int_{-\infty}^{+\infty} \bar{f}(t)\exp(-jwt).dt \tag{12}$$

$$= \frac{1}{T} \sum_{n=-\infty}^{+\infty} \int_{-\infty}^{+\infty} f(t)\exp(j(2\pi n/T)t)\ \exp(-jwt).dt \; . \tag{13}$$

Using the standard identity

$$\int_{-\infty}^{+\infty} f(t)\exp(-at)\exp(-jwt).dt = F(jw + a), \tag{14}$$

where $a > 0$, it can be seen that

$$\bar{F}(jw) = \frac{1}{T} \sum_{n=-\infty}^{+\infty} F(jw - j2\pi n/T). \tag{15}$$

Equation 15 shows that the Fourier transform of a sampled data set consists of an infinite number of regularly spaced Fourier transforms of the analogue signal. The spacing is $2\pi/T$ radians. This result comes as no surprise having seen figure A2b.

Provided that the analogue waveform contains no component frequencies higher than π/T rad s^{-1} the repetitive spectrum of the sample set poses no problems. If the analogue signal has components at frequencies higher than π/T rad s^{-1} then the shifted analogue spectra overlap. The regions of overlap are known as aliased frequency spectra. When aliasing occurs the original analogue waveform can no longer be recovered. An example of aliasing is shown in figure A7. Shannon's sampling theorem follows from these

conclusions:

a continuous signal which contains no significant components above w rad s^{-1} may in principle be recovered from its sampled version if the sampling interval is less than π / w seconds.

Next comes a statement on aliasing:

given a sampling period of T seconds, frequency components at u and u + n/T Hz, where n = 0, $\pm$ 1, $\pm$ 2, $\pm$ 3 -----, are indistinguishable because they have the same sample values.

For instance, if the analogue signal were a sine wave at exactly half the sampling frequency the sample set would be identical to that of a DC level, and any reconstruction procedure would be bound to interpret the sample set as a DC level.

Now that the principle of unambiguous sampling has been seen, how can the analogue signal be reconstructed? An outline of this operation can be seen in figure A3. In the frequency domain the difference between the sample set and the analogue signal is that the sample set contains frequencies above π/T rad $.s^{-1}$ and that the spectrum is weighted by a factor 1/T. Passing the sample set through a perfect low pass filter with a step cut off frequency at π /T rad s^{-1} and a gain of T therefore recreates the analogue signal. Numerically this may be achieved by interpolation between the sampling points using Whittaker's cardinal function[63,62]. For a set of N values taken at a rate of 1/T Hz, Whittaker's cardinal function to recreate f(t) is

$$f^*(t) = \sum_{n=0}^{N-1} f_n \frac{\sin((\pi/T)(t - nT))}{(\pi/T)(t - nT)} \quad , \qquad (16)$$

f_n is the nth value within the sample set. Notice that $f^*(t) = f(t)$ at the sampling points: only the nth term can be non-zero if t = nT in equation 16.

Figure A3. A diagram illustrating the recovery of f(t) from $\overline{f}$ (t).

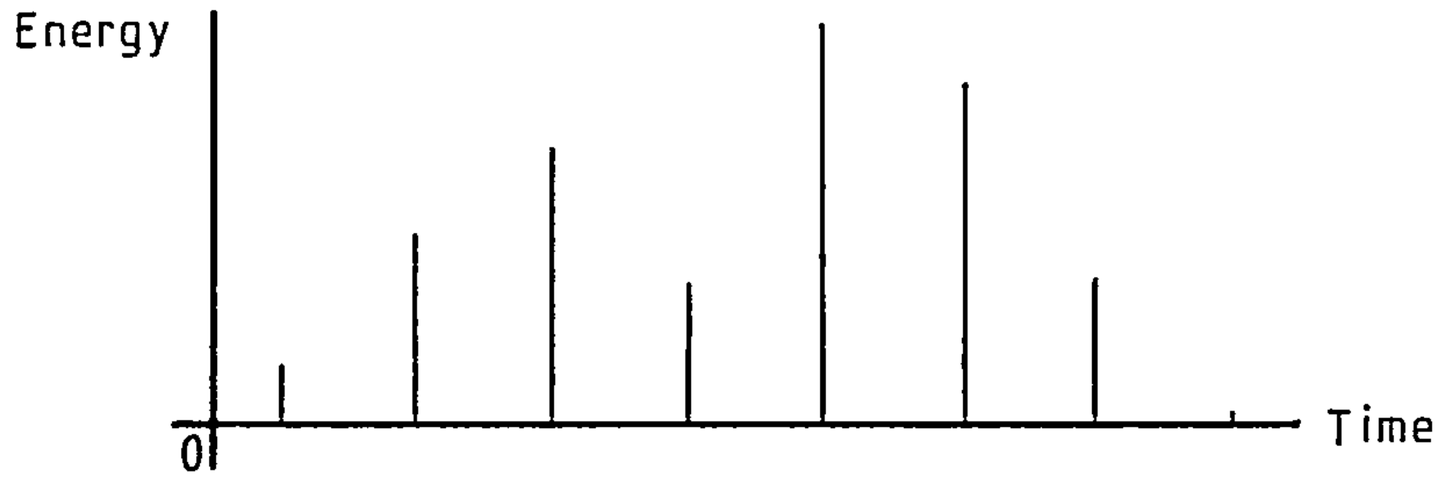

a. The sample set $\overline{f}$ (t).

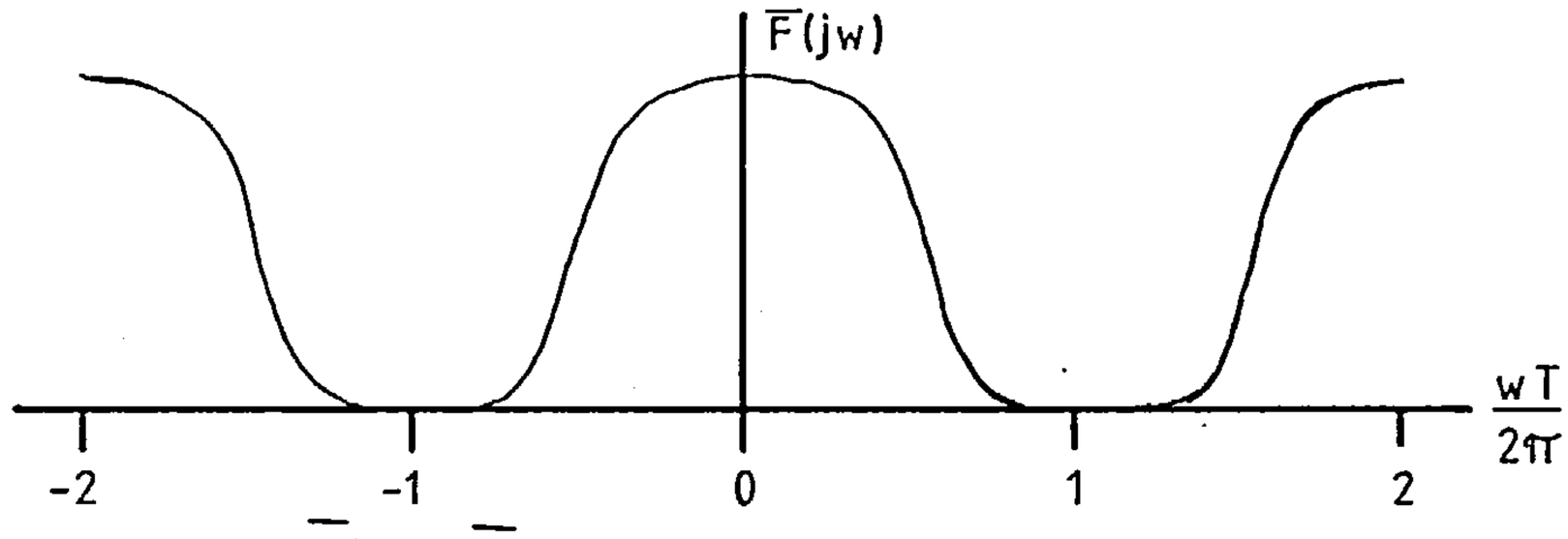

b. The spectrum of $\overline{f}$(t), $\overline{F}$ (jw).

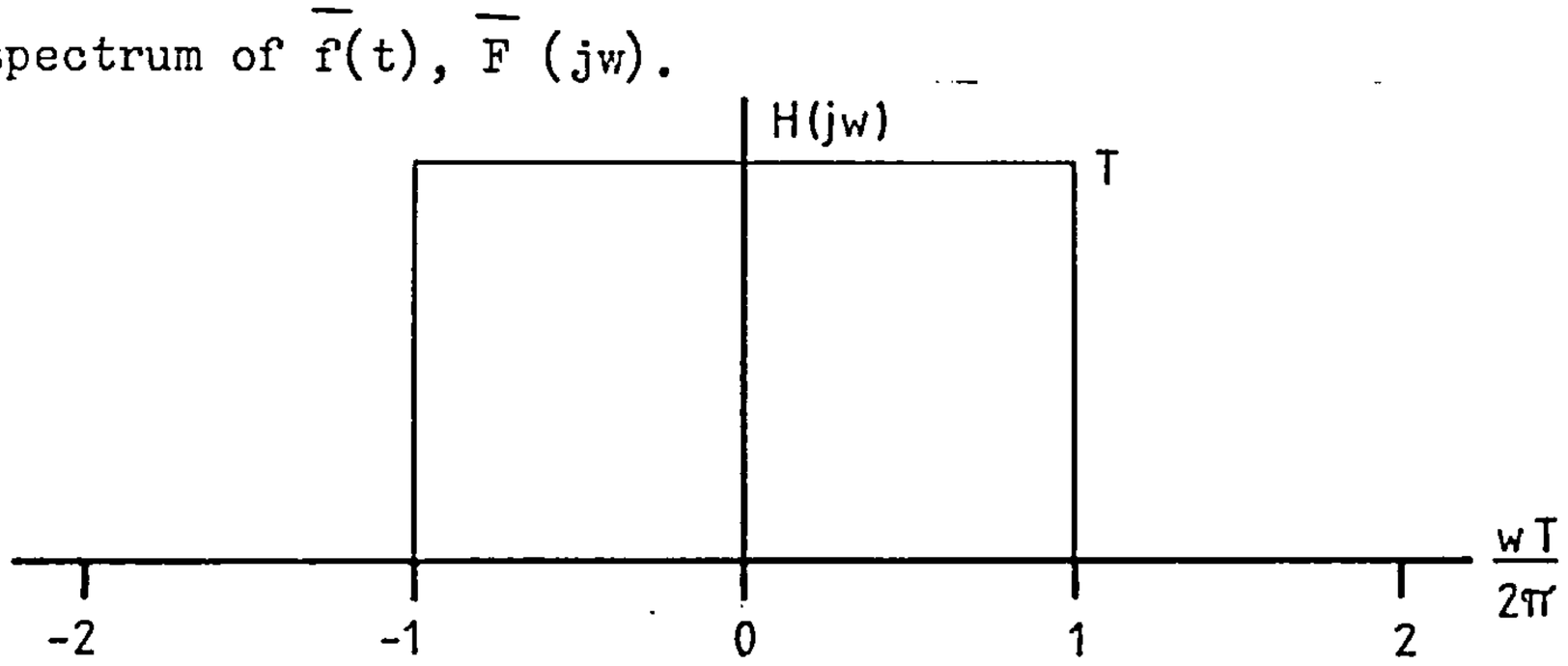

c. The ideal reconstruction filter.

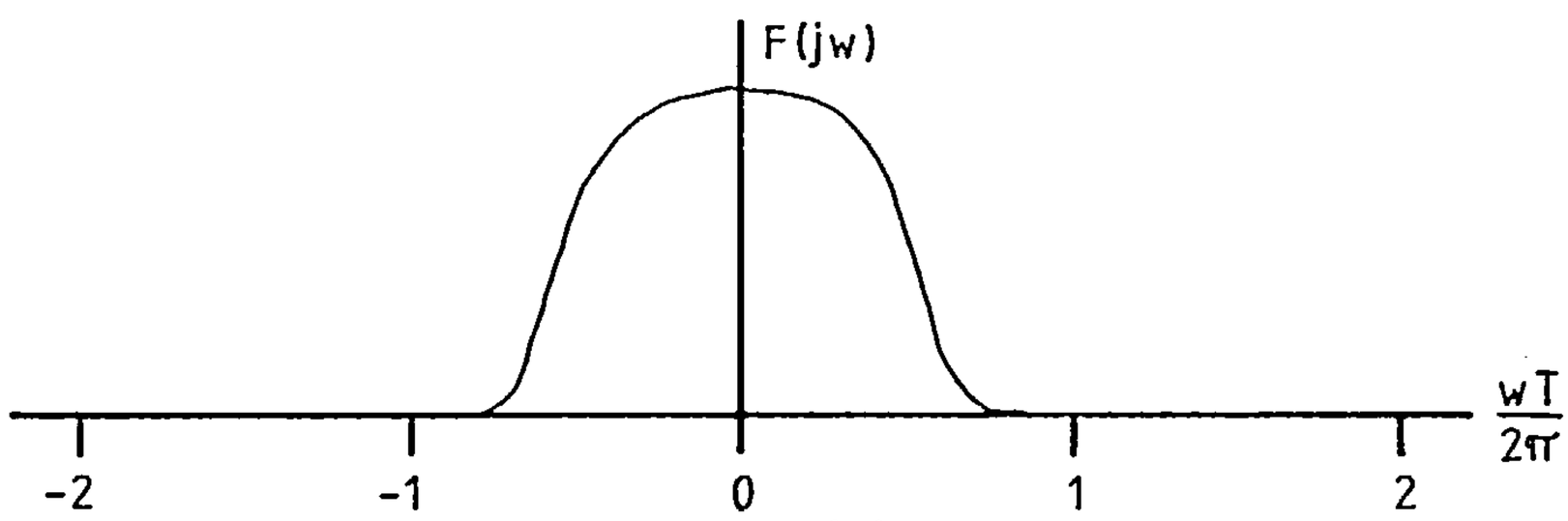

d. The recovered analogue spectrum F*(t).

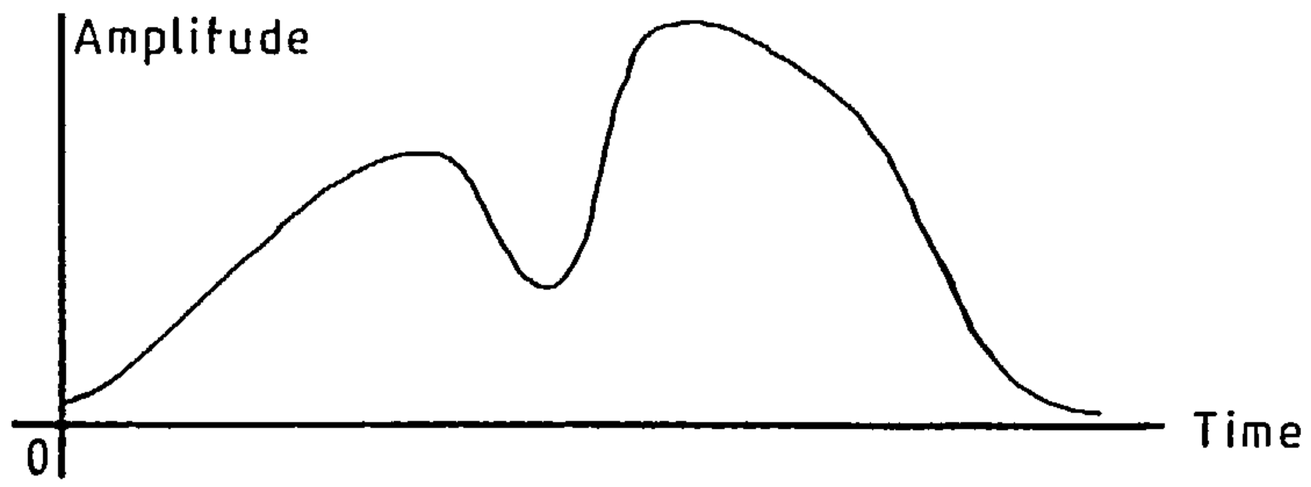

e. The recovered analogue signal f* (t).

A1.3 Practical sampling and reconstruction errors

A system for digitally processing an analogue waveform is shown as a block diagram in figure A4. The purpose of this section is to show how the performance of a practical real-time processing system differs from the ideal system just discussed.

A1.3.1 The quantization error

Digital systems cannot deal with the continuous amplitude distribution of an analogue signal. Instead, the amplitude is represented as an integer and there is a quantization error incurred by doing this. When instructed by the sample clock, the sample and hold circuit (SH) stores the instantaneous value of the analogue signal. The stored value is converted to a digital sample by the analogue to digital converter (ADC). The details of the operation and design of ADC's are discussed by Tietze and Schenk [49,427]. The resolution of an ADC is one least significant bit (LSB), the ADC's output for a full scale analogue input is 2^N LSB's where N may range from 3 to 18 depending on the price and conversion speed of the ADC. The maximum quantization error is $\pm$ 1/2 LSB, but the error usually lies within these bounds. The distribution of the quantization error in a typical set of samples is shown in figure A5.

It is not difficult to calculate the r.m.s. amplitude of the quantization error. For a sufficient number of samples the quantization error is a random variable that may be treated as random noise. The errors are uniformly distributed in the range $\pm$ 1/2 LSB provided that 1 LSB is a small fraction of the maximum output (2^N LSB). The root mean square error is given by [63,45]

$$V_e \text{ r.m.s.} = 2^{-N} / \sqrt{12} = V_{LSB} / \sqrt{12}, \qquad (17)$$

where V_{LSB} is the voltage represented by 1 LSB. For any ADC, the maximum output signal to noise ratio for a sinusoid can now be calculated. For a full scale sinusoidal input swing the r.m.s. output

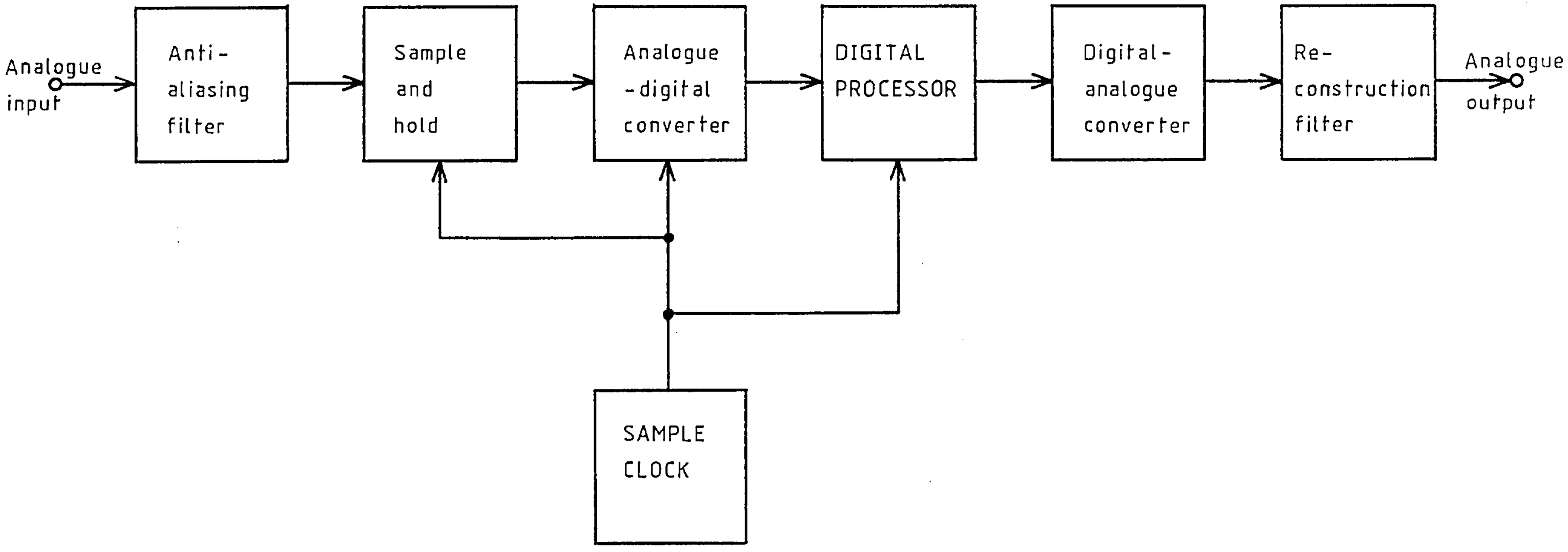

Figure A4. A system for the real-time digital processing of an analogue signal.

Figure A5. An illustration of the quantization error in an analogue to digital converter.

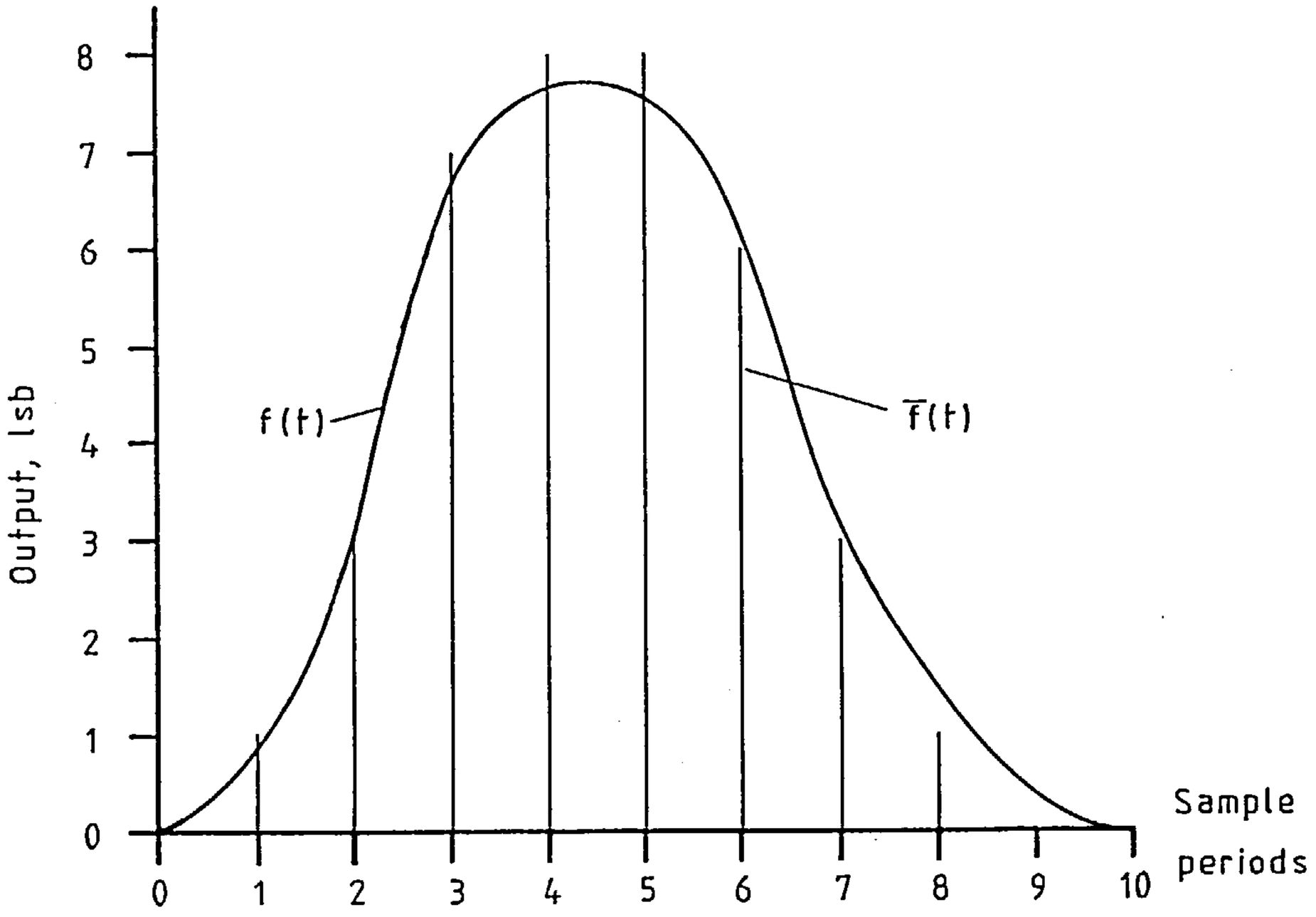

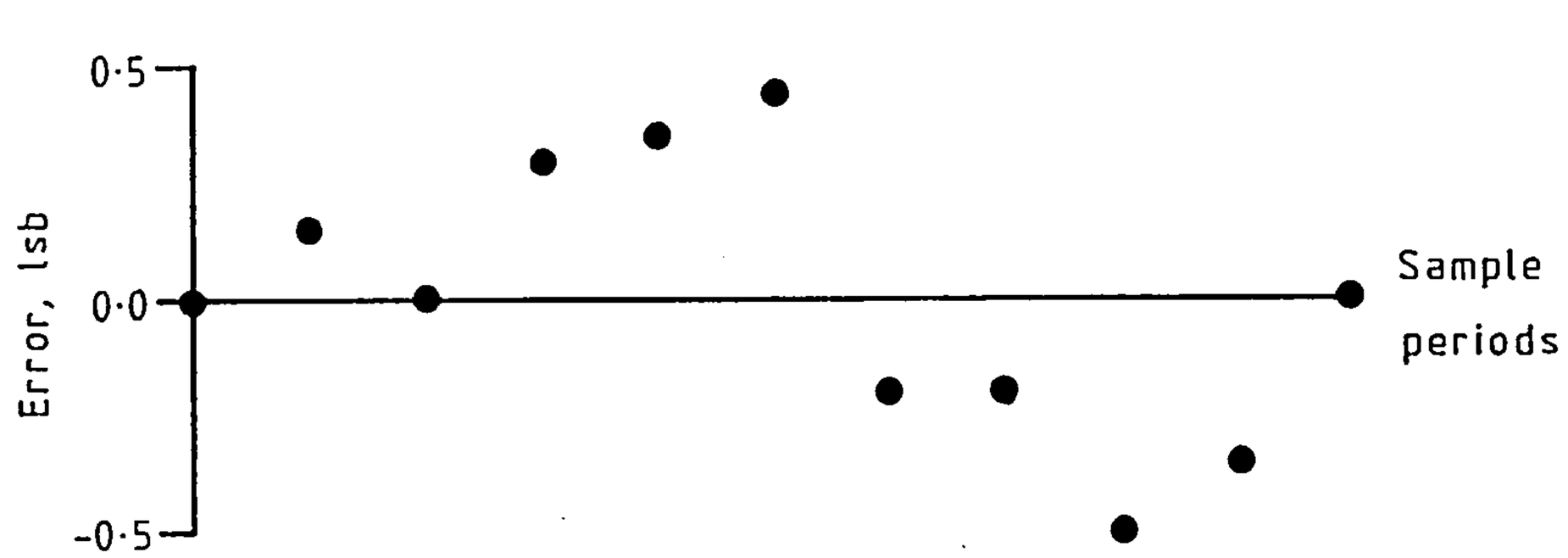

Figure A6. The weighting function due to the finite sample pulse width.

signal voltage for an N bit converter is

$$V_s \text{ r.m.s.} = \frac{1}{2^{0.5}} \ (2^N) \ \frac{1}{2} V_{LSB} \ . \qquad (18)$$

The signal to noise ratio is

$$SNR = 20 \log_{10} \left[\frac{V_s \text{ r.m.s.}}{V_e \text{ r.m.s.}} \right] ,$$

that is

$$SNR = (6N + 1.8)dB \ . \qquad (19)$$

A1.3.2 The finite aperture time

A real sample and hold circuit cannot take instantaneous sample values of the analogue waveform. Instead, there is an aperture time during which the SH records the waveform's amplitude by storing some of the waveform's energy on an input capacitance C. Because the waveform comes from a source of output impedance R there is an inbuilt RC time constant which ensures that the aperture time is finite. RC time constants in this form act as low pass filters and it is therefore not surprising that high frequency components on the incoming waveform are attenuated. The finite aperture time can be reasonably modelled by changing the delta sampling pulse to a flat topped sampling pulse of width W and height T/W. The spectrum of the sample set is then weighted by the Fourier transform of the sample pulse:

$$F(jw) = \frac{\sin(wW/2)}{wW/2} \ , \qquad (20)$$

where w is any frequency component of the sample set. The weighting function is illustrated in figure A6. The function's importance lies in showing that Shannon's sampling theorem may be too lax in practice for there to be minimal distortion of the sampled data set.

A1.3.3 Aperture jitter

Phase noise in the sample clock produces an uncertainty ΔT in the sample period, this creates an error ΔV in the sampled voltage.

In the case of a sine wave with a peak value V_m and a frequency w, the worst jitter error occurs when a sample is taken close to the sinusoid's zero crossings. At the zero crossings,

$$\frac{\Delta V}{\Delta t} = wV_m \quad , \qquad (21)$$

the jitter error is therefore

$$\Delta V = wV_m . \Delta T \quad . \qquad (22)$$

If this error is to be kept smaller than the amplitude of 1 LSB, labelled V_{LSB}, the restriction on the uncertainty in the sample period is

$$\Delta T < \frac{V_{LSB}}{wV_m} \quad . \qquad (23)$$

A1.3.4 The anti-alias filter

It is desirable to reduce the sampling rate as far as is possible in keeping with the sampled data system's purpose. One way of doing this is to use a low pass filter prior to the SH to remove any analogue signal frequencies above the range of interest. The sampling frequency can then be reduced without any worries about high frequency noise, or useless high frequency signals, causing aliasing distortion in the useful signal. This low pass filter is known as an anti-aliasing filter.

Practicable anti-alias filters do not have an infinitely steep cut off and so some aliasing noise is inevitable. The best that can be done is to keep the amplitude of this noise less than the magnitude of 1 LSB. The filter brings in its wake the penalty of phase distortion. In general, the better the filter's performance in the frequency domain the worse its performance in the time domain. These points are illustrated in figure A7.

Choosing a sampling frequency requires a knowledge of the filter's frequency characteristics, the likely amplitude of the unwanted frequency components and the amount of phase distortion that is acceptable.

Figure A7.

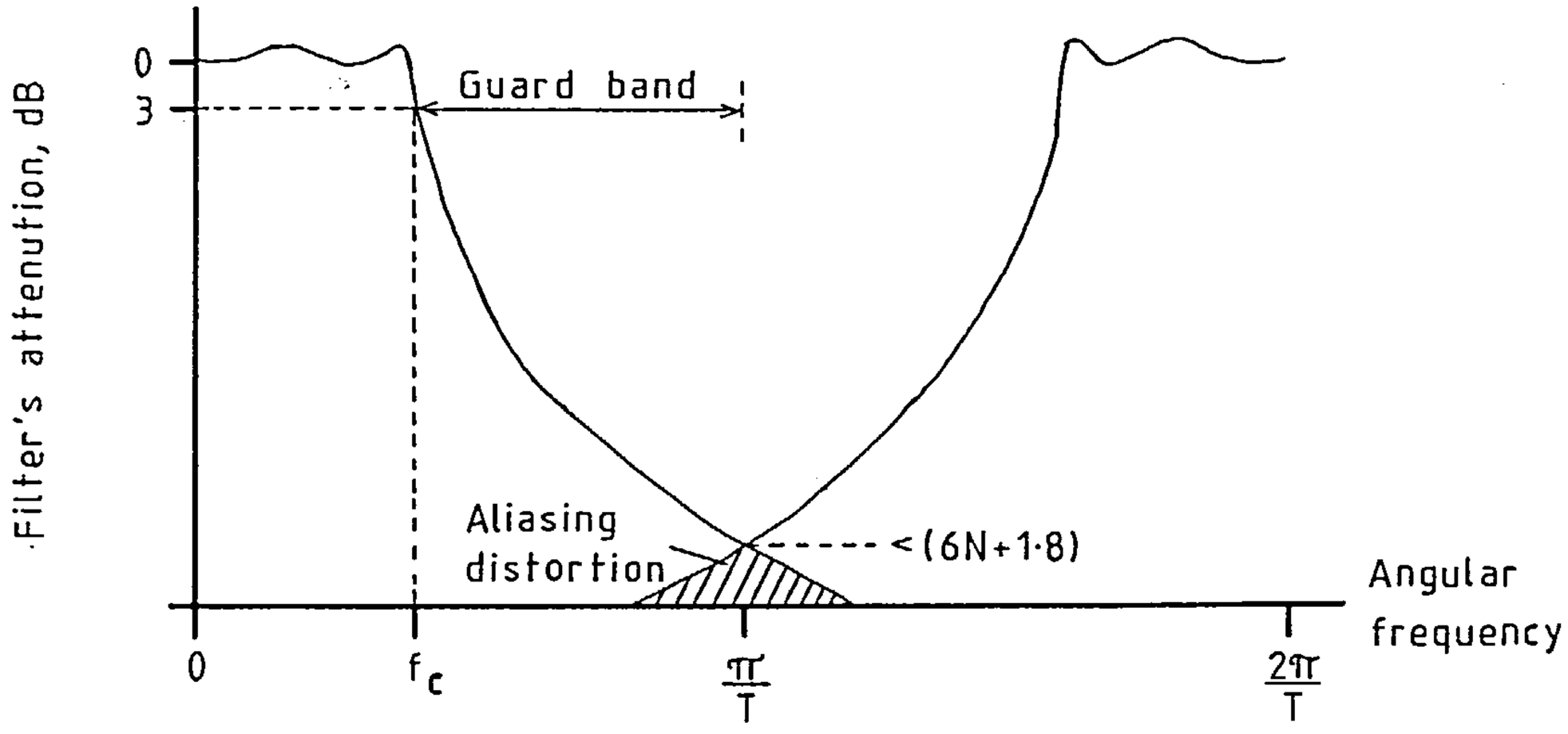

a. Using an anti-alias filter to tailor the signal's amplitude spectrum,...,.

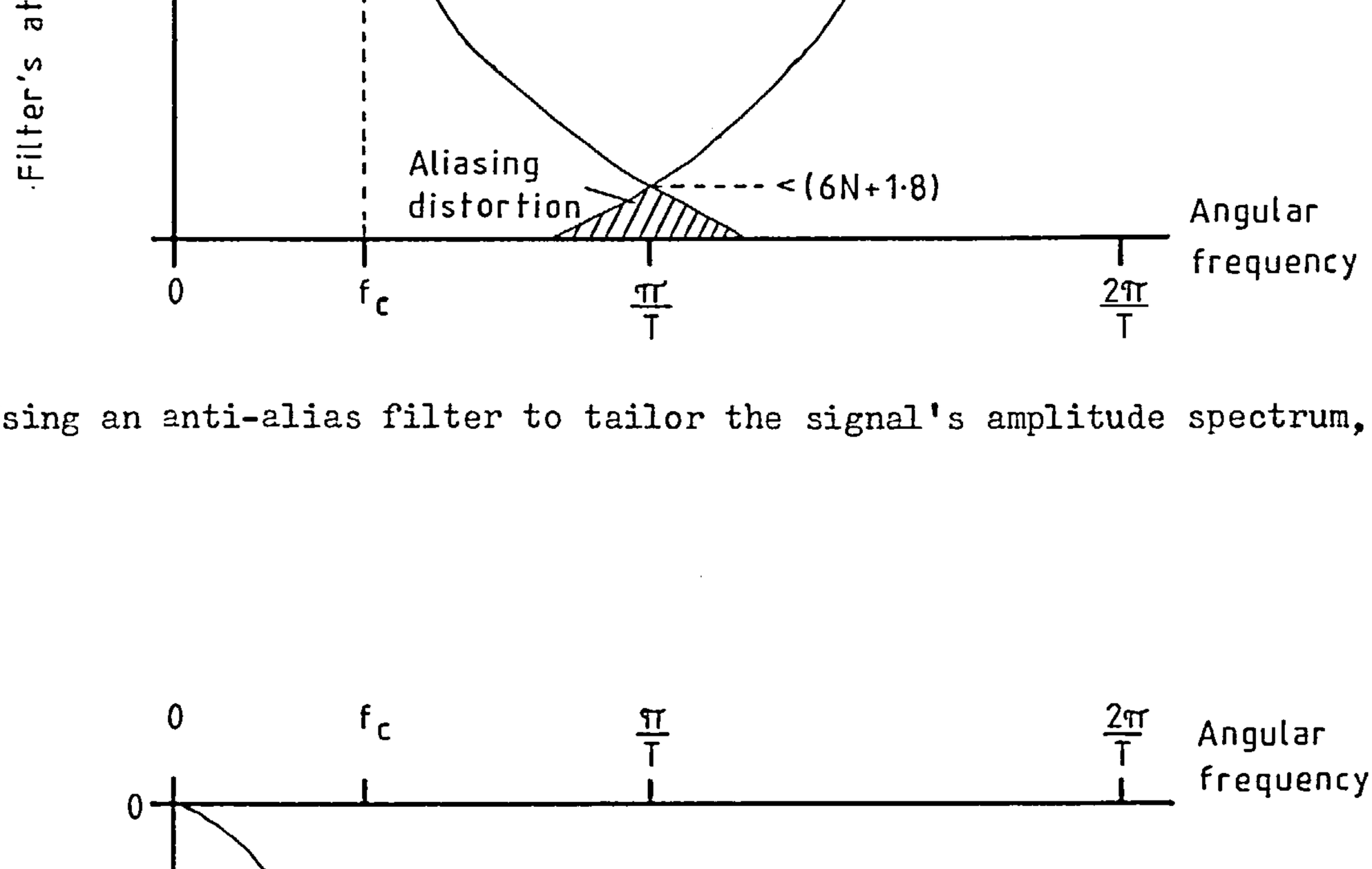

b. .... will distort the signal's phase spectrum.

A1.3.5 Digital to analogue conversion

The ideal reconstruction of an analogue signal requires that pulses of energy, each with an infinitely short duration and an infinite height, be passed through a perfect low pass filter. After the discussion on analogue to digital conversion, the problems here are obvious.

The digital to analogue converter (DAC) turns what is usually a binary number into any one of 2^N discrete analogue levels. The design of DAC's is discussed by Tietze and Schenk[49,411]. It is common practice to update the output of the DAC once every sample period, the output remains constant in between times. The output pulses therefore have a width of T seconds which creates an undesirable spectrum weighting function of

$$F(jw) = \frac{\sin(wT/2)}{wT/2} . \qquad (24)$$

Finally, the perfect analogue reconstruction filter cannot be built. Once again, the sampling rate of the system has to be high enough to allow the reconstruction filter to sufficiently attenuate the high frequency components without significantly affecting the useful components.

A.1.4 The z transform

The z transform is perfectly adapted to sampled data signals. The definition of the transform is:

$$z = \exp(sT) \qquad (25)$$

where s is the Laplace transform variable $\sigma + jw$. Therefore,

$$z = \exp(\sigma T)\exp(jwT)$$

$$= \exp(\sigma T)\cos wT + j\exp(\sigma T)\sin wT. \qquad (26)$$

z is commonly described as a shift operator, multiplying by z represents a time advance of T seconds and dividing by z represents a time delay of T seconds. The z transform of a sequence of samples is just

Figure A8.

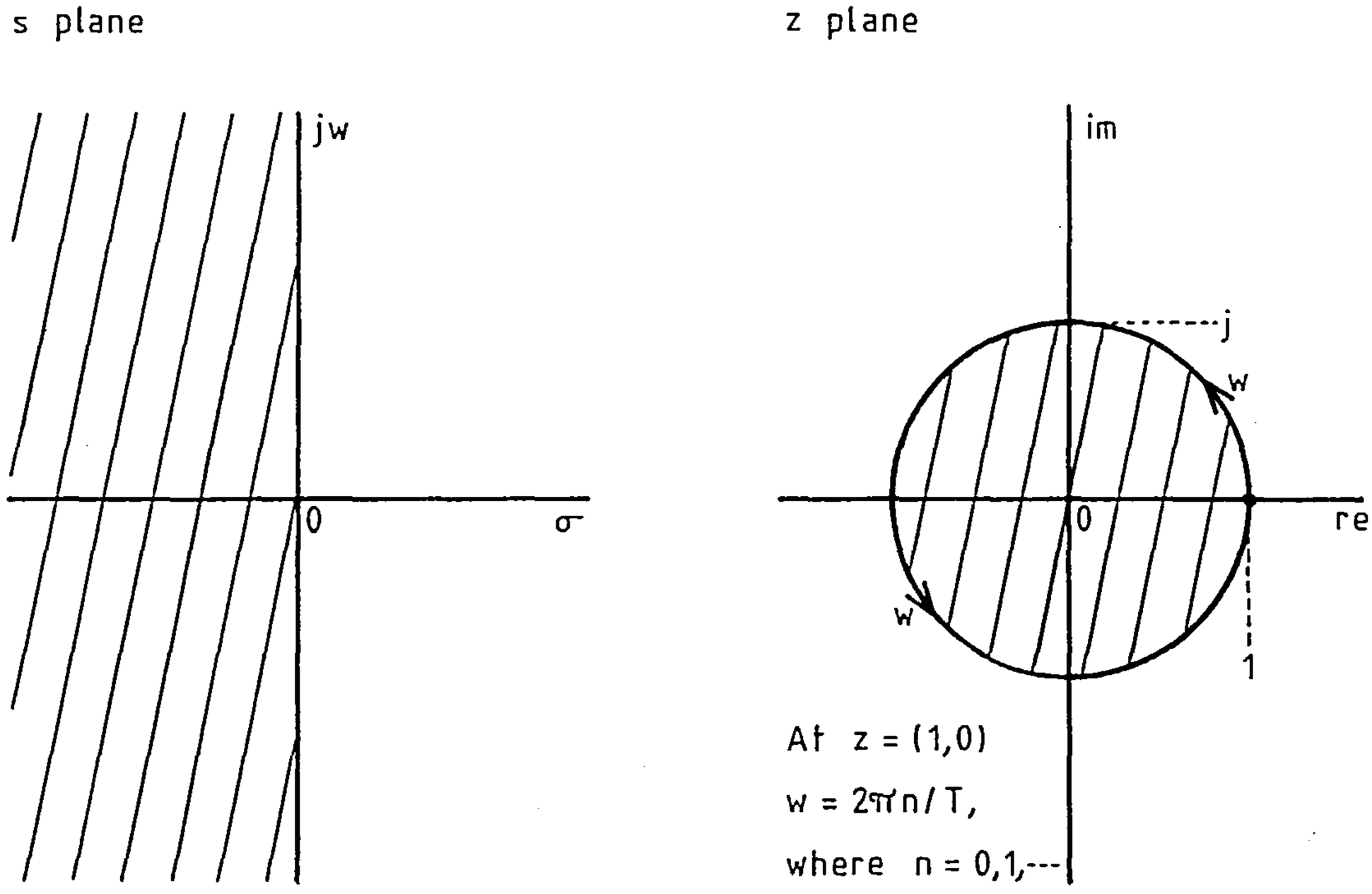

a. Mapping the s plane onto the z plane.

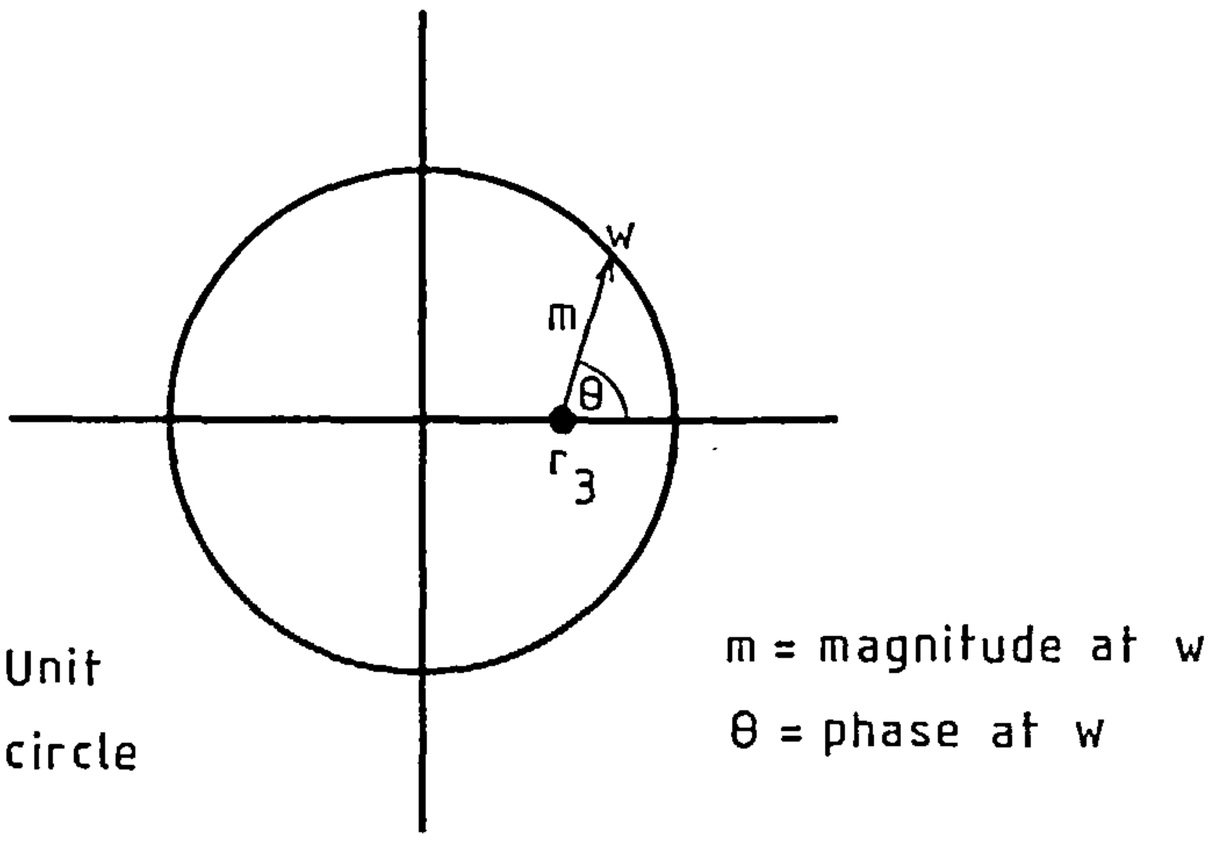

b. A stable time sequence described by a single pole at $z = r_3$.

the samples' complete spectrum, or the response of the digital system, may be described by just one set of z plane poles and zeros. A pole or zero at the point $\sigma + jw$ in the s plane maps to $r = \exp(\sigma T)$ and $\theta = wT$ in the z plane.

By way of illustration, the data set

$$G(z) = z^{-1} + r_3 z^{-2} + r_3{}^2 z^{-3} + r_3{}^3 z^{-4} \ldots \qquad (30)$$

is more conveniently written as

$$G(z) = \frac{1}{(z - r_3)} \quad . \qquad (31)$$

This function corresponds to a pole at $z = r_3$ in the z plane. If $r_3 < 1$ the sequence in equation 45 decreases as $t \longrightarrow \infty$. Thus, poles within the unit circle represent stable sequences. This would be expected as the inside of the unit circle is the counterpart of the left hand side of the s plane. For $r_3 > 1$ the pole lies outside the unit circle and the sequence grows without limit as $t \longrightarrow \infty$.

The spectrum of the sequence is found by substituting jw for z so that

$$G(jw) = (\exp(jwT) - r_3)^{-1} \quad . \qquad (32)$$

This expression represents a vector drawn from the pole to a frequency w on the unit circle. As w is increased from 0 to ∞ the unit circle is traced out repeatedly by the vector. The changes in the vector's modulus and argument then give the magnitude and phase spectra - see figure A8 b.

This concludes the appendix.

APPENDIX 2

AN ANNOTATED LISTING OF THE SOFTWARE FOR THE DISPLACEMENT TRANSDUCER

This appendix gives a complete listing of the software code for a 6502 microprocessor. All addresses and numbers are hexadecimal. The symbol £ is used to denote immediate data as opposed to a page zero address. A general hardware memory map is given in figure 86, a detailed page zero memory map is given in figure 104. Details of the microprocessor's registers and instructions can be found in figures 98, 99 and 100. The code corresponds to the flowcharts and explanations given in section 9.3.

ANALOGUE TO DIGITAL CONVERSION MODULE

HEXADECIMAL ADDRESS	LABEL	INSTRUCTION	COMMENTS
F800	ADCONV	LDA £40	Wait for sample
F802	TEST	BIT 900D	clock's instruction to
F805		BEQ TEST	start - T1 interrupt.
F807		STA 9180	Initiate conversion.
F80A		LDX £03	Wait for 34 us
F80C	WAIT	NOP	
F80D		DEX	
F80E		BNE WAIT	
F810		LDA 9004	Clear TI interrupt.
F813		LDA 9180	Put m.s. 8 bits in 01
F816		STA 01	
F818		LDA 9181	Put l.s. 4 bits in 00
F81B		STA 00	
F81D		LSR 01	Remove 4 trailing
F81F		ROR 00	zeros of result
F821		LSR 01	
F823		ROR 00	
F825		LSR 01	
F827		ROR 00	
F829		LSR 01	
F82B		ROR 00	
F82D		RTS	End of subroutine.

BINARY TO BCD CONVERSION MODULE

HEXADECIMAL ADDRESS	LABEL	INSTRUCTION	COMMENTS
F82E	BINBCD	LDA £00	Set DNUM = 0
F830		STA 02	
F832		STA 03	
F834		LDX £0C	Set INDEX = 12_{10}
F836		SED	Set DECIMAL mode
F837		ASL 04	Shift 12 bit BNUM left
F839		ROL 05	4 times such that MS Bit
F83B		ASL 04	will enter CARRY on
F83D		ROL 05	next shift left.
F83F		ASL 04	
F841		ROL 05	
F843		ASL 04	
F845		ROL 05	
F847	NXTBIT	CLC	Double DNUM. Note
F848		LDA 02	that shifting left is
F84A		ADC 02	no good for decimal
F84C		STA 02	mode numbers.
F84E		LDA 03	
F850		ADC 03	
F852		STA 03	
F854		ASL 04	Shift BNUM left
F856		ROL 05	CARRY ← MS Bit
F858		LDA 02	Add CARRY to DNUM
F85A		ADC 00	
F85C		STA 02	
F85E		LDA 03	
F860		ADC 00	
F862		STA 03	
F864		DEX	Decrement index.
F865		BNE NXTBIT	Index = 0? If not, go back to NXTBIT
F867		CLD	Clear DECIMAL mode.
F868		RTS	End of subroutine.

16 BIT UNSIGNED BINARY MULTIPLY MODULE

HEXADECIMAL ADDRESS	LABEL	INSTRUCTION		COMMENT
F869	MLTPLY	LDX	£11	Set INDEX = 17
F86B		LDA	£00	Set A' = B' = 0
F86D		STA	0B	
F86F		STA	0A	
F871		CLC		Clear CARRY
F872	CCHECK	BCC	ROTATE	If CARRY = 0, branch to ROTATE
F874		CLC		Clear CARRY for addition
F875		LDA	06	Add MULTIPLICAND (E',F')
F877		ADC	0A	to A', B'.
F879		STA	0A	
F87B		LDA	07	
F87D		ADC	0B	
F87F		STA	0B	
F881	ROTATE	ROR	0B	Rotate A', B', C', D'.LS Bit
F883		ROR	0A	of D' enters CARRY.
F885		ROR	09	
F887		ROR	08	
F889		DEX		Decrement INDEX
F88A		BNE	CCHECK	If INDEX ≠ 0 branch to CCHECK.
F88C		RTS		End of subroutine

ANALOGUE FILTER SETTLING DELAY MODULE

HEXADECIMAL ADDRESS	LABEL	INSTRUCTION		COMMENT
F88D	DELAY	LDX	£23	Set INDEX = 35
F88F	REPEAT	LDA	£40	Has T1 set interrupt yet?
F891	CLKTST	BIT	900D	If not, go back to
F894		BEQ	CLKTST	CLKTST and try again
F896		LDA	9004	Reset T1 interrupt
F899		DEX		Decrement INDEX
F89A		BNE	REPEAT	Counted out 35 cycles? If not, go back to REPEAT.
F89C		RTS		End of subroutine.

THE ANALOGUE OFFSET SUBROUTINE

HEXADECIMAL ADDRESS	LABEL	INSTRUCTION		COMMENT
F89D	OFFSET	STA	91A0	Set gain HIGH; first set
F8A0		STA	91A8	it low and then toggle it
F8A3		LDA	£0F	Put D OFF (Device
F8A5		STA	9190	OFF set) on display.
F8A8		LDA	£1F	
F8AA		STA	9190	
F8AD		LDA	£20	
F8AF		STA	9190	
F8B2		LDA	£3D	
F8B4		STA	9190	
F8B7		JSR	DELAY	Call DELAY module to let analogue filter settle
F8BA		LDY	£FF	Set INDEX = 255_{10}
F8BC	NEWSMP	JSR	ADCONV	Call ADC module to get an offset sample
F8BF		CLC		Add offset into TOTAL
F8C0		LDA	0C	
F8C2		ADC	00	
F8C4		STA	0C	
F8C6		LDA	0D	
F8C8		ADC	01	
F8CA		STA	0D	
F8CC		DEY		Decrement index
F8CD		BNE	NEWSMP	Index = 0? If not, get another sample.
F8CF		LDA	0D	High gain offset = TOTAL/256
F8D1		STA	0F	Store high gain offset
F8D3		LSR	A	Low gain offset
F8D4		LSR	A	$= \frac{TOTAL}{2048} + 3$
F8D5		LSR	A	
F8D6		CLC		
F8D7		ADC	£03	
F8D9		STA	0E	Store low gain offset
F8DB		LDA	£01	Set GAIN TEST bit
F8DD		STA	14	
F8DF		RTS		End of subroutine

THE GAIN CHECKING AND RANGE SETTING SUBROUTINE

HEXADECIMAL ADDRESS	LABEL	INSTRUCTION	COMMENT
F8E0	GRCHK	JSR ADCONV	Call ADC module
F8E3		LDA £01	Load GAIN TEST bit
F8E5		BIT 14	If gain HIGH, branch to
F8E7		BNE HIGAIN	high gain section.
F8E9	LOGAIN	SEC	As this is low gain section,
F8EA	OFFLO	LDA 00	remove the low gain offset
F8EC		SBC 0E	and store result at 11, 10.
F8EE		STA 10	
F8F0		LDA 01	
F8F2		SBC £00	
F8F4		STA 11	
F8F6	CHKRLO	SEC	Is signal < 0E, FF?
F8F7		LDA 10	Yes: next question.
F8F9		SBC £FF	No: magnet too close,
F8FB		LDA 11	tell operator.
F8FD		SBC £0E	
F8FF		BMI CHKGLO	
F901	TCLOSE	LDA £00	As magnet is too close
F903		STA 9189	put CCCC on display
F906		STA 918A	and zero deflection on
F909		LDA £0C	D.A.C.
F90B		STA 9190	
F90E		LDA £1C	
F910		STA 9190	
F913		LDA £0C	
F915		STA 9190	
F91B		LDA £3C	
F91A		STA 9190	
F91D		JMP GRCHK	Jump back to start of subroutine.
F920	CHKGLO	SEC	Is signal ⩾ 01, 80?
F921		LDA 10	Yes: stick with low gain.
F923		SBC £80	No: change to high gain.
F925		LDA 11	
F927		SBC £01	
F929		BPL GROKLO	

HEXADECIMAL ADDRESS	LABEL	INSTRUCTION		COMMENT
F92B	CHGGLO	STA	91A8	Toggle gain
F92E		LDA	£01	Set GAIN TEST bit.
F930		STA	14	
F932		JSR	DELAY	Allow analogue settling
F935		JMP	GRCHK	Go back to start of routine
F938	GROKLO	LDA	£7F	Identify low gain look-up
F93A		STA	12	table.
F93C		RTS		Exit gain and range check routine.
F93D	HIGAIN	SEC		This is the high branch.
F93E	OFFHI	LDA	00	Remove the high gain offset
F940		SBC	0F	from the signal.
F942		STA	10	
F944		LDA	01	
F946		SBC	£00	
F948		STA	11	
F94A	CHKRHI	SEC		Is signal $\geqslant$ 00, 05?
F94B		LDA	10	
F94D		SBC	£05	Yes: next question.
F94F		LDA	11	No: magnet TOO FAR, tell
F951		SBC	£00	operator.
F953		BPL	CHKGHI	
F955	TFAR	LDA	£E8	As magnet is too far
F957		STA	9189	put FFFF on display
F95A		LDA	£03	and put 1000_{10} on D.A.C.
F95C		STA	918A	
F95F		LDA	£0F	i.e. 1 bit on D.A.C.
F961		STA	9190	= 0.4 mm
F964		LDA	£1F	
F966		STA	9190	
F969		LDA	£2F	
F96B		STA	9190	
F96E		LDA	£3F	
F970		STA	9190	
F973		JMP	GRCHK	Jump back to start of this subroutine.

HEXADECIMAL ADDRESS	LABEL	INSTRUCTION	COMMENT
F976	CHKGHI	SEC	Is 0E, 7F ⩾ signal?
F977		LDA £7F	
F979		SBC 10	Yes: stick with high gain
F97B		LDA £0E	No: change to low gain.
F97D		SBC 11	
F97F		BPL GROKHI	
F981	CHGGHI	STA 91A0	Set low gain.
F984		LDA £00	Reset GAIN TEST bit.
F986		STA 14	
F988		JSR DELAY	Delay for analogue settling
F98B		JMP GRCHK	Jump back to start of this subroutine.
F98E	GROKHI	LDA £BF	Identify high gain look up
F990		STA 12	table.
F992		RTS	Exit gain and range check subroutine.

CALIBRATION DATA FETCHING SUBROUTINE

HEXADECIMAL ADDRESS	LABEL	INSTRUCTION	COMMENT
F993	FETCH	JSR ADCONV	Get sample and store
F996		LDA 00	in output of
F998		STA 24	interpolation subroutine
F99A		LDA 01	
F99C		STA 25	
F99E		RTS	Leave this subroutine.

THE FIELD TO DISTANCE INTERPOLATION SUBROUTINE

HEXADECIMAL ADDRESS	LABEL	INSTRUCTION	COMMENT
F99F	INTERP	LDA 11	Get MS Byte (ADC output
F9A1		STA 15	- analogue offset.)
F9A3		LDA 10	Get LS Byte of above.
F9A5		ROL A	Put bit 7 into CARRY
F9A6		ROL 15	Get X/128
F9A8		ASL 15	Get (X/128) x 2
F9AA		LDY 15	Store in Y Register for indexed indirect addressing
F9AC		LDA 10	
F9AE		AND £7F	Find $X-X_i$ Know that last
F9B0		STA 16	7 bits of X_j are zero and that upper 9 bits of two variables are identical.
F9B2		LDA (12),Y	Find and store f.
F9B4		STA 17	
F9B6		INY	
F9B7		LDA (12), Y	
F9B9		STA 18	
F9BB		LDA 16	$X_i + 1 - X$ is two's
F9BD		EOR £7F	complement of $X - X_i$
F9BF		CLC	
F9C0		ADC £01	
F9C2		STA 19	
F9C4		INY	Find and store f_{i+1}
F9C5		LDA (12),Y	
F9C7		STA 1A	
F9C9		INY	
F9CA		LDA (12),Y	
F9CC		STA 1B	
F9CE		INY	Find and store f_{i+2}
F9CF		LDA (12),Y	
F9D1		STA 1A	
F9D3		INY	
F9D4		LDA (12),Y	
F9D6		STA 1B	
F9D8		SEC	Find and store
F9D9		LDA 17	
F9DB		SBC 1A	$-\Delta f_{i+1} = f_{i+1} - f_{i+2}$
F9DD		STA 1E	

HEXADECIMAL ADDRESS	LABEL	INSTRUCTION		COMMENT
F9DF		LDA	18	
F9E1		SBC	1B	
F9E3		STA	1F	
F9E5		SEC		Find and store
F9E6		LDA	1A	
F9E8		SBC	1C	$-\Delta f_{i+1} = f_{i+1} - f_{i+2}$
F9EA		STA	20	
F9EC		LDA	1B	
F9EE		SBC	1D	
F9F0		STA	21	
F9F2		SEC		Find and store
F9F3		LDA	1E	
F9F5		SBC	20	$\Delta^2 f_i = -\Delta f_i - (-\Delta f_{i+1})$
F9F7		STA	22	
F9F9		LDA	1F	
F9FB		SBC	21	
F9FD		STA	23	
F9FF		LDA	17	TOTAL = f_i
FA01		STA	24	
FA03		LDA	18	
FA05		STA	25	
FA07		LDA	16	Put $(X - X_i)$ in multiplicand
FA09		STA	06	
FA0B		LDA	£00	
FA0D		STA	07	
FA0F		LDA	1E	Put $-\Delta f_i$ in multiplier.
FA11		STA	08	
FA13		LDA	1F	
FA15		STA	09	
FA17		JSR	MLTPLY	Call MULTIPLY subroutine, gives P1.

HEXADECIMAL ADDRESS	LABEL	INSTRUCTION		COMMENT
FA1A		ASL	08	Find P1/128 by
FA1C		ROL	09	shifting A', B', C', D' left
FA1E		ROL	0A	once and reading B', C'.
FA20		ROL	0B	
FA22		SEC		TOTAL = TOTAL - $\frac{P1}{128}$
FA23		LDA	24	
FA25		SBC	09	
FA27		STA	24	
FA29		LDA	25	
FA2B		SBC	0A	
FA2D		STA	25	
FA2F		LDA	16	Put $(x - x_i)$ in multiplicand.
FA31		STA	06	
FA33		LDA	£00	
FA35		STA	07	
FA37		STA	09	Put $(X_{i+1} - X)$ in multiplier
FA39		LDA	19	
FA3B		STA	08	
FA3D		JSR	MLTPLY	Call MULTIPLY subroutine, gives P2.
FA40		LDA	22	Put $\Delta^2 f_i$ in multiplicand.
FA42		STA	06	P2 is already in multiplier.
FA44		LDA	23	
FA46		STA	07	
FA48		JSR	MLTPLY	Call MULTIPLY to get P3.
FA4B		ROL	09	Shift left once and read A', B'
FA4D		ROL	0A	equivalent to dividing by $2h^2$
FA4F		ROL	0B	
FA51		SEC		TOTAL = TOTAL - $\frac{P3}{2h^2}$
FA52		LDA	24	
FA54		SBC	0A	
FA56		STA	24	
FA58		LDA	25	
FA5A		SBC	0B	
FA5C		STA	25	
FA5E		RTS		Leave this subroutine

THE DIGITAL FILTER SUBROUTINE

HEXADECIMAL ADDRESS	LABEL	INSTRUCTION	COMMENT
FA5F	FILTER	LDA £0F	Put 32 D into
FA61		STA 06	MULTIPLICAND
FA63		LDA £34	
FA65		STA 07	
FA67		LDA 26	Put X from XSTORE
FA69		STA 08	into MULTIPLIER
FA6B		LDA 27	
FA6D		STA 09	
FA6F		JSR MLTPLY	Call MULTIPLY: $32D_0.X$
FA72		LDA 0B	Get MS byte of 2A
FA74		STA 2B	
FA76		LSR A	Generate MS byte of A
FA77		STA 2F	
FA79		LDA 0A	
FA7B		STA 2A	
FA7D		ROR A	
FA7E		STA 2E	
FA80		LDA 09	
FA82		STA 29	
FA84		ROR A	
FA85		STA 2D	
FA87		LDA 08	Get LS byte of 2A
FA89		STA 28	
FA8B		ROR A	Generate LS byte of A
FA8C		STA 2C	
FA8E		LDA £06	Put C_0 into
FA90		STA 06	MULTIPLICAND.
FA92		LDA £D3	
FA94		STA 07	
FA96		LDA 40	Put K into MULTIPLIER.
FA98		STA 08	
FA9A		LDA 41	
FA9C		STA 09	

HEXADECIMAL ADDRESS	LABEL	INSTRUCTION	COMMENT
FA9E		JSR MLTPLY	Call MULTIPLY: C_o.K
FAA1		SEC	Find and store
FAA2		LDA 08	-B = C_oK - A
FAA4		SBC 2C	
FAA6		STA 30	
FAA8		LDA 09	
FAAA		SBC 2D	
FAAC		STA 31	
FAAE		LDA 0A	
FAB0		SBC 2E	
FAB2		STA 32	
FAB4		LDA 0B	
FAB6		SBC 2F	
FAB8		STA 33	
FABA		LDA £84	Start to find
FABC		STA 06	F = 2A - C_1 K - (-E).
FABE		LDA £CC	Put (-C_1 -1) into
FAC0		STA 07	MULTIPLICAND.
FAC2		LDA 40	Put K into MULTIPLIER.
FAC4		STA 08	
FAC6		LDA 41	
FAC8		STA 09	
FACA		JSR MLTPLY	Call MULTIPLY: (-C_1 -1).K
FACD		CLC	Find and store
FACE		LDA 28	F = F + 2A - (C_1 + 1) K
FAD0		ADC 08	
FAD2		STA 38	
FAD4		LDA 29	
FAD6		ADC 09	
FAD8		STA 39	
FADA		LDA 2A	
FADC		ADC 0A	
FADE		STA 3A	
FAE0		LDA 2B	
FAE2		ADC 0B	
FAE4		STA 3B	

HEXADECIMAL ADDRESS	LABEL	INSTRUCTION		COMMENT
FAE6		SEC		Find and store:
FAE7		LDA	38	F = F - (-E).
FAE9		SBC	34	
FAEB		STA	38	
FAED		LDA	39	
FAEF		SBC	35	
FAF1		STA	39	
FAF3		LDA	3A	
FAF5		SBC	36	
FAF7		STA	3A	
FAF9		LDA	3B	
FAFB		SBC	37	
FAFD		STA	3B	
FAFF		CLC		Now complete calculation
FB00		LDA	40	of F:
FB02		ADC	3A	F = F + K.
FB04		STA	3A	
FB06		LDA	41	
FB08		ADC	3B	
FB0A		STA	3B	
FB0C		LDA	24	Get a new value of
FB0E		STA	26	X from INTERPOLATION
FB10		LDA	25	routine, put into
FB12		STA	27	XSTORE.
FB14		LDA	38	
FB16		STA	3C	Transfer:
FB18		LDA	39	
FB1A		STA	3D	G = F
FB1C		LDA	3A	
FB1E		STA	3E	
FB20		LDA	3B	
FB22		STA	3F	

HEXADECIMAL ADDRESS	LABEL	INSTRUCTION		COMMENT
FB24		LDA	30	
FB26		STA	34	Transfer:
FB28		LDA	31	
FB2A		STA	35	-E = -B.
FB2C		LDA	32	
FB2E		STA	36	
FB30		LDA	33	
FB32		STA	37	
FB34		CLC		Find: K = G + A.
FB35		LDA	2C	First add lower two
FB37		ADC	3C	bytes to check for
FB39		LDA	2D	CARRY to upper two
FB3B		ADC	3D	bytes. Store result.
FB3D		TAX		
FB3E		LDA	2E	
FB40		ADC	3E	
FB42		STA	40	
FB44		LDA	2F	
FB46		ADC	3F	
FB48		STA	41	
FB4A		CPX	£80	Check to see if lower
FB4C		LDA	40	two bytes ≥ £10,00.
FB4E		ADC	£00	
FB50		STA	40	If so, add 1 to upper
FB52		STA	04	two bytes of K. Store
FB54		LDA	41	result in BINBCD input.
FB56		ADC	£00	
FB58		STA	41	
FB5A		STA	05	
FB5C		LSR	05	Find: Y = K/16.
FB5E		ROR	04	
FB60		LSR	05	
FB62		ROR	04	
FB64		LSR	05	
FB66		ROR	04	
FB68		LSR	05	
FB6A		ROR	04	

HEXADECIMAL ADDRESS	LABEL	INSTRUCTION	COMMENT
FB6C		LDA 04	Check for round up
FB6E		ADC £00	
FB70		STA 04	
FB72		LDA 05	
FB74		ADC £00	
FB76		STA 05	
FB78		LDA 05	Put Y in MULTIPLICAND.
FB7A		STA 07	
FB7C		LDA 04	
FB7E		STA 06	
FB80		LDA £60	Put 0.4_{10} in MULTIPLIER.
FB82		STA 08	
FB84		LDA £66	
FB86		STA 09	
FB88		JSR MLTPLY	Call MULTIPLY.
FB8B		LDA 0A	Store in DAC slot.
FB8D		STA 42	
FB8F		LDA 0B	
FB91		STA 43	
FB93		RTS	Leave this subroutine.

THE SOFTWARE CONTROLLER

HEXADECIMAL ADDRESS	LABEL	INSTRUCTION		COMMENT
FB94	CONTRL	CLD		Set BINARY MODE.
FB95		SEI		Block external interrupts
FB96		LDX	£FF	Locate stack at 01FF
FB98		TXS		
FB99		LDA	£00	Clear X register.
FB9B		TAX		
FB9C	CLEAR	STA	00,X	Clear page 0 store
FB9E		INX		spaces.
FB9F		CPX	£44	
FBA1		BNE	CLEAR	
FBA3		LDA	£C0	Enable T1's interrupt.
FBA5		STA	900E	T1 free running, output on
FBA8		STA	900B	PB7.
FBAB		LDA	9198	Get switches, invert to
FBAE		EOR	£FF	recover settings and store.
FBB0		STA	44	
FBB2		AND	£10	Test most significant
FBB4		BNE	FAST	switch nibble.
FBB6	SLOW	LDA	£12	If = 1, set FAST sample
FBB8		STA	9004	rate. Otherwise, set
FBBB		LDA	£7A	SLOW (32Hz) sample
FBBD		STA	9005	rate.
FBC0		JMP	MODE	Jump to MODE test.
FBC3	FAST	LDA	£6A	Set 160 Hz sample.
FBC5		STA	9004	rate.
FBC8		LDA	£18	
FBCA		STA	9005	
FBCD	MODE	LDA	£FE	STORE MSB base
FBCF		STA	13	address.
FBD1		JSR	OFFSET	Call OFFSET subroutine.

HEXADECIMAL ADDRESS	LABEL	INSTRUCTION	COMMENT
FBD4	LOOP	LDA 44	Test least significant
FBD6		AND £01	switch nibble. If = 1,
FBD8		BNE DISTCE	do DISPLACEMENT.
FBDA	CALBRT	JSR FETCH	Otherwise, do
FBDD		JSR FILTER	VOLTMETER.
FBE0		JMP DACONV	
FBE3	DISTCE	JSR GRCHK	DISPLACEMENT operation.
FBE6		JSR INTERP	
FBE9		JSR FILTER	
FBEC	DACONV	LDA 42	Output result on DAC.
FBEE		STA 9189	
FBF1		LDA 43	
FBF3		STA 918A	
FBF6		INC 45	Increment loop counter
FBF8		LDA 45	Done 16 times?
FBFA		CMP £10	No: go back again.
FBFC		BNE LOOP	Yes: display.
FBFE	DSPLAY	LDA £00	Clear counter.
FC00		STA 45	Call BIN-BCD conversion.
FC02		JSR BINBCD	
FC05		LDA 02	Display LSD.
FC07		AND £0F	
FC09		STA 9190	
FC0C		LDA 02	Display next digit.
FC0E		SEC	
FC0F		ROR A	
FC10		LSR A	
FC12		LSR A	
FC13		STA 9190	
FC16		LDA 03	Display next digit.
FC18		AND £0F	
FC1A		ORA £20	
FC1C		STA 9190	

HEXADECIMAL ADDRESS	LABEL	INSTRUCTION	COMMENT
FC1F		LDA 03	Display MSD
FC21		SEC	
FC22		ROR A	
FC23		SEC	
FC24		RDR A	
FC25		LSR A	
FC26		LSR A	
FC27		STA 9190	
FC2A		JMP LOOP	Return for next cycle

APPENDIX 3

SOME RELEVANT PAPERS

A simple method for the measurement of the temperature variation of initial magnetic susceptibility between 77 and 1000 K

A Stephenson and A de Sa
Department of Geophysics and Planetary Physics, School of Physics, University of Newcastle upon Tyne

MS *received 8 August 1969*

Abstract Two identical multi-layered solenoids each enclosing a water jacket are used in an a.c. bridge circuit so that inclusion of a sample in either coil produces an out of balance signal proportional to the susceptibility of the sample. This signal is then amplified with low noise field effect transistors, converted to direct current with a phase sensitive detector, and displayed against temperature on an XY recorder. The water jacket of one solenoid contains a furnace capable of reaching 700 °C, while the other contains a cooling assembly for use between liquid nitrogen and room temperature. The temperature variation of susceptibility allows determination of Curie and transition temperatures.

1 Introduction

Magnetic susceptibility is defined by the equation $K = J/H$ where J is the intensity of magnetization and H is the effective magnetic field within the sample. H differs from the applied field H_a by an amount H_d known as the demagnetizing field. Thus $H = H_a - H_d$. This equation may also be written as $H = H_a - NJ$ where N is known as the demagnetizing factor and depends on the shape of the sample. ($N = 4\pi/3$ for a sphere.) Thus the true susceptibility differs from the apparent susceptibility K_a ($= J/H_a$) by a factor of $1 + NK$, i.e.

$$K_a = \frac{K}{1 + NK}.$$

It is thus the apparent susceptibility which is measured by this apparatus and by those mentioned below. For minerals of low susceptibility, however, where $NK \ll 1$, the true susceptibility is measured.

Apparatus for low field susceptibility measurements on rocks at room temperature has been described previously by Girdler (1961) who used air cored coils in a transformer bridge and by Collinson *et al.* (1963) who used a pair of high permeability ferrite cores. The latter method is, however, not suitable for temperature measurements because the ferrite cores are extremely sensitive to microphony and small temperature changes. The method described here uses a conventional inductance bridge with air cored coils (De Vries and Livius 1966) to minimize the above sources of instability. One coil is used for measurements above room temperature and the other for low temperatures. The apparatus was originally devised for measurements on small single crystal titanomagnetite samples (about 20 mg) grown by one of the authors (Hauptman and Stephenson 1968).

For high temperature measurements the sample may either be heated in the correct gas mixture for the equilibrium oxygen pressure or it may be placed in a sealed quartz tube. Alternatively the furnace may be evacuated. The field in which the sample is measured is 2·5 Oe (200 A m^{-1}) rms.

2 The heating assembly

For measurements between room temperature and 700 °C the arrangement shown in figure 1 is used. The coil of resistance 200 Ω consists of 5000 turns of 32 swg copper wire on a perspex former. It has an internal diameter of 2·2 cm and is of length 3·6 cm. Immediately within the coil, which is screened with 80 mesh copper gauze, is a Pyrex glass water jacket which encloses a small furnace consisting of a narrow walled quartz tube, 8 mm internal diameter, wound non-inductively with Nichrome wire. This is heated by an alternating current of up to 1 A which does not cause any disturbance to the bridge. After balancing the bridge, the sample

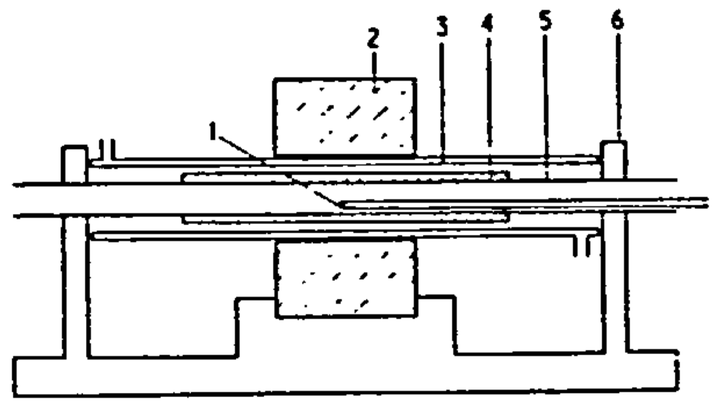

Figure 1 The heating assembly. 1, platinum–platinum/13% rhodium thermocouple; 2, coil; 3, water jacket; 4, furnace-winding; 5, quartz tube; 6, supports

to be measured is placed within the tube and moved until the out of balance signal reaches a maximum. A platinum–platinum/13% rhodium thermocouple is then placed in contact with the sample. Because of this juxtaposition of thermocouple and sample, the small size of the sample, and the low thermal inertia of the system, fast heating and cooling rates can be employed (typically, ten minutes to reach 700 °C).

Figure 2 shows a typical result on a sintered pellet of magnetite powder of mass 5·7 mg and total susceptibility $3{\cdot}7 \times 10^{-4}$ G cm^3 Oe^{-1} (5·8 fH m^2). The Curie point can be determined to within about ±3 degC.

3 The cooling assembly

For low temperature measurements down to liquid nitrogen temperature (77 °K), the second coil is used – the coil containing the furnace being used as a reference. The arrangement used is shown in figure 3.

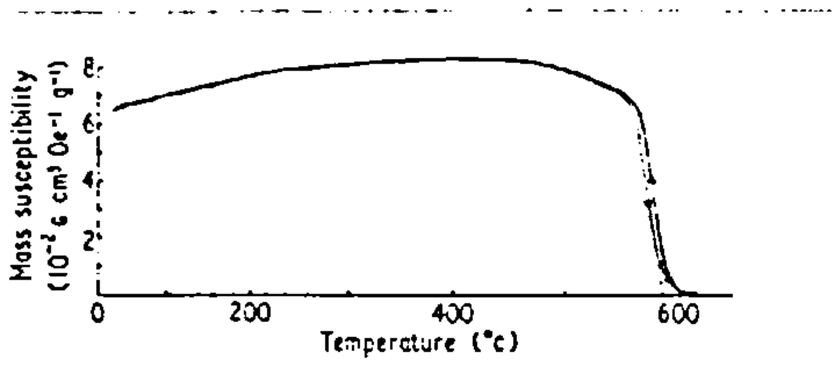

Figure 2 Variation of initial susceptibility of a magnetite sintered pellet of mass 5·7 mg between room temperature and the Curie point

Within the coil is a water jacket which contains an inner closed-end, thin-walled tube which is used to hold the sample. Between this tube and the water jacket is a thin layer of expanded polystyrene insulation, about 1 mm thick. This ensures that the rate of cooling of the water in the jacket is low enough to prevent freezing. On the outside surface of the inner tube, in contact with the polystyrene, is a non-inductively wound thin Nichrome wire heating coil. The sample to be cooled, e.g. a small crystal, is embedded in a sphere of Plasticine which holds the copper–constantan thermocouple junction in contact with it. A plug of cotton wool is placed above the sample to minimize temperature inhomogeneities. A powder

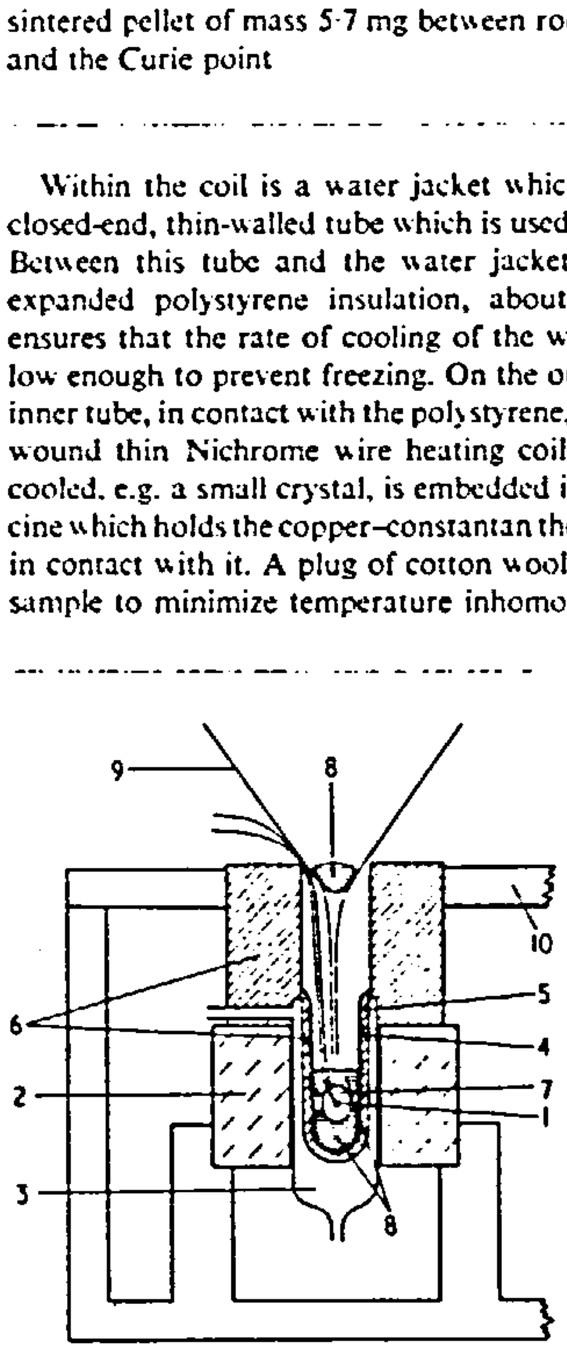

Figure 3 The low temperature assembly. 1, copper–constantan thermocouple; 2, coil; 3, water jacket; 4, heating coil; 5, inner glass tube; 6, expanded polystyrene insulation; 7, Plasticine sphere containing sample; 8, cotton wool plugs; 9, liquid nitrogen feed funnel; 10, wooden box enclosing both low temperature and heating assemblies

may be placed in an open-ended capsule with the thermocouple junction embedded in it. The method of cooling is to pour liquid nitrogen slowly into the funnel. By this means the temperature can be slowly lowered to 77 K, at which point the funnel is removed. Any liquid nitrogen left at the bottom of the tube is then allowed to boil off after which the temperature begins to rise as heat is conducted through the polystyrene insulation from the water jacket. When the temperature has risen to about −80 C a small current is passed through the heating coil, which then continues to increase the temperature to room temperature. A typical cooling and heating cycle takes about 20 min.

During this operation both the low and high temperature assemblies are enclosed in a wooden box, as shown, so that the cold air produced by the liquid nitrogen cannot reach the coils and cause a drift of the zero. Figure 4 shows a typical result on a synthetic magnetite crystal of mass 6·6 mg. The low temperature transition exhibits very little hysteresis and can be measured with an accuracy to about ±2 degc.

4 Electronic circuits

The method used is shown in figure 5. A 1·5 kHz thermistor controlled Wien's bridge oscillator drives the bridge through an isolating transformer T. The two identical solenoids form two arms of the bridge while the other two are made of resistors, one of which has provision for fine adjustment. A

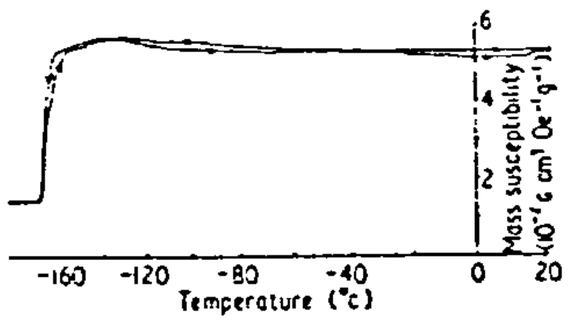

Figure 4 Low temperature variation of initial susceptibility of a synthetic magnetite crystal of mass 6·6 mg

high impedance detector is used consisting of a low noise field effect transistor tuned amplifier. The amplifier is converted to d.c. output using a phase sensitive detector. A square wave reference voltage with an adjustable phase is derived from the oscillator and enables the in phase component of the signal, proportional to the susceptibility, to be displayed on a digital voltmeter or a pen recorder. For good linearity the amplitude of the input signal is controlled by an attenuator.

5 Linearity and sensitivity

For a bridge consisting of elements of equal impedance Z, the out of balance signal is equal to $E\delta/4(1+\delta/2)$ provided that the impedance of the source of electromotive force E is zero and that of the detector is infinite. These approximations may be made in practice. δ is the fractional change in impedance of one of the elements due to the presence of a sample. Thus for $\delta/2 \ll 1$, the off balance signal will be proportional to δ, and, provided that δ is always less than 0·02, the deviation from linearity of the bridge output never exceeds 1%. In practice such an output corresponds to a sample of total susceptibility $7{\cdot}5 \times 10^{-2}$ G cm³ Oe⁻¹ (1·2 pH m²) for a cylindrical sample of dimensions 10 mm length and 4 mm

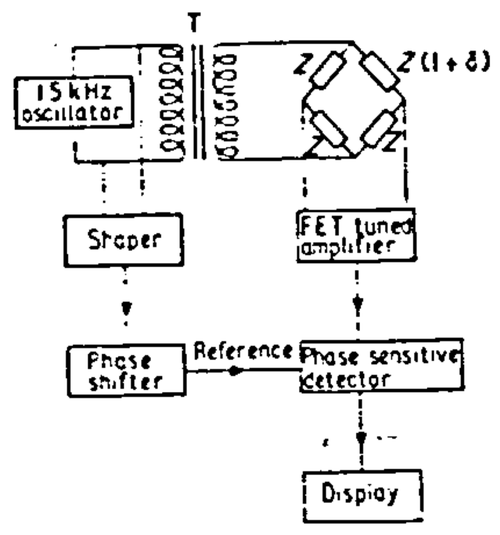

Figure 5 Block diagram of electronics

diameter. Samples stronger than this must be reduced in size if a linear output is required. The linearity may be improved by a factor of up to 2 by using a high value of Z_s/Z where Z_s is the impedance of the source. In this case, however, care must be taken to avoid distortion of the waveform due to loading. The noise at the output is equivalent to a total susceptibility of about $\pm 1 \times 10^{-6}$ G cm^3 Oe^{-1} (16 μH m^2) for the above size of sample, the time constant of the output circuit being about 0.2 s. The zero drift over the measuring time of about 20 min is typically less than 20×10^{-6} G cm^3 Oe^{-1} (320 μH m^2).

The proportionality between the output and the susceptibility was checked by using known amounts of magnetite powder dispersed in a matrix of Al_2O_3 and made into pellets of uniform size.

6 Conclusion

In addition to being used to determine the temperature variation of initial susceptibility, absolute measurements at room temperature may be obtained on very weak samples by removing the water jacket from the low temperature assembly and inserting a much larger sample of the weak material than otherwise possible. Because the field within the coil is fairly homogeneous, the sensitivity is only weakly dependent on the size of sample and thus the noise level remains at about $\pm 1 \times 10^{-6}$ G cm^3 Oe^{-1} (16 μH m^2) for a sample of volume 10 cm^3, which is about the maximum usable size. For accurate measurements of the susceptibility, recalibration with a paramagnetic salt in a container the same size as the sample may be carried out. The apparatus is especially useful for the determination of Curie points since a much sharper transition occurs for many samples than by other methods such as the measurement of saturation magnetization for example. Since it is easy to orientate specimens, the temperature variation of the susceptibility in a particular direction may be obtained for anisotropic materials.

Acknowledgments

The authors wish to thank Professor K M Creer and Dr D W Collinson for valuable comments. One of us (A S) is indebted to NERC for their financial support.

References

Collinson D W Molyneux L and Stone D B 1963 *J. Sci. Instrum.* 40 310–2

De Vries A J and Livius J W M 1966 *Appl. Sci. Res.* 17 31–64

Girdler R W 1961 *Geophys. J.R.A.S.* 5 34–44

Hauptman Z and Stephenson A 1968 *J. Phys.* E: *Sci. Instrum.* 1 1236–7

J. Phys. E: Sci. Instrum., Vol. 14, 1981. Printed in Great Britain

A radio frequency method for the measurement of initial magnetic susceptibility

M P Cooke and A de Sa
School of Physics, The University, Newcastle upon Tyne, NE1 7RU, UK

Received 13 November 1980, in final form 13 May 1981

Abstract A method of displaying simultaneously the real and imaginary parts of the complex initial susceptibility of rocks and rock powders is described. A Q-multiplier in conjunction with two feedback loops separates distinctly and linearly the contributions of the real component, X' and imaginary component X'' of a given sample. Temperature variations of susceptibility may also be studied using a furnace. In the absence of the furnace the sample's coupling factor and hence the signal-to-noise ratio of the instrument is substantially enhanced. At present the noise level of the X'' loop is equivalent to $\pm 5\times10^{-12}$ m^3 and that of the X' loop is equivalent to $\pm 1.4\times10^{-11}$ m^3 with the furnace in position. The sample volumes are 0.2 cm^3 or less.

1 Introduction

The variation of initial magnetic susceptibility with frequency is of some geophysical interest. It has been predicted (Vincenz 1965) that the apparent AC susceptibility of rock samples should decrease with increasing frequency of measurement. The expected decrease, for a random assembly of magnetite particles, is about 1% per decade although there is some disagreement about this (Blathal and Stacey 1969). Wilson's results (1978) appear to show that rocks yielding unreliable palaeomagnetic information exhibit a relatively large decrease in apparent susceptibility of about 2.5% per decade. In this context, it is X' that is of interest and so it is important to separate X' from X''. These two components have opposite trends with increasing frequency.

In his investigation, Wilson used a marginal oscillator from 1 kHz to 10 MHz. The wide range was an advantage as it made any change in X' more apparent. However, the results are difficult to interpret when looking for small changes (Hughes and Smith 1971). de Vries and Livius (1966) and Markert *et al* (1974) built devices that truly separate X' and X''. The former built a wide range AC bridge (200 Hz up to 1 MHz) which was sensitive but of very complex construction. The device built by the latter was not suitable for use at more than one frequency.

The instrument to be described distinguishes between X' and X'', is linear and requires no balancing. It can be used over a wide frequency range although the present results pertain to a fixed frequency of 5 MHz. A later section outlines the instrument's development for wide range use and suggests some applications for X''. At present, the drift and random noise levels are comparable with those of existing AC instruments e.g. Stephenson and de Sa (1970).

2 Principle of operation

The sample is inserted into an air-cored coil where it is subjected to a 5 MHz radio frequency field having a peak magnetic intensity of about 1.8 A m^{-1}. The induced motion of domain walls and rotation of domain magnetisation generates an internal field in phase with the applied field. This is represented by X'. Another component is introduced in quadrature to the applied field through hysteresis and eddy current losses. This is represented by X''.

Kneller (1962) has shown that X' changes the inductance, L of the air cored coil. X'' acts as an increase in the coil's series resistance, R. The sample's susceptibility may be written

$$X = X' - jX''. \tag{1}$$

When the sample is inserted into the coil, the changes in L and R are

$$\Delta R = \left(\frac{N^2A}{l}\eta\mu_0\right)WX'' \tag{2}$$

and

$$\Delta L = \left(\frac{N^2A}{l}\eta\mu_0\right)X' \tag{3}$$

where W = angular frequency (rad s^{-1}), A = cross sectional area of the coil (m^2), l = length of coil (m), N = number of turns in coil, η = coil-sample coupling factor, $\mu_0 = 4\pi\times10^{-7}$ H m^{-1}.

The relative permeability of air has been taken to be unity.

The crystal oscillator (figure 1) drives the tuned circuit at its resonant frequency W_0 through a 1 MΩ series resistance. Under these conditions, signals from the oscillator and tuned circuit are in phase and the tuned circuit looks like a real resistance $Z = (W_0L)\,Q$ where the quality factor, Q is W_0L/R. Clearly, X' produces a phase shift by altering the resonant frequency of the tuned circuit. X'' alters the voltage divider

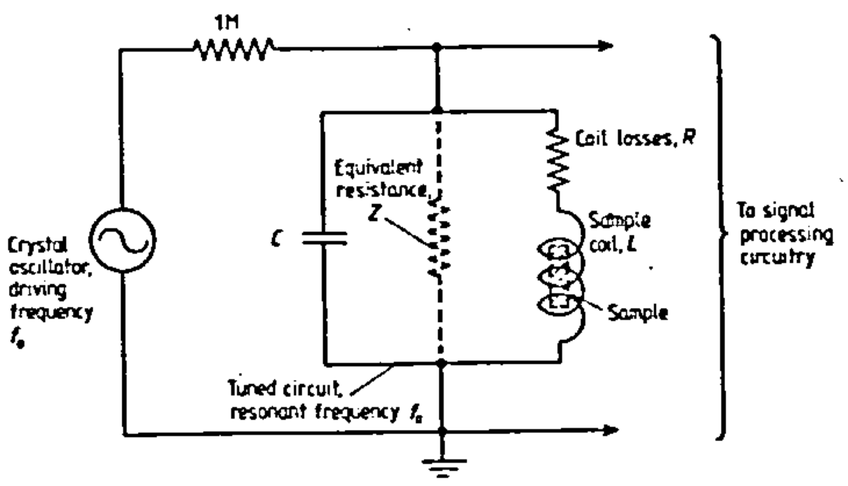

Figure 1 Simplified circuit illustrating principle of operation.

ratio between the tuned circuit and the 1 MΩ resistance producing a decrease in signal amplitude. Although Q is a function of L and R the effect of a change in L is neglected. In a typical case this means that ΔR is underestimated by 8% or less (see appendix 1). The Q is made large (about 10^3) such that $W_0^2 = (LC)^{-1}(1-1/Q^2)$ reduces to $W_0^2 = (LC)^{-1}$. This means that a small change ΔQ can not affect W_0 and so

0022-3735/81/101192+05 $01.50

cannot induce an unwanted phase shift. Finding the magnitudes of X' and X'' for a given sample reduces to monitoring a phase shift, from a change in L and an alteration in amplitude, from a change in Q. This is done using two closed feedback loops, which act in such a way that the tuned circuit is restored to its initial state. The feedback therefore prevents undesirable mixing of X' and X''.

3 Practical implementation (figure 2)

A 5.0 MHz crystal oscillator drives the resonant circuit (1) via a 1 MΩ isolating resistance. The oscillator has a stable amplitude and a frequency stability of better than one part in 10^5. The single layer sample coil is made of 16 SWG silver wire, it has an inductance of 1.3 μH. Inside the sample coil is a water jacket (2) and non-inductively wound furnace (3) made of 40 SWG nichrome wire. The water jacket and lagging (4) thermally isolate the sample coil from the furnace. The furnace can heat the sample in its holder (5) to over 700°C. The sample's temperature is monitored by the Pt–13% Pt/Rh thermocouple (6). The Q-multiplier (Harris 1951) produces an overall Q of 1.1×10^3.

The amplitude of the voltage across the resonant circuit is examined using a voltage follower, an RF amplifier and a peak rectifier. The DC output of the peak rectifier, representing the Q of the resonant circuit, is subtracted from a DC reference voltage representing the initial Q. This generates an error signal which is amplified and applied to an FET used as an voltage variable resistance. The variable resistance serves as the control element of the Q-multiplier. Concurrently, a phase comparator gives a DC voltage proportional to the phase difference between the crystal oscillator and the resonant circuit signals. The output is subtracted from a DC reference voltage representing the initial, in phase, condition. Waveshaping circuitry ensures that the phase error voltage is not sensitive to the amplitudes of the two signals being compared. This error voltage is amplified and passed to a voltage variable capacitance formed from two varicap diodes. The varicaps compensate for the increase in the coil's inductance by reducing the parallel capacitance, so keeping the product LC constant.

The two feedback loops are closed via switches S_1 and S_2. The loop response times are adjusted such that the phase loop responds faster than the Q loop. This ensures that the loops are independent. The two output signals are taken via voltage followers.

Quantitatively it can be shown (see appendices 1 and 2),

$X' \propto \Delta V_c$ to within 4.5% provided

$$X' \leqslant (8.1 \pm 0.5) \times 10^{-9}\ \mathrm{m}^3$$

$X'' \propto \Delta V_f$ to within 8% provided

$$X'' \leqslant (3.4 \pm 0.3) \times 10^{-9}\ \mathrm{m}^3$$

where ΔV_c = change in control voltage to the varicaps, ΔV_f = change in control voltage to the FET.

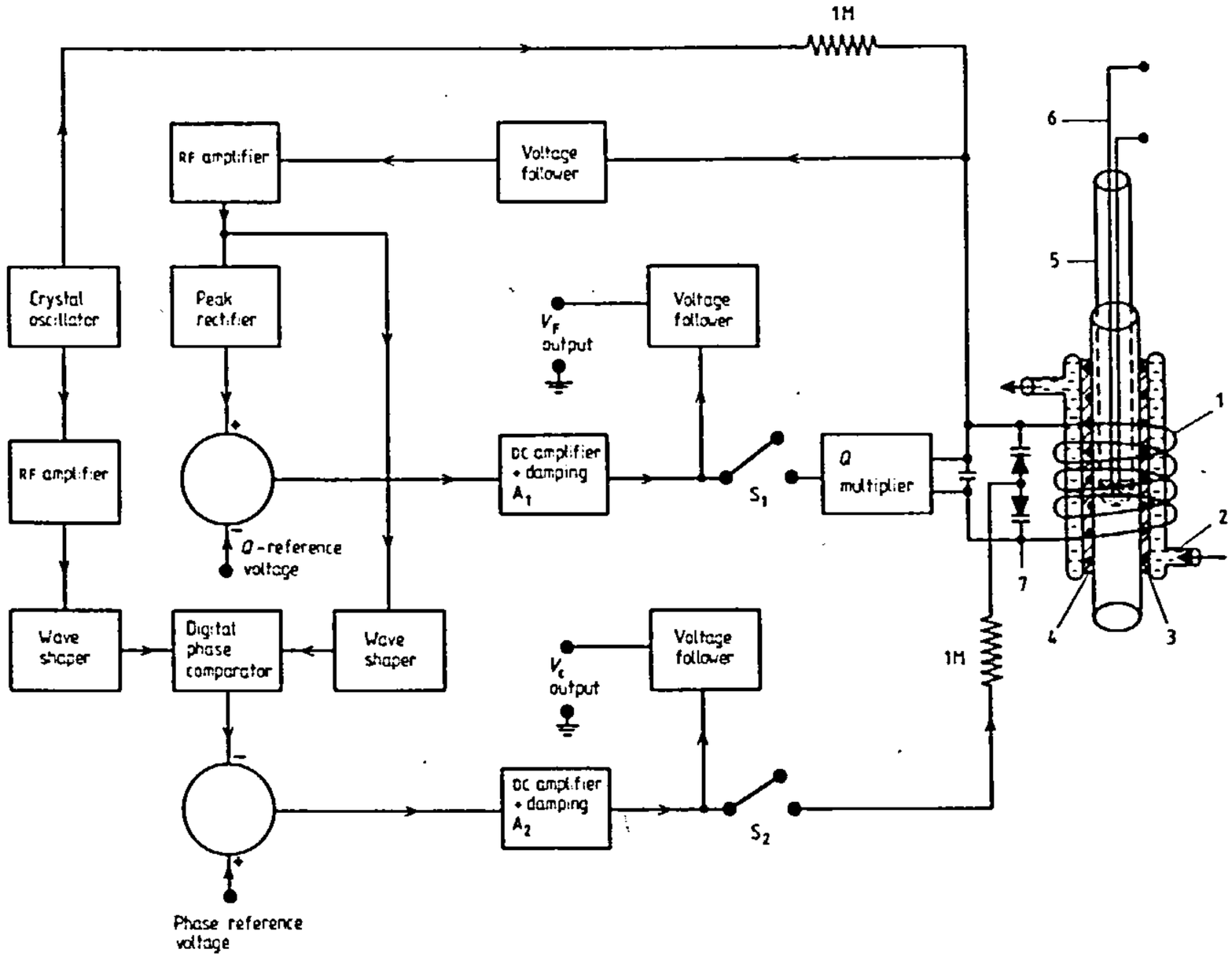

Figure 2 Block diagram of circuitry: 1, resonant LCR circuit; 2, water jacket; 3, non-inductively wound furnace; 4, thermal lagging; 5, sample holder; 6, Pt–Pt/Rh thermocouple; 7, varicaps.

4 Calibration and linearity

The DC outputs of amplifiers A_1 and A_2 are adjusted to set the Q-multiplier and the varicaps to their predetermined operating points. The feedback loops are then closed via switches S_1 and S_2.

A glass tube containing 238 mg of $FeSO_4 \cdot 7H_2O$ having a total susceptibility $(1.24 \pm 0.02) \times 10^{-10}$ m^3 is inserted into the sample coil. The change in the phase control voltage, ΔV_c is noted and the calibration factor K_1 is calculated from

$$X' = K_1 \Delta V_c. \tag{4}$$

This gives

$$K_1 = (2.52 \pm 0.15) \times 10^{-8} \text{ m}^3 \text{ V}^{-1}$$

The uncertainty in K_1 is principally caused by $FeSO_4 \cdot 7H_2O$ having a weak susceptibility. This substance is used because its susceptibility is independent of frequency to well above 5 MHz and it is a commonly used standard. This permits results from different instruments or different frequencies to be compared.

An indirect procedure is adopted to find a calibration factor, K_2 for the Q loop. Using equation (18) from appendix 2,

$$\eta = \left(\frac{a}{2C} \frac{\Delta V_c}{V_c^{3/2}}\right) \left(\frac{L}{X'} \frac{l}{N^2 A \mu_0}\right). \tag{5}$$

Combining equation (5) with equation (12) from appendix 1

$$X'' = \frac{X'}{\Delta V_c} \left(\frac{2C}{a} V_c^{3/2}\right) \left(\frac{\theta}{Q^2}\right) \Delta V_f \tag{6}$$

where θ is the open loop rate of change of Q with respect to V_f and a is a constant connected with the varicaps.

Finally,

$$X'' = K_2 \Delta V_f. \tag{7}$$

$(X'/\Delta V_c)$ is found whilst calibrating the phase loop and the other constants are easily measured giving

$$K_2 = (2.4 \pm 0.2) \times 10^{-9} \text{ m}^3 \text{ V}^{-1}.$$

The linearity of the instrument is checked in the following manner. Samples of powdered magnetite are made up to constant mass (50 mg) by dispersing the powder in pure LiF. LiF gives no signal on its own. The maximum amount of magnetite used is about 20 mg to ensure that it is well dispersed in all the samples.

Figure 3 shows the mass of magnetite plotted against ΔV_c and ΔV_f at room temperature. The linearity of the instrument is seen to be within the error of the measurements.

5 Performance and future work

The noise in V_c is equivalent to $X' = \pm 1.4 \times 10^{-11}$ m^3 and the drift is 3×10^{-11} m^3 per minute. The noise in V_f is equivalent to $X'' = \pm 5 \times 10^{-12}$ m^3 and the drift is 5×10^{-12} m^3 per minute. When the water jacket and furnace are running the noise level increases by a factor of 2.5. On removing the furnace, the coupling factor, and therefore the noise level, improves by a factor of 3.0. In future, the furnace will be run from a DC supply to reduce the 50 Hz noise that it generates. Figure 4 shows a plot of X' against temperature for 13.0 mg of natural magnetite. The Curie point occurs at (580 ± 3)°C

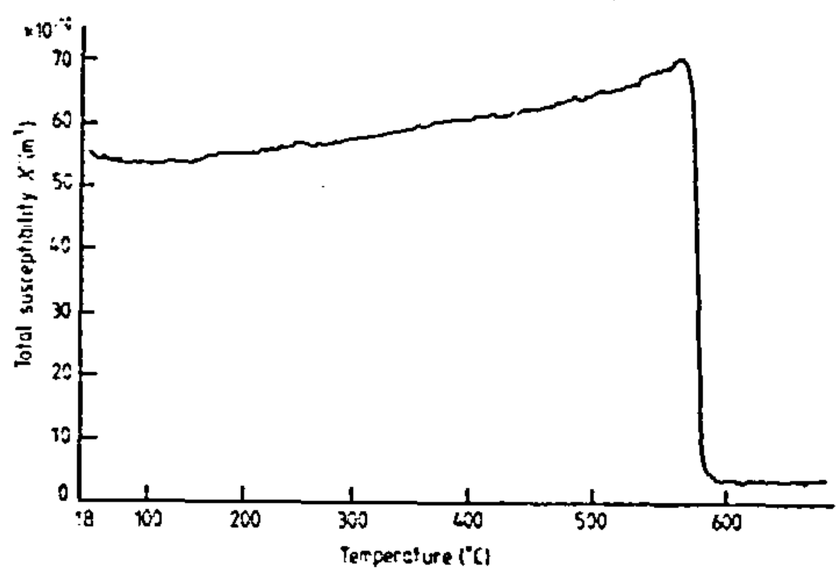

Figure 4 X–Y plot of X' against temperature for a 13.0 mg sample of natural magnetite.

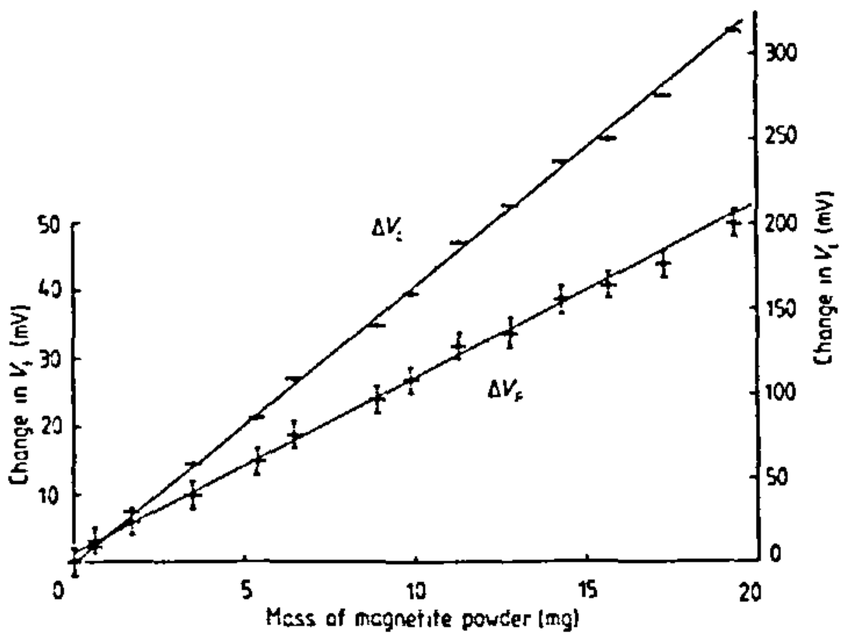

Figure 3 Changes in V_f and V_c for varying masses of magnetite powder.

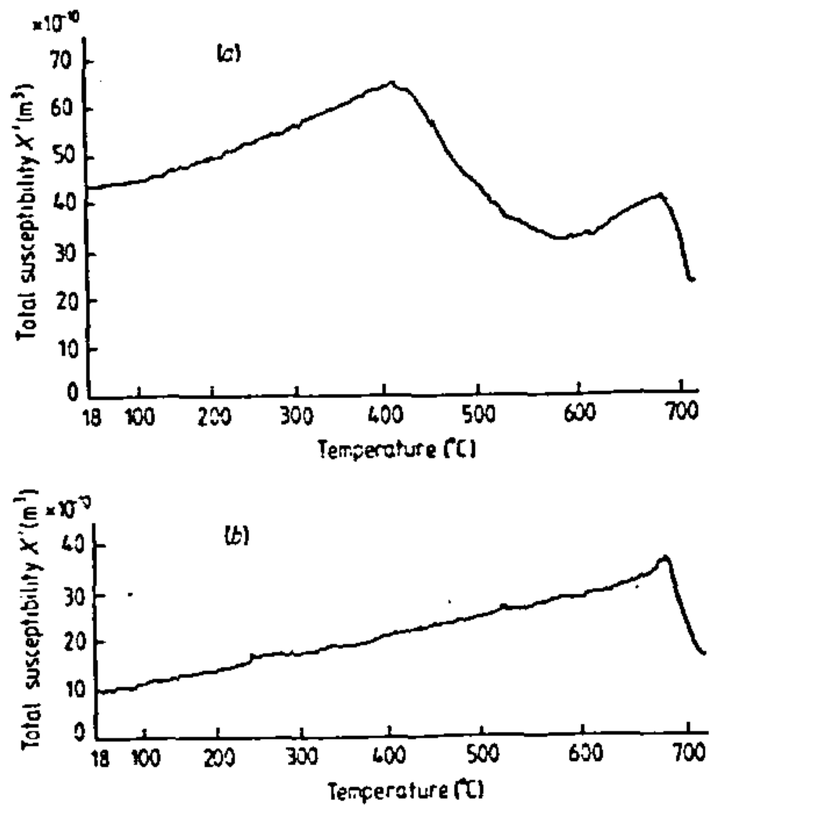

Figure 5 X–Y plot of X' against temperature for a mixture of 9.5 mg of powdered magnetite and 206 mg of powdered Brazilian haematite during (*a*) heating and (*b*) cooling.

and the Hopkinson peak shows up plainly. Figure 5 depicts X' against temperature for 9.5 mg of powdered magnetite mixed with 206 mg of powdered Brazilian haematite. When heating the sample, figure 5(*a*), the magnetite oxidises but the haematite's Curie point is visible. On cooling the sample, figure 5(*b*) shows only the haematite Curie transition. The transition is smeared because it is difficult to maintain a uniform heat throughout a relatively bulky sample while running the furnace close to its limits. This explains why figure 5 puts the haematite's Curie point as 710 C and not 675 C as expected.

X'' is a source of useful information. For instance, El-Hanany (1973) shows that if conducting grains are dispersed in a nonconducting matrix then the average grain size can be found from X''. This is true provided that the grains' permeability is close to unity and that their radii are smaller than the RF skin depth. More importantly, Curie transitions are associated with maxima in X''. Petersen (1967) suggests that this is useful when examining materials that exhibit a number of Curie points lying close together. Markert *et al* (1974) have obtained some interesting results in this respect.

Useful information can be obtained by observing the thermal variation of X' and X'' at low temperatures. It is intended to extend the useful temperature range to 77 K.

The instrument is readily adaptable for use at different frequencies: the processing circuitry is broadband, so that only the oscillator frequency and resonant circuit would need to be altered. By using a square wave to drive the resonant circuit, a master crystal oscillator could easily be subdivided to produce different drive frequencies.

Acknowledgments

The authors wish to thank Dr D W Collinson and colleagues for their valuable comments. One of us (MPC) is indebted to the NERC for their financial support.

Appendix 1 – Relating ΔV_t to X''

The resistance in series with the sample coil after Q multiplication is R. On inserting the sample the increase in resistance is ΔR and the increase in inductance is ΔL. This alters the Q such that

$$Q-\Delta Q=\frac{W_0(L+\Delta L)}{(R+\Delta R)}. \tag{8}$$

As $\Delta R/R$ is small and accepting for the moment that the losses dominate

$$\Delta Q/Q=\Delta R/R. \tag{9}$$

It was found experimentally that neglecting ΔL caused ΔR to be underestimated by 8% for a magnetite sample with grain radii in the range $4.3<r<7.7$ μm. This error decreases with increasing conductivity and with the square of the grain size; the experimenter may well have control over the latter parameter.

The Q loop acts such that $\Delta Q \to 0$. In this case

$$\Delta Q=\theta \Delta V_t \tag{10}$$

where θ is the open loop rate of change of Q with respect to V_t and is a constant.

From equations (9) and (10)

$$\Delta R=\frac{R\theta \Delta V_t}{Q}. \tag{11}$$

Recalling equation (2)

$$X''=\frac{1}{W}\left(\frac{l}{N^2A\eta\,\mu_0}\right)\left(\frac{R\theta}{Q}\right)\Delta V_t. \tag{12}$$

Limits on X'' are placed by the region of linear control of the Q-multiplier. The linear range was found to be

$$\Delta V_t \leqslant 1.4 \text{ V}.$$

Appendix 2 – Relating ΔV_c to X'

When a sample is inserted into the sample coil the phase loop acts on the varicaps such that the product LC is kept constant. As $\Delta L/L \ll 1$ this can be expressed as

$$\Delta L/L=\Delta C/C \tag{13}$$

where ΔC is the decrease in resonant circuit capacitance.

The relation between a varicap's capacitance, C_v and the applied reverse bias voltage V_c is

$$C_v=\frac{a}{V_c^{1/2}}, \text{ F} \tag{14}$$

where a is a constant of proportionality.

In compensating for an increase in inductance V_c changes to $(V_c+\Delta V_c)$ and so

$$\Delta C=a\left(\frac{1}{V_c^{1/2}}-\frac{1}{(V_c+\Delta V_c)^{1/2}}\right) \tag{15}$$

$$=a\left(\frac{(1+\Delta V_c/V_c)^{1/2}-1}{(V_c+\Delta V_c)^{1/2}}\right).$$

Expanding to first order

$$\Delta C=\frac{a}{2}\frac{\Delta V_c}{V_c^{3/2}}\left(\frac{1}{1+\Delta V_c/2V_c}\right). \tag{16}$$

$\Delta V_c=0.06\ V_c$ for the largest sample of magnetite and to 4.5% or better over the range examined

$$\frac{\Delta C}{C}=\frac{a}{2C}\frac{\Delta V_c}{V_c^{3/2}}. \tag{17}$$

Recalling equations (3) and (13).

$$X'=\left(\frac{a}{2C}\frac{1}{V_c^{3/2}}\right)\left(\frac{L}{\eta}\frac{l}{N^2A\mu_0}\right)\Delta V_c. \tag{18}$$

References

Blathal R S and Stacey F D 1969 Frequency independence of low-field magnetic susceptibility of rocks
J. Geophys. Res. **74** 2025–7

El-Hanany U 1973 A Q-meter method for measuring the grain size and resistivity temperature dependence of metallic powders
Rev. Sci. Instrum. **44** 1067–8

Harris H E 1951 Simplified Q multiplier
Electronics May 130–4

Hughes D G and Smith M R 1971 On the nuclear magnetic resonance detection characteristics of marginal and Robinson oscillators
J. Phys. E: Sci. Instrum. **4** 13–20

Kneller E 1962 *Ferromagnetismus* (Berlin: Springer) pp 598–604

Markert H, Trissl K H and Zimmerman G J 1974 On a high frequency method for the measurement of susceptibilities and hysteresis losses of rocks and minerals between nitrogen temperature and 700 C
J. Geophys. **40** 303–28

Petersen N 1967 A high frequency method for the measurement of Curie temperatures of ferrimagnetic minerals
Methods in Palaeomagnetism eds D W Collinson, K M Creer and S K Runcorn (Amsterdam: Elsevier) pp 445–6

Stephenson A and de Sa A 1970 A simple method for the measurement of the temperature variation of initial magnetic susceptibility between 77 and 1000 K
J Phys. E: Sci. Instrum. 3 59–61

Vincenz S A 1965 Frequency dependence of magnetic susceptibility of rocks in weak alternating fields
J. Geophys. Res. 70 1371–7

de Vries A J and Livius J W M 1966 A sensitive and rapid bridge for the study of magnetic susceptibilities at frequencies from 200 to 10^6 Hz
Appl. Sci. Res. 17 31–64

Wilson D 1978 Some instrumentation techniques in rock magnetism
PhD Thesis School of Physics, Newcastle University

J. Phys. E: Sci. Instrum., Vol. 15, 1982. Printed in Great Britain

A new method of non-contact measurement of linear displacement

M P Cooke and A de Sa
School of Physics, The University, Newcastle-upon-Tyne NE1 7RU, UK

Received 8 February 1982, in final form 31 March 1982

Abstract. The new method of non-contact measurement of linear displacement described in this paper utilises the large changes in the field of a permanent magnet with distance. The output of a magnetic field detector is fed to a microprocessor programmed to display the distance between the magnet and the detector directly. The maximum measurable displacement is limited by the size of the permanent magnet and the noise level of the detector.

In the present version of the instrument, the accuracy is better than 2.0% of full-scale deflection (FSD) over the entire useful range of 250 mm and better than 0.1% FSD for displacements less than 110 mm.

1. Introduction

Combining a magnetometer and permanent magnet to make non-contact measurements of displacement has never been popular because of the inherent non-linearity. Analogue linearisation techniques are not suited to low frequencies (<10 Hz) and digital linearisation has been prohibitively expensive. In addition, magnetic materials with a strong magnetisation, for an adequate signal-to-noise ratio and reasonable magnet volume, have often lacked the stability necessary for use in adverse environments.

The present availability of strong and stable magnetic materials, sensitive magnetometers and low-cost microcomputers makes this technique feasible. The method described makes accurate and continuous non-contact measurements of displacement along a single axis.

2. Principle of operation

A small magnet is attached to the object whose axial displacement is to be measured. The probe of a magnetometer and the magnetic dipole are both permanently aligned with the axis of motion, thereby eliminating any orientational dependence. The voltage output of the magnetometer is passed to an analogue-to-digital converter (ADC) and collected by a microcomputer. Here the effects of unwanted environmental fields are removed, leaving the signal due to the magnet alone. The unknown displacement, up to 250 mm, is then calculated using a pre-recorded calibration table and the result is displayed directly. The hardware and software to be described show how the technique was verified.

3. Hardware

A samarium–cobalt magnet, with a volume of 400 mm^3 and a total moment of 3.1×10^{-7} Wb m, is mounted on a perspex

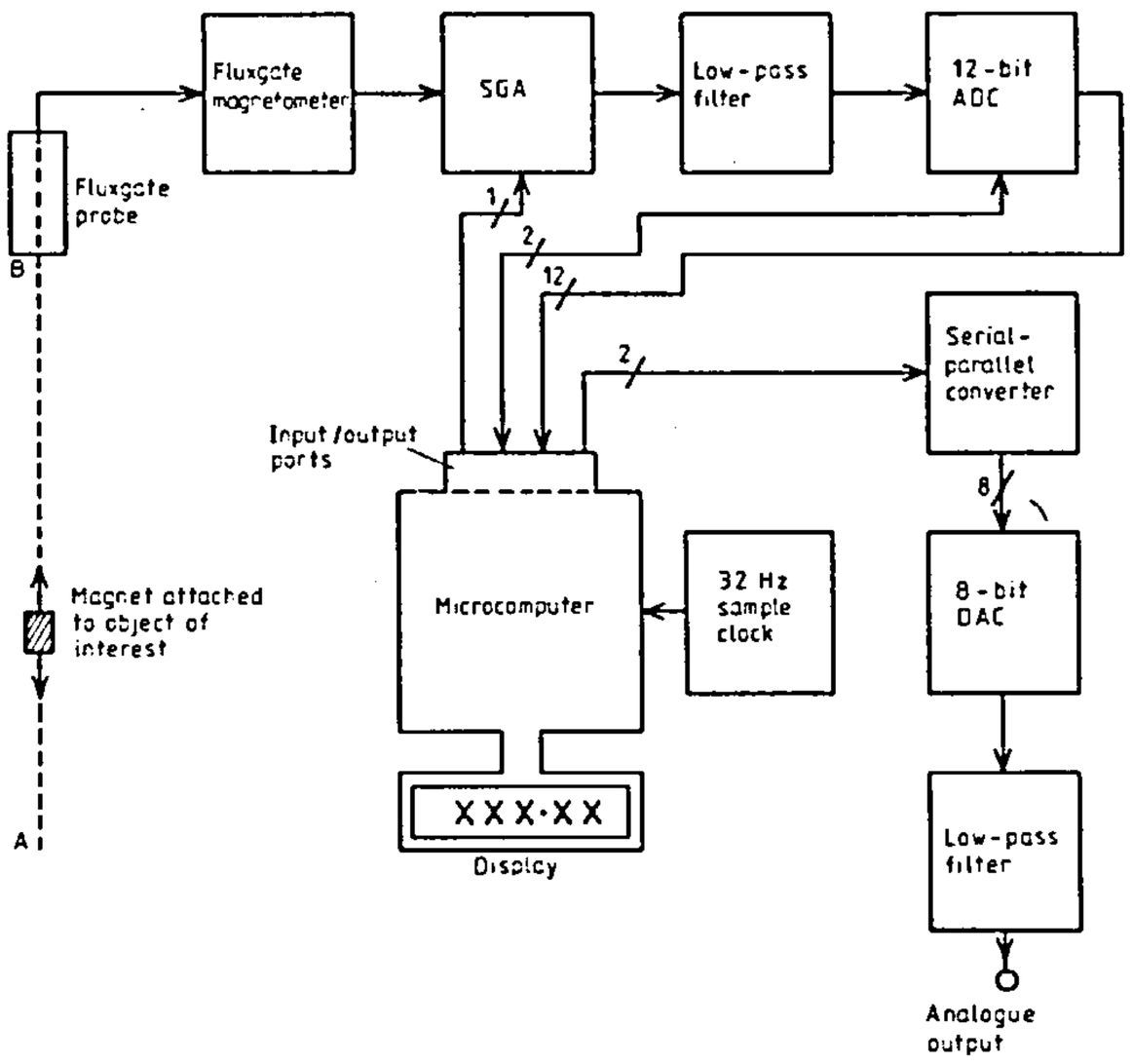

Figure 1. Block diagram of hardware for non-contact measurement of displacement. SGA stands for Switched Gain Amplifier.

0022-3735/82/080843 + 05 $02.00

carriage which moves along AB (see figure 1). The magnetic field sensor is a feedback fluxgate magnetometer that was originally developed for another application. It has a noise level, in its working environment, of 40 nT RMS over a 2 Hz bandwidth. Commercial feedback fluxgate magnetometers are available with, for example, noise levels of 0.3 nT RMS over a 10 Hz bandwidth. In general, feedback magnetometers are much more stable than open-loop types (Primdahl 1979) and this is important in monitoring displacement over long periods.

To improve the dynamic range of the ADC, a switched-gain amplifier (SGA) follows the magnetometer. When the magnet is close to the fluxgate probe, a gain of 2.00 is selected so that the amplifier's output does not overload the ADC. When the magnet is distant, a gain of 16.0 is chosen. This ensures that the quantisation noise does not significantly degrade the weak signal from the magnetometer. The SGA is constructed using CMOS analogue switches to swop the gain-setting resistors about an operational amplifier.

The ADC sampling frequency is 32 Hz, giving an aliasing frequency of 16 Hz (Stearns 1976). Signals above 16 Hz would be folded below it as aliasing noise. The magnetometer has a 3 dB response roll-off at 12 Hz. A sixth-order, low-pass Chebyshev filter, with a passband ripple of 0.5 dB and a 3 dB attenuation at 7.0 Hz (Tietze and Schenk 1978, ch. 3), is effective in suppressing unwanted signal components. The Chebyshev filter's desirable amplitude characteristics outweigh its poor phase performance.

The processed signal from the magnetometer is digitised at the request of the microcomputer. There are two control lines to the ADC. One line passes the order to hold and convert a sample: the other line alerts the microcomputer when conversion is complete, after about 25 μs. The microcomputer then picks up the data available on twelve parallel input lines and performs the relevant calculations.

The new result is sent to an LED display and an analogue output for a chart recorder. The analogue output is updated 32 times per second using data sent out serially by the microcomputer. The data are converted back to a parallel format and passed to an eight-bit digital-to-analogue converter (DAC). The resolution of 255:1 is adequate for most chart recorders; more accurate results can be taken from the display. Strictly, a low-pass reconstruction filter is required to smooth the output samples. In this case, the filter is obviated by the chart recorder's own time constant.

The microcomputer used is the Rockwell AIM-65 equipped with an 8k monitor. The input/output ports are all part of one R6522 versatile interface adapter (VIA). The 32 Hz sample clock, which orchestrates information flow through the instrument, is also included on the VIA as a programmable timer. There should be no problem in using a different microcomputer provided that it can be programmed at the assembler level. A high-level language such as BASIC could be used, but this would be at the expense of the instrument's bandwidth. In terms of short program execution times, a general-purpose, high-level language cannot compete with carefully tailored assembler level routines.

4. Software

A calibration curve of the magnetometer's processed output against the magnet's displacement is stored as a table in the memory. Though the exact coordinates of the curve are known only at a few points along its length, the curve between these points can be recovered by interpolation. Each calibration is specific to the magnet and magnetometer used and so the software incorporates a calibration facility. The hardware and software described will work for any choice of magnetometer and magnet.

Figure 2 shows a simplified flowchart of the program used. First, the VIA is configured to handle the ADC, the DAC and the switched-gain amplifier. One of the VIA's timers is set to continuously generate 32 interrupts per second. No sample can be taken unless this sample clock gives permission via an interrupt.

Subroutine 1 compensates for long-term drifts in the analogue circuitry or changes in the ambient magnetic environment. The subroutine assumes that the magnet is sited at its maximum useful displacement. The analogue gain is automatically set to $\times 16$ and the digitised output of the magnetometer is averaged over 256 samples, or 8 s. This average is compared with the expected output obtained whilst calibrating the instrument. The difference represents a shift in offset and is accounted for in subsequent calculations. The offset pertaining to a gain of $\times 2$ is exactly $\frac{1}{8}$th of the previous result.

The function of subroutine 2, shown in more detail in figure 3, is to find the best amplifier gain and to check that valid measurements can be made. The choice of gain is decided on the basis of the magnetometer's output; thus a weak signal requires a high gain and a strong signal requires a low gain. The high-to-low and low-to-high thresholds are offset to produce hysteresis (see figure 4). This prevents random noise causing repeated

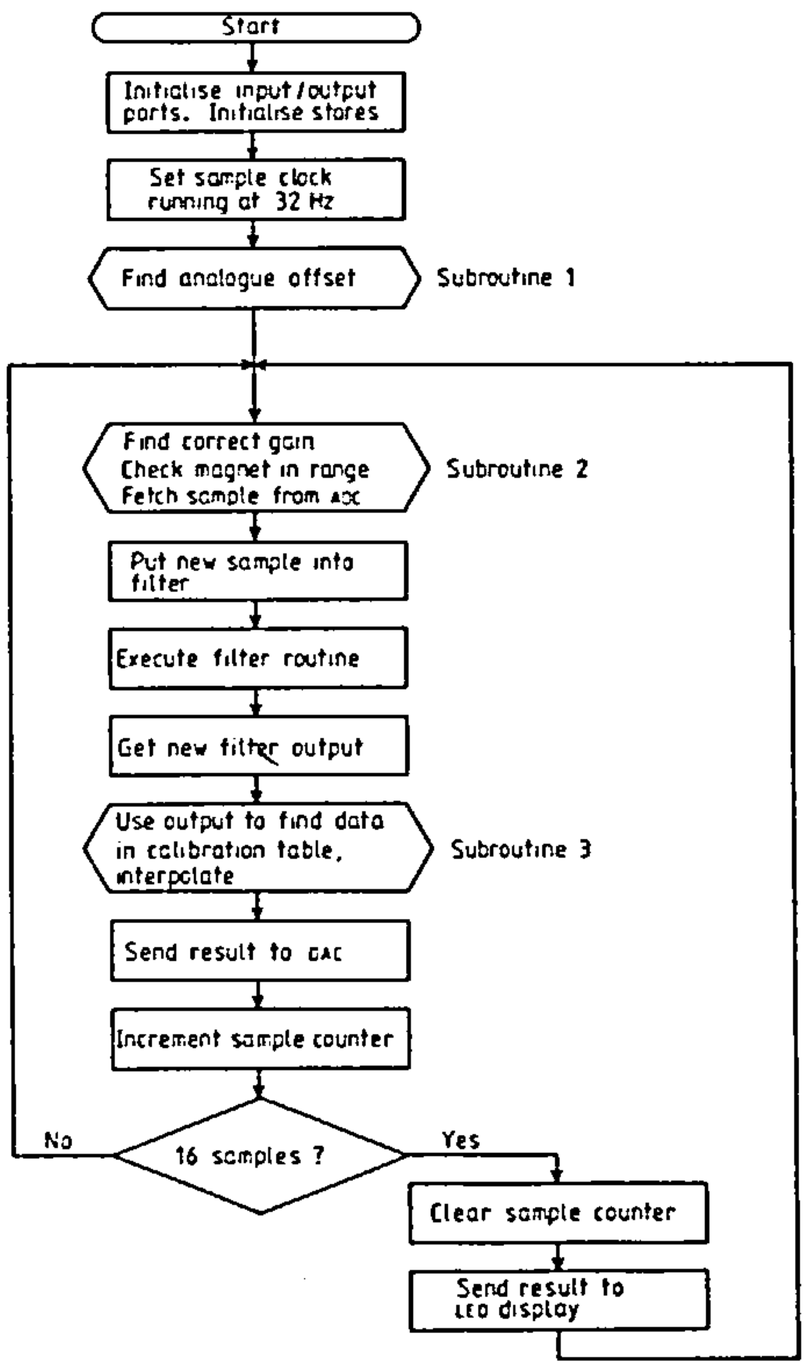

Figure 2. Simplified software flowchart for non-contact measurement of displacement.

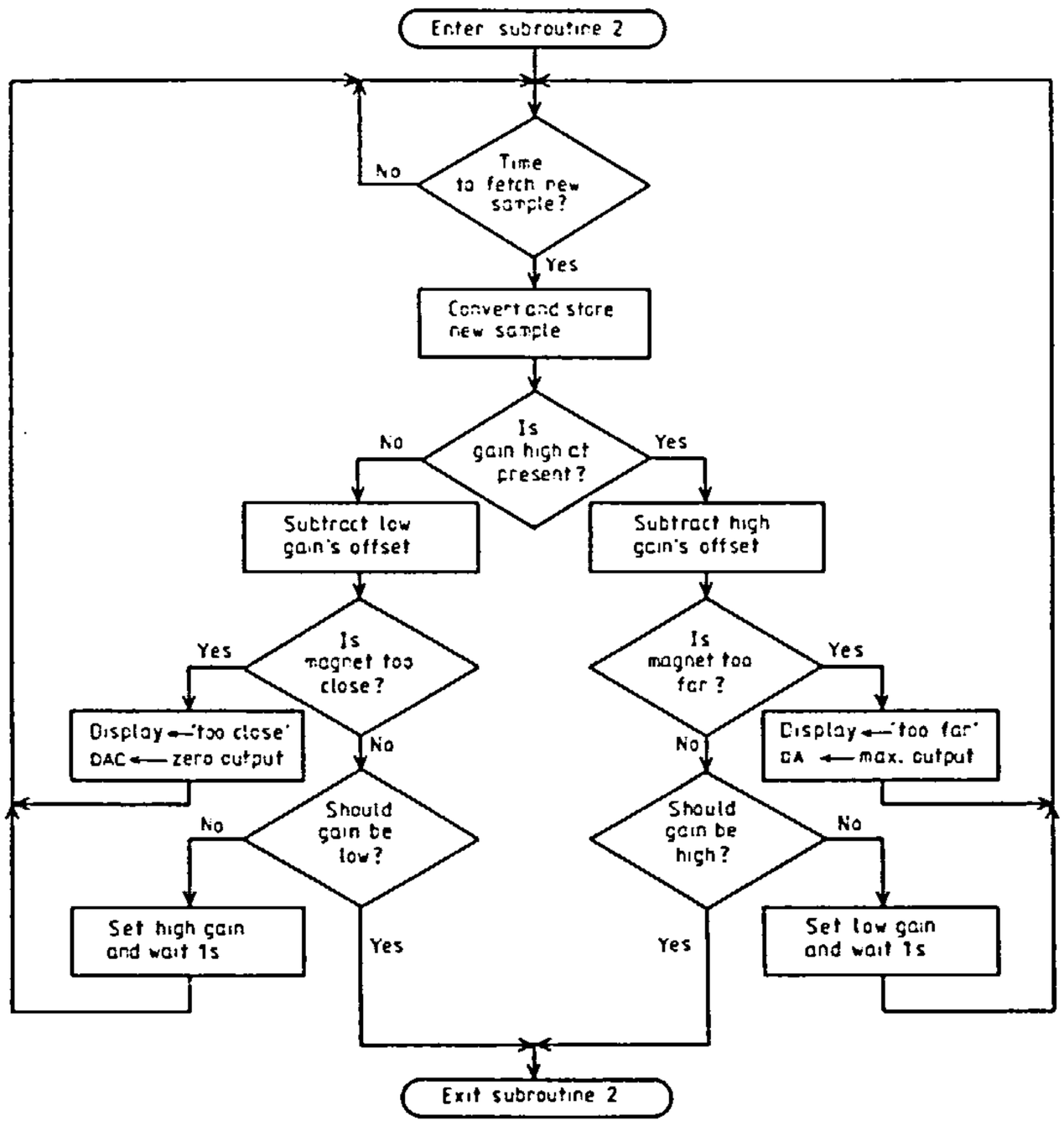

Figure 3. Detailed software flowchart for subroutine 2.

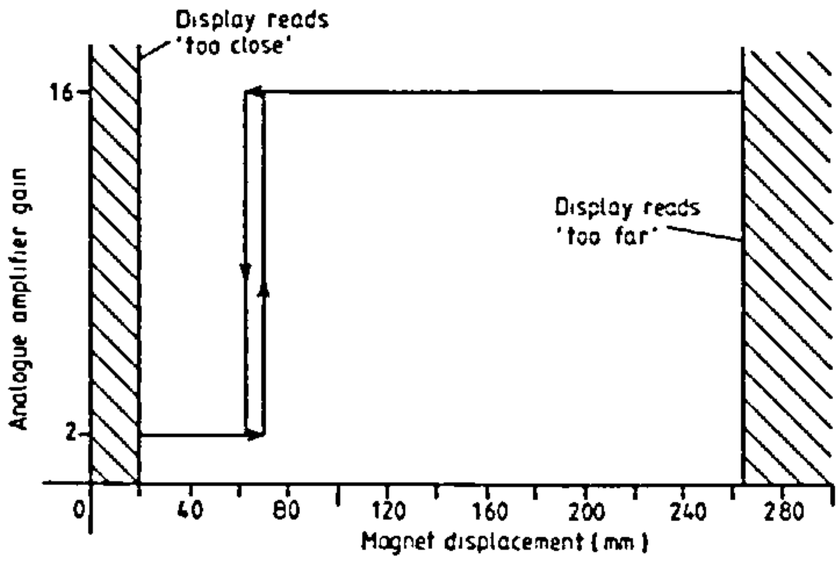

Figure 4. Diagram relating the actions of subroutine 2 to the magnet's displacement.

changes of gain when the magnetometer's output is in the gain transition region. A delay is added to allow the analogue filter to settle after a change of gain. Subroutine 2 checks whether the magnet is in a valid measurement range by seeing if the magnetometer's output is too large or too small. If either of these conditions is detected, the operator is informed accordingly. No measurements will be made until the condition is rectified.

The program now has a valid sample which it places into a 16-bit digital filter. The filter has the amplitude characteristic of a second-order, low-pass Chebyshev filter with 0.5 dB ripple in the passband and an attenuation of 3 dB at 1.0 Hz. It is modelled on its analogue counterpart using the bilinear transform (Tietze and Schenk 1978, ch. 12). The bandwidth of the filter, and hence the instrument, is easily altered by changing the sampling rate.

Subroutine 3 (figure 2) uses the filter output to make a new estimate of displacement. This subroutine first selects either the high-gain or the low-gain calibration table. It calculates an offset into the table chosen and picks out the relevant displacement data. Newton's second-order forward-difference method is used to make the interpolation (Seim 1978). A 16 x 16-bit binary multiply routine is required both here and in the filter above (Peatman 1977).

At the moment, a change in gain presents the digital filter with a voltage step. This is a nuisance because of the filter's poor settling behaviour. More subtly, the magnet velocity that can be successfully followed is greater at large displacements than at small displacements. For a given magnet velocity, the rate of

change of magnetometer output increases dramatically as the displacement decreases; the slew rate of the filter is fixed and is increasingly less able to follow the accelerating change at its input. Both problems could be avoided by placing the filter after subroutine 3 (figure 2). The overriding advantage of the present arrangement is that the filter is used in the same manner when aiding calibration as it is when aiding measurement of displacement.

It only remains to display the new result before recycling. The most significant eight bits of the binary result are sent to the DAC in each cycle. This permits a proper reconstruction of the magnet's motion. The LED display is updated once every 16 cycles, or every half second as each cycle takes $\frac{1}{32}$nd of a second (unless the gain is changed or the magnet is out of range). An algorithm (Peatman 1977) is used to convert the result from binary to binary-coded decimal before it is passed to the display.

The scheme for calibrating the instrument is simple to understand. When the instrument is instructed to start, it immediately checks a switch to see whether the calibration or displacement measurement mode is selected. If the former mode is required, the software simply omits calling subroutines 1, 2 and 3. In place of subroutine 2 it inserts a magnetometer data-fetch instruction that is synchronous with the sample clock. The amplifier gain can be set manually as well as through software. The instrument, acting as a voltmeter with a filter, can now be calibrated easily.

5. Calibration and performance

The magnet, on its guided carriage, ran along the line AB (figure 1) to maximise the magnetometer output for any given displacement. A cathetometer was used to measure the positions of the tip of the fluxgate probe and the edge of the magnet to ± 0.02 mm. The cathetometer was situated 1.5 m from the probe: it did not influence the magnetometer in any measurable way. No special precautions were taken with regard to ambient magnetic noise in the environment.

The instrument was put into the calibration mode and the amplifier gain was set to $\times 16$. The magnet carriage was moved away from the probe until the magnetometer's output was reduced to 128 bits, according to the instrument's display. This probe–magnet separation was noted. It was used in future as a reference displacement for calculating changes in offset through changes in the ambient magnetic field or analogue circuitry drifts. The magnet was next moved towards the probe until the display read 256 bits and again the displacement was noted. This process was repeated in steps of 128 bits, thereby forming a list of 32 displacements ($128 \times 32 = 2^{12}$ bits) for the high-gain calibration table. The gain was then switched to $\times 2$ and, starting from 128 bits, another 32 displacements were obtained to form the low-gain calibration table. Both tables were converted into 16-bit binary code and stored in the microcomputer's memory. The calibration error worsened at large displacements because of the reduction in the magnetometer's signal-to-noise ratio. The limited resolution of the cathetometer became a significant calibration error at small displacements.

It was now possible to find how accurately the instrument measured displacement. Using the cathetometer, the magnet was set at a series of known displacements. In each case, the microcomputer's display was noted and the instrument's error was found. Figure 5 is a plot of the non-contact measurement error against magnet displacement. The error is shown as a percentage of the true displacement set with the cathetometer. The uncertainty in the 'true' displacement was ± 0.04 mm, and this is represented by the broken curves above and below the displacement axis.

At larger displacements of about 200 mm, the interpolation

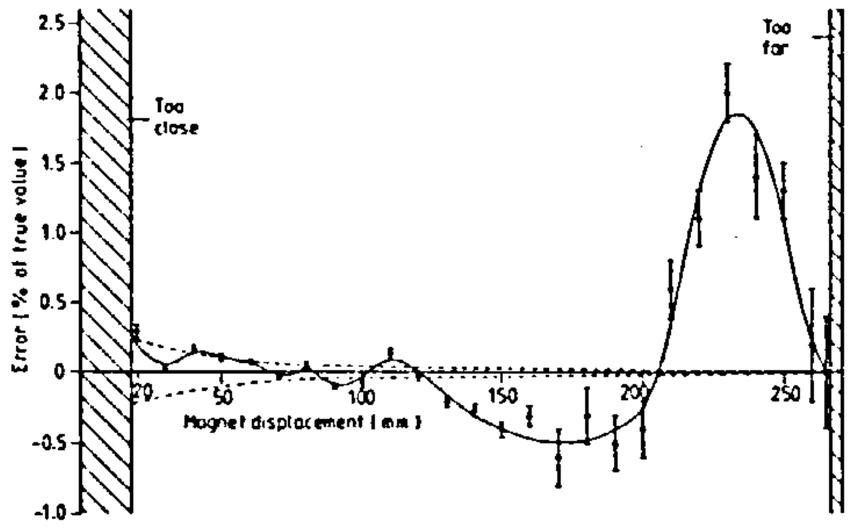

Figure 5. A plot of non-contact measurement error against magnet displacement. The broken curves show the bounds of uncertainty in the true value of the displacement.

error was dominant. This error could have been reduced using closer spaced entries in the high-gain calibration table. The ultimate limit to the reduction of interpolation error was the quantisation error of the ADC. At the maximum displacement of 266 mm, a change of one least significant bit corresponded to 0.7 mm or 0.26% of 266 mm. At the minimum displacement of 18 mm, a change of one least significant bit corresponded to 4.5 μm or 0.025% of 18 mm. The quantisation error was always less important than the random noise when the gain was $\times 16$. The error bars on the plot show the effects of the random noise level compared with the interpolation error. Random noise errors, like interpolation errors, shrank in significance as the displacement decreased.

At smaller displacements, about 40 mm, the errors in the method used to test performance were most important. The method exaggerated an underlying increase in calibration error that was itself caused by limited cathetometer resolution.

It is normal to quote performance in terms of the full-scale deflection (FSD). The minimum measurable displacement was 18 mm and the maximum measurable displacement was 266 mm, giving a full-scale deflection of 248 mm. This instrument had an accuracy of better than 2.0% FSD over the whole working range and better than 0.1% FSD over the range 18–130 mm. In the range 18–80 mm, the measured performance was better than 0.02% FSD.

The maximum execution time of a software cycle was 29 ms (see figure 2): the sampling rate of 32 Hz was therefore reasonable. A cycle that excluded sending a result to the display took 4.7 ms. Subroutines resident in the AIM-65's monitor took 23 ms to display a new binary-coded decimal result. It was assumed that these subroutines were efficiently written and so no attempt was made to improve on them. Clearly, a special-purpose display could increase the maximum possible sampling rate dramatically.

6. Applications and improvements

The only link between the sensor and the object whose displacement is to be found is a magnetic field. The method is therefore ideally suited for experimental situations where a displacement or thickness is to be measured or monitored without the use of optical instruments, variable capacitance or reluctance techniques, ultrasonics, x-rays or radioactive sources. DC magnetic fields pass unattenuated through copper, lead, aluminium, glass, flesh and many other materials.

A new method of non-contact measurement of linear displacement

The effects of undesirable AC and DC magnetic fields in the environment can be minimised using a differential fluxgate magnetometer which would only respond to changes in the local field gradient. This makes it worthwhile employing a more sensitive magnetometer, allowing an increase in working range and a decrease in magnet volume.

The dynamic range of a 16-bit ADC would make the switched-gain amplifier redundant. This would eliminate the annoying delays necessary when changing gains. It would also reduce quantisation error.

Improved calibration would guarantee a better performance at small displacements. A better approach to interpolation and closer spaced calibration table entries would improve performance at large displacements.

It is intended to construct a software-compatible, purpose designed microcomputer system in which the ADC, DAC and display decoder/driver will be connected directly to the system's bus. This will allow a maximum sampling rate of 200 Hz. It will then be realistic to improve the phase characteristics of the analogue and digital filters so that motion of the magnet can be followed with a minimum of distortion.

Acknowledgment

One of us (MPC) is indebted to the NERC for its financial support.

References

Peatman J B 1977 *Microcomputer Based Design* (New York: McGraw-Hill) pp 401–5, 416–20

Primdahl F 1979 The fluxgate magnetometer *J. Phys. E: Sci. Instrum.* **12** 241–53

Seim T A 1978 Numerical interpolation for microprocessor based systems *Computer Design* February 111–6

Stearns S D 1976 *Digital Signal Analysis* (New Jersey: Hayden) pp 36–73

Tietze U and Schenk Ch 1978 *Advanced Electronic Circuits* (Berlin: Springer) pp 76–111, 373–93

REFERENCES

1. Bleaney, B.I. and Bleaney, B., 1976; " Electricity and magnetism", O.U.P., 3rd edition.
2. Collinson, D., 1982; "Methods in rock magnetism and palaeomagnetism, techniques and instrumentation", Chapman and Hall (London).
3. Chikazumi, S., 1978; "Physics of magnetism", Robert E. Krieger (New York).
4. Craik, D.J., 1971; "The structure and properties of magnetic materials", Pion (London).
5. Stacey, F.D. and Banerjee, S.K., 1974; "The physical principles of rock magnetism", Elsevier Scientific Publishing Company (Amsterdam).
6. Stephenson, A., 1971; "Single domain grain distributions. 1. A method for the determination of single domain grain distributions"; Phys. Earth Planet. Int., 4, pp. 353-360.
7. Day, R., Fuller, M. and Schmidt, V.A., 1977; "Hysterysis properties of titanomagnetites: grain size and compositional dependence", Phys. Earth Planet. Int ., 13, pp. 260-267.
8. Smit, J. and Wijn, H.P.J., 1959; "Ferrites", Philips Technical Library.
9. Parasnis, D.S., 1979; " Principles of applied geophysics", Chapman and Hall (London), 3rd Edition.
10. Anderson, J.C., 1968; "Magnetism and magnetic materials", Chapman and Hall (London).
11. Galt, J.K., 1952; "Motion of a ferromagnetic domain wall in Fe_3O_4", Phys. Rev., 85, pp. 664-669.
12. Galt, J.K., 1957; Losses in ferrites: single crystal studies", Proc. IEE (London), 104B, pp. 189-197.
13. Stephenson, A., 1971; "Single domain grain distributions. 2. The distribution of single domain iron grains in Apollo II Lunar dust", Phys. Earth Planet. Int., 4, pp. 361 -369.
14. Neubert, H.K.P., 1975; " Instrument transducers, an introduction to their performance and design", O.U.P., 1975.

15. Pollack, D., 1937; "The design of inductances for frequencies between 4 and 25 Mc/s", Trans. AIEE, 56, pp. 1169-1176.

16. Becker A. and Collett, L.S., 1978; "Magnetic losses in lunar materials", Earth Planet. Sci. Lett., 41, pp. 139-142.

17. Stephenson, A. and de Sa, A., 1969; "A simple method for the measurement of the temperature variation of initial magnetic susceptibility between 77 and 1000 K", J. Phys. E: Sci. Inst., 3, pp. 59-61.

18. Markert, H., Trissl, K.-H. and Zimmerman, G.J., 1974; "On a high frequency method for the measurement of susceptibilities and hysterysis losses of rocks and minerals between nitrogen temperature and 700°C", J. Geophys., 40, pp. 303-328.

19. Petersen, N., 1967; " A high frequency method for the measurement of Curie temperatures of ferrimagnetic materials", in "Methods in palaeomagnetism", eds. Collinson, D.W., Creer, K.M. and Runcorn, S.K., Elsevier (Amsterdam), pp. 445-6.

20. Rollin, B.V., 1946; Nature, 158, pp.669-670.

21. Donally, B. and Sanders, T.M., 1960; "Simple transistor marginal oscillator for magnetic resonance", Rev. Sci. Inst., 31, 9, pp. 977-978.

22. Pound, R.V. and Knight, W.D., 1950; Rev. Sci. Inst., 31, 9, pp. 977-978.

23. Robinson, F.N.H., 1959; "Nuclear resonance absorption circuit", J. Sci. Instrum., 36, pp. 481-487.

24. Faulkner, E.A. and Holman, A., 1967; "An improved circuit for nuclear magnetic resonance detection", J. Sci. Instrum., 44, 391-392.

25. de Sa, A., 1968; "A radio frequency method for determining Curie point temperatures", J. Phys. E: Sci. Instrum., 1, pp. 1136-1137.

26. Riedi, P.C., 1973; "An automatic radio frequency method for determining Curie point temperatures", J. Phys. E: Sci. Instrum., 6, pp. 1172-1174.

27. Terman, F.E., 1955; "Radio and electronic engineering", McGraw-Hill (New York).

28. Wind, R.A., 1970; "The sensitivities of fine transistorised nuclear magnetic resonance spectrometers", J. Phys. E: Sci. Instrum., 3, pp. 31-35.

29. Robinson, F.N.H., 1982; "A sensitive nuclear quadrupole resonance spectrometer for 2-60 MHz", J. Phys. E: Sci. Instrum., 15, pp. 814-823.

30. Lee, J. and Ho Choh, S., 1982; "Robinson type nuclear quadrupole resonance spectrometer adapted to field effect transistors", Rev. Sci. Instrum., 53, 2, pp. 232-235.

31. Hughes, D.G. and Smith, M.R., 1971; "On the nuclear magnetic resonance detection characteristics of marginal and Robinson oscillators", J. Phys. E: Sci. Instrum., 4, pp. 13-20.

32. Strauss, L., 1970; "Wave generation and shaping", McGraw - Hill Kogakusha (Tokyo), 2nd edition.

33. Cooke, M.P. and de Sa, A., 1981; "A radio frequency method for the measurement of initial magnetic susceptibility", J. Phys. E: Sci. Instrum., 14, pp. 1192-1196.

34. Jones, B.E., 1979; "Feedback in instruments and its applications", J. Phys. E: Sci. Instrum., 12, pp. 145-158.

35. Shinners, S.M., 1978; "Modern control system theory and its application", Addison-Wesley, (Reading, Mass.), 2nd edition.

36. Harris, H.E., 1951; "Simplified Q multiplier", Electronics, May, pp. 130-134.

37. Sze, S.M., 1981; "The physics of semiconductor devices", Wiley (New York), 2nd edition.

38. Mullard, 1979; "Applications of field effect transistors", Technical note 86, Mullard Ltd. (London).

39. Watson, J., 1978; "Semiconductor circuit design", Adam Hilger (Bristol) 3rd edition.

40. Nagata, T., 1967; "Identification of magnetic minerals in rocks using methods based on their magnetic properties", in "Methods in palaeomagnetism", eds. Collinson, D.W., Creer, K.M. and Runcorn, S.K., Elsevier (Amsterdam), pp. 501-513.

41. de Sa, A., 1981; "Fixed frequency f-2f signal source with phase shift", New Electronics, August, pp. 17-18.

42. Egan, W.F., 1981; "Frequency synthesis by phase lock", Wiley (New York)

43. Gardner, F.M., 1979; "Phaselock techniques", Wiley (New York), 2nd edition.

44. Blair, D.P. and Sydenham, P.H., 1975; "Phase sensitive detection as a means to recover signals buried in noise", J. Phys. E: Sci. Inst., 8, pp. 621-627.

45. Meade, M.L., 1982; "Advances in lock in amplifiers", J. Phys. E: Sci. Instrum., 15, pp. 395-403.

46. Robinson, F.N.H., 1974; "Noise and fluctuations", Clarendon Press (Oxford).

47. Boyle, A.G., 1940; "The effective inductance and resistance of screened coils", JIEE (Wireless Soc.), 15, pp. 299-316.

48. Frerking, M.E., 1978; " Crystal oscillator design and temperature compensation", Van Nostrand Rheinhold (New York).

49. Tietze, U. and Schenk, Ch., 1978; "Advanced electronic circuits", Springer - Verlag (Berlin).

50. Morrison, R., 1977; "Grounding and shielding techniques in instrumentation", Wiley (New York), 2nd edition.

51. Comer, D.J., 1976; "Modern electronic circuit design", Addison-Wesley (Reading, Mass.).

52. Caplan, L.C. and Stern, R., 1971; "An inexpensive lock in amplifier, Rev. Sci. Instrum., 42, 5, pp. 689-695.

53. Creer, K.M. and de Sa, A., 1970; "An automatic translation balance for recording variation of magnetization", J. Phys. E: Sci. Inst., 3, pp. 74-75.

54. Radhakrishnamurty, C. and Likhite, S.D., 1970; "Hopkinson effect, blocking temperature and Curie point in basalts", Earth Planet. Sci. Lett., 7, pp. 389-395.

55. Dunlop, D.J., 1974; "Thermal enhancement of magnetic susceptibility", J. Geophys., 40, pp. 439-451.

56. Dunlop, D.J., 1981; "The rock magnetism of fine particles", Phys, Earth Planet. Int., 26, pp. 1-26.

57. Tyler, F., 1931; "The magnetization-temperature curves of iron, cobalt and nickel", Phil. Mag., 11, p. 596-602.

58. El-Hanary, U., 1973; "A Q-meter method for measuring the grain size and resistivity temperature dependence of metallic powders", Rev. Sci. Instrum., 44, 8, pp. 1067-1068.

59. 1962; "Handbook of chemistry and physics", The Chemical and Rubber Company, 47th edition.

60. Creer, K.M., 1967; "Rock magnetic investigations at low temperatures", in "Methods in palaeomagnetism", eds. Collinson, D.W., Creer, K.M. and Runcorn, S.K., Elsevier (Amsterdam), pp. 514-528.

61. Schwartz, M. and Shaw, L., 1981; "Signal processing: discrete spectral analysis, detection and estimation", McGraw-Hill (New York).

62. Lynn, P.A., 1979; "An introduction to the analysis and processing of signals", MacMillan (London).

63. Stearns, S.D., 1975; "Digital signal analysis", Hayden Book Company (New Jersey).

64. Wieder, H.H., 1971; "Hall generators and magnetoresistors", Pion Ltd. (London).

65. Cooke, M.P. and de Sa, A., 1982; "A new method of non-contact measurement of linear displacement", J. Phys. E: Sci. Inst., 15, pp. 843-847.

66. Garratt, J.D., 1979; "Survey of displacement transducers below 50 mm", J. Phys. E: Sci. Inst., 12, pp. 563-573.

67. Sydenham, P.H., 1980; "Transducers in measurements and control", Adam Hilger Ltd (Bristol).

68. Hugill, A.L. 1982; "Displacement transducers based on reactive sensors in transformer ratio bridge circuits", J. Phys. E: Sci. Inst., 15, pp. 597-606.

69. Mehrdadi, B., Kaghazchi, B. and Beck, M.S., 1982; "Non-contacting level measurement of irregular surfaces using coded ultrasound and cross correlation analysis", J. Phys. E: Sci. Inst., 15, pp. 367-372.

70. Magnetic Developments Ltd; "Samarium cobalt magnet data and applications", Unit 7, Headlands Road, Swindon.

71. Vacuumschmelze data sheet M040; "Vacomax permanent magnets", Telcon Metals Ltd., Manor Royal, Crawley, Sussex.

72. Stuart, W.F., 1972; "Earth's field magnetometry", Rep. Progr. Phys., 35, pp.803-81.

73. Wilson, B and Jones, B.E., 1982; "Feed-forward temperature compensation for Hall effect devices", J. Phys. E: Sci. Inst., 15, pp. 364-366.

74. Primdahl, F., 1979; "The fluxgate magnetometer", J. Phys. E: Sci. Inst., 12, pp. 241-253.

75. Swithenby, S.J., 1980; "SQUIDS and their applications to the measurement of weak magnetic fields", J. Phys. E: Sci. Inst., 13, pp.801-813.

76. Kelvin Hughes publication KH3050/G0; "Fluxgate elements", New North Road, Hainault, Ilford, Essex.

77. Domain Micro-Systems Ltd., Stafford Street, Stafford, ST16 2BP.

78. Control Universal Ltd., 11-15 Bush House, Bush Fair, Harlow, Essex.

79. Analogue Devices, 1980; "Data acquisition components and subsystems", Central Avenue, East Molesey, Surrey.

80. Intersil, 1980; "ICM 7211 (LCD), ICM 7212 (LED) four digit CMOS display decoder/drivers", Farnell Technical Data Service, Canal Road, Leeds.

81. National Semiconductor, 1980; "Linear databook", Farnell Technical Data Service, Canal Road, Leeds.

82. Klingman, E.E., 1977; "Microprocessor systems design", Prentice-Hall (New Jersey).

83. Leventhal, L.A., 1976; "Introduction to microprocessors; software, hardware, programming", Prentice-Hall (New Jersey).

84. Peatman, J.B., 1977; "Microcomputer based design", McGraw-Hill (New York).

85. Kreysig, E., 1979; "Advanced engineering mathematics", Wiley (New York), 4th edition.

86. Scheid, F., 1968; "Theory and problems of numerical analysis", Schaum's Outline Series, McGraw-Hill (New York).

87. Seim, T.A., 1978; "Numerical interpolation for microprocessor based systems", Computer Design, February, pp. 111-116.

88. Bozic, S.M., 1979; "Digital and Kalman filtering", Edward Arnold (London).

89. Grimbleby, J.B., 1980; "Averaging filter circuits for signal recovery applications", J. Phys. E: Sci. Inst., 13, pp. 557-561.

90. Sorenson, H.W., 1970; "Least squares estimation: from Gauss to Kalman", IEEE Spectrum, 7, pp. 63-68 .